



FACULTY
OF MATHEMATICS
AND PHYSICS
Charles University

HABILITATION THESIS

Josef Stráský

**Advanced Titanium Alloys
for Medical Applications**

Prague 2020

Josef Stráský

Advanced Titanium Alloys for Medical Applications

Habilitation Thesis

Prague 2020

Charles University

Faculty of Mathematics and Physics

Department of Physics of Materials

Ke Karlovu 5

121 16 Praha 2

Czech Republic

Content

1. Structure of the thesis	1
2. Introduction	2
2.1. Titanium and classification of titanium alloys	2
2.2. Phase transformations in metastable β -Ti alloys	3
2.3. Strengthening mechanisms in Ti alloys	4
2.4. Titanium as an implant material	6
2.5. Ultra-fine grained Ti alloys	7
3. Development of Ti-Nb-Ta-Zr-O biomedical alloys	9
4. Ultra-fine grained Ti alloys for biomedical use.....	16
5. Conclusion and outlook	21
6. Reprints of included publications	27

Acknowledgement

I would like to thank prof. Miloš Janeček for bolstering my scientific career and letting me write on my own several hundreds of pages of manuscripts, chapters, grant applications and grant reports within last ten years. I acknowledge my colleague Petr Hrcuba for plenty of experimental work he did and for never-ending fruitful discussions. I acknowledge Jana Šmilauerová and Hanuš Seiner for their kind help with writing this thesis. I would like to thank my hard-working students: Jiří Kozlík, Dalibor Preisler, Anna Veverková and Kristína Bartha who work for their own benefits, but also significantly contributed to this thesis. Above all I would like to express my appreciation to my wife Jitka for a thorough support.

1. Structure of the thesis

This habilitation thesis presents the main achievements of my research at the Department of Physics of Materials during the years 2014 – 2020. My scientific activities focused mainly on the development of titanium-based materials for medical applications. The range of research spans from theoretical considerations and experimental characterization to applied research projects aiming to achieve commercially utilizable materials. I conducted a significant part of this investigation, but a successful research in such a complex topic requires a team consisting of members with different abilities, experiences and interests. Such team at the Department of Physics of Materials made this thesis possible.

The habilitation thesis is a compilation of previously published works. However, the structure of the thesis is affected by the fact that recently I was invited and had the privilege to publish two chapters in the monograph *Titanium in medical and dental applications* published by Woodhead Publishing, Elsevier. Each of these two chapters introduced the topic, reviewed existing literature and presented some of our own experimental results. Based on these two chapters, which are included in this habilitation thesis, the scientific content of the thesis can be divided into two following parts:

- 1) *Development of Ti-Nb-Ta-Zr-O biomedical alloys*
- 2) *Ultra-fine grained Ti alloys for biomedical use*

How to read this thesis

Chapter 2 *Introduction* aims on introducing the reader to the topic of titanium alloys with the focus on medical applications. The text of this chapter is partly based on the introduction to the diploma thesis of my former PhD student Kristina Bartha: *Microstructure and mechanical properties of ultra-fine grained titanium alloys*.

Chapter 3 *Development of Ti-Nb-Ta-Zr-O biomedical alloys* first briefly introduces this research topic. More detailed scientific overview is included in the chapter *Biocompatible beta-Ti alloys with enhanced strength due to increased oxygen content* from the monograph *Titanium in medical and dental applications*, which is reprinted in this thesis. The chapter 3 continues with a list of published papers and their annotations. At the end of this chapter, some interesting, yet unpublished, results are presented.

Chapter 4 *Ultra-fine grained Ti alloys for biomedical use* has a similar structure to the previous chapter. After a brief overview, the reader is referred to the chapter *Microstructure and lattice defects in ultrafine grained biomedical $\alpha+\beta$ and metastable β Ti alloys* from the monograph *Titanium in medical and dental applications*, which is attached to this thesis. The description of 7 published papers follows. At the end of this chapter, some unpublished results are presented.

Chapter 5 *Conclusion and outlook* summarizes the thesis and describes current activities of myself and my research team in the field of titanium alloys.

2. Introduction

2.1. Titanium and classification of titanium alloys

Titanium was discovered by the English chemist William Gregor in 1791 in the mineral ilmenite (FeTiO_3). In 1795 it was named after the Titans due to its resistance to be isolated as a pure metal. Titanium is a transition metal and as a chemical element with the atomic number of 22 it belongs to the Group 4 of the periodic table of elements [Lutjering2007].

Titanium and its alloys are of great interest due to their outstanding properties such as high specific strength and excellent corrosion resistance. Titanium is not a noble metal, but it owes its corrosion resistance to a passivation layer, consisting mainly of TiO_2 , which is formed virtually immediately on the exposed surface and is stable at high temperatures and in many chemically aggressive environments [Welsch1993].

Aircraft industry comprises the biggest market for titanium alloys. Other applications include architecture, jewellery, sport goods and, most importantly for this thesis, medicine [Geetha2009].

Under different conditions, titanium can exist in different crystal structures, which are referred to as allotropic modifications. Above so-called β -transus temperature (882°C), the structure of the material is the body-centered cubic (bcc) which is referred to as β phase. Upon cooling, the material transforms to the hexagonal close-packed (hcp) structure referred to as α phase. Nevertheless, the stability ranges of the α and β phases can be affected by additions of alloying elements as schematically shown in Figure 1. The β -transus temperature can be shifted by alloying, and a two phase region $\alpha + \beta$ is introduced. The β stabilizing elements decrease the β -transus temperature and shift the β -phase field towards lower temperatures. The β stabilizing elements are divided to β -isomorphous and β -eutectoid. Sufficient amount of the β -isomorphous elements can stabilize β phase at room temperature, while the β -eutectoid elements can form a stable intermetallic compound. However, the intermetallic compound usually forms only at elevated temperatures and after a long time and, in many alloys containing β -eutectoid elements, it can be avoided completely [Smilauerova2017].

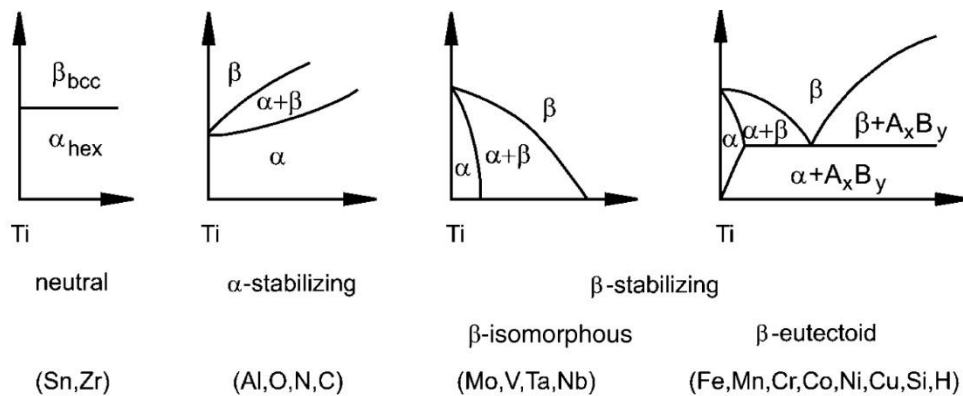


Figure 1. Effect of alloying elements on phase composition of titanium alloys (schematically) [Lutjering2007]

The schematic phase diagram depicted in Figure 2 shows qualitatively the effect of the content of the β -stabilizing elements (horizontal axis) and temperature (vertical axis) on the phase composition. Equilibrium phase diagram is shown by the solid black curves, while the dashed red curve shows a martensite start (M_s) temperature corresponding to the beginning of a $\beta \rightarrow \alpha''$ phase transformation. α'' is an orthorhombic martensite phase [Davis1979]. The martensite start temperature decreases with increasing content of β -stabilizers.

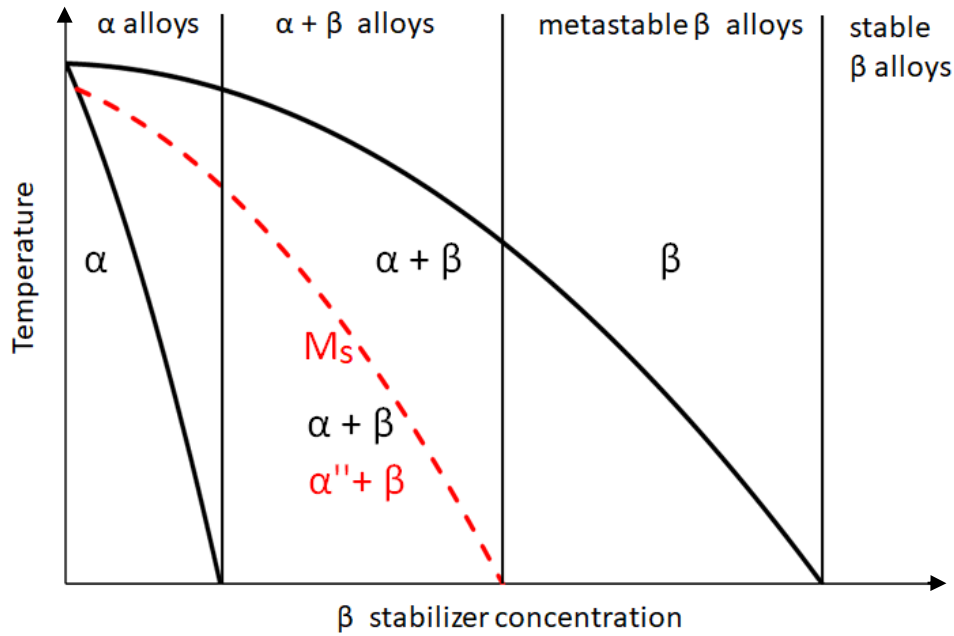


Figure 2. Pseudo-binary β isomorphous phase diagram (schematically)

Based on this phase diagram, titanium alloys are divided into four classes according to their phase composition at room temperature. α phase is the only stable phase at room temperature for pure titanium and α alloys. Increasing content of the β -stabilizing element(s) stabilizes some amount of β phase at room temperature which is characteristic for $\alpha + \beta$ alloys. When the martensite start temperature is lowered below the room temperature, the formation of α phase and martensitic α'' phase can be fully suppressed. Such alloys are called metastable β -Ti alloys and currently represent the most studied group of Ti alloys. Finally, a Ti alloy can be β stabilized to such extent that β phase is thermodynamically stable at ambient temperature, and the alloy is referred to as the stable β -Ti alloy.

2.2. Phase transformations in metastable β -Ti alloys

Apart from above mentioned stable α and β phases, many unstable and metastable phases were found in titanium alloys. Many titanium alloys in commercial practice are intentionally used in a metastable condition (metastable phase composition).

The majority of the results presented in this thesis concerns metastable β -Ti alloys. Metastable β -Ti alloys, by definition, do not contain α , α' , or α'' phase after quenching from a temperature above the β -transus temperature of the particular alloy (typically around 700 – 800 °C) – this condition is referred to as beta solution treated condition.

After quenching, ω phase can be formed in some metastable β -Ti alloys by a diffusionless displacive transformation (ω athermal phase). ω phase can be also formed via diffusion-assisted process at temperatures 200 – 550 °C depending on the alloy composition (ω isothermal phase). This phase has been thoroughly studied in numerous reports [DeFontaine1971, Devaraj2009]. A comprehensive discussion can be found in the PhD thesis by J. Šmilauerová [Smilauerova2016]. For the purpose of the present thesis, it must be stressed that ω phase causes a significant increase of elastic modulus [Tang2000].

Controlled precipitation of incoherent α phase particles in the β matrix is the major strengthening mechanism in metastable β -Ti alloys and has been thoroughly studied by numerous researchers since 1960s. The nucleation of the α phase occurs heterogeneously at preferential sites - including grain and subgrain boundaries, dislocations and other types of lattice defects [Makino1996, Ivasishin2005].

In diffusion controlled transformations, such as precipitation of α phase particles in the β matrix, the formation of a new phase is accompanied by a change of composition, which is controlled by diffusion. At high cooling rates, diffusion fails to accomplish required compositional changes and phase transformations are generally suppressed. However, with increasing under-cooling, the driving forces for the transformation increase considerably and the crystal structure may change spontaneously without a change in chemical composition. These transformations are referred to as martensitic. Martensitic transformations involve organized movement (shift) of atoms from their initial positions in the crystal lattice into new positions creating a new crystal structure. The martensitic transformation is athermal, i.e. time-independent at a given temperature. The transformation initiates below M_s (martensite start) temperature, and the material is fully transformed below M_f (martensite finish) temperature [Gottstein2004]. Two main martensite phases occurring in titanium alloys are hexagonal α' phase and orthorhombic α'' (alpha double prime). α'' can be formed martensitically upon quenching in alloys with composition near the borderline between $\alpha + \beta$ and metastable β -Ti alloys [Kharia2001, Elmay2013]. M_s temperature of the α'' phase formation is schematically shown in Figure 2 by a red dashed line. Martensite can be also formed with the aid of stress which causes organized mutual movement of atomic planes (stress induced martensite - SIM) [Orgeas1998]. α'' martensitic phase might be formed by mechanical loading in some metastable β -Ti alloys [Koul1970], which results in pseudo-elasticity and shape memory effect [Kim2007, Kent2010].

2.3. Strengthening mechanisms in Ti alloys

Plastic deformation in metals is promoted predominantly by dislocation movement. Shear stress necessary for activation of the dislocation slip (Peierls stress τ_p) in a defect-free single-crystal is surprisingly low, and strategies for material strengthening must be employed in order to achieve commercially viable properties.

Deformation strengthening is a basic strengthening mechanism and is utilized in materials prepared by severe plastic deformation (SPD) methods described below. Strength of a polycrystalline material is also increased by grain boundaries. This strengthening effect is related to the mean grain size d via Hall – Petch relationship [Hall1951, Petch1953]:

$$\sigma_y = \sigma_0 + k_y d^{-1/2}, \quad (1)$$

where σ_y is the yield stress of the material, σ_0 represents the friction stress, k_y is a material constant and d is the mean size of grains. Increasing strength via grain refinement is the main motivation for the development and production of so-called ultra-fine grained (UFG) materials [Valiev1993].

In alloys, solute atoms interact with dislocations and increase the stress required for dislocation movement. The absolute increase of the mechanical strength strongly depends on the strength of the obstacle – for instance on the type of solute atom. Moreover, the strengthening effect is significantly enhanced if solute atoms impose large anisotropic distortions.

It must be recalled that β -Ti alloys studied in this thesis have bcc structure and that interstitial strengthening by oxygen is of our primary interest. Oxygen atoms (along with carbon and nitrogen atoms) are interstitial atoms and considered as “heavy” interstitials (contrary to hydrogen or helium atoms). Interstitial oxygen atoms induce anisotropic elastic dipoles with tetragonal symmetry in bcc materials [Savino1981], because an interstitial atom in an octahedral void is closer to the pair of its neighbours and causes a significant asymmetric tetragonal distortion of the lattice. The effect of tetragonal distortions on hardening was described in a seminal paper by Fleischer [Fleischer1962]. The distortion increases the interaction of the interstitial atom with both edge and screw dislocations and promotes strengthening significantly. As a result, strengthening by interstitial atoms is more effective in bcc alloys than, for instance, in face-centered cubic (fcc) materials, where the lattice distortion is more isotropic [Cochardt1955].

Interstitial strengthening by increased oxygen content is used in commercially pure Ti (i.e. in hcp α phase). This type of strengthening is very efficient as recently explained in [Yu2015]. So-called commercially pure titanium (CP Ti) may contain up to 0.4 wt. % of oxygen, which guarantees its strength of 550 MPa. Titanium with higher oxygen content becomes brittle [Welsch1993]. Interstitial hardening by oxygen atoms also affects the strength and the ductility of Ti alloys. In $\alpha + \beta$ alloys or metastable β -Ti alloys, maximum allowed oxygen content is limited typically to 0.2 wt % [Welsch1993]. Interstitial strengthening by oxygen is also efficient in bcc structure of β alloys as explained above. Moreover, ductility of some β alloys is preserved even for oxygen content exceeding 0.5 wt % [Qazi2004].

In metastable β -Ti alloys used in the commercial practice, the most used strengthening mechanism is the controlled precipitation of homogeneously distributed α phase particles [Lutjering2007]. α phase precipitation is usually achieved via elaborated thermal or thermomechanical treatment [Zheng2016]. One of the topics of this thesis is the investigation of the effect of severely deformed microstructure on α phase precipitation.

2.4. Titanium as an implant material

Replacement of big joints is considered as a major achievement in orthopaedic surgery in 20th century. One of the most delicate issues in a hip endoprosthesis design is the femoral stem that is crucial for preventing the implant from loosening. Development of orthopaedic implants is a complex and multi-field scientific issue.

Titanium alloys have been extensively applied in the orthopaedics due to their superior mechanical properties, excellent corrosion resistance and favourable biocompatibility for several decades. There are numerous studies reviewing outstanding properties of these materials for medical use [Long1998, Katti2004, Geetha2009]. Excellent biocompatibility of titanium was proven by many authors both in vitro and in vivo [Rao1997, Okazaki2005, Gepreel2013]. In the last two decades, specialized biocompatible β -Ti alloys were developed. Among commonly used alloying elements, Nb, Ta, Zr and also Mo are regarded as the most biocompatible, whereas V, Cr and Co are considered inappropriate [Steinemann 1998], although Ti-6Al-4V alloy is still used for load-bearing implants [Niinomi2008].

Ti-6Al-4V alloy is a two-phase $\alpha + \beta$ alloy originally developed for aerospace applications in 1950s and still constitutes the workhorse of titanium industry. The strength of Ti-6Al-4V alloy can exceed 1000 MPa after proper thermomechanical treatment. The elastic modulus of the alloy is around 115 GPa, which is half of the elastic modulus of steels [Welsch1993]. Despite its original application in aerospace industry, Ti-6Al-4V alloy is nowadays used for manufacturing of vast majority of load-bearing body implants such as hip joint implants [Rack2006].

The strength of the implant material is the most important parameter for implant construction. The yield stress above 800 MPa is a typical requirement as this is the low-limit of the strength of Ti-6Al-4V alloy. Common elastic modulus of Ti and Ti alloys is around 100 GPa, which is much higher than the elastic modulus of the cortical bone (10-30 GPa) [Niinomi2012]. This difference in stiffness of the implant and the surrounding bone causes so-called stress shielding effect. The applied load is transmitted through the implant stem, and therefore the surrounding bone is not loaded and becomes atrophied and prone to failure. As a result, a material with a sufficient strength and a reduced elastic modulus is required [Niinomi2008].

Metastable β -Ti alloys have been developed since 1960s [Lutjering2007]. The principal advantages of these alloys is their increased strength. The dominant area of application is the aircraft manufacturing – namely landing gear structures. However, in the last three decades, specialized biocompatible alloys have also been developed [Kaur2019].

2.5. Ultra-fine grained Ti alloys

Ultra-fine grained (UFG) materials are defined as polycrystalline materials with grain sizes lower than 1 μm but typically greater than 100 nm. These materials usually have excellent mechanical properties – high strength, hardness and fatigue resistance. A common disadvantage is a reduced ductility of the material [Langdon2013]. The reduction of grain size in polycrystalline materials results in changes in mechanical and physical properties, namely an increase in strength.

UFG bulk materials can be fabricated by severe plastic deformation (SPD) methods, which refer to techniques that introduce intensive plastic deformation to the material by repetitive processing [Valiev2000, Huang2013]. The most used SPD methods are Equal Channel Angular Pressing (ECAP) [Segal1981] and High Pressure Torsion (HPT) [Smirnova1986].

The principle of ECAP is a repetitive pressing of a small rod or billet through a die consisting of two intersecting channels with the same cross-section. The geometry of the die is characterized by two angles: Φ and Ψ shown in Figure 3.

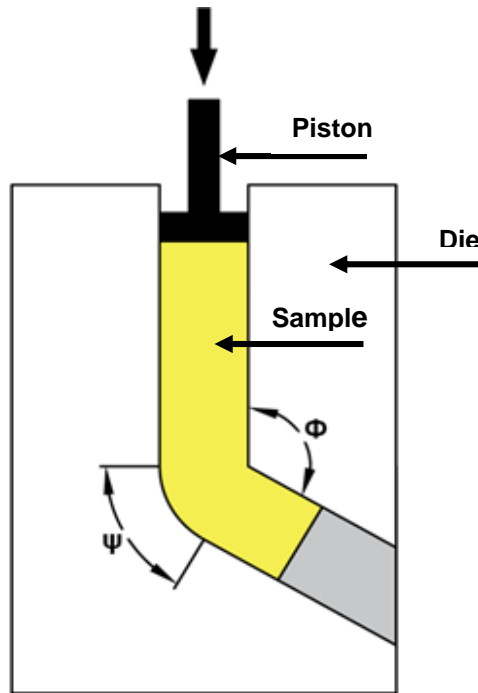


Figure 3. Schematic representation of the ECAP process

A conventional ECAP die has the angle Φ equal to 90° ; however, titanium alloys, due to their high strength and limited ductility, can be usually repeatedly successfully processed only using a die with an increased angle Φ (e.g. 120° as shown in Figure 3).

The specimen pressed through the ECAP die is deformed by a simple shear, and the imposed von Mises strain after N passes can be expressed [Iwahashi1996]:

$$\varepsilon_{VM} = \frac{N}{\sqrt{3}} \left[2 \cotg \left(\frac{\phi}{2} + \frac{\psi}{2} \right) + \psi \operatorname{cosec} \left(\frac{\phi}{2} + \frac{\psi}{2} \right) \right]. \quad (2)$$

The equivalent von Mises strain calculated from eq. (2) for a die with angles $\Phi = 120^\circ$ and $\psi = 0^\circ$ is $\varepsilon_{VM} = 0.67$ for each pass. Pressing temperature is a crucial parameter of the ECAP which influences both the processability and the microstructure of the deformed material.

During high pressure torsion (HPT) a disc-shaped sample is placed between two anvils which compress the sample at high pressure (several GPa). One of the anvils is subsequently rotated and deforms the sample in torsion. The schematic representation of the procedure is shown in Figure 4.

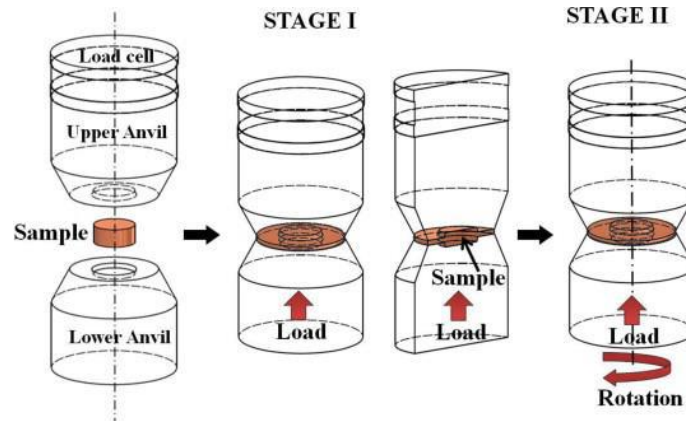


Figure 4. Schematic representation of the HPT process [Song2011]

The total von Mises strain imposed by HPT in the sample can be expressed using a simple torsion model [Valiev1996]:

$$\varepsilon_{VM} = \frac{2\pi Nr}{\sqrt{3}h}, \quad (3)$$

where N is the number of rotations, r is the distance from the sample centre and h is the sample thickness. Due to the geometry of the deformation, the imposed strain is not homogeneous and increases from the centre to the edge of the sample. HPT is usually carried out at room temperature and its main advantage is the high degree of imposed deformation. Small size of samples and inhomogeneous deformation which restrict commercial production are the main disadvantages of HPT processing [Zhilyaev2008]. In contrast, ECAP is capable of producing specimens with a reasonable size for various biomedical applications [Valiev2009].

Ultra-fine grained titanium was first prepared by the SPD methods at Ufa State Aviation Technical University (USATU), Ufa, Russia [Popov1997]. Ultra-fine grained titanium alloy Ti-6Al-4V was later prepared by ECAP [Semenova2004]. Manufacturing of dental implants benefits from the enhanced strength of UFG titanium [Valiev2009]. Recently, SPD processing has been proposed to fabricate ultra-fine grained metastable β -Ti alloys with high strength, reduced modulus of elasticity and excellent biocompatibility [Xu2009, Zafari2015, Polyakov2019]. It has been shown that severe plastic deformation of these alloys leads to improved strength due to grain refinement and substructure evolution [Valiev2014]. These materials are of significant interest for biomedical use [Xie2013].

3. Development of Ti-Nb-Ta-Zr-O biomedical alloys

This chapter describes our achievements in the field of development and characterization of new biocompatible β -Ti alloys.

Within the last 25 years, the development of biocompatible β -Ti alloys with decreased modulus of elasticity focused mainly on the Ti-Nb-Ta-Zr alloying system due to an excellent biocompatibility of the used alloying elements [Okazaki2005]. The two most investigated alloys are Ti-29Nb-13Ta-4.6Zr [Kuroda1998] (Japan alloy) and Ti-35Nb-7.3Zr-5.7Ta (US alloy). The latter alloy was developed in the 1990s in the USA, patented in 1999 [Ahmed1999] and used as a benchmark material for alloy development described in this thesis. The alloy was designed experimentally by testing many different chemical compositions aiming to achieve the minimum elastic modulus. Ti-35Nb-7Zr-5Ta was the most β -stabilized alloy tested in [Tang2000]. The elastic modulus of this alloy can be as low as 50 GPa, because α , α' and ω phases are avoided in the β solution treated condition. The main disadvantage of this alloy is its low strength of only 500 MPa that is not sufficient for manufacturing of implants of big joints.

The main objective of our own investigation was to develop strategies for increasing strength of Ti-35Nb-7Zr-6Ta alloy while maintaining low elastic modulus and good biocompatibility. The majority of our research in this field focuses on biocompatible β -Ti alloys with an increased oxygen content. Our findings, along with a comprehensive literature review, are summarized in the chapter in the monograph:

[A0] J. Stráský, M. Janeček, P. Harcuba, D. Preisler, M. Landa, *Chapter 4.2.: Biocompatible beta-Ti alloys with enhanced strength due to increased oxygen content*, in *Titanium in Medical and Dental Applications*, Editors: Francis H. Froes, Ma Qian, Woodhead Publishing in Materials, Elsevier 2018

This chapter provides the very first comprehensive review on β -Ti alloys with increased oxygen content. This class of alloys intended for biomedical applications with knowledge-based design is very promising for manufacturing of load-bearing orthopaedic implants. The chapter describes theoretical considerations of interstitial strengthening of bcc materials, which include β -Ti alloys. Moreover, it provides a comprehensive literature review of reports on β -Ti alloys in which the oxygen content was increased (intentionally or unintentionally) and properly measured. The immense effect of interstitial oxygen atoms on the strength enhancement was documented. Our experimental results describing the development of biomedical Ti-Nb-Zr-Ta-O alloys with varied oxygen content are introduced in the text, as well.

I wrote the whole chapter with the help of my student Dalibor Preisler who prepared the overview of the properties of various alloys characterized in available literature. Other co-authors contributed by the experimental characterization.

[A1] I. Kopová, J. Stráský, P. Hrcuba, M. Landa, M. Janeček, L. Bačáková: *Newly developed Ti-Nb-Zr-Ta-Si-Fe biomedical beta titanium alloys with increased strength and enhanced biocompatibility*, Materials Science & Engineering C, Vol. 60, 2016, 230 -238

The paper published already in 2016 represents our first attempt to increase the strength of Ti-35Nb-7Zr-6Ta alloy by utilizing the combined strengthening effect of iron and silicon. Fe causes simple solution strengthening in β -Ti alloys, while Si addition causes precipitation of silicides which may increase the strength via precipitation strengthening. The results show that the strength of the material increased from 500 MPa to 800 MPa. However, the modulus of elasticity increased from 60 GPa to 80 GPa. We ascribe such significant increase of modulus of elasticity to the stabilization of β phase by Fe content.

This contribution resulted from a long-term cooperation between Department of Physics of Materials and the Institute of Physiology, Czech Academy of Sciences. This cooperation initially focused on surface treatment of Ti alloys [Hrcuba2012, Stráský2013, Havlíková2014]. Biocompatibility (cell adhesion and toxicity) of the newly developed biomedical Ti-based alloys was assessed at the Institute of Physiology headed by prof. Lucie Bačáková and complemented by the investigation of mechanical properties conducted by our group. The most important original finding is that the addition of other alloying elements does not have any harmful effect on the biomedical response of the alloys, and the biocompatibility of all studied alloys was superior to that of benchmark Ti-6Al-V alloy.

Based on discussions in our team, I designed the new alloys arranged for their manufacturing and managed their experimental characterization. I wrote the introduction to the paper and the part describing the development, microstructure and mechanical properties of the alloys.

[A2] J. Stráský, P. Hrcuba, K. Václavová, K. Horváth, M. Landa, O. Srba, M. Janeček: *Increasing strength of a biomedical Ti-Nb-Ta-Zr alloy by alloying with Fe, Si and O*, Journal of Mechanical Behavior of Biomaterials, Vol. 71, 2017, 329 – 336

This is the key publication in which we describe the strengthening of the Ti-35Nb-7Zr-6Ta titanium alloy by three different mechanisms: substitutional solid solution strengthening by Fe, precipitation hardening by silicide particles and interstitial strengthening by oxygen. It was proven that interstitial strengthening is much more efficient than the other mechanisms, and increased content of oxygen proved to be the most promising for achieving optimal combination of desired mechanical properties. Addition of oxygen, which is obviously a biotolerant element, resulted in doubled strength of the material. At the same time, ductility of the material exceeded 20 %, which is sufficient for practical use. On the other hand, modulus of elasticity increased to 80 GPa due to reasons explained below.

The strategy of designing new alloys was developed by me and my colleague Petr Hrcuba. I performed the measurements of mechanical properties, summarized all achieved results, discussed them and wrote the manuscript.

[A3] D. Preisler, J. Stráský, P. Hrcuba, F. Warchomicka, M. Janeček, *Enhancing mechanical properties and microstructure of Ti-Nb-Zr-Ta-O biomedical alloy through hot working*. Acta Physica Polonica A, Vol. 134 (2018)

The newly developed alloy with composition Ti-35Nb-7.3Zr-5.7Ta-0.7O was granted a Czech patent no. 307793 in 2018. The alloy was thoroughly characterized with the focus on its use as a material for manufacturing of load-bearing implants of big joints, namely for the stem of the hip joint endoprosthesis. The paper investigates hot-formability of this alloy. Deformation tests at high temperatures with high strain rates were undertaken to determine parameters of hot-working of the material, which is commonly required for the manufacturing of the implant.

The publication could not be possible without a close cooperation between our team and the team of dr. Fernando Warchomicka, Technical University Graz, Austria. This foreign partner provided us the possibility to use Gleeble machine allowing deformation at high temperatures and at high strain rates, and immediate water quench after the deformation.

[A4] J. Stráský, D. Preisler, K. Bartha, M. Janeček, *Manufacturing of Biomedical Ti-Based Alloys with High Oxygen Content and Various Amount of Beta-Stabilizing Elements*, Materials Science Forum, Conference proceedings: Thermec 2018, Paris

The above mentioned drawback of oxygen addition is the undesired increase of elastic modulus. We found that elastic modulus can be retained at low level (60 GPa) by decreasing content of the β stabilizing elements. The paper *Manufacturing of Biomedical Ti-Based Alloys with High Oxygen Content and Various Amount of Beta-Stabilizing Elements* in the conference proceeding of conference Thermec 2018 represents the first experimental characterization of alloys with reduced content of β stabilizing elements. This paper with limited length shows only initial experimental results. Most achievements remain unpublished and are described below in this thesis.

[A5] D. Preisler, M. Janeček, P. Hrcuba, J. Džugan, K. Halmešová, J. Málek, A. Veverková, J. Stráský, *The Effect of Hot Working on the Mechanical Properties of High Strength Biomedical Ti-Nb-Ta-Zr-O Alloy*, Materials 12 (2019) 4233

Our most recent published contribution in the field of development and characterization of Ti-Nb-Ta-Zr-O based alloys describes the possible thermomechanical treatment of the alloy. Most importantly, this paper includes experimental results from fatigue testing. Fatigue performance is a key property which decides applicability of the developed material and determines the life-time of an implant. Testing of fatigue properties is extremely material demanding and rarely published for newly developed biomedical β -Ti alloys. The publication results from a long-term cooperation between our team and Beznoska Ltd., an important Czech implant manufacturer. Cooperation with industrial partner (currently supported by a project by Ministry of Industry and Trade, Czech Republic) is promising in terms of application and commercialization of achieved results.

My current research in the development of new biocompatible β -Ti alloys with increased oxygen content focuses on the reduction of elastic modulus without sacrificing strength. The majority of this research has not been published yet and therefore is introduced in the rest of this section.

Elastic modulus (E) of different phases in Ti alloy can be ordered as: $E_{\beta} \approx E_{\alpha'} \approx 70 \text{ GPa} < E_{\alpha} \approx 100 \text{ GPa} < E_{\omega} \approx 130 \text{ GPa}$ [Fischer 1970, Niinomi 1998, Tane 2013, Nejezhlebova 2016]. The stability of individual phases is connected to the electron-per-atom ratio (e/a ratio) and the elastic modulus decreases with decreasing e/a ratio as long as the material retains the pure β phase [Hao 2007]. Therefore, in order to achieve material with a reduced elastic modulus, an alloy should retain the pure β phase, but the stability of this phase must be low: in ‘proximity’ to $\beta \rightarrow \alpha''$ martensitic transformation [Tane 2010].

During elastic deformation, atoms are slightly shifted from their initial positions due to stress, but after relieving the stress, atoms return to their original positions. Elastic deformation in shear is crucial for overall macroscopic Young’s modulus of polycrystalline materials. Therefore, in the proximity of the martensitic transformation, which would occur at slightly lower temperature, the atoms can be shifted further away from their initial positions by the shear stress, although they return back after relieving the stress without any change in crystal structure. Such material exhibits lower elastic constants (so-called abnormal softening) due to the ‘proximity’ to the martensitic transformation, although no martensitic transformation actually occurs [Nakanishi1980].

The effect of ‘proximity’ of martensitic transformation was studied in different systems such as Ti-Ni [Ren2001] or Co-Ni-Al [Seiner2013]. Abnormal softening of elastic constants was measured in single crystals of biomedical Ti-Nb-Ta-Zr alloy, but it was not ascribed directly to the ‘proximity’ of martensitic transformation [Tane2010]. Biomedical alloys with the lowest elastic modulus such as Ti-29Nb-13Ta-4.6Zr, Ti-35Nb-7Zr-5Ta or GUM Metal (Ti-35Nb-2Ta-3Zr-0.3O) were developed mostly experimentally and in my opinion these alloys owe their low-modulus property to the ‘proximity’ of martensitic transformation, although the inventors of these alloys may have not realized this at the time of the alloy development.

In the Ti-35Nb-7Zr-6Ta-0.7O alloy, which we have thoroughly studied, high oxygen content affects the phase stability of the β matrix. Oxygen is an α stabilizing element in terms of increasing the β transus temperature in pure Ti [Waldner1999] and in metastable β -Ti alloys [Qazi2005, Geng2011]. The relationship between oxygen content and $\beta \rightarrow \alpha''$ martensitic transformation is less understood. Results from a few experimental studies suggest that in the competition between β and α'' phases, interstitial oxygen acts as a β stabilizing element and shifts the martensite start (M_s) temperature of α'' formation to lower temperatures [Furuta2007, Tane2016, Abdel-Hady2006, Obbard2011]. Consequently, by adding significant amount of oxygen to a low-modulus β -Ti alloy, the stability of β phase increases, causing an increase of the elastic modulus.

These considerations are depicted in Figure 5 which presents a schematic pseudo-binary phase diagram of Ti-Zr-Nb-Ta-O alloys. The diagram is pseudo-binary in terms that one constituent is not pure Ti (cf. Figure 2), but Ti-7Zr composition. The other constituent is a β -Ti stabilizing element (cf. Figure 2), in this particular case the total Nb + Ta content.

Horizontal axis therefore represents the content of Nb + Ta in wt % (the effect of Ta on phase stability is similar to Nb within the limits used in the studied alloys). This unusual construction allows us to show the position of quaternary Ti-35Nb-7Zr-6Ta alloy in the diagram. Note that blue lines are relevant for the alloys without oxygen.

The effect of oxygen is incorporated into the diagram such that the first constituent in the diagram (along vertical axis on the left hand side) is not Ti-7Zr but Ti-7Zr-0.7O composition, and the diagram is drawn by red lines. It can be observed that oxygen increases the stability of α phase. This diagram allows us to depict the position of Ti-35Nb-7Zr-6Ta-0.7O alloy.

Apart from solid lines representing the equilibrium diagram, the dotted lines represent the start of martensitic transformation $\beta \rightarrow \alpha''$ (cf. Figure 2). In the diagram, elastic modulus of Ti-35Nb-7Zr-6Ta and Ti-35Nb-7Zr-6Ta-0.7O is also shown. Low modulus of the former alloy is given by the partial abnormal softening due to the ‘proximity’ of martensitic transformation. On the other hand, the elastic modulus of Ti-35Nb-7Zr-6Ta-0.7O alloy is much higher, because oxygen is a β stabilizing element with respect to $\beta \rightarrow \alpha''$ martensitic transformation (M_s line is shifted to the left).

The key idea is therefore to decrease the total content of β stabilizing elements (Nb and Ta) to restore the low elastic-modulus of the alloy with high oxygen content, which must be kept sufficiently high to retain the high strength. In this respect, Ti-29Nb-7Zr-0.7O alloy was tested, and its elastic modulus of 65 GPa confirms the discussed effects.

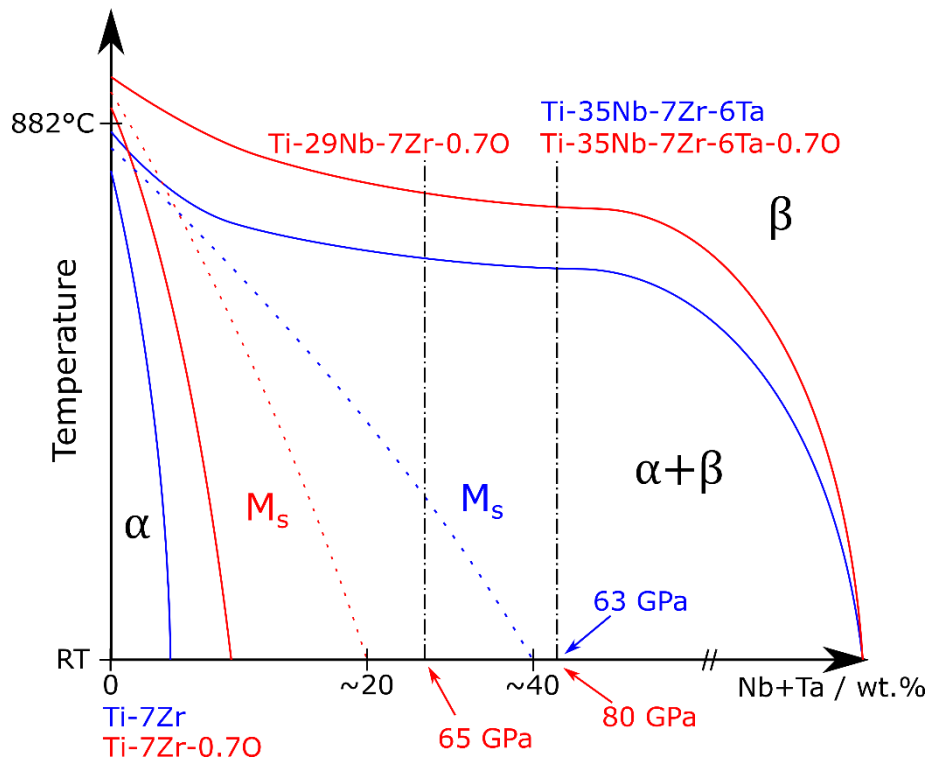


Figure 5. Schematic pseudo-binary phase diagram. Blue lines are drawn for the addition of β -stabilizing Nb/Ta to Ti-7Zr alloy. Red lines correspond to adding of Nb/Ta to Ti-7Zr-0.7O composition.

Recently, we have manufactured and tested several alloys derived from the Ti-35Nb-7Zr-6Ta-0.7O alloy with reduced Nb content (26 – 35 wt % Nb) and reduced Ta content (0 or 6 wt %). Figure 6 shows the elastic moduli of the developed Ti-Nb-(Ta)-Zr-O alloys and clearly demonstrates that the elastic modulus decreases with decreasing Nb content and also when Ta is absent. These alloys were subjected to tensile testing and all of them achieved the high yield strength of at least 800 MPa (Figure 7), which is attributed to the interstitial strengthening by oxygen.

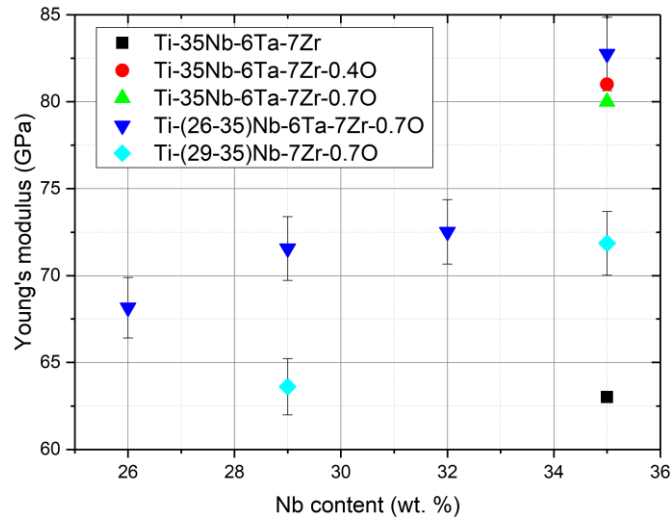


Figure 6. Elastic modulus of Ti-Nb-(Ta)-Zr-O alloys with various content of Nb and Ta

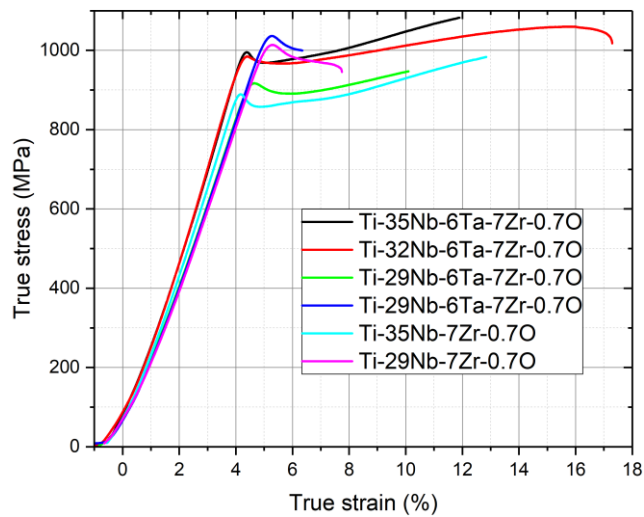


Figure 7. Flow curves for Ti-Nb-(Ta)-Zr-O alloys with various content of Nb and Ta

Simultaneous achievement of low elastic modulus and high strength is very promising in terms of potential application in implant manufacturing. Figure 8 shows a comparison of the newly developed alloys with results from other authors. Our newly developed alloys possess the strength of around 900 MPa and the elastic modulus of around 70 GPa. Such combination of mechanical properties has not been reported, yet.

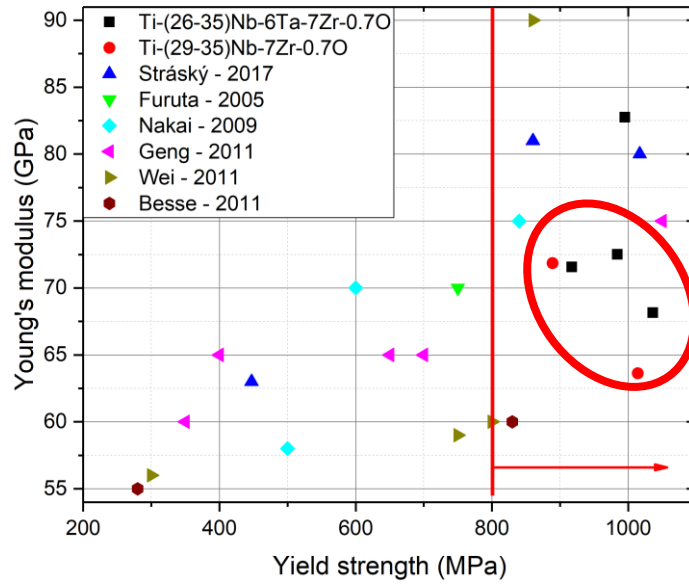


Figure 8. Elastic modulus and yield strength of our Ti-Nb-(Ta)-Zr-O alloys (highlighted by the red circle) in comparison with results of other authors. Materials having the strength above 800 MPa are prospective candidates for load-bearing implants of big joints.

4. Ultra-fine grained Ti alloys for biomedical use

This chapter summarizes our results achieved in the development, manufacturing and characterization of ultra-fine grained (UFG) Ti based materials for biomedical use. Our contribution of this long-term research is mainly in the methodology of experimental characterization.

Ultra-fine grained (UFG) materials contain, by definition, the high amount of grain boundaries. SPD methods for fabrication of UFG materials also typically produce high density of dislocations. Complex characterization of the UFG metallic materials requires utilizing numerous experimental methods such as x-ray diffraction (XRD), scanning electron microscopy (SEM), transmission electron microscopy (TEM) and indirect methods such as electrical resistivity measurement, positron annihilation spectroscopy or microhardness measurement [Čížek2016]. Defect structure significantly affects mechanical properties of materials and is therefore of significant importance.

Our work in investigation of lattice defects and microstructure of UFG titanium alloys is thoroughly reviewed in the chapter:

[B0] J. Stráský, M. Janeček, I. Semenova, J. Čížek, K. Bartha, P. Harcuba, V. Polyakova, S. Gatina, *Microstructure and lattice defects in ultrafine grained biomedical $\alpha+\beta$ and metastable β Ti alloys*, in: Titanium in Medical and Dental Applications, ed. F. Froes, M. Qian, pp. 455-475 (2018)

The chapter in the monograph contains a thorough introduction to UFG Ti alloys, methods of their manufacturing and methods of experimental characterization of UFG Ti-based materials. The chapter contains our own experimental data and underlines the importance of employing various complementary experimental techniques. Output of each of the experimental methods must be thoroughly understood in order to get the full picture about microstructure and properties of these novel materials. Superior properties of the UFG materials are based on strengthening via grain refinement and increase of dislocation density.

The chapter was written by me in a cooperation with my former PhD student Kristina Bartha.

[B1] M. Janeček, J. Stráský, J. Čížek, P. Harcuba, K. Václavová, V.V. Polyakova, I.P. Semenova: *Mechanical properties and dislocation structure evolution in Ti6Al7Nb alloy processed by high pressure torsion*, Metallurgical and Materials Transactions, Vol. 45A, 2014, 7 – 15.

As mentioned in the Introduction, the workhorse of Ti industry is Ti-6Al-4V alloy, which is still used for implant manufacturing despite known toxicity of vanadium. Vanadium-free Ti-6Al-7Nb alloy is an $\alpha + \beta$ alloy for biomedical applications which was developed as a non-toxic alternative to Ti-6Al-4V alloy. Our first study on an UFG biomedical alloy, summarized in the paper, describes the evolution of microstructure and mechanical properties in Ti-6Al-7Nb alloy prepared by high pressure torsion (HPT). The material was studied by microscopic methods, microhardness measurement and an advanced method of positron annihilation spectroscopy, which is able to determine the density of dislocations and also the concentration of vacancies or vacancy clusters. I wrote the majority of the

manuscript in cooperation with prof. M. Janeček and I supervised my student K. Bartha (neé Václavová) during preparation of this publication.

The publication is the first outcome of the cooperation between our research group and the research team at the Ufa State Aviation University, Ufa, Russia. This team was formed by one of the leading experts in the field of UFG materials prof. Ruslan Z. Valiev and is headed by prof. Irina P. Semenova. Intensive cooperation is based on the complementarity of the research groups and available equipment. The UFG materials were manufactured by SPD methods in Ufa and thoroughly characterized at the Department of Physics of Materials and at other cooperating institutes in Prague.

[B2] J. Stráský, P. Hrcuba, M. Hájek, K. Václavová, P. Zháňal, M. Janeček, V. Polyakova, I. Semenova: *Microstructure evolution in ultrafine-grained Ti and Ti-6Al-7Nb alloy processed by severe plastic deformation*, NanoSPD6, IOP Conference Series: Materials Science and Engineering, Vol. 63, 2014, pp. UNSP 012072.

The contribution in the conference proceedings from the conference NanoSPD (nanostructured materials prepared by SPD methods) *Microstructure evolution in ultrafine-grained Ti and Ti-6Al-7Nb alloy processed by severe plastic deformation* investigates the use of in-situ electrical resistivity measurement to reveal microstructural changes during heating of UFG commercially pure Ti and UFG biomedical Ti-6Al-7Nb alloy. Results from the electrical resistivity measurements were compared to the results from other experimental techniques. The UFG condition is thermodynamically unstable and undergoes processes of recovery and recrystallization at elevated temperatures. Moreover, in the case of Ti-6Al-7Nb alloy, the transition between α and β phases occurs during heating. Enhanced thermal stability of the UFG structure was revealed for the Ti-6Al-7Nb alloy in comparison to commercially pure Ti. Thermal stability at high temperatures discussed in this paper is clearly not important for the use of the material in human body, but it is of significant importance for manufacturing of implants from semi-products which is performed at high temperatures.

[B3] K. Bartha, P. Zháňal, J. Stráský, J. Čížek, M. Dopita, F. Lukáč, P. Hrcuba, M. Hájek, V. Polyakova, I. Semenova, M. Janeček: *Lattice defects in severely deformed biomedical Ti-6Al-7Nb alloy and thermal stability of its ultra-fine grained microstructure*, Journal of Alloys and Compounds, Vol. 788, 2019, pp. 881-890

This extensive paper underlines the necessity of using several complementary methods for comprehensive microstructural characterization of multi-phase UFG materials. Indirect methods, namely electrical resistivity measurement, x-ray diffraction or positron annihilation spectroscopy are combined with direct observations by scanning electron microscopy. The investigation focused on UFG microstructure and its thermal stability in Ti-6Al-7Nb alloy. The publication completed our investigation of this $\alpha + \beta$ biomedical Ti alloy. I coordinated the research and wrote the manuscript with significant help of my PhD student K. Bartha.

- [B4] K. Václavová, J. Stráský, V. Polyakova, J. Stráská, J. Nejezchlebová, H. Seiner, I. Semenova, M. Janeček: *Microhardness and microstructure evolution of ultra-fine grained Ti-15Mo and TIMETAL LCB alloys prepared by high pressure torsion*, Materials Science and Engineering A Vol. 682, 2017, pp. 220-228

Since 2014, our investigation focused on UFG *metastable* β -Ti alloys [Janecek2014]. Two metastable β -Ti alloys were studied. Binary Ti15Mo alloy is intended and currently also certified for biomedical use. Ti-6.8Mo-4.5Fe-1.5Al (TIMETAL LCB) is referred to as low-cost β -Ti alloy (LCB) and is designed for application in aerospace and automotive industry. Both materials were deformed by high pressure torsion (HPT) and thoroughly characterized. The results are summarized in publication *Microhardness and microstructure evolution of ultra-fine grained Ti-15Mo and TIMETAL LCB alloys prepared by high pressure torsion*. Detailed observations by electron back-scattered diffraction (EBSD) technique proved that the twinning (and multiple twinning – i.e. formation of secondary twins in primary twins) significantly contributes to the grain refinement in these body-centred cubic titanium alloys. This fact was reported for the first time in a β -Ti alloy. The alloys were investigated in the β solution treated condition, which typically exhibits a low strength. Nevertheless, the microhardness of the studied UFG alloys in the β solution treated condition exceeded the microhardness achievable by standard thermomechanical treatment involving precipitation of α phase. It is therefore of significant interest to combine microstructural refinement by SPD methods and subsequent ageing treatment to achieve even higher strength levels.

The manuscript was prepared in a close cooperation between me and my student Kristina Bartha (neé Václavová).

- [B5] K. Bartha, A. Veverková, J. Stráský, J. Veselý, P. Minárik C.A. Corrêa, V. Polyakova, I. Semenova, M. Janeček, *Effect of the severe plastic deformation by ECAP on microstructure and phase transformations in Ti-15Mo alloy*, Materials Today Communications 22 (2020) 100811

The effect of SPD deformation on phase transformations was studied in Ti15Mo alloy prepared by two SPD methods: ECAP and HPT. The article *Effect of the severe plastic deformation by ECAP on microstructure and phase transformations in Ti-15Mo alloy* summarizes the characterization of phase transformations in the biomedical Ti15Mo alloy prepared by ECAP in the β solution treated condition, which is a thermodynamically metastable condition. As described in the Introduction, achieving the stable composition requires the precipitation of α phase particles by heterogeneous nucleation and growth. UFG structure significantly affects both the nucleation and growth process.

The publication was prepared by K. Bartha under my supervision. It results from continuing cooperation with the research team in Ufa, Russia.

[B6] K. Bartha, J. Stráský, A. Veverková, P. Barriobero-Vila, F. Lukáč, P. Doležal, P. Sedlák, V. Polyakova, I. Semenova, M. Janeček, *Effect of the High-Pressure Torsion (HPT) and Subsequent Isothermal Annealing on the Phase Transformation in Biomedical Ti15Mo Alloy*, Metals 9 (2019) 1194

Ti15Mo alloy prepared by high pressure torsion (HPT) contains a high density of dislocations and the grain structure is significantly refined. The nucleation of α phase therefore occurs at lower temperatures and results in very fine equiaxed α phase precipitates upon isothermal heating due to the dense net of nuclei. Combination of severe deformation, grain refinement and subsequent thermal processing is promising in terms of achieving enhanced mechanical properties of the alloy.

Apart from the isothermal annealing and ex-situ measurements included in the last mentioned publication, the phase transformation in Ti15Mo alloy were studied also in-situ during linear heating by high energy synchrotron x-ray diffraction (HEXRD). These results have not been published yet and therefore are presented here.

Phase transformation in Ti15Mo alloy were studied both in the coarse-grained solution treated condition and the UFG condition prepared by HPT.

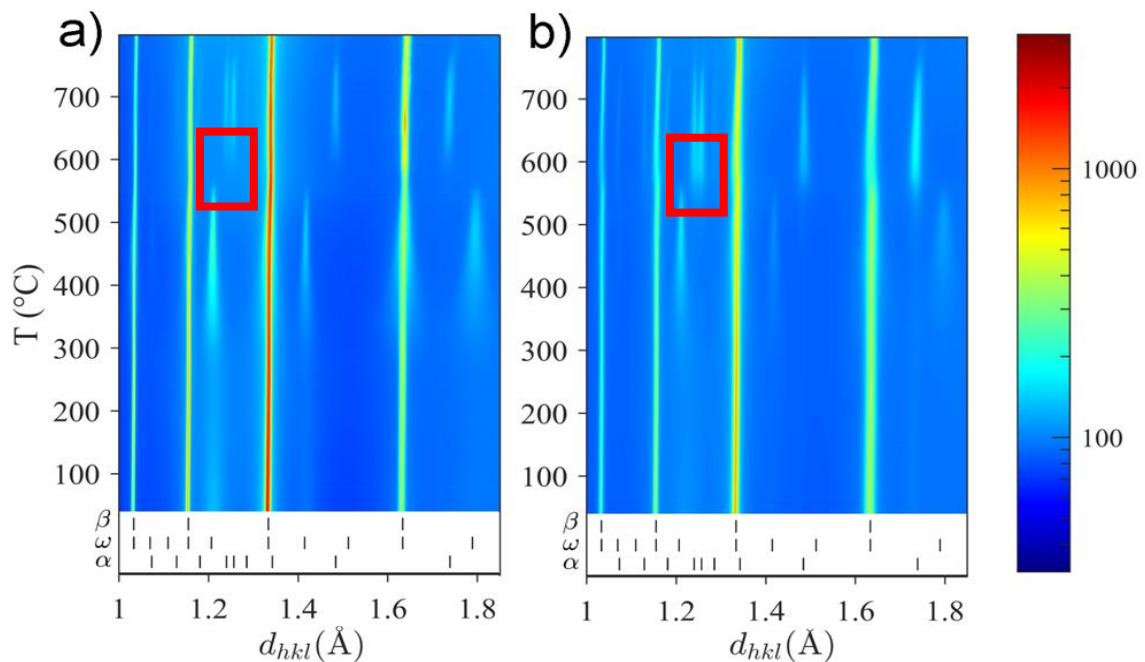


Figure 9 High energy synchrotron x-ray diffraction (HEXRD) of Ti15Mo alloy *in-situ* during linear heating at the rate of 5 °C/min from room temperature to 800 °C.

a) non-deformed material, b) UFG material deformed by HPT. Horizontal axis represents interplane distances d_{hkl} ; temperature is shown on the vertical axis and the measured intensity is represented by the colour code.

Figure 9 shows the HEXRD patterns measured *in-situ* during linear heating at the rate of 5 °C/min from room temperature up to 800 °C. The horizontal axis represents the interplane distances d_{hkl} ; temperature is shown on the vertical axis and the measured intensity is represented by the colour code. The most intense peaks are those of β phase; however, more interesting peaks are related to ω phase and to α phase. Peaks corresponding to ω phase often

coincide with the more intense β phase peaks. A notable exception is the peak at $d_{hkl} = 1.2$ Å. ω peaks are most intense at 450 °C, while α peaks at 650 °C. Figure 9 a) shows HEXRD patterns for the coarse-grained material, while in Figure 9 b), HEXRD patterns for the UFG material deformed by HPT are presented. Red boxes highlight the biggest difference between the two studied conditions. In the non-deformed material, ω phase dissolves completely at 550 °C and only at a higher temperature, α phase starts to precipitate [Zhanal2018]. On the other hand, in the UFG condition, the severe plastic strain introduced by SPD enhances the α phase precipitation, which occurs at lower temperatures already in the presence of ω particles and the co-existence of all three phases (ω , α and β) was observed.

For a comprehensive description of the effect of microstructure on the α phase precipitation, the reader is referred to the dissertation thesis *Phase transformations in ultra-fine grained titanium alloys* by my former doctoral student Kristina Bartha [Bartha2019].

[B7] R. Z. Valiev, E. A. Prokofiev, N. A. Kazarinov, G. I. Raab, T. B. Minasov, J. Stráský, *Developing nanostructured Ti alloys for innovative implantable medical devices*, Materials 13 (2020) 967

The last publication included in this habilitation thesis is a review paper by a team of authors headed by prof. Ruslan Z. Valiev. This invited review paper was published in a special issue *Alloys for Biomedical Use* of journal Materials, MDPI. I had the privilege to serve as a guest editor of this issue and used this opportunity to invite prof. Valiev to submit a review paper to this issue. I contributed to this paper by a comprehensive literature review of the UFG β -Ti alloys for biomedical use. The paper discusses not only properties of UFG Ti-based alloys, but also describes specific applications of these materials in practical medical use.

5. Conclusion and outlook

Research and development of titanium alloys still represent a vast scientific field for exploration. This habilitation thesis is devoted to two important scientific areas. The first one – development of biomedical titanium alloys – is of primary interest to the titanium community and I am convinced that our contribution will lead to application of the newly developed alloys in medical practice.

The second part is devoted to ultra-fine grained Ti alloys for biomedical use. UFG materials constitute a very interesting field of materials science as they exhibit superior mechanical properties. Potential application of metallic UFG materials is still in the beginning. Manufactured products suffer from small size and the low efficiency of production. Despite that, first potential biomedical applications of UFG Ti alloys have already emerged.

Apart from continuing research in the areas described in this thesis, my scientific activities in the field of Ti alloys include two other topics.

1. Powder metallurgy (PM) is an emerging processing technology. PM is particularly useful for manufacturing products from Ti alloys, because conventional manufacturing methods (casting, forging and machining) are complicated in Ti alloys due to their affinity to oxygen, high toughness and low thermal conductivity. One of the promising PM methods is so-called Spark Plasma Sintering (SPS) allowing compaction of powder materials at shorter times and lower temperatures than conventional sintering methods. My PhD student Jiří Kozlík demonstrated the feasibility of processing of commercially pure Ti by cryogenic milling followed by compaction by SPS [Kozlik2019, Kozlik2020].

Currently we focus on manufacturing of bulk material by SPS from Ti alloys – either from a pre-alloyed powder or from elemental powders. We used Ti15Mo alloy powder to show the effect of cryogenic milling and SPS on phase composition and microstructure of the alloy [Veverkova2019] Our recent, yet unpublished, results show that it is possible to manufacture biomedical β -Ti Ti-Nb-Zr-O alloy with homogeneous composition, controlled oxygen content and promising mechanical properties from elemental powders and TiO₂ powder.

Another important branch of powder metallurgy is the Additive Manufacturing (3D printing), which is believed to be a feasible option for net-shape or near-net-shape production. Apart from interesting technological issues associated with 3D printing, the possibility of additive manufacturing opens a brand new field for alloy development and characterization. Required properties of 3D printed materials will significantly differ from the properties required for ‘standard’ metallic materials, for instance in terms of high temperature formability. Simultaneously, new issues emerge, such as limited fracture toughness and overall fatigue performance of final products prepared by additive manufacturing. A breakthrough in this field is anticipated – in terms of new technologies, new materials and new applications.

2. The second area of my interest relates to the investigation of plastic deformation mechanisms associated with phase transformations in metastable β -Ti alloys. Although dislocation movement is a major mechanism of plastic deformation in metals, in some advanced metallic materials, other plastic deformation mechanisms such as transformation induced plasticity (TRIP) and twinning induced plasticity (TWIP) operate. Well-known examples include so-called TRIP/TWIP steels. Nevertheless, recently also TRIP/TWIP Ti alloys emerged. It is now qualitatively clear that TRIP and TWIP effects depend on the chemical composition of an alloy – in particular on the degree of its β phase stabilization. However, interrelations between martensitic transformation, twinning in various twinning systems and activity of dislocation slip systems are not fully explored and deserve systematic investigation.

References

- [Abdel-Hady2006] M. Abdel-Hady, K. Hinoshita, M. Morinaga, General approach to phase stability and elastic properties of β -type Ti-alloys using electronic parameters, *Scripta Materialia* 55 (2006) 477–480
- [Ahmed1999] T. Ahmed, H.J. Rack, Alloy of titanium, zirconium, niobium and tantalum for prosthetics. *US Patent 5871595 A*, 1999
- [Bartha2019] K. bartha, *Phase transformations in ultra-fine grained titanium alloys*, Doctoral Thesis, Charles University (2019).
- [Cochardt1955] A. W. Cochardt, G. Schoek, H. Wiedersich, Interaction between dislocations and interstitial atoms in body-centered cubic metals, *Acta Metallurgica* 3 (1955) 533–537
- [Čížek2016] J. Čížek, M. Janeček, T. Krajňák, J. Stráská, P. Hruška, J. Gubicza, H.S. Kim, Structural characterization of ultrafine-grained interstitial-free steel prepared by severe plastic deformation, *Acta Materialia* 105 (2016) 258-272
- [Davis1979] R. Davis, H. M. Flower, D. R. F. West, Martensitic transformations in Ti-Mo alloys, *Journal of Materials Science* 14 (1979) 712-722
- [DeFontaine1971] D. De Fontaine, N.E. Paton, J.C. Williams, The omega phase transformation in titanium alloys as an example of displacement controlled reactions, *Acta Metallurgica* 19 (1971) 1153–1162
- [Devaraj2009] A. Devaraj, R.E.A. Williams, S. Nag, R. Srinivasan, H.L. Fraser, R. Banerjee, Three-dimensional morphology and composition of omega precipitates in a binary titanium-molybdenum alloy, *Scripta Materialia* 61 (2009) 701–704
- [Elmay2013] W. Elmay, F. Prima, T. Gloriant, R. Bolle, Y. Zhong, E. Patoor, P. Laheurte, Effects of thermomechanical process on the microstructure and mechanical properties of a fully martensitic titanium-based biomedical alloy, *Journal of the Mechanical Behavior of Biomedical Materials* 18 (2013) 47–56.
- [Fleisher1962] R. L. Fleischer, Solution hardening by tetragonal distortions: Application to irradiation hardening in F.C.C. crystals, *Acta Metallurgica* 10 (1962) 835-842
- [Fisher1970] E. S. Fisher, D. Dever, Relation of the c' elastic modulus to stability of b.c.c. transition metals, *Acta Metallurgica* 18 (1970) 265-269
- [Furuta2007] T. Furuta, S. Kuramoto, J. Hwang, K. Nishino, T. Saito, M. Niinomi, Mechanical properties and phase stability of Ti-Nb-Ta-Zr-O alloys, *Materials Transactions* 48 (2007) 1124–1130
- [Geetha2009] M. Geetha, A. K. Singh, R. Asokamani, A. K. Gogia, Ti based biomaterials, the ultimate choice for orthopaedic implants – A review. *Progress in Materials Science* 54 (2009) 397–425
- [Geng2011] F. Geng, M. Niinomi, M. Nakai, Observation of yielding and strain hardening in a titanium alloy having high oxygen content. *Materials Science and Engineering A* 528 (2011) 5435 - 5445
- [Gepreel2013] M. Abdel-Hady Gepreel, M. Niinomi, Biocompatibility of Ti-alloys for long-term implantation, *Journal of the Mechanical Behavior of Biomedical Materials* 20 (2013) 407–415
- [Gottstein2004] G. Gottstein, *Physical Foundations of Materials Science*, Springer 2004
- [Hall1951] E. O. Hall, The deformation and ageing of mild steel, *Proceedings of the Physical Society of London Section B* 64 (1951) 747
- [Hao2007] Y.L. Hao, S.J. Li, S.Y. Sun, C.Y. Zheng, R. Yang, Elastic deformation behaviour of Ti-24Nb-4Zr-7.9Sn for biomedical applications, *Acta Biomaterialia* 3(2) (2007) 277–286
- [Harcuba2012] P. Harcuba, L. Bačáková, J. Stráský, M. Bačáková, K. Novotná, M. Janeček, Surface treatment by electric discharge machining of Ti–6Al–4V alloy for potential application in orthopaedics, *Journal of the Mechanical Behavior of Biomedical Materials* 7 (2012) 96-105
- [Havlíková2014] J. Havlíková, J. Stráský, M. Vandrovcová, P. Harcuba, M. Mhaede, M. Janeček, L. Bačáková, Innovative surface modification of Ti–6Al–4V alloy with a positive effect on osteoblast proliferation and fatigue performance, *Materials Science and Engineering: C* 39 (2014) 371-379
- [Huang2013] Y. Huang, T. G. Langdon, Advances in ultrafine-grained materials, *Materials Today* 16 (2013) 85-93

- [Iwahashi1996] Y. Iwahashi, J. Wang, Z. Horita, M. Nemoto, T. G. Langdon, Principle of equal-channel angular pressing for the processing of ultra-fine grained materials, *Scripta Materialia* 35 (1996) 143-146
- [Ivasishin2005] O. M. Ivasishin, P. E. Markovsky, S. L. Semiatin, C. H. Ward, Aging response of coarse- and fine-grained β titanium alloys, *Materials Science and Engineering: A* 405 (2005) 296-305
- [Janeček2014] M. Janeček, J. Čížek, J. Stráský, K. Václavová, P. Hruška, V. Polyakova, S. Gatina, I. Semenova, Microstructure evolution in solution treated Ti15Mo alloy processed by high pressure torsion, *Materials Characterization* 98 (2014) 233-240
- [Katti2004] K. S. Katti, Biomaterials in total joint replacement, *Colloids and Surfaces B: Biointerfaces*. 39 (2004) 133-142.
- [Kaur2019] M. Kaur, K. Singh, Review on titanium and titanium based alloys as biomaterials for orthopaedic applications, *Materials Science and Engineering: C* 102 (2019) 844-862
- [Kent2010] D. G. Kent, G. Wang, Z. Yu, M. S. Dargusch, Pseudoelastic behaviour of a β Ti-25Nb-3Zr-3Mo-2Sn alloy, *Materials Science and Engineering A* 527 (2010) 2246-2252
- [Kharia2001] K. K. Kharia, H. J. Rack, Martensitic phase transformations in IMI 550 (Ti-4Al-4Mo-2Sn-0.5 Si), *Metallurgical and Materials Transactions A* 32 (2001) 671-679
- [Kim2007] H. S. Kim, S. H. Lim, I. D. Yea, W. Y. Kim, Stress-induced martensitic transformation of metastable β -titanium alloy, *Materials Science and Engineering A* 449-451 (2007) 322-325
- [Koul1970] M. K. Koul, J. F. Breedis, Phase transformations in beta isomorphous titanium alloys, *Acta Metallurgica* 18 (1970) 579-588.
- [Kozlík2019] J. Kozlík, P. Hrcuba, J. Stráský, H. Becker, J. Šmilauerová, M. Janeček, Microstructure and texture formation in commercially pure titanium prepared by cryogenic milling and spark plasma sintering, *Materials Characterization* 151 (2019) 1-5
- [Kozlík2020] J. Kozlík, P. Hrcuba, J. Stráský, H. Becker, M. Janeček, Manufacturing of fine-grained titanium by cryogenic milling and spark plasma sintering, *Materials Science and Engineering: A* 772 (2020) 138783
- [Kuroda1998] D. Kuroda, M. Niinomi, M. Morinaga, Y. Kato, T. Yashiro, Design and mechanical properties of new β type titanium alloys for implant materials, *Materials Science and Engineering A* 243 (1998) 244-249
- [Langdon2013] T. G. Langdon, Twenty-five years of ultrafine-grained materials: Achieving exceptional properties through grain refinement, *Acta Materialia* 61 (2013) 7035-7059
- [Long1998] M. Long, H. J. Rack, Titanium alloys in total joint replacement—a materials science perspective *Biomaterials* 19 (1998) 1621-1639
- [Lütjering2007] G. Lütjering, J. C. Williams, *Titanium*, Springer 2007
- [Makino1996] T. Makino, R. Chikaizumi, T. Nagaoka, T. Furuhashi, T. Makino, Microstructure development in a thermomechanically processed Ti15V3Cr3Sn3Al alloy, *Materials Science and Engineering A* 213 (1996) 51-60
- [Nakanishi1980] N. Nakanishi, Elastic constants as they relate to lattice properties and martensite formation, *Progress in Materials Science* 24 (1980) 143-265
- [Nejezchlebova2016] J. Nejezchlebová, M. Janovská, H. Seiner, P. Sedlák, M. Landa, J. Šmilauerová, J. Stráský, P. Hrcuba, M. Janeček, The effect of athermal and isothermal ω phase particles on elasticity of β -Ti single crystals, *Acta Materialia* 110 (2016) 185-191
- [Niinomi1998] M. Niinomi, Mechanical properties of biomedical titanium alloys, *Materials Science and Engineering A* 243 (1998) 231-236
- [Niinomi2008] M. Niinomi, Mechanical biocompatibilities of titanium alloys for biomedical applications, *Journal of the Mechanical Behavior of Biomedical Materials* 1 (2008) 30-42
- [Niinomi2012] M. Niinomi, M. Nakai, J. Hieda, Development of new metallic alloys for biomedical applications, *Acta Biomaterialia* 8 (2012) 3888-3903
- [Obbard2011] E. G. Obbard, Y. L. Hao, R. J. Talling, S. J. Li, Y. W. Zhang, D. Dye, R. Yang, The effect of oxygen on α'' martensite and superelasticity in Ti-24Nb-4Zr-8Sn, *Acta Materialia* 59 (2011) 112-125
- [Okazaki2005] Y. Okazaki, E. Gotoh, Comparison of metal release from various metallic biomaterials in vitro, *Biomaterials* 26 (2005) 11-21

- [Orgéas1998] L. Orgéas, D. Favier, Stress-induced martensitic transformation of a NiTi alloy in isothermal shear, tension and compression, *Acta Materialia* 46 (1998) 5579-5591
- [Petch1953] N. J. Petch: The cleavage strength of polycrystals, *Journal of the Iron and Steel Institute* 174 (1953) 25-28
- [Popov1997] A.A. Popov, I.Yu. Pyshmintsev, S.L. Demakov, A.G. Illarionov, T.C. Lowe, A.V. Sergeyeva, R.Z. Valiev, Structural and mechanical properties of nanocrystalline titanium processed by severe plastic deformation, *Scripta Materiala* 37 (1997) 1089-1094
- [Polyakov2019] A.V. Polyakov, I.P. Semenova, E. Ivanov, R.Z. Valiev, Ultra-fine grained β -type TNZr ELI alloy with high strength and low elastic modulus, *IOP Conference Series: Materials Science Engineering* 461 (2019) 012077
- [Qazi2004] J. I. Qazi, H. J. Rack, B. Marquardt, High-strength metastable beta-titanium alloys for biomedical applications, *Journal of Materials Science* 56 (2004) 49–51
- [Qazi2005] J. I. Qazi, B. Marquardt, L. F. Allard, H. J. Rack, Phase transformations in Ti–35Nb–7Zr–5Ta–(0.06–0.68)O alloys, *Materials Science and Engineering C* 25 (2005) 389–397
- [Rack2006] H. J. Rack, J. I. Qazi, Titanium alloys for biomedical applications, *Materials Science and Engineering: C* 26 (2006) 1269–1277.
- [Rao1997] S. Y.Rao, Y. Okazaki, T. Tateishi, T. Ushida, Y. Ito, Cytocompatibility of new Ti alloy without Al and V by evaluating the relative growth ratios of fibroblasts L929 and osteoblasts MC3T3-E1 cells, *Materials Science and Engineering: C* 4 (1997) 311–314
- [Ren2001] X. Ren, N. Miura, J. Zhang, K. Otsuka, K. Tanaka, M. Koiwa, T. Suzuki, Y. Chumlyakov, M. Asai, A comparative study of elastic constants of Ti–Ni-based alloys prior to martensitic transformation, *Materials Science and Engineering A* 312 (2001) 196-206
- [Savino1981] E. J. Savino, A. Seeger, Octahedral and tetrahedral interstitial sites in a BCC lattice, *Scripta Metallurgica* 15 (1981) 431–435
- [Segal1981] V. M. Segal, V. I. Reznikov, A. D. Drobyshevsky, V. I. Kopylov, Plastic working of metals by simple shear, *Russian Metallurgy* 1 (1981) 99
- [Seiner2013] H. Seiner, J. Kopeček, P. Sedlák, L. Bodnárová, M. Landa, P. Sedmák, O. Heczko, Microstructure, martensitic transformation and anomalies in c' -softening in Co–Ni–Al ferromagnetic shape memory alloys, *Acta Materialia* 61 (2013) 5869-5876
- [Semenova2004] I. P. Semenova, G. I. Raab, L. R. Saitova, R. Z. Valiev, The effect of equal-channel angular pressing on the structure and mechanical behavior of Ti-6Al-4V alloy, *Materials Science and Engineering A* 387-389 (2004) 805-808
- [Smilauerova2016] J. Šmilauerová, *Phase transformations in modern titanium alloys, Doctoral Thesis*, Charles University (2016).
- [Smilauerova2017] J. Šmilauerová, M. Janeček, P. Hrcuba, J. Stráský, J. Veselý, R. Kužel, H.J. Rack, Ageing response of sub-transus heat treated Ti–6.8Mo–4.5Fe–1.5Al alloy, *Journal of Alloys and Compounds* 724 (2017) 373-380
- [Smirnova1986] N. A. Smirnova, V. I. Levit, V. I. Pilyugin, R. I. Kuznetsov, L. S. Davydova, V. A. Sazonova, Evolution of the structure of FCC single crystals subjected to strong plastic deformation, *Fizika metallov i metallovedenie* 61 (1986) 1170-1177
- [Song2011] Y. Song, E. Y. Yoon, D. J. Lee, J. H. Lee, H. S. Kim, Mechanical properties of copper after compression stage of high-pressure torsion, *Materials Science and Engineering A*, 528 (2011) 4840-4844
- [Steinmann 1998] S. G. Steinmann, Titanium--the material of choice?, *Periodontology* 2000 17 (1998) 7–21
- [Stráský2013] J. Stráský, J. Havlíková, L. Bačáková, P. Hrcuba, M. Mhaede, M. Janeček, Characterization of electric discharge machining, subsequent etching and shot-peening as a surface treatment for orthopedic implants, *Applied Surface Science* 281 (2013) 73-78
- [Tane2010] M. Tane, S. Akita, T. Nakano, K. Hagihara, Y. Umakoshi, M. Niinomi, H. Mori, H. Nakajima, Low Young's modulus of Ti–Nb–Ta–Zr alloys caused by softening in shear moduli c' and c_{44} near lower limit of body-centered cubic phase stability, *Acta Materialia* 58 (2010) 6790–6798
- [Tane2013] M. Tane, Y. Okuda, Y. Todaka, H. Ogi, A. Nagakubo, Elastic properties of single-crystalline ω phase in titanium, *Acta Materialia* 61 (2013) 7543-7554

- [Tane2016] M. Tane, K. Hagihara, M. Ueda, T. Nakano, Y. Okuda, Elastic-modulus enhancement during room-temperature aging and its suppression in metastable Ti-Nb-based alloys with low body-centered cubic phase stability, *Acta Materialia* 102 (2016) 373–384
- [Tang2000] X. Tang, T. Ahmed, H. J. Rack, Phase transformations in Ti-Nb-Ta and Ti-Nb-Ta-Zr alloys, *Journal of Materials Science* 35 (2000) 1805–1811
- [Valiev1993] R.Z. Valiev, A.V. Korznikov, R.R. Mulyukov, Structure and properties of ultrafine-grained materials produced by severe plastic deformation, *Materials Science and Engineering A* 168 (1993)141-148
- [Valiev1996] R. Z. Valiev, Y. Ivanisenko, E. F. Rauch, B. Baudelet, Structure and deformation behaviour of Armco iron subjected to severe plastic deformation, *Acta Materialia*. 44 (1996) 4705-4712
- [Valiev2000] R.Z Valiev, R.K Islamgaliev, I.V Alexandrov, Bulk nanostructured materials from severe plastic deformation, *Progress in Materials Science* 45 (2000) 103-189
- [Valiev2009] R. Z. Valiev, I.P. Semenova, V.V. Latysh, H. Rack, T.C. Lowe, J. Petruzella, L. Dluhos, D. Hrusak, J. Sochova - Nanostructured titanium for biomedical applications, *Advanced Engineering Materials* 10 (2009) B15–B17
- [Valiev2014] R.Z. Valiev, Superior strength in ultrafine-grained materials produced by SPD processing. *Materials Transactions* 55 (2014) 13-18
- [Veverkova2019] A. Veverková, J. Kozlík, K. Bartha, T. Chráska, C. A. Corrêa, J. Stráský, Mechanical Properties of Ti-15Mo Alloy Prepared by Cryogenic Milling and Spark Plasma Sintering, *Metals* 9 (2019) 1280
- [Waldner1999] P. Waldner, G. Eriksson, Thermodynamic modelling of the system titanium-oxygen, *Calphad* 23 (1999) 189–218
- [Welsch1993] G. Welsch, R. Boyer, E. W. Collings, *Materials Properties Handbook: Titanium Alloys*, ASM International, 1993
- [Xie2013] K. Xie, Y. Wang, Y. Zhao, L. Chang, G. Wang, Z. Chen, Y. Cao, X. Liao, E. Lavernia, R. Valiev, B. Sarrafpour, H. Zoellner, S. Ringer, Nanocrystalline β -Ti alloy with high hardness, low Young's modulus and excellent in vitro biocompatibility for biomedical applications, *Materials Science and Engineering C* 33 (2013) 3530-3536
- [Xu2009] W. Xu, X. Wu, M. Calin, M. Stoica, J. Eckert, K. Xia, Formation of an ultrafine-grained structure during equal-channel angular pressing of a β -titanium alloy with low phase stability, *Scripta Materialia* 60 (2009) 1012-1015
- [Yu2015] Qian Yu, Liang Qi, Tomohito Tsuru, Rachel Traylor, David Rugg, J. W. Morris Jr., Mark Asta, D. C. Chrzan, Andrew M. Minor, Origin of dramatic oxygen solute strengthening effect in titanium, *Science* (2015) Vol. 347, Issue 6222, pp. 635-639
- [Zafari2015] A. Zafari, X.S. Wei, W. Xu, K. Xia, Formation of nanocrystalline β structure in metastable beta Ti alloy during high pressure torsion: The role played by stress induced martensitic transformation, *Acta Materialia* 97 (2015) 146-155
- [Zhanal2018] P. Zhanal, P. Harcuba, M. Hajek, B. Smola, J. Stráský, J. Šmilauerová, J. Veselý, M. Janeček, Evolution of omega phase during heating of metastable beta titanium alloy Ti-15Mo, *Journal of Materials Science* 53 (2018) 837 - 845
- [Zheng2016] Y. Zheng, R. Williams, D. Wang, R. Shi, S. Nag, P. Kami, J. M. Sosa, R. Banerjee, Y. Wang, H. L. Fraser, Role of ω phase in the formation of extremely refined intragranular α precipitates in metastable β -titanium alloys, *Acta Materialia* 103 (2016) 850-858
- [Zhilyaev2008] A. P. Zhilyaev, T. G. Langdon, Using high-pressure torsion for metal processing: fundamentals and applications, *Progress in Materials Science* 53 (2008) 893-979

6. Reprints of included publications

This habilitation thesis includes two authored chapters from book *Titanium in Medical and Dental Applications* published in 2018 and 12 contributions in journals and conference proceedings published in years 2014 – 2020. This section consists of the reprints of the aforementioned publications.

- [A0] J. Stráský, M. Janeček, P. Harcuba, D. Preisler, M. Landa, *Chapter 4.2.: Biocompatible beta-Ti alloys with enhanced strength due to increased oxygen content*, in *Titanium in Medical and Dental Applications*, Editors: Francis H. Froes, Ma Qian, Woodhead Publishing in Materials, Elsevier 2018

<https://doi.org/10.1016/B978-0-12-812456-7.00017-2>

<https://www.sciencedirect.com/science/article/pii/B9780128124567000172>

- [A1] I. Kopová, J. Stráský, P. Harcuba, M. Landa, M. Janeček, L. Bačáková: *Newly developed Ti-Nb-Zr-Ta-Si-Fe biomedical beta titanium alloys with increased strength and enhanced biocompatibility*, Materials Science & Engineering C, Vol. 60, 2016, 230 -238

<https://doi.org/10.1016/j.msec.2015.11.043>

<https://www.sciencedirect.com/science/article/pii/S0928493115305786>

- [A2] J. Stráský, P. Harcuba, K. Václavová, K. Horváth, M. Landa, O. Srba, M. Janeček: *Increasing strength of a biomedical Ti-Nb-Ta-Zr alloy by alloying with Fe, Si and O*, Journal of Mechanical Behavior of Biomaterials, Vol. 71, 2017, 329 – 336

<https://doi.org/10.1016/j.jmbbm.2017.03.026>

<https://www.sciencedirect.com/science/article/pii/S1751616117301443>

- [A3] D. Preisler, J. Stráský, P. Harcuba, F. Warchomicka, M. Janeček, *Enhancing mechanical properties and microstructure of Ti-Nb-Zr-Ta-O biomedical alloy through hot working*. Acta Physica Polonica A, Vol. 134 (2018)

<https://doi.org/10.12693/APhysPolA.134.636>

<http://przyrbwn.icm.edu.pl/APP/PDF/134/app134z3p05.pdf>

- [A4] J. Stráský, D. Preisler, K. Bartha, M. Janeček, *Manufacturing of Biomedical Ti-Based Alloys with High Oxygen Content and Various Amount of Beta-Stabilizing Elements*, Materials Science Forum, Conference proceedings: Thermec 2018, Paris
<https://doi.org/10.4028/www.scientific.net/MSF.941.2471>
<https://www.scientific.net/MSF.941.2471>
- [A5] D. Preisler, M. Janeček, P. Hrcuba, J. Džugan, K. Halmešová, J. Málek, A. Veverková, J. Stráský, *The Effect of Hot Working on the Mechanical Properties of High Strength Biomedical Ti-Nb-Ta-Zr-O Alloy*, Materials 12 (2019) 4233
<https://doi.org/10.3390/ma12244233>
<https://www.mdpi.com/1996-1944/12/24/4233>
- [B0] J. Stráský, M. Janeček, I. Semenova, J. Čížek, K. Bartha, P. Hrcuba, V. Polyakova, S. Gatina, *Microstructure and lattice defects in ultrafine grained biomedical $\alpha+\beta$ and metastable β Ti alloys*, in: Titanium in Medical and Dental Applications, ed. F. Froes, M. Qian, pp. 455-475 (2018)
<https://doi.org/10.1016/B978-0-12-812456-7.00020-2>
<https://www.sciencedirect.com/science/article/pii/B9780128124567000202>
- [B1] M. Janeček, J. Stráský, J. Čížek, P. Hrcuba, K. Václavová, V.V. Polyakova, I.P. Semenova: *Mechanical properties and dislocation structure evolution in Ti6Al7Nb alloy processed by high pressure torsion*, Metallurgical and Materials Transactions, Vol. 45A, 2014, 7 – 15.
<https://doi.org/10.1007/s11661-013-1763-2>
<https://link.springer.com/article/10.1007/s11661-013-1763-2>
- [B2] J. Stráský, P. Hrcuba, M. Hájek, K. Václavová, P. Zháňal, M. Janeček, V. Polyakova, I. Semenova: *Microstructure evolution in ultrafine-grained Ti and Ti-6Al-7Nb alloy processed by severe plastic deformation*, NanoSPD6, IOP Conference Series: Materials Science and Engineering, Vol. 63, 2014, pp. UNSP 012072.
<https://doi.org/10.1088/1757-899X/63/1/012072>
<https://iopscience.iop.org/article/10.1088/1757-899X/63/1/012072>

- [B3] K. Bartha, P. Zháňal, J. Stráský, J. Čížek, M. Dopita, F. Lukáč, P. Hrcuba, M. Hájek, V. Polyakova, I. Semenova, M. Janeček: *Lattice defects in severely deformed biomedical Ti-6Al-7Nb alloy and thermal stability of its ultra-fine grained microstructure*, Journal of Alloys and Compounds, Vol. 788, 2019, pp. 881-890
<https://doi.org/10.1016/j.jallcom.2019.02.173>
<https://www.sciencedirect.com/science/article/abs/pii/S0925838819306255>
- [B4] K. Václavová, J. Stráský, V. Polyakova, J. Stráská, J. Nejezchlebová, H. Seiner, I. Semenova, M. Janeček: *Microhardness and microstructure evolution of ultra-fine grained Ti-15Mo and TIMETAL LCB alloys prepared by high pressure torsion*, Materials Science and Engineering A Vol. 682, 2017, pp. 220-228
<https://www.sciencedirect.com/science/article/abs/pii/S0921509316313892>
<https://doi.org/10.1016/j.msea.2016.11.038>
- [B5] K. Bartha, A. Veverková, J. Stráský, J. Veselý, P. Minárik C.A. Corrêa, V. Polyakova, I. Semenova, M. Janeček, *Effect of the severe plastic deformation by ECAP on microstructure and phase transformations in Ti-15Mo alloy*, Materials Today Communications 22 (2020) 100811
<https://doi.org/10.1016/j.mtcomm.2019.100811>
<https://www.sciencedirect.com/science/article/pii/S235249281931308X>
- [B6] K. Bartha, J. Stráský, A. Veverková, P. Barriobero-Vila, F. Lukáč, P. Doležal, P. Sedlák, V. Polyakova, I. Semenova, M. Janeček, *Effect of the High-Pressure Torsion (HPT) and Subsequent Isothermal Annealing on the Phase Transformation in Biomedical Ti15Mo Alloy*, Metals 9 (2019) 1194
<https://doi.org/10.3390/met9111194>
<https://www.mdpi.com/2075-4701/9/11/1194>
- [B7] R. Z. Valiev, E. A. Prokofiev, N. A. Kazarinov, G. I. Raab, T. B. Minasov, J. Stráský, *Developing nanostructured Ti alloys for innovative implantable medical devices*, Materials 13 (2020) 967
<https://doi.org/10.3390/ma13040967>
<https://www.mdpi.com/1996-1944/13/4/967/htm>

Biocompatible beta-Ti alloys with enhanced strength due to increased oxygen content

4.2

J. Stráský*, M. Janeček*, P. Harcuba*, D. Preisler*, M. Landa†

*Charles University, Prague, Czech Republic, †Institute of Thermomechanics, Academy of Sciences, Prague, Czech Republic

4.2.1 Introduction

In commercially pure Ti (α -Ti), oxygen content significantly affects the strength of the material [1]. Depending on the amount of oxygen, commercially pure Ti is divided into four grades. The strongest, Grade 4, contains 0.4 wt% of oxygen. It is known that oxygen content exceeding 0.4 wt% leads to embrittlement [2]. This is caused by immobilization of dislocations by interstitial oxygen atoms [3].

Excessive oxygen content is a serious concern in the casting and processing of Ti alloys, including high strength metastable β -Ti alloys used in the aerospace industry. These alloys are used in fully aged $\alpha + \beta$ condition and excessive oxygen content reduces the ductility due to the brittleness of the α phase. On the other hand, β -Ti alloys for biomedical use should be used in a pure β condition due to lower elastic modulus of the β phase. It was found that bcc β phase accommodates higher amounts of oxygen without deterioration of ductility. This chapter aims to review the outstanding properties of biomedical Ti alloys with increased oxygen content.

An apparent effect of oxygen on the strength of the biomedical Ti-35.3Nb-7.3Zr-5.7Ta (TNTZ) alloy is shown in Fig. 4.2.1. Three alloys were prepared by arc melting and tested in tension. The oxygen content was 0.06O (TNTZ), 0.35O (TNTZ+0.4O), and 0.66O (TNTZ+0.7O) in weight %. One can see in Fig. 4.2.1 that both the yield stress and the ultimate tensile strength (UTS) are more than doubled by the addition of 0.7 wt% of oxygen content without sacrificing the ductility.

4.2.1.1 Oxygen as an interstitial element in bcc materials

Oxygen atoms in titanium and titanium alloys occupy interstitial positions. There are tetrahedral voids with $r_{\text{void}}/r_{\text{atom}} = 0.225$ ratio and larger octahedral voids with $r_{\text{void}}/r_{\text{atom}} = 0.414$ in a hexagonal closed packed structure (α -Ti). Oxygen atoms occupy larger octahedral sites surrounded by six titanium atoms [1]. In a body-centered cubic structure (β -Ti), tetrahedral sites are bigger than octahedral ones with $r_{\text{void}}/r_{\text{atom}} = 0.291$, and 0.155, respectively [4]. It is well known that interstitial carbon atoms in bcc Fe occupy octahedral sites; it was also proven that O occupies octahedral

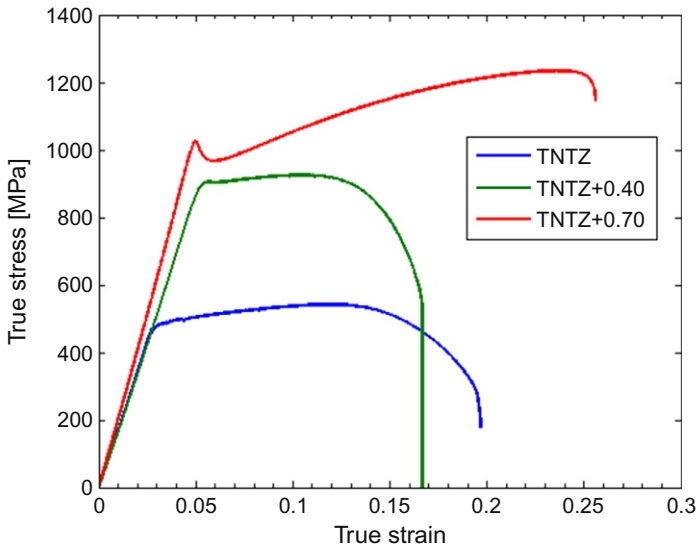


Fig. 4.2.1 Tensile properties of Ti-35.3Nb-7.3Zr-5.7Ta alloys with different oxygen content.

sites in bcc vanadium [5]. Also O in Ti is believed to be in octahedral sites, which also follows from thermodynamic and first principle calculations [6,7].

Oxygen atoms (along with carbon and nitrogen atoms) are considered to be “heavy” interstitials and to induce anisotropic elastic dipoles with tetragonal symmetry [8]. In other words, an interstitial atom in an octahedral void is closer to two of its neighbors and causes an asymmetric distortion of the lattice. Two interesting consequences follow from this fact.

Firstly, there are three groups of octahedral sites with equal distribution of the interstitial atoms. However, the application of stress leads to a redistribution of interstitials because one group of sites is preferred. The redistribution of interstitial atoms gives rise to anelastic relaxation, which can be identified by internal friction measurements and is known as the Snoek relaxation [9,10]. Measurements of the Snoek effect allow us to determine solution-interstitial interactions. For instance, the region around the substitutional iron forbidden to oxygen was reported to extend to the second nearest neighbor [11]. Such repulsive interaction affects the solubility of interstitial atoms and may affect the elastic modulus [10,12].

Secondly, the anisotropy of lattice distortion increases interaction of interstitial atom with dislocations and promotes hardening. Therefore, the hardening by interstitial atoms is more effective in bcc alloys than in fcc materials, where the lattice distortion is isotropic. At larger solute concentrations, the interstitial atoms interact and may occupy one of three types of octahedral sites leading to long-range distortion and change of the crystal lattice from bcc to body-centered tetragonal (bct) [13]. A very hard bct phase forms due to carbon interstitials in bcc iron and is famously known as the martensite. A similar effect in bcc titanium due to oxygen interstitials has yet to be discovered.

4.2.1.2 Controlling amount of oxygen during casting

During production of titanium ingots, a large effort is put on limiting the oxygen content below a certain level. In the production of β titanium alloys, the task is usually how to add a controlled amount of oxygen during casting of the alloy from pure constituents. The most-used approach is based on dissolution of an appropriate amount of titanium dioxide in the melt [14–17]. The melting point of rutile (TiO_2) is 1855°C while other forms of TiO_2 , such as anatase and brookite, have lower melting points. These melting temperatures are much lower than the melting temperatures of other typical constituents, namely niobium and tantalum. Note that due to these alloying elements, the melting temperatures of the manufactured alloys are significantly higher than those of pure Ti. Common precautions during melting must be taken, such as processing in pure inert atmosphere, reduced contamination from a crucible [18], and patient mixing of constituents.

An alternative (and probably more commercially viable) option for manufacturing of alloys with increased oxygen content is to use an appropriate amount of low-purity Ti with high oxygen content (3 at.%) [19]. The disadvantage of this approach is that low-purity Ti usually contains not only excessive amounts of oxygen but also excessive iron and nitrogen. The former influences the stability of the β phase affecting the modulus of elasticity while the latter has a negative effect on the ductility, although technical standards restricting interstitial content of nitrogen for α -titanium (0.07 wt% N) might be unnecessarily strict for alloys used in the pure β condition. A unique approach for manufacturing of alloys with different oxygen content was presented in [20] and can be rephrased as “waiting for good fortune”: The different oxygen contents were achieved by selecting different melt batches [20].

4.2.1.3 On the design of low-modulus biocompatible β -Ti alloys—a brief overview

The outstanding properties of biomedical β titanium alloys are reviewed elsewhere in this book, namely in chapters by Dr. Carsten Siemers and Prof. Mitsuo Niinomi. Moreover, the background for designing low-modulus alloys was provided in the chapter “The Molecular Orbital Approach and its Application to Biomedical Titanium Alloy Design” by Prof. Masahiko Morinaga. In this section, the main considerations are briefly reviewed along with an overview of the most common alloying systems.

Multiple (and often contradictory) requirements include using biocompatible elements only, achieving the lowest elastic modulus possible, and simultaneously reaching sufficient strength.

Among commonly used alloying elements, Nb, Ta, Zr, and Mo are regarded as the most biocompatible ones whereas V, Cr, and Co are inappropriate [21]. The typical elastic modulus of Ti is around 100 GPa, which is the half of the elastic modulus of steel but still five times higher than the elastic modulus of the cortical bone (10–30 GPa) [22]. The elastic modulus (E) of different phases typical for various titanium alloys can be ordered as:

$$E_{\beta} \approx E_{\alpha'} \approx 60\text{--}90 \text{ GPa} < E_{\alpha} \approx 100 \text{ GPa} < E_{\omega} \approx 130\text{--}220 \text{ GPa} \quad [23\text{--}26].$$

It is now generally believed that the lowest elastic modulus can be achieved in alloys that retain pure β phase; at the same time these alloys possess a low phase stability due to “proximity” to the $\beta \rightarrow \alpha''$ martensitic transformation [27]. As discussed in [28], the phase stability is connected to the electron-per-atom ratio (e/a ratio) and the elastic modulus decreases with decreasing e/a ratio as long as the material retains a pure β phase [29]. Another approach relates the elastic modulus of Ti alloys to the bond order (Bo value) and d-electron-orbital energy (Md value) in the so-called Bo - Md diagram [30–32]. Unfortunately, the latter approach does not allow us to include the effect of oxygen directly.

In order to stabilize the β phase at room temperature in Ti alloys, an appropriate β -stabilizing element must be used. In biomedical β -Ti alloys, such alloying elements are molybdenum and niobium. Despite the fact that the only commercially used orthopedic implant made of β -Ti alloy (Stryker Accolade TMZF Femoral Hip Stem) is made from a Ti-12Mo-6Zr-2Fe alloy, the majority of developed biomedical alloys are based on the Ti-Nb system. Apart from the high biocompatibility of Nb, the Ti-Nb based alloys are less prone to the adverse formation of ω phase.

The beneficial effects of using other alloying elements such as Ta and Zr were also reported. Tantalum is another biocompatible β -stabilizing element providing some solid solution strengthening. Finally, Zr prevents formation of both the ω phase and martensite α'' phase. As a result, Ti-Nb-Ta-Zr (abbreviated as TNTZ) quaternary system provides an optimal combination of mechanical properties. Three different compositions of the TNTZ system became the most investigated: Ti-35.3Nb-5.7Ta-7.3Zr developed by American inventors [33], Ti-29Nb-13Ta-4.6Zr developed in Japan [34], and finally Ti-35Nb-2Ta-3Zr known as Gum Metal [35] (see also Table 4.2.1). All three alloys contain only the β phase at room temperature and possess the low elastic modulus due to proximity to $\beta \rightarrow \alpha''$ transformation, despite the fact that the macroscopic α'' phase does not form even during deformation (so-called stress induced martensite).

The Ti-35Nb-2Ta-3Zr-0.3O alloy famously known as Gum Metal [36] possess several unique properties, including good biocompatibility [37], a low elastic modulus, and high strength in cold-worked condition. These properties were attributed to dislocation-free plastic deformation by ideal shear, which is possible due to elastic softening and by a simultaneous increase of critical stress for the dislocation slip by interstitial oxygen [35]. This explanation supported by the observation of so-called “giant faults” by TEM [38,39] was, however, later. It is assumed that stress-induced martensite (SIM) is formed before the alloy can be deformed by ideal shear. The SIM in this particular alloy was not found before, because

Table 4.2.1 Ti-Nb-Ta-Zr based biomedical alloys

Gum Metal	Ti-35Nb-2Ta-3Zr	[35]
“Japanese” TNTZ	Ti-29Nb-13Ta-4.6Zr	[34]
“American” TNTZ	Ti-35.3Nb-5.7Ta-7.3Zr	[33]

- (i) The volume fraction of SIM is low due to the presence of oxygen that limits the α'' growth via an increase of the C' elastic constant [40].
- (ii) SIM grows only in nanodomains due to the presence of oxygen that limits the size of α'' regions [41].
- (iii) SIM is fully reversible and therefore cannot be identified after unloading [42].

As a result, Gum Metal is stronger but has a lower superelastic strain when compared to other superelastic β -Ti alloys, which undergo massive $\beta \rightarrow \alpha''$ stress-induced transformation. However, due to the low stability of the β phase, the material is elastic and a low elastic modulus of the β phase dominates over the superelastic effect.

Summary

Oxygen in bcc (β) titanium is an interstitial element and its atoms occupy octahedral interstitial positions. Oxygen causes significant interstitial strengthening. A Ti-Nb-Ta-Zr quaternary alloying system is often used for designing low-modulus biocompatible β titanium alloys. A minimum elastic modulus is achieved in alloys with low β phase stability due to the “proximity” to martensitic $\beta \rightarrow \alpha''$ transformation, which may occur either during cooling to room temperature or during deformation at room temperature (stress-induced martensite—SIM). Oxygen affects the formation of the α'' phase.

4.2.2 Effect of oxygen content on phase stability and elastic modulus in biomedical β -Ti alloys

The reason for using controlled amounts of oxygen as an “alloying element” is simple—oxygen affects mechanical properties of biomedical β -Ti alloys. Two major mechanisms were outlined in the previous section:

- (a) Oxygen atoms cause strong interstitial strengthening.
- (b) Oxygen affects phase composition and phase stability, which subsequently influences the elastic modulus of the material.

In this section, the particular effects of oxygen on the phase composition and phase stability are reviewed, followed by discussion on the influence of oxygen on the elastic modulus. The strengthening effect of oxygen is reviewed at the end of this section.

4.2.2.1 Effect of oxygen on phase stability

4.2.2.1.1 Oxygen and α phase

Oxygen is an α stabilizing element. Increased oxygen content significantly increases the β transus temperature in pure Ti [7] and in (metastable) β -Ti alloys. The β transus temperature was determined in the Ti-29Nb-13Ta-4.6Zr alloy with 0.14, 0.33, and 0.70 wt% of oxygen. The alloy was annealed at different temperatures for 3 days and water quenched. Optical microscopy revealed α phase particles, which

disappeared after annealing at temperatures higher than the β transus temperature. It was found that β transus temperature equals to $(429 O + 619)^\circ\text{C}$ where O is oxygen content in wt% [2].

The diffusion of oxygen atoms into α phase in alloys with two-phase $\alpha + \beta$ composition also demonstrates the α stabilizing ability of oxygen. Direct proof of this fact was obtained by a 3D atom probe tomography in Refs. [43,44].

The α stabilizing effect of oxygen can also be traced after aging of metastable β -Ti alloys, provided that temperatures are sufficient for α phase particle precipitation (typically $>400^\circ\text{C}$) but still below the β transus temperature. It was found that oxygen slightly increases both the volume fraction and the size of α phase particles after aging the Ti-29Nb-13Ta-4.6Zr alloy at 450°C [16]. On the other hand, the α stabilizing effect of oxygen was not seen after annealing at $850^\circ\text{C}/30\text{min}$ of Ti-30Nb-12Zr-(0.08–0.50)O alloys. It is argued that the annealing temperature of 850°C might have been just around the β transus temperature even for the alloy with the highest oxygen content [45]. On the other hand, the same study showed that 0.49 wt% of nitrogen increased the β transus temperature to a temperature $>850^\circ\text{C}$ and α phase is present. It is therefore suggested that the α stabilizing effect of oxygen is weaker than that of nitrogen [45].

4.2.2.1.2 Oxygen and ω phase

The ω phase is a hexagonal phase (but not hexagonal close packed) that is present in various bcc metals including many β -Ti alloys [46]. The ω phase is formed upon quenching by a diffusionless displacive transformation [47,48]. The transformation can be described as a collapse of two neighboring $(111)_\beta$ planes into a single one. Such hexagonal structure is coherent with the parent β phase [49]. This displacive $\beta \rightarrow \omega$ transformation is completely reversible at low temperatures at which diffusion does not play a role. This ω phase is often referred to as the athermal ω phase (ω_{ath}). The particles of the ω phase further evolve and grow during aging through a diffusion-controlled reaction [50]. This process is irreversible and is accompanied by the rejection of β stabilizing elements from the ω phase. This ω phase is referred to as the isothermal ω phase (ω_{iso}).

It is widely agreed that interstitial oxygen suppresses the diffusionless $\beta \rightarrow \omega_{\text{ath}}$ transformation. In an extensive TEM study of Ti-(17–19V)-(0.025–0.125)O alloys, Paton and Williams [51] showed that the ω_{ath} -start temperature decreases below the room temperature with increased oxygen content. Furthermore, oxygen creates a hysteresis of the nondiffusional $\beta \leftrightarrow \omega_{\text{ath}}$ transformation, suggesting that interstitial oxygen pins linear defects required for this shuffle transformation. This hypothesis is supported by theoretical considerations in [47,49], assuming that the collapse of atomic planes associated with ω_{ath} can be hindered by interstitial atoms.

A reduced amount of ω_{ath} due to increased oxygen content was also observed in solution-treated Ti-(11–12)Cr-(0.2–0.6)O alloys [18,52]. Furthermore, selected alloys were subjected to intensive cold-rolling. Selected area electron diffraction (SAED) in TEM proved that cold-rolling is responsible for the formation of the deformation-induced ω phase, the amount of which decreases with increasing oxygen

content [18,53]. The deformation-induced ω phase increases the elastic modulus and therefore the elastic modulus in the studied alloys can be varied by cold rolling [18,53]. Unfortunately, the lowest achieved elastic modulus values are around 80 GPa.

The evolution of the ω_{iso} phase is associated with the diffusion of β stabilizing elements from ω_{iso} particles while α stabilizing elements (and also Ti atoms) diffuse from the β matrix into ω_{iso} particles. It is natural to assume that oxygen as an α stabilizing element diffuses into ω_{iso} particles, but direct supporting evidence was delivered only recently using a 3D atom probe (atom probe tomography) in [44]. Two alloys with different oxygen content—Ti-29Nb-13Ta-4.6Zr-0.1O and Ti-29Nb-13Ta-4.6Zr-0.4O—were subjected to annealing at 300°C/72 h, which is ideal for ω_{iso} phase evolution without α phase precipitation. A higher-volume fraction of the ω_{iso} phase was found in the alloy with higher oxygen content. Furthermore, after the second step of annealing at 450°C/24 h, ω_{iso} was present only in the alloy with higher oxygen content. It is therefore suggested that oxygen extends the stability of the ω_{iso} phase to higher temperatures [44].

Conversely, in another recent study [54] oxygen atoms are claimed to cluster at the $\beta/\omega_{\text{iso}}$ interface and to be responsible for precipitation of α phase platelets just next to ellipsoidal ω particles. Finally, under the coexistence of all three β , α , and ω_{iso} phases, oxygen seems to predominantly stabilize the α phase and therefore the overall ω_{iso} content is decreased due to oxygen in Ti-35Nb-5Ta-7Zr-(0.06–0.68)O [55].

4.2.2.1.3 Oxygen and α'' phase

Understanding the relationship between oxygen content and martensitic $\beta \rightarrow \alpha''$ transformation seems to be crucial for designing low-modulus alloys with increased oxygen content.

α'' is an orthorhombic martensitic phase formed by lattice displacement, which significantly affects the geometry of the octahedral interstitial positions [41,56,57].

An assertion that oxygen prevents the formation of the α'' phase in Ti-Nb-based alloys is based on numerous experimental studies reviewed below and also supported by first principles theoretical studies [56,58]. In competition between β and α'' phases, interstitial oxygen acts as a β stabilizing element and shifts the martensite start temperature of α'' (M_s) to lower temperatures, as documented in Ti-(32–36)Nb-2Ta-3Zr-(0.3–0.5)O [59] or in Ti-35Nb-2Ta-3Zr-(0.09–0.51)O single crystals [60]. Interstitial oxygen has therefore a similar effect on the M_s of α'' phase as substitutional zirconium atoms [61]. Moreover, first principles calculations indicated that Zr-O bonding is energetically favorable and leads to Zr-O nanoclustering, which was confirmed experimentally by 3D atom-probe tomography. Consequently, the coexistence of Zr substitutional atoms and oxygen interstitial atoms improves the elastic stability of the β phase in Gum Metal [62].

Alloys with increased oxygen content are often developed from benchmark low-modulus alloys in which substitutional β stabilizing elements are finely tuned to allow for superelastic behavior at room temperature. The formation of SIM by $\beta \rightarrow \alpha''$ martensitic transformation, which is fully reversible upon unloading, causes a very high nonlinear recoverable strain referred to as superelastic behavior. Once oxygen is

added to such finely tuned superelastic alloys, the β stability is enhanced and the SIM formation is either fully or partially suppressed.

In Ti-30Nb-12Zr-(0.08–0.50)O alloys, already 0.20 wt% of oxygen completely suppresses the double yielding behavior, which is typical for SIM transformation during loading [45]. In a Ti-37Nb benchmark alloy, 0.28 wt% of added oxygen postpones SIM transformation to higher strength levels [57]. As described in [20], interstitial oxygen atoms reduce the nonlinear recoverable strain by two mechanisms

- (a) Raising the critical stress for α'' formation and reducing ultimate α'' volume fraction.
- (b) Reducing the transformation strain of displacive $\beta \rightarrow \alpha''$ transformation due to structural convergence of parent β and martensite α'' phases with increased interstitial content.

As the result, the stress plateau that is typical for superelastic behavior is shifted to higher stress levels closer to the critical stress for common dislocation slip. Simultaneously, the stress plateau is shorter (in strain) due to lower transformation strains. Both effects contribute to diminishing the double yielding behavior with increasing interstitial oxygen content [20].

The β stabilizing effect of oxygen was used in cold-rolled Ti-38Nb-0.14O alloys, in which oxygen postpones the SIM transformation to high stress values. In such alloys, the stability of the β phase at room temperature is very low (i.e., very close to $\beta \rightarrow \alpha''$ transformation). As a result, the elastic modulus of the β phase is very low and can be tuned by oxygen content [63]. A Ti-38Nb-0.14O alloy after 90% of cold rolling achieves an elastic modulus of only 54 GPa without apparent SIM transformation [17].

Note that stabilization of the β phase by oxygen has only been rarely studied in alloys with oxygen content >0.5 wt%.

4.2.2.2 Oxygen and elastic modulus

Elastic deformation is conventionally defined as a reversible deformation. Elastic deformation in metals commonly occurs by (small) changes in the shape of the atomic lattice (mainly by shear). Such elastic deformation is linear and therefore obeys the Hooke's law, which allows the determination of Young's modulus (in this chapter simply referred to as "elastic modulus"). An alternative mechanism of reversible deformation is a reversible martensitic transformation—the formation and vanishing of SIM upon loading and unloading, respectively—referred to as pseudoelasticity or superelasticity. Such reversible deformation is nonlinear and the elastic modulus cannot be unambiguously determined.

The "true" Young's modulus (elastic modulus) unaffected by martensitic transformation can be evaluated by resonance techniques—namely by the electromagnetic acoustic resonance (EMAR) [64] and resonant ultrasound spectroscopy [65]. On the other hand, the determination of the elastic modulus from tensile tests often leads to underestimated values due to the deformation of the tensile machine and possible SIM formation.

The relation between oxygen content and the resulting linear elastic deformation of a Ti alloy is predominantly related to the phase composition and stability of particular phases. The formation of α and ω_{iso} phases should be avoided due to their high elastic

modulus. Both phases are formed during annealing by the diffusion transformation; oxygen contributes to their stabilization and may increase their volume fraction [16,44].

The elastic modulus of bcc material strongly depends on the number of valence electrons per atom (e/a ratio). For instance, the elastic modulus of bcc chromium or molybdenum having 6 valence electrons is close to 300 GPa while the elastic modulus of vanadium and niobium with 5 valence electrons is 128 and 105 GPa, respectively. The elastic modulus of the bcc β phase further decreases with a decreasing e/a ratio until approximately $e/a = 4.2$, when the bcc β phase loses its stability and transforms by displacive transformation to α'' martensite or partially to ω_{ath} , depending on the type of alloying elements. However, it is not clear how to include interstitial oxygen into the e/a ratio calculation. One approach is to include six valence electrons per oxygen atom into the sum of electrons (e), but not to include oxygen atoms into the sum of atoms (a) because interstitial atoms do not occupy lattice positions. This approach is consistent with calculations of valence electron concentration (VEC) which subsequently affects bulk moduli [66]. However, the effect of oxygen on the e/a ratio is often completely neglected in the reports on low-modulus β -Ti alloys [35,67].

However, the elastic modulus cannot be estimated directly from the e/a ratio [27,68]. Anomalous softening of elastic constants (namely c_{44}) can be explained by features in the electron band structure in the immediate vicinity of the Fermi level as determined for Nb-based alloys in [69,70]. The contribution of interstitial oxygen to bonding, the Fermi level, the density of states at the Fermi level, and consequently to elastic constants unfortunately remains for such complicated alloying systems unknown [71].

The relationship between the elastic modulus and the proximity to martensitic transformation is described by the measurement of temperature evolution of the elastic modulus in the range of 200–300 K [27]. The temperature corresponding to the minimum in elastic modulus increases with decreasing Nb content, suggesting that β stabilizing niobium shifts the M_s temperature associated with the lowest elastic modulus to lower temperatures. Similar measurement in the same temperature range was performed for three Ti-35-2Ta-3Zr-based alloys containing 0.09, 0.36, and 0.51 wt% oxygen [67]. In the 0.09 O alloy, the elastic modulus increases with decreasing temperature below RT. This alloy contains both β and α'' phases and with decreasing temperature, the volume fraction of stiffer α'' (and even ω_{ath}) increases. On the other hand, in 0.36 and 0.51 O alloys, the M_s temperature is shifted far below room temperature. Therefore, the elastic modulus decreases with decreasing temperature, which is explained by the decreasing stability of the β phase [67]. The same alloys were subjected to cold rolling, which caused an increase in the elastic modulus due to deformation induced α'' and ω_{ath} . However, the increase in the elastic modulus due to cold rolling was the smallest in the alloy with the highest oxygen content, because oxygen reduced the amount of newly formed stiff phases.

The anisotropy of the elastic modulus was measured by EMAR and RUS in single crystals of biomedical β -Ti alloys. The lowest elastic modulus of 35 GPa was found in direction $\langle 100 \rangle$ in the Ti-29Nb-13Ta-4.6Zr alloy while in the direction $\langle 111 \rangle$, the

elastic modulus reached 80 GPa [68]. A less-stabilized Ti-25Nb-13Ta-5Zr alloy exhibits qualitatively similar anisotropy but a higher stiffness due to ω_{ath} particles [68]. The results are consistent with a detailed study on the Ti-15Mo alloy [24]. The elastic modulus was determined in three different directions in the Ti-36Nb-2Ta-3Zr-0.3O alloy single crystal by tensile tests [72]. The softest direction was again $\langle 100 \rangle$ (40 GPa) while the stiffest one (85 GPa) is $\langle 111 \rangle$. Note that SIM was observed in the $\langle 110 \rangle$ direction (the initial elastic modulus before the SIM was 60 GPa) while it was absent in other directions. The results on single crystals indicate that the strong texture of polycrystalline material would affect the elastic modulus of the material via the anisotropy of the bcc β phase and possible anisotropy of the SIM formation. A detailed investigation is, however, not available.

Summary

Oxygen increases the temperature range of stability of α and ω_{iso} phases and stabilizes them by diffusion. On the other hand, interstitial oxygen atoms prevent the formation of ω_{ath} and α'' phases by displacive transformations. A martensite start temperature of $\beta \rightarrow \alpha''$ transformation is shifted to lower temperatures and the formation of SIM is either fully suppressed or postponed to higher stress levels due to oxygen. Such β stabilizing effects of oxygen lead to an increase in elastic modulus.

4.2.3 Effect of oxygen on strength

Oxygen significantly increases the strength of the bcc β phase by interstitial strengthening. The relative magnitude of the effect is comparable to the effect of oxygen content of commercially pure Ti (Grades 1–4). Interstitial oxygen atoms create a Cottrell atmosphere around edge dislocations and a Snoek atmosphere around screw dislocations while acting as obstacles for dislocation motions [2,9,73].

Table 4.2.2 presents an overview of the mechanical properties of Ti-Nb-based biomedical β -Ti alloys focusing on the effect of oxygen content. As discussed above, a low elastic modulus is achieved when the precipitation of α and ω_{iso} phases during aging is avoided. Therefore, Table 4.2.2 includes only alloys after solution treatment and eventual cold working. The third column in Table 4.2.2 shows whether the SIM formation occurs in the material during a tensile test. Note that if SIM is present, then both the elastic modulus and yield stress are not properly defined. The elastic modulus is usually determined from the initial stage of the deformation and the yield stress is resolved as the first deviation from linearity (therefore associated with SIM formation rather than the dislocation slip).

The effect of oxygen on mechanical properties is rather complex. Several mechanisms of plastic deformation—namely the slip, twinning, SIM α'' , and stress-induced ω_{ath} —can operate in a single alloy [74]. The dominant mechanisms of plastic deformation change with increasing content of oxygen and of other alloying elements, previous thermomechanical treatment, and even during tensile plastic deformation.

Table 4.2.2 Overview of mechanical properties of Ti-Nb-based biomedical alloys with increased oxygen content

Composition (wt%)	Oxygen (wt%)	SIM	Elastic modulus	Yield stress (MPa)	UTS (MPa)	Elong. (%)	Thermomechanical treatment	Ref.
Ti-35Nb-5.7Ta-7.3Zr	0.06	NO	–	530	590	21	ST 850°C 1h WQ	[75]
Ti-35Nb-5.7Ta-7.3Zr	0.46	NO	–	937	1014	19	ST 850°C 1h WQ	[75]
Ti-35Nb-5.7Ta-7.3Zr	0.68	NO	–	1081	1097	21	ST 850°C 1h WQ	[75]
Ti-29Nb-13Ta-4.6Zr	0.12	NO	58	500	600	27	ST 790°C 1h WQ	[16]
Ti-29Nb-13Ta-4.6Zr	0.20	NO	70	600	700	20	ST 800°C 1h WQ	[16]
Ti-29Nb-13Ta-4.6Zr	0.42	NO	75	840	900	17	ST 820°C 1h WQ	[16]
Ti-35Nb	0	YES	–	350	500	38	CR (98.5%)+ST 900°C 0.5h WQ	[76]
Ti-35Nb	0.14	YES	–	170	700	27	CR (98.5%)+ST 900°C 0.5h WQ	[76]
Ti-35Nb	0.28	YES	–	350	850	27	CR (98.5%)+ST 900°C 0.5h WQ	[76]
Ti-35Nb	0.41	YES	–	450	900	9	CR (98.5%)+ST 900°C 0.5h WQ	[76]
Ti-35Nb	0.55	YES	–	500	1050	6	CR (98.5%)+ST 900°C 0.5h WQ	[76]
Ti-36Nb	0.04	YES	–	180	250	–	CR (98.5%)+ST 900°C 0.5h WQ	[57]
Ti-36Nb	0.28	YES	–	350	500	–	CR (98.5%)+ST 900°C 0.5h WQ	[57]
Ti-38Nb	0	YES	60	300	445	32	CR (90%)+ST 850°C 0.5h WQ	[17]
Ti-38Nb	0.14	YES	54	665	810	21	CR(90%)+ST 850°C 0.5h WQ	[17]
Ti-30Nb-2Ta-3Zr	0.49	YES	58	–	1500	8	Hot rolled + cold worked (90%)	[59]
Ti-33Nb-2Ta-3Zr	0.49	NO	50	–	1250	14	Hot rolled + cold worked (90%)	[59]
Ti-36Nb-2Ta-3Zr	0.47	NO	60	–	1100	15	Hot rolled + cold worked (90%)	[59]
Ti-30Nb-12Zr	0.08	YES	67	–	545	48	ST 850°C 0.5h WQ	[45]
Ti-30Nb-12Zr	0.20	NO	67.4	–	675	37	ST 850°C 0.5h WQ	[45]
Ti-30Nb-12Zr	0.29	NO	68.2	–	720	30	ST 850°C 0.5h WQ	[45]
Ti-30Nb-12Zr	0.37	NO	68.9	–	850	25	ST 850°C 0.5h WQ	[45]
Ti-30Nb-12Zr	0.50	NO	72	–	995	18	ST 850°C 0.5h WQ	[45]

Continued

Table 4.2.2 Continued

Composition (wt%)	Oxygen (wt%)	SIM	Elastic modulus	Yield stress (MPa)	UTS (MPa)	Elong. (%)	Thermomechanical treatment	Ref.
Ti-35Nb-2Ta-3Zr	0.26	NO	65	650	750	17	ST 780°C 30 min AC	[77]
Ti-35Nb-2Ta-3Zr	0.38	NO	59	750	770	10	ST 780°C 30 min AC	[77]
Ti-35Nb-2Ta-3Zr	0.52	NO	60	800	840	4	ST 780°C 30 min AC	[77]
Ti-35Nb-2Ta-3Zr	0.59	NO	90	860	883	1	ST 780°C 30 min AC	[77]
Ti-35Nb-2Ta-3Zr	0.14	YES	60	350	600	21	Hot rolled + ST 730°C 1 h WQ	[2]
Ti-35Nb-2Ta-3Zr	0.33	NO	65	700	800	13	Hot rolled + ST 810°C 1 h WQ	[2]
Ti-35Nb-2Ta-3Zr	0.70	NO	75	1050	1050	19	Hot rolled + ST 970°C 1 h WQ	[2]
Ti-35Nb-2Ta-3Zr	0	YES	55	280	400	33	ST 850°C 0.5h WQ	[14]
Ti-35Nb-2Ta-3Zr	0.32	NO	60	830	880	12	ST 850°C 0.5h WQ	[14]
Ti-35Nb-2Ta-3Zr	0.44	YES	45.3	880	940	5	Cold-worked (96%)	[78]

Table 4.2.3 The effect of cold working on strength in the Ti-35Nb-2Ta-3Zr-0.32O alloy [19]

Elastic modulus (GPa)	Yield stress (MPa)	Elongation (%)	Cold working
70	750	18	0%
60	900	10	20%
58	900	10	40%
55	900	10	60%
55	950	10	80%
55	1050	10	90%

The strength values in [Table 4.2.2](#) unambiguously document the strength enhancement by oxygen. UTS exceeds 800MPa in all alloys with oxygen content around 0.4wt%. A positive effect of combining Zr and O on strength can be also revealed.

Cold working—usually either cold rolling (CR) or rotary swaging—is beneficial for strength enhancement due to induced deformation and microstructural refinement as well as for decreasing the elastic modulus, arguably due to the crystallographic texture. The direct effect of cold rolling in the Ti-35Nb-2Ta-3Zr-0.32O alloy is demonstrated in [Table 4.2.3](#) [19]. On the other hand, cold rolling without subsequent solution treatment reduces the total plastic elongation.

Material ductility generally decreases with increasing oxygen content [45,76] and especially the low elongation values reported in [77] were attributed to intergranular failure, which may be caused by oxygen segregation at grain boundaries. However, nitrogen content, which deteriorates the ductility of β -Ti alloys, is not quoted in [77].

Despite the fact that oxygen content reduces the ductility, two exceptions can be found in [Table 4.2.2](#)—for alloys with oxygen content higher than 0.6wt%. In the Ti-35Nb-5.7Ta-7.3Zr alloy [75] and the Ti-35Nb-2Ta-3Zr alloy [2], the elongation was found to increase when the oxygen content was increased from approx. 0.3wt% and 0.7wt%. The reason is described in [2] and can be seen in [Fig. 4.2.1](#) in the introduction to this chapter. When the oxygen content exceeds a certain level (approx. 0.6wt%), the material exhibits significant work hardening. Work hardening suppresses the premature necking and higher plastic elongation is achieved. Moreover, in the flow curves (see [Fig. 4.2.1](#)), the sharp-yield point is observed, which demonstrates the interaction between the atmosphere of interstitial oxygen atoms and dislocations in the alloys.

Ti-35Nb-5.7Ta-7.3Zr alloys with increased oxygen content, high strength, and high ductility were recently studied by the authors of this chapter; the main results are presented in the following section.

Summary

Oxygen significantly increases the strength by interstitial strengthening, but generally leads to some reduction in ductility. In alloys exhibiting SIM formation, the yield stress defined as the deviation from the linear deformation is usually low. Cold rolling

increases the strength of the material but usually reduces the elongation. The yield stress of 800 MPa is achievable by 0.4 wt% of oxygen. Even higher yield stress levels are found in alloys with 0.7 wt% oxygen. These alloys also exhibit enhanced elongation due to work hardening during tensile straining.

4.2.4 The case study: The Ti-Nb-Zr-Ta-O alloy for load-bearing implant manufacturing

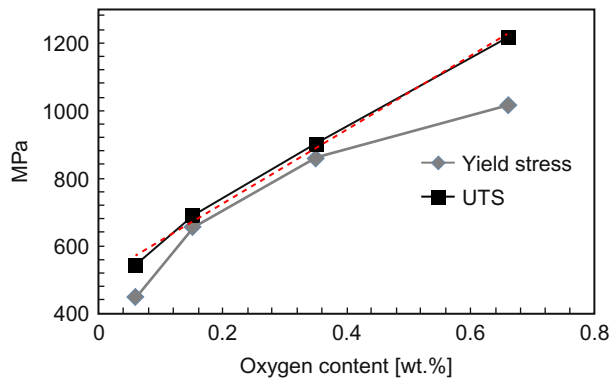
A laboratory amount of Ti-35.3Nb-5.7Ta-7.3Zr-based alloys was cast by arc melting with appropriate TiO₂ addition to achieve the final oxygen content of 0.06, 0.15, 0.35, and 0.66 wt%. The as-cast material was subsequently hot forged at approximately 1100°C. Tensile tests performed at room temperature indicated the apparent strength enhancement by oxygen. Fig. 4.2.2 shows that true yield stress increased from 400 MPa to almost 1000 MPa and seems to saturate with increasing O content while the UTS increases almost linearly. The difference between yield stress and UTS indicates clearly that the alloy with 0.66 exhibits significant work hardening (see also Fig. 4.2.1).

4.2.4.1 Alloy manufacturing

Based on achieved results, the Ti-35.3Nb-5.7Ta-7.3Zr-0.7O alloy was selected for larger-scale manufacturing. The alloy was prepared at Retech Co. by plasma-arc melting of pure elements and TiO₂ to produce small compacts (approx. 150 g). These compacts were subsequently remelted by sequential pour melting; ingots with the diameter of 50 mm and the length of 1 m were prepared.

The as-cast material was subsequently processed by two different industrial techniques. A hip implant semiproduct was successfully manufactured by die forging of the as-cast material heated to 1100°C. Another piece of as-cast material was processed by hot rolling of the material heated to 1200°C. In both cases, the material was water quenched after the last processing step.

Fig. 4.2.2 The evolution of the yield stress and the ultimate tensile strength (UTS) with increasing oxygen content in Ti-35.3Nb-5.7Ta-7.3Zr-based alloys.



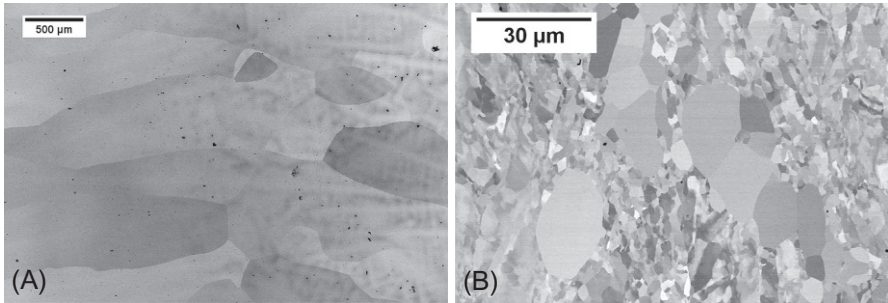


Fig. 4.2.3 (A) Ti-35.3Nb-5.7Ta-7.3Zr-0.7O alloy as cast. (B) Ti-35.3Nb-5.7Ta-7.3Zr-0.7O alloy, die forged.

4.2.4.2 Microstructure

The microstructure of as-cast material is shown in Fig. 4.2.3A. The very coarse grain structure of pure β -Ti phase contains micropores (black spots) and chemical inhomogeneity due to the lack of homogenization treatment on the right side of the image.

The microstructure after die forging is significantly refined and partly recrystallized as depicted in Fig. 4.2.3B. Pores could not be found (rare black spots are remnants from polishing as evidenced by more detailed observations).

4.2.4.3 Mechanical properties

Elastic moduli of as-cast alloys with 0.06, 0.35, and 0.66 wt% O determined by resonant ultrasound spectroscopy are 63, 81, and 80 GPa, respectively. The increase of elastic modulus is attributed to the stabilization of the β phase.

Typical flow curves (selected out of three samples per condition) of the as-cast, the as-(die)-forged and the as-rolled material are shown in Fig. 4.2.4. The yield stress of

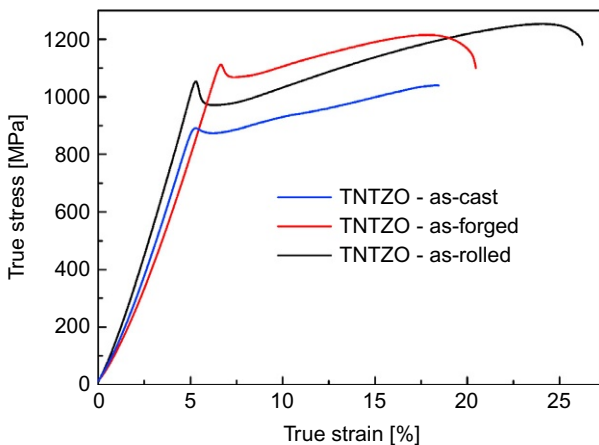


Fig. 4.2.4 Flow curves of Ti-35.3Nb-5.7Ta-7.3Zr-0.7O in different processing conditions.

the hot-worked material is significantly increased while the difference between the die-forged and rolled conditions is insignificant. All specimens exhibited an apparent sharp-yield point but it was more pronounced in hot-worked ones, which suggested that oxygen atoms clustered around dislocations during hot working. Elongation is also slightly increased by hot working; in particular, as-cast material fails without significant necking.

4.2.4.4 The applicability of the developed alloy for load-bearing implant manufacturing

A reduced elastic modulus and high biocompatibility [79] are the key advantages of a developed alloy as compared to the common Ti-6Al-4V alloy. The developed TNTZO alloy exhibits sufficient strength and ductility at room temperature to be used for orthopedic implants of big joints. The initial as-cast material prepared by sequential pour melting has sufficient dimensions while preliminary tests indicate that hot formability allows cost-effective implant manufacturing. The key requirement for implant material—the fatigue performance—has, however, not yet been mentioned throughout this chapter. Fatigue tests indicate that there is only a limited correlation between material performance under static and dynamic loading. The fatigue performance of the as-cast condition was found to be inferior to hot-worked conditions. The complete understanding of the relation between the processing, the microstructure, and fatigue performance is yet unclear.

Summary

A Ti-35.3Nb-5.7Ta-7.3Zr-0.7O alloy was manufactured in the form of a rod with the diameter of 50mm. The material was successfully hot rolled and also die forged. Resulting hot worked conditions exhibit the high strength (>1000MPa) and satisfactory elongation (>15%).

4.2.5 The applicability of biomedical β -Ti alloys with increased oxygen content in orthopedics

Biomedical β -Ti alloys with increased oxygen content simultaneously achieve low elastic modulus, high strength, and sufficient ductility. It is assumed that oxygen does not deteriorate material biocompatibility, which has been thoroughly studied for Ti-Nb-based alloys. However, several issues must be resolved to produce the material for industrial application.

Fatigue: Fatigue properties are critical for employment of the material in orthopedics. Unfortunately, results on fatigue resistance of biomedical β -Ti alloys with increased oxygen content are not available. Fatigue testing is extremely material-demanding but investigated alloys are usually prepared only in laboratory amounts.

It is assumed that performance under dynamic loading will be more sensitive to particular microstructural conditions than properties determined during static loading.

Dimensions: The most-demanded metallic implants are endoprostheses of big joints—hip and knee. Certain dimensions of input material—typically a rod with the diameter of 20–30 mm or a plate with thickness around 10 mm—are required. This fact literally disqualifies material prepared by intensive cold rolling. In extreme cases, cold rolling with a thickness reduction of 98.5% led to the final thickness of 150 μm [57]. Despite these facts, there are several applications of Ti alloys in small implants (mainly in traumatology).

Product manufacturing: β -Ti alloys with increased oxygen have many disadvantages as compared to other groups of Ti alloys: extreme reactivity with gases, high toughness, and low thermal conductivity. Moreover, alloying with Nb and Ta is complicated due to the very high melting temperatures of these elements. As a result, the melting point of these alloys is high and forging temperatures exceed those typical for steels. Biomedical alloys with increased oxygen have another specific disadvantage. High strength levels due to interstitial oxygen are almost unknown, but it can be assumed that the effect of oxygen will prevail up to relatively high temperatures, which may further complicate hot forming. Furthermore, these alloys should be used in pure β conditions, which exhibit even higher toughness than the more-common aged $\alpha+\beta$ conditions. Data on machinability of these alloys are not available. The optimal processing route of biomedical alloys is to be determined. However, it is clear that the processing route will be completely different from those of Ti-6Al-4V alloy or high-strength metastable β -Ti alloys in the aircraft industry.

It must be considered that the final products of specialized Ti-Nb-based alloys will be much more expensive than that of Ti-6Al-4V alloy, both due to expensive alloying elements and complicated processing. On the other hand, production for medical use has high added value and direct material costs create only a small margin of the final price of biomedical products.

Summary

Biomedical β -Ti alloys with increased oxygen content are promising candidates for manufacturing of orthopedic and other medical implants. Depending on the required application, an alloy with a favorable combination of strength and elastic modulus can be selected. For the manufacturing of big joint implants, detailed assessment of fatigue performance and optimization of processing parameters remain critical issues.

Acknowledgments

The Czech Science Foundation (project 17-20700Y) and the grant agency of Charles University (project 1530217) are gratefully acknowledged for financial support.

References

- [1] H. Conrad, Effect of interstitial solutes on the strength and ductility of titanium, *Prog. Mater. Sci.* 26 (1981) 123–403, [https://doi.org/10.1016/0079-6425\(81\)90001-3](https://doi.org/10.1016/0079-6425(81)90001-3).
- [2] F. Geng, M. Niinomi, M. Nakai, Observation of yielding and strain hardening in a titanium alloy having high oxygen content, *Mater. Sci. Eng. A* 528 (2011) 5435–5445, <https://doi.org/10.1016/j.msea.2011.03.064>.
- [3] G. Welsch, R. Boyer, E.W. Collings, *Materials Properties Handbook: Titanium Alloys*, ASM International, Ohio, 1993 ISBN: 978-0-87170-481-8.
- [4] M. Chandran, P.R. Subramanian, M.F. Gigliotti, Energetics of interstitial oxygen in β -TiX (X = transition elements) alloys using first principles methods, *J. Alloys Compd.* 571 (2013) 107–113, <https://doi.org/10.1016/j.jallcom.2013.03.140>.
- [5] K. Hiraga, T. Onozuka, M. Hirabayashi, Locations of oxygen, nitrogen and carbon atoms in vanadium determined by neutron diffraction, *Mater. Sci. Eng.* 27 (1977) 35–38, [https://doi.org/10.1016/0025-5416\(77\)90191-4](https://doi.org/10.1016/0025-5416(77)90191-4).
- [6] J.H. Dai, Y. Song, W. Li, R. Yang, L. Vitos, Influence of alloying elements Nb, Zr, Sn, and oxygen on structural stability and elastic properties of the Ti2448 alloy, *Phys. Rev. B* 89 (2014) 014103, <https://doi.org/10.1103/PhysRevB.89.014103>.
- [7] P. Waldner, G. Eriksson, Thermodynamic modelling of the system titanium-oxygen, *Calphad* 23 (1999) 189–218, [https://doi.org/10.1016/S0364-5916\(99\)00025-5](https://doi.org/10.1016/S0364-5916(99)00025-5).
- [8] E.J. Savino, A. Seeger, Octahedral and tetrahedral interstitial sites in a BCC lattice, *Scr. Metall.* 15 (1981) 431–435, [https://doi.org/10.1016/0036-9748\(81\)90225-8](https://doi.org/10.1016/0036-9748(81)90225-8).
- [9] J.L. Snoek, Effect of small quantities of carbon and nitrogen on the elastic and plastic properties of iron, *Physica* 8 (1941) 711–733, [https://doi.org/10.1016/S0031-8914\(41\)90517-7](https://doi.org/10.1016/S0031-8914(41)90517-7).
- [10] M. Weller, The Snoek relaxation in bcc metals—from steel wire to meteorites, *Mater. Sci. Eng. A* 442 (2006) 21–30, <https://doi.org/10.1016/j.msea.2006.02.232>.
- [11] T. Shkama, S. Ishino, Y. Mishima, The interaction between interstitial impurities and substitutional solutes in vanadium, *J. Nucl. Mater.* 68 (1977) 315–323, [https://doi.org/10.1016/0022-3115\(77\)90256-2](https://doi.org/10.1016/0022-3115(77)90256-2).
- [12] Z.C. Szkoziak, J.T. Smith, The internal friction of Nb-1 at.% substitutional alloys, *J. Phys. D Appl. Phys.* 8 (1975) 1273, <https://doi.org/10.1088/0022-3727/8/11/006>.
- [13] A.W. Cochardt, G. Schoek, H. Wiedersich, Interaction between dislocations and interstitial atoms in body-centered cubic metals, *Acta Metall.* 3 (1955) 533–537, [https://doi.org/10.1016/0001-6160\(55\)90111-5](https://doi.org/10.1016/0001-6160(55)90111-5).
- [14] M. Besse, P. Castany, T. Gloriant, Mechanisms of deformation in gum metal TNTZ-O and TNTZ titanium alloys: a comparative study on the oxygen influence, *Acta Mater.* 59 (2011) 5982–5988, <https://doi.org/10.1016/j.actamat.2011.06.006>.
- [15] H. Lu, C.X. Li, F.X. Yin, Q.F. Fang, O. Umezawa, Effects of alloying elements on the Snoek-type relaxation in Ti-Nb-X-O alloys (X = Al, Sn, Cr, and Mn), *Mater. Sci. Eng. A* 541 (2012) 28–32, <https://doi.org/10.1016/j.msea.2012.01.113>.
- [16] M. Nakai, M. Niinomi, T. Akahori, H. Tsutsumi, M. Ogawa, Effect of oxygen content on microstructure and mechanical properties of biomedical Ti-29Nb-13Ta-4.6Zr alloy under solutionized and aged conditions, *Mater. Trans.* 50 (2009) 2716–2720, <https://doi.org/10.2320/matertrans.MA200904>.
- [17] A. Ramarolahy, P. Castany, F. Prima, P. Laheurte, I. Péron, T. Gloriant, Microstructure and mechanical behavior of superelastic Ti-24Nb-0.5O and Ti-24Nb-0.5N biomedical alloys, *J. Mech. Behav. Biomed. Mater.* 9 (2012) 83–90, <https://doi.org/10.1016/j.jmbbm.2012.01.017>.

- [18] H. Liu, M. Niinomi, M. Nakai, J. Hieda, K. Cho, Deformation-induced changeable Young's modulus with high strength in β -type Ti-Cr-O alloys for spinal fixture, *J. Mech. Behav. Biomed. Mater.* 30 (2014) 205–213, <https://doi.org/10.1016/j.jmbbm.2013.11.001>.
- [19] T. Furuta, S. Kuramoto, J. Hwang, K. Nishino, T. Saito, Elastic deformation behavior of multi-functional Ti-Nb-Ta-Zr-O alloys, *Mater. Trans.* 46 (2005) 3001–3007, <https://doi.org/10.2320/matertrans.46.3001>.
- [20] E.G. Obbard, Y.L. Hao, R.J. Talling, S.J. Li, Y.W. Zhang, D. Dye, et al., The effect of oxygen on α'' martensite and superelasticity in Ti-24Nb-4Zr-8Sn, *Acta Mater.* 59 (2011) 112–125, <https://doi.org/10.1016/j.actamat.2010.09.015>.
- [21] S.G. Steinemann, Titanium—the material of choice?, *Periodontol* 2000 17 (1998) 7–21, <https://doi.org/10.1111/j.1600-0757.1998.tb00119.x>.
- [22] M. Niinomi, M. Nakai, J. Hieda, Development of new metallic alloys for biomedical applications, *Acta Biomater.* 8 (2012) 3888–3903, <https://doi.org/10.1016/j.actbio.2012.06.037>.
- [23] E.S. Fisher, D. Dever, Relation of the c' elastic modulus to stability of b.c.c. transition metals, *Acta Metall.* 18 (1970) 265–269, [https://doi.org/10.1016/0001-6160\(70\)90033-7](https://doi.org/10.1016/0001-6160(70)90033-7).
- [24] J. Nejezchlebová, M. Janovská, H. Seiner, P. Sedlák, M. Landa, J. Šmilauerová, et al., The effect of athermal and isothermal ω phase particles on elasticity of β -Ti single crystals, *Acta Mater.* 110 (2016) 185–191, <https://doi.org/10.1016/j.actamat.2016.03.033>.
- [25] M. Niinomi, Mechanical properties of biomedical titanium alloys, *Mater. Sci. Eng. A* 243 (1998) 231–236, [https://doi.org/10.1016/S0921-5093\(97\)00806-X](https://doi.org/10.1016/S0921-5093(97)00806-X).
- [26] M. Tane, Y. Okuda, Y. Todaka, H. Ogi, A. Nagakubo, Elastic properties of single-crystalline ω phase in titanium, *Acta Mater.* 61 (2013) 7543–7554, <https://doi.org/10.1016/j.actamat.2013.08.036>.
- [27] M. Tane, S. Akita, T. Nakano, K. Hagihara, Y. Umakoshi, M. Niinomi, et al., Low Young's modulus of Ti-Nb-Ta-Zr alloys caused by softening in shear moduli c' and c_{44} near lower limit of body-centered cubic phase stability, *Acta Mater.* 58 (2010) 6790–6798, <https://doi.org/10.1016/j.actamat.2010.09.007>.
- [28] C.A. Luke, R. Taggart, D.H. Polonis, Electronic factors and the metastable constitution of quenched alloys based on titanium and zirconium, *J. Nucl. Mater.* 16 (1965) 7–18, [https://doi.org/10.1016/0022-3115\(65\)90086-3](https://doi.org/10.1016/0022-3115(65)90086-3).
- [29] Y.L. Hao, S.J. Li, S.Y. Sun, C.Y. Zheng, R. Yang, Elastic deformation behaviour of Ti-24Nb-4Zr-7.9Sn for biomedical applications, *Acta Biomater.* 3 (2007) 277–286, <https://doi.org/10.1016/j.actbio.2006.11.002>.
- [30] M. Abdel-Hady, K. Hinoshita, M. Morinaga, General approach to phase stability and elastic properties of β -type Ti-alloys using electronic parameters, *Scr. Mater.* 55 (2006) 477–480, <https://doi.org/10.1016/j.scriptamat.2006.04.022>.
- [31] W. Elmay, P. Laheurte, A. Eberhardt, B. Bolle, T. Gloriant, E. Patoor, et al., Stability and elastic properties of Ti-alloys for biomedical application designed with electronic parameters, *EPJ Web Conf.* 6 (2010)29002, <https://doi.org/10.1051/epjconf/20100629002>.
- [32] M. Morinaga, M. Kato, T. Kamimura, M. Fukumoto, I. Harada, K. Kubo, Theoretical design of β -type titanium alloys, *Titan 1992 Sci Technol Proc 7th Int Conf Titan, San Diego, CA, USA, 1992*, pp. 276–283.
- [33] Ahmed T, Rack HJ. Alloy of titanium, zirconium, niobium and tantalum for prosthetics, *US 5871595 A*, 1999.
- [34] D. Kuroda, M. Niinomi, M. Morinaga, Y. Kato, T. Yashiro, Design and mechanical properties of new β type titanium alloys for implant materials, *Mater. Sci. Eng. A* 243 (1998) 244–249, [https://doi.org/10.1016/S0921-5093\(97\)00808-3](https://doi.org/10.1016/S0921-5093(97)00808-3).

- [35] T. Saito, T. Furuta, J.-H. Hwang, S. Kuramoto, K. Nishino, N. Suzuki, et al., Multifunctional alloys obtained via a dislocation-free plastic deformation mechanism, *Science* 300 (2003) 464–467, <https://doi.org/10.1126/science.1081957>.
- [36] T. Saito, T. Furuta, J.H. Hwang, S. Kuramoto, K. Nishino, N. Suzuki, et al., Multi functional titanium alloy “GUM METAL”, *Mater. Sci. Forum* 426–432 (2003) 681–688, <https://doi.org/10.4028/www.scientific.net/MSF.426-432.681>.
- [37] D.M. Gordin, R. Ion, C. Vasilescu, S.I. Drob, A. Cimpean, T. Gloriant, Potentiality of the “Gum Metal” titanium-based alloy for biomedical applications, *Mater. Sci. Eng. C* 44 (2014) 362–370, <https://doi.org/10.1016/j.msec.2014.08.003>.
- [38] M.Y. Gutkin, T. Ishizaki, S. Kuramoto, I.A. Ovid’ko, N.V. Skiba, Giant faults in deformed Gum Metal, *Int. J. Plast.* 24 (2008) 1333–1359, <https://doi.org/10.1016/j.ijplas.2007.09.009>.
- [39] S. Kuramoto, T. Furuta, J.H. Hwang, K. Nishino, T. Saito, Plastic deformation in a multifunctional Ti-Nb-Ta-Zr-O alloy, *Metall. Mater. Trans. A* 37 (2006) 657–662, <https://doi.org/10.1007/s11661-006-0037-7>.
- [40] W. Guo, M.Z. Qadir, M. Ferry, The mode of deformation in a cold-swaged multifunctional Ti-Nb-Ta-Zr-O alloy, *Metall. Mater. Trans. A* 44 (2013) 2307–2318, <https://doi.org/10.1007/s11661-012-1598-2>.
- [41] H.Y. Kim, L. Wei, S. Kobayashi, M. Tahara, S. Miyazaki, Nanodomain structure and its effect on abnormal thermal expansion behavior of a Ti-23Nb-2Zr-0.7Ta-1.2O alloy, *Acta Mater.* 61 (2013) 4874–4886, <https://doi.org/10.1016/j.actamat.2013.04.060>.
- [42] R.J. Talling, R.J. Dashwood, M. Jackson, D. Dye, On the mechanism of superelasticity in gum metal, *Acta Mater.* 57 (2009) 1188–1198, <https://doi.org/10.1016/j.actamat.2008.11.013>.
- [43] A. Behera, S. Nag, K. Mahdak, H. Mohseni, J. Tiley, R. Banerjee, Influence of oxygen ingress on fine scale precipitation of α -Ti during oxidation of Beta21S β -Ti alloy, *J. Mater. Sci.* 48 (2013) 6700–6706, <https://doi.org/10.1007/s10853-013-7470-y>.
- [44] M. Niinomi, M. Nakai, M. Hendrickson, P. Nandwana, T. Alam, D. Choudhuri, et al., Influence of oxygen on omega phase stability in the Ti-29Nb-13Ta-4.6Zr alloy, *Scr. Mater.* 123 (2016) 144–148, <https://doi.org/10.1016/j.scriptamat.2016.06.027>.
- [45] F.Q. Hou, S.J. Li, Y.L. Hao, R. Yang, Nonlinear elastic deformation behaviour of Ti-30Nb-12Zr alloys, *Scr. Mater.* 63 (2010) 54–57, <https://doi.org/10.1016/j.scriptamat.2010.03.011>.
- [46] B.A. Hatt, J.A. Roberts, The ω -phase in zirconium base alloys, *Acta Metall.* 8 (1960) 575–584, [https://doi.org/10.1016/0001-6160\(60\)90112-7](https://doi.org/10.1016/0001-6160(60)90112-7).
- [47] D. De Fontaine, N.E. Paton, J.C. Williams, The omega phase transformation in titanium alloys as an example of displacement controlled reactions, *Acta Metall.* 19 (1971) 1153–1162, [https://doi.org/10.1016/0001-6160\(71\)90047-2](https://doi.org/10.1016/0001-6160(71)90047-2).
- [48] D. De Fontaine, Simple models for the omega phase transformation, *Metall. Trans. A* 19 (1988) 169–175, <https://doi.org/10.1007/BF02652523>.
- [49] J.C. Williams, D. De Fontaine, N.E. Paton, The ω -phase as an example of an unusual shear transformation, *Metall. Trans. A* 4 (1973) 2701–2708, <https://doi.org/10.1007/BF02644570>.
- [50] A. Devaraj, R.E.A. Williams, S. Nag, R. Srinivasan, H.L. Fraser, R. Banerjee, Three-dimensional morphology and composition of omega precipitates in a binary titanium-molybdenum alloy, *Scr. Mater.* 61 (2009) 701–704, <https://doi.org/10.1016/j.scriptamat.2009.06.006>.

- [51] N.E. Paton, J.C. Williams, The influence of oxygen content on the athermal β - ω transformation, *Scr. Metall.* 7 (1973) 647–649, [https://doi.org/10.1016/0036-9748\(73\)90229-9](https://doi.org/10.1016/0036-9748(73)90229-9).
- [52] X. Zhao, M. Niinomi, M. Nakai, J. Hieda, Beta type Ti-Mo alloys with changeable Young's modulus for spinal fixation applications, *Acta Biomater.* 8 (2012) 1990–1997, <https://doi.org/10.1016/j.actbio.2012.02.004>.
- [53] H. Liu, M. Niinomi, M. Nakai, K. Cho, K. Narita, M. Şen, et al., Mechanical properties and cytocompatibility of oxygen-modified β -type Ti-Cr alloys for spinal fixation devices, *Acta Biomater.* 12 (2015) 352–361, <https://doi.org/10.1016/j.actbio.2014.10.014>.
- [54] T. Li, D. Kent, G. Sha, L.T. Stephenson, A.V. Ceguerra, S.P. Ringer, et al., New insights into the phase transformations to isothermal ω and ω -assisted α in near β -Ti alloys, *Acta Mater.* 106 (2016) 353–366, <https://doi.org/10.1016/j.actamat.2015.12.046>.
- [55] J.I. Qazi, B. Marquardt, L.F. Allard, H.J. Rack, Phase transformations in Ti-35Nb-7Zr-5Ta-(0.06–0.68)O alloys, *Mater. Sci. Eng. C* 25 (2005) 389–397, <https://doi.org/10.1016/j.msec.2005.01.022>.
- [56] J.G. Niu, W.T. Geng, Oxygen-induced lattice distortion in β -Ti3Nb and its suppression effect on β to α'' transformation, *Acta Mater.* 81 (2014) 194–203, <https://doi.org/10.1016/j.actamat.2014.07.060>.
- [57] M. Tahara, H.Y. Kim, T. Inamura, H. Hosoda, S. Miyazaki, Lattice modulation and superelasticity in oxygen-added β -Ti alloys, *Acta Mater.* 59 (2011) 6208–6218, <https://doi.org/10.1016/j.actamat.2011.06.015>.
- [58] J.H. Dai, Y. Song, R. Yang, Influence of impurities on phase stability of martensites in titanium, *Philos. Mag.* 92 (2012) 2272–2285, <https://doi.org/10.1080/14786435.2012.669075>.
- [59] T. Furuta, S. Kuramoto, J. Hwang, K. Nishino, T. Saito, M. Niinomi, Mechanical properties and phase stability of Ti-Nb-Ta-Zr-O alloys, *Mater. Trans.* 48 (2007) 1124–1130, <https://doi.org/10.2320/matertrans.48.1124>.
- [60] M. Tane, K. Hagihara, M. Ueda, T. Nakano, Y. Okuda, Elastic-modulus enhancement during room-temperature aging and its suppression in metastable Ti-Nb-based alloys with low body-centered cubic phase stability, *Acta Mater.* 102 (2016) 373–384, <https://doi.org/10.1016/j.actamat.2015.09.030>.
- [61] Y.L. Hao, S.J. Li, S.Y. Sun, R. Yang, Effect of Zr and Sn on Young's modulus and superelasticity of Ti-Nb-based alloys, *Mater. Sci. Eng. A* 441 (2006) 112–118, <https://doi.org/10.1016/j.msea.2006.09.051>.
- [62] N. Nagasako, R. Asahi, D. Isheim, D.N. Seidman, S. Kuramoto, T. Furuta, Microscopic study of gum-metal alloys: a role of trace oxygen for dislocation-free deformation, *Acta Mater.* 105 (2016) 347–354, <https://doi.org/10.1016/j.actamat.2015.12.011>.
- [63] P. Castany, A. Ramarolahy, F. Prima, P. Laheurte, C. Curfs, T. Gloriant, In situ synchrotron X-ray diffraction study of the martensitic transformation in superelastic Ti-24Nb-0.5N and Ti-24Nb-0.5O alloys, *Acta Mater.* 88 (2015) 102–111, <https://doi.org/10.1016/j.actamat.2015.01.014>.
- [64] M. Hirao, H. Ogi, Electromagnetic acoustic resonance and materials characterization, *Ultrasonics* 35 (1997) 413–421, [https://doi.org/10.1016/S0041-624X\(97\)00030-9](https://doi.org/10.1016/S0041-624X(97)00030-9).
- [65] A. Migliori, J.L. Sarrao, W.M. Visscher, T.M. Bell, M. Lei, Z. Fisk, et al., Resonant ultrasound spectroscopic techniques for measurement of the elastic moduli of solids, *Phys. B Condens. Matter* 183 (1993) 1–24, [https://doi.org/10.1016/0921-4526\(93\)90048-B](https://doi.org/10.1016/0921-4526(93)90048-B).
- [66] J.N. Lalena, D.A. Cleary, *Principles of Inorganic Materials Design*, John Wiley & Sons, New Jersey, 2010 ISBN: 978-0-470-40403-4.

- [67] M. Tane, T. Nakano, S. Kuramoto, M. Hara, M. Niinomi, N. Takesue, et al., Low Young's modulus in Ti-Nb-Ta-Zr-O alloys: cold working and oxygen effects, *Acta Mater.* 59 (2011) 6975–6988, <https://doi.org/10.1016/j.actamat.2011.07.050>.
- [68] M. Tane, S. Akita, T. Nakano, K. Hagihara, Y. Umakoshi, M. Niinomi, et al., Peculiar elastic behavior of Ti-Nb-Ta-Zr single crystals, *Acta Mater.* 56 (2008) 2856–2863, <https://doi.org/10.1016/j.actamat.2008.02.017>.
- [69] J. Ashkenazi, M. Dacorogna, M. Peter, Y. Talmor, E. Walker, S. Steinemann, Elastic constants in Nb-Zr alloys from zero temperature to the melting point: experiment and theory, *Phys. Rev. B* 18 (1978) 4120–4131, <https://doi.org/10.1103/PhysRevB.18.4120>.
- [70] P. Bujard, R. Sanjines, E. Walker, J. Ashkenazi, M. Peter, Elastic constants in Nb-Mo alloys from zero temperature to the melting point: experiment and theory, *J. Phys. F: Met. Phys.* 11 (1981) 775, <https://doi.org/10.1088/0305-4608/11/4/011>.
- [71] G.P. Tiwari, R.V. Ramanujan, Review the relation between the electron to atom ratio and some properties of metallic systems, *J. Mater. Sci.* 36 (2001) 271–283, <https://doi.org/10.1023/A:1004853304704>.
- [72] N. Takesue, Y. Shimizu, T. Yano, M. Hara, S. Kuramoto, Single-crystal growth of Ti-Nb-Ta-Zr-O alloys and measurement of elastic properties, *J. Cryst. Growth* 311 (2009) 3319–3324, <https://doi.org/10.1016/j.jcrysgro.2009.03.052>.
- [73] A.H. Cottrell, B.A. Bilby, Dislocation theory of yielding and strain ageing of iron, *Proc. Phys. Soc. Sect. B* 62 (1949) 49–62, <https://doi.org/10.1088/0370-1298/62/1/308>.
- [74] Y. Yang, W. SQ, G.P. Li, Y.L. Li, L. YF, K. Yang, et al., Evolution of deformation mechanisms of Ti-22.4Nb-0.73Ta-2Zr-1.34O alloy during straining, *Acta Mater.* 58 (2010) 2778–2787, <https://doi.org/10.1016/j.actamat.2010.01.015>.
- [75] J.I. Qazi, H.J. Rack, B. Marquardt, High-strength metastable beta-titanium alloys for biomedical applications, *JOM* 56 (2004) 49–51, <https://doi.org/10.1007/s11837-004-0253-9>.
- [76] J.I. Kim, H.Y. Kim, H. Hosoda, S. Miyazaki, Shape memory behavior of Ti-22Nb-0.5-2.0O(at%) biomedical alloys, *Mater. Trans.* 46 (2005) 852–857, <https://doi.org/10.2320/matertrans.46.852>.
- [77] Q. Wei, L. Wang, Y. Fu, J. Qin, W. Lu, D. Zhang, Influence of oxygen content on microstructure and mechanical properties of Ti-Nb-Ta-Zr alloy, *Mater. Des.* 32 (2011) 2934–2939, <https://doi.org/10.1016/j.matdes.2010.11.049>.
- [78] W. Guo, M.Z. Quadir, S. Moricca, T. Eddows, M. Ferry, Microstructural evolution and final properties of a cold-swaged multifunctional Ti-Nb-Ta-Zr-O alloy produced by a powder metallurgy route, *Mater. Sci. Eng. A* 575 (2013) 206–216, <https://doi.org/10.1016/j.msea.2013.03.029>.
- [79] I. Kopová, J. Stráský, P. Harcuba, M. Landa, M. Janeček, L. Bačáková, Newly developed Ti-Nb-Zr-Ta-Si-Fe biomedical beta titanium alloys with increased strength and enhanced biocompatibility, *Mater. Sci. Eng. C* 60 (2016) 230–238, <https://doi.org/10.1016/j.msec.2015.11.043>.



Newly developed Ti–Nb–Zr–Ta–Si–Fe biomedical beta titanium alloys with increased strength and enhanced biocompatibility



Ivana Kopova^{a,*}, Josef Stráský^b, Petr Hrcuba^b, Michal Landa^c, Miloš Janeček^b, Lucie Bačáková^a

^a Department of Biomaterials and Tissue Engineering, Institute of Physiology of the Czech Academy of Sciences, Videnska 1083, 14220 Prague 4, Czech Republic

^b Department of Physics of Materials, Faculty of Mathematics and Physics, Charles University in Prague, Ke Karlovu 5, 121 16 Prague 2, Czech Republic

^c Institute of Thermomechanics, Academy of Sciences of the Czech Republic, Doležalkova 5, 182 00 Prague 8, Czech Republic

ARTICLE INFO

Article history:

Received 13 February 2015

Received in revised form 16 August 2015

Accepted 16 November 2015

Available online 17 November 2015

Keywords:

Elastic modulus

Alloy hardening

Cell growth

Osteogenic cell differentiation

Bone implants

ABSTRACT

Beta titanium alloys are promising materials for load-bearing orthopaedic implants due to their excellent corrosion resistance and biocompatibility, low elastic modulus and moderate strength. Metastable beta-Ti alloys can be hardened via precipitation of the alpha phase; however, this has an adverse effect on the elastic modulus. Small amounts of Fe (0–2 wt.%) and Si (0–1 wt.%) were added to Ti–35Nb–7Zr–6Ta (TNZT) biocompatible alloy to increase its strength in beta solution treated condition. Fe and Si additions were shown to cause a significant increase in tensile strength and also in the elastic modulus (from 65 GPa to 85 GPa). However, the elastic modulus of TNZT alloy with Fe and Si additions is still much lower than that of widely used Ti–6Al–4V alloy (115 GPa), and thus closer to that of the bone (10–30 GPa). Si decreases the elongation to failure, whereas Fe increases the uniform elongation thanks to increased work hardening. Primary human osteoblasts cultivated for 21 days on TNZT with 0.5Si + 2Fe (wt.%) reached a significantly higher cell population density and significantly higher collagen I production than cells cultured on the standard Ti–6Al–4V alloy. In conclusion, the Ti–35Nb–7Zr–6Ta–2Fe–0.5Si alloy proves to be the best combination of elastic modulus, strength and also biological properties, which makes it a viable candidate for use in load-bearing implants.

© 2015 The Authors. Published by Elsevier B.V. This is an open access article under the CC BY-NC-ND license (<http://creativecommons.org/licenses/by-nc-nd/4.0/>).

1. Introduction

Titanium alloys have been applied extensively in orthopaedics for several decades due to their superior mechanical properties, excellent corrosion resistance and favourable biocompatibility [1,2]. Numerous studies have reviewed the outstanding properties of these materials for medical use. Excellent biocompatibility of titanium has been proven by many authors, both in vitro and in vivo [3,4]. Commercially pure titanium is used in some orthopaedic and dental applications. However, limited strength (up to 500 MPa) disallows its use as a material for orthopaedic endoprostheses, which constitute most of the market for metallic implants [2].

Although Ti–6Al–4V alloy was developed for the aerospace industry, it is still the workhorse of the orthopaedic implants industry [5]. Despite the generally good properties of this alloy, there are several limitations. Special concern relates to the presence of vanadium, because an increasing number of studies have reported a cytotoxic effect of this element [6,7]. The presence of aluminium has been associated with the induction of neurotoxicity and neurodegenerative diseases reviewed in [8].

Moreover, there is a risk of implant-induced oxidative stress and subsequent inflammatory activation caused by Ti–6Al–4V [9].

Another principal adverse property is its excessively high elastic modulus (around 115 GPa for Ti–6Al–4V alloy), which is much higher than the elastic modulus of cortical bone (10–30 GPa) [10]. The load, which is normally applied to the bone is carried by the stiff implant, and the bone tissue atrophies due to lack of functional stimulation. Consequent osteoporosis results in fractures of the surrounding bone or loosening of the implant. For any of these reasons, the lifetime of an orthopaedic implant made of Ti–6Al–4V alloy is usually limited to 15–20 years [11,12]. At the same time, the excessively low elastic modulus causes large amounts of shear motion between the stem and the bone, leading to the formation of fibrous tissue and to failure [13]. Current interest is therefore focused on metastable β -titanium alloys with increased biocompatibility and a moderate elastic modulus [10].

1.1. Metastable beta-Ti alloys

The first metastable β -Ti alloys were developed in the 1960s [14]. The principal advantages of these alloys are their good response to heat treatment, their enhanced ductility, weldability and high strength [15]. The dominant area of application has been in the aerospace industry [16]. However, in the last two decades, specialized biocompatible

* Corresponding author.

E-mail address: ivana.kopova@biomed.cas.cz (I. Kopova).

alloys have also been developed. The most widely-used alloying elements are vanadium, chromium, iron, molybdenum and niobium. Nb and Zr are regarded as biocompatible alloying elements, whereas V, Cr and Co are considered inappropriate due to their potential cytotoxicity [17].

Metastable beta-Ti alloys after quenching from a temperature above the beta transus (typically around 600–800 °C) do not contain the alpha phase. The major hardening mechanism in metastable β -Ti alloys is the formation of omega and alpha phases by subsequent ageing. Underlying phase transitions including schematic phase diagrams for metastable beta-Ti alloys and effects on mechanical properties are overviewed in [18]. It has been shown experimentally and explained theoretically that the Young's modulus of β -phase is lower than the Young's modulus of the alpha phase or the omega phase [19,20]. Ageing treatment therefore increases the elastic modulus of the alloys. Alternative strengthening mechanisms are solid solution strengthening and precipitation strengthening by small dispersed particles. Both of these mechanisms are utilized and investigated in the present study.

1.2. TNZT alloy

Ti-Nb-Zr-Ta based alloys are known as highly biocompatible materials with favourable mechanical properties. Various types of Ti-Nb-Zr-Ta have been developed. The two most widely used and most widely investigated compositions are Ti-29Nb-13Ta-4.6Zr [12] and Ti-35.3Nb-7.3Zr-5.7Ta (in the following text abbreviated as TNZT). TNZT was developed in the 1990s in the USA and was patented in 1999 [21]. This particular composition was used as a benchmark material for experimental investigations in this study. The TNZT alloy contains only biocompatible elements [11], and consists of beta phase only after quenching from temperatures above the beta transus. In this condition, the elastic modulus is as low as 55 GPa. A considerable disadvantage is the relatively low strength of this alloy of around 550 MPa, depending on oxygen content [22].

The aim of this study is to investigate TNZT alloys as an implant material for hip total endoprostheses, which constitute the majority of market. The strength of basic TNZT alloy in solution treated condition does not exceed 500 MPa and as such cannot be used for hip implant. A relatively low bending strength (e.g. in comparison with Ti-12Cr) of Ti-29Nb-13Ta-4.6Zr limits its application in spinal fixation [23]. In another TNZT alloy, i.e. Ti-35Nb-5.7Ta-7.2Zr, attempts were made to improve its strength by small boron addition and TiB formation. However, the presence of boron decreased the attachment of human osteoblast-like MG-63 cells to the material [24] and also deteriorates its wear resistance of the alloy [25].

The strength can be significantly improved by ageing involving alpha precipitation [26]. However, the elastic modulus is increased to above 100 GPa, which is similar to the modulus of widely-used alpha + beta alloys. The purpose of our study is to employ small Fe and Si additions to strengthen TNZT alloy without increasing the elastic modulus excessively, and to assess the effects of Fe and Si on the biocompatibility of the material.

1.3. Fe and Si additions

The solubility of iron in beta-Ti matrix reaches 22 at.% [27]. Iron acts as a strong beta stabilizer and causes simple solution strengthening in beta alloys due to different electron bonding. However, Si has very low solubility in both the alpha and beta phases and contributes to hardening via the creation of dispersed precipitates Ti_5Si_3 [28]. Moreover, the even more stable $(Ti,Zr)_5Si_3$ compound is formed in alloys containing Zr [28]. An Si content of 0.2–0.4 wt.% is often utilized in high-strength and high-temperature alloys in the aerospace industry to increase the strength and to suppress excessive creep [15,29]. The combined effect of Fe and Si was explored by Lee et al. [30] for the alpha phase only. According to Lee et al., Si increases the strength up

to 2 wt.% content, and the most pronounced increase is achieved already for 0.5 wt.% content. On the other hand, Si content in excess of 1 wt.% reduces elongation drastically. Fe additions above 2 wt.% increase the strength substantially. As a result, combined alloying by Fe and Si leads to higher strength levels. Kim et al. [31] studied Ti-(18–28)Nb-(0.5–1.5)Si metastable beta Ti alloys. It is reported that an Si content up to 1 wt.% decreases the elastic modulus to 48 GPa. However, this fact is related to the lower concentration of beta stabilizing elements which leads to the lower stability of the beta phase rather than to an intrinsic effect of Si on the beta phase matrix. To the best of our knowledge, no other authors have yet considered combined additions of Fe and Si to a biomedical beta Ti alloy.

Apart from the mechanical properties, the effect of Fe and Si on the cells and tissues of the living organism must be evaluated. In vivo animal experiments on pure iron stents showed good biocompatibility, with no evidence of local or systemic toxicity or of an inflammatory reaction [32, 33]. Similarly, porous silicon microparticles studied as a multistage delivery carrier showed biocompatibility with immune cells, endothelial cells, and erythrocytes [34]. Internalization of these microparticles by endothelial cells did not affect cellular integrity, proliferation, viability, mitosis or the release of pro-inflammatory cytokines [35]. Moreover, in vivo studies demonstrated that acute or subchronic intravenous administration of these silicon microparticles produced no obvious changes in blood chemistry, microscopic histology or immunoreactivity in mice [36,37]. In addition, the combination of Fe and Si in silica-iron phosphate nanocomposites exhibited good biocompatibility, and there was no cytotoxicity or reduced viability of the human mesenchymal stem cells, even if the nanocomposites penetrated the cells [38]. Porous silicon is already clinically used for drug delivery, and also by pSivida Corp as a sustained release device for the treatment of chronic eye disease. Moreover, great biocompatibility of different alloys containing Fe (Fe-Mn, Ti-Zr-Nb-Fe, Ti-Fe-Mo-Mn-Nb-Zr, Au-Fe, Fe-Pd) was reported in numerous studies [39–43]. Alloys with silicon additions (Ti-Zr-Pd-Si-(Nb) and Mg-Si) or Si-coating also show good cell proliferation, viability and biocompatibility [44–47]. However to verify these finding, adhesion, proliferation and potential cytotoxicity as well as differentiation of the cells cultivated on all manufactured TNZT-Si-Fe alloys was performed in this study.

2. Material and experimental procedure

2.1. Manufacturing TNZT alloys

Six different alloys were designed and manufactured. A TNZT alloy with chemical composition 51.7Ti-35.3Nb-7.3Zr-5.7Ta (wt.%) or 68.7Ti-24.2Nb-5.1Zr-2.0Ta (at.%) was used as a benchmark. Six tailored alloys with 0–2 wt.% Fe and 0–1 wt.% Si additions are listed in Table 1.

All alloys were prepared by arc melting of pure elements under low pressure of a clean He atmosphere (350 mbar). Each part of the sample was remelted at least six times by the electric arc to ensure homogeneity. Samples approximately 200 g in weight were homogenized at 1400 °C for two hours and were furnace cooled. Before forging into the shape of rods, the material was heated to approximately 1100 °C; however, the forging temperature was not precisely controlled. This is referred to as the as-forged condition. Some samples were sealed into a quartz tube and a beta solution treated at 1000 °C/2 h, followed by water quenching. This is referred to as the solution treated (ST) condition. The final samples (flat rounded discs, 11 mm in diameter) were

Table 1
Manufactured alloys with different amounts of Fe and Si (wt.%).

Ti-35Nb-7Zr-5Ta	Ti-35Nb-7Zr-5Ta-0.5Si-1Fe
Ti-35Nb-7Zr-5Ta-1Si	Ti-35Nb-7Zr-5Ta-0.5Si-2Fe
Ti-35Nb-7Zr-5Ta-2Fe	Ti-35Nb-7Zr-5Ta-1Si-1Fe

polished by common grinding and polishing techniques using grinding papers and alumina.

2.2. Mechanical and microstructural characterization

Samples for observations by scanning electron microscopy were carefully polished using SiC abrasive papers. Subsequently, a three-step procedure using alumina (0.3 μm and 0.05 μm) and colloidal silica on a vibratory polisher (Buehler–Vibromet) was employed to obtain an optimally clean and flat sample surface.

Extensive SEM observations were performed using the FEI Quanta 200F scanning electron microscope with the FEG cathode at an accelerating voltage of 20 kV, and the EDX analyser. The elastic modulus was measured on samples 3 mm in thickness, using a resonant ultrasound spectroscopic pulse-echo method [48]. For the tensile tests, we employed a computer controlled Instron 5882 machine and a strain rate of 10^{-4} s^{-1} .

2.3. Simulated body fluid (SBF)

To evaluate mineralization of TNZT samples, simulated body fluid experiment following Kokubo's protocol was performed [49]. Samples were incubated for 14 days in Hank's Balanced Salt Solution (Life technologies, Cat. No. 14,025,092) at 37 °C in a humidified air atmosphere containing 5% of CO_2 . The samples were subsequently analysed by SEM and TF-XRD.

2.4. Cells and culture conditions

TNZT alloys with various Fe and Si additions, and also the benchmark Ti–6Al–4V alloy, were sterilized by autoclaving and were inserted into polystyrene 24-well tissue culture plates (TPP, well diameter 15.4 mm). For the initial experiments (to evaluate cell adhesion and proliferation), sterile samples were seeded with human osteoblast-like U-2 OS cells (ATCC-LGC, Cat. No HTB-96) with an initial density of about 6000 cells/ cm^2 and were cultured for 7 days in 1 mL of Dulbecco's Modified Eagle's Medium (D-MEM; Sigma, Cat. No D5648) supplemented with 10% fetal bovine serum (Sebak GmbH,) and gentamicin (40 $\mu\text{g}/\text{mL}$; LEK,). For differentiation experiments, human primary osteoblasts (HOB-p; PromoCell, Cat. No C12760) in an initial density of about 9000 cells/ cm^2 were seeded on samples and were grown in the osteoblast growth medium (PromoCell, Cat. No C 27001) to cell confluence. After confluence was reached, the cells were differentiated for 14 days in the osteoblast growth medium with additives promoting osteogenic differentiation: 10 mM β -glycerolphosphate, 2 mM L-glutamin, 1 μM $1,\alpha,25$ dihydroxyvitamin D_3 , 100 nM dexamethasone, 280 μM L-ascorbic acid (all purchased from Sigma). Both cell types were cultivated at 37 °C in a humidified air atmosphere containing 5% of CO_2 . The SSM1 Mini Orbital Shaker (circular motion with an orbit of 16 mm; Stuart) was used for cultivation under dynamic conditions. The seeding speed was set to 40 rpm for the first 24 h, followed by 90 rpm for the rest of the cultivation. A polystyrene culture dish and Ti–6Al–4V alloy were used as reference materials. Three samples were analysed for each experimental group and time interval.

2.5. Cell adhesion

After 3 and 7 days of cultivation, all samples seeded with U-2 OS cells were vigorously shaken in 0.5 mL of a four times more concentrated trypsin-EDTA solution (2 g porcine trypsin and 0.8 g EDTA per liter of saline; Sigma) for 15 min at 37 °C on the SSM1 Mini Orbital Shaker. The detached cells were washed away with phosphate-buffered saline (PBS; Sigma). The samples with cells, which remained attached to the samples, were fixed with 4% paraformaldehyde (PFA; Sigma) for 20 min, followed by permeabilization with 0.1% Triton X-100 in PBS (Sigma) for 20 min and incubation in propidium iodide (5 $\mu\text{g}/\text{mL}$;

Sigma) for 5 min at room temperature (RT). The stained cells were photographed using an Olympus IX-71 epifluorescence microscope equipped with a DP-71 digital camera.

2.6. Evaluation of proliferation and potential cytotoxicity (XTT assay)

The commercial II XTT Cell Proliferation Kit (Roche, Cat. No 11 465 015 001) was used to investigate the proliferation of human osteoblast-like U-2 OS cells. After 3 and 7 days of cultivation, a 1 mL solution of XTT and D-MEM without phenol red (Gibco, Cat. No 11053-028) supplemented with 10% fetal bovine serum (Sebak GmbH) and gentamicin (40 $\mu\text{g}/\text{mL}$; LEK) in the ratio of 1 portion of XTT to 2 portions of D-MEM (according the manufacturer's protocol) were added to each sample. After 4–6 h of incubation at 37 °C, the absorbance of the resulting solution was measured at a wavelength of 470 nm. Solutions from alloys or a polystyrene culture dish without seeded cells were used as the blank samples. Three parallel samples were used for each experimental group and time interval.

2.7. Differentiation study: evaluation of cell number and collagen I staining

After 14 days of differentiation (induced after reaching the confluence of human primary osteoblasts HOB-p), all samples were fixed in 4% PFA (Sigma) for 20 min at RT. Subsequently, the cells were permeabilized with 0.1% Triton X-100 in PBS (Sigma) for 20 min at RT. Primary antibody anti-collagen type I (2.5 $\mu\text{g}/\text{mL}$; Sigma), followed by secondary antibody coupled to Alexa Fluor 488 (4 $\mu\text{g}/\text{mL}$; Invitrogen) for 1 h at RT were used. The nuclei were visualized by DAPI (1 $\mu\text{g}/\text{mL}$; Sigma). To determine the cell numbers, the cell nuclei were counted on the microphotographs that were obtained. For each experimental group, three samples were used, and from each sample, 10 randomly taken microphotographs (homogeneously distributed on the surface of the sample) were evaluated.

2.8. Statistical analysis

The quantitative data were presented as the mean \pm S.E.M. (Standard Error of the Mean). Three samples for each experimental group and time interval were evaluated. A comparison between the groups was analysed with the ANOVA, Student–Newman–Keuls method. *p*-Values equal to or less than 0.05 were considered statistically significant.

3. Results

3.1. SEM observations

Fig. 1a–f shows SEM micrographs of the microstructure of all prepared alloys in as-forged condition. The channelling contrast makes it possible to distinguish between individual grains, thanks to their different crystallographic orientation. The microstructure of the alloys without an Si content (Fig. 1a and c) is very coarse, with grain sizes $>100 \mu\text{m}$. The iron content has no observable effect on the grain size. However, Si serves as a grain growth inhibitor. The grain size decreases with increasing Si content (compare Fig. 1d and e with Fig. 1b and f). Small black dots in Fig. 1b, d, e and f are silicide intermetallic precipitates and are depicted in greater detail in Fig. 2. Energy dispersive X-ray spectroscopy (EDS) measurements summarized in Table 2 proved that particles observed in Fig. 2 are indeed silicide particles, which are additionally enriched by zirconium. Note that EDS results should be taken only qualitatively. Two types of silicide particles are present in the material. Bigger particles (2–3 μm) are usually formed along grain boundaries that serve as preferential nucleation sites, whereas smaller particles (~1 μm) are distributed more homogeneously.

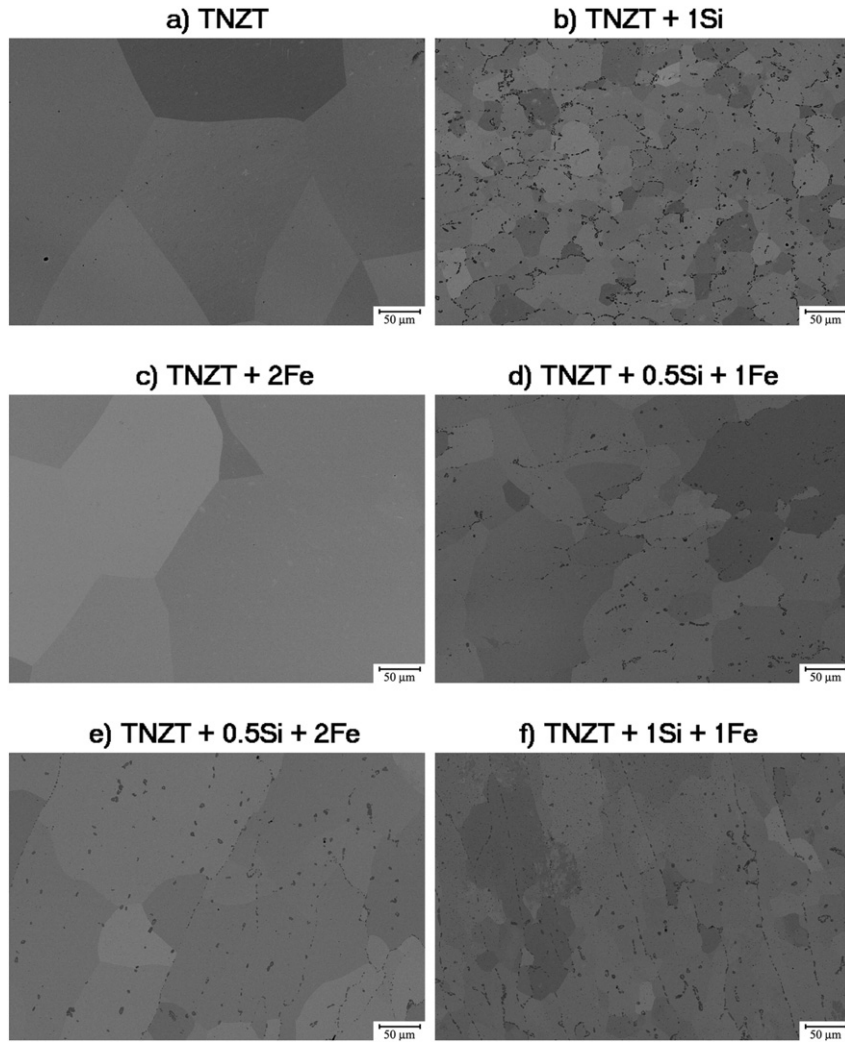


Fig. 1. SEM micrographs of TNZT alloys in as-forged condition (channelling contrast).

3.2. Mechanical properties

The elastic modulus of all alloys was measured by a pulse-echo method for both as-forged and solution treated (ST) conditions. The results of the measurements are summarized in Fig. 3. The elastic modulus of the benchmark TNZT alloy is around 65 GPa, which is in accordance with the literature [21]. The elastic modulus increases with increasing

Fe and Si content. The highest elastic modulus is observed for TNZT + 0.5Si + 2Fe alloy. However, the value of 85 GPa is still significantly lower than the value for the widely-used Ti–6Al–4V alloy. Fig. 4 shows the yield stress and the ultimate tensile strength (UTS) of the studied alloys (as-forged condition) determined from the flow curves. The values presented here are the averages from three samples, and the standard deviation is shown by the error bar. The yield stress of the benchmark TNZT alloy is below 500 MPa. Both Fe and Si increase the yield stress and UTS and, moreover, the combined effect of Fe and Si leads to an even higher strength level. TNZT + 0.5Si + 2Fe alloy yields above 700 MPa, and its ultimate strength is higher than 800 MPa. These are relatively high values, considering that the alloy is not hardened by ageing treatment.

Fig. 5a summarizes the total plastic elongation measured after fracture (as-forged condition). All the alloys are ductile at room temperature, but Si significantly reduces the total elongation. Fe content

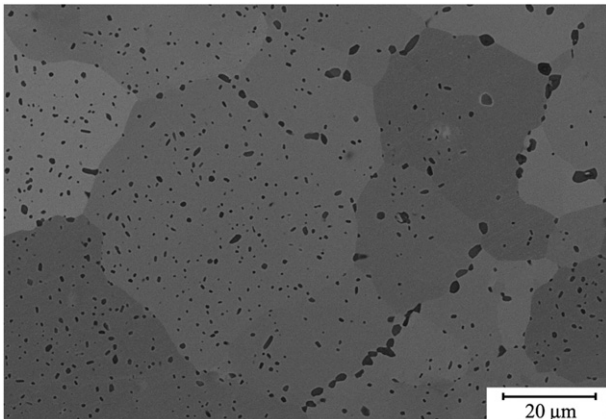


Fig. 2. SEM image of silicides of the TNZT + 1Si alloy.

Table 2

Chemical composition of TNZT + 1Si alloy and composition of silicide particles determined by EDS (qualitative results).

wt.%	Matrix	Particle #1	Particle #2
Ti	46.4	24.8	33.5
Nb	40	11.8	16.7
Zr	7.1	45.7	34.8
Ta	5.5	1.8	3.0
Si	1.0	15.9	12.0

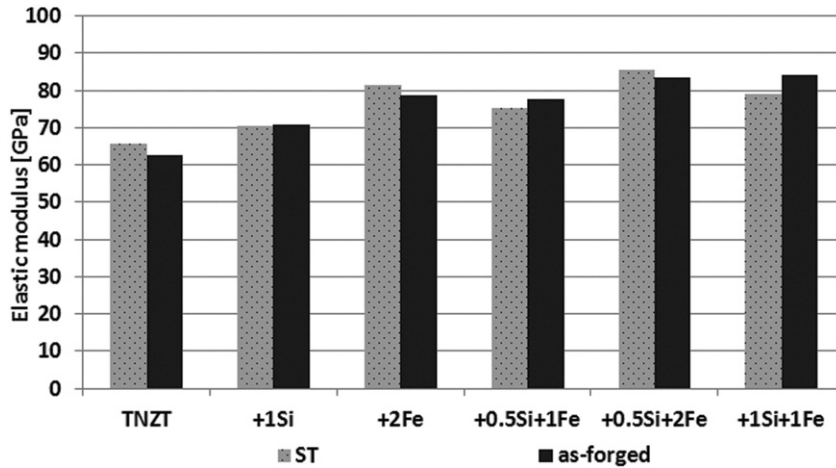


Fig. 3. Elastic modulus measurements of TNZT alloys (solution treated and as-forged condition).

surprisingly increased the total elongation when compared to the benchmark alloy. Flow curves in Fig. 5b show that Fe contrary to Si is responsible for work hardening, which avoids premature necking and therefore increases the overall ductility.

3.3. Cell adhesion

The initial biological experiments showed that human U-2 OS osteoblast-like cells adhered well on all evaluated alloys. Interestingly, stronger adhesion and higher resistance of cells to the detachment by a trypsin-EDTA solution was observed on TNZT alloys (especially on the benchmark TNZT and on TNZT with the addition of 1Si, 2Fe or 0.5Si + 1Fe) than on reference materials, such as Ti-6Al-4V alloy and a polystyrene culture dish (Fig. 6).

3.4. Cell proliferation

In order to investigate the proliferation of human osteoblast-like cells on different alloys, the XXT assay was used to measure the activity of mitochondrial enzymes. This activity is considered to be proportional to the cell number; the XXT assay is therefore often used for evaluating cell proliferation. U-2 OS cells were cultivated for seven days under static or dynamic conditions. The metabolic activity of the cells grown on all tested TNZT alloys under static conditions was comparable to the activity on the reference polystyrene culture dish, and was significantly higher than the metabolic activity

of cells cultured on the reference Ti-6Al-4V alloy (Fig. 7 a). These significant differences were not observed on cells cultivated under dynamic conditions, where the metabolic activity of cells cultured on all tested samples was similar (Fig. 7b).

3.5. Cell differentiation study: cell number and collagen I production

The counting of primary human osteoblast HOB-p cells on day 21 after seeding within the cell differentiation study showed significantly higher population densities of HOB-p grown on TNZT with the addition of 2Fe and 0.5Si + 2Fe (wt.%) than on the standard Ti-6Al-4V alloy (Fig. 8). Production of collagen I was used as a marker of the osteogenic differentiation of the cells. Higher collagen I production was observed in cells cultured on TNZT with the addition of 2Fe, 0.5Si + 1Fe and 0.5Si + 2Fe (wt.%) than on the reference polystyrene culture dish. Moreover, TNZT with 0.5Si + 2Fe additions promoted better differentiation of HOB-p cells (evaluated by collagen I production) than the standard Ti-6Al-4V alloy (Fig. 9).

4. Discussion

It follows from the SEM results (Figs. 1 and 2) that Si serves as a grain growth inhibitor. Grain growth suppression during annealing is caused by underpinning the grain boundaries by silicide intermetallic particles. It is known that the composition of intermetallic silicides in zirconium-containing Ti alloys is $(\text{Ti,Zr})_5\text{Si}_3$ [28]. EDS analysis summarized in

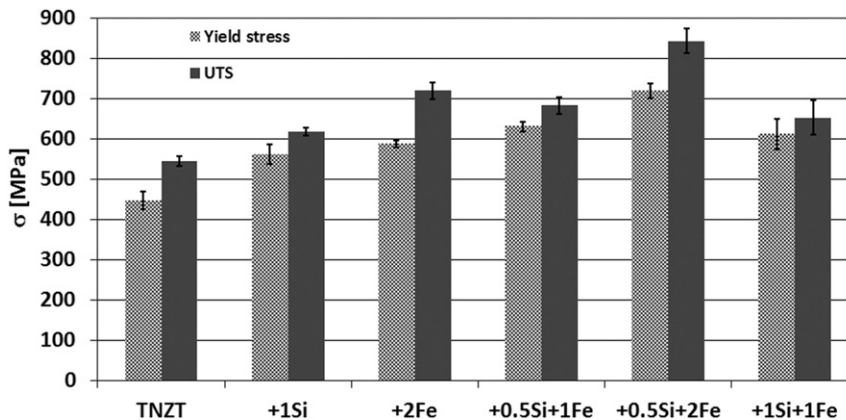


Fig. 4. Yield stress and ultimate tensile strength (UTS) of TNZT alloys (as-forged condition).

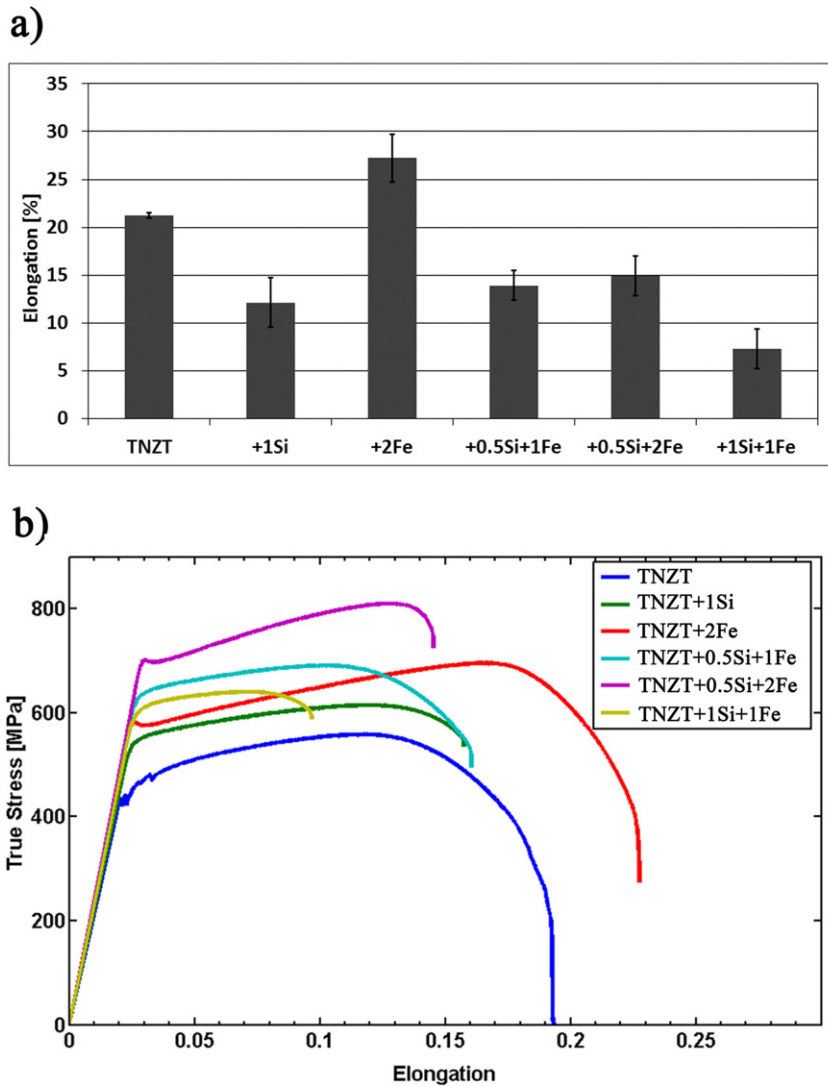


Fig. 5. Total elongation (A5 elongation) (a) and true strain curves (b) of TNZT alloys (as-forged condition).

Table 2 proved that these precipitates are obviously Si enriched and also strongly Zr enriched, which confirms that Zr is preferred for the formation of silicide particles. However, it is impossible to determine the exact chemical composition of these tiny particles by EDS. It has been argued that these particles are also responsible for the increased elastic modulus of Si containing alloys. In addition, these incoherent homogeneously distributed fine particles cause significant precipitation strengthening, as described by the Orowan mechanism [50].

An Fe content of 2 wt.% significantly increased both the elastic modulus and the ultimate strength of the material. The effect on the elastic modulus is related to the strong beta stabilization effect of iron. Two recent approaches relate the e/a ratio and the position in the so-called Bo-Md diagram to the elastic modulus of metastable beta Ti alloys in as-quenched condition [51,52]. The electron per atom ratio, the bonding-order (Bo) and the metal d -orbital energy (Md) values can be calculated simply, and are shown in Table 3 for the benchmark TNZT alloy and TNZT + 2Fe alloy (the effect of the Si additions on the e/a , Bo and Md values is negligible). Fe increases the average electron per atom ratio (e/a ratio) in the alloy, which is associated with an increased elastic modulus [53,54]. Similarly, the beta stabilization effect of Fe decreases the Md value and increases the elastic modulus. This is in excellent agreement with a study by Laheurte et al. [55].

Fe addition also increased the plastic elongation of the material at room temperature, as shown in Fig. 5a. This surprising effect is

associated with work-hardening occurring during the tensile test, which is apparent from the flow curves (Fig. 5 b) and also from the difference between the yield stress and the UTS for the TNZT + 2Fe alloy (Fig. 4). More pronounced work-hardening avoids premature necking and increases the uniform elongation. It is argued that Fe atoms (or their clusters) cause dislocation pinning and consequent dislocation multiplication during straining resulting in work hardening. This also explains the sharp yield point observed for alloys containing 2 wt.% of Fe. The dislocation created during hot-working might be pinned in the atmosphere (clusters) of Fe atoms and the macroscopic stress decreases once dislocations are released from Fe atmosphere during yielding.

The biological experiments proved that all TNZT alloys are biocompatible and promote stronger adhesion as well as higher proliferation of U-2 OS cells cultured under static conditions than the standard Ti-6Al-4V alloy. These observations are in accordance with another study comparing a similar TNZT alloy with Ti-6Al-4V alloy, where a higher proliferation of MG-63 cells cultured on Ti-35Nb-3Zr-2Ta was observed [56]. Similarly, higher viability of L-929 cells (proven by MTT assay) when incubated in a solution extracted from Ti-29Nb-13Ta-4.6Zr rather than in a Ti-6Al-4V extract has been reported [57]. The lack of differences in proliferation under dynamic conditions could be explained by the mechanical forces on the cells, and also by better diffusion of oxygen and nutrients associated with circulation of the culture

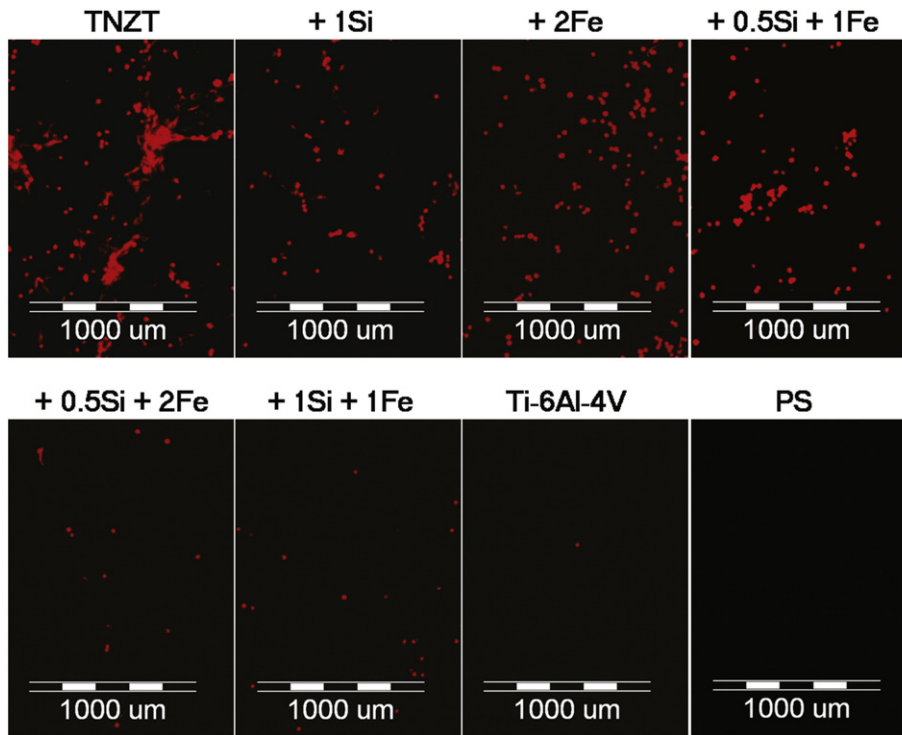


Fig. 6. Adhesion and higher resistance of human U-2 OS osteoblast-like cells to detachment by a four times more concentrated trypsin-EDTA solution from the evaluated materials. Attached cells visualized by propidium iodide. PS – polystyrene culture dish, reference material.

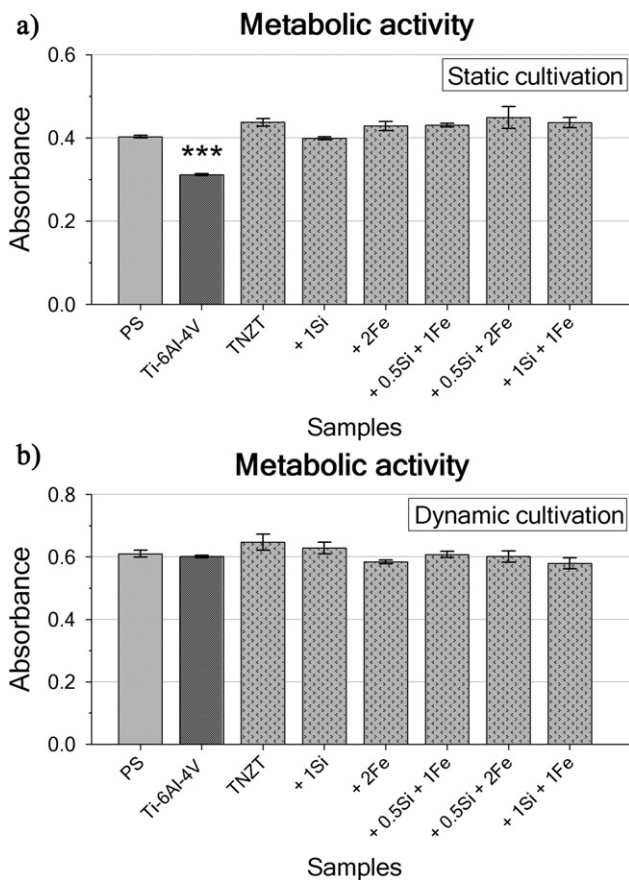


Fig. 7. Metabolic activity measured per culture of human osteoblast-like U-2 OS cells on day seven after seeding cultivated under static (a) and dynamic (b) conditions. PS – polystyrene culture dish, reference material. ***Significant difference from all samples, $p \leq 0.001$.

medium, which are known to enhance cell proliferation [58]. Dynamic cultivation is an approach that better mimics the in vivo environment and therefore promotes the formation of extracellular matrix. This facilitates cell adhesion in the first week of dynamic cultivation [59]. This facilitation may have diminished the effect of the materials on the cells, and may have led to better proliferation of cells cultured on the Ti-6Al-4V alloy.

Our experiments performed on primary human osteoblast (HOB-p) revealed a beneficial effect of Si and Fe additions (especially 0.5Si + 2Fe) to the TNZT alloy on the proliferation and differentiation of these cells. Similarly, in human hFOB1.19 osteoblasts, moderate concentrations of iron in the cell culture media (adjusted with 5 $\mu\text{mol/L}$ of deferoxamine) promoted the proliferation and osteogenic differentiation, manifested by the activity of alkaline phosphatase, expression of collagen I and osteocalcin as well as matrix mineralization. However,

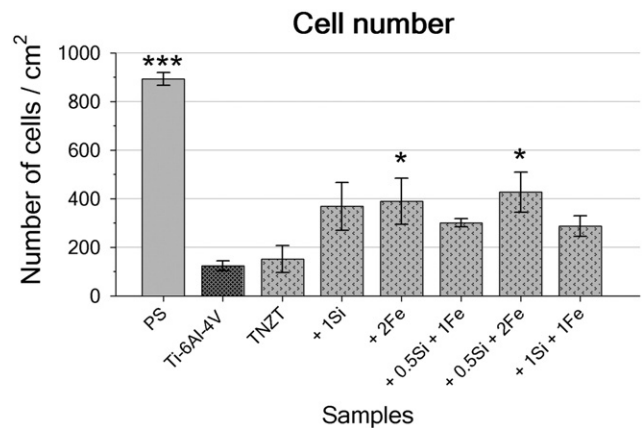


Fig. 8. The number of primary human osteoblast cells (HOB-p) on day 21 after seeding (14 days of differentiation) obtained by counting the cell nuclei. PS – polystyrene culture dish, reference material. ***Significant difference from all samples, $p \leq 0.001$. *Significant difference from Ti-6Al-4V, $p \leq 0.05$.

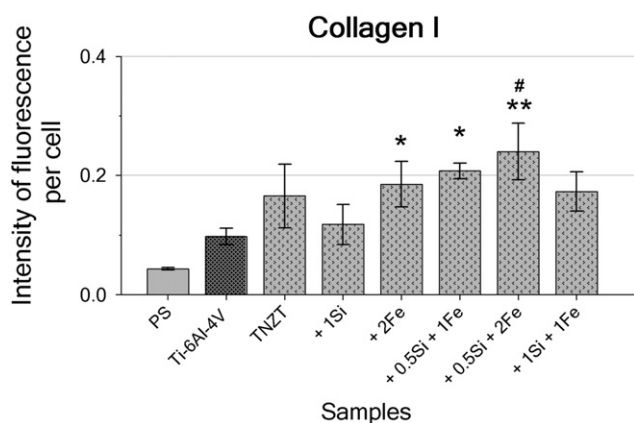


Fig. 9. The amount of collagen I produced by primary human osteoblast cells (HOB-p) after 21 days of cultivation (14 days of differentiation). PS – polystyrene culture dish, reference material. **Significant difference from PS, $p \leq 0.01$. *Significant difference to PS, $p \leq 0.05$. #Significant difference from Ti-6Al-4 V, $p \leq 0.05$.

very low concentrations (at 10–20 $\mu\text{mol/L}$ deferoxamine) or high concentrations of iron (adjusted by 50–200 $\mu\text{mol/L}$ of ferric ammonium citrate) inhibited the growth and differentiation of osteoblasts [60]. Iron also stimulated proliferation and collagen synthesis in other cell types, namely rat lung fibroblasts [61], tracheal cells [62] and rat hepatic stellate cells [63]. As in the case of silicon, Si-containing calcium phosphate [64,65] and silicatein/biosilica substrates [66,67] increased the proliferation of human osteoblast-like MG-63 and Saos-2 cells and rat bone marrow stromal cells, which can be explained e.g. by the increased expression of transforming growth factor beta 1 (TGF- β_1), a potent mitogen for osteoblasts [68]. At the same time, Si-containing materials, such as calcium phosphates, zeolite A, silk–silica composites or silicatein/biosilica matrix, stimulated the expression and synthesis of collagen [66,69] and other markers of osteogenic cell differentiation, such as alkaline phosphatase [65,68], Runx-2, osteopontin, bone sialoprotein, osteocalcin [64,66] and bone morphogenetic protein 2 (BMP-2), an inducer of bone formation [67].

To evaluate potential mineralization of TNZT alloys, in-vitro bioactivity study in simulated body fluid was performed (results not shown). The samples after 14 days of immersion in Hank's Balanced Salt Solution were analysed by scanning electron microscopy (SEM) and Thin Film X-ray diffraction (TF-XRD). All investigated titanium (TNZT) alloys behaved as biologically inert material and no remnants from immersion in SFB were observed.

Unlike the hydroxyapatite scaffolds (intended for degradable implants, which are supposed to be replaced by formation of new bone), where the bioactivity and mineralization is necessary requirement, our TNZT alloys were designed for long-term implantation. In these biostable implants, no extensive mineralization in order to replace the degraded materials is needed. In long-term implantation the great biocompatibility and support of the alloy for cell adhesion and differentiation is more important. It is well known (and our differentiation study also confirmed), that differentiated cells are capable of producing and releasing extracellular matrix components. As mentioned above, the osteoblasts growing on TNZT alloys doped with Si and/or Fe produced more collagen I, which contains binding sites for calcium and phosphate ions, i.e. carboxyl, hydroxyl and amine functional groups. These groups then serve as nucleation sites for formation of hydroxyapatite, and thus for the bone matrix mineralization [70,71].

Table 3

e/a, Bo and Md values computed for benchmark TNZT alloy and TNZT + 2Fe alloy.

Alloy	e/a	Bo	Md
TNZT	4.26	2.887	2.468
TNZT + 2Fe	4.36	2.884	2.434

5. Conclusion

The effect of Fe and Si on the mechanical properties and the biocompatibility of Ti-35Nb-7Zr-6Ta alloy has been evaluated and discussed. All alloys that were developed showed an elastic modulus lower than that of the widely-used Ti-6Al-4V alloy, and a positive effect of Fe and Si on the strength of the alloys was demonstrated.

The newly-developed alloys also displayed superior biocompatibility to that of the widely-used Ti-6Al-4V alloy. The alloy with composition Ti-35Nb-7Zr-6Ta-2Fe-0.5Si provided the best combination of mechanical and biological properties, which makes it a viable candidate for biomedical use in load-bearing bone implants.

Acknowledgements

Financial support from the Czech Science Foundation under grant P107/12/1025 is gratefully acknowledged. We also thank Mr. Robin Healey (Czech Technical University, Prague) for his language revision of the manuscript.

References

- [1] M. Geetha, A.K. Singh, R. Asokamani, A.K. Gogia, Ti based biomaterials, the ultimate choice for orthopaedic implants – a review, *Prog. Mater. Sci.* 54 (2009) 397–425.
- [2] M. Long, H.J. Rack, Titanium alloys in total joint replacement – a materials science perspective, *Biomaterials* 19 (1998) 1621–1639.
- [3] Y. Okazaki, E. Gotoh, Comparison of metal release from various metallic biomaterials in vitro, *Biomaterials* 26 (2005) 11–21.
- [4] S. Rao, Y. Okazaki, T. Tateishi, T. Ushida, Y. Ito, Cytocompatibility of new Ti alloy without Al and V by evaluating the relative growth ratios of fibroblasts L929 and osteoblasts MC3T3-E1 cells, *Mater. Sci. Eng. C* 4 (1997) 311–314.
- [5] K.S. Katti, Biomaterials in total joint replacement, *Colloids Surf. B* 39 (2004) 133–142.
- [6] G.C. McKay, R. Macnair, C. MacDonald, M.H. Grant, Interactions of orthopaedic metals with an immortalized rat osteoblast cell line, *Biomaterials* 17 (1996) 1339–1344.
- [7] J.L. Domingo, Vanadium: a review of the reproductive and developmental toxicity, *Reprod. Toxicol.* 10 (1996) 175–182.
- [8] S.C. Bondy, The neurotoxicity of environmental aluminum is still an issue, *Neurotoxicology* 31 (2010) 575–581.
- [9] R. Tsaryk, K. Peters, S. Barth, R.E. Unger, D. Scharnweber, C.J. Kirkpatrick, The role of oxidative stress in pro-inflammatory activation of human endothelial cells on Ti6Al4V alloy, *Biomaterials* 34 (2013) 8075–8085.
- [10] M. Niinomi, M. Nakai, J. Hieda, Development of new metallic alloys for biomedical applications, *Acta Biomater.* 8 (2012) 3888–3903.
- [11] M. Abdel-Hady Gepreel, M. Niinomi, Biocompatibility of Ti-alloys for long-term implantation, *J. Mech. Behav. Biomed. Mater.* 20 (2013) 407–415.
- [12] D. Kuroda, M. Niinomi, M. Morinaga, Y. Kato, T. Yashiro, Design and mechanical properties of new β type titanium alloys for implant materials, *Mater. Sci. Eng. A* 243 (1998) 244–249.
- [13] M. Niinomi, Mechanical biocompatibilities of titanium alloys for biomedical applications, *J. Mech. Behav. Biomed. Mater.* 1 (2008) 30–42.
- [14] G. Lütjering, J.C. Williams, *Titanium*, Springer, 2007.
- [15] G. Welsch, R. Boyer, E.W. Collings, *Materials Properties Handbook: Titanium Alloys*, ASM International, 1993.
- [16] C. Leyens, M. Peters (Eds.), *Titanium and Titanium Alloys*, Wiley-VCH Verlag GmbH & Co. KGaA, 2003.
- [17] S.G. Steinemann, Titanium – the material of choice? *Periodontol.* 17 (1998) 7–21.
- [18] I. Weiss, S.L. Semiatin, Thermomechanical processing of beta titanium alloys—an overview, *Mater. Sci. Eng. A* 243 (1998) 46–65.
- [19] J. Sun, Q. Yao, H. Xing, W.Y. Guo, Elastic properties of β , α' and ω metastable phases in Ti-Nb alloy from first-principles, *J. Phys. Condens. Matter* 19 (2007) 486215.
- [20] J. Zhao, H. Duan, H. Li, Microstructure and mechanical properties of biomedical Ti-27Nb-8Zr alloy with low elastic modulus, *Rare Metal Mater. Eng.* 39 (2010) 1707–1710.
- [21] Ahmed T, Rack, HJ Low modulus biocompatible titanium base alloys for medical devices. United States Patent, 5,871,595, 1999.
- [22] J.I. Qazi, B. Marquardt, L.F. Allard, H.J. Rack, Phase transformation in Ti-35Nb-7Zr-5Ta-(0.06–0.68)O alloys, *Mater. Sci. Eng.* 25 (2005) 389–397.
- [23] H. Liu, M. Niinomi, M. Nakai, J. Hieda, K. Cho, Bending springback behavior related to deformation-induced phase transformations in Ti-12Cr and Ti-29Nb-13Ta-4.6Zr alloys for spinal fixation applications, *J. Mech. Behav. Biomed. Mater.* 34 (2014) 66–74.
- [24] P. Majumdar, S.B. Singh, S. Dhara, M. Chakraborty, Influence of in situ TiB reinforcements and role of heat treatment on mechanical properties and biocompatibility of β Ti-alloys, *J. Mech. Behav. Biomed. Mater.* 10 (2012) 1–12.
- [25] P. Majumdar, S.B. Singh, M. Chakraborty, The influence of heat treatment and role of boron on sliding wear behaviour of β -type Ti-35Nb-7.2Zr-5.7Ta alloy in dry condition and in simulated body fluids, *J. Mech. Behav. Biomed. Mater.* 4 (2011) 284–297.

- [26] J.I. Qazi, H.J. Rack, B. Marguardt, High-strength metastable beta-titanium alloys for biomedical applications, *JOM* 11 (2004) 49–51.
- [27] J. Matyka, F. Faudot, J. Bigot, Study of iron solubility in α titanium, *Scr. Metall.* 13 (1979) 645–648.
- [28] S. Ankem, D. Banerjee, D.J. McNeish, J.C. Williams, S.R. Seagle, Silicide formation in Ti–3Al–8V–6Cr–4Zr–4Mo, *Metall. Trans. A* 18 (1987) 2015–2025.
- [29] K. Chaudhuri, J.H. Perepezko, Microstructural study of the titanium alloy Ti–15Mo–2.7Nb–3Al–0.2Si (TIMETAL 21S), *Metall. Mater. Trans. A* 25 (1994) 1109–1118.
- [30] D.B. Lee, K.B. Park, H.W. Jeong, S.E. Kim, Mechanical and oxidation properties of Ti–xFe–ySi alloys, *Mater. Sci. Eng.* 328 (2002) 161–168.
- [31] H.S. Kim, W.Y. Kim, S.H. Lim, Microstructure and elastic modulus of Ti–Nb–Si ternary alloys for biomedical applications, *Scr. Mater.* 54 (2006) 887–891.
- [32] M. Peuster, C. Hesse, T. Schloo, C. Fink, P. Beerbaum, C. von Schnakenburg, Long-term biocompatibility of a corrodible peripheral iron stent in the porcine descending aorta, *Biomaterials* 27 (2006) 4955–4962.
- [33] R. Waksman, R. Pakala, R. Baffour, R. Seabron, D. Hellinga, F.O. Tio, Short-term effects of biocorrosible iron stents in porcine coronary arteries, *J. Interv. Cardiol.* 21 (2008) 15–20.
- [34] B. Godin, J. Gu, R.E. Serda, S. Ferrati, X. Liu, C. Chiappini, T. Tanaka, P. Decuzzi, M. Ferrari, Multistage mesoporous silicon-based nanocarriers: biocompatibility with immune cells and controlled degradation in physiological fluids, *Control. Release Newsl.* 25 (2008) 9–11.
- [35] R.E. Serda, S. Ferrati, B. Godin, E. Tasciotti, X. Liu, M. Ferrari, Mitotic trafficking of silicon microparticles, *Nanoscale* 1 (2009) 250–259.
- [36] Q. He, Z. Zhang, F. Gao, Y. Li, J. Shi, In vivo biodistribution and urinary excretion of mesoporous silica nanoparticles: effects of particle size and PEGylation, *Small* 7 (2011) 271–280.
- [37] T. Tanaka, B. Godin, R. Bhavane, R. Nieves-Alicea, J. Gu, X. Liu, C. Chiappini, J.R. Fakhoury, S. Amra, A. Ewing, Q. Li, I.J. Fidler, M. Ferrari, In vivo evaluation of safety of nanoporous silicon carriers following single and multiple dose intravenous administrations in mice, *Int. J. Pharm.* 402 (2010) 190–197.
- [38] J. Athinarayanan, V.S. Periasamy, A.A. Alshatwi, Biogenic silica–metal phosphate (metal = Ca, Fe or Zn) nanocomposites: fabrication from rice husk and their biomedical applications, *J. Mater. Sci. Mater. Med.* 25 (2014) 1637–1644.
- [39] A. Drynda, T. Hassel, F.W. Bach, M. Peuster, In vitro and in vivo corrosion properties of new iron–manganese alloys designed for cardiovascular applications, *J. Biomed. Mater. Res. B Appl. Biomater.* 103 (3) (2015) 649–660.
- [40] P. Xue, Y. Li, K. Li, D. Zhang, C. Zhou, Superelasticity, corrosion resistance and biocompatibility of the Ti–19Zr–10Nb–1Fe alloy, *Mater. Sci. Eng. C* 50 (2015) 179–186.
- [41] S.R. Yu, X.P. Zhang, Z.M. He, Y.H. Liu, Z.H. Liu, Effects of Ce on the short-term biocompatibility of Ti–Fe–Mo–Mn–Nb–Zr alloy for dental materials, *J. Mater. Sci. Mater. Med.* 15 (6) (2004) 687–691.
- [42] V. Amendola, S. Scaramuzza, L. Litti, M. Meneghetti, G. Zuccolotto, A. Rosato, E. Nicolato, P. Marzola, G. Fracasso, C. Anselmi, M. Pinto, M. Colombatti, Magneto-plasmonic Au–Fe alloy nanoparticles designed for multimodal SERS–MRI–CT imaging, *Small* 10 (12) (2014) 2476–2486.
- [43] U. Allenstein, Y. Ma, A. Arabi-Hashemi, M. Zink, S.G. Mayr, Fe–Pd based ferromagnetic shape memory actuators for medical applications: biocompatibility, effect of surface roughness and protein coatings, *Acta Biomater.* 9 (3) (2013) 5845–5853.
- [44] A. Hynowska, A. Blanquer, E. Pellicer, J. Fornell, S. Suriñach, M.D. Baró, A. Gebert, M. Calin, J. Eckert, C. Nogués, E. Ibáñez, L. Barrios, J. Sort, Nanostructured Ti–Zr–Pd–Si–(Nb) bulk metallic composites: novel biocompatible materials with superior mechanical strength and elastic recovery, *J. Biomed. Mater. Res. B Appl. Biomater.* (2014).
- [45] X. Gu, Y. Zheng, Y. Cheng, S. Zhong, T. Xi, In vitro corrosion and biocompatibility of binary magnesium alloys, *Biomaterials* 30 (4) (2009) 484–498.
- [46] Y. Xin, J. Jiang, K. Huo, G. Tang, X. Tian, P.K. Chu, Corrosion resistance and cytocompatibility of biodegradable surgical magnesium alloy coated with hydrogenated amorphous silicon, *J. Biomed. Mater. Res. A* 89 (3) (2009) 717–726.
- [47] M.A. Arenas, E. Frutos, L. Saldaña, A. Conde, L. Labajos-Broncano, M.L. González-Martín, J.L. González-Carrasco, N. Vilaboa, Corrosion behaviour and biocompatibility of a novel Ni-free intermetallic coating growth on austenitic steel by hot dipping in an Al–12.6%Si alloy, *J. Mater. Sci. Mater. Med.* 22 (4) (2011) 1005–1014.
- [48] M. Landa, J. Plešek, Contrast enhancement of ultrasonic imaging of internal stresses in materials, *Ultrasonics* 40 (2002) 531–535.
- [49] T. Kokubo, H. Takadama, How useful is SBF in predicting in vivo bone bioactivity? *Biomaterials* 27 (2005) 2907–2915.
- [50] E. Orowan, Zur Kristallplastizität, *Z. Phys.* 89 (1934) 605–659.
- [51] M. Morinaga, M. Kato, T. Kamimura, M. Fukumoto, I. Farada, K. Kubo, Theoretical design of β -type titanium alloys, *Titanium 1992, Science and Technology, Proc. 7th Int. Conf. on Titanium, San Diego, CA, USA, vol. 1992 1992*, pp. 276–283.
- [52] M. Abdel-Hady, K. Hinoshita, M. Morinaga, General approach to phase stability and elastic properties of β -type Ti-alloys using electronic parameters, *Scr. Mater.* 55 (2006) 477–480.
- [53] C.A. Luke, R. Taggart, D.H. Polonis, Electronic factors and the metastable constitution of quenched alloys based on titanium and zirconium, *J. Nucl. Mater.* 16 (1965) 7–18.
- [54] Y.L. Hao, S.J. Li, S.Y. Sun, C.Y. Zheng, R. Yang, Elastic deformation behaviour of Ti–24Nb–4Zr–7.9Sn for biomedical applications, *Acta Biomater.* 3 (2007) 277–286.
- [55] P. Laheurte, F. Prima, A. Eberhardt, T. Gloriant, M. Wary, E. Patoor, Mechanical properties of low modulus beta titanium alloys designed from the electronic approach, *J. Mech. Behav. Biomed. Mater.* 3 (2010) 565–573.
- [56] Y. Guo, D. Chen, M. Cheng, W. Lu, L. Wang, X. Zhang, The bone tissue compatibility of a new Ti35Nb2Ta3Zr alloy with a low Young's modulus, *Int. J. Mol. Med.* 31 (2013) 689–697.
- [57] M. Niinomi, Fatigue performance and cyto-toxicity of low rigidity titanium alloy, Ti–29Nb–13Ta–4.6Zr, *Biomaterials* 24 (2003) 2673–2683.
- [58] I. Martin, D. Wendt, M. Heberer, The role of bioresorbable in tissue engineering, *Trends Biotechnol.* 22 (2004) 80–86.
- [59] J.V. Araujo, C. Cunha-Reis, T. Rada, M.A. da Silva, M.E. Gomes, Y. Yang, N. Ashammakhi, R.L. Reis, A.J. El-Haj, N.M. Neves, Dynamic culture of osteogenic cells in biomimetically coated poly(caprolactone) nanofibre mesh constructs, *Tissue Eng. A* 16 (2010) 557–563.
- [60] G.Y. Zhao, L.P. Zhao, Y.F. He, G.F. Li, C. Gao, K. Li, Y.J. Xu, A comparison of the biological activities of human osteoblast hFOB1.19 between iron excess and iron deficiency, *Biol. Trace Elem. Res.* 150 (2012) 487–495.
- [61] C. Gardi, P. Calzoni, M. Ferrali, M. Comperti, Iron mobilization from crocidolite as enhancer of collagen content in rat lung fibroblasts, *Biochem. Pharmacol.* 53 (1997) 1659–1665.
- [62] J. Dai, A. Churg, Relationship of fiber surface iron and active oxygen species to expression of procollagen, PDGF-A, and TGF-beta(1) in tracheal explants exposed to amosite asbestos, *Am. J. Respir. Cell Mol. Biol.* 24 (2001) 427–435.
- [63] C. Gardi, B. Arezzini, V. Fortino, M. Comperti, Effect of free iron on collagen synthesis, cell proliferation and MMP-2 expression in rat hepatic stellate cells, *Biochem. Pharmacol.* 64 (2002) 1139–1145.
- [64] W. Duan, C. Ning, T. Tang, Cytocompatibility and osteogenic activity of a novel calcium phosphate silicate bioceramic: silicocarnotite, *J. Biomed. Mater. Res. A* 101 (2013) 1955–1961.
- [65] X. Qiu, P. Wan, L. Tan, X. Fan, K. Yang, Preliminary research on a novel bioactive silicon doped calcium phosphate coating on AZ31 magnesium alloy via electrodeposition, *Mater. Sci. Eng. C Mater. Biol. Appl.* 36 (2014) 65–76.
- [66] A.J. Mieszawska, N. Fourligas, I. Georgakoudi, N.M. Ouhib, D.J. Belton, C.C. Perry, D.L. Kaplan, Osteoinductive silk–silica composite biomaterials for bone regeneration, *Biomaterials* 31 (2010) 8902–8910.
- [67] M. Wiens, X. Wang, U. Schlossmacher, I. Lieberwirth, G. Glasser, H. Ushijima, H.C. Schröder, W.E. Müller, Osteogenic potential of biosilica on human osteoblast-like (SaOS-2) cells, *Calcif. Tissue Int.* 87 (2010) 513–524.
- [68] P.E. Keating, M.J. Oursler, K.E. Wiegand, S.K. Bonde, T.C. Spelsberg, B.L. Riggs, Zeolite A increases proliferation, differentiation, and transforming growth factor beta production in normal adult human osteoblast-like cells in vitro, *J. Bone Miner. Res.* 7 (1992) 1281–1289.
- [69] I.S. Byun, S.K. Sarkar, M. Anirban Jyoti, Y.K. Min, H.S. Seo, B.T. Lee, H.Y. Song, Initial biocompatibility and enhanced osteoblast response of Si doping in a porous BCP bone graft substitute, *J. Mater. Sci. Mater. Med.* 21 (2010) 1937–1947.
- [70] M. Ngiam, S. Liao, A.J. Patil, Z. Cheng, C.K. Chan, S. Ramakrishna, The fabrication of nano-hydroxyapatite on PLGA and PLGA/collagen nanofibrous composite scaffolds and their effects in osteoblastic behavior for bone tissue engineering, *Bone* 45 (2009) 4–16.
- [71] N. Almora-Barrios, N.H. de Leeuw, A density functional theory study of the interaction of collagen peptides with hydroxyapatite surfaces, *Langmuir* 26 (18) (2010) 14535–14542.



Research Paper

Increasing strength of a biomedical Ti-Nb-Ta-Zr alloy by alloying with Fe, Si and O



Josef Stráský^{a,*}, Petr Harcuba^a, Kristína Václavová^a, Klaudia Horváth^a, Michal Landa^b, Ondřej Srba^c, Miloš Janeček^a

^a Department of Physics of Materials, Faculty of Mathematics and Physics, Charles University in Prague, Ke Karlovu 5, 121 16 Prague 2, Czech Republic

^b Institute of Thermomechanics, Academy of Sciences of the Czech Republic, Dolejškova 5, 182 00 Prague 8, Czech Republic

^c Structural and system diagnostic, Research Centre Rez, Hlavní 130, Husinec-Rez, Czech Republic

ARTICLE INFO

Keywords:

β-Ti alloys
Orthopaedic implants
Elastic modulus
Strengthening mechanisms
Ductility
Ultrasound spectroscopy

ABSTRACT

Low-modulus biomedical beta titanium alloys often suffer from low strength which limits their use as load-bearing orthopaedic implants. In this study, twelve different Ti-Nb-Zr-Ta based alloys alloyed with Fe, Si and O additions were prepared by arc melting and hot forging. The lowest elastic modulus (65 GPa) was achieved in the benchmark TNTZ alloy consisting only of pure β phase with low stability due to the ‘proximity’ to the β to α’ martensitic transformation. Alloying by Fe and O significantly increased elastic modulus, which correlates with the electrons per atom ratio (e/a). Sufficient amount of Fe/O leads to increased yield stress, increased elongation to fracture and also to work hardening during deformation. A 20% increase in strength and a 20% decrease in the elastic modulus when compared to the common Ti-6Al-4V alloy was achieved in TNTZ-Fe-Si-O alloys, which proved to be suitable for biomedical use due to their favorable mechanical properties.

1. Introduction

Replacement of large joints is considered as a major achievement in the orthopaedic surgery. However, an appropriate implant material is also a big challenge for material scientists. Along with knee arthroplasty, the hip endoprosthesis is the most demanded joint implant. One of the most delicate issues in hip implant design is the femoral stem that is crucial to prevent the implant from loosening. In fact, the loosening of the implant is one of the most frequent causes of implant failure (Chu et al., 2002). 152,000 hip joint replacements were performed in the US in 2000, thereof almost 13% were revisions and reoperations of previous hip replacement (Long and Rack, 1998). The percentage of reoperations will rise due to the longer life expectation and more active life-style. Therefore, the demand for implants with enhanced life-time will be increasing.

Development of orthopaedic implants is a complex and multi-field scientific issue. Titanium alloys have been extensively applied in orthopaedics for several decades due to their superior mechanical properties, excellent corrosion resistance and favourable biocompatibility (Geetha et al., 2009, Katti, 2004, Long and Rack, 1998, Rack and Qazi, 2006). Elastic modulus of the implant material determining its stiffness is currently a widely discussed topic. Typical elastic modulus of Ti and common Ti alloys is around 100 GPa, while elastic modulus of the cortical bone ranges from 20 to 30 GPa and elastic modulus of

cancellous bone is even lower (7–15 GPa) (Niinomi et al., 2012, Rho et al., 1993, Zysset et al., 1999). This difference in stiffness of implant and surrounding bone leads to the transmission of the applied load through the implant stem and consequently, the surrounding bone is not loaded (so-called stress-shielding effect). The bone tissue that is not regularly loaded becomes atrophied and is prone to failure. Therefore, materials with reduced elastic modulus are being developed.

The relationship between the elastic moduli (E) of different phases in Ti can be expressed as follows $E_{\beta} \approx E_{\alpha'} \approx 60\text{--}85 \text{ GPa} < E_{\alpha} \approx 100 \text{ GPa} < E_{\omega} \approx 130 \text{ GPa}$ (Niinomi, 1998, Nejezchlebová et al., 2016, Sun et al., 2007, Tane et al., 2013), which demonstrates the interest in β-Ti alloys.

Metastable β-Ti alloys have been developed since 1960s (Lütjering and Williams, 2007). The dominant area of application is the aerospace industry. However, two decades ago, specialized biocompatible alloys also emerged. The most used β stabilizing alloying elements are vanadium, chromium, iron, molybdenum and niobium. Nb and Zr are regarded as biocompatible alloying elements, whereas V, Cr and Co are considered inappropriate (Steinemann, 1998).

The design of biomedical alloys for orthopaedic use therefore faces several limitations. Firstly, only biotolerant elements can be used. Secondly, sufficient strength level must be achieved. And thirdly, elastic modulus should be reduced well below 100 GPa. Note that the latter two requirements are often in a trade-off relationship.

The Ti-Nb-Ta-Zr alloying system is a highly biocompatible material

* Corresponding author.

with favourable mechanical properties. The benchmark alloy for this study, Ti-35.3Nb-5.7Ta-7.3Zr (TNTZ), was developed in 1990s in the USA and patented in 1999 (Ahmed and Rack, 1999). The particular alloy composition was selected empirically aiming to minimize the elastic modulus which can be as low as 60 GPa in the solution treated condition (Tang et al., 2000). Ti-Nb-Ta-Zr alloy is predetermined for biomedical use also due to low metal release in vitro, which is advantageous especially for long-term implants (Okazaki and Gotoh, 2015). On the other hand, a considerable disadvantage of this alloy is its low strength. Despite both Zr and Ta provide some solution strengthening when compared to Ti-Nb binary alloys (Ferrandini et al., 2007, Sakaguchi et al., 2005), the ultimate tensile strength reaches only 550 MPa. The major issue for applicability of this alloy for manufacturing of large joint implants is increasing its strength.

The main hardening mechanism in metastable β -Ti alloys is the formation of α phase precipitates. However, the presence of α phase precipitates leads to an unfavourable increase of elastic modulus. Precipitation hardening can be achieved also by titanium carbides and titanium borides (Chen and Hwang, 2012, Du et al., 2014, Zhang et al., 2012) and by titanium silicides. Si has a very low solubility in both the α and β phase and contributes to hardening via creation of dispersed precipitates of Ti_5Si_3 . Moreover, in alloys containing Zr even more stable $(\text{Ti,Zr})_5\text{Si}_3$ compound is formed (Ankem et al., 1987, Headley and Rack, 1979). Si content of 0.2–0.4 wt% is often utilized in high-strength and high-temperature alloys in aerospace industry to increase the strength and to suppress excessive creep (Chaudhuri and Perepecko, 1994, Welsch et al., 1993).

Solid solution strengthening is the fundamental hardening mechanism in alloys. Among bio-tolerable elements, Fe and Ta are known to cause significant solid solution hardening (Kudrman et al., 2007), whereas the effect of Mo and Nb is low. However, the experimental results are often affected by undergoing phase transitions and changes in deformation mechanisms (Min et al., 2008, Min et al., 2010).

Considering interstitial hardening, enhanced hardness due to oxygen increase from 0.3 wt% to 0.5 wt% was reported in Ti-Nb-Ta-Zr single crystals (Takesue et al., 2009) and 0.46 wt% O content increases the strength of Ti-35Nb-7Zr-5Ta-0.46 O alloy to 1000 MPa in solution treated condition (Qazi et al., 2004). Nakai et al. (2009) reported the increase of the elastic modulus and the strength for similar Ti-29Nb-13Ta-4.6Zr alloy by increased oxygen content. Niinomi et al. (2016) recently discussed the effect of oxygen on phase transformations in the same alloy.

Ti-Nb-Ta-Zr-O alloys with various Nb and O content and comparatively low Ta and Zr are often referred to as gum-metal due to very low elastic modulus and unusual dislocation-free plastic deformation mechanism (Furuta et al., 2007, Nagasako et al., 2016, Saito et al., 2003, Tane et al., 2011). Enhanced publication activity in the last years illustrates high research interest in the biomedical Ti alloys with increased oxygen content.

The combined effect of Fe and/or Si on strengthening of the TNTZ alloy was investigated in detail in our previous study (Kopová et al., 2016). However, to our best knowledge, no study examining combined effect of oxygen and Fe/Si on the strength and the elastic modulus of biomedical β -Ti alloy has been reported yet.

2. Material and experimental methods

The material was prepared at the company UJP Praha, Czech Republic by arc melting of pure elements under low pressure of clean He atmosphere (350 mbar). Oxygen was introduced during melting by adding appropriate amount of TiO_2 , which dissolved in the melt. Each part of the sample was remelted at least six times by electric arc to ensure the chemical homogeneity. Samples of an approximate weight of 200 g in the shape of small bricks were homogenized at 1400 °C in

Table 1

Chemical composition of investigated alloys. TNTZ refers to Ti-35.3Nb-5.7Ta-7.3Zr. Contents of alloying elements are given in wt%. Fe, Si and O are added at the extent of Ti. An asterisk (*) marks the alloys which could not be successfully forged.

Ti-35.3Nb-5.7Ta-7.3Zr (TNTZ)	TNTZ-2Fe
TNTZ-0.25Si	TNTZ-2Fe-0.25Si*
TNTZ-0.4O	TNTZ-2Fe-0.4O
TNTZ-0.25Si-0.4O	TNTZ-2Fe-0.25Si-0.4O*
TNTZ-0.7O	TNTZ-2Fe-0.7O*
TNTZ-0.25Si-0.7O	TNTZ-2Fe-0.25Si-0.7O*

vacuum for two hours and furnace cooled. This condition is referred to as the as-cast condition. Despite slow furnace cooling, the alloys did not contain any α phase particles observable by scanning electron microscopy.

The as-cast material was subsequently forged using forging hammer into the shape of rods by company Comtes FHT, Czech Republic. Prior to the forging and between the forging steps the material was heated to approximately 1100 °C in argon atmosphere to avoid excessive oxidation. The forging process was performed in air with cold tools and the temperature of the workpiece was not further controlled. Since no α phase was observed in the interior of the rods, the forging temperature of bulk material did not fall below β -transus temperature. The forged rods were machined to the diameter of 8–10 mm depending on surface damage. This condition is referred to as the as-forged condition.

The nominal composition of twelve alloys investigated in this study is summarized in Table 1. The oxygen content was checked by carrier-gas-hot-extraction (CGHE) method. The resulting oxygen content was 0.06, 0.35 and 0.66 wt% of O for alloys with the nominal oxygen content of 0, 0.4 and 0.7 wt%, respectively. The differences in the measured oxygen content between the alloys with the same nominal oxygen content were below 0.01 wt%. Nitrogen contamination was below 0.03 wt%. The forgeability of alloys with high content of Fe, Si and O was generally poor. Alloys marked by asterisk in Table 1 could not be successfully forged.

SEM observations were performed using scanning electron microscopes FEI Quanta 200 F and Tescan LYRA 3GMU both equipped with field emission gun (FEG) operated at the accelerating voltage of 20 kV. Microhardness was measured using automatic micro-hardness tester Qness Q10a according to Vickers with load of 0.5 kg and indentation time 10 s.

A computer-controlled DAKEL-CONTI-4 acoustic emission system was used to monitor acoustic emission (AE) signal during tensile tests. Four channels with different amplification (0–20–30–40 dB) and 2 MHz sampling frequency were used to detect and store data. More details on the method and the data analysis are reported elsewhere (Bohlen et al., 2004, Dobroň et al., 2012).

Tensile tests were performed at room temperature employing the computer controlled Instron 5882 machine using the strain rate of 10^{-4} s^{-1} . Round samples with the diameter of 3 mm and the gauge length of 15 mm were used for the tensile tests.

Elastic constants were evaluated by the ultrasonic pulse-echo method (Papadakis and Lerch, 2000). Elastic constants are determined from velocities of propagation of quasi-longitudinal (qL) and quasi-transverse (qT) acoustic waves. Calculation of elastic coefficients from the set of velocities is relatively simple for materials with cubic crystal symmetry, which is the case of studied β -Ti alloys. Two sets of delayed broadband transducers for generating and receiving acoustic waves (10 MHz or 30 MHz for qL waves and 5 MHz or 20 MHz for qT-waves) were used with a pulse/receiver system DPR50+ (JSR Ultrasonics). Time of flight measurements were carried out by a pulse overlapping technique implemented in a digital storage oscilloscope LT264M (LeCroy) (Landa and Plešek, 2002).

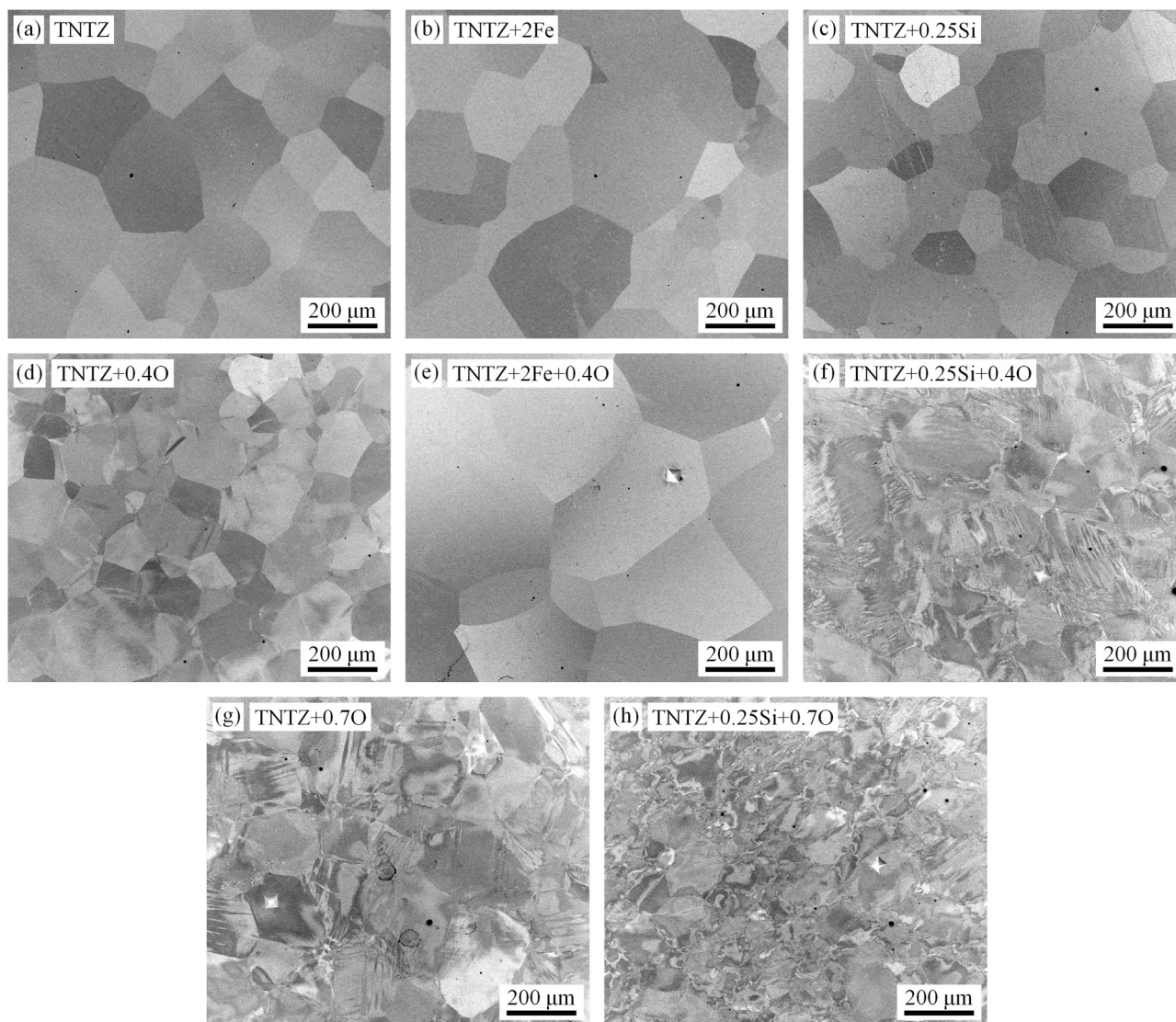


Fig. 1. SEM micrographs of microstructure of selected alloys in the as-forged condition.

3. Results

3.1. Microstructure of studied alloys

The microstructure of the investigated alloys in the as-forged condition observed by SEM employing channelling contrast of BSE is shown in Fig. 1. The benchmark TNTZ alloy and all alloys with 2 wt% of Fe contain large equiaxed grains without apparent deformation, while most alloys with oxygen additions are deformed. Neither α phase nor α'' phase is observed in any alloy suggesting that the β phase is sufficiently stabilized by Nb, Ta and possibly even Zr and the α -stabilizing effect of oxygen is surpassed. Small black spots are remnants from polishing and traces of microhardness indents can also be seen.

Alloys with 0.25 wt% of Si contain small silicide particles with the size of $\sim 1 \mu\text{m}$. A detail of a representative area containing silicides is shown in Fig. 2. The composition of these precipitates is $(\text{Ti,Zr})_5\text{Si}_3$ according to (Chaudhuri and Perepezko, 1994). Energy dispersive spectroscopy (EDS) study (not shown) could not unambiguously confirm the stoichiometric composition, but it revealed that these particles are significantly Zr enriched suggesting that Zr is preferred to Ti in silicide formation. Similar alloys were studied by EDS in our previous study (Kopová et al., 2016). Silicide particles seem to be distributed homogeneously, but particles precipitated along grain

boundaries were also observed (Fig. 2b).

3.1.1. Mechanical properties

Table 2 summarizes the mechanical properties of all studied alloys. Elastic modulus (E) and microhardness (HV) were measured in the as-cast condition while tensile tests were performed in the as-forged condition.

The benchmark TNTZ alloy has a very low elastic modulus of $\sim 65 \text{ GPa}$. Si slightly increases the elastic modulus of the benchmark alloy. Additions of Fe or O result in an increase in elastic modulus to 80 GPa , which is typical for β phase (Welsch et al., 1993). Si addition in alloys containing also Fe or O further slightly increases elastic modulus in these alloys. A different situation is in the alloys containing both Fe and O which exhibit high elastic modulus $> 100 \text{ GPa}$. Si addition in alloys containing Fe and O significantly reduces the elastic modulus, which is a rather surprising result and will be discussed below.

The increase of elastic modulus due to oxygen was explained theoretically for α phase (Lee and Welsch, 1990, Song et al., 2002). However, almost the same values of elastic modulus were found in this study in alloys containing 0.4 and 0.7 wt% of O (81 and 80 GPa , respectively).

The effect of elemental additions (Si, Fe, O) on the microhardness is more straightforward, since any of these elements contribute to the

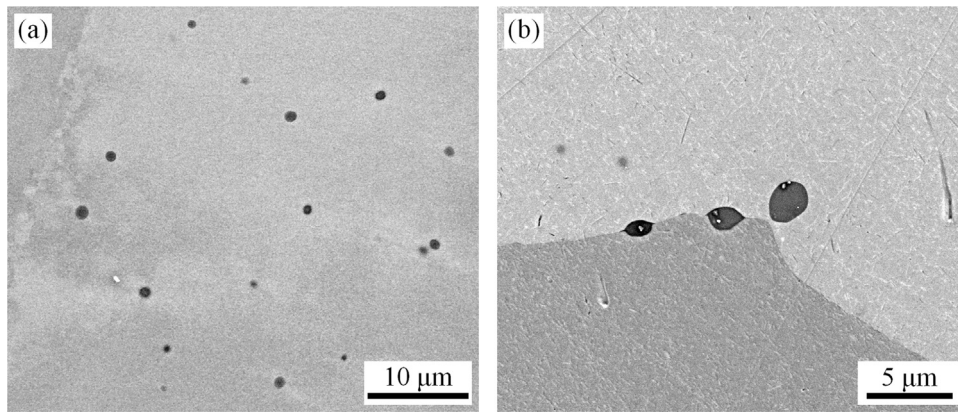


Fig. 2. Detailed SEM micrographs of silicide particles. a) Homogeneous distribution of silicide particles (TNTZ+0.25Si+0.7O alloy), b) Example of grain boundary silicide particles (TNTZ+2Fe+0.25Si+0.4O alloy).

Table 2
Mechanical properties of the studied alloys.

	E [GPa]	HV [HV0.5]	YTS [MPa]	UTS [MPa]	Elongation [%]
Ti-35.3Nb-5.7Ta-7.3Zr (TNTZ)	63	164	447	545	21
TNTZ-0.25Si	65	219	629	716	13
TNTZ-2Fe	79	236	587	719	27
TNTZ-2Fe-0.25Si	82	263	N/A	N/A	N/A
TNTZ-0.4O	81	270	860	903	16
TNTZ-0.25Si-0.4O	87	294	885	1099	22
TNTZ-2Fe-0.4O	107	321	817	1130	28
TNTZ-2Fe-0.25Si-0.4O	85	328	N/A	N/A	N/A
TNTZ-0.7O	80	335	1017	1217	21
TNTZ-0.25Si-0.7O	87	337	1085	1373	24
TNTZ-2Fe-0.7O	109	371	N/A	N/A	N/A
TNTZ-2Fe-0.25Si-0.7O	94	390	N/A	N/A	N/A

microhardness increase. However, the combined effect of two or more additions is always lower than the sum of individual effects. The effect of interstitial oxygen is very pronounced. Alloying by 0.4 wt% (1.4 at%) of O increased the microhardness of the material more than alloying by 2 wt% (2.3 at%) of Fe. The microhardness of the benchmark alloy was increased by 100% by 0.7 wt% of O. Combined alloying by O and Fe further enhances the microhardness.

Tensile tests were conducted for 8 alloys in the *as-forged* condition and the results are summarized in Table 2 and graphically displayed in Fig. 3. Fe and Si additions increase the yield stress up to 600 MPa. More significant increase in the yield stress is achieved by oxygen. TNTZ-0.4 O alloy exceeds the yield stress of 800 MPa and the yield stress of TNTZ-0.7 O reaches 1000 MPa. Note that these two alloys

differ significantly in strength, while their elastic moduli are equal. In alloys with increased oxygen content, Fe and Si additions have low effect on the yield stress. Very high true ultimate tensile strength (UTS) is achieved due to work hardening in some alloys. UTS of 1200 MPa is achieved by addition of 0.7 wt% of oxygen. Such value corresponds to high strength metastable β-alloys and is much higher than the typical UTS of Ti-6Al-4V alloy (Lütjering and Williams, 2007). Note also that UTS values correlate well with HV values.

Figs. 4a and 4b show stress-strain curves from a representative sample of each investigated alloy. The benchmark alloy, the alloy with 0.4O and the alloy with 0.25 Si do not show significant work hardening. Note that significant work hardening correlates with the higher total elongation to fracture (see also Table 2).

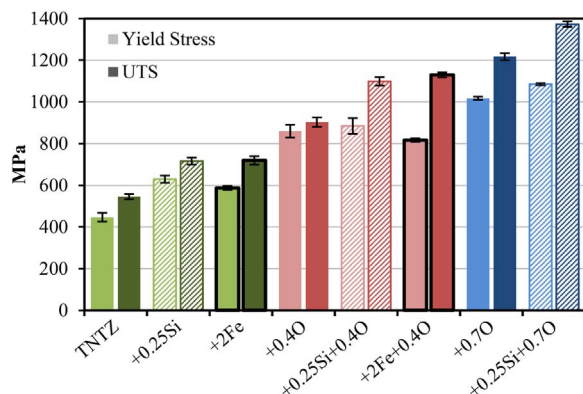


Fig. 3. Yield stress and ultimate tensile strength (UTS) determined from true stress–true strain curves.

3.1.2. Twinning in the benchmark Ti-35.3Nb-5.7Ta-7.3Zr

All tensile tests were complemented by acoustic emission (AE) measurement. All alloys, except the benchmark TNTZ alloy, did not exhibit any distinct behaviour – acoustic signal (not shown here) was detectable only at around the yield point and at fracture. On the other hand, the stress-strain curve of the benchmark TNTZ alloy (Fig. 5) showed distinct serrated character around the yield point accompanied by a strong acoustic emission signal over the range of 4% of strain (~400 s of experiment). The strong acoustic emission signal in the benchmark TNTZ alloy can be attributed to twinning as proven by EBSD image (Fig. 6) taken from the gauge of the specimen after the tensile test.

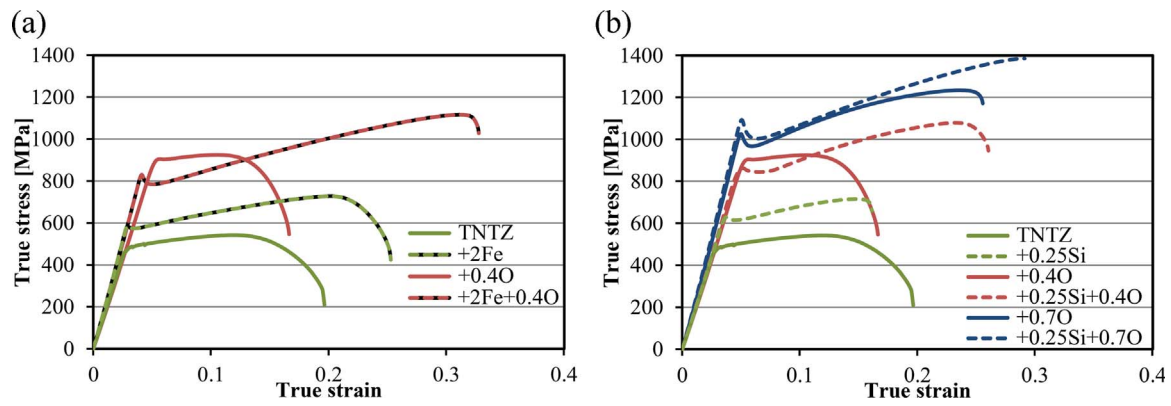


Fig. 4. Stress-strain curves a) TNTZ+Si+O, b) TNTZ+Fe+O.

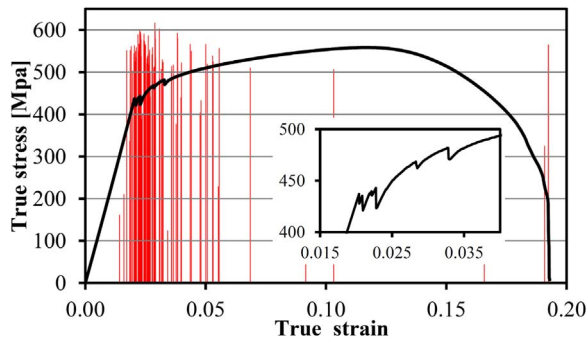


Fig. 5. Stress-strain curve of Ti-35.3-5.7Ta-7.3Zr alloy accompanied with acoustic emission measurement in red (arbitrary units in log-scale). Inset: serrated character of the stress-strain curve around the yield point.

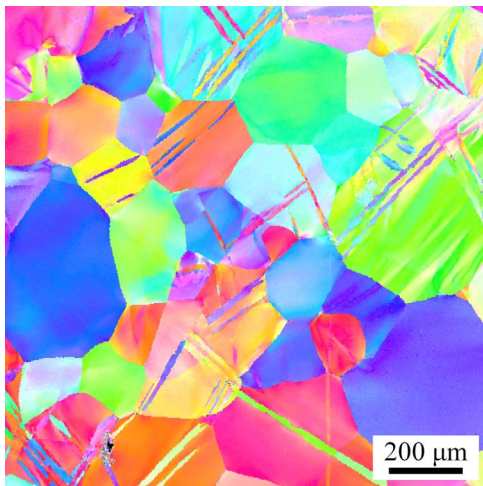


Fig. 6. Benchmark TNTZ alloy. EBSD image (IPF map) of the gauge of specimen after the tensile test.

4. Discussion

4.1. Elastic modulus

High elastic modulus E of α and ω phases implies that hardening by particles of these phases have an adverse effect on elastic modulus. Furthermore, the lowest modulus is achieved in alloys containing only β phase with low stability due to the ‘proximity’ to the $\beta \rightarrow \alpha'$ transformation (Tane et al., 2010). As first described in (Morinaga et al., 1992), the elastic modulus of Ti alloys can be deduced from a bond-order (Bo value) and the d-electron-orbital energy (Md value) of the alloy using so-called Bo - Md diagram (Morinaga et al., 1992, Song et al., 2016).

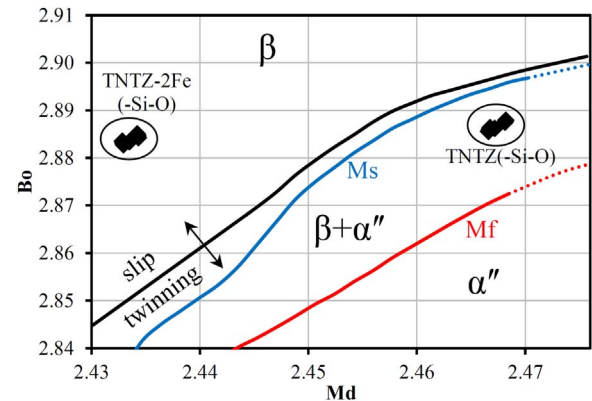


Fig. 7. Bo - Md diagram. The dependence of phase composition and dominant deformation mechanism on the Bo and Md values, applicable mainly to Ti-Nb alloys. \blacklozenge symbols mark the positions of the investigated alloys. Fe has the most pronounced effect on the Md value, while the effect of Si is low and the effect of O is omitted. As a consequence, the investigated alloys form two distinct groups.

This approach is based on calculating Bo and Md values for various alloying elements in bcc Ti reported in (Abdel-Hady et al., 2006). Average values weighted by atomic concentrations are used to calculate the Bo and Md values for alloys. Fig. 7 presents so called Bo - Md diagram adapted from (Abdel-Hady et al., 2006, Laheurte et al., 2010). The empirical Bo - Md space is divided into three regions by M_s and M_f curves which refer to the martensite start and the martensite finish of the $\beta \rightarrow \alpha''$ transformation. Another curve divides the Bo - Md space into two regions that differ in dominant deformation mechanism - slip and twinning. The minimum elastic modulus is believed to be achieved just along the M_s curve especially for higher values of Bo and Md (Laheurte et al., 2010). In Saito et al. (2003), the values of $Bo = 2.87$ and $Md = 2.45$ associated with the low elastic modulus were reported.

The Bo and Md values were calculated for the alloys investigated in this study and their positions are represented by \blacklozenge symbol. The effect of oxygen on the overall Bo and Md values is omitted since Bo and Md values for oxygen in bcc Ti were not reported (Saito et al., 2003). However, it is known that oxygen stabilizes the β phase against α'' phase and shifts the M_s curve to the lower values of Bo (Abdel-Hady et al., 2006).

All studied alloys therefore form two groups in the Bo - Md diagram. Alloys containing Fe are placed on the left in the β stable region, while alloys without Fe lie in the $\beta + \alpha''$ region. It can be concluded that Bo - Md analysis is not valid for the studied alloys without Fe, since none of the studied alloys contains α'' phase and only the benchmark TNTZ alloy deforms by twinning. It is therefore argued that the Bo - Md diagram does not fully capture the relation between chemical composition, phase composition and dominant plastic deformation mechanism. In particular, the effect of interstitial oxygen should be taken into account separately.

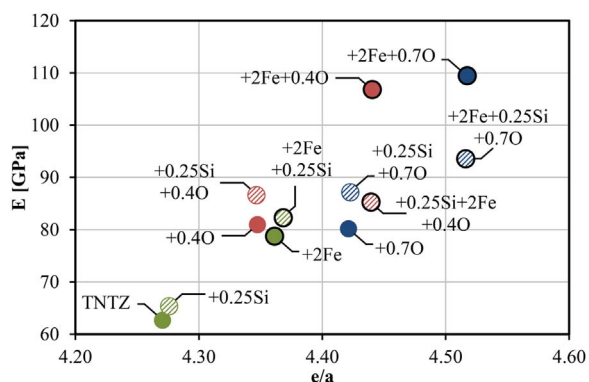


Fig. 8. The dependence of elastic modulus on e/a ratio.

As discussed in Luke et al. (1965), the phase stability is related to the electron-per-atom ratio (e/a ratio) which follows from the electron theory of transition metals. Fig. 8 shows the dependence of the elastic modulus on the e/a ratio for the investigated alloys. e/a ratio is calculated as the weighted average of valence electrons of all alloying elements.

Note that it is not clear how to include interstitial oxygen into the e/a ratio calculation. We decided to include 6 valence electrons per oxygen atom into the sum of electrons (e), but not to include oxygen atoms into the sum of atoms (a) since interstitial atoms do not occupy lattice positions. This approach is consistent with calculations of valence electron concentration (VEC) which subsequently affects the bulk modulus (Lalena and Cleary, 2010). The contribution of interstitial oxygen to bonding, Fermi level, the density of states at Fermi level and consequently elastic constants remains unknown for such complicated alloying systems (see also (Toth, 1971, Tiwari and Ramanujan, 2001)) and the effect of oxygen on e/a ratio is often completely neglected in the low-modulus β -Ti alloys (Saito et al., 2003, Tane et al., 2011).

According to Saito et al. (2003), the minimum elastic modulus in Ti-Nb based bcc alloys is achieved for $e/a = 4.24$, while elastic modulus rises with increasing e/a ratio due to increasing stability of β phase (Hao et al., 2007). The correlation between the calculated e/a ratio and the measured elastic modulus (Fig. 8) is only partial.

Note that the addition of both O and Fe causes very high elastic modulus >100 GPa that is not typical for the β phase. Such pronounced increase in stiffness might be caused by the interaction of substitutional Fe with interstitial O atoms in bcc β phase. These interactions were studied by investigating relaxation processes identified in the internal friction spectrum known as Snoek effect (Snoek, 1939). Snoek type relaxation processes were studied in Ti-Nb based alloys with interstitial oxygen when exploring high damping β titanium alloys (Chaves et al., 2014, Lu et al., 2012, Yin et al., 2006). Solute (Ti) – interstitial (O) interactions were also reported for Nb and V alloys (Shikama et al., 1977, Szkoziak and Smith, 1975). The interaction between solute Fe and interstitial O is repulsive resulting in ‘forbidden regions’ around Fe solutes (Shikama et al., 1977). Therefore, it increases the oxygen concentration in other areas. Increasing content of interstitial oxygen atoms increases the elastic modulus in some bcc metals (Fischer et al., 1975, Greiner et al., 1979), despite data on Ti-Nb based bcc alloys are not available. It is therefore suggested, that the repulsion of interstitial oxygen atoms from substitutional Fe atoms may contribute to the overall increase of elastic modulus. On the other hand, adding Si to alloys with both Fe and O suppresses this stiffening effect. High chemical affinity of Si to oxygen was documented in steels (Svedung and Vannerberg, 1974) and indirectly observed in α -Ti (Chaze and Coddet, 1986; Vojtěch et al., 2003). It might be therefore speculated, that substitutional Si atoms act as traps for interstitial oxygen atoms and may compensate the repulsion of O from Fe.

4.2. Strength, elongation and sharp yield point

Oxygen additions increase both the yield stress and UTS of TNTZ-based alloys. The yield stress reaches 1000 MPa while the UTS reaches 1200 MPa, which significantly exceeds the tensile strength of the most used Ti-6Al-4V alloy. Fe and Si also increase the tensile strength, but their effect is comparatively lower.

Work hardening is clearly associated with the substitutional atoms (Fe) and interstitial atoms (O) which, at sufficient concentrations, cause pinning and multiplication of dislocations. Szkoziak (Szkoziak and Smith, 1975) argues that in the bcc materials substitutional solute atoms (Fe) create Cottrell atmosphere pinning edge dislocations, while interstitial atoms (O) create Snoek atmosphere pinning the screw dislocations.

It is argued that 0.4 wt% O is not sufficient for multiplication of dislocations during deformation and therefore work hardening is not observed (Furuta et al., 2007, Saito et al., 2003). On the other hand, 0.7 wt% O is sufficient in this respect. Furthermore, premature necking is prevented by work hardening and results in a higher elongation to failure. This leads to an unexpected result that the elongation first decreases for low O concentration (0.4 wt% O), while it increases for higher O content (0.7 wt% O). Note that oxygen content > 0.4 wt% is detrimental for room temperature ductility of the α phase titanium (Geng et al., 2011). On the other hand, the ductility of β -Ti alloys containing a substantial amount of oxygen remains relatively high (Qazi et al., 2004, Nakai et al., 2009). The main practical result is that additions of oxygen or combined Fe/Si/O results in the material with the high yield stress, significant work hardening and high room temperature elongation while keeping the elastic modulus at around 80 GPa. Mechanical properties of developed alloys exceed those of TNTZ-O alloys in solution treated condition (Qazi et al., 2004, Nakai et al., 2009), while subsequent ageing leads to significant increase of elastic modulus. Promising mechanical properties, similar to those presented in this study, were achieved in Ti-Nb based alloys by intensive cold rolling or cold swaging (Furuta et al., 2005, Kim et al., 2005). Despite promising mechanical properties, the final size of the product has the thickness of 0.13 mm (Kim et al., 2005) or of few millimetres only (Furuta et al., 2005). Such product sizes are not utilizable for manufacturing implants of big joints. On the other hand, mechanical properties of alloys presented in this study were achieved without intensive working procedure and products can be prepared in virtually any size – depending on size of the initial cast ingot.

Finally, note also that comparatively low-purity Ti and Nb (with high Fe and O content) can be used for manufacturing of these alloys to reduce material costs.

5. Conclusions

- Twelve different Ti-Nb-Zr-Ta based alloys with oxygen content of 0%, 0.4% and 0.7% (wt%); Fe content of 0% and 2%; and Si content of 0% and 0.25% were prepared by arc melting and hot forging.
- Silicide precipitates were observed by SEM in alloys containing 0.25% of Si.
- The elastic modulus of the benchmark of Ti-35.3Nb-5.7Ta-7.3Zr alloy was as low as 65 GPa, while the elastic modulus of alloys containing Fe and/or O exceeded 80 GPa. This was attributed to an increased stability of β phase associated with increased electrons per atom ratio.
- The 0.7 wt% of oxygen addition doubled the yield strength and UTS of the benchmark TNTZ alloy to values of 1000 MPa and 1200 MPa, respectively. Fe and Si further increase the tensile strength, but the effect is not so pronounced.
- Fe and/or O additions enhance the work hardening and cause sharp yield point suggesting that substitutional Fe atoms and interstitial oxygen atoms interact with dislocations already during hot working.
- By alloying of Ti-Nb-Zr-Ta alloy with low amount of O/Fe/Si a 20%

increase in strength and a 20% decrease in elastic modulus was achieved when compared to the common Ti-6Al-4V alloy.

- Despite Fe and Si provide some additional strengthening, TNTZ-0.7O alloy already exhibits excellent mechanical properties and is a prospective candidate for load-bearing orthopaedic implants manufacturing.

Acknowledgements

This work was financially supported by the AdMat project of the Czech Science Foundation (14-36566G). O.S. acknowledges the financial support by the Ministry of Education, Youth and Sport Czech Republic Project LQ1603 (Research for SUSEN). This work has been realized within the SUSEN Project (established in the framework of the European Regional Development Fund (ERDF) in project CZ.1.05/2.1.00/03.0108).

References

- Abdel-Hady, M., Hinoshita, K., Morinaga, M., 2006. General approach to phase stability and elastic properties of β -type Ti-alloys using electronic parameters. *Scr. Mater.* 55, 477–480.
- Ahmed T. and Rack H.J., 1999. Alloy of titanium, zirconium, niobium and tantalum for prosthetics, US Patent: US 5871595A.
- Ankem, S., Banerjee, D., McNeish, D.J., Williams, J.C., Seagle, S.R., 1987. Silicide formation in Ti-3Al-8V-6Cr-4Zr-4Mo. *Metall. Trans. A* 18, 2015–2025.
- Bohlen, J., Chmelík, F., Dobroň, P., Letzig, D., Lukáč, P., Kainer, K.U., 2004. Orientation effects on acoustic emission during tensile deformation of hot rolled magnesium alloy AZ31. *J. Alloy. Compd.* 378, 207–213.
- Chaudhuri, K., Perepezko, J.H., 1994. Microstructural study of the titanium alloy Ti-15Mo-2.7Nb-3Al-0.2Si (TIMETAL 21S). *Metall. Mater. Trans. A* 25, 1109–1118.
- Chaves, J.M., Florêncio, O., Silva, P.S., Marques, P.W.B., Schneider, S.G., 2014. An elastic relaxation associated to phase transformations and interstitial atoms in the Ti-35Nb-7Zr alloy. *J. Alloy. Compd.* 616, 420–425.
- Chaze, A.M., Coddet, C., 1986. The role of nitrogen in the oxidation behaviour of titanium and some binary alloys. *J. Less-Common Met.* 124, 73–84.
- Chen, B.-Y., Hwang, K.-S., 2012. Sintered Ti-Fe alloys with in situ synthesized TiC dispersoids. *Mater. Sci. Eng. A* 541, 88–97.
- Chu, P.K., Chen, J.Y., Wang, L.P., Huang, N., 2002. Plasma-surface modification of biomaterials. *Mater. Sci. Eng. R: Rep.* 36, 143–206.
- Dobroň, P., Chmelík, F., Parfenenko, K., Letzig, D., Bohlen, J., 2012. On the effect of the extrusion speed on microstructure and plastic deformation of ZEK10 and ZEK100 magnesium alloys – an acoustic emission study. *Acta Phys. Pol. A* 122, 593–596.
- Du, Z.X., Xiao, S.L., Wang, P.X., Xu, L.J., Chen, Y.Y., Rahoma, H.K.S., 2014. Effects of trace TiB and TiC on microstructure and tensile properties of β titanium alloy. *Mater. Sci. Eng. A* 596, 71–79.
- Ferrandini, P.L., Cardoso, F.F., Souza, S.A., Afonso, C.R., Caram, R., 2007. Aging response of the Ti-35Nb-7Zr-5Ta and Ti-35Nb-7Ta alloys. *J. Alloy. Compd.* 433, 207–210.
- Fischer, E.S., Westlake, D.G., Ockers, S.T., 1975. Effects of hydrogen and oxygen on the elastic moduli of vanadium, niobium, and tantalum single crystals. *Phys. Stat. Sol.* 28, 591–602.
- Furuta, T., Kuramoto, S., Hwang, J., Nishino, K., Saito, T., 2005. Elastic deformation behavior of multi-functional Ti-Nb-Ta-Zr-O alloys. *Mater. Trans.* 46, 3001–3007.
- Furuta, T., Kuramoto, S., Hwang, J., Nishino, K., Saito, T., Niinomi, M., 2007. Mechanical properties and phase stability of Ti-Nb-Ta-Zr-O alloys. *Mater. Trans.* 48, 1124–1130.
- Geetha, M., Singh, A.K., Asokamani, R., Gogia, A.K., 2009. Ti based biomaterials, the ultimate choice for orthopaedic implants – a review. *Prog. Mater. Sci.* 54, 397–425.
- Geng, F., Niinomi, M., Nakai, M., 2011. Observation of yielding and strain hardening in a titanium alloy having high oxygen content. *Mater. Sci. Eng. A* 528, 5435–5445.
- Greiner, J.D., Carlson, O.N., Smith, J.F., 1979. Single-crystal elastic constants of vanadium and vanadium with oxygen additions. *J. Appl. Phys.* 50, 4394–4398.
- Hao, Y.L., Li, S.J., Sun, S.Y., Zheng, C.Y., Yang, R., 2007. Elastic deformation behaviour of Ti-24Nb-4Zr-7.9Sn for biomedical applications. *Acta Biomater.* 3, 277–286.
- Headley, T.J., Rack, H.J., 1979. Phase transformations in Ti-3Al-8V-6Cr-4Zr-4Mo. *Metall. Trans. A* 10, 909–920.
- Katti, K.S., 2004. Biomaterials in total joint replacement. *Colloids Surf. B Biointerfaces* 39, 133–142.
- Kim, J.I., Kim, H.Y., Hosoda, H., Miyazaki, S., 2005. Shape memory behavior of Ti-22Nb-(0.5–2.0)O (at%) biomedical alloys. *Mater. Trans.* 46, 852–857.
- Kopová, I., Stráský, J., Harcuba, P., Landa, M., Janeček, M., Bačáková, L., 2016. Newly developed Ti-Nb-Zr-Ta-Si-Fe biomedical beta titanium alloys with increased strength and enhanced biocompatibility. *Mater. Sci. Eng. C* 60, 230–238.
- Kudrman, J., Fousek, J., Březina, V., Míková, R., Veselý, J., 2007. Titanium alloys for implants in medicine. *Met. Mater.* 45, 199–208.
- Lalena, J.N., Cleary, D.A., 2010. *Principles of Inorganic Materials Design*. Wiley, New Jersey.
- Laheurte, P., Prima, F., Eberhardt, A., Gloriant, T., Wary, M., Patoor, E., 2010. Mechanical properties of low modulus titanium alloys designed from the electronic approach. *J. Mech. Behav. Biomed. Mater.* 3, 565–573.
- Landa, M., Plešek, J., 2002. Contrast enhancement of ultrasonic imaging of internal stresses in materials. *Ultrasonics* 40, 531–535.
- Lee, Y.T., Welsch, G., 1990. Young's modulus and damping of Ti-6Al-4V alloy as a function of heat treatment and oxygen concentration. *Mater. Sci. Eng. A* 128, 77–89.
- Long, M., Rack, H.J., 1998. Titanium alloys in total joint replacement—a materials science perspective. *Biomaterials* 19, 1621–1639.
- Lu, H., Li, C.X., Yin, F.X., Fang, Q.F., Umezawa, O., 2012. Effects of alloying elements on the Snoek-type relaxation in Ti-Nb-X-O alloys (X = Al, Sn, Cr, and Mn). *Mater. Sci. Eng. A* 541, 28–32.
- Luke, C.A., Taggart, R., Polonis, D.H., 1965. Electronic factors and the metastable constitution of quenched alloys based on titanium and zirconium. *J. Nucl. Mater.* 16, 7–18.
- Lütjering G. and Williams J.C., 2007. *Titanium*, Springer.
- Min, X.H., Emura, S., Zhang, L., Tsuzaki, K., 2008. Effect of Fe and Zr additions on ω phase formation in β -type Ti-Mo alloys. *Mater. Sci. Eng. A* 497, 74–78.
- Min, X.H., Emura, S., Sekido, N., Nishimura, T., Tsuchiya, K., Tsuzaki, K., 2010. Effects of Fe addition on tensile deformation mode and crevice corrosion resistance in Ti-15Mo alloy. *Mater. Sci. Eng. A* 527, 2693–2701.
- Morinaga M., Kato M., Kamimura T., Fukumoto M., Harada I., Kubo K., 1992. Theoretical design of b-type titanium alloys, Titan. Sci. Technol. In: Proceedings of the 7th International Conference Titan. San Diego CA USA, 1992, pp. 276–28.
- Nagasako, N., Asahi, R., Isheim, D., Seidman, D.N., Kuramoto, S., Furuta, T., 2016. Microscopic study of gum-metal alloys: a role of trace oxygen for dislocation-free deformation. *Acta Mater.* 105, 347–354.
- Nakai, M., Niinomi, M., Akahori, T., Tsutsumi, H., Ogawa, M., 2009. Effect of oxygen content on microstructure and mechanical properties of biomedical Ti-29Nb-13Ta-4.6Zr alloy under solutionized and aged conditions. *Mater. Trans.* 50, 2716–2720.
- Nejzchlebová, J., Janovská, M., Seiner, H., Sedlák, P., Landa, M., Šmilauerová, J., Stráský, J., Harcuba, P., Janeček, M., 2016. The effect of athermal and isothermal ω phase particles on elasticity of β -Ti single crystals. *Acta Mater.* 110, 185–191.
- Niinomi, M., 1998. Mechanical properties of biomedical titanium alloys. *Mater. Sci. Eng. A* 243, 231–236.
- Niinomi, M., Nakai, M., Hieda, J., 2012. Development of new metallic alloys for biomedical applications. *Acta Biomater.* 8, 3888–3903.
- Niinomi, M., Nakai, M., Hendrickson, M., Nandwana, P., Alam, T., Choudhuri, D., Banerjee, R., 2016. Influence of oxygen on omega phase stability in the Ti-29Nb-13Ta-4.6Zr alloy. *Scr. Mater.* 123, 144–148.
- Okazaki, Y., Gotoh, E., 2005. Comparison of metal release from various metallic biomaterials in vitro. *Biomaterials* 26, 11–21.
- Papadakis, E.P., Lerch, T., 2000. *Pulse Superposition, Pulse Echo Overlap and Related Techniques Handbook of Elastic Properties of Solids, Liquids, and Gases* 2000. Academic Press.
- Qazi, J.I., Rack, H.J., Marquardt, B., 2004. High-strength metastable beta-titanium alloys for biomedical applications. *JOM* 56, 49–51.
- Rack, H.J., Qazi, J.I., 2006. Titanium alloys for biomedical applications. *Mater. Sci. Eng. C* 26, 1269–1277.
- Rho, J.Y., Ashman, R.B., Turner, C.H., 1993. Young's modulus of trabecular and cortical bone material: ultrasonic and microtensile measurements. *J. Biomech.* 26, 111–119.
- Saito, T., Furuta, T., Hwang, J.H., Kuramoto, S., Nishino, K., Suzuki, N., Chen, R., Yamada, A., Ito, K., Seno, Y., Nonaka, T., Ikehata, H., Nagasako, N., Iwamoto, C., Ikuhara, Y., Sakuma, T., 2003. Multifunctional alloys obtained via a dislocation-free plastic deformation mechanism. *Science* 300, 464–467.
- Sakaguchi, N., Niinomi, M., Akahori, T., Takeda, J., Toda, H., 2005. Effect of Ta content on mechanical properties of Ti-30Nb-XTa-5Zr. *Mater. Sci. Eng. C* 25, 370–376.
- Shikama, T., Ishino, S., Mishima, Y., 1977. The interaction between interstitial impurities and substitutional solutes in vanadium. *J. Nucl. Mater.* 68, 315–323.
- Snoek, J.L., 1939. Letter to the editor. *Physica* 6, 591–592.
- Song, Y., Guo, Z.-X., Yang, R., 2002. First principles estimation of bulk modulus and theoretical strength of titanium alloys. *Mater. Trans.* 43, 3028–3031.
- Song, Y., Dai, J.H., Yang, R., 2016. Application of first principles theory to the design of advanced titanium alloys. In: Tiwari, A., Murugan, A., Ahuja, R. (Eds.), *Advanced Engineering Materials and Modelling*. Scrivener Publishing.
- Steinemann, S.G., 1998. Titanium – the material of choice? *J. Periodontol.* 17, 7–21.
- Sun, J., Yao, Q., Xing, H., Guo, W.Y., 2007. Elastic properties of β , α' and ω metastable phases in Ti-Nb alloy from first-principles. *J. Phys. Condens. Matter* 19, 486215.
- Svedung, I., Vannerberg, N.-G., 1974. The influence of silicon on the oxidation process of iron. *Corr. Sci.* 14, 391–399.
- Szkopiak, Z.C., Smith, J.T., 1975. The internal friction of Nb-1 at% substitutional alloys. *J. Phys. Appl. Phys.* 8, 1273.
- Takesue, N., Shimizu, Y., Yano, T., Hara, M., Kuramoto, S., 2009. Single-crystal growth of Ti-Nb-Ta-Zr-O alloys and measurement of elastic properties. *J. Cryst. Growth* 311, 3319–3324.
- Tane, M., Akita, S., Nakano, T., Hagihara, K., Umakoshi, Y., Niinomi, M., Mori, H., Nakajima, H., 2010. Low Young's modulus of Ti-Nb-Ta-Zr alloys caused by softening in shear moduli c' and c_{44} under lower limit of body-centered cubic phase stability. *Acta Mater.* 58, 6790–6798.
- Tane, M., Nakano, T., Kuramoto, S., Hara, M., Niinomi, M., Takesue, N., Yano, T., Nakajima, H., 2011. Low Young's modulus in Ti-Nb-Ta-Zr-O alloys: cold working and oxygen effects. *Acta Mater.* 59, 6975–6988.
- Tane, M., Okuda, Y., Todaka, Y., Ogi, H., Nagakubo, A., 2013. Elastic properties of single-crystalline ω phase in titanium. *Acta Mater.* 61, 7543–7554.
- Tang, X., Ahmed, T., Rack, H.J., 2000. Phase transformations in Ti-Nb-Ta and Ti-Nb-Ta-Zr alloys. *J. Mater. Sci.* 35, 1805–1811.
- Tiwari, G.P., Ramanujan, R.V., 2001. Review: the relation between the electron to atom ratio and some properties of metallic systems. *J. Mater. Sci.* 36, 271–283.

- Toth, L.E., 1971. Transition Metal Carbides and Nitrides. Academic Press, New York and London.
- Vojtěch, D., Bártová, B., Kubatík, T., 2003. High temperature oxidation of titanium–silicon alloys. *Mater. Sci. Eng. A* 361, 50–57.
- Welsch, G., Boyer, R., Collings, E.W., 1993. *Materials Properties Handbook: Titanium Alloys*. ASM International.
- Yin, F., Iwasaki, S., Ping, D., Nagai, K., 2006. Snoek-type high-damping alloys realized in beta-Ti alloys with high oxygen solid solution. *Adv. Mater.* 18, 1541–1544.
- Zhang, C.J., Kong, F.T., Xiao, S.L., Zhao, E.T., Xu, L.J., Chen, Y.Y., 2012. Evolution of microstructure and tensile properties of in situ titanium matrix composites with volume fraction of (TiB+TiC) reinforcements. *Mater. Sci. Eng. A* 548, 152–160.
- Zysset, P.K., Guo, X.E., Hoffer, C.E., Moore, K.E., Goldstein, S.A., 1999. Elastic modulus and hardness of cortical and trabecular bone lamellae measured by nanoindentation in the human femur. *J. Biomech.* 32, 1005–1012.

Proceedings of the International Symposium on Physics of Materials (ISPMA 14), September 10–15, 2017, Prague

High Temperature Mechanical Properties and Microstructure of Ti–Nb–Zr–Ta–O Biomedical Alloy

D. PREISLER^{a,*}, J. STRÁSKÝ^a, P. HARCUBA^a, F.G. WARCHOMICKA^b AND M. JANEČEK^a

^aCharles University, Department of Physics of Materials, Ke Karlovu 5, 121 16 Prague, Czech Republic

^bGraz University of Technology, Institute of Materials Science and Welding, Kopernikusgasse 24/I, Graz, Austria

Sufficient biocompatibility and high strength are fundamental properties required for total joint endoprostheses material. Recently developed Ti-based alloy Ti–35.3Nb–7.3Zr–5.7Ta–0.7O (wt%) exhibits these properties. However, the as-cast material does not meet requirements for fatigue resistance due to pores and very coarse grain structure and therefore a feasible forming procedure must be established. Gleeble apparatus was used to deform the studied alloy at high temperatures (from 800 °C to 1400 °C) and high strain rates (up to 1 s⁻¹) to the total strain of 0.5. Mechanical properties at elevated temperatures were evaluated. The resulting microstructure was investigated by scanning electron microscopy and electron backscatter diffraction (EBSD). It was found that forming procedure should be performed at temperatures higher than 1400 °C to reach conditions similar to forming of Ti–6Al–4V. Calculation of kernel average misorientation from EBSD data showed that most deformation is stored in the material in the vicinity of grain boundaries without any apparent recrystallization.

DOI: [10.12693/APhysPolA.134.636](https://doi.org/10.12693/APhysPolA.134.636)

PACS/topics: 81.05.Bx, 81.40.Lm, 81.70.Bt, 68.37.Hk

1. Introduction

Titanium and its alloys have been traditionally used in medicine and orthopaedics [1, 2]. There are numerous applications where these materials take advantage from excellent corrosion resistance, high biocompatibility and low Young's modulus. Commercially pure Ti has been successfully used as tooth replacement material and $\alpha+\beta$ Ti alloy Ti–6Al–4V (wt%) (Ti64), primarily developed for aerospace industry, has been used for decades as a material for implants of big body joints. Ti64 has a very high strength (around 1000 MPa), but the drawback is the content of toxic vanadium and high Young's modulus (110 GPa [3]) — although very low when compared to steels, it is still much higher than that of a bone (10–30 GPa [4]).

Alloys that retain pure β phase after quenching, which ensures lower Young's modulus [5], and contain only biocompatible elements (Nb, Ta, Mo, Zr) [6] are extensively studied nowadays. Several biocompatible Ti–Nb–Zr–Ta based alloys exhibiting the Young's modulus as low as 50–60 GPa have emerged recently; one of them having the composition Ti–35.3Nb–7.3Zr–5.7Ta (wt%; all composition values are in wt% from now on) [7]. However, their strength is approximately only one half of that of Ti64. Small amount of oxygen addition, typically 0.3%–0.5%, has a great strengthening effect on this type of β -Ti alloys [8–11] and adding more than 0.5% of oxygen, as in Ti–35.3Nb–7.3Zr–5.7Ta–0.7O, yields even higher strength, sharp yield point and deformation strengthening [12, 13]. The addition of 0.7% of oxygen raises Young's modulus to the value of 80 GPa that is still significant improvement to 110 GPa of Ti64.

The alloy with the composition Ti–35.3Nb–7.3Zr–5.7Ta–0.7O, studied in this work, contains very large grains (0.5–3 mm), small pores (5–30 μm) and dendritic inhomogeneities after casting. As a consequence, it exhibits a reduced strength [14] and poor fatigue performance. Forming procedure is therefore necessary. The goal of the current work is to find suitable conditions of working, namely the temperature and the speed of forming to allow its feasible procedure.

2. Material and methods

The alloy used in this study was cast at Retech, Co., USA in helium atmosphere. Rod with diameter 55 mm was produced by plasma arc melting of pure Ti, Nb, Zr, Ta and TiO₂ (for oxygen addition) into small compacts and remelting these compacts into final ingot. Cylindrical samples with the diameter of 8 mm and the length of 12 mm were cut from the cast ingot for compression testing using Gleeble[®] 1500 machine equipped with a servo-hydraulic system. Compression tests were performed at temperatures of 800 °C–1400 °C with strain rates $\dot{\epsilon} = 0.01 \text{ s}^{-1}$ and $\dot{\epsilon} = 1 \text{ s}^{-1}$ up to the total strain of 0.5. Duration of a compression test was 0.5 s and 50 s for high strain rate of $\dot{\epsilon} = 1 \text{ s}^{-1}$ and lower strain rate of $\dot{\epsilon} = 0.01 \text{ s}^{-1}$, respectively. Each sample was heated with the rate of 5 K/s up to the final temperature of deformation. Compressive flow curves were recorded *in situ*. Each sample was immediately water quenched after deformation. The resulting microstructure was studied by scanning electron microscope (SEM) Quanta FEG 200FX equipped with EDAX electron backscatter diffraction (EBSD) detector. Samples for microstructural observations were ground with SiC papers up to the grit of 2400 and polished with Buehler vibratory polisher with alumina 0.3 μm , 0.05 μm (for 8 h each) and colloidal silica (for 3 h) suspensions.

*corresponding author; e-mail: preisler.dalibor@gmail.com

3. Results and discussion

Flow curves from compression tests at elevated temperatures are shown in Fig. 1. It should be noted that curves recorded at high strain rate of $\dot{\epsilon} = 1 \text{ s}^{-1}$ contained artefacts and heavy noise and massive smoothing procedure was employed which resulted in wavy curves (mostly recognizable at temperature $1400 \text{ }^\circ\text{C}$). As expected, lower temperatures and higher strain rates lead to higher compressive strength. The sample deformed at $T = 800 \text{ }^\circ\text{C}$ with $\dot{\epsilon} = 0.01 \text{ s}^{-1}$ exhibits the sharp yield point similarly to the tensile flow curves performed at room temperature [13]. On the other hand, flow curves measured at higher temperatures did not exhibit the sharp yield point because the temperature is sufficiently high to activate diffusion of oxygen in matrix and prevent pinning dislocations by interstitial oxygen atoms. Note that the flow curve at $1100 \text{ }^\circ\text{C}$ with $\dot{\epsilon} = 1 \text{ s}^{-1}$ does not exhibit the sharp yield point. The origin of this undulation is the smoothing of recorded curve only.

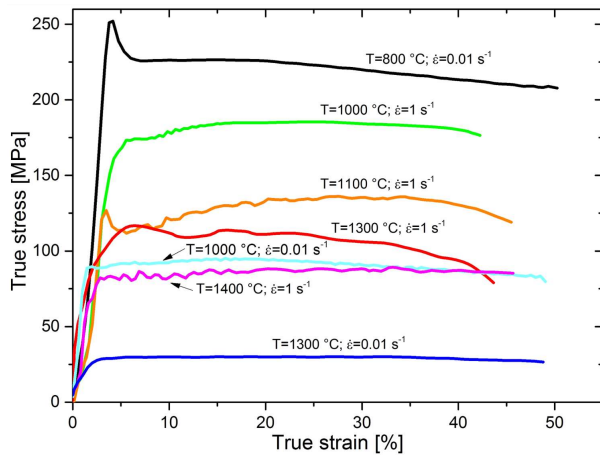


Fig. 1. Compression flow curves at various temperatures and strain rates.

Ultimate compressive strength (UCS) was determined from each flow curve. The temperature dependence of UCS is shown in Figure 2 for the $\dot{\epsilon} = 1 \text{ s}^{-1}$ and $\dot{\epsilon} = 0.01 \text{ s}^{-1}$. Fitted lines indicate that the slope is steeper for the $\dot{\epsilon} = 0.01 \text{ s}^{-1}$ than for $\dot{\epsilon} = 1 \text{ s}^{-1}$. The main reason of this difference is the sharp yield point of the sample deformed at $800 \text{ }^\circ\text{C}$. On the other hand, the slope between samples deformed at $1000 \text{ }^\circ\text{C}$ and $1300 \text{ }^\circ\text{C}$ is very similar to that at high strain rates. The strength of studied material at $\dot{\epsilon} = 1 \text{ s}^{-1}$ exceeds 170 MPa at $1000 \text{ }^\circ\text{C}$ and decreases below 100 MPa only at $1400 \text{ }^\circ\text{C}$. This behaviour is much different from that of Ti64 that has strength value at $1000 \text{ }^\circ\text{C}$ and $\dot{\epsilon} = 1 \text{ s}^{-1}$ already below 50 MPa [15] but similar to commercial stainless steel AISI 304 [16].

SEM observations revealed that porosity present in the cast condition was not completely removed by high temperature deformation. Two types of pores were found

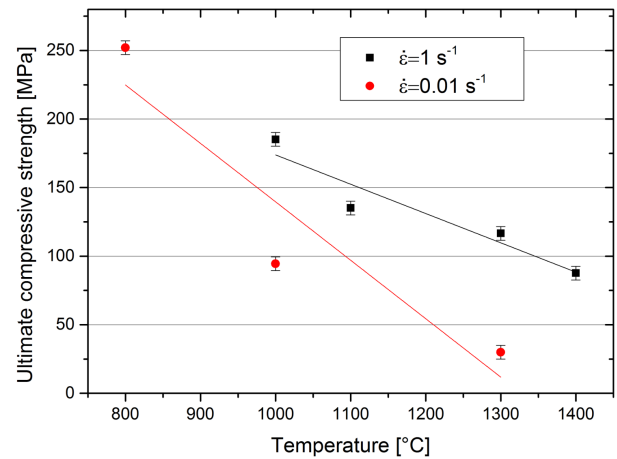


Fig. 2. The temperature dependence of the ultimate compressive strength for two strain rates.

in the deformed material: (i) small, homogeneously distributed pores and (ii) larger pores mainly along grain boundaries. Smaller pores of the size of a few micrometers were formed already during casting and Gleeble processing deformed the area around them and closed some of them. The deformed zones can be observed in backscattered electrons in Fig. 3a (sample deformed at $T = 1100 \text{ }^\circ\text{C}$ and $\dot{\epsilon} = 1 \text{ s}^{-1}$) as lighter area near both pores. The deformed area appears lighter in the SEM micrographs thanks to channelling contrast of the deformed crystal lattice that has locally different scattering condition. Larger pores have sizes of tens of micrometers and are located at the grain boundaries, especially in triple points, as in Fig. 3b for sample deformed at $T = 1300 \text{ }^\circ\text{C}$ and $\dot{\epsilon} = 1 \text{ s}^{-1}$. Note that these pores were not observed in all deformed samples and the correlation with temperature or strain rate of deformation is rather inconclusive.

EBSD measurements were performed to analyse the degree and the distribution of deformation present in samples. The area of $1300 \mu\text{m} \times 1800 \mu\text{m}$ and the step size of $4 \mu\text{m}$ were employed. For this purpose, kernel average misorientation (KAM) was determined for each data point as the mean misorientation of all points within the maximum distance of the triple step size around each point (note that hexagonal grid was used for measurements). Grain boundaries (points with misorientation higher than 5° from reference point) were excluded from each kernel. Example of inverse pole figure (IPF) map for sample deformed at $T = 1300 \text{ }^\circ\text{C}$ and $\dot{\epsilon} = 1 \text{ s}^{-1}$ is shown in Fig. 4a, corresponding KAM map is displayed together with the colour code of respective misorientations in Fig. 4b. It is clearly seen that the deformation (higher KAM value) is concentrated near the grain boundaries, especially near triple points. This phenomenon was present in all samples deformed at the strain rate $\dot{\epsilon} = 1 \text{ s}^{-1}$ and is typical in β -Ti deformed at high strain rates and/or relatively low temperatures [17].

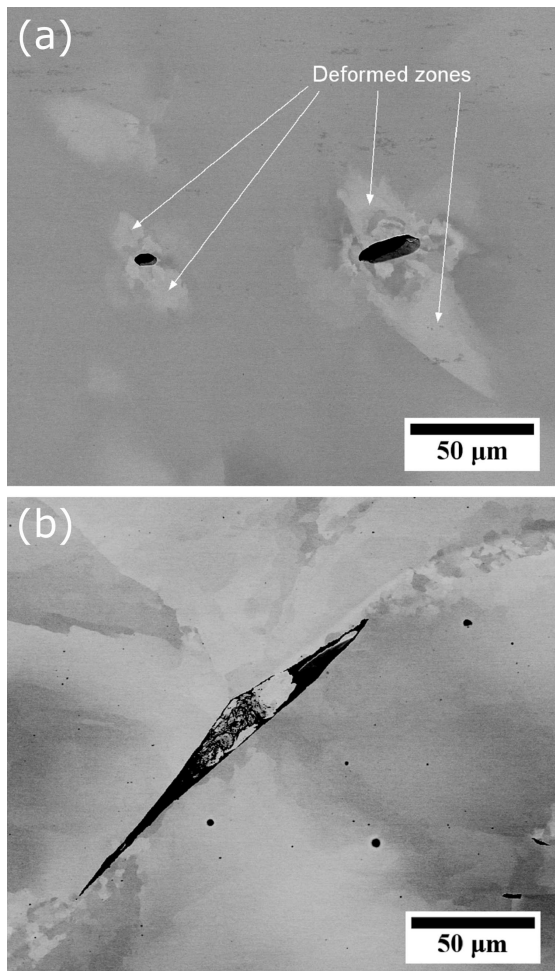


Fig. 3. (a) Small pores (formed during casting) in the sample deformed at $T = 1100\text{ °C}$ and $\dot{\epsilon} = 1\text{ s}^{-1}$, deformed zones are indicated by white arrows. (b) Large pore on grain boundary in sample deformed at $T = 1300\text{ °C}$ and $\dot{\epsilon} = 1\text{ s}^{-1}$, small black dots are remnants from polishing suspensions.

The KAM distribution of samples deformed at the lower strain rate of $\dot{\epsilon} = 0.01\text{ s}^{-1}$ depends strongly on the temperature of deformation. Figure 5a shows that at lowest temperature of 800 °C the KAM values are distributed very homogeneously while at higher temperature of 1000 °C (Fig. 5b), the deformation is concentrated at grain boundaries similarly as at the faster strain rate; *cf.* Fig. 4b. In addition, several spots of enhanced deformation (higher KAM value) can be seen in Fig. 5a. These spots indicate the presence of pores around which the material is highly deformed. The highest deformation temperature of 1300 °C leads to lowest amount of deformation which will be discussed below; *cf.* Fig. 5c. The area fraction of individual misorientations was computed from the KAM maps.

The respective KAM distributions for strain rates of $\dot{\epsilon} = 0.01\text{ s}^{-1}$ and $\dot{\epsilon} = 1\text{ s}^{-1}$ are shown in Fig. 6. At the $\dot{\epsilon} = 0.01\text{ s}^{-1}$, deformation stored in the material decreases with increasing temperature. The sample de-

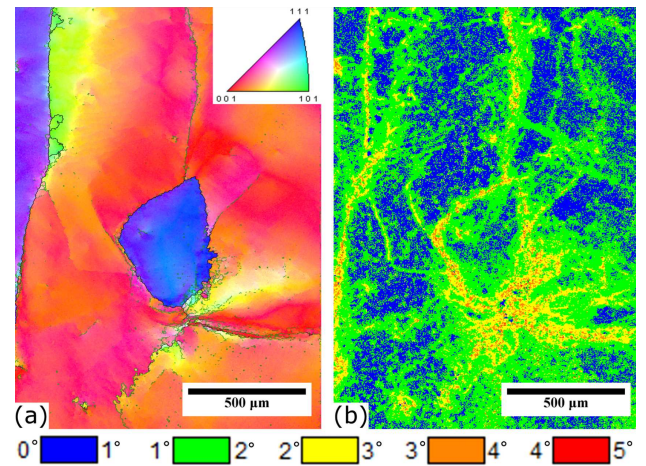


Fig. 4. Sample deformed at $T = 1300\text{ °C}$ and $\dot{\epsilon} = 1\text{ s}^{-1}$. (a) IPF map, (b) KAM map.

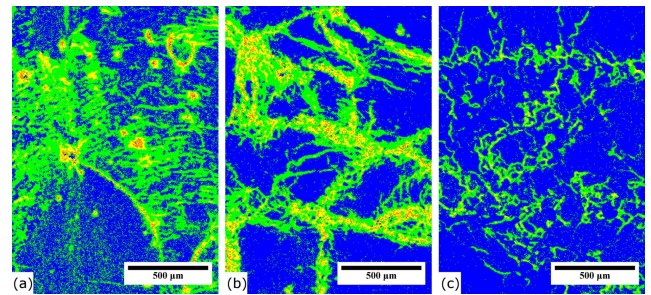


Fig. 5. KAM maps of samples deformed at $\dot{\epsilon} = 0.01\text{ s}^{-1}$ and (a) $T = 800\text{ °C}$, (b) $T = 1000\text{ °C}$ and (c) $T = 1300\text{ °C}$. For the orientation colour code, see Fig. 4.

formed at the highest temperature (1300 °C), contains almost 80% of area with KAM value less than 1° . At this slow strain rate, recovery processes are probably fast enough to reduce the dislocation density. The recovery rate increases with the increasing temperature. Similar behaviour has been recently observed in other β -Ti alloy and was ascribed to high stacking fault energy of β -Ti [17] which enhanced the dynamic recovery and prevented the dynamic recrystallization. On the other hand, at the high strain rate $\dot{\epsilon} = 1\text{ s}^{-1}$, the deformation stored in material does not vary monotonously with increasing temperature. It increases up to 1100 °C , then decreases up to 1300 °C . As a consequence, one may assume that the effect of deformation temperature on the stored strain is only minor at the highest strain rate $\dot{\epsilon} = 1\text{ s}^{-1}$.

KAM analysis of EBSD data indicate that dynamic recovery occurs at the lower strain rates of $\dot{\epsilon} = 0.01\text{ s}^{-1}$ at the whole temperature range employed ($800\text{--}1300\text{ °C}$). On the other hand, even the highest temperature of 1300 °C was not high enough to initiate the recrystallization. In contrast, the stainless steel recrystallizes already at 900 °C to 1100 °C [16].

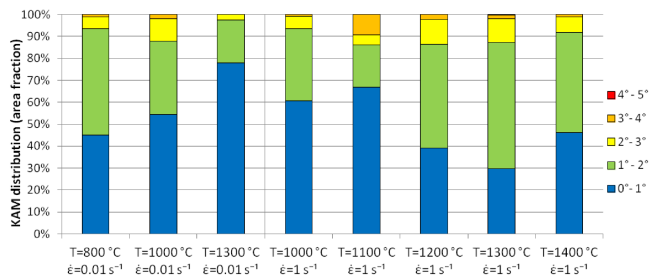


Fig. 6. Distribution of KAM values computed from each EBSD map as area fraction.

4. Conclusions

The mechanical properties of a biomedical alloy Ti–Nb–Zr–Ta–O were investigated at high temperatures and correlated with microstructure evolution. The following conclusion may be drawn from this experimental study:

- The deformation at elevated temperatures up to 1300 °C and the strain rate up to $\dot{\epsilon} = 1 \text{ s}^{-1}$ results in the dynamic recovery without any apparent recrystallization.
- The material is mostly deformed near grain boundaries and in the vicinity of pores formed already during casting.
- At the lower strain rate $\dot{\epsilon} = 0.01 \text{ s}^{-1}$ the deformation inside material drops with increasing temperature due to dynamic recovery.
- The minimum forming temperature of this alloy resulting in the strength comparable to that of Ti64 seems to be 1400 °C.

Acknowledgments

This work was financially supported by the Czech Science Foundation (project No. 17-20700Y) and by the joint project of the Ministry of Education, Youth and Sports of the Czech Republic (7AMB16AT012) and the Austrian Science Fund (FWF) (project No. I2391-N23). D.P. acknowledges financial support

by the Grant Agency of Charles University (project GAUK No. 1530217). M.J. and P.H. acknowledge partial financial support by ERDF under the project CZ.02.1.01/0.0/0.0/15_003/0000485.

References

- [1] H.J. Rack, J.I. Qazi, *Mater. Sci. Eng. C* **26**, 1269 (2006).
- [2] M. Geetha, A.K. Singh, R. Asokamani, A.K. Gogia, *Prog. Mater. Sci.* **54**, 397 (2009).
- [3] Y.T. Lee, G. Welsch, *Mater. Sci. Eng. A* **128**, 77 (1990).
- [4] J.-Y. Rho, T.Y. Tsui, G.M. Pharr, *Biomaterials* **18**, 1325 (1997).
- [5] M. Niinomi, *J. Mech. Behav. Biomed. Mater.* **1**, 30 (2008).
- [6] E. Eisenbarth, D. Velten, M. Müller, R. Thull, J. Brems, *Biomaterials* **25**, 5705 (2004).
- [7] A.T. Rack, *HJ Low modulus biocompatible titanium base alloys for medical devices*, United States Patent, 5,871,595, (1999).
- [8] J.I. Kim, H.Y. Kim, H. Hosoda, S. Miyazaki, *Mater. Trans.* **46**, 852 (2005).
- [9] M. Nakai, M. Niinomi, T. Akahori, H. Tsutsumi, M. Ogawa, *Mater. Trans.* **50**, 2716 (2009).
- [10] Q. Wei, L. Wang, Y. Fu, J. Qin, W. Lu, D. Zhang, *Mater. Des.* **32**, 2934 (2011).
- [11] M. Besse, P. Castany, T. Gloriant, *Acta Mater.* **59**, 5982 (2011).
- [12] J.I. Qazi, H.J. Rack, B. Marquardt, *JOM* **56**, 49 (2004).
- [13] J. Stráský, P. Hrcuba, K. Václavová, K. Horváth, M. Landa, O. Srba, M. Janeček, *J. Mech. Behav. Biomed. Mater.* **71**, 329 (2017).
- [14] D. Preisler, K. Václavová, J. Stráský, M. Janeček, P. Hrcuba, in: *METAL 2016, 25rd Int. Conf. on Metallurgy and Materials*, Ostrava Tanger Ltd, 2016, p. 1509.
- [15] R. Pederson, R. Gaddam, M.-L. Antti, *Cent. Eur. J. Eng.* **2**, 347 (2012).
- [16] S.-I. Kim, Y.-C. Yoo, *Mater. Sci. Eng. A* **311**, 108 (2001).
- [17] J. Zhao, J. Zhong, F. Yan, F. Chai, M. Dargusch, *J. Alloys Comp.* **710**, 616 (2017).

Manufacturing of Biomedical Ti-Based Alloys with High Oxygen Content and Various Amount of Beta-Stabilizing Elements

Josef Stráský^{1,a*}, Dalibor Preisler^{1,b}, Kristína Bartha^{1,c} and Miloš Janeček^{1,d}

¹Charles University, Department of Physics of Materials, Ke Karlovu 5, 121 16, Prague, Czech Republic

^ajosef.strasky@gmail.com, ^bbartha.kristina@gmail.com, ^cpreisler.dalibor@gmail.com, ^djanecek@met.mff.cuni.cz

Keywords: titanium alloys, biomedical materials, interstitial strengthening, scanning electron microscopy, microhardness

Abstract. High strength and low elastic modulus are key properties of biomedical Ti-based alloys. Body centred cubic beta phase shows lowest elastic modulus, especially if the stability of the beta phase is low due to the ‘proximity’ to martensitic β to α ’ transformation. It was previously shown that Ti-35Nb-6Ta-7Zr alloy contains biotolerant elements only and exhibits low modulus. By enriching this alloy by 0.7 wt. % of oxygen the strength is significantly enhanced, but elastic modulus increases as well. This fact can be attributed to apparent beta stabilizing effect of oxygen with respect to martensitic β to α ’ transformation. In the present study, six different alloys with reduced niobium and/or tantalum content were prepared by vacuum arc melting. Their microstructure in beta solution treated condition was studied by scanning electron microscopy including energy dispersive spectroscopy and mechanical properties were evaluated by microhardness measurements.

Introduction

Titanium is a hexagonal metal with a unique combination of properties such as high strength, excellent corrosion resistance, good biocompatibility and comparatively low elastic modulus of 100 GPa. Titanium based alloys containing substantial amount of so-called β -stabilizing elements (for instance V, Fe, Nb, Mo or Ta) retain bcc structure (referred to as β phase) after quenching from high temperatures [1]. Elastic modulus of bcc β phase is significantly lower (80 GPa) than that of hcp α phase [2]. Reduced elastic modulus partially prevents stress shielding which makes β -Ti alloys prospective material for application in medicine as permanent implant material [3].

Due to biocompatibility requirements, only some alloying elements can be used – namely: Nb, Mo, Ta and Zr [4]. By the end of 20th century, few specialized biomedical β -Ti alloys were developed and Ti-35Nb-6Ta-7Zr alloy was patented in the United States [5]. Chemical composition of biomedical alloys was optimized to achieve minimum elastic modulus (60 GPa or even less), which is attained in the alloys containing pure β phase whose stability is low at room temperature due to ‘proximity’ to the $\beta \rightarrow \alpha$ ’ martensitic transformation [6]. Nevertheless, these β -Ti alloys in a solution treated single phase condition exhibited limited strength of approx. 500 MPa, which is not sufficient for implant material for manufacturing of endoprostheses of big joints (hip, knee) [7].

Significant strengthening of β -Ti alloys by increased oxygen content was demonstrated in several studies [8-11]. Quazi et al. [8] and Stráský et al. [11] show that the tensile strength of Ti-35Nb-6Ta-7Zr alloy with a controlled content of 0.7 wt.% of oxygen exceeded 1000 MPa. Oxygen strengthened material also exhibited satisfactory ductility and retained pure β phase. However, the elastic modulus increased back to 80 GPa [11]. Sharp increase in elastic modulus is arguably caused by the effect of oxygen on the stability of β phase.

Oxygen is known as an α stabilizing element. Increased oxygen content significantly increases β transus temperature in pure Ti and in β -Ti alloys [12,13]. On the other hand, oxygen prevents the formation of α ’ martensite phase in Ti-Nb based alloys and therefore in fact increases relative

stability of the β phase [14,15]. In summary, if oxygen is added to the finely tuned low-modulus alloy, the stability of the β phase increases and so does the elastic modulus.

In this study, the Ti-35Nb-6Ta-7Zr alloy patented by Ahmed and Rack [5] is considered as the starting alloy composition. By adding 0.7 wt.% O, the strength of the alloy increases sharply, however modulus of elasticity also increases. Such Ti-35Nb-6Ta-7Zr-0.7O alloy was introduced first in [8] and thoroughly investigated in [11,16]. Considering the relative β stabilizing effect of oxygen with respect to martensitic transformation, six different alloys with reduced content of β stabilizing elements (Nb, Ta) were designed and manufactured for this investigation.

Material and Experimental Methods

Compositions of six newly designed and manufactured alloys differ in Nb and Ta content and are given in Tab. 1.

Table 1 Chemical composition of studied Ti-Nb-Ta-Zr-O alloys

		Ti (wt.%)	Nb (wt.%)	Ta (wt.%)	Zr (wt.%)	O (wt.%)
1	Ti-35Nb-6Ta-7Zr-0.7O	bal.	35	6	7	0.7
2	Ti-32Nb-6Ta-7Zr-0.7O	bal.	32	6	7	0.7
3	Ti-29Nb-6Ta-7Zr-0.7O	bal.	29	6	7	0.7
4	Ti-26Nb-6Ta-7Zr-0.7O	bal.	26	6	7	0.7
5	Ti-35Nb-7Zr-0.7O	bal.	35	0	7	0.7
6	Ti-29Nb-7Zr-0.7O	bal.	29	0	7	0.7

The alloys were prepared by arc melting of pure elements under low pressure of clean He atmosphere (350 mbar). Oxygen was introduced during melting by adding appropriate amount of TiO₂, which dissolved in the melt. Resulting casts in the shape of bricks (approx. 200 g per alloy) were wire cut to few small rods with the diameter of 8 mm. These rods were then encapsulated in quartz tubes with the pure argon atmosphere. Material was subsequently solution treated at 850°C/1h. Since this treatment proved to be insufficient for dissolution of α -phase in all alloys, small parts of the rods were subsequently annealed at 1000°C for 15 min in air.

SEM observations were performed using the scanning electron microscopes FEI Quanta 200F and Zeiss Auriga Compact CrossBeam FIB-SEM, both equipped with field emission gun (FEG) operated at the accelerating voltage of 20 kV and energy dispersive spectroscopy (EDS) detector. Microhardness was measured using automatic micro-hardness tester Qness Q10a according to Vickers with load of 0.5 kg and indentation time 10 s.

Results and Discussion

All designed alloys could be successfully manufactured and wire cut. Solution treatment at 850°C for 1 hour was selected as it is sufficient for most metastable β -Ti alloys. However, α -phase was retained in the least stabilized alloys: Ti-26Nb-6Ta-7Zr-0.7O and Ti-29Nb-7Zr-0.7O. Figure 1 a) shows single phase microstructure of Ti-32Nb-6Ta-7Zr-0.7O using back-scattered electrons. Very large grains can be observed in the image due to channeling contrast. Moreover, within the grains and disregarding grain boundaries, slightly 'brighter' and slightly 'darker' areas with the size of approx. 100 μ m are visible due to chemical Z-contrast. These differences are even better observed in Figure 2 and investigated in detail below.

In the Figure 1 (b), the microstructure of less stabilized Ti-26Nb-6Ta-7Zr-0.7O alloy is shown. 'Brighter' and 'darker' areas are again observed. However within the darker areas, tiny black spots are visible. These spots are α -phase particles as proven by detail observations (not shown). Heavier β stabilizing elements (Nb, Ta) are expelled from the α -phase particles which therefore appear black. α -phase particles could be observed in each 'darker' area and also in chains (in the image progressing from both bottom corners). Since α -phase particles precipitate preferentially at grain

boundaries [17], these chains can be associated with grain boundaries in the material or with the former grain boundaries that existed in these positions after casting, but subsequently moved during annealing leaving the chain of α -phase particles behind.

Solution treatment at 850°C might have been sufficient even for less stabilized alloys (in other words, β transus temperature might be below 850°C even in materials with composition Ti-26Nb-6Ta-7Zr-0.7O or Ti-29Nb-7Zr-0.7O), but due to chemical inhomogeneities, α -phase particles precipitated in the regions with lower local content of β stabilizing elements.

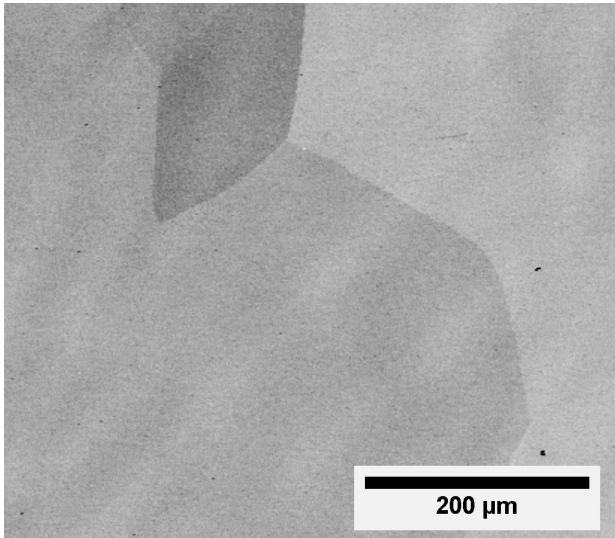


Figure 1 a): Ti-32Nb-6Ta-7Zr-0.7O alloy, after annealing at 850°C/1h

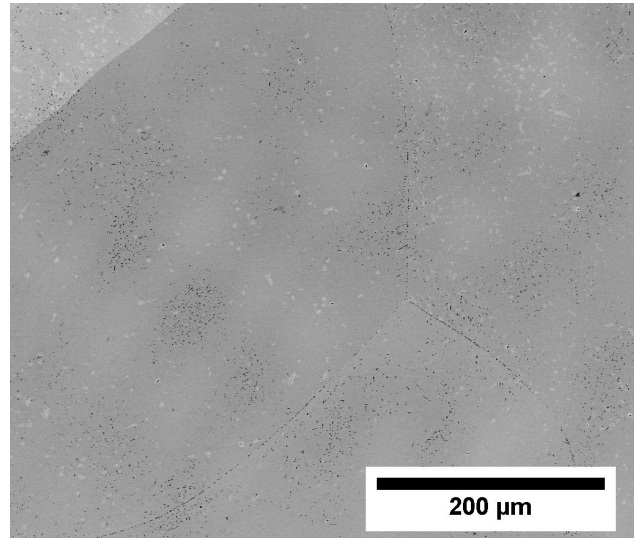


Figure 1 b): Ti-26Nb-6Ta-7Zr-0.7O alloy, after annealing at 850°C/1h

After annealing at 1000°C for 15 minutes, α -phase particles dissolved in all alloys as shown in Figure 2. Note that images in Figure 2 have enhanced contrast to visualize grain structure and chemical inhomogeneities. Grains are large, ranging from hundreds of micrometers to the millimeter sized grains which is typical for non-deformed material. Chemical inhomogeneities have shape of dendrites and were formed during casting. 'Brighter' areas have higher content of heavier Nb and Ta elements that are characterized by significantly higher melting points than that of titanium. It is therefore argued that during melting these Nb/Ta rich dendrites solidified first and expel excessive Ti into areas that solidified slightly later resulting in inhomogeneous microstructure. Homogenization procedure must be developed to remove these inhomogeneities, however, such homogenization treatment is complicated due to very high required temperatures (around 1400°C) and strict requirements on purity of environment in the furnace.

Note that in Figure 2 f), the dendrites cannot be observed. It is argued, that the formation of dendrites strongly depends on the cooling rate during solidification. Different parts of the cast may therefore exhibit different dendritic structure. We believe that the absence of dendrites in Figure 2 f) is related to the cooling rate of this particular area rather than to the particular alloy composition.

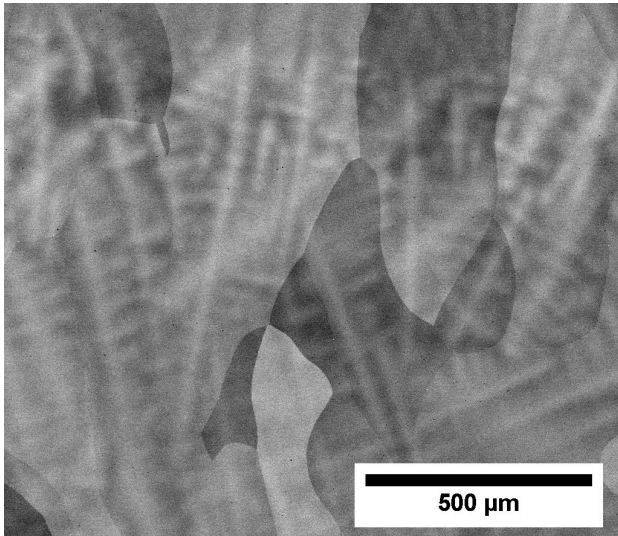


Figure 2 a): Ti-35Nb-6Ta-7Zr-0.7O alloy, after annealing at 1000°C/15 min

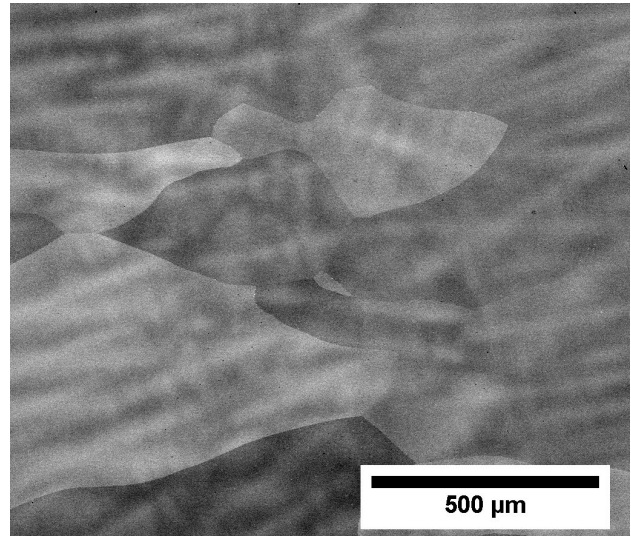


Figure 2 b): Ti-32Nb-6Ta-7Zr-0.7O alloy, after annealing at 1000°C/15 min

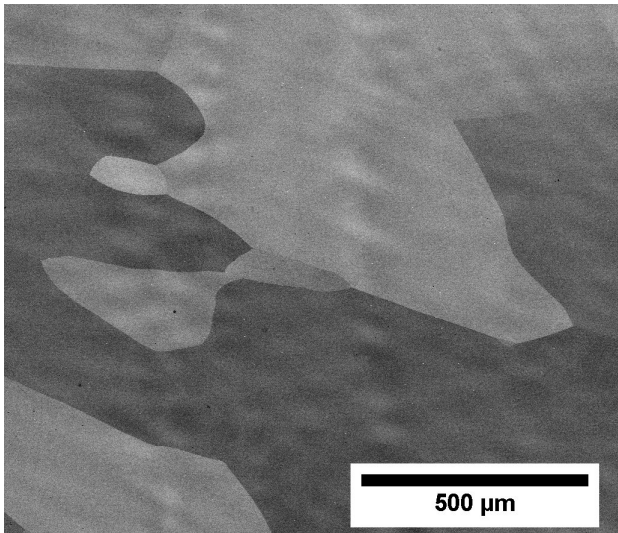


Figure 2 c): Ti-29Nb-6Ta-7Zr-0.7O alloy, after annealing at 1000°C/15 min

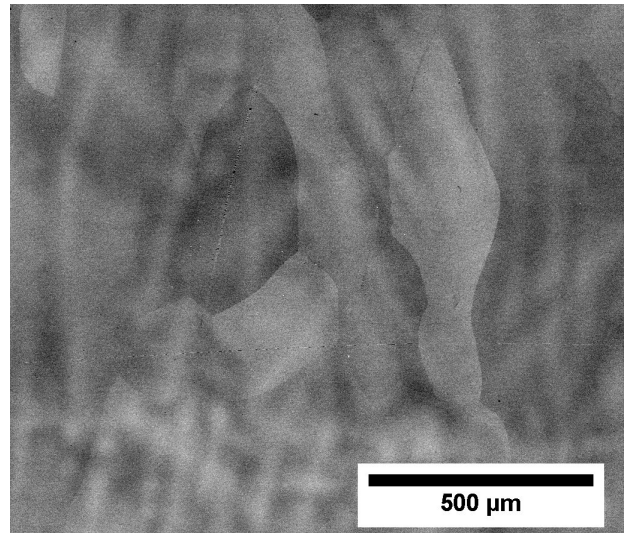


Figure 2 d): Ti-26Nb-6Ta-7Zr-0.7O alloy, after annealing at 1000°C/15 min

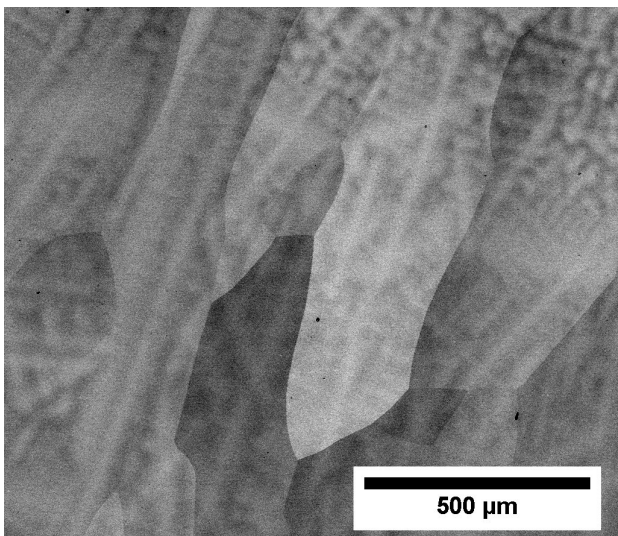


Figure 2 e): Ti-35Nb-7Zr-0.7O alloy, annealed at 1000°C/15 min

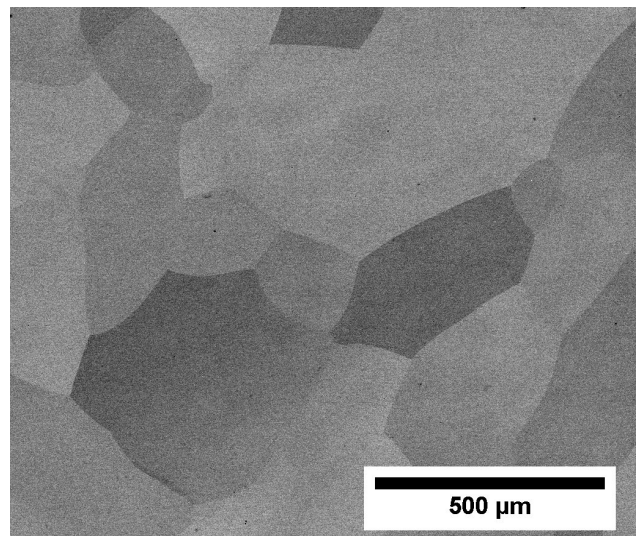


Figure 2 f): Ti-29Nb-7Zr-0.7O alloy, annealed at 1000°C/15 min

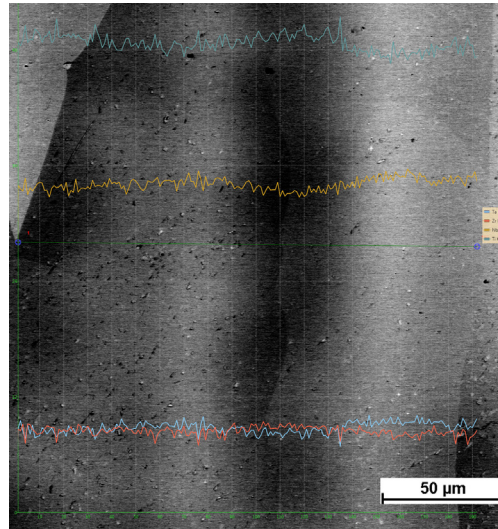


Figure 3 Ti-35Nb-6Ta-7Zr-0.7O alloy after solution treatment, detail. Overlapped by results of EDS measurement of (from the top): Ti, Nb, Ta (light blue), Zr (red)

Figure 3 shows detailed image of Ti-35Nb-6Ta-7Zr-0.7O alloy in back-scattered electrons with very high contrast (small black and white dots are remnants from polishing). EDS line scan was performed along green horizontal line in the middle of the image and the results of EDS investigation are overlapped over the BSE image. The differences in chemical composition are best observed for Nb (orange line). Nb content clearly increases in the ‘brighter’ regions and decreases in the ‘dark’ one. The difference in Nb content is, however, within 3 weight percentage points. Similar behavior can be found for Ta (though with lower magnitude due to the lower overall content of Ta). Measured amount of Ta (light blue) is higher than that of Zr (red) in ‘bright’ areas and vice-versa. Opposite behavior was found for titanium (shown in the upper part of the image). In the Ti based alloys with high content of β stabilizing elements, Ti serves as a relative α stabilizer. It can be thus concluded that ‘brighter’ dendrites contain higher amount of β stabilizing Nb and Ta at the extent of Ti.

Table 2 Microhardness of studied Ti-Nb-Ta-Zr-O alloys

	HV 0.5		HV 0.5		HV 0.5
Ti-35Nb-6Ta-7Zr [11]	164	Ti-32Nb-6Ta-7Zr -0.7O	333	Ti-26Nb-6Ta-7Zr -0.7O	333
Ti-35Nb-6Ta-7Zr-0.4O [11]	270	Ti-29Nb-6Ta-7Zr -0.7O	328	Ti-35Nb-7Zr -0.7O	329
Ti-35Nb-6Ta-7Zr -0.7O	333	Ti-26Nb-6Ta-7Zr -0.7O	328		

Microhardness measurements are summarized in Tab. 2. Sharp increase of microhardness with increasing oxygen content can be observed by comparing microhardness values from [11]. Otherwise, microhardness remain unchanged disregarding the content of Nb and Ta. The relative error of measurement is as low as 3%, which corresponds approximately to ± 5 HV for the studied alloys. The microhardness of the material is therefore homogeneous, but the differences between the alloys with equivalent oxygen content are within the measurement uncertainty.

Summary

Biomedical β -Ti alloys such as Ti-35Nb-6Ta-7Zr are characterized by low elastic modulus due to the low stability of the β phase caused by the ‘proximity’ to martensitic β to α ’ transformation. Oxygen addition (0.7 wt. %) is capable of doubling the strength of these alloys, but also causes significant increase of elastic modulus due to relative stabilization of the β phase. To compensate for these effect, six different alloys with reduced amount of β stabilizing elements were prepared and following conclusions can be drawn from this investigation:

- Ti-(29-35)Nb-(0-6)Ta-7Zr-0.7O alloys were prepared by arc melting.

- Solution treatment at 850°C for 1h is not sufficient for complete removal of α phase. α phase particles are present in less β -stabilized alloys in the regions with locally lower content of Nb and Ta and along (former) grain boundaries.
- Solution treatment at 1000°C for 15 min results in single β phase composition.
- Material is not fully chemically homogeneous and contains dendrites with increased content of Nb and Ta.
- Microhardness is comparatively high due to high oxygen content, but does not depend on the content of Nb and Ta.

Acknowledgment






Financial support by Czech Science Foundation under project 17-20700Y and by Grant Agency of Charles University under project 1530217 is gratefully acknowledged.

References

- [1] G. Lütjering, J. C. Williams, Titanium, Springer-Verlag, Berlin, Heidelberg (2003).
- [2] H. J. Rack and J. I. Qazi, Titanium alloys for biomedical applications, *Mater Sci Eng C*, 26 (2006) 1269–1277
- [3] M. Niinomi, Mechanical properties of biomedical titanium alloys, *Mater Sci Eng A*, 243 (1998) 231-236.
- [4] S. G. Steinemann, Titanium — the material of choice?, *Periodontol* 17 (1998) 7–21
- [5] T. Ahmed and H. J. Rack, Alloy of titanium, zirconium, niobium and tantalum for prosthetics, US Patent: US 5871595 A, 1999.
- [6] M. Tane et al., Low Young's modulus of Ti–Nb–Ta–Zr alloys caused by softening in shear moduli c' and c_{44} near lower limit of body-centered cubic phase stability. *Acta Mater* 2010;**58**:6790–6798.
- [7] P. L. Ferrandini, F. F. Cardoso, S. A. Souza, C. R. Afonso, and R. Caram: Aging response of the Ti–35Nb–7Zr–5Ta and Ti–35Nb–7Ta alloys, *J Alloys Compd* 433 (2007) 207–210
- [8] J. I. Qazi, H. J. Rack, and B. Marquardt: High-strength metastable beta-titanium alloys for biomedical applications, *JOM* 56 (2004) 49–51
- [9] M. Nakai et al., Effect of oxygen content on microstructure and mechanical properties of biomedical Ti-29-Nb-13Ta-4.6Zr alloy under solutionized and aged conditions, *Mater Trans*, 50 (2009) 2716-2720
- [10] M. Niinomi, M. Nakai, M. Hendrickson, P. Nandwana, T. Alam, D. Choudhuri, R. Banerjee: Influence of oxygen on omega phase stability in the Ti-29-Nb-13Ta-4.6Zr alloy, *Scripta Mater* 123 (2016) 144-148
- [11] J. Stráský *et al.*, Increasing strength of a biomedical Ti-Nb-Ta-Zr alloy by alloying with Fe, Si and O, *J. Mech. Behav Biomed Mater* 71, (2017), pp. 329–336.
- [12] P. Waldner and G. Eriksson, Thermodynamic modelling of the system titanium-oxygen. *Calphad* 23 (1999) 189–218.
- [13] F. Geng, M. Niinomi, M. Nakai, Observation of yielding and strain hardening in a titanium alloy having high oxygen content. *Mater Sci Eng A* 528 (2011) 5435–5445.
- [14] M. Tane et al. Elastic-modulus enhancement during room-temperature aging and its suppression in metastable Ti-Nb based alloys with low body-centered cubic phase stability *Acta Mater* 102 (2016) 373-384
- [15] Y.L. Hao, S.J. Li, S.Y. Sun, R. Yang, Effect of Zr and Sn on Young's modulus and superelasticity of Ti–Nb based alloys. *Mater Sci Eng A* 441 (2006) 112-118
- [16] D. Preisler, K. Vaclavova, J. Strasky, M. Janecek, P. Harcuba, Microstructure and mechanical properties of Ti-Nb-Zr-Ta-O biomedical alloy, *Conference Metal 2016*, (2016) 1509-1513.
- [17] J. Šmilauerová, M. Janeček, P. Harcuba, J. Stráský, J. Veselý, R. Kužel, H.J. Rack, Ageing response of sub-transus heat treated Ti-6.8Mo-4.5Fe-1.5Al alloy, *J Alloys Comp* 724 (2017)373-380

Article

The Effect of Hot Working on the Mechanical Properties of High Strength Biomedical Ti-Nb-Ta-Zr-O Alloy

Dalibor Preisler ^{1,*} , Miloš Janeček ¹ , Petr Harcuba ¹ , Jan Džugan ², Kristýna Halmešová ² , Jaroslav Málek ³ , Anna Veverková ¹  and Josef Stráský ^{1,*}

¹ Department of Physics of Materials, Charles University, 121 16 Prague, Czech Republic;

janecek@met.mff.cuni.cz (M.J.); harcuba.p@gmail.com (P.H.); annaterynkova@gmail.com (A.V.)

² COMTES FHT, 334 41 Dobřany, Czech Republic; jdžugan@comtesfht.cz (J.D.); khalmesova@comtesfht.cz (K.H.)

³ Faculty of Mechanical Engineering, Czech Technical University in Prague, 121 35 Prague, Czech Republic; jardamalek@seznam.cz

* Correspondence: preisler.dalibor@gmail.com (D.P.); josef.strasky@gmail.com (J.S.)

Received: 7 October 2019; Accepted: 13 December 2019; Published: 17 December 2019



Abstract: Beta titanium alloy Ti-35Nb-6Ta-7Zr-0.7O (wt%) was developed as a material intended for the manufacturing of a stem of a hip joint replacement. This alloy contains only biocompatible elements and possesses a very high yield strength already in the cast condition (900 MPa). However, the porosity, large grain size and chemical inhomogeneity reduce the fatigue performance below the limits required for utilization in the desired application. Two methods of hot working, die forging and hot rolling, were used for processing of this alloy. Microstructural evolution, tensile properties and fatigue performance of the hot worked material were investigated and compared to the cast material. Microstructural observations revealed that porosity is removed in all hot-worked conditions and the grain size is significantly reduced when the area reduction exceeds 70%. Static tensile properties were improved by both processing methods and ultimate tensile strength (UTS) of 1200 MPa was achieved. Fatigue results were more reproducible in the hot rolled material due to better microstructural homogeneity, but forging leads to an improved fatigue performance. Fatigue limit of 400 MPa was achieved in the die-forged condition after 70% of area reduction and in the hot rolled condition after 86% of area reduction.

Keywords: titanium alloys; hot working; biomedicine; tensile testing; fatigue testing

1. Introduction

Designing a new implant material for total hip replacement with improved properties provides a major market opportunity in the field of medical implants, and, at the same time, a major challenge for material scientists [1]. Several requirements must be fulfilled simultaneously; in particular, the high strength in static loading, acceptable fatigue limit in high cycle fatigue test, positive biological response and sufficient size of initial material for product manufacturing. Beta titanium alloys constitute the most promising and also the most explored material class in this regard [2,3]. Despite years of intensive research, Accolade™ hip implant made from TMZF (Ti-12Mo-6Zr-2Fe) alloy by Stryker Co represents the only commercial β -Ti based hip implant [4,5].

Excellent biocompatibility of titanium was proven by many authors both in vitro and in vivo [6–8]. In the last two decades, specialized biocompatible β -Ti alloys have been developed. Among utilizable alloying elements, Nb, Ta, Zr and also Mo are regarded as the most biocompatible, whereas V, Cr and Co are inappropriate [9].

The modulus of elasticity of Ti and common Ti alloys is around 100 GPa, which is half of the elastic modulus of steels, but still much higher than the elastic modulus of the cortical bone (10–30 GPa) [10]. The development of biocompatible β -Ti alloys with reduced modulus of elasticity focused mainly on the Ti-Nb-Ta-Zr alloying system due to the excellent biocompatibility of these alloying elements [7]. Ti-29Nb-13Ta-4.6Zr [11] (Japan alloy, TNTZ) and Ti-35Nb-7Zr-6Ta (US alloy, TNZT) [12] are the two most studied alloys of this type. The latter alloy was developed in USA and patented in 1999 [13]. The alloy was designed empirically by testing many different chemical compositions aiming to achieve the minimum elastic modulus [14]. The elastic modulus of this alloy is below 60 GPa, because α , α'' and ω phases are avoided in the β solution treated condition. Excellent biocompatibility of the alloy was recently confirmed in [15]. Low strength is the main disadvantage of this class of alloys [16].

Interstitial strengthening by oxygen is one of the major strengthening mechanisms in commercially pure Ti [17]. Interstitial strengthening is efficient also in bcc metals (β phase) [18]. The immense effect of oxygen content on the strength of TNZT alloy was first mentioned in [19]. Moreover, the ductility of this alloy is preserved even for oxygen content of 0.7 wt%, until the alloy contains only β phase. In contrast, in alloys containing α phase (either $\alpha + \beta$ alloys or metastable β alloys aged to $\alpha + \beta$ condition), the maximum allowed oxygen content is limited typically to 0.2 wt% to avoid embrittlement [20]. Interstitial strengthening by oxygen has been thoroughly studied in our previous work on as-cast Ti-35Nb-7Zr-6Ta based alloys with various oxygen contents [21].

As-cast Ti-35.3Nb-7.3Zr-5.7Ta-0.7O (TNZTO) alloy contains very large grains with the size ranging from 0.5 to 3 mm. Despite that, the alloy shows promising properties under static loading [22]. On the other hand, fatigue performance of the as-cast material is rather poor, as shown below.

Investigation of hot working of the alloy is of critical importance not only for improvement of fatigue performance, but also because hot working (namely, die forging) is currently used for implant semi-product manufacturing. Determination of forging conditions is, therefore, of clear practical importance.

Hot working of β -Ti alloys is done either below or above the beta-transus temperature [23]. The studied TNZTO alloy was deformed in the pure β phase condition. Restoration mechanism in the beta phase field is dominated by dynamic recovery; however, continuous recrystallization in the vicinity of grain boundaries may occur at higher strains [23]. Recovery is a dominant process due to the high stacking fault energy of β -Ti alloys [24].

Hot forging is commonly used for thermomechanical processing of biomedical β -Ti alloys. Ti-36Nb-2Ta-3Zr-0.35O alloy prepared by sintering was successfully hot forged at 800–1150 °C, which caused significant improvement of both the strength and ductility [25]. The authors also claimed that hot forging was comparatively easy due to fine grained structure of the material after sintering. Forging from the diameter of 40 mm to 10 mm at 950 °C was possible in Ti-30Nb-10Ta-5Zr [26]. Ti-xNb-3Zr-2Ta alloy and Ti-35Nb-(10-x)Ta-xZr alloys were successfully forged at 910 °C with 50% reduction and at 900–1000 °C with the reduction of 40%, respectively [27,28].

There are also studies concerning the hot working of β alloys intended for aerospace applications. Dynamic recovery is found as a major restoration mechanism in Ti-5553 (Ti-5Al-5V-5Mo-3Cr) alloy during hot deformation [29]. Most studies, however, discuss deformation of Ti-5553 alloy in the $\alpha + \beta$ field [30–32]. In the β field, dynamic recrystallization is preferred to dynamic recovery when high forming temperatures are used [30].

The most important difference between above mentioned alloys and the studied TNZTO alloy is that the TNZTO alloy is much stronger at elevated temperatures, which can be attributed to the strengthening by oxygen. For instance, at the temperature of 800 °C and the strain rate of 0.01 s⁻¹, the Ti-5553 alloy deforms already at the stress of approximately 80 MPa [29], while stress of 250 MPa is required for the deformation of TNZTO alloy at these conditions [33].

This study aims to develop a manufacturing procedure of the cast material in pure β -phase to achieve a condition suitable for implant production. A sufficiently high temperature of deformation has to be used not only to prevent α phase formation but, more importantly, to reduce the forming forces.

2. Materials and Methods

2.1. Alloy Casting

The alloy with nominal composition Ti-35.3Nb-6Ta-7.3Zr-0.7O (wt%) was produced on demand at the company Retech Systems LLC (Ukiah, USA) in the form of a rod with the diameter of 53 mm in two steps. In the first stage, a sponge of Ti and Zr, pieces of Nb and Ta and powder of TiO₂, were plasma arc melted into compacts with 100 mm diameters, 75 mm lengths and weights of approximately 3 kg. The melting took place under a protective atmosphere of pure He to prevent excessive contamination by oxygen and nitrogen. In the second stage, the compacts were remelted by the sequential pour melting process into a mold with the inner diameter of 55 mm, again in the pure He atmosphere. Each compact was consecutively inserted into melting hearth and poured into mold. The material remains molten at the top but solid at the bottom. The bottom part of the mold can be opened, and with each melted compact added to mold, the ingot is pulled down by about 75 mm. Thus, the process is quasi-continuous and two ingots with the length over 1 m each were produced.

The elemental composition was checked at the top and at the bottom of each produced ingot by the supplier. The content of metallic elements was determined by inductively coupled plasma-atomic emission spectroscopy (ICP-AES) and the contents of non-metallic elements were measured by combustion-infrared absorption (CIA). Results in Table 1 show that the desired nominal composition was achieved. The content of oxygen was accurate and the contents of contaminants (most importantly nitrogen) were negligible.

Table 1. Chemical composition of cast ingots determined by ICP-AES and CIA. Standard errors of measured contents of metallic elements were not determined.

Element (wt%)	Ingot 1-Top	Ingot 1-Bottom	Ingot 2-Top	Ingot 2-Bottom
Titanium	balance	balance	balance	balance
Niobium	35.5	35.6	35.8	35.3
Zirconium	7.36	7.28	7.40	7.36
Tantalum	5.90	6.17	6.01	5.88
Iron	0.049	0.052	0.055	0.050
Oxygen	0.726 ± 0.012	0.702 ± 0.003	0.699 ± 0.002	0.719 ± 0.010
Nitrogen	0.012 ± 0.002	0.012 ± 0.002	0.0108 ± 0.0004	0.012 ± 0.001
Carbon	0.0093 ± 0.0007	0.0101 ± 0.0003	0.0098 ± 0.0009	0.0119 ± 0.0002
Hydrogen	0.0051 ± 0.0001	0.0080 ± 0.0013	0.0061 ± 0.0012	0.0023 ± 0.0001

Altogether, 5 different conditions were produced by two different hot working processes. Two rods with the diameter of 35 mm (area reduction—AR 40%) and 25 mm (AR 70%) were prepared by die forging. Three rods with the diameter of 33 mm (AR 64%), 25 mm (AR 77%) and 20 mm (AR 86%) were manufactured by hot rolling.

2.2. Die Forging

Two die-forged conditions were produced at ALPER Co., Prostějov, Czech Republic. In the first stage, pieces of initial ingot were machined to 45 mm and heated to 1220 °C in an electrical laboratory furnace in air for approximately 25 min. Heated pieces were forged to the diameter of 35 mm (AR 40%) by hydraulic press using a closed die of the cylindrical shape (diameter 35 mm) preheated to 300 °C. About 10 forging steps were used during the die-forging, while rotating the forged piece after each step to achieve round cross-section. The whole process took approximately 1 min. One of the forged rods was water quenched (WQ) and the other was put again into the furnace.

This piece was reheated to 1220 °C (within approximately 15 min) and forged to the diameter of 25 mm (AR 70%) using a closed cylindrical die with the diameter of 25 mm. During the forging of the rod with smaller diameter, the temperature of the sides of the forged rod dropped below approximately 800 °C and this piece was reheated back to 1220 °C (5 min) before the final forging to the 25 mm and

water quenched. In total, 20 forging steps were used to achieve the piece with the diameter of 25 mm and this piece was reheated three times to reduce diameter from 45 mm to final 25 mm.

The rod forged to 35 mm (AR 40%) was round with the desired diameter, and surface cracks were less than 0.5 mm deep. Material outflow from the die occurred during hot forging to 25 mm. The outflow was machined off. A few surface cracks up to 2 mm in depth were formed.

Photographs of pieces of both forged rods are shown in Figure 1a.



Figure 1. Photographs of (a) forged rods and (b) rolled rods. The samples for tensile and fatigue testing were already machined from the processed conditions parallel to the axial direction. SEM samples were prepared from cross-section of rods.

2.3. Hot Rolling

Two pieces of the second manufactured cast ingot (53 mm in diameter) were hot rolled at Technical University Ostrava, Czech Republic. 3 rods with oval cross-sections with larger axes of 33 mm, 25 mm and 20 mm, and smaller axes of 25 mm, 22 mm and 18 mm, respectively, were manufactured. Area reductions were calculated according to actually-achieved cross-sections: 64%, 77% and 86%, respectively. The rolling was performed in a machine with grooves for rolling of round rods along their central axes. The pieces were heated to 1200 °C before the process. Several passes through rolling grooves were used without reheating to achieve the 33 mm diameter and the rods were rotated by 90° after each pass to preserve round or oval shape. One of the rolled rods was water quenched (AR 64%) while the other rod was reheated back to 1200 °C and rolled to the diameter of 25 mm (AR 77%), again in several passes while rotating by 90° after each pass. After rolling to 25 mm, the rod was water quenched and cut into two pieces. One of the pieces was again reheated back to 1200 °C and rolled to the diameter of 20 mm (AR 86%), and finally, water quenched.

Due to the necessity of reheating, the whole process took about 3 h and the rods were heated and processed in air.

The produced rods had a white surface, indicating the presence of titanium/niobium oxide, and large surface cracks up to 3 mm in depth. The shape of the rod rolled with AR 86% was almost round while the other two rolled rods had more oval shapes. The photograph of pieces of produced rods is shown in Figure 1b.

2.4. Experimental Techniques

Samples for microstructural observations by scanning electron microscopy (SEM), including electron back-scatter diffraction (EBSD) and energy dispersive X-ray spectroscopy (EDX), and for microhardness measurements, were cut from the forged/rolled rods perpendicular to the axial direction of produced rods. The samples were ground with SiC papers up to grit 2400. Grinding was followed by three-step vibratory polishing employing Alumina 0.3 µm suspension for 6–9 h, Alumina 0.05 µm suspension for 6–9 h and Colloidal Silica for 3–4 h. Field emission SEM FEI Quanta 200FX (FEI, now under Thermo Fisher Scientific, Eindhoven, Netherlands) was used for back-scattered electrons (BSE) observations operating at 10 kV and for EBSD and EDX measurement (both by EDAX, Tilburg, Netherlands) at 20 kV.

Microhardness was measured using Vickers method with the load of 0.5 kgf and dwell time of 10 s.

Round samples for tensile and fatigue testing were prepared parallel to the axial direction of the forged/rolled rods and at sufficient distance from the surface to avoid the influence of surface cracks or oxidation. Tensile tests of the samples with the gauge length of 15 mm and the diameter of 3 mm were conducted at strain rate of 10^{-4} s^{-1} and 3–4 samples were tested for each condition. Samples for fatigue testing had a typical hour-glass shape with the diameter of 3 mm and the radius of 30 mm. Measurements were done in tension-compression with $R = -1$ at 50 Hz. Schematic drawings of the tensile and fatigue samples are shown in Figure 2.

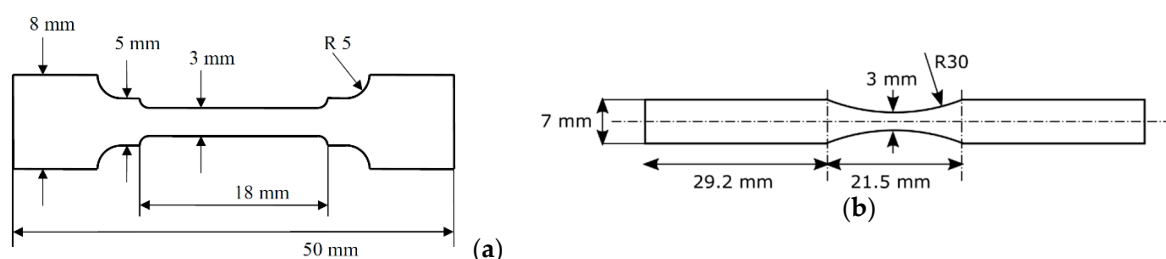


Figure 2. Schematic drawings of (a) tensile sample and (b) fatigue sample.

3. Results and Discussion

3.1. Microstructure—Cast Ingot

Figure 3a shows a SEM micrograph of the cast ingot. Very large grains with sizes over 1 mm are present in the material. Porosity appears as black spots with the size of 5–20 μm . In the right half of the image in Figure 3a (i.e., closer to the center of the cast ingot), there are dendritic chemical inhomogeneities, as proven by EDX line scan in Figure 3b. Darker areas are Ti and Zr enriched while lighter areas are Nb and Ta enriched. The compositional fluctuations around mean values are approximately 3%. The chemical inhomogeneity and porosity were located mainly in the central part of the cast ingot.

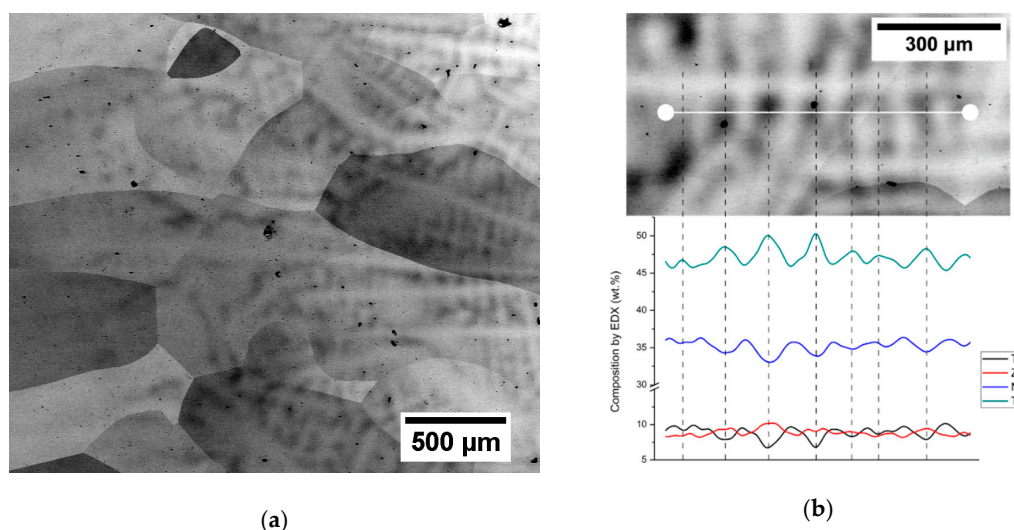


Figure 3. (a) SEM micrograph of cast ingot. Left part is closer to the edge; right part is closer to the center of the ingot. More pores and chemical inhomogeneities are seen closer to the center. (b) Line scan of composition by EDX along a dendrite.

The alpha phase was not found either in the interior of grains or at the grain boundaries, indicating that the cooling of ingot during production was sufficient to prevent alpha phase precipitation and that the material contains only beta phase. No beta solution treatment was carried out after casting.

3.2. Microstructure—Die-Forging

Figure 4 shows the microstructure of the rod forged with the AR 40% in three different areas located in the central part of the rod. Note that grains retain the same size as in the cast ingot. On the other hand, they are heavily deformed, as manifested by parallel deformation bands. However, the deformation is not homogeneous and non-deformed regions can also be found (Figure 4a, marked by red arrow). These structures are formed by dislocation slip, as further inspected by EBSD below. Note also that porosity from casting is removed by forging. On the other hand, dendritic chemical inhomogeneities can be still observed, especially in the lower part of Figure 4a (marked by green arrow). Apart from dendritic inhomogeneities, there is a larger chemical inhomogeneity appearing as a darker area in Figure 4b; i.e., Nb and Ta depleted and Ti enriched. The results of EDX analysis of points A and B are shown in Table 2.

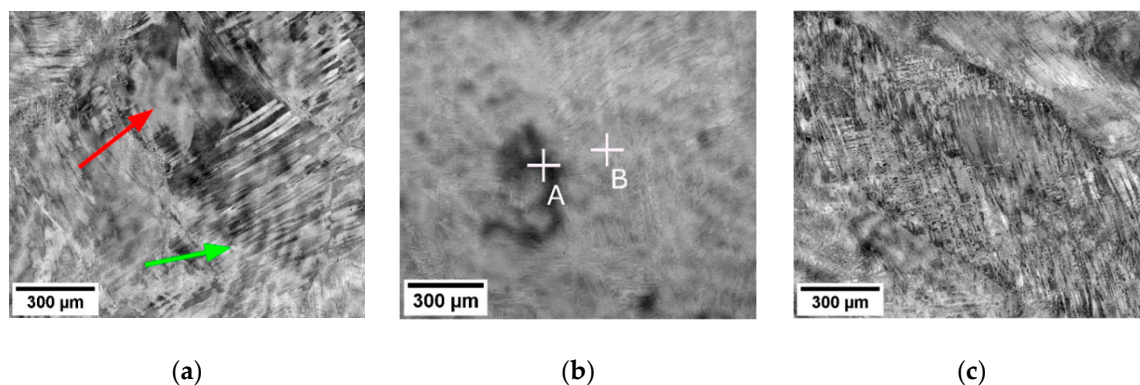


Figure 4. Micrographs of the rod forged with AR 40% showing distinct features: (a) non-deformed area (denoted by red arrow) and dendritic inhomogeneity (denoted by green arrow); (b) local chemical inhomogeneity; (c) grain deformed by slip in parallel directions. Dendritic inhomogeneities can be observed in all micrographs.

Table 2. Chemical composition (EDX) at positions A and B marked in Figure 3b. Position A is depleted of Nb and Ta.

Position	Ti	Nb	Zr	Ta
A	52.9	31.6	9.4	6.1
B	46.3	36.7	6.8	10.2

In order to examine the origin of parallel bands in Figure 4c in detail, the EBSD inverse pole figure (IPF) map of the central part of forged rod with the AR 40% is shown in Figure 5a, along with orientation triangle (Figure 5b) and misorientation profile (Figure 5c) along a line drawn in white in the IPF map. The misorientation profile shows that the misorientations between two grains never exceeds 40° . The misorientation angles of twins occurring in β Ti are 60° in case of $\{112\} \langle 111 \rangle$ twinning and 50.57° for $\{332\} \langle 113 \rangle$ twinning [34]. Therefore, the parallel bands that are intersecting each other are slip bands formed by dislocations. Apart from dislocation bands, significant lattice rotation within the original large grains was observed.

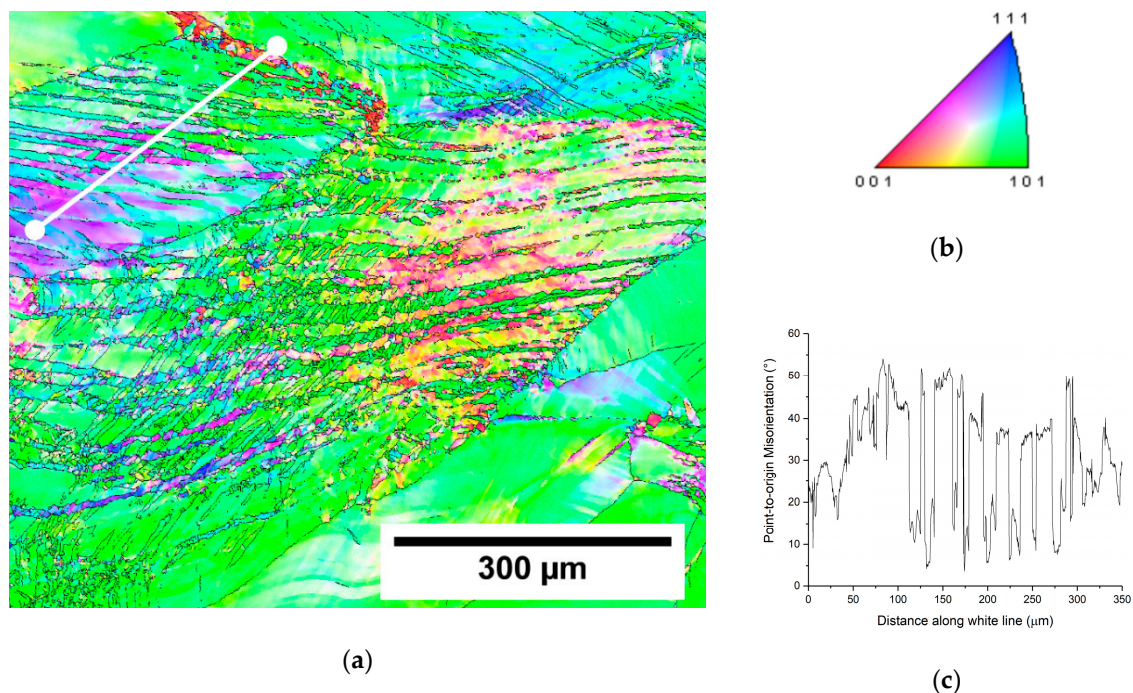


Figure 5. EBSD measurement of the forged rod with AR 40%. (a) inverse pole figure (IPF) map, (b) orientation triangle (BCC structure) and (c) point-to-origin misorientation profile along white line drawn in (a).

Dynamic (continuous [23]) recrystallization occurred only in the areas with the highest deformation—mainly along grain boundaries of large grains after casting and also along some of the newly formed high angle boundaries.

The microstructure of the rod forged with AR 70% was studied at two different cross-section samples. One was taken from the middle part of the rod, while the other one from the end of the rod (side). While in the forged rod with AR 40%, the orientation of SEM samples was not established, as this rod was round, in the rod forged to AR 70% the direction of last forging step was up/down. The microstructure is completely different from the rod with the AR 40%.

In Figure 6a,b the grain structure of the middle and the side of the forged rod with AR 70% are compared (both cross-sections studied showed similar microstructures in their centers and closer to their surfaces, but the middles and sides of the forged rods differ significantly). The microstructure is heavily deformed, as indicated by the channeling contrast of BSE. Due to the high deformation, it is difficult to recognize the individual grains in Figure 6a or Figure 6b. The layered structure observed in the middle part of the rod (Figure 6a) is caused mainly by elongation of grains. The observed contrast is, however, also caused by elongated areas of chemical inhomogeneities (varying Nb content).

EBSD measurements for the rod with the AR 70% are shown in Figure 7 as IPF maps. The difference between the middle and the side of the rod is clearly manifested. The microstructure in the area close to the side of the rod contains equiaxed grains with the size below 50 μm . These grains contain only few deformation bands which indicates that they recrystallized from the deformed structure during the three-step heating and deformation (rods forged with the AR 70% were heated three times before reaching the final diameter, as described in Section 2.2). The grains are, however, slightly deformed, which suggests that the recrystallization itself did not occur in the final deformation step.

In the cross-section from the middle of the rod, the grains are elongated and contain high fraction of low-angle GBs.

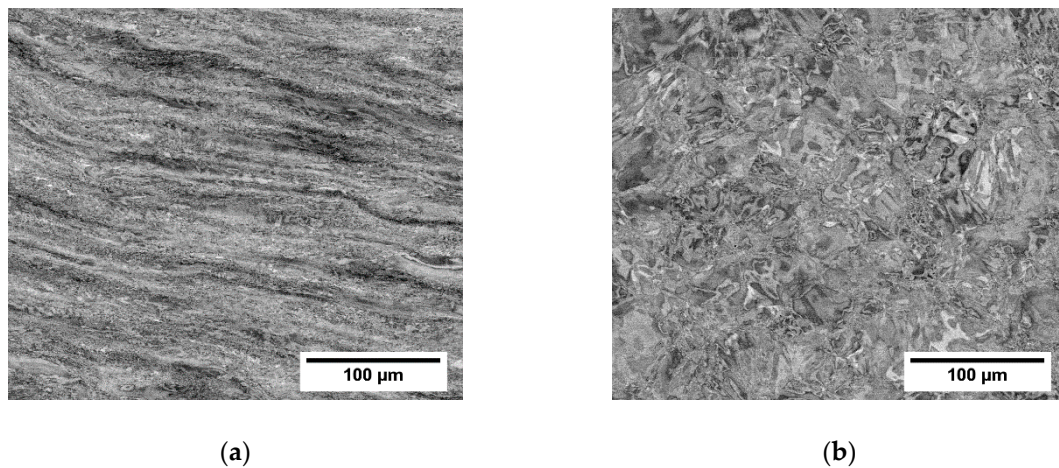


Figure 6. Microstructure of the forged rod (AR 70%) cross sections: (a) middle part; (b) side of the rod.

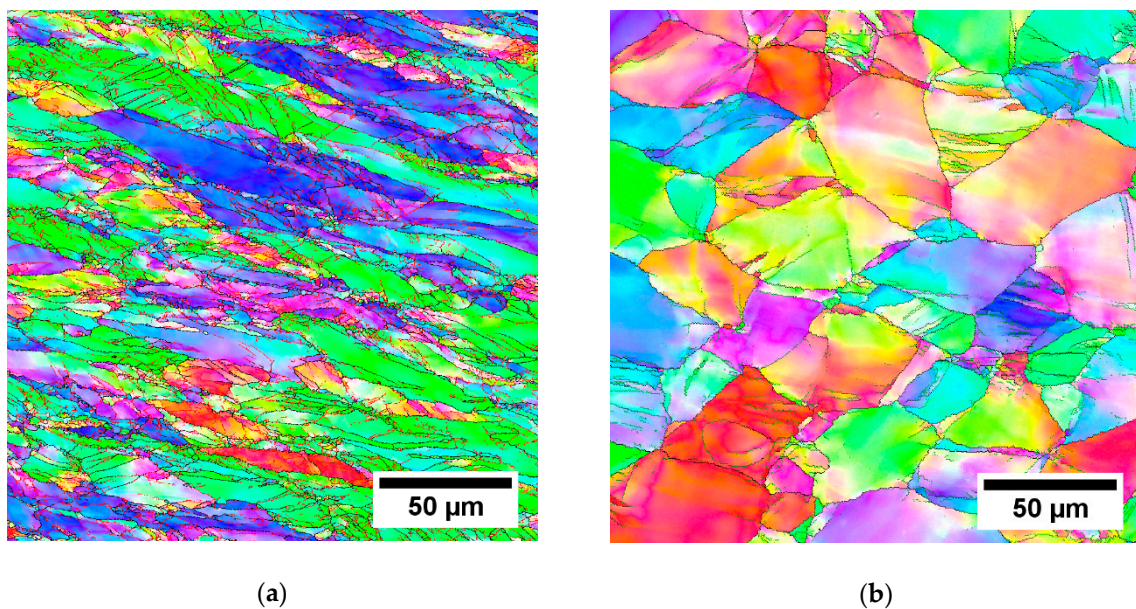


Figure 7. IPF maps of 25 mm forged rod (AR 70%). (a) Middle part; (b) side of the rod.

3.3. Microstructure—Hot Rolling

BSE images of the three hot rolled rods from the centers of the cross-sections are shown in Figure 8. Similarly to the forged rods, no porosity was found in the hot rolled rods. The refinement of microstructure increases with the increasing area reduction, as can be observed mainly by comparing Figure 8a,c. The dark shades in Figure 8a,b are chemical inhomogeneities from casting that were distorted by the rolling procedure, as proven by EDX point analysis of points A, B, C and D, as summarized in the Table 3. Large deformed grains and new small grains can be distinguished in Figure 8, EBSD measurements were performed for a detailed inspection.

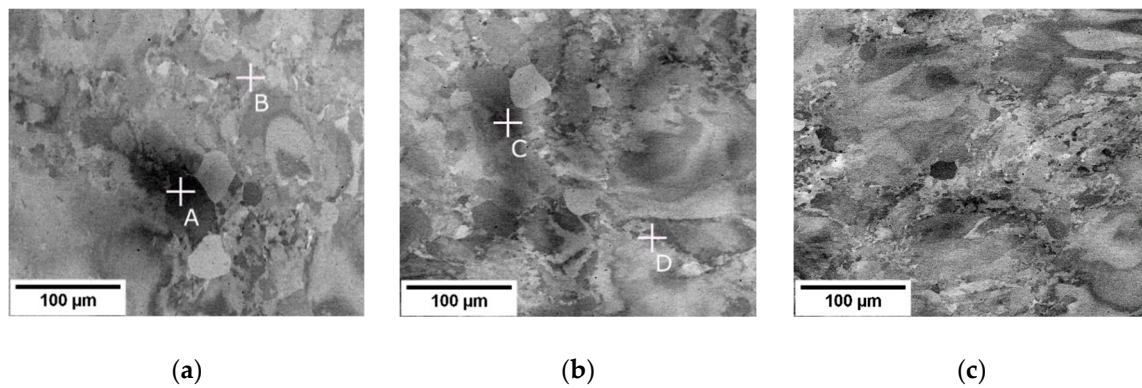


Figure 8. Microstructures of centers of cross-sections in hot rolled rods. Rods with (a) AR 64%, (b) AR 77% and (c) AR 86%.

Table 3. Chemical composition (EDX) at positions A, B, C and D marked in Figure 8a,b. Positions A and C are depleted of Nb and Ta.

Position	Ti	Nb	Zr	Ta
A	51.1	31.3	13.4	4.2
B	45.4	38.4	8.6	7.6
C	49.0	34.8	10.9	5.3
D	50.9	36.8	5.1	7.2

EBSD measurements were performed on the rolled conditions in the cross-section center and edge. Figures 9–11 show IPF maps of conditions rolled to AR 64%, 77% and 86%, respectively. In each figure shows (a) the IPF map of the center of cross-section, (b) the grain orientation spread (GOS) map of the center and (c) the IPF map near the edge of cross-section.

The GOS was computed for each grain as a mean deviation of crystalline orientations in the grain from the average grain orientation [35]. In other words, high GOS means that the grain is significantly deformed, and vice-versa: low GOS represents grains with a low deformation—for instance, recrystallized (RX) grains. GOS is normalized to the grain size; i.e., low GOS values are not caused by the small size of grains. The threshold between the GOS values of RX and non-RX fractions was determined on the basis of the histogram of GOS values (not-shown) as 1° , which is a common choice for β -Ti alloys [36]. GOS maps are only shown for centers of each rod as the edges did not contain recrystallized grains with low GOS values.

It is clear from the EBSD images that with the increasing area reduction, the fraction of recrystallized (RX) grains (size of 20–30 μm) increased. New small grains were formed in the areas with higher deformation; namely, at the grain boundaries. This resembles a so-called necklace continuous recrystallization reported in [23]. The recrystallized grains evolve during multiple heating and deformation. Note that there is the lowest RX fraction in the condition with AR of only 64%, which was not reheated. However, the deformed grains also have a smaller size in the rods with higher AR. This can be associated with continuous dynamic recrystallization, which is supported by several incomplete low-angle grain boundaries (marked by black arrows in IPF images), that separate sub-grains.

Quantitative analysis is provided in Table 4, comparing each condition in terms of the grain sizes in both the RX fraction ($\text{GOS} < 1^\circ$) and non-RX fraction ($\text{GOS} > 1^\circ$). In the centers of cross-sections, both the grains from the RX and non-RX fraction are significantly smaller for higher area reductions, while on the cross-sectional edges, the grain sizes are comparable in AR 64% and AR 77% and smaller only in AR 86% condition.

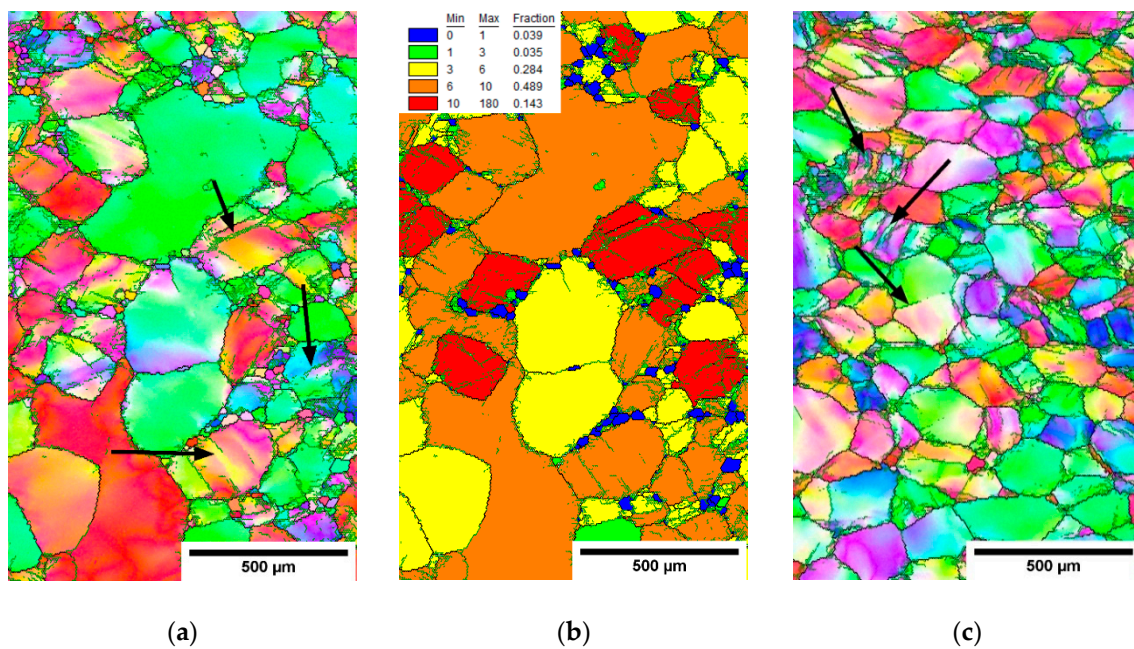


Figure 9. Microstructure of the cross-section of the hot-rolled rod with AR 64%. (a) IPF map-center, (b) grain orientation spread (GOS) map-center and (c) IPF map-edge.

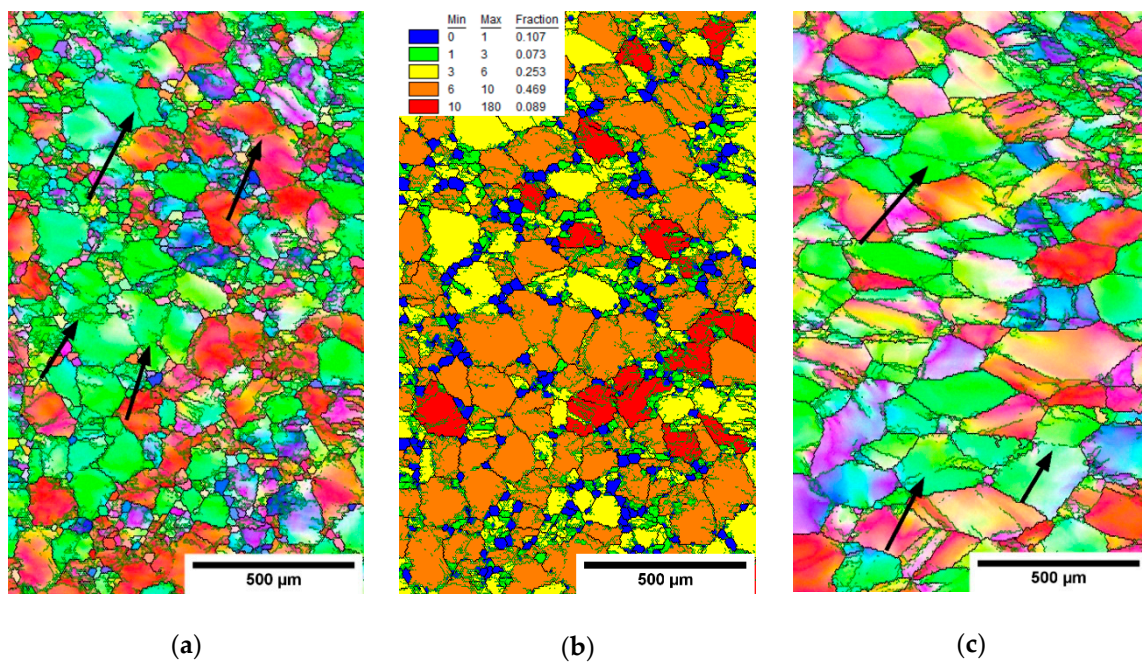


Figure 10. Microstructure of the cross-section of the hot-rolled rod with AR 77%. (a) IPF map-center, (b) GOS map-center and (c) IPF map-edge.

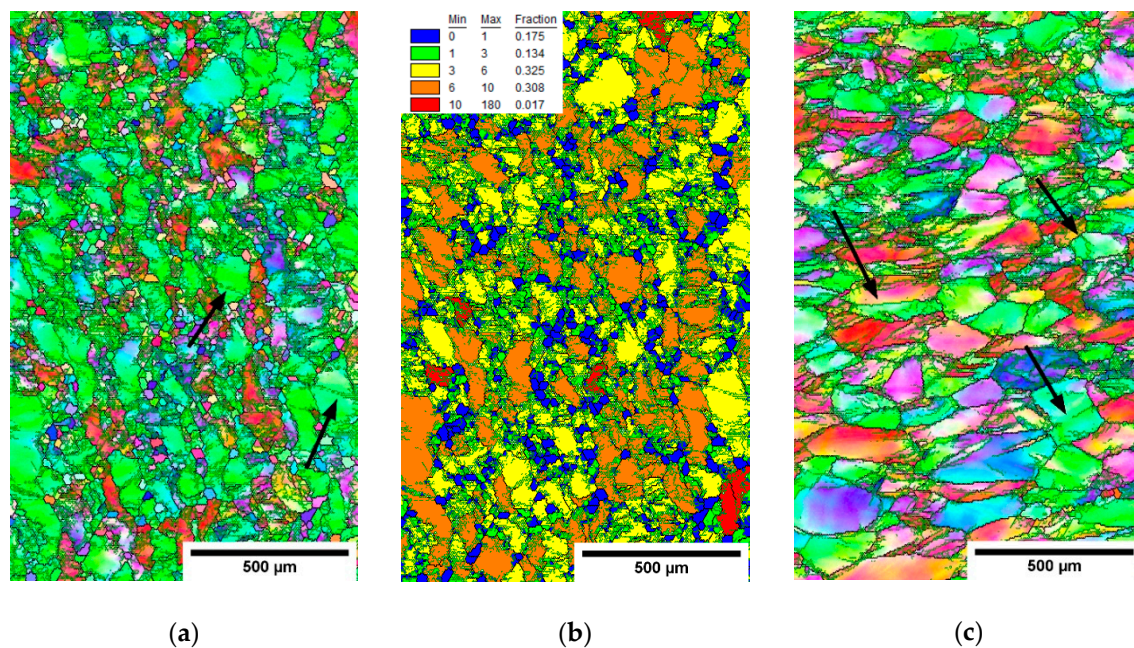


Figure 11. Microstructure of the cross-section of the hot-rolled rod with AR 86%. (a) IPF map-center, (b) GOS map-center and (c) IPF map-edge.

Table 4. Comparison of microstructural parameters of each condition produced by hot-rolling and die-forging. The error values shown are the widths of the grain size distributions of each fraction.

Hot-Rolled Rods				
Area Reduction	Fraction of Grains with GOS < 1° in Center	Grain Size in Fraction with GOS < 1°	Grain Size in Fraction with GOS > 1°	Grain Size on the Edges
64%	4%	28 ± 12 μm	270 ± 180 μm	145 ± 65 μm
77%	11%	25 ± 11 μm	114 ± 62 μm	157 ± 66 μm
84%	22%	20 ± 10 μm	78 ± 56 μm	103 ± 64 μm
Die-Forged Rods				
Area Reduction	Grain size—Middle Part		Grain Size—Side of the Rod	
40%	0.5 ± 0.3 mm		-	
70%	15 ± 10 μm		38 ± 15 μm	

The die-forged rods contained a limited fraction (<1%) of grains with GOS < 1°. The average grain sizes are shown in Table 4 with errors estimated as the distribution widths. Hot-rolled rods showed larger grain size in comparison with die-forged rod with AR 70%. The rod die-forged to 40% was not significantly refined. The dominating restoration mechanism during hot-rolling is recovery. The grains are deformed and their size decreases with larger area reduction. Necklace recrystallization was observed in the centers of rods cross-section. Differences between center and edge are mainly due to temperature, strain and strain rate gradients according to calculations of a similar rolling process [37].

In contrast, deformation bands were observed in the forged rod with AR 40% and only limited recrystallization was present at the grain boundaries. Meanwhile, in a rod forged with AR 70%, fully recrystallized microstructure was present, presumably via continuous recrystallization [23,29]. The grains were equiaxed on side of the rod, while elongated and more refined grains were in the middle of the rod. In comparison with hot-rolled rod with AR 86%, the grain size in rod die-forged to 70% was significantly lower, both on the side and in the middle part. The differences observed between both methods of forming are mainly due to much shorter exposition to the high temperature and much higher strain rate during the forging procedure.

3.4. Microhardness Measurements

The microhardness was measured in the as-cast condition and in the forged and rolled rods. The cast ingot exhibited the microhardness of 326 ± 6 HV, while all other conditions showed the microhardness of 344 ± 10 HV. This small though significant difference is clearly caused by thermomechanical processing. On the other hand, the mutual differences in microhardness between hot-worked conditions are negligible, while microstructure differs considerably. This might be caused by the fact that dominant strengthening mechanism in the alloy studied is the interstitial strengthening by oxygen. Other strengthening mechanisms are of lower importance and cause only limited differences in microhardness.

The microhardness of the hot rolled rods near the surface, was much higher than in the bulk, as shown in Figure 12a. Microhardness decreases with increasing distance from the surface for all hot-rolled conditions. In the closest vicinity to the surface, the microhardness exceeds 550 HV, and this value decreases with the increasing distance from surface to the value of 340 HV at 1.7 mm below the surface. The reason for this behavior was undoubtedly the increased oxygen content during exposure to air during the rolling process, which took several hours. Oxygen increases hardness, causes embrittlement in titanium [20] and also stabilizes the α phase. As shown in the Figure 12b, both the α phase precipitation and cracking were observed in the surface region of the condition hot rolled to AR 86%. Note that the α phase precipitates only to a depth of approximately 0.5 mm, while the layer with increased hardness—presumably increased oxygen content—is thicker. The clear practical implication of this behavior is that long-term exposure of the material to air at high temperature should be avoided. For instance, the hot die-forging process described above was designed to limit the time of exposure to high temperatures.

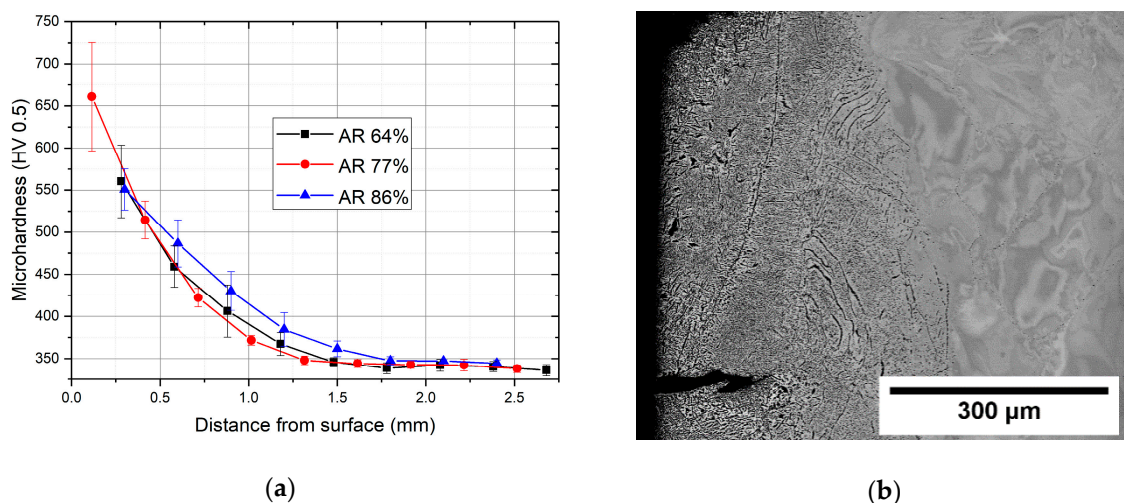


Figure 12. (a) Microhardness in the surface region of hot rolled rods; (b) SEM image of the α phase precipitated at the surface of hot rolled rod with the AR 86%.

3.5. Tensile Testing

Flow curves from static tensile tests are shown in Figure 13 for all manufactured conditions. Three or four samples were measured for each condition, and representative flow curves (with yield stress, ultimate tensile strength and ductility closest to the average) are shown. Tensile parameters, namely, the yield strength, the ultimate tensile strength and the total plastic elongation, derived from the flow curves, are summarized in Table 5. Extensometer was not used in the measurements and flow curves were determined only from the movement of the cross-head. Elastic parts, were thus subtracted from the true stress–true strain curves to obtain flow curves.

In the cast condition, the upper yield stress was just below 900 MPa; then, the stress slightly decreased (sharp yield point phenomenon), and was followed by a work hardening stage. The flow

curve ends with the brittle fracture, apparently without any strain localization (necking) with ultimate tensile strength over 1000 MPa.

Both forged conditions showed higher yield stress and higher ultimate tensile strength, but with considerably larger spread of measured values, as manifested by higher errors in Table 5. The elongation of the forged rod with AR 40% is comparable to the cast condition (approximately 15%) while in the rod with AR 70%, the achieved elongation was only about 10%. At this condition the highest yield strength exceeding 1200 MPa was achieved. In contrast to the cast condition, a significant neck was formed before rupture in the forged samples and was much more pronounced in the rod with AR 70%.

The yield stress of the hot-rolled rods slightly increases with increasing area reduction from 1050 MPa in rod with AR 64% to 1090 MPa in rod with AR 86%. The ultimate tensile strength is approximately 1250 MPa and elongation around 20%. The tensile tests results of the hot-rolled conditions are more reproducible than those from forged conditions. This is consistent with microstructural observations—more homogeneous microstructure in hot-rolled conditions.

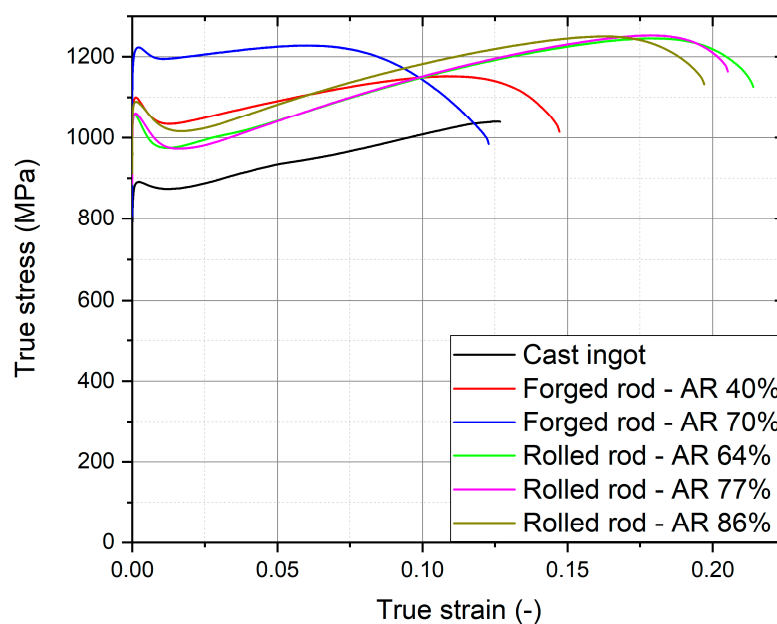


Figure 13. Flow curves of production conditions: cast, forged and rolled rods.

The sharp yield points are more pronounced in all deformed conditions in comparison to the cast ingot. In the rolled conditions, the yield points are significantly “sharper” compared to forged conditions. The reason for the occurrence of a sharp yield point was the interaction of dislocations with interstitial oxygen atoms [21,38].

Table 5. Yield strength, ultimate tensile strength and elongation of production conditions.

Condition	Yield Strength (MPa)	Ultimate Tensile Strength (MPa)	Plastic Elongation (%)
Cast ingot	870 ± 25	1039 ± 38	14.8 ± 1.4
Forged rod-AR 40%	1053 ± 71	1129 ± 76	14.1 ± 2.9
Forged rod-AR 70%	1256 ± 68	1264 ± 62	10.4 ± 2.0
Rolled rod-AR 64%	1053 ± 4	1251 ± 4	21.6 ± 0.5
Rolled rod-AR 77%	1078 ± 14	1256 ± 6	20.9 ± 1.2
Rolled rod-AR 86%	1084 ± 7	1237 ± 19	20.0 ± 1.2

3.6. Fatigue Testing

The S–N plots of fatigue tests in tension-compression ($R = -1$) are shown in two separate graphs for better orientation. Figure 14a shows results from the forged rods compared to the cast condition, while Figure 14b shows results from the hot rolled rods compared to the cast condition.

Fatigue properties of the rod rolled to AR 77% were not determined due to insufficient amount of material. In addition, stress amplitude lower than 350 MPa was not used for testing since lower stress amplitudes are not relevant for the foreseen application—manufacturing of the stem of the hip implant.

The cast ingot showed a very poor fatigue resistance, especially when compared with its high strength. The fatigue properties are negatively influenced by very large grain size, by the casting porosity and possibly by the chemical inhomogeneity. Both the die-forging and hot-rolling had removed the porosity and refined the grain structure; therefore, improvement in fatigue properties was expected.

The results of fatigue performance of the two forged rods are not systematic, which can be attributed to the inhomogeneous microstructure. Nevertheless, the rod forged to AR 70% showed generally improved fatigue performance as compared to the rod forged to AR 40%. This clearly correlates with much finer grain structure in the rod forged to AR 70% and its higher tensile strength. The microstructure of the forged rod with AR 70% was, however, not homogeneous, which resulted in the low reproducibility of the fatigue results. The fatigue limit can be estimated as approximately 400 MPa.

The fatigue results of two rolled rods were much more homogeneous. Variations between samples still existed due to differences in the grain size and the fraction of recrystallized grains between the center and surface regions of the hot rolled rods. The hot rolling to AR 64% did not significantly improve fatigue properties. The reduction of the grain size was apparently insufficient. However, the rolling to AR 86% increased the fatigue properties, and in this condition, the fatigue limit could be established as approximately 390 MPa. The reason for this improvement is more homogeneous deformation and refined grain size, together with the absence of the casting porosity.

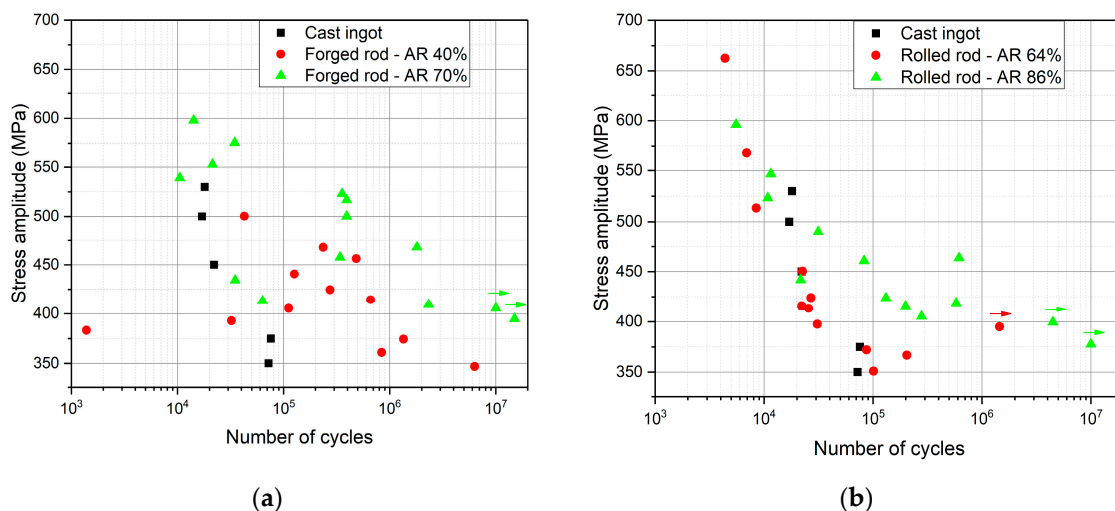


Figure 14. S–N plots of fatigue results: (a) cast ingot and die-forged rods; (b) cast ingot and hot-rolled rods.

Rolled conditions showed much more homogeneous grain structures. The forged condition of AR 70% showed, overall, the highest fatigue performance. The most significant differences were seen at stress amplitudes between 450 and 550 MPa, where the lifetime of rolled rods was significantly inferior to the rod forged to AR 70%. This is consistent with the grain size differences between these conditions: the rod forged to AR 70% contains grains of the size of 40 μm on the sides and 15 μm in the middle, while the rod hot-rolled to 86% exhibits grain sizes of the deformed fraction (80% of area) of about 80 μm . However, the effect of microstructure on fatigue properties in the alloy is not fully resolved.

Rolling of a rod to the AR 86% and forging to the AR 70% resulted in the fatigue limits (σ_f) of 390 MPa and 400 MPa, respectively. However, it constituted only 30% of the UTS values (approximately 1250 MPa for both), while the more common ratio σ_f/UTS is 0.5 in bcc metals [39]. Studies on fatigue

performance of β -Ti alloys in pure β (bcc) conditions are surprisingly scarce. Fatigue limit of 350 MPa was found in Ti-29Nb-13Ta-4.6Zr alloy in the beta solution treated condition [40]. Fatigue limit can be increased to 500 MPa by formation of ω phase or with the use of CeO₂ particles [41,42]. Low strength alloys Ti-22Nb-6Zr and Ti-24Nb-4Zr-7.9Sn exhibited fatigue limits of 200 MPa and 300 MPa, respectively [43,44]. Fatigue limits in the rotating bending tests of Ti-35.3Nb-7.3Zr-5.7Ta and Ti-35.3Nb-7.3Zr-5.7Ta-0.48O alloys were 280 and 450 MPa, respectively, as reported in [45]. This comprehensive study confirms the σ_f /UTS ratio of 0.5 and demonstrates the effect of the grain size, and, in particular, the average grain misorientation on σ_f . The initial damage accumulation is caused by coarse planar slip bands which propagate across low angle grain boundaries through several grains [45]. Our microstructural observations showed a high amount of low-angle grain boundaries in the conditions with lower accumulated deformation, and therefore are consistent with this theory. Conditions with the best fatigue performance—as-forged rod with AR 70% and as-rolled rod with AR 86%—are characterized by the smallest grain size and the highest misorientations between grains.

From practical point of view, the diameter of initial material for hip implant manufacturing must be at least 35 mm. Furthermore, the area reduction of approximately 85% is required to achieve satisfactory fatigue performance and oxidized surface layer must be removed after hot working [25]. Therefore, the initial diameter of the cast ingot should be approximately 100 mm.

4. Conclusions

Metastable β titanium alloy Ti-35.3Nb-6Ta-7.3Zr-0.7O (wt%) was prepared in several conditions: cast ingot, die-forged rods and hot-rolled rods. The influence of processing route on microstructure evolution, tensile properties and fatigue performance was investigated. The following conclusions can be drawn from this experimental study.

- Casting porosity and very large grains negatively affect mechanical properties, especially fatigue performance.
- Both hot working processes were successful in closing the casting pores.
- Area reduction over 70% for die-forging and over 80% for hot-rolling is required for significant grain size refinement. Apart of achieved strain, recrystallization processes are affected by exact temperature history and distribution of strain rate.
- Tensile properties were improved by both die-forging and hot-rolling.
- Fatigue performance of hot-rolled rods was more homogeneous to that of forged rods due to more homogeneous microstructure, but the rod forged with the AR 70% showed better fatigue performance.

Fatigue limits of the hot-rolled rod with the area reduction of 86% and die-forged rod with the area reduction of 70% were approximately 400 MPa.

Author Contributions: D.P. conducted majority of the SEM and EBSD experiments and tensile tests and wrote part of the manuscript. M.J. co-developed the studied alloy, coordinated the research and participated in the manuscript writing. P.H. co-developed the alloy and participated in the SEM experiments. J.D. and K.H. developed hot working procedures. J.M. participated in the alloy design and manufacturing. A.V. participated in the specimen preparation and SEM experiments. J.S. co-developed the studied alloy, coordinated the research, participated in the fatigue testing and wrote part of the manuscript.

Funding: Financial support by Czech Science Foundation under project 17-20700Y and by the Ministry of Industry and Trade under FV20147 is gratefully acknowledged. M.J. acknowledges partial financial support by ERDF under project No. CZ.02.1.01/0.0/0.0/15 003/0000485. D.P. acknowledges the Grant Agency of Charles University (project 1530217).

Conflicts of Interest: The authors declare no conflict of interest.

References

1. Long, M.; Rack, H.J. Titanium alloys in total joint replacement—A materials science perspective. *Biomaterials* **1998**, *19*, 1621–1639. [[CrossRef](#)]
2. Geetha, M.; Singh, A.K.; Asokamani, R.; Gogia, A.K. Ti based biomaterials, the ultimate choice for orthopaedic implants—A review. *Prog. Mater. Sci.* **2009**, *54*, 397–425. [[CrossRef](#)]
3. Katti, K.S. Biomaterials in total joint replacement. *Colloids Surfaces B Biointerfaces* **2004**, *39*, 133–142. [[CrossRef](#)] [[PubMed](#)]
4. Lettich, T.; Tierney, M.G.; Parvizi, J.; Sharkey, P.F.; Rothman, R.H. Primary Total Hip Arthroplasty with an Uncemented Femoral Component: Two- to Seven-Year Results. *J. Arthroplast.* **2007**, *22*, 43–46. [[CrossRef](#)] [[PubMed](#)]
5. Casper, D.S.; Kim, G.K.; Restrepo, C.; Parvizi, J.; Rothman, R.H. Primary Total Hip Arthroplasty with an Uncemented Femoral Component: Five- to Nine-Year Results. *J. Arthroplast.* **2011**, *26*, 838–841. [[CrossRef](#)]
6. Abdel-Hady Gepreel, M.; Niinomi, M. Biocompatibility of Ti-alloys for long-term implantation. *J. Mech. Behav. Biomed. Mater.* **2013**, *20*, 407–415. [[CrossRef](#)]
7. Okazaki, Y.; Gotoh, E. Comparison of metal release from various metallic biomaterials in vitro. *Biomaterials* **2005**, *26*, 11–21. [[CrossRef](#)]
8. Rao, S.; Okazaki, Y.; Tateishi, T.; Ushida, T.; Ito, Y. Cytocompatibility of new Ti alloy without Al and V by evaluating the relative growth ratios of fibroblasts L929 and osteoblasts MC3T3-E1 cells. *Mater. Sci. Eng. C* **1997**, *4*, 311–314. [[CrossRef](#)]
9. Steinemann, S.G. Titanium—The material of choice? *Periodontology 2000* **1998**, *17*, 7–21. [[CrossRef](#)]
10. Niinomi, M.; Nakai, M.; Hieda, J. Development of new metallic alloys for biomedical applications. *Acta Biomater.* **2012**, *8*, 3888–3903. [[CrossRef](#)]
11. Kuroda, D.; Niinomi, M.; Morinaga, M.; Kato, Y.; Yashiro, T. Design and mechanical properties of new β type titanium alloys for implant materials. *Mater. Sci. Eng. A* **1998**, *243*, 244–249. [[CrossRef](#)]
12. Ahmed, T.; Silvestri, J.; Ruiz, C.; Rack, H. A New Low Modulus, Biocompatible Titanium Alloy. In Proceedings of the 8th World Conference on Titanium, 22–26 October 1995; Institute of Materials: Birmingham, UK, 1995; Volume 620, pp. 1760–1767.
13. Ahmed, T.; Rack, H. Low modulus biocompatible titanium base alloys for medical devices. U.S. Patent 5,871,595, 16 February 1999.
14. Tang, X.; Ahmed, T.; Rack, H.J. Phase Transformations in Ti-Nb-Ta and Ti-Nb-Ta-Zr Alloys. *J. Mater. Sci.* **2000**, *35*, 1805–1811. [[CrossRef](#)]
15. Kopova, I.; Stráský, J.; Hrcuba, P.; Landa, M.; Janeček, M.; Bačáková, L. Newly developed Ti-Nb-Zr-Ta-Si-Fe biomedical beta titanium alloys with increased strength and enhanced biocompatibility. *Mater. Sci. Eng. C* **2016**, *60*, 230–238. [[CrossRef](#)] [[PubMed](#)]
16. Rack, H.J.; Qazi, J.I. Titanium alloys for biomedical applications. *Mater. Sci. Eng. C* **2006**, *26*, 1269–1277. [[CrossRef](#)]
17. Lütjering, G.; Williams, J.C. Engineering Materials and Processes. In *Titanium*, 2nd ed.; Springer: Berlin/Heidelberg, Germany, 2007; ISBN 978-3-540-71397-5.
18. Cocharadt, A.W.; Schoek, G.; Wiedersich, H. Interaction between dislocations and interstitial atoms in body-centered cubic metals. *Acta Metall.* **1955**, *3*, 533–537. [[CrossRef](#)]
19. Qazi, J.I.; Rack, H.J.; Marquardt, B. High-strength metastable beta-titanium alloys for biomedical applications. *JOM* **2004**, *56*, 49–51. [[CrossRef](#)]
20. Welsch, G.; Boyer, R.; Collings, E.W. *Materials Properties Handbook: Titanium Alloys*; ASM International: Novelty, USA, 1993; ISBN 978-0-87170-481-8.
21. Stráský, J.; Hrcuba, P.; Václavová, K.; Horváth, K.; Landa, M.; Srba, O.; Janeček, M. Increasing strength of a biomedical Ti-Nb-Ta-Zr alloy by alloying with Fe, Si and O. *J. Mech. Behav. Biomed. Mater.* **2017**, *71*, 329–336. [[CrossRef](#)]
22. Preisler, D.; Václavová, K.; Stráský, J.; Janeček, M.; Hrcuba, P. Microstructure and mechanical properties of Ti-Nb-Zr-Ta-O biomedical alloy. In Proceedings of the METAL 2016: 25rd International Conference on Metallurgy and Materials, Brno, Czech Republic, 25–27 May 2016; TANGER: Ostrava, Czech Republic, 2016; pp. 1509–1513.

23. Weiss, I.; Semiatin, S.L. Thermomechanical processing of beta titanium alloys—An overview. *Mater. Sci. Eng. A* **1998**, *243*, 46–65. [[CrossRef](#)]
24. Huang, J.; Xing, H.; Sun, J. Structural stability and generalized stacking fault energies in β Ti–Nb alloys: Relation to dislocation properties. *Scr. Mater.* **2012**, *66*, 682–685. [[CrossRef](#)]
25. ZHANG, W.; LIU, Y.; WU, H.; LIU, B.; CHEN, Z.; TANG, H. Microstructural evolution during hot and cold deformation of Ti–36Nb–2Ta–3Zr–0.35O alloy. *Trans. Nonferrous Met. Soc. China* **2016**, *26*, 1310–1316. [[CrossRef](#)]
26. Sakaguchi, N.; Niinomi, M.; Akahori, T.; Takeda, J.; Toda, H. Effect of Ta content on mechanical properties of Ti–30Nb–XTa–5Zr. *Mater. Sci. Eng. C* **2005**, *25*, 370–376. [[CrossRef](#)]
27. Zhu, Y.; Wang, X.; Wang, L.; Fu, Y.; Qin, J.; Lu, W.; Zhang, D. Influence of forging deformation and heat treatment on microstructure of Ti–xNb–3Zr–2Ta alloys. *Mater. Sci. Eng. C* **2012**, *32*, 126–132. [[CrossRef](#)]
28. Málek, J.; Hnilica, F.; Veselý, J.; Smola, B.; Bartáková, S.; Vaněk, J. The influence of chemical composition and thermo-mechanical treatment on Ti–Nb–Ta–Zr alloys. *Mater. Des.* **2012**, *35*, 731–740. [[CrossRef](#)]
29. Dikovits, M.; Poletti, C.; Warchomicka, F. Deformation Mechanisms in the Near- β Titanium Alloy Ti-55531. *Metall. Mater. Trans. A* **2014**, *45*, 1586–1596. [[CrossRef](#)]
30. Hua, K.; Xue, X.; Kou, H.; Fan, J.; Tang, B.; Li, J. Characterization of hot deformation microstructure of a near beta titanium alloy Ti-5553. *J. Alloy. Compd.* **2014**, *615*, 531–537. [[CrossRef](#)]
31. Jones, N.G.; Dashwood, R.J.; Dye, D.; Jackson, M. Thermomechanical processing of Ti-5Al-5Mo-5V-3Cr. *Mater. Sci. Eng. A* **2008**, *490*, 369–377. [[CrossRef](#)]
32. Li, K.; Yang, P. Strain-induced α -to- β phase transformation during hot compression in Ti–5Al–5Mo–5V–1Cr–1Fe alloy. *Trans. Nonferrous Met. Soc. China* **2019**, *29*, 296–304. [[CrossRef](#)]
33. Preisler, D.; Stráský, J.; Harcuba, P.; Warchomicka, F.G.; Janeček, M. High Temperature Mechanical Properties and Microstructure of Ti-Nb-Zr-Ta-O Biomedical Alloy. *Acta Phys. Pol. A* **2018**, *134*, 636–639. [[CrossRef](#)]
34. Bertrand, E.; Castany, P.; Péron, I.; Gloriant, T. Twinning system selection in a metastable β -titanium alloy by Schmid factor analysis. *Scr. Mater.* **2011**, *64*, 1110–1113. [[CrossRef](#)]
35. Wright, S.I. Quantification of recrystallized fraction from orientation imaging scans. In Proceedings of the National Research Council of Canada, Proceedings of the Twelfth International Conference on Textures of Materials (ICOTOM-12), Montreal, QC, Canada, 9–13 August 1999; Volume 1, pp. 104–109.
36. Zhao, J.; Zhong, J.; Yan, F.; Chai, F.; Dargusch, M. Deformation behaviour and mechanisms during hot compression at supertransus temperatures in Ti-10V-2Fe-3Al. *J. Alloy. Compd.* **2017**, *710*, 616–627. [[CrossRef](#)]
37. Glowacki, M.; Kuziak, R.; Malinowski, Z.; Pietrzyk, M. Modelling of heat transfer, plastic flow and microstructural evolution during shape rolling. *J. Mater. Process. Technol.* **1995**, *53*, 159–166. [[CrossRef](#)]
38. Geng, F.; Niinomi, M.; Nakai, M. Observation of yielding and strain hardening in a titanium alloy having high oxygen content. *Mater. Sci. Eng. A* **2011**, *528*, 5435–5445. [[CrossRef](#)]
39. Ferro, A.; Mazzetti, P.; Montalenti, G. On the effect of the crystalline structure on fatigue: Comparison between body-centred metals (Ta, Nb, Mo and W) and face-centred and hexagonal metals. *The Philos. Mag. A J. Theor. Exp. Appl. Phys.* **1965**, *12*, 867–875. [[CrossRef](#)]
40. Niinomi, M.; Nakai, M. Titanium-Based Biomaterials for Preventing Stress Shielding between Implant Devices and Bone. Available online: <https://www.hindawi.com/journals/ijbm/2011/836587/> (accessed on 7 October 2019).
41. Nakai, M.; Niinomi, M.; Oneda, T. Improvement in Fatigue Strength of Biomedical β -type Ti-Nb-Ta-Zr Alloy While Maintaining Low Young's Modulus Through Optimizing ω -Phase Precipitation. *Metall. Mater. Trans. A* **2012**, *43*, 294–302. [[CrossRef](#)]
42. Song, X.; Wang, L.; Niinomi, M.; Nakai, M.; Liu, Y.; Zhu, M. Microstructure and fatigue behaviors of a biomedical Ti–Nb–Ta–Zr alloy with trace CeO₂ additions. *Mater. Sci. Eng. A* **2014**, *619*, 112–118. [[CrossRef](#)]
43. Sheremetyev, V.; Brailovski, V.; Prokoshkin, S.; Inaekyan, K.; Dubinskiy, S. Functional fatigue behavior of superelastic beta Ti-22Nb-6Zr(at%) alloy for load-bearing biomedical applications. *Mater. Sci. Eng. C* **2016**, *58*, 935–944. [[CrossRef](#)]

44. Li, S.J.; Cui, T.C.; Hao, Y.L.; Yang, R. Fatigue properties of a metastable β -type titanium alloy with reversible phase transformation. *Acta Biomater.* **2008**, *4*, 305–317. [[CrossRef](#)]
45. Long, M.; Crooks, R.; Rack, H.J. High-cycle fatigue performance of solution-treated metastable- β titanium alloys. *Acta Mater.* **1999**, *47*, 661–669. [[CrossRef](#)]



© 2019 by the authors. Licensee MDPI, Basel, Switzerland. This article is an open access article distributed under the terms and conditions of the Creative Commons Attribution (CC BY) license (<http://creativecommons.org/licenses/by/4.0/>).

Microstructure and lattice defects in ultrafine grained biomedical $\alpha + \beta$ and metastable β Ti alloys

4.5

*J. Stráský**, *M. Janeček**, *I. Semenova[†]*, *J. Čížek**, *K. Bartha**, *P. Harcuba**,
V. Polyakova[†], *S. Gatina[†]*

*Charles University, Prague, Czech Republic, [†]Ufa State Aviation Technical University, Ufa, Russia

4.5.1 Introduction

Ultrafine-grained (UFG) titanium has been prepared for the first time by methods of severe plastic deformation (SPD) at Ufa State Aviation Technical University (USATU), Ufa, Russia, more than two decades ago [1]. UFG commercially pure titanium (CP Ti) Grade 2 and Grade 4 as well as a Ti-6Al-4V alloy prepared by different SPD methods were thoroughly investigated in numerous studies. SPD methods and properties of ultrafine-grained Ti materials are reviewed in this book by Prof. Ruslan Z. Valiev in the chapter “Nanostructured Commercially Pure Titanium for Development of Miniaturized Biomedical Implants.” This chapter focuses on investigations of the microstructure of ultrafine-grained Ti alloys designed for biomedical use. Such alloys include $\alpha + \beta$ Ti-6Al-7Nb alloy as a biomedical alternative of Ti-6Al-4V and biomedical β Ti alloys based on Ti-Mo and Ti-Nb systems.

The microstructure of metallic material is determined by alloy composition and processing conditions. On the other hand, the microstructure determines the mechanical and other physical properties of metallic materials. Moreover, ultrafine-grained microstructure was shown to affect biological response as reviewed by Prof. Yuri Estrin in this book in the chapter “Mechanical Performance and Cell Response of Pure Titanium with Ultrafine-Grained Structure Produced by Severe Plastic Deformation.” Therefore, microstructural studies provide a link between processing and properties. Especially in UFG materials, proper assessment of the microstructure is critical for their applications.

Ti-6Al-4V is still a workhorse of the titanium industry even in orthopedics, despite the fact that the adverse effect of toxic vanadium is widely discussed [2,3]. In order to avoid potential harmful effects to an organism, a new vanadium-free Ti-6Al-7Nb alloy was developed [4,5]. Despite the different composition of these two materials, the Ti-6Al-7Nb alloy has similar metallurgical and mechanical

properties as Ti-6Al-4V. The microstructure evolution of the UFG Ti-6Al-7Nb alloy is also described in detail in this chapter.

Nevertheless, the most-studied Ti alloys are currently β titanium alloys, which profit from enhanced biocompatibility and reduced modulus of elasticity. β alloys can be divided into metastable β alloys that can be hardened by dispersion of α phase particles and stable β alloys that are nonhardenable by a simple thermal treatment. Despite a long history of intensive investigations of UFG materials, ultrafine-grained biomedical β -Ti alloys were prepared and investigated only recently [6].

SPD methods refer to metal-forming processes that impose a very high strain on a bulk solid resulting in exceptional grain refinement [7]. The most-used SPD methods for achieving the UFG structure in β titanium alloys are high-pressure torsion (HPT), equal channel angular pressing (ECAP) and accumulative roll bonding (ARB) [8,9].

In this chapter, the original results of the authors are presented along with the review of other studies focusing on the microstructure of ultrafine-grained biomedical Ti alloys. Special attention is paid to the experimental methods for microstructural analysis.

4.5.2 Strain accumulation, grain refinement, and Hall-Petch strengthening

SPD methods are based on the repetitive application of straining using special geometries of tools such that straining does not reduce product dimensions. In the case of ECAP, a metallic billet is pressed through a special die comprising two intersecting channels. At the point of intersection, the billet is deformed by a simple shear. The typical angle of intersecting channels is 90 degrees. For this die geometry, the von Mises equivalent deformation after one pass reaches approx. $\epsilon_{\text{von Mises}} \approx 1$ (=100%). In order to process strong and hard-to-deform materials such as titanium alloys, ECAP dies with bigger angles (120 or 135 degrees) are often used. Repetitive application of ECAP can impose the total von Mises equivalent deformation of $\epsilon_{\text{von Mises}} \approx 10$ depending on the number of passes and the die geometry.

The technique of ARB uses conventional rolling deformation. A sheet is rolled to a 50% reduction in thickness, then cut into two pieces and stacked together to reform the initial dimensions. The sheet sandwich is subsequently repetitively rolled. The rolling in the ARB processing is in fact a bonding process. The von Mises equivalent strain per each rolling pass is $\epsilon_{\text{von Mises}} \approx 0.8$. The ARB rolling is limited to few rolling passes due to the deterioration of both surface and bonding quality [10].

In HPT, a thin disk sample is placed between two massive anvils, then subjected to a high applied compressive pressure (several GPa) followed by the rotation of one anvil, introducing torsional straining [11]. The von Mises equivalent strain calculation utilizing a simple torsion gives the strain as:

$$\epsilon_{\text{von Mises}} = \frac{2\pi Nr}{\sqrt{3}h} \quad (4.5.1)$$

where N is the number of rotations, r represents the radius of the sample, and h its thickness. Note that the strain is inhomogeneous over the sample disk and increases with

distance from the sample center. The radius of the sample is typically 10–20 mm while its thickness is usually around 1 mm. The number of rotations can reach $N > 10$ and therefore the maximum achieved von Mises equivalent strain easily exceeds 100, which is by one order of magnitude higher than in the case of ARB or ECAP.

Homogeneous and equiaxed microstructures with grain size $< 1 \mu\text{m}$ are characteristic for the ultrafine-grained materials. The most accepted mechanism of grain fragmentation is the continuous dynamic recrystallization mechanism based on dislocation movement, agglomeration, formation of dislocation walls, subgrain boundaries, and, finally, creation of high-angle grain boundaries [12]. Other models include the effect of so-called disclinations [13]. The effect of mechanical twinning on grain refinement was also reported [14]. For a review on mechanisms of grain refinement in materials after SPD, the reader is referred to [15].

The reduction of grain size in polycrystalline materials causes changes in mechanical and physical properties. The strength of the polycrystalline material changes with the grain size d according to the Hall-Petch equation [16,17]:

$$\sigma_y = \sigma_0 + k_y d^{-1/2} \quad (4.5.2)$$

where σ_y is the yield stress of the material, σ_0 represents the friction stress, and k_y is a material constant. The strength of the UFG material is also determined by the dislocation density, spatial arrangements of dislocations [12], texture, or even vacancy concentration [18].

4.5.2.1 Refinement of Ti-6Al-7Nb $\alpha+\beta$ alloy

Ti-6Al-7Nb is a biomedical two-phase alloy designed as a vanadium-free alternative of the Ti-6Al-4V alloy. Fig. 4.5.1 depicts the initial material after thermal treatment in the $\alpha+\beta$ region [19]. A scanning electron microscopy (SEM) micrograph employing back-scattered electrons (BSE) reveals the duplex microstructure of the Ti-6Al-7Nb alloy. The contrast between darker and lighter areas is given by chemical composition—the so-called Z-contrast. Darker areas include elements with a lower atomic number (higher concentration of Al) and lighter areas with a higher atomic number (higher concentration of Nb). Primary α grains are globular with the size of $\sim 10 \mu\text{m}$. The central part of primary α grains contains a higher concentration of Al due to the two-step thermal treatment [19]; therefore they appear darker. White particles are Nb-rich β phase. The microstructure after thermal treatment contains α lamellae within the so-called $\alpha+\beta$ areas.

Samples with a diameter of 20 mm and a thickness of 1 mm were prepared by HPT, applying the compressive pressure of 6 GPa at room temperature. The lower anvil was rotated by the speed of 0.5 rpm to achieve torsion deformation. The sample after $N = 5$ HPT revolutions was selected for further characterization. The maximum von Mises equivalent strain near the sample edge reaches $\varepsilon_{\text{von Mises}} \approx 200$.

The material after deformation by HPT was examined by SEM in three different zones. The scheme of zones of the observation is presented in Fig. 4.5.2A. Fig. 4.5.2B shows the microstructure of the specimen center after five turns. The α grains are still

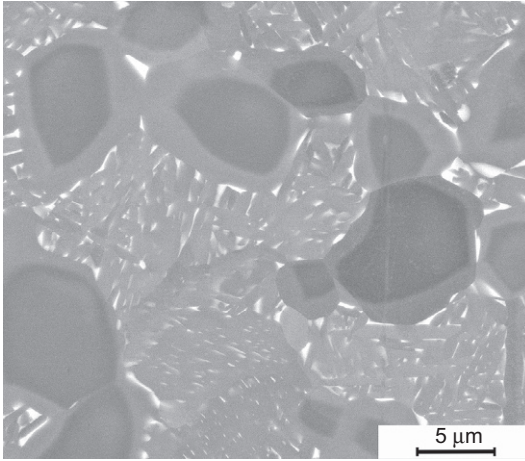


Fig. 4.5.1 Ti-6Al-7Nb alloy, initial material, SEM image (BSE).

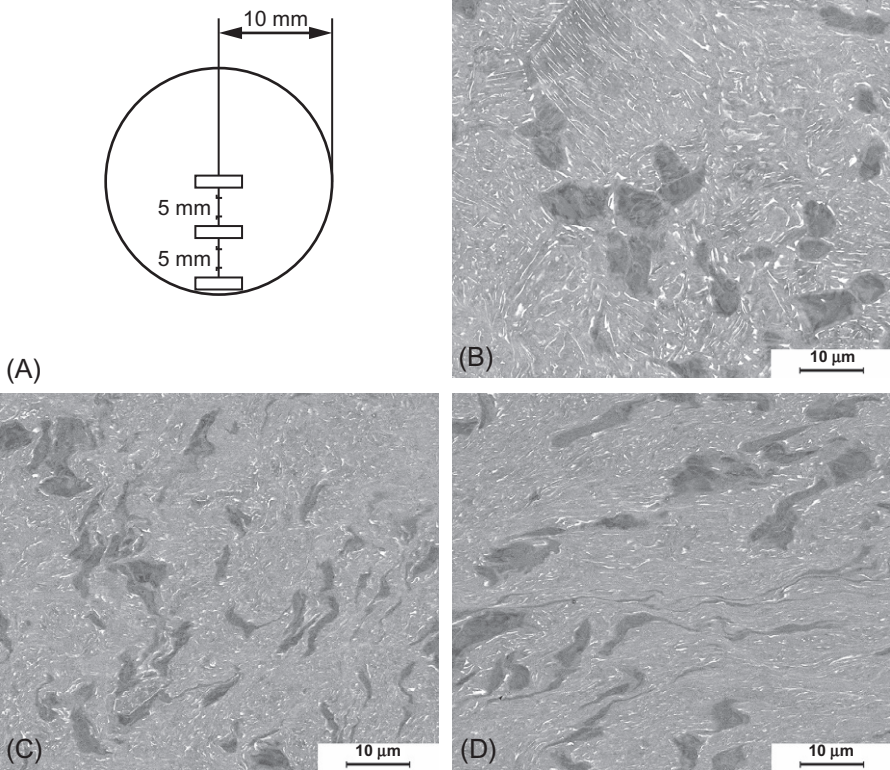


Fig. 4.5.2 (A) Scheme of SEM observations. (B) HPT deformed material ($N=5$), center of the sample. (C) HPT deformed material ($N=5$), 5 mm from the center of the sample. (D) HPT deformed material ($N=5$), periphery of the sample.

well distinguishable and remain mostly equiaxed—similar to the initial material. However, each grain is obviously strongly deformed. The α areas have uneven shade due to the deformation contrast. The $\alpha+\beta$ phase lamellar areas remain straight in some zones but in other areas they are already heavily deformed.

In Fig. 4.5.2C, the typical microstructure of the region 5 mm from the center of the sample (middle radius) is shown, while Fig. 4.5.2D displays the zone near the edge of the specimen. The areas of initial primary α grains are still visible; their shape is elongated and they are strongly deformed. The lamellar part is also deformed.

4.5.2.2 Refinement of Ti-15Mo alloy prepared by HPT

Ti-15Mo is a metastable β titanium alloy that can be used in biomedicine since it does not contain any toxic elements. The so-called solution-treated condition exhibits reduced elastic modulus due to the absence of a stiffer α phase.

The Ti-15Mo alloy was deformed by HPT employing the same procedure as the Ti-6Al-7Nb alloy described above. The microstructure of the initial material consists of large grains with a typical size of 50 μm . An EBSD image of the microstructure after the initial stage of HPT deformation ($N=1/4$, center of the sample) is shown in Fig. 4.5.3. Large grains present in the initial material can still be recognized. These grains are heavily deformed (uneven color/orientation within grains), heavily

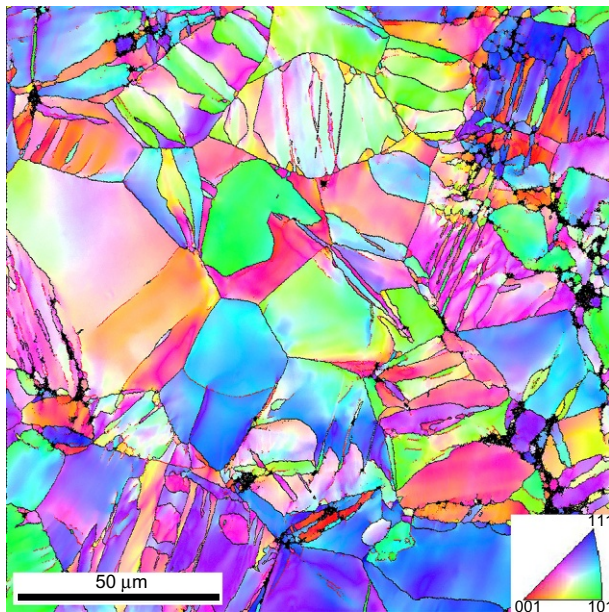


Fig. 4.5.3 EBSD image of Ti-15Mo alloy deformed by HPT, $N=1/4$, center of the sample.

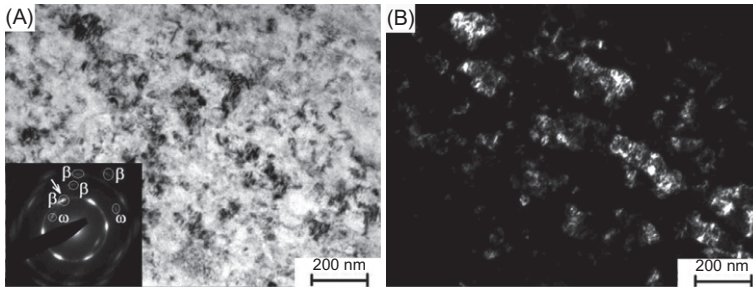


Fig. 4.5.4 Bright field (A) and dark field (B) TEM image of Ti-15Mo alloy deformed by HPT, $N = 5$, periphery of the sample.

twinned, and, in some areas, the microstructure is clearly refined. EBSD observations prove the activity of the common mechanism of the grain refinement consisting of accumulation of dislocations, lattice rotation, formation of dislocation walls, and sub-grain boundaries. Simultaneously, the activity of the twinning system $\{112\}\langle 111\rangle$ in the Ti-15Mo alloy is also clearly documented. Moreover, it can be seen that the primary twins undergo additional secondary twinning. One may therefore conclude that multiple mechanical twinning significantly contributes to the microstructure refinement in the Ti-15Mo alloy [14].

Additional HPT straining leads to the formation of a nanocrystalline structure. Such a structure cannot be distinguished by SEM and therefore transmission electron microscopy (TEM) with higher resolution is employed. The heavily deformed microstructure typical for Ti alloys after severe deformation by HPT is shown in a bright field TEM micrograph in Fig. 4.5.4A. The dark field image in Fig. 4.5.4B reveals the average grain size around 100 nm.

Fig. 4.5.5 displays an image obtained by a special technique referred to as ACOM-TEM [20], which has been rarely employed for the characterization of Ti alloys [21]. This technique is based on the reconstruction of the crystalline symmetry (phase) and the determination of crystalline orientation from the point diffraction patterns in TEM. A TEM with electron beam precession must be used to enhance the quality of orientation indexing. The result of the measurement is qualitatively similar to an EBSD image but the resolution is by one order of magnitude higher. The ACOM-TEM method confirms the nanocrystalline microstructure in Ti-15Mo after HPT deformation.

4.5.2.3 Refinement in Ti-Nb based alloys prepared by SPD methods

β Ti alloys with a high content of β stabilizing elements that often contain other alloying elements such as Ta or Zr are promising candidates for replacing the Ti-6Al-4V alloy in biomedical use [22–24]. The Ti-29Nb-13Ta-4.6Zr (TNTZ) alloy was prepared by HPT in order to enhance the strength of the material without

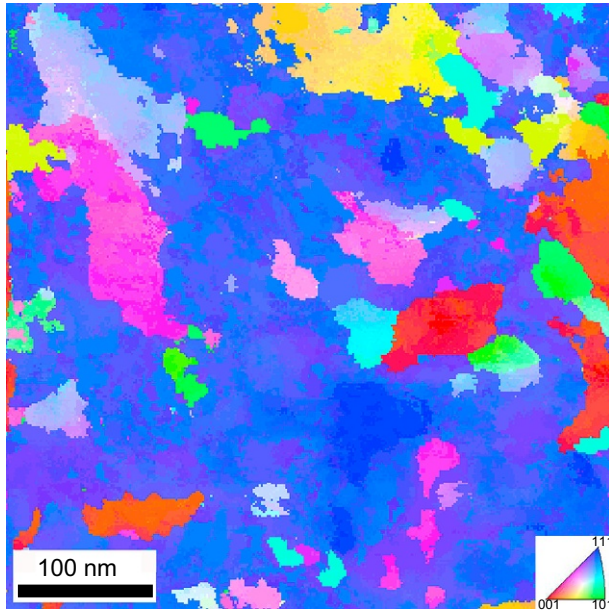


Fig. 4.5.5 Orientation map of Ti-15Mo alloy deformed by HPT, $N = 1$, periphery of the sample.

unwanted increase of the elastic modulus [25]. TEM observations of the cold-rolled TNTZ alloy subjected to $N = 5$ and $N = 20$ HPT turns showed reduction of the grain size to 100 and 50 nm, respectively [26]. Elongated grains with a thickness of 50 nm were formed in a simple binary biomedical alloy Ti45Nb processed by 15 HPT revolutions. These alloys contain sufficient amounts of β stabilizing elements (Nb and Ta) to prevent $\beta \rightarrow \alpha''$ stress-induced martensitic transformation. Stress-induced martensite (SIM) is formed in the early stages of plastic deformation while at high strains the backward $\alpha'' \rightarrow \beta$ transformation occurs in addition to microstructure refinement [27]. The formation of SIM leads to more pronounced grain refinement. Grain sizes smaller than 50 nm can be achieved in the Ti5553 alloy, which undergoes stress-induced martensitic transformation, while in a stable Ti-20Mo alloy, the grain size was approximately 100 nm after equivalent HPT straining. The authors in [27] claim that once β grains are refined to submicrometer sizes, the formation of α'' requires too high energy, resulting in backward transformation.

Because the maximum achievable equivalent strain imposed by ECAP is much lower than the strain imposed by HPT, the minimum achievable grain sizes are larger. In a Ti-20Nb-5Ta-2Cr alloy processed by ECAP, the grain size reduction to 1.4 μm was reported. On the other hand, in the Ti-25Nb-5Zr-3Sn beta phase alloy with low stability, β grains of an average size of 400 nm were formed by an identical ECAP procedure. This difference was attributed to observed SIM and reverse SIM transformations [28].

A similar alloy Ti-36Nb-3Zr-2Ta was processed by ECAP (channel angle 120 degrees) at room temperature by three and six passes and grain sizes of the β matrix of 600 nm and 250 nm were reported, respectively. Numerous α'' laths were observed in the microstructure due to processing at room temperature [29]. On the other hand, the α'' SIM formation can be prevented by higher processing temperatures. A similar Ti-35Nb-3Zr-2Ta biomedical alloy was prepared by four passes of ECAP at temperatures of 500°C and 600°C [30]. The grain size determined from TEM images is 300 nm and 600 nm for pressing temperatures of 500°C and 600°C, respectively. No traces of α'' SIM were observed.

Finally, a commercial Ti-13Nb-13Zr alloy was subjected to ECAP after previous annealing in the $\alpha + \beta$ field. TEM images reveal the grain size in the range of hundreds of nanometers, which was confirmed by a detailed EBSD analysis indicating the high fraction of low-angle grain boundaries [31].

Summary

HPT is capable of decreasing grain size down to 100 nm while grain sizes after ECAP are typically in the range of hundreds of nanometers. Grain refinement is enhanced by mechanical twinning and stress-induced phase transformations during SPD processing. A nanocrystalline β Ti matrix prevents the formation of α'' and ω phases.

4.5.3 Dislocations and vacancies/point defects in biomedical Ti alloys prepared by severe plastic deformation

4.5.3.1 Dislocation density determination by XRD

Dislocations in severely deformed material can be qualitatively observed by TEM. However, quantitative analysis from TEM images is usually not possible due to their high density. More often, dislocation density in heavily deformed material may be indirectly determined by an X-ray line profile analysis (XLPA) [18]. In heavily deformed materials, the effect of crystallite size and dislocation density on peak broadening must be simultaneously considered.

The dislocation density in the order of 10^{14} m^{-2} was determined in the Ti-36Nb-3Zr-2Ta alloy processed by ECAP by X-ray diffraction (XRD) methods [29]. Dislocation density was found to increase with increasing strain imposed by ECAP. On the other hand, in [31], the estimated dislocation density from XRD data (from a single peak) was reported as high as 10^{16} m^{-2} in Ti-13Nb-13Zr deformed by ECAP in the annealed $\alpha + \beta$ condition. Dislocation density is reported to increase with ECAP straining up to four passes and followed by a drop during subsequent straining up to eight passes. Similar behavior was also found in Mg alloys [32].

4.5.3.2 Positron annihilation spectroscopy

An alternative and extraordinary method for the determination of dislocation density and also point defects and their conglomerates concentrations in deformed materials is positron annihilation spectroscopy (PAS), which deserves a short introduction.

PAS is a nondestructive method of investigation of lattice defects in material. The radioactive source ^{22}Na decays by β^+ -decay during which the positron is created. This event is accompanied by the simultaneous emission of a γ -photon of the energy of 1274 keV (the so-called start signal). The positron source is placed between two identical samples of the studied material. The high-energy positron enters the material and reduces its energy from hundreds of keV down to $kT \approx 0.03$ eV within 10 ps (so-called thermalization). Subsequently, the thermalized positron diffuses through the lattice until it encounters an electron. Positron-electron pair annihilates by emitting two γ -photons with the energy of 511 keV. One of these γ -photons is detected as a stop signal by one or two detectors. The time between the start and stop signal determines the positron lifetime. Positron lifetime was measured by a fast-fast spectrometer with a time resolution of 150 ps [33]. The measurement of the positron lifetime is schematically shown in Fig. 4.5.6.

In a defect-free lattice, the electron density is comparatively higher and consequently the positron lifetime is shorter (free positron annihilation). If the material contains open-volume defects such as vacancies or dislocations, the positron can be trapped in the defect. The electron density around defects is lower, the probability of annihilation of the electron and positron is also lower, and the average positron lifetime is therefore longer. As a consequence, the mean positron lifetime correlates with the density of lattice defects. The positron lifetime spectrum can be divided into components associated with different lifetimes. These lifetimes are ascribed to different types of defects [34] whereas the intensities of the components provide information about concentrations/densities of types of defects.

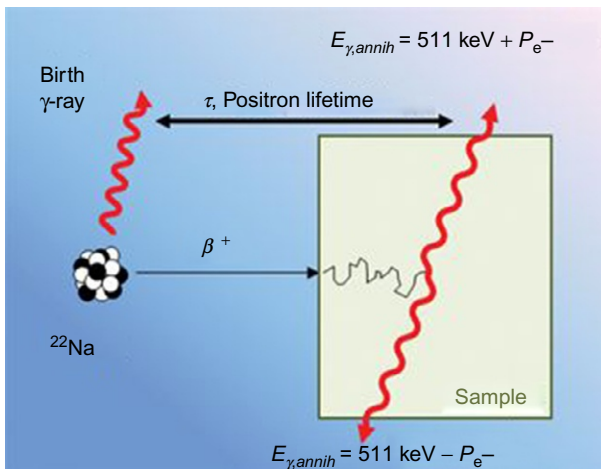


Fig. 4.5.6 Schematic representation of measurement of positron lifetime.

Other experimental data from the annihilation of positrons can be obtained by measuring the Doppler broadening (DB), which corresponds to the difference in energies of two γ -photons emitted after annihilation of a positron-electron pair caused by a nonzero momentum of interacting particles. Because the momentum of a thermalized positron is negligible, the energy broadening is given solely by the momentum of the electron. If the positron annihilates with low-momentum valence electrons, the DB is lower, while for the high-momentum core electrons the opposite is true. In order to quantify this effect, the so-called S-parameter is introduced. The S-parameter is calculated as the ratio of the area near the center of the Doppler-broadened peak and the total area of the peak. The S-parameter therefore determines the proportion of the positrons annihilated with low-momentum valence electrons. Positrons trapped in defects annihilate with much higher probability with outer low-momentum electrons, rather than with core electrons. Under the assumption that the nature of defects does not change, the S-parameter correlates well with the density of defects [35].

4.5.3.3 Dislocations and vacancy clusters in Ti-6Al-7Nb and Ti-15Mo alloys

In the biomedical $\alpha + \beta$ Ti-6Al-7Nb alloy prepared by HPT, two types of defects were found by PAS: dislocations and vacancy clusters containing typically 2–10 vacancies. Fig. 4.5.7 shows the intensities of free positrons, dislocations, and vacancy cluster components in the positron lifetime spectrum as a function of the number of HPT revolutions (N). It can be observed that the dislocation density increases in the initial stages of HPT straining while vacancy cluster concentration is rather constant.

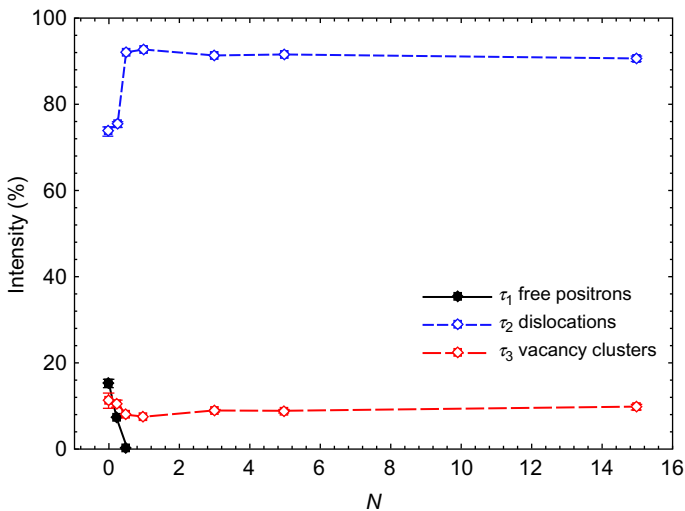


Fig. 4.5.7 Intensities of free positrons, dislocations, and vacancy cluster components in the positron lifetime spectrum of the Ti-6Al-7Nb alloy as a function of the number of HPT revolutions (N).

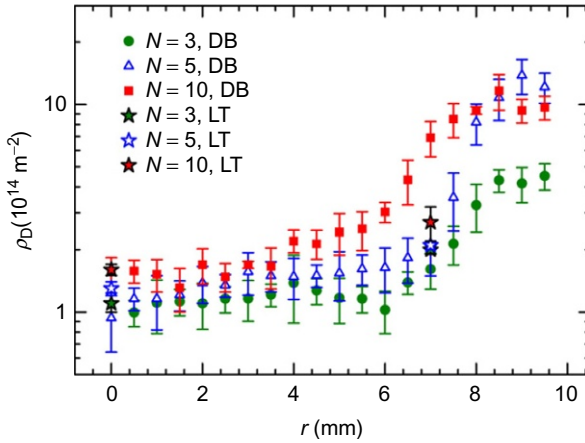


Fig. 4.5.8 The dislocation densities for HPT-deformed Ti-15Mo samples calculated from lifetime spectra and Doppler broadening results and plotted as a function of the distance r from the center of the sample for three different samples ($N=3, 5, 10$).

In samples subjected to a higher degree of HPT straining ($N > 1/2$), the concentration of defects cannot be determined because of saturated positron trapping, which leads to the disappearance of the free positron component. Taking into account the ratio between dislocation and vacancy cluster intensities, the dislocation density of the order of 10^{15} m^{-2} and simultaneously the concentration of vacancy clusters of at least 15 ppm [36] were determined. Note that dislocation density might increase during further HPT processing. If this occurs, the concentration of vacancy clusters must increase proportionally.

Contrary to $\alpha+\beta$ Ti-6Al-7Nb alloy, in the β Ti-15Mo alloy deformed by HPT under comparable conditions, vacancy clusters were not found. The positron lifetime spectra of Ti-15Mo samples after HPT ($N=3, 5, 10$) can be well fitted by two components—a free positron component and a dislocations component. The dislocation density was calculated from these intensities using a two-state single-trapping model [35]. Estimated dislocation density at the center of the sample and at a distance $r=7$ mm from the center is shown in Fig. 4.5.8 (asterisk symbols). DB was measured along the sample radius with the step of 1 mm. Resulting S-parameter values are dimensionless but they can be calibrated using results from lifetime spectra and dislocation density can be calculated from the S-parameter values. The overall evolution of the dislocation density as a function of the distance r from the center of the sample for three different samples ($N=3, 5, 10$) is depicted in Fig. 4.5.8. It can be observed that the dislocation density in the β phase increases with increasing equivalent strain. No saturation was reached even in heavily deformed conditions.

Summary

SPD processing significantly increases the dislocation density. Apart from TEM and XRD, PAS provides a valuable tool for the determination of dislocation density and concentration of vacancies and vacancy clusters in heavily deformed UFG materials.

In the $\alpha + \beta$ alloy after HPT, vacancy clusters were found along with dislocations while in the β phase only high dislocation density was resolved.

4.5.4 Mechanical properties of UFG biomedical Ti alloys

Despite the fact that this chapter focuses on the microstructure of UFG biomedical materials, the microstructure determines the mechanical properties. Due to the limited size of the samples, especially after HPT, microhardness measurements are often used for the estimation of material strength. Microhardness of the Ti-6Al-7Nb alloy reported in [36] increases from 330 to 400 HV due to HPT deformation. The most pronounced increase is observed in the early stages of deformation while microhardness saturates at very high strains $\epsilon_{\text{von Mises}} > 50$. Fig. 4.5.9 shows the microhardness variation on the disk sample surface in the Ti-15Mo alloy processed by the different number of HPT revolutions using color-coded graphs.

The microhardness of the Ti-15Mo alloy in the β solution treated condition may be increased from 310 to more than 450 HV by HPT. This value exceeds the microhardness of commercially aged $\alpha + \beta$ material. Enhanced microhardness corresponds to the increased dislocation density and microstructure refinement [37].

Microhardness values of 220 and 300 HV in the Ti-29Nb-13Ta-4.6Zr alloy prepared by cold rolling and cold rolling + HPT, respectively, were reported in [25]. Microhardness heterogeneity over HPT samples correlates with heterogeneous grain refinement. Tensile tests carried out using small samples cut from HPT disks of the same alloy showed that the yield stress increased from 550 MPa (cold-rolled material) to 800 MPa (material after cold rolling and $N=5$ HPT revolutions).

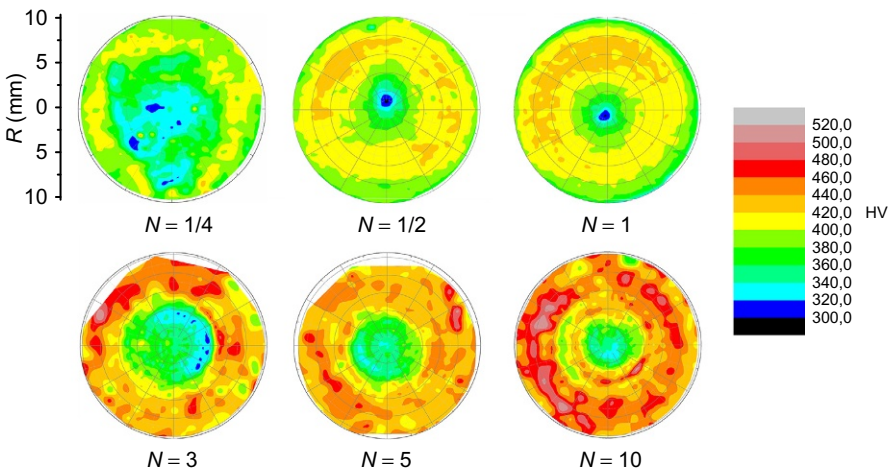


Fig. 4.5.9 Microhardness of the Ti-15Mo alloy processed by HPT.

On the other hand, the elongation to fracture for UFG material was only 7% [26]. Similar results were achieved in the Ti45Nb alloy, in that the strength increased from 400 to 1000 MPa due to HPT but elongation decreased to approximately 10% [38]. In other reports, the effect of grain refinement on strength is obscured by phase transformations. In the Ti-35Nb-3Zr-2Ta alloy processed by ECAP at 500°C, the ultimate tensile strength is enhanced from 500 to 765 MPa but the yield stress remains as low as 400 MPa due to the SIM α'' that forms during the tensile test at room temperature [30]. On the other hand, in the Ti-35Nb-3Zr-2Ta alloy processed by ECAP at room temperature, the α'' martensite is already present after ECAP pressing. After six passes of ECAP, an increase of the yield stress of previously hot-extruded material from 360 to 670 MPa and of ultimate tensile strength from 500 to 750 MPa were reported. However, the effects of grain refinement and strengthening by α'' martensite cannot be separated [29].

4.5.4.1 The effect of UFG microstructure on elastic modulus

The elastic modulus is a key issue in designing new biomedical alloys. However the direct effect of the UFG microstructure on the elastic modulus remains unresolved due to concurrently occurring phase transformations that prevent the determination of the direct effect of grain size. Furthermore, any alterations in crystallographic texture affect the elastic modulus of polycrystalline β matrix due to the elastic anisotropy of β single-crystals [39]. In general, any open volume defects such as dislocations, vacancies, grain boundaries, and nonequilibrium grain boundaries [40] should reduce the macroscopic modulus of elasticity [41], but this effect might be very low [42].

In a comparatively more β -stabilized Ti-29Nb-13Ta-4.6Zr alloy, the elastic modulus determined from tensile stress-strain curves increased from 60 to 64 GPa after the initial stages of HPT straining and upon further deformation the value of elastic modulus returned back to 60 GPa [26]. Nevertheless, these differences might be within the experimental error or might be caused by local texture changes. A Ti-35Nb-3Zr-2Ta alloy produced by ECAP at 500°C exhibits a comparable elastic modulus of 59 GPa [30].

In less β -stabilized alloys, the martensitic α'' phase or even the ω phase may form during SPD processing. Both these phases have a higher elastic modulus than β phase [39]—and their effect on the elastic modulus reduction is therefore adverse.

The Young's modulus of the Ti-15Mo alloy deformed by HPT was evaluated by the resonant ultrasound spectroscopy (RUS) [43,44]. RUS measurement allows the determination of the Young's modulus with high precision (± 1 GPa). The initial stages of HPT deformation led to an increase of the elastic modulus while further straining resulted in elastic modulus reversion. The initial increase of the elastic modulus was attributed to the deformation induced ω phase [45], which subsequently reverts to the β matrix [46] (Table 4.5.1).

Table 4.5.1 Young's modulus of the Ti-15Mo alloy after a different number of HPT turns

	Young's modulus E (GPa)	
	Center	Periphery
Ti-15Mo ST	91.0	
Ti-15Mo $N=1$	98.1	92.8
Ti-15Mo $N=5$	96.6	91.4

Summary

Microstructural refinement and increased dislocation density significantly increase the microhardness and strength but simultaneously decreased the elongation to fracture. High strength significantly improves the applicability of low-modulus biomedical β Ti alloys. Microstructure refinement itself does not influence the elastic modulus. On the other hand, the elastic modulus might be significantly increased by phase transformation occurring during SPD processing.

4.5.5 Microstructural stability and phase transformations in UFG biomedical Ti alloys

4.5.5.1 Microstructure stability in commercially pure Ti and biomedical Ti alloys

The application of the biomedical materials in a human body is obviously at the temperature of 37°C. None of the UFG Ti materials would recover or recrystallize at this temperature. However, for processing of specific products for biomedical use (e.g., hip implants), hot-forming procedures are often used. Possible recovery and recrystallization may significantly deteriorate mechanical properties. Therefore, the investigation of microstructure stability is of primary importance.

Thermal stability of UFG commercially pure Ti Grade 4 prepared by ECAP during linear heating (5°C/min) was evaluated by postmortem SEM observations. The microstructure after heating to 440°C and 640°C is shown in Fig. 4.5.10A and B, respectively. The specimens were water quenched after reaching the temperature during linear heating with the rate of 5°C/min. Heating to 440°C does not cause any visible changes when compared to material after ECAP (not shown here). On the other hand, heating to 660°C led to extensive grain growth, which resulted in a significant microhardness decrease [47]. These results are consistent with other studies [19,48].

The thermal stability of UFG biomedical Ti-6Al-7Nb was studied in a similar manner. Fig. 4.5.11A and B show SEM observations of microstructure after linear heating to 440°C and 660°C, respectively. Heating to 440°C again does not show signs of recovery or recrystallization while heating to 660°C led to the recrystallization of α grains and the globularization of β phase particles. The adverse effect of heating

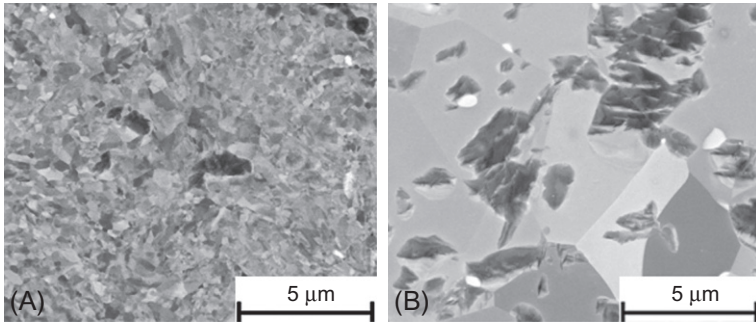


Fig. 4.5.10 (A) CP Ti—heated to 440°C. (B) CP Ti—heated to 640°C.

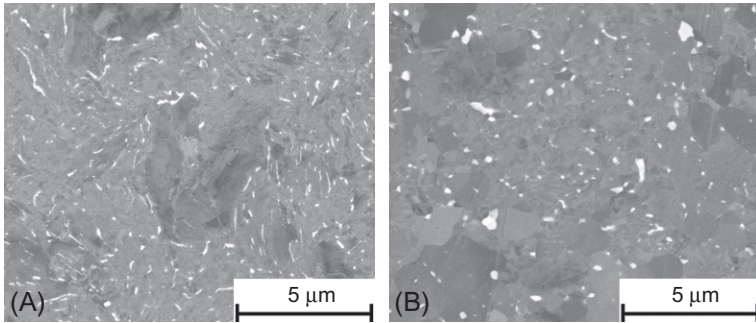


Fig. 4.5.11 (A) CP Ti—heated to 440°C. (B) Ti-6Al-7Nb—heated to 660°C.

to 660°C on microhardness was negligible [47]. The microstructural stability of UFG Ti-6Al-7Nb extends to higher temperatures (or longer annealing times) when compared to UFG CP Ti.

As mentioned in [30], the grain size of Ti-Nb-Zr-Ta-based alloys depends on the temperature of ECAP processing. This suggests that thermally activated recovery and recrystallization processes may already occur during SPD at elevated temperatures. The thermal stability of the UFG Ti-25Nb-3Zr-3Mo-2Sn biomedical alloy prepared by ARB extends to 500°C for short annealing times and only to 400°C for longer annealing as reported in [49], which is one of very few comprehensive studies discussing this issue.

4.5.5.2 Phase transformations in UFG β alloys

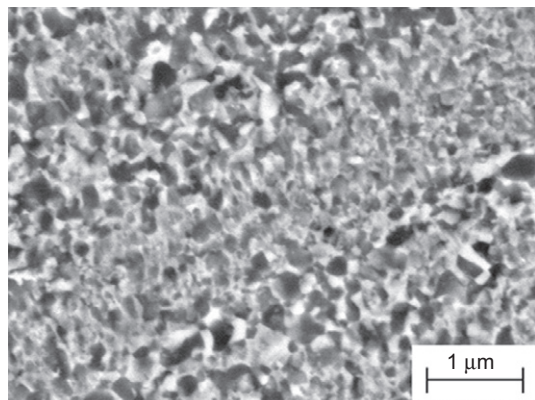
Phase transformations in metastable β alloys represent a broad topic even if we focus on biomedical alloys only. The aim of this short section is to stress a few peculiarities of phase transformations in UFG biomedical Ti alloys. The high volume fraction of α'' martensite after ECAP pressing at room temperature is reported in [29], while no α'' martensite is observed after ECAP at 500°C, 600°C, or 700°C in an almost identical

alloy [30]. Increased pressing temperature prevents the formation of α'' martensite, which is consistent with the nonequilibrium phase diagram of TiNb-based metastable β alloys. The α'' martensite may form in the early stages of ECAP deformation and subsequently transform back to beta during continued deformation, as suggested in [29]. The relation between the UFG structure after ECAP and the formation of α'' SIM phase during a tensile test at room temperature is discussed in [30]. The amount of SIM and its effect on pseudoelastic behavior depend significantly on the temperature of previous ECAP processing, therefore on a particular microstructural UFG condition.

In less β -stabilized alloys, even deformation-induced ω phase may form as suggested in Section 4.5.4.1. Bulk nanocrystalline omega phase is formed by HPT in Ti-16.1Nb alloy with ω grain size of ~ 100 nm. Despite UFG structure and very high hardness, the material is not in a favorable microstructural condition for biomedical applications due to the high elastic modulus of 110 GPa, which is not significantly reduced even by subsequent annealing [50]. On the other hand, HPT deformation of Ti-45Nb does not lead to any phase transformation and elastic modulus remains low (60 GPa) while HPT processing increases the microhardness by 60% when compared to the initial extruded material [51]. It is well known that α grains in metastable β alloys preferentially precipitate heterogeneously at grain boundaries (grain boundary α) [52,53,54]. In coarse-grained materials, these GB α particles are large and do not positively contribute to mechanical properties.

On the other hand, in UFG materials, grain boundaries form dense network. As a result, heterogeneously precipitated α particles at grain boundaries are small, equiaxed, and homogeneously distributed. Such microstructure is reported in [55] where GB α particles have sizes in the range of hundreds of nanometers in a Ti-20Mo alloy after HPT ($N=10$ passes) and subsequent annealing at 550°C/1 h. A similar submicrocrystalline microstructure was observed by the authors of this chapter after annealing of Ti-15Mo alloy deformed by HPT at 500°C/4 h as displayed in Fig. 4.5.12.

Fig. 4.5.12 Ti-15Mo alloy deformed by HPT and annealed at 500°C for 4h.



Summary

UFG structure is not thermodynamically stable and undergoes recovery and recrystallization at elevated temperatures. Thermal stability must be considered during manufacturing of products from the UFG material. UFG structure in biomedical Ti alloys is stable usually up to 450°C. It may be exposed to even higher temperatures for a limited time. SIM α'' phase and ω phase may form during SPD processing. UFG structure can be used for the precipitation of small, equiaxed, and homogeneously distributed grain boundary α particles.

4.5.6 Applicability of UFG Ti and Ti alloys as orthopedic implants

4.5.6.1 Size matters

Products prepared by SPD usually suffer from limited sizes. The typical diameter of the channel in the ECAP die is 10 mm; plates resulting from ARB have a thickness of few millimeters and HPT samples are coin-sized. This is clearly insufficient for highly demanded implants of big joints (hip and knee). On the other hand, many other small-sized devices (such as plates, fixations, screws, or dental implants) might be successfully manufactured from UFG materials.

4.5.6.2 Structural stability matters

Hot-forming procedures are cost efficient for product manufacturing. The thermal stability of the material must be carefully assessed and, in some cases, the standard commercial processes should be changed when utilizing UFG materials. On the other hand, the need for thermally stable material opens new challenges in alloy design. Special alloy designs with solute atoms or particles pinning grain boundaries are yet to come. SPD materials themselves are much more expensive than common materials and this disadvantage must be more than outweighed by improved functional properties to achieve commercial breakthrough.

4.5.6.3 Hip implant made from UFG Ti-6Al-4V prepared by large-scale ECAP

In order to overcome the size effect, the research team at the University in Ufa, Russia, up-scaled the ECAP device to produce rods of CP Ti and Ti-6Al-4V with a diameter of 55 mm. In Fig. 4.5.13, the semiproduct for hip implant manufacturing is shown. This semiproduct is made from UFG Ti-6Al-4V alloy prepared by ECAP and subsequent rolling and bending. The dimensions are sufficient for implant manufacturing by common wire cutting and machining. Recent results showed that the fatigue performance of the implant made of UFG Ti-6Al-4V under standardized testing conditions significantly exceeds that of the commercial Ti-6Al-4V material. This opens a new

Fig. 4.5.13 Ti-6Al-4V prepared by ECAP. Semi-product for hip implant manufacturing.



application potential of this material. Firstly, a new design of hip implants will be possible due to outstanding fatigue performance. Secondly, CP Ti would be capable of substituting the Ti-6Al-4V alloy because its mechanical properties can be significantly improved by grain refinement. And thirdly, and most importantly, the highly biocompatible biomedical low-modulus alloys may gain sufficient strength and fatigue performance to surpass both Ti-6Al-4V and CP Ti.

Acknowledgments

Czech Science Foundation (project 14-36566G) and Grant Agency of Charles University (project 1106216) are gratefully acknowledged for financial support.

References

- [1] A.A. Popov, I.Y. Pyshmintsey, S.L. Demakov, A.G. Illarionov, T.C. Lowe, A.V. Sergeyev, R.Z. Valiev, Structural and mechanical properties of nanocrystalline titanium processed by severe plastic deformation, *Scr. Mater.* 37 (1997) 1089–1094.
- [2] S.G. Steinemann, Titanium—the material of choice? *Periodontol* 17 (1998) 7–21.
- [3] S. Rao, Y. Okazaki, T. Tateishi, T. Ushida, Y. Ito, Cytocompatibility of new Ti alloy without Al and V by evaluating the relative growth ratios of fibroblasts L929 and osteoblasts MC3T3-E1 cells, *Mater. Sci. Eng. C* 4 (1997) 311–314.
- [4] K. Katti, Biomaterials in total joint replacement, *Colloids Surf. B Biointerfaces* 39 (2004) 133–142.
- [5] M. Niinomi, Mechanical biocompatibilities of titanium alloys for biomedical applications, *J. Mech. Behav. Biomed. Mater.* 1 (2008) 30–42.
- [6] W. Xu, X. Wu, R.B. Figueiredo, M. Stoica, M. Calin, J. Eckert, T.G. Langdon, K. Xia, Nanocrystalline body-centred cubic beta-titanium alloy processed by high-pressure torsion, *Int. J. Mater. Res.* 100 (2009) 1662–1667.
- [7] R.Z. Valiev, R.K. Islamgaliev, Bulk nanostructured materials from severe plastic deformation, *Prog. Mater. Sci.* 45 (2000) 103–189.
- [8] D. Kent, G. Wang, Z. Yu, X. Ma, M. Dargusch, Strength enhancement of a biomedical titanium alloy through modified accumulative roll bonding technique, *J. Mech. Behav. Biomed. Mater.* 4 (2011) 405–416.

- [9] B. Jiang, Effect of Severe Plastic Deformation on Microstructure in Metastable β -Ti Alloys (Doctoral Thesis), University of Tsukuba, 2015.
- [10] R.Z. Valiev, Y. Estrin, Z. Horita, T.G. Langdon, M.J. Zehetbauer, Y.T. Zhu, Producing bulk ultrafine-grained materials by severe plastic deformation, *JOM* 58 (4) (2006) 33–39.
- [11] T.G. Langdon, Twenty-five years of ultrafine-grained materials: achieving exceptional properties through grain refinement, *Acta Mater.* 61 (2013) 7035–7059.
- [12] Y. Estrin, L.S. Tóth, A. Molinari, Y. Bréchet, A dislocation-based model for all hardening stages in large strain deformation, *Acta Mater.* 46 (1998) 5509–5522.
- [13] A.E. Romanov, A.L. Kolesnikova, Application of disclination concept to solid structures, *Prog. Mater. Sci.* 54 (2009) 740–769.
- [14] K. Václavová, J. Stráský, V. Polyakova, J. Stráská, J. Nejezchlebová, H. Seiner, I. Semenova, M. Janeček, Microhardness and microstructure evolution of ultra-fine grained Ti-15Mo and TIMETAL LCB alloys prepared by high pressure torsion, *Mater. Sci. Eng. A* 682 (2017) 220–228.
- [15] Y. Estrin, A. Vinogradov, Extreme grain refinement by severe plastic deformation: a wealth of challenging science, *Acta Mater.* 61 (2013) 782–817.
- [16] E.O. Hall, The deformation and ageing of mild steel, *Proc. R. Soc. B* 64 (1951) 747.
- [17] N.J. Petch, The cleavage strength of polycrystals, *J. Iron Steel Inst.* 174 (1953) 25.
- [18] J. Čížek, M. Janeček, T. Krajňák, J. Stráská, P. Hruška, J. Gubicza, H.S. Kim, Structural characterization of ultrafine-grained interstitial-free steel prepared by severe plastic deformation, *Acta Mater.* 105 (2016) 258–272.
- [19] V. Polyakova, I.P. Semenova, R.Z. Valiev, Influence of annealing on the structure and mechanical properties of ultrafine-grained alloy Ti-6Al-7Nb, processed by severe plastic deformation, *Mater. Sci. Forum* 667–669 (2011) 943–948.
- [20] E.F. Rauch, M. Véron, Automated crystal orientation and phase mapping in TEM, *Mater. Charact.* 98 (2014) 1–9.
- [21] F. Sun, J.Y. Zhang, M. Marteleur, C. Brozek, E.F. Rauch, M. Veron, P. Vermaut, P.J. Jacques, F. Prima, A new titanium alloy with a combination of high strength, high strain hardening and improved ductility, *Scr. Mater.* 94 (2015) 17–20.
- [22] J.I. Qazi, H.J. Rack, B. Marquardt, High-strength metastable beta-titanium alloys for biomedical applications, *J. Mater. Sci.* 56 (2004) 49–51.
- [23] D. Kuroda, M. Niinomi, M. Morinaga, Y. Kato, T. Yashiro, Design and mechanical properties of new β type titanium alloys for implant materials, *Mater. Sci. Eng. A* 243 (1998) 244–249.
- [24] M. Niinomi, M. Nakai, J. Hieda, Development of new metallic alloys for biomedical applications, *Acta Biomater.* 8 (2012) 3888–3903.
- [25] H. Yilmazer, M. Niinomi, M. Nakai, J. Hieda, Y. Todaka, T. Akahori, T. Miyazaki, Heterogeneous structure and mechanical hardness of biomedical β -type Ti-29Nb-13Ta-4.6Zr subjected to high-pressure torsion, *J. Mech. Behav. Biomed. Mater.* 10 (2012) 235–245.
- [26] H. Yilmazer, M. Niinomi, M. Nakai, K. Cho, J. Hieda, Y. Todaka, T. Miyazaki, Mechanical properties of a medical β -type titanium alloy with specific microstructural evolution through high-pressure torsion, *Mater. Sci. Eng. C* 33 (2013) 2499–2507.
- [27] A. Zafari, X.S. Wei, W. Xu, K. Xia, Formation of nanocrystalline β structure in metastable beta Ti alloy during high pressure torsion: the role played by stress induced martensitic transformation, *Acta Mater.* 97 (2015) 146–155.
- [28] W. Xu, X. Wu, M. Calin, M. Stoica, J. Eckert, K. Xia, Formation of an ultrafine-grained structure during equal-channel angular pressing of a β -titanium alloy with low phase stability, *Scr. Mater.* 60 (2009) 1012–1015.

- [29] Z. Li, B. Zheng, Y. Wang, T. Topping, Y. Zhou, R.Z. Valiev, A. Shan, E.J. Lavernia, Ultrafine-grained Ti-Nb-Ta-Zr alloy produced by ECAP at room temperature, *J. Mater. Sci.* 49 (2014) 6656–6666.
- [30] Z. Lin, L. Wang, X. Xue, W. Lu, J. Qin, D. Zhang, Microstructure evolution and mechanical properties of a Ti-35Nb-3Zr-2Ta biomedical alloy processed by equal channel angular pressing (ECAP), *Mater. Sci. Eng. C* 33 (2013) 4551–4561.
- [31] K.S. Suresh, N.P. Gurao, D.S. Singh, S. Suwas, K. Chattopadhyay, S.V. Zherebtsov, G.A. Salishchev, Effect of equal channel angular pressing on grain refinement and texture evolution in a biomedical alloy Ti-13Nb-13Zr, *Mater. Charact.* 82 (2013) 73–85.
- [32] J. Vrátná, M. Janeček, J. Čížek, D.J. Lee, E.Y. Yoon, H.S. Kim, Mechanical properties and microstructure evolution in ultrafine-grained AZ31 alloy processed by severe plastic deformation, *J. Mater. Sci.* 48 (2013) 4705–4712.
- [33] F. Bečvář, J. Čížek, L. Lesták, I. Novotný, I. Procházka, F. Šebesta, A high-resolution BaF₂ positron-lifetime spectrometer and experience with its long-term exploitation, *Nucl. Instrum. Methods Phys. Res. Sect. A* 443 (2000) 557–577.
- [34] J.M.C. Robles, E. Ogando, F. Plazaola, Positron lifetime calculation for the elements of the periodic table, *J. Phys. Condens. Matter* 19 (2007) 176–222.
- [35] R.N. West, Positron studies of lattice defects in metals, in: P. Hautojärvi (Ed.), *Positrons in Solids*, Springer-Verlag, Berlin, 1979, pp. 89–144.
- [36] M. Janeček, J. Stráský, J. Čížek, P. Hrcuba, K. Václavová, V.V. Polyakova, I.P. Semenova, Mechanical properties and dislocation structure evolution in Ti-6Al-7Nb alloy processed by high pressure torsion, *Metall. Mater. Trans. A* 45A (2014) 7–15.
- [37] M. Janeček, J. Čížek, J. Stráský, K. Václavová, P. Hruška, V. Polyakova, S. Gatina, I. Semenova, Microstructure evolution in solution treated Ti-15Mo alloy processed by high pressure torsion, *Mater. Charact.* 98 (2014) 233–240.
- [38] B. Völker, N. Jäger, M. Calin, M. Zehetbauer, J. Eckert, A. Hohenwarter, Influence of testing orientation on mechanical properties of Ti-45Nb deformed by high pressure torsion, *Mater. Des.* 114 (2017) 40–46.
- [39] J. Nejezchlebová, M. Janovská, H. Seiner, P. Sedlák, M. Landa, J. Šmilauerová, J. Stráský, P. Hrcuba, M. Janeček, The effect of athermal and isothermal ω phase particles on elasticity of β -Ti single crystals, *Acta Mater.* 110 (2016) 185–191.
- [40] X. Sauvage, G. Wilde, S.V. Divinski, Z. Horita, R.Z. Valiev, Grain boundaries in ultrafine grained materials processed by severe plastic deformation and related phenomena, *Mater. Sci. Eng. A* 540 (2012) 1–12.
- [41] A.B. Lebedev, Y.A. Burenkov, A.E. Romanov, V.I. Kopylov, V.P. Filonenko, V.G. Gyaznov, Softening of the in submicrocrystalline copper, *Mater. Sci. Eng. A* 203 (1995) 165–170.
- [42] T.D. Shen, C.C. Koch, T.Y. Tsui, G.M. Pharr, On the elastic moduli of nanocrystalline Fe, Cu, Ni, and Cu-Ni alloys prepared by mechanical milling/alloying, *J. Mater. Res.* 10 (1995) 2892–2896.
- [43] A. Migliori, J.L. Sarrao, W.M. Visscher, T.M. Bell, M. Lei, Z. Fisk, R.G. Leisure, Resonant ultrasound spectroscopic techniques for measurement of the elastic moduli of solids, *Phys. B Condens. Matter* 183 (1993) 1–24.
- [44] P. Sedlák, H. Seiner, J. Zídek, M. Janovská, M. Landa, Determination of all 31 independent elastic coefficients of generally anisotropic solids by resonant ultrasound spectroscopy: benchmark examples, *Exp. Mech.* 54 (2014) 1073–1085.
- [45] B. Koch, B. Skrotzki, Strain controlled fatigue testing of the metastable β -titanium alloy Ti-6.8Mo-4.5Fe-1.5Al (Timetal LCB), *Mater. Sci. Eng. A* 528 (2011) 5999–6005.

- [46] S. Gatina, I. Semenova, J. Leuthodl, R. Valiev, Nanostructuring and phase transformations in the β -alloy Ti-15Mo during high-pressure torsion, *Adv. Eng. Mater.* 17 (2015) 1742–1747.
- [47] P. Zhaňal, K. Václavová, B. Hadzima, P. Harcuba, J. Stráský, M. Janeček, V. Polyakova, I. Semenova, M. Hájek, K. Hajizadeh, Thermal stability of ultrafine-grained commercial purity Ti and Ti-6Al-7Nb alloy investigated by electrical resistance, microhardness and scanning electron microscopy, *Mater. Sci. Eng. A* 651 (2016) 886–892.
- [48] M. Hoseini, M.H. Pourian, F. Bridier, H. Vali, J.A. Szpunar, P. Bocher, Thermal stability and annealing behaviour of ultrafine grained commercially pure titanium, *Mater. Sci. Eng. A* 532 (2012) 58–63.
- [49] D. Kent, W.L. Xiao, G. Wang, Z. Yu, M.S. Dargusch, Thermal stability of an ultrafine grain β -Ti alloy, *Mater. Sci. Eng. A* 556 (2012) 582–587.
- [50] A. Panigrahi, M. Bönisch, T. Waitz, E. Schafner, M. Calin, J. Eckert, W. Skrotzki, M. Zehetbauer, Phase transformations and mechanical properties of biocompatible Ti-16.1Nb processed by severe plastic deformation, *J. Alloys Compd.* 628 (2015) 434–441.
- [51] A. Panigrahi, B. Sulkowski, T. Waitz, K. Ozaltin, W. Chrominski, A. Pukenas, J. Horky, M. Lewandowska, W. Skrotzki, M. Zehetbauer, Mechanical properties, structural and texture evolution of biocompatible Ti-45Nb alloy processed by severe plastic deformation, *J. Mech. Behav. Biomed. Mater.* 62 (2016) 93–105.
- [52] E. Sarath Kumar Menon, H.I. Aaronson, Nucleation, growth, and overall transformation kinetics of grain boundary allotriomorphs of proeutectoid α in Ti-3.2 At. Pct Co and Ti-6.6 At. Pct Cr alloys, *Metall. Mater. Trans. A* 17A (1986) 1703–1715.
- [53] D. Bhattacharyya, G.B. Viswanathan, H.L. Fraser, Crystallographic and morphological relationships between β phase and the Widmanstätten and allotriomorphic α phase at special β grain boundaries in an α/β titanium alloy, *Acta Mater.* 55 (2007) 6765–6778.
- [54] M. Salib, J. Teixeira, L. Germain, E. Lamielle, N. Gey, E. Aeby-Gautier, Influence of transformation temperature on microtexture formation associated with α precipitation at β grain boundaries in a β metastable titanium alloy, *Acta Mater.* 61 (2013) 3758–3768.
- [55] W. Xu, D.P. Edwards, X. Wu, M. Stoica, M. Calin, U. Kühn, J. Eckert, K. Xia, Promoting nano/ultrafine-duplex structure via accelerated α precipitation in a β -type titanium alloy severely deformed by high-pressure torsion, *Scr. Mater.* 68 (2013) 67–70.

Mechanical Properties and Dislocation Structure Evolution in Ti6Al7Nb Alloy Processed by High Pressure Torsion

MILOŠ JANEČEK, JOSEF STRÁSKÝ, JAKUB ČÍŽEK, PETR HARCUBA, KRISTÍNA VÁCLAVOVÁ, VERONIKA V. POLYAKOVA, and IRINA P. SEMENOVA

Ultrafine-grained biocompatible Ti-6Al-7Nb alloy was produced by high pressure torsion (HPT). Lattice defects—vacancies and dislocations—investigated by positron annihilation spectroscopy, observations by scanning electron microscopy, and microhardness evaluation are linked to the strain imposed by different numbers of HPT revolutions and to the distance from the specimen center. Positron annihilation spectroscopy showed significant increase of dislocation density and concentration of vacancy clusters after $\frac{1}{2}$ of the HPT revolution. Microhardness increases by 20 pct with increasing strain, but it is heterogenous due to duplex microstructure. The heterogeneity of the microhardness increases with increasing strain, suggesting that a heavily deformed and fragmented $\alpha + \beta$ lamellar microstructure is more hardened than primary alpha grains. The defect structure is homogenous after $\frac{1}{2}$ HPT revolution, while the microhardness becomes homogenous after 3 HPT revolutions only.

DOI: 10.1007/s11661-013-1763-2

© The Minerals, Metals & Materials Society and ASM International 2013

I. INTRODUCTION

FOR several decades, titanium alloys have been the most used material for load-bearing orthopedic implants.^[1] Their unique combination of properties includes extreme corrosion resistance, relatively high strength, sufficient biocompatibility, and moderate elastic modulus.^[2] Commercially pure titanium is used in some dental and orthopedic applications mainly due to its excellent biocompatibility. However, limited strength (up to 500 MPa) disallows using commercially pure titanium as a material for orthopedic endoprostheses, which constitute a majority of the market of metallic implants. The most commonly used one is still one of the oldest Ti alloys—Ti-6Al-4V—that belongs to the alpha + beta alloys. Despite the generally good properties of this alloy, there are several limitations. A special concern relates to the presence of vanadium which is considered to be a toxic element. A similar alpha + beta Ti alloy Ti-6Al-7Nb has been developed to avoid the adverse effect of vanadium.^[3,4] Ti-6Al-7Nb alloy has similar mechanical properties and undergoes a similar phase transformation as the common Ti-6Al-4V alloy.

The mechanical and other essential properties determining the application of titanium alloys may be improved by refining the grain size to the submicrometer

or even nanometer level. A variety of special techniques are used for the production of bulk ultrafine-grained (UFG) materials, *e.g.*, equal channel angular pressing (ECAP),^[5] high pressure torsion (HPT),^[6,7] accumulative roll bonding (ARB),^[8] twist extrusion,^[9] or multi-directional forging.^[10] Among these techniques, which introduce severe plastic deformation (SPD) in the material, HPT provides an opportunity for achieving exceptional grain refinement often to the nanometer level in many FCC and HCP metals and alloys.^[11] Due to the fundamentally non-homogenous deformation by HPT, important properties evolve with the number of HPT revolutions and with the distance from the specimen center. HPT therefore allows getting fundamental knowledge of the evolution of the structure refinement and the nature of physical strengthening.

The aim of this study is therefore twofold:

- (a) to fabricate the ultrafine-grained structure in the Ti-6Al-7Nb alloy by HPT and
- (b) to characterize its microstructure features, the lattice defect evolution, and mechanical properties

In addition to high resolution scanning microscopy and microhardness measurements, positron annihilation spectroscopy (PAS) was used to evaluate the spatial distribution of lattice defects. Our previous investigations proved the feasibility of PAS to determine the lattice defect structure in UFG materials.^[12–15]

II. MATERIAL AND EXPERIMENTAL METHODS

Hot-rolled rods of the Ti-6Al-7Nb ELI (IMI 367) alloy for medical application, 20 mm in diameter, manufactured by TIMET were used for the investigation.

MILOŠ JANEČEK, Professor, JOSEF STRÁSKÝ, Ph.D. Student, PETR HARCUBA, Research Fellow, and KRISTÍNA VÁCLAVOVÁ, Undergraduate Student, are with the Department of Physics of Materials, Charles University, Ke Karlovu 5, 12116 Prague 2, Czech Republic. Contact e-mail: janecek@met.mff.cuni.cz JAKUB ČÍŽEK, Professor, is with the Department of Low Temperature Physics, Charles University, Prague, Czech Republic. VERONIKA V. POLYAKOVA, Ph.D. Student, and IRINA P. SEMENOVA, Professor, are with the Ufa State Aviation Technical University, Ufa, Russia.

Manuscript submitted March 1, 2013.

Article published online April 30, 2013

The chemical composition of the alloy was the following: Ti—basic; Al—6.17 pct; Nb—7.05 pct; Fe—0.14 pct; O—0.17 pct; C—0.01 pct; N—0.03 pct; and Ti—balance. The beta-transus temperature according to the material certificate was 1278 K (1005 °C).

Samples in the initial condition were subjected to thermal treatment (TT), including incomplete quenching from 1258 K (985 °C) (20 K below the beta-transus temperature) to room temperature followed by annealing at 973 K (700 °C) for 4 h. The microstructure of the as-received and TT conditions was observed using a light microscope Olympus GX51.

For the HPT process, samples 20 mm in diameter and 2 mm thick were cut from the thermally processed rods by the electrospark method. The sample surface was polished before deformation. During the HPT, the sample was placed between the anvils with a groove of 0.8 mm and pressed under an imposed pressure of 6 GPa. The lower anvil was rotated, and the sample was deformed by shear under the surface friction. The use of the groove excludes sliding of the sample during torsion. Torsion was performed with the rotation speed of 0.5 rpm at room temperature, and a series of specimens after 1/4, 1/2, 1, 3, 5, and 15 rotations were processed.

The high resolution scanning electron microscope FEI Quanta 200 FEG operated at 20 kV was employed for detail investigation of UFG microstructure of the specimens after HPT (10 kV was used to enhance the image contrast in some cases). Back-scattered electron, Z-contrast, and channeling contrast were used for revealing the different microstructural features in the UFG specimens.

An automatic microhardness tester Qness Q10a was used for the evaluation of microhardness variations throughout the surface of specimens after HPT. More than 1000 indents were applied in a square grid with higher density near the specimen center. As a result, more than 100 indents within each ring of 1 mm width were applied.

Lattice defect density variations in individual specimens after HPT were determined by PAS. A Na_2CO_3 positron source with an activity of 1.2 MBq deposited on an approx. 2- μm -thick Mylar foil was used for positron annihilation studies. The source contribution representing a contribution of positrons annihilated in the $^{22}\text{Na}_2\text{CO}_3$ spot and the covering mylar foil consisted of two weak components with lifetimes of 0.368 and 1.5 ns and relative intensities of 8 pct and 1 pct, respectively. Positron lifetime (LT) measurements were carried out using a high resolution digital spectrometer.^[16] The detector part of the digital LT spectrometer consists of two Hamamatsu H3378 photomultipliers coupled with BaF_2 scintillators. Detector pulses are sampled by two ultrafast Acqiris DC211 8 bit digitizers at a sampling frequency of 4 GHz. The digitized pulses are acquired by a PC and analyzed off-line by software using a new algorithm for integral constant fraction timing.^[17] The time resolution of the digital LT spectrometer was 145 ps [full width at half maximum (FWHM) of the resolution function for ^{22}Na positron source]. At least 10^7 annihilation events were accumulated in each LT spectrum. Decomposition of LT spectra into exponential compo-

nents was performed by a maximum likelihood code described in Reference 18.

III. RESULTS

A. Light Microscopy

The coarse-grained Ti-6Al-7Nb alloy was received as hot-rolled rods having a duplex structure with grains of the primary α -phase (light area) of an average size of 5.3 μm and a volume fraction of 66 pct distributed in the $\alpha + \beta$ matrix (dark area), see Figure 1.

One of the authors, Polyakova, has shown recently^[19] that in order to create the homogeneous UFG structure by the ECAP method, it is effective to enhance the fraction of the thin-plate β -transformed structure, the fragmentation of which occurs easier in the process of SPD. It is also necessary to preserve the fraction of the primary α phase (usually about 20 pct)^[20] in the microstructure in order to provide sufficient ductility.^[21] In this paper, such a microstructure was obtained by the TT described in the previous section. The structure after TT is characterized by homogeneous distribution of the globular primary α grains in the $\alpha + \beta$ lamellar microstructure—see Figure 2. The volume fraction and the average size of the α phase were 18 pct and 5.3 μm , respectively. The packages of α -phase plates with the average cross size of 330 nm formed in the position of the former martensite occupy about 80 pct of the structure.

B. SEM Observations

The microstructure of the as-pressed specimen (*i.e.*, the specimen compressed between the anvils by a pressure of 6 GPa, but without any rotation) and the specimen prepared by HPT (5 revolutions) was observed by SEM using back-scattered electrons.

1. As-pressed ($N = 0$) material

Figure 3 shows the detailed micrograph of the as-pressed material. The contrast of the picture is given by a chemical composition—so-called Z-contrast. Darker

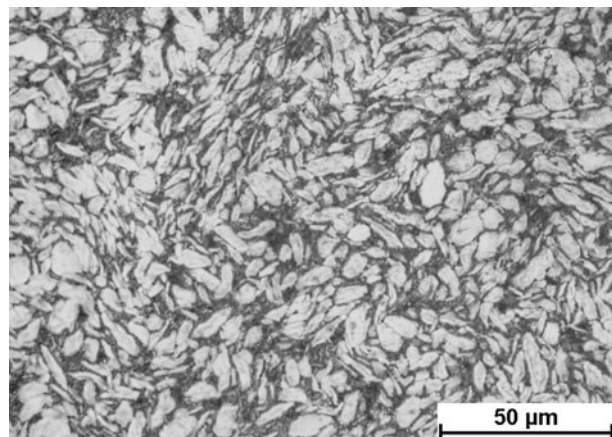


Fig. 1—Light microscopy image of as-rolled Ti-6Al-7Nb cross section.

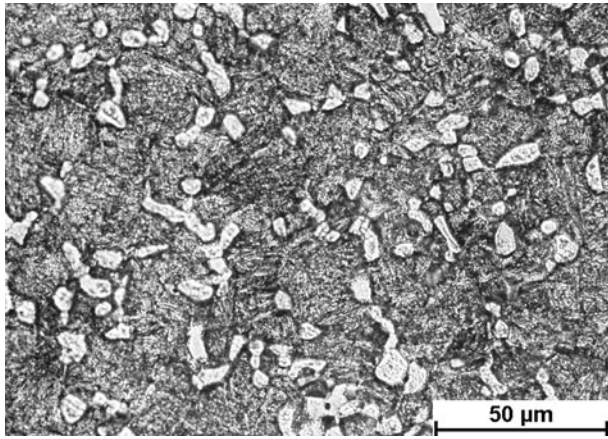


Fig. 2—Light microscopy image of Ti-6Al-7Nb after TT.

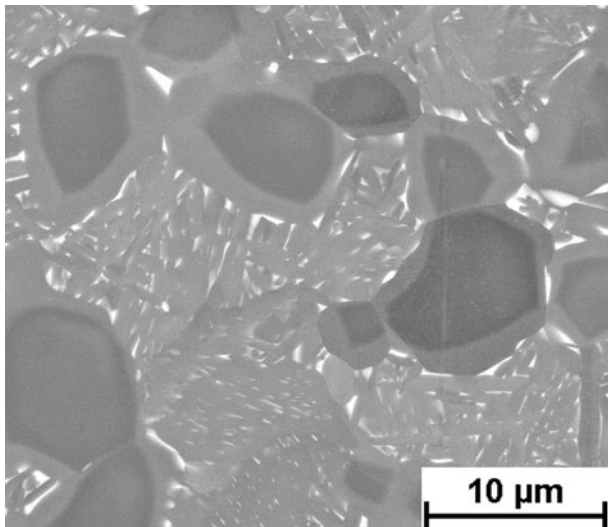


Fig. 3—As-pressed sample ($N = 0$), detail SEM image (back-scattered electrons, Z-contrast).

equiaxed grains are primary alpha grains.^[20] Within those grains, two chemically different regions can be distinguished. The interior parts of the grains contain more aluminum and less niobium (see Table I) and therefore appear darker. Diffusion of alpha-stabilizing aluminum and beta-stabilizing niobium must have occurred during thermal processing. The white parts are beta phase particles that are either between primary alpha grains or elongated between alpha lamellae. The resulting microstructure is known as bimodal or duplex. It must be also noted that alpha grains are known to be softer than lamellar areas.^[21,22]

Figure 4 is an overview SEM image. Two types of contrast are present: the above-discussed Z-contrast and also the channeling contrast (grains with different orientations may have different contrasts due to different absorption of back-scattered electrons). The white arrows point to the two adjacent alpha grains with different shades, which are caused by their different orientations only. More interestingly, channeling contrast allows the observation

Table I. Chemical Composition of Different Microstructural Features, Measured by EDX

Weight Percent	Average	Alpha—Edge	Alpha—Int.	Beta
Ti	83.0	83.2	85.1	75.7
Al	8.6	8.5	10.0	6.4
Nb	8.5	8.3	4.9	16.4
Fe	0.0	0.0	0.0	1.4

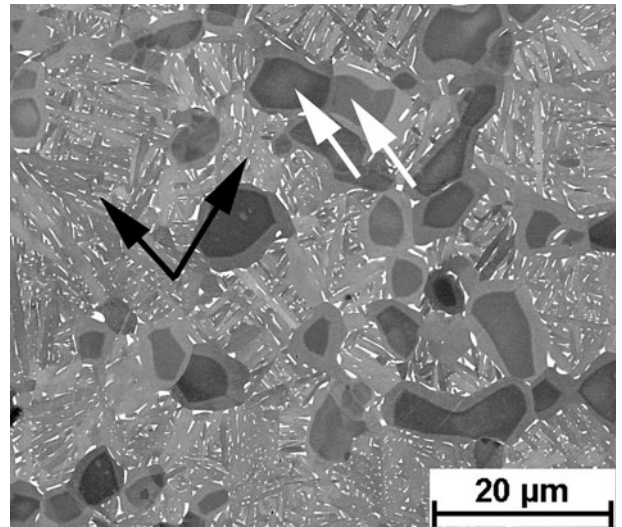


Fig. 4—As-pressed sample ($N = 0$), an overview SEM image. Arrows point to the areas with different channeling contrast.

of different families of parallel lamellae formed in the original beta grain during cooling from the beta region^[23] (illustrated by black arrows in two different grains).

The chemical composition was determined by energy dispersive x-ray scattering (EDX). The results are presented in Table I. Note that the results from the EDX may be used only for mutual comparison of different measurements by this method. However, they cannot be quantitatively compared to the results of other methods. Firstly, the average chemical composition was evaluated by x-ray signal acquisition over a sufficiently large area so that the composition is averaged over all microstructural features. The chemical composition slightly differs from the nominal composition of the Ti-6Al-7Nb alloy, proving the qualitative character of these results only. Secondly, the chemical composition was locally measured near the edge and in the interior of alpha grains and in beta particles. The presented results are average values from three different points, but those data should be taken as qualitative only, especially for the beta phase where the beta particle size is comparable to the interaction volume of the electron beam.

2. Material after HPT ($N = 5$)

Figure 5 shows the microstructure of the center of the specimen after 5 revolutions. Alpha grains are well distinguishable and their shape is mostly round—similar

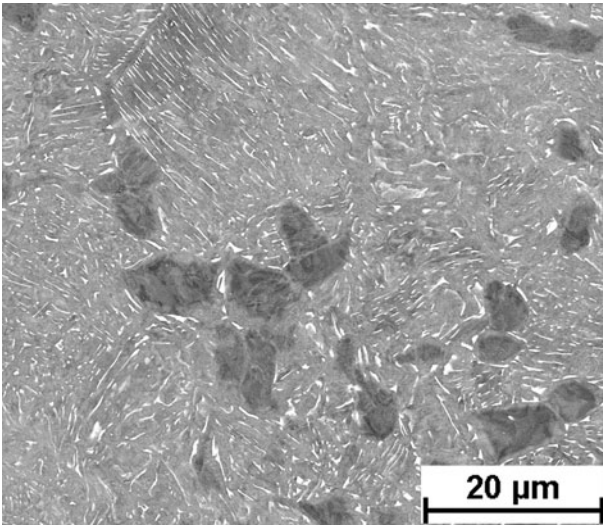


Fig. 5—HPT-deformed material ($N = 5$), center of the sample.

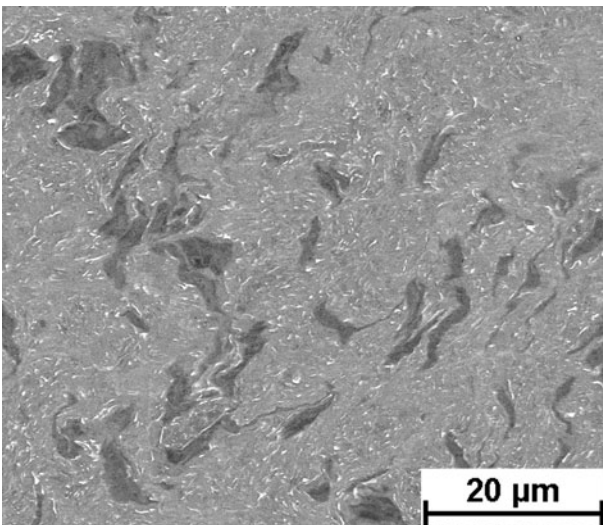


Fig. 6—HPT-deformed material ($N = 5$), 5 mm from the center of the sample.

to the original material. However, each grain is obviously strongly deformed (uneven shade within grain). Alpha + beta phase lamellar areas remain straight in some zones—similar to the as-pressed material—but in other areas, they are already heavily deformed.

Figure 6 shows the typical microstructure of the area that is 5 mm from the center (see scheme in Figure 7). A more deformed microstructure can be observed. Alpha grains are still visible, but their shape is altered due to strong deformation. Each alpha grain is also internally deformed and the whole lamellar part is also deformed.

The microstructure of the zone near the edge of the specimen after 5 revolutions is shown in Figure 8. An even more deformed structure with clear directionality along the direction of deformation (left to right) is seen. However, the original alpha grains are still recognizable.

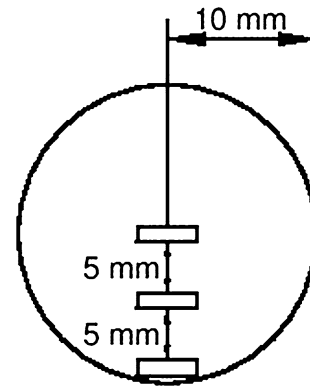


Fig. 7—Scheme of SEM observations.

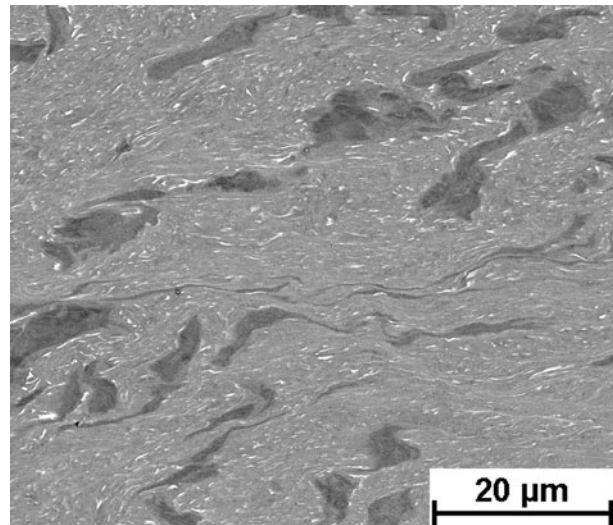


Fig. 8—HPT-deformed material ($N = 5$), edge of the sample.

C. Microhardness

Figure 9 shows the microhardness line profiles, *i.e.*, the microhardness variations with the distance from the specimen center toward its edge, in samples subjected to different numbers of HPT revolutions. Each point is an average calculated from more than 100 indents. Error bars show standard deviations. The low precision of measured data is given only by the heterogeneity of the material. Measurement precision is higher by more than one order of the magnitude. Locally heterogeneous microhardness might be associated with heterogeneous microstructure; more specifically, the hardness may differ for an indent (with diagonals of approx. $50 \mu\text{m}$) in the lamellar area and for another one placed in the alpha grains that are softer.

The results of the measurements indicate that there is a significant increase of microhardness with increasing number of revolutions until $N = 3$. On the other hand, no significant increase of microhardness with distance from the center of the specimen is observed. Some increase is seen only for $N = 1/4$ and $N = 1/2$. For $N = 3$ and higher strains, the microhardness is

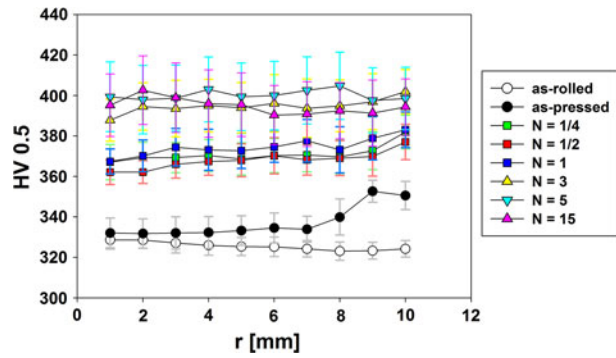


Fig. 9—Dependence of the microhardness on number of HPT turns and the distance from the center of the specimen.

homogenous over the whole specimen, which is a favorable result for any potential application, *e.g.*, in microforming technology such as MEMS,^[23] microgears,^[24] microcups,^[25] heat exchangers,^[26] *etc.* Finally, an increase in microhardness at the edge of the as-preserved ($N = 0$) specimen is due to material outflow from underneath the pressing anvils, which effectively causes plastic deformation accompanied with microhardness increase. A similar effect was also observed in other materials.^[27]

D. Evolution of Lattice Defects with Strain Due to HPT (Positron Annihilation Spectroscopy)

Figure 10 shows the dependence of the mean positron lifetime on the radial distance r from the center of the sample subjected to various numbers N of HPT revolutions. In the sample, which was only pressed without any HPT straining ($N = 0$), the mean lifetime at the periphery ($r \geq 6$) is remarkably higher than in the center of the sample, which might be caused by material flowing out of the area of pressing anvils.

HPT straining causes a significant increase of the mean lifetime due to defects introduced by SPD. In the sample subjected to $N = 1/4$ HPT revolution, the mean lifetime is increased in the center and becomes approximately constant across the whole sample. Further HPT straining ($N = 1/2$) leads to an additional increase of the mean lifetime, which finally saturates at the value of ≈ 190 ps. All samples subjected to more HPT revolutions ($N > 1/2$) exhibit very similar mean lifetimes. The spatial dependence of the mean lifetime across the sample disk is approximately uniform in all samples subjected to HPT straining ($N \geq 1/4$), which proves the formation of a relatively homogeneous structure of defects across the whole sample.

More information can be obtained from the decomposition of positron lifetime spectra into individual components. Figure 11 shows the dependence of the lifetimes of components resolved in positron lifetime spectra on the radial distance r from the center of the sample for materials subjected to various numbers N of HPT rotations. The spatial dependence of relative intensities of these components is plotted in Figure 12.

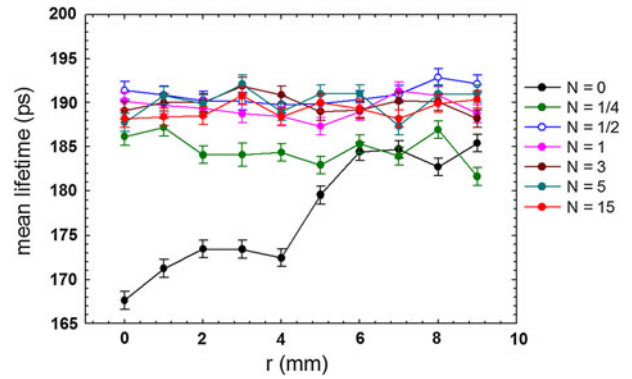


Fig. 10—The mean positron lifetime as a function of the radial distance r from the center of the samples subjected to various number N of HPT revolutions.

One can see in Figure 11 that there are three components in the positron lifetime spectra of the samples studied:

- A short lived component with lifetime $\tau_1 < 100$ ps and relative intensity I_1 represents a contribution of free positrons annihilated in the delocalized state, *i.e.*, not trapped at defects. This component was found in samples subjected to $N = 0$ and $1/4$ HPT revolution only. In samples subjected to more HPT revolutions ($N \geq 1/2$), the density of defects becomes so high that virtually all positrons are trapped at defects and the free positron component disappeared (saturated positron trapping).^[28]
- A component with lifetime $\tau_2 \approx 180$ ps and relative intensity I_2 . This component which dominates in the positron lifetime spectra of all samples studied can be attributed to positrons trapped at dislocations.
- A long-lived component with lifetime $\tau_3 \approx 300$ ps and relative intensity I_3 comes from positrons trapped at larger point defects with open volume corresponding to several vacancies. These defects were likely formed by the agglomeration of deformation-induced vacancies. In order to estimate the size of these vacancy clusters, we performed *ab initio* theoretic calculations of positron parameters for vacancy clusters of various sizes in Ti. Figure 13 shows the calculated dependence of positron lifetime on the size of vacancy clusters consisting of different numbers of vacancies. Obviously, positron lifetime strongly increases with increasing size of vacancy clusters and gradually saturates for large clusters. From the comparison of calculated dependence with experimental lifetimes in Figure 11, one can conclude that the average size of vacancy clusters in HPT-deformed samples corresponds to 4 vacancies.

The as-received material comprises only two components: free positrons with the lifetime $\tau_1 = 84 \pm 3$ ps and the relative intensity $I_1 = 17.6 \pm 0.7$ pct, and positrons trapped at dislocations with the lifetime $\tau_2 = 170 \pm 1$ ps and the relative intensity $I_2 = 82.4 \pm 0.7$ pct. No

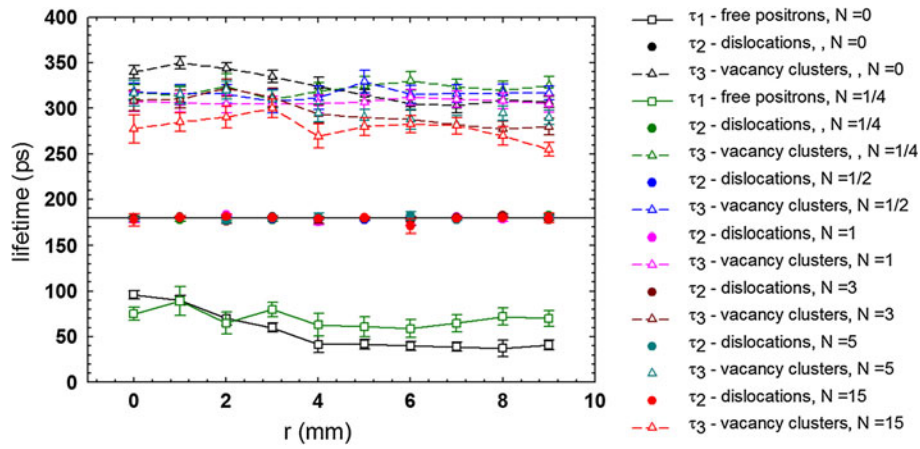


Fig. 11—Dependence of lifetimes of individual positron components on the radial distance r from the center of the sample for materials subjected to various numbers N of HPT rotations.

vacancy clusters were detected in the as-received material.

From the detailed inspection of Figure 12, it becomes clear that in the sample which was only pressed ($N = 0$), the intensity I_1 of the free positron component decreases with increasing distance from the center of the sample, while the intensity I_3 of positrons trapped at vacancy clusters increases. This proves that the concentration of vacancy clusters at the periphery of the sample ($N = 0$) is higher than in the center, most probably due to higher deformation at the periphery where deformed material can flow out of the area of pressing anvils. HPT straining introduces dislocations, which are reflected by an increase of the intensity I_2 . One can see in Figure 12 that I_2 increases for the sample subjected to $1/4$ HPT revolution, and a further increase of I_2 occurs also in the sample strained to $1/2$ HPT revolution. In the latter sample, the density of defects becomes so high that virtually all positrons are trapped and the free positron component cannot be resolved in the spectrum anymore. With increasing torsional strain ($N > 1/2$), I_2 saturates and remains approximately constant.

Moreover, one can see in Figure 12 that samples subjected to HPT straining ($N \geq 1/4$) exhibit approximately uniform spatial dependence of the intensities I_1 , I_2 , and I_3 across the whole sample disk. This proves that an almost homogeneous structure of defects across the whole sample has already been achieved after $1/4$ HPT revolution.

Since the samples subjected to HPT straining ($N \geq 1/4$) do not exhibit any systematic dependence of positron parameters across the sample except of statistical scattering, the average lifetimes and relative intensities were calculated by averaging of all data measured at each sample. These averaged lifetimes and corresponding relative intensities are plotted in Figure 14 as a function of the number of HPT revolutions. From inspection of the figure, it becomes clear that the density of dislocations strongly increases in the beginning of HPT straining ($N < 1$) and it is accompanied by a disappearance of the free positron component. During

further deformation ($N \geq 1$), the dislocation component remains approximately unchanged. The average size of vacancy clusters slightly decreases during HPT straining; see the upper panel in Figure 14.

In the samples $N = 0$ and $N = 1/4$ where the free positron component is present in the positron lifetime spectra, one can determine the dislocation density ρ_D by application of the three-state simple trapping model (3-STM)^[29]

$$\rho_D = \frac{1}{v_D} \frac{I_2}{I_1} \left[\frac{1}{\tau_B} - \frac{1}{\tau_2} + I_3 \left(\frac{1}{\tau_2} - \frac{1}{\tau_3} \right) \right], \quad [1]$$

where $\tau_B = 144$ ps is the bulk positron lifetime in Ti^[30] and v_D is the specific positron trapping rate for dislocations, which is known to fall into the range 10^{-5} to 10^{-4} $\text{m}^2 \text{s}^{-1}$ for most metals.^[31] For the estimation of the dislocation density, we used the average value $v_D \approx 0.5 \times 10^{-5}$ $\text{m}^2 \text{s}^{-1}$. The dislocation density in the as-received sample is $\rho_D = 1 \times 10^{14}$ m^{-2} . The dislocation density in samples $N = 0$ and $N = 1/4$ estimated using the average value $v_D \approx 0.5 \times 10^{-5}$ $\text{m}^2 \text{s}^{-1}$ is plotted in Figure 15 as a function of the radial distance from the center. The dislocation density in both samples slightly increases from the center of the sample toward the edge. The mean dislocation density in the sample subjected to $1/4$ HPT revolution is 4 times higher than in the as-received material.

The concentration of the vacancy clusters c_{vc} in samples $N = 0$ and $1/4$ can be estimated within 3-STM from the expression

$$c_{vc} = \frac{1}{n_v v_v} \frac{I_3}{I_1} \left[\frac{1}{\tau_B} - \frac{1}{\tau_3} + I_2 \left(\frac{1}{\tau_3} - \frac{1}{\tau_2} \right) \right], \quad [2]$$

where $n_v = 4$ is the average number of vacancies per cluster and $v_v \approx 10^{14}$ s^{-1} is the specific positron trapping rate for a vacancy.^[31] The concentration of vacancy clusters estimated from Eq. [2] for samples $N = 0$ and $1/4$ is plotted in Figure 16 as a function of the distance from the center. Obviously, the sample which was only pressed exhibits remarkably higher c_{vc} at the periphery

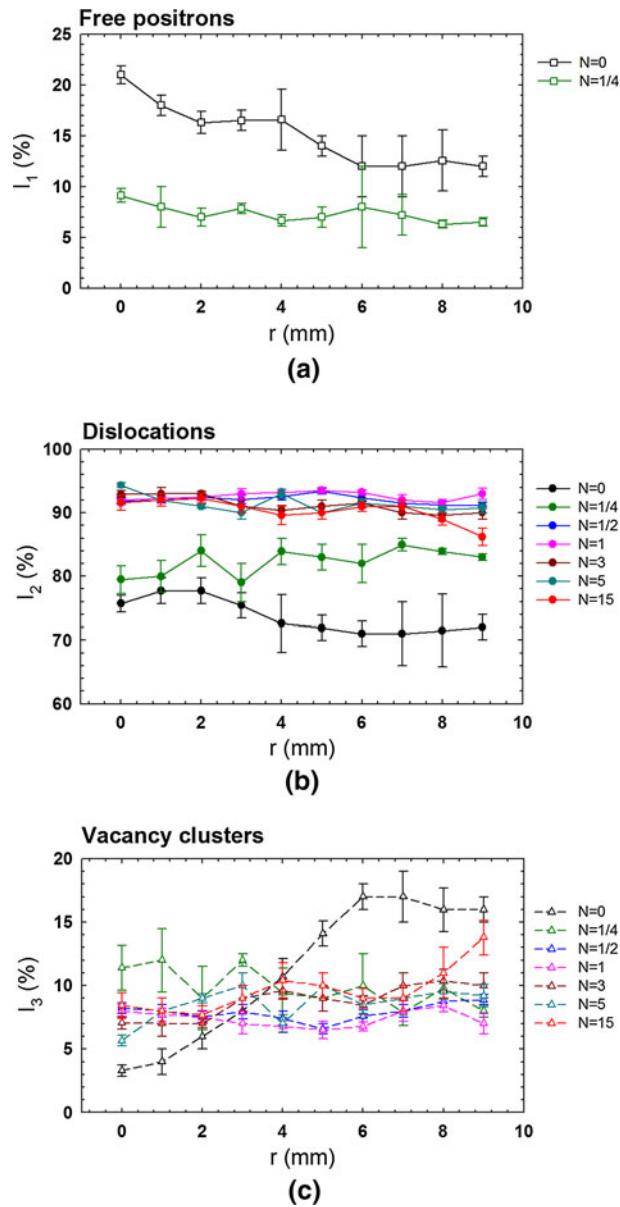


Fig. 12—Relative intensities I_1 , I_2 , and I_3 for the free positron component (a), the contribution of positrons trapped at dislocations (b) and vacancy clusters (c) for samples subjected to various numbers N of HPT revolutions plotted as a function of the radial distance r from the center of the sample.

compared to the center. On the other hand, the sample subjected to $1/4$ HPT revolution exhibits a relatively uniform spatial distribution of vacancy clusters. The concentration of vacancy clusters in the sample $N = 1/4$ is comparable with that at the periphery of the sample which was only pressed, see Figure 16. An increase of c_{vc} in the center of the sample $N = 1/4$ is obviously due to agglomeration of vacancies created by SPD during HPT straining.

In samples subjected to a higher degree of HPT straining ($N \geq 1/2$), the concentration of defects cannot be determined because of saturated positron trapping which leads to disappearance of the free positron component. Taking into account that the free positron

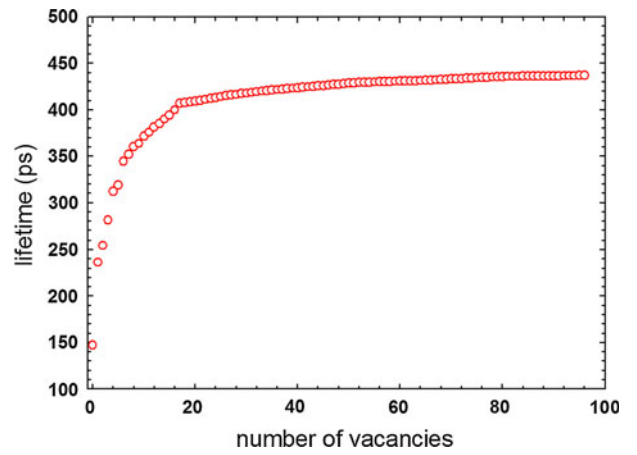


Fig. 13—Calculated positron lifetimes for vacancy clusters in Ti consisting of various numbers of vacancies.

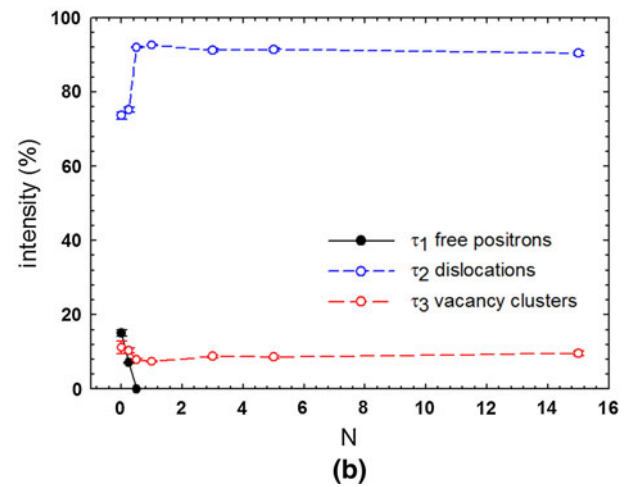
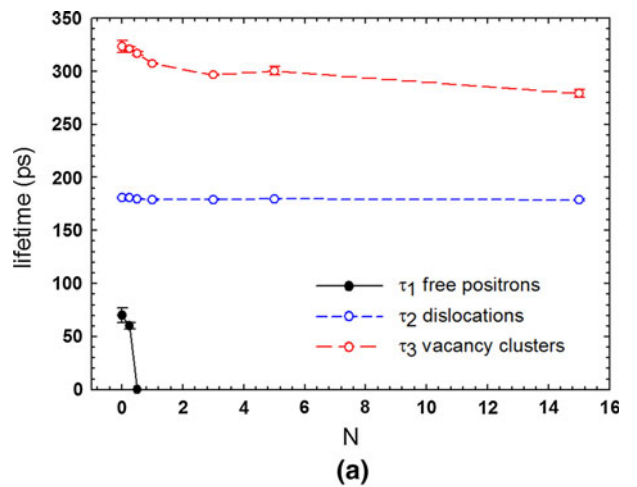


Fig. 14—Positron lifetimes (a) and corresponding relative intensities (b) averaged over whole sample and plotted as the number of HPT revolutions.

component cannot be resolved when $I_1 < 5$ pct and using the ratio of intensities I_2 and I_3 , one can estimate that straining to $N = 1/2$ leads to an increase of

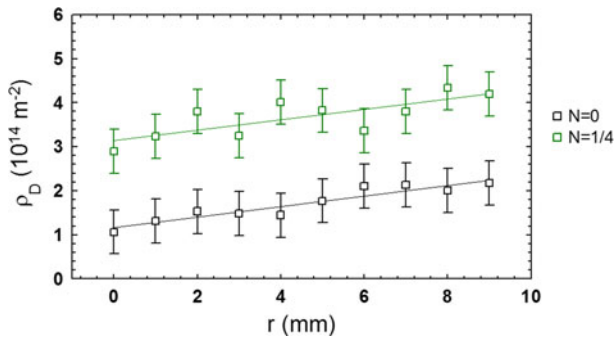


Fig. 15—Dislocation density ρ_D in the sample, which was only pressed ($N = 0$) and the sample subjected to $1/4$ HPT revolution ($N = 1/4$), plotted as a function of the radial distance r from the center.

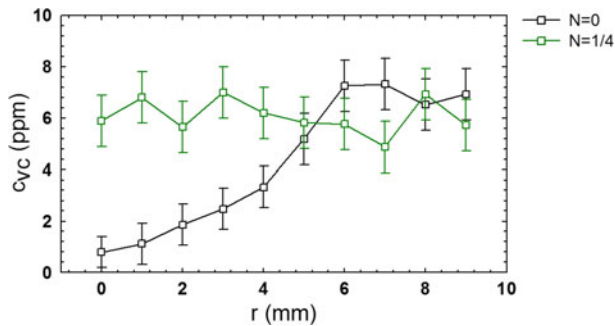


Fig. 16—The concentration c_{vc} of vacancy clusters in the sample which was only pressed ($N = 0$) and the sample subjected to $1/4$ HPT revolution ($N = 1/4$), plotted as a function of the radial distance r from the center.

dislocation density to at least 10^{15} m^{-2} and simultaneously to an increase of c_{vc} to at least 15 ppm. Note that dislocation density might increase during further HPT processing ($N > 1/2$), but it cannot be detected due to saturated positron trapping. However, if so, then the concentration of vacancy clusters increases in a similar manner and the ratio of concentrations of these two kinds of defects remains unchanged.

IV. DISCUSSION

A. Effect of Thermal Treatment

Two-step TT results in a typical duplex microstructure consisting of round primary alpha grains and lamellar $\alpha + \beta$ structure. Chemical analysis proved that the interiors of the primary alpha grains are aluminum enriched and niobium depleted, whereas the rim of those grains has the average composition. We assume that the interior of the primary alpha grains having the volume fraction of approximately 10 pct are original alpha grains of the as-received (as-rolled) material that remain in the material during annealing at 1258 K (985 °C). These alpha grains started to grow during annealing at 973 K (700 °C), but the temperature is not sufficiently high to cause the diffusional change in the composition of the primary alpha grains in favor of α -stabilizing elements. As

a result, the interiors of the primary alpha grains have different chemical compositions than their rims.

Contrarily, beta particles are aluminum depleted and strongly niobium enriched. Beta particles also include detectable iron content. Iron is the typical impurity in Ti alloys and even in a low content (<1 wt pct), it helps to stabilize the beta phase.^[32]

B. Relation Between Defect Structure, Microstructure, and Microhardness

SEM observations confirm that after HPT deformation, primary alpha grains and $\alpha + \beta$ lamellae are present in the microstructure. However, microhardness measurements and PAS cannot distinguish between those microstructural features. The approximate size of an indent is $50 \mu\text{m}$ and therefore it is too large to distinguish between these two regions. On the other hand, each indentation does not represent the measurement of a truly average material. The results of microhardness are therefore heterogeneous. Interestingly, the heterogeneity (represented as standard deviation from the mean value) increases with increasing strain. This suggests that the difference between hardness of the alpha grains and $\alpha + \beta$ lamellar structure increases with increasing strain. Most probably, $\alpha + \beta$ lamellar structure is significantly hardened. The final answer to this assumption may be provided by more detailed microhardness or nanohardness measurements.

For the as-pressed sample ($N = 0$), the outflow of the material between the anvils is captured by significant increase in vacancy clusters in the periphery region, but no increase in dislocation density occurs. Microhardness increases significantly, proving the important effect of vacancy hardening.^[33]

The defect structure is already homogenous from $N = 1/2$ HPT revolution, while the microhardness is homogenous from $N = 3$ HPT revolutions only. On the other hand, the microstructure is not entirely homogenous even after $N = 5$ HPT revolutions. The evolution of primary alpha grains as observed by SEM is rather independent of the evolution of point and line defects as evaluated by PAS. Several mechanisms like vacancy hardening, dislocation density, and microstructure refinement are responsible for the significant hardness increase which is not directly related to a single characteristic quantity.

V. CONCLUSIONS

The following conclusions can be drawn from the presented investigations of the ultrafine-grained Ti-6Al-7Nb biocompatible alloy prepared by HPT up to 15 revolutions:

1. Thermal treatment before HPT resulted in duplex microstructure with chemically heterogeneous primary alpha grains having 18 pct volume fraction. Primary alpha grains provide sufficient ductility for SPD, whereas the major $\alpha + \beta$ lamellar microstructure becomes more easily fragmented and hardened.

2. SEM observations revealed heavily deformed primary alpha grains surrounded by significantly fragmented $\alpha + \beta$ microstructure after 5 HPT revolutions.
3. Microhardness significantly increases (from 330 to 400 HV 0.5) with increasing strain, but it is heterogeneous due to heterogeneous microstructure. Heterogeneity of microhardness increases with increasing strain, suggesting that the $\alpha + \beta$ lamellar microstructure is more hardened than primary alpha grains.
4. Positron annihilation spectroscopy showed significant increase of dislocation density (approx. 10^{15} m^{-2}) and of the concentration of vacancy clusters (15 ppm) after $\frac{1}{2}$ of the HPT revolution.
5. The defect structure is already homogenous after $\frac{1}{2}$ HPT revolution, while the microhardness becomes homogenous after three HPT revolutions.

ACKNOWLEDGMENTS

This work was financially supported by the Czech Ministry of Education and Youth under the grant LH12217. Partial financial support by the Czech Science Foundation under the project P107/12/1025 is also acknowledged. One of the authors J.C. acknowledges financial support from the Czech Science Foundation (project P108/12/G043).

REFERENCES

1. M. Geetha, A.K. Singh, R. Asokamani, and A.K. Gogia: *Prog. Mater. Sci.*, 2009, vol. 54, pp. 397–425.
2. C. Leyens and M. Peters: *Titanium and Titanium Alloys*, Wiley-VCH Verlag, 2003, pp. 423–51.
3. K.S. Katti: *Colloids Surf. B*, 2004, vol. 39, pp. 133–42.
4. M. Niinomi: *J. Mech. Behav. Biomed. Mater.*, 2008, vol. 1, pp. 30–42.
5. R.Z. Valiev and T.G. Langdon: *Prog. Mater. Sci.*, 2006, vol. 51, pp. 881–981.
6. A.P. Zhilyaev and T.G. Langdon: *Prog. Mater. Sci.*, 2008, vol. 53, pp. 893–979.
7. H.S. Kim: *J. Mater. Proc. Technol.*, 2001, vol. 113, pp. 622–26.
8. Y. Saito, H. Utsunomiya, N. Tsuji, and T. Sakai: *Acta Mater.*, 1999, vol. 47, pp. 579–83.
9. V.N. Varyutkhin, Y. Beygelzimer, S. Synkov, and D. Orlov: *Mater. Sci. Forum*, 2006, vols. 503–504, pp. 335–38.
10. X. Yang, Y. Okabe, H. Miura, and T. Sakai: *J. Mater. Sci.*, 2012, vol. 47, pp. 2823–30.
11. Z. Horita, D.J. Smith, M. Furukawa, M. Nemoto, R.Z. Valiev, and T.G. Langdon: *J. Mater. Res.*, 1996, vol. 11, pp. 1880–90.
12. R. Kužel, Z. Matěj, V. Cherkaska, J. Pešička, J. Čížek, I. Procházka, and R.K. Islamgaliev: *J. Alloys Compd.*, 2004, vol. 378, pp. 242–47.
13. M. Janeček, J. Čížek, M. Dopita, R. Král, and O. Srba: *Mater. Sci. Forum*, 2008, vols. 584–586, pp. 400–45.
14. Z. Matěj, R. Kužel, M. Dopita, M. Janeček, J. Čížek, and T. Brunátová: *Int. J. Mater. Res.*, 2009, vol. 100, pp. 880–83.
15. R. Kužel, M. Janeček, Z. Matěj, J. Čížek, M. Dopita, and O. Srba: *Metall. Mater. Trans. A*, 2010, vol. 41A, pp. 1174–90.
16. F. Bečvář, J. Čížek, I. Procházka, and J. Janotová: *Nucl. Instrum. Methods A*, 2005, vol. 539, pp. 372–85.
17. F. Bečvář: *Nucl. Instrum. Methods B*, 2007, vol. 261, pp. 871–74.
18. I. Procházka, I. Novotný, and F. Bečvář: *Mater. Sci. Forum*, 1997, vols. 255–257, pp. 772–74.
19. V.V. Polyakova and I.P. Semenova: *Modern Problems of Science and Education*, 2012, vol. 6, in Russian.
20. J. Mueller, H.J. Rack, and L. Wagner: *Ti-2007, Science and Technology*, M. Niinomi, S. Akiyama, M. Hagiwara, M. Ikeda, and K. Maryama, eds., JIMIC 5, 2007, pp. 383–87.
21. R. Boyer, G. Welsh, and E. Collings: *Material Properties Handbook—Titanium Alloys*, ASM International, Materials Park, OH, 1994.
22. N. Poondla, T.S. Srivatsan, A. Patnaik, and M. Petraroli: *J Alloys Compd.*, 2009, vol. 486, pp. 162–67.
23. Y. Estrin, M. Janeček, G.I. Raab, R.Z. Valiev, and A. Zi: *Metall. Mater. Trans. A*, 2007, vol. 38A, pp. 1906–09.
24. W.J. Kim and Y.K. Sa: *Scripta Mater.*, 2006, vol. 54, pp. 1391–95.
25. X. Ma, R. Lapovok, C. Gu, A. Molotnikov, Y. Estrin, E.V. Pereloma, C.H.J. Davies, and P.D. Hodgson: *J. Mater. Sci.*, 2009, vol. 44, pp. 3807–12.
26. X.G. Qiao, N. Gao, Z. Moktadir, M. Kraft, and M.J. Starink: *J. Micromech. Microeng.*, 2010, vol. 20, p. 045029.
27. J. Vrátná, M. Janeček, J. Čížek, D.J. Lee, E.Y. Yoon, and H.S. Kim: *J. Mater. Sci.*, 2013, DOI:10.1007/s10853-013-7151-x.
28. J. Čížek, M. Janeček, O. Srba, R. Kužel, Z. Barnovská, I. Procházka, and S. Dobatkin: *Acta Mater.*, 2011, vol. 59, pp. 2322–29.
29. R. West: *Positrons in Solids, Topics in Current Physics*, P. Hautojärvi, ed., Springer, Berlin, 1979, pp. 89–115.
30. J.M. Campillo Robles, E. Ogando, and F. Plazaola: *J. Phys. Condens. Matter*, 2007, vol. 19, p. 176222.
31. P. Hautojärvi and C. Corbel: *Proceedings of the International School of Physics “Enrico Fermi”, Course CXXV*, A. Dupasquier and A.P. Mills, eds., IOS Press, Varena, 1995, pp. 491–506.
32. M. Mhaede, L. Wagner, and K. Ibrahim: *Int. J. Mater. Res.*, 2013, doi:10.3139/146.110920.
33. M. Zehetbauer: *Key Eng. Mater.*, 1995, vols. 97–98, pp. 287–306.

Microstructure evolution in ultrafine-grained Ti and Ti-6Al-7Nb alloy processed by severe plastic deformation

J Strasky¹, P Harcuba¹, M Hajek¹, K Vaclavova¹, P Zhanal¹, M Janecek¹, V Polyakova², I Semenova²

¹ Charles University in Prague, Prague, Czech Republic, Ke Karlovu 5, 121 16, Prague. Czech Republic

² Ufa State Aviation Technical University, Ufa, Russia, K. Marx Street 12, 450 000, Ufa, Russia

E-mail: josef.strasky@gmail.com

Abstract. Unique in-situ electric resistivity measurement was utilized to identify microstructural changes in ultra-fine grained commercially pure titanium and Ti-6Al-7Nb alloy. Both materials were prepared by equal channel angular pressing. Changes in resistivity evolution during in-situ heating were compared to scanning electron microscopy observations. Both materials are stable up to 440°C. Further heating at rate 5°C/min causes recovery and recrystallization of UFG structure. At 650°C the microstructure is fully recrystallized. High resolution in-situ electric resistivity measurement is capable of detecting recovery and recrystallization in UFG CP Ti and Ti-6Al-7Nb alloy.

1. Introduction

The importance of titanium and titanium alloys including their biomedical use is unquestionable [1,2]. The ultra-fine grained (UFG) commercial purity titanium (CP Ti) and Ti-6Al-4V alloy have already been prepared by severe-plastic deformation techniques (SPD) [3,4,5]. UFG commercial purity Ti and Ti alloys became known for their increased strength and enhanced fatigue performance [6]. Moreover, UFG materials exhibit also higher corrosion resistance and improved biocompatibility [7,8]. Recently, biocompatible UFG beta-Ti alloys have also been thoroughly investigated [9,10,11,12].

On the other hand, thermal stability of UFG microstructure in Ti and Ti alloys has been only rarely discussed [13,14], despite its significant importance for material processing and eventual low temperature superplasticity [15].

This investigation focuses on thermal stability of UFG microstructure of commercially pure Ti and biocompatible Ti-6Al-7Nb alloy. Ti-6Al-7Nb alloy has been developed as a biocompatible alternative to the common Ti-6Al-4V alloy. It belongs to $\alpha+\beta$ alloys consisting of both phases at room temperature. Its beta-transus temperature is 1010 °C [16]. UFG microstructure was obtained by the most popular technique of severe plastic deformation - equal channel angular pressing. The UFG microstructure of this alloy including its thermal stability was investigated by one of the co-authors [14]. The thermal treatment at 500°C is often used to increase the strength of Ti-6Al-4V alloy [17] and the same proved to increase the strength of UFG Ti-6Al-7Nb alloy [14]. The thermal stability of UFG microstructure around this temperature is therefore of major importance.

The principal experimental method used in this study is in-situ measurement of electric resistivity. This method has been successfully used to investigate phase transformations in metastable beta Ti alloys [18]. In this paper, we focus on recovery and recrystallization of microstructure during linear heating. Recovery and recrystallization were studied by in-situ electrical resistivity measurements in copper based alloys and composites [19,20] or in NiTi compound [21]. To our knowledge, there was no attempt up to date to study recovery and recrystallization by in-situ electric resistivity measurements in UFG Ti and Ti alloys.

2. Material and experimental



Two different materials – CP Ti and Ti-6Al-7Nb alloy were prepared by equal channel angular pressing using slightly different procedure. Both materials were procured from ATI Alvac Ltd. in as-rolled condition.

2.1. Preparation of CP Ti

The billets of CP Ti grade 4 were pressed through ECAP die having a round channel and the channel angle $\Phi = 105^\circ$ and the corner angle $\Psi = 20^\circ$. The diameter of the channel was 15 mm. The temperature of the die during pressing was between 300 and 310 °C. The studied billets were pressed 6 times via the route B_C at a constant ram speed of 1 mm/s. The mixture of 1/3 MoS₂ and 2/3 grease was used as a lubricant. More details about the ECAP processing of CP Ti be found elsewhere [22].

2.2. Preparation of Ti-6Al-7Nb alloy

Ti-6Al-7Nb alloy was at first thermally treated to enable successful processing by ECAP. The thermal treatment consisted of two annealing steps. Initially annealing at a temperature just below β transus was applied for one hour followed by water quenching. In the second step annealing for 4 hours at a temperature of 780 °C was applied. The microstructure after this thermal treatment is standard ‘duplex’ structure consisting of 18 vol.% of primary alpha phase, which allows successful ECAP processing (compared to initial microstructure with more than 60% of primary alpha).

The ECAP die with the diameter of 20 mm angles $\Phi = 120^\circ$ and $\Psi = 0^\circ$ was employed. The pressing was repeated six times (6 passes) at 600°C. Finally, extrusion to 10 mm was applied at 300°C. More details on material and its processing can be found elsewhere [14].

2.3. Experimental procedure

Electric resistivity was measured in situ using a self-made experimental setup. DC four-point method and rapid commutation of current were implemented in order to minimize parasitic effects. By utilizing Keithley 2182A nanovoltmeters we are able to achieve measurement with relative error lower than 0.0001 within each measured point while obtaining about 2 points per second. The dynamics of microstructural changes will be thus undoubtedly revealed.

The electric resistivity was measured during linear heating with the rate of 5°C/min up to 700°C and 800°C for CP Ti and Ti-6Al-7Nb alloy, respectively. UFG conditions of both materials were investigated along with their annealed counterparts in which no microstructural transformations occurred.

Microstructure changes in both materials were observed by high resolution scanning electron microscope FEI Quanta 200 FEG operated at 20 kV using backscattered electrons. Employing of Z-contrast allowed distinguishing α and β phases in Ti-6Al-7Nb alloy and the channeling contrast revealed the grain structure. The microstructure of both the as pressed materials and its evolution after subsequent heating were investigated. The samples for SEM observations were heated in the furnace with the rate of 5°C/min up to selected temperatures (see the section Results) and then water quenched. This heating procedure aims to mimic the thermal processing during resistivity measurements. Specimens were then prepared by automatic grinding in Struers Accutom 50 precision cut-off machine (0.3 mm removed), followed by standard metallographic grinding and vibratory polishing in three 8-hour steps using successively 0.3 μm alumina, 0.05 μm alumina and colloidal silica.

3. Results

3.1. In-situ electrical resistivity measurements

Fig. 1 shows the dependence of relative resistivity of CP Ti after ECAP and of the annealed material. The resistivity increases almost three times during heating to 700°C. Initially, the resistivity increases linearly, above 300°C the course slightly deviates from linearity. Small

difference between annealed and ECAP samples is observable. In order to see the difference more clearly, the first and the second derivatives were computed numerically using Savitzky-Golay algorithm with smoothing. Fig. 2 shows the first derivative of electrical resistivity. The course of both curves is similar with two small deviations at about 500°C and 600°C. Those deviations appear as clear peaks in the plot of the second derivative of relative resistivity which is shown in Fig. 3. Based on the assumption that these peaks correspond to undergoing microstructural changes, the temperatures of 440°C, 520°C and 640°C were chosen for subsequent SEM observations.

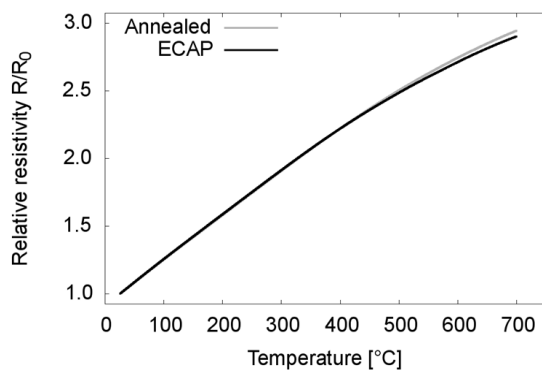


Fig. 1 Relative resistivity during heating 5°C/min – CP Ti

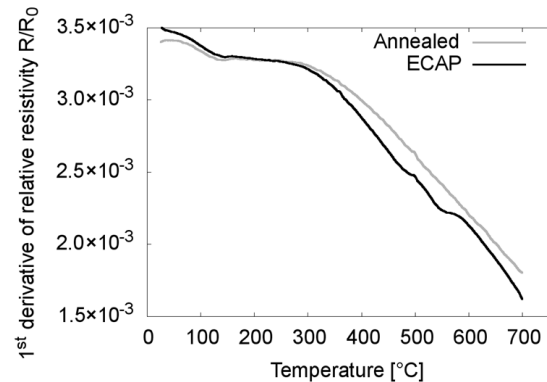


Fig. 2 First derivative of relative resistivity CP Ti

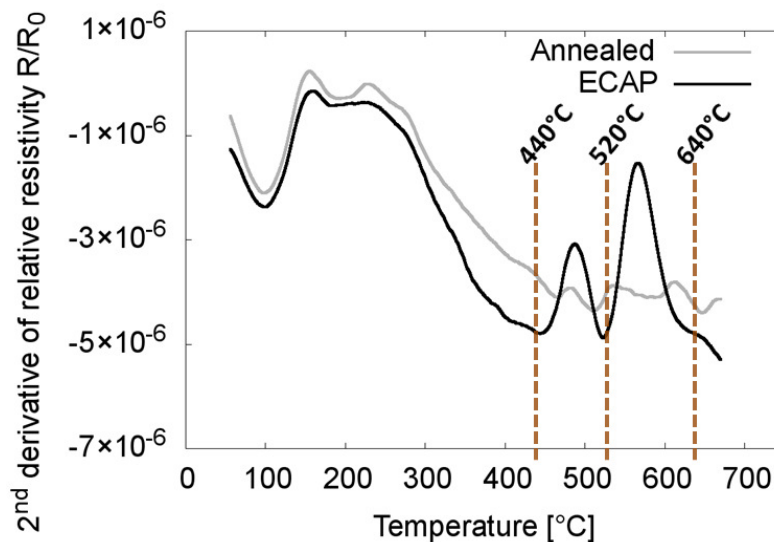


Fig. 3 Second derivative of relative resistivity - CP Ti, temperatures chosen for SEM observations

The results of resistivity measurements of Ti-6Al-7Nb alloy are processed and presented in the similar way. Fig. 4 shows the temperature dependence of relative resistivity for the UFG material after ECAP and also in the as-annealed condition. The relative resistivity increases only by approx. 10%, which contrasts to the CP Ti. The difference of the ECAP and as-annealed condition is therefore well visible. The course of both curves is similar (concave) up to 650°C. For higher temperatures, the electrical resistivity even declines. Fig. 5 shows the first derivative with two distinct peaks around 500°C and 650°C for the material after ECAP.

The differences between the two conditions are accentuated by plotting the second derivative of electrical resistivity as shown in Fig. 6. The temperatures of 440°C, 550°C and 660°C were chosen for microstructure observation by SEM.

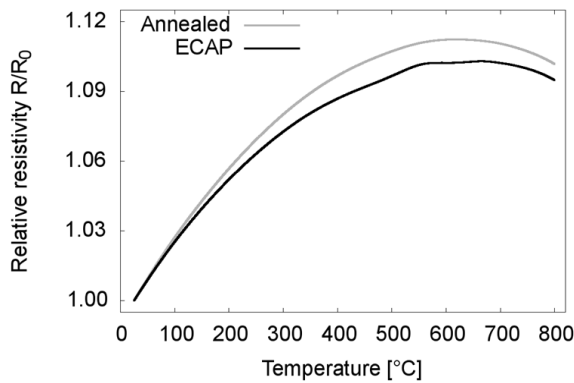


Fig. 4 Relative resistivity during heating 5°C/min – Ti-6Al-7Nb

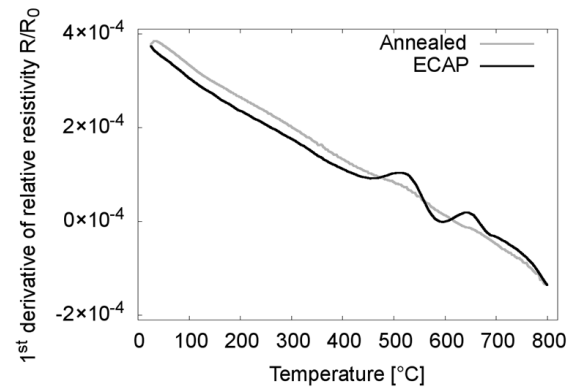


Fig. 5 First derivative of relative resistivity Ti-6Al-7Nb

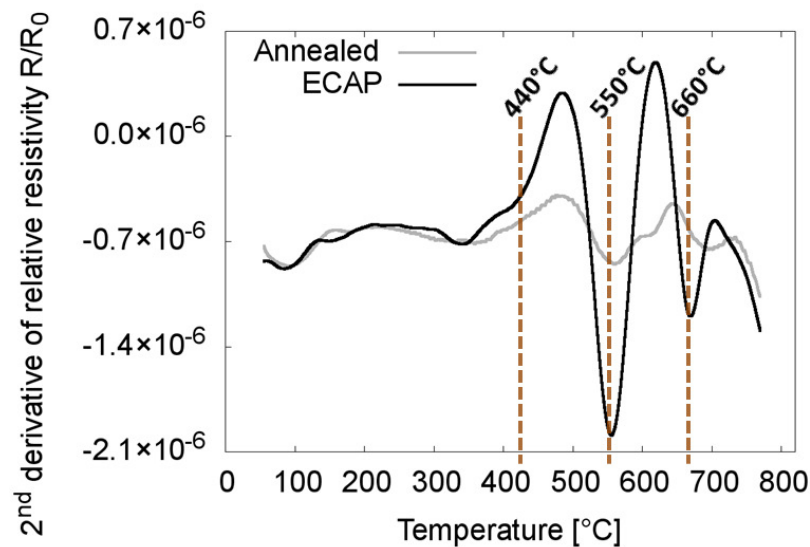


Fig. 6 Second derivative of relative resistivity - Ti-6Al-7Nb, temperatures chosen for SEM observations

3.2. SEM observations

Based on resistivity measurements, four conditions were chosen for SEM observations in each material; namely the as-ECAPed condition and three annealed conditions – samples heated up to selected temperatures.

Fig. 7 displays the microstructure of CP Ti. In Fig 7a the ultra-fine grained microstructure of as-ECAPed material is shown. It is a typical heavily deformed structure and the grains of the average size of 1 μm [3, 22]. No significant change of the microstructure was observed in the sample heated to 440°C, see Fig. 7b. On the other hand, the microstructure in Fig. 7c (condition after heating up to 520°C) differs significantly. Individual grains are much clearer, which indicates that some recovery process occurred during heating between 440°C and 520°C. Grain size is also slightly increased indicating some grain growth. The dark spots in

the micrograph are relicts from polishing – in fact parts of grains that fell out from the surface during vibratory polishing - those relicts should be excluded from the consideration. Microstructure in the condition after heating to the highest temperature (640°C) is shown in Fig. 7d. It is a completely recrystallized microstructure with grains of the average size of approximately of 5µm.

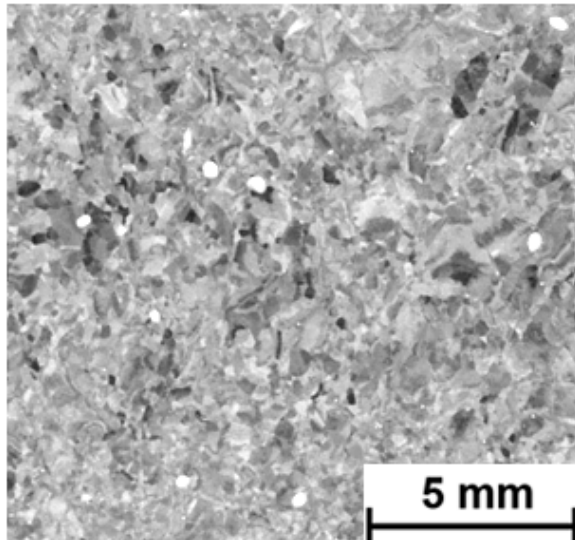


Fig. 7a CP Ti – as-ECAPed condition

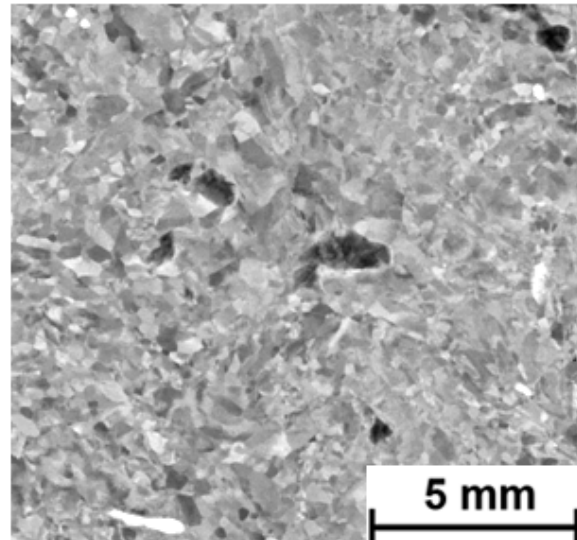


Fig. 7b CP Ti – heated up to 440°C

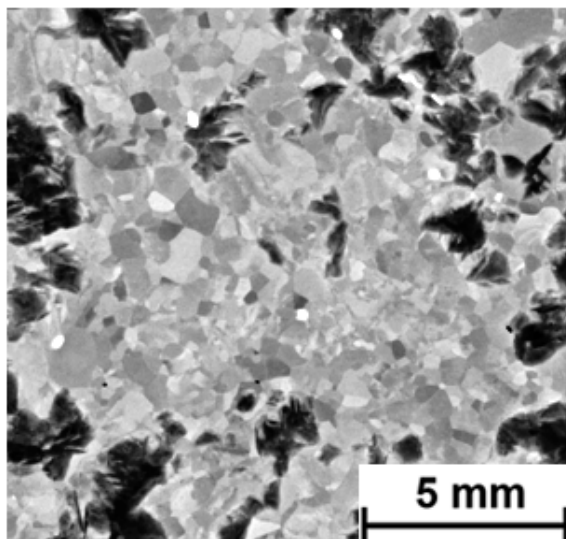


Fig. 7c CP Ti – heated up to 520°C

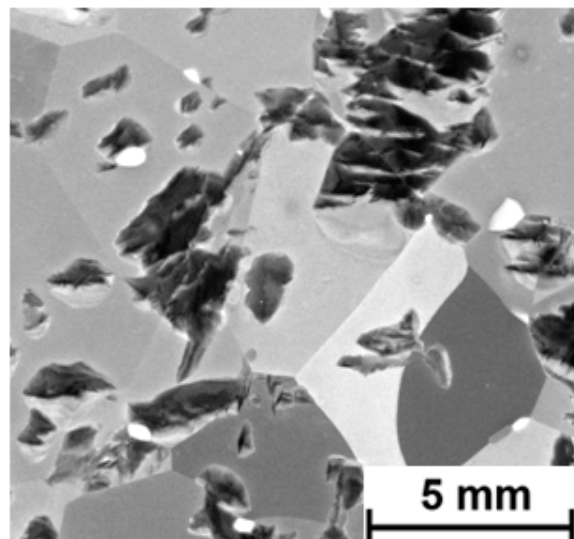


Fig. 7d CP Ti – heated up to 640°C

The microstructure of Ti-6Al-7Nb alloy after ECAP and annealed conditions are shown in Fig. 8. In Fig. 8a the typical microstructure of the ultrafine-grained material after ECAP and extrusion is shown. Lower magnifications (not presented here) show that the microstructure can be described as duplex with approx. 20% of heavily deformed primary alpha phase and fragmented $\alpha + \beta$ region. The microstructure is significantly less deformed then after processing by HPT [23]. Fig. 8b shows microstructure after deformation and subsequent heating up to 440°C. The microstructure is similar as the as ECAPed one (cf. Figs. 8a and 8b). Large (~5 µm) alpha grain remains heavily deformed. Surrounding $\alpha + \beta$ region is fragmented and contains slightly elongated beta phase particles appearing white. Fig. 8c

corresponds to the material heated to 550°C (after the first 'peak' in second derivative of resistivity). Detail inspection of the micrograph reveals that a negligible fraction of small grains in $\alpha + \beta$ region are non-deformed (clear contrast) and the higher proportion of beta phase particles are more equiaxed. Finally, Fig. 8d shows partly recrystallized microstructure of the condition heated up to 660°C containing bigger and more equiaxed beta phase particles.

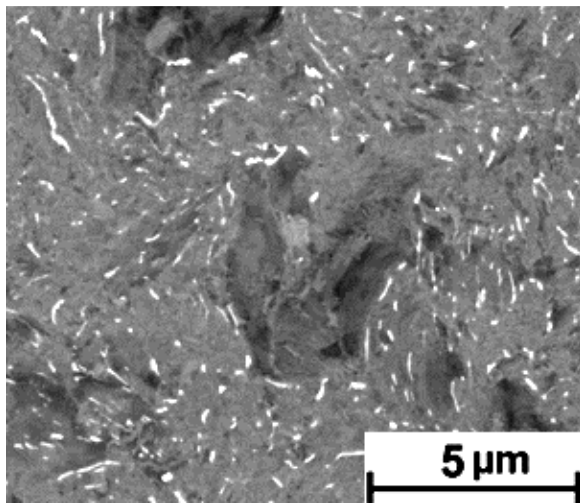


Fig. 8a Ti-6Al-7Nb – as-deformed condition

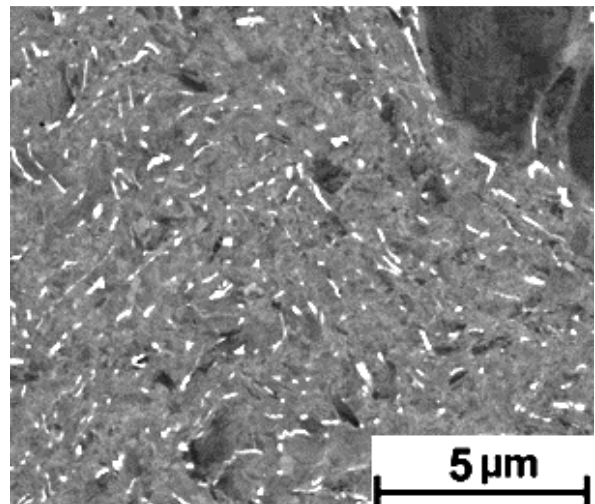


Fig. 8b Ti-6Al-7Nb – heated up to 440°C

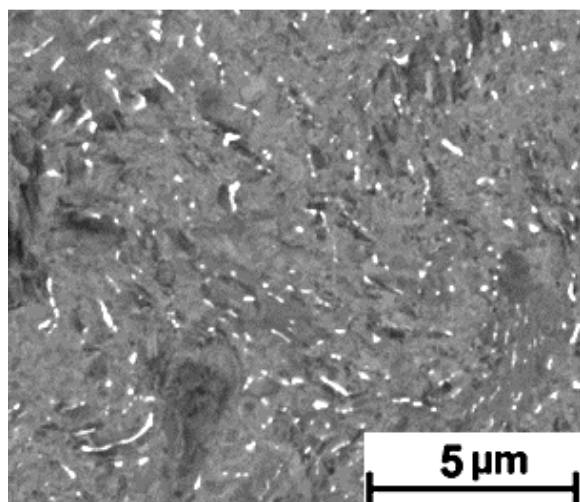


Fig. 8c Ti-6Al-7Nb – heated up to 550°C

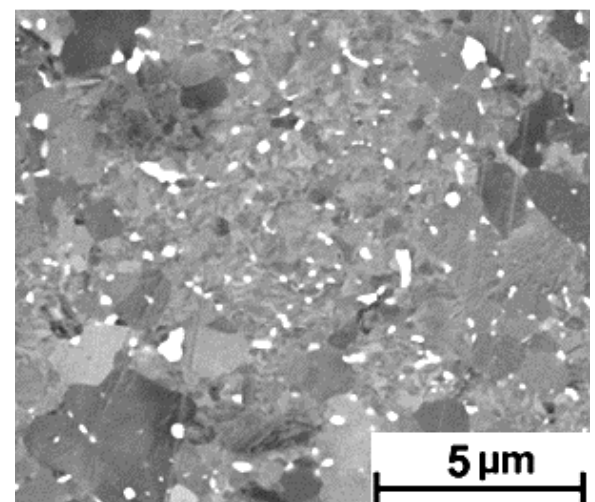


Fig. 8d Ti-6Al-7Nb – heated up to 660°C

4. Discussion

4.1. Overall resistivity evolution

The increase of electric resistivity of pure Ti during heating to 700°C (three times) is reasonable and depends on the amount of impurities, mainly the oxygen content [24]. Much smaller increase of resistivity (by only 10%) in Ti-6Al-7Nb alloy confirms also for Ti-alloys the well-known fact that the structural/compositional component in alloyed systems is of higher importance than the temperature dependent component [25].

The decrease of the resistivity in Ti-6Al-7Nb alloy above 700°C is caused by increased amount of beta phase. Similar alloy - Ti-6Al-4V - contains around 15% of beta phase at 750°C

and 20% of beta phase at 800°C and that this difference causes the decrease in resistivity [26].

4.2. Microstructural changes identified by resistivity measurements and SEM observations in CP Ti

SEM observations of CP Ti did not reveal any microstructure change after heating to 440°C. It is consistent with resistivity measurements and in perfect agreement with other authors [13]. No thermally activated process is observable by SEM or identifiable by in-situ resistivity measurement in CP Ti during heating to 440°C.

Further heating to 520°C caused significant recovery and possibly even the initial stage of recrystallization/grain growth. Heating up to 640°C caused complete recovery and significant grain growth. These processes were apparently detected by in-situ measurement of electric resistivity. Recovery processes were identified by electric resistivity measurements in copper alloys [19], copper-based composites [20] and in NiTi alloy [21]. Some differences in resistivity between severely deformed material and solution treated material were found in [27], however, only for isothermal high-temperature annealing of a beta titanium alloy. Our results proved that high sensitivity in-situ measurement of electric resistivity is capable of detecting recovery and/or recrystallization processes in temperature regions that are decisive for microstructure stability of UFG pure Ti.

4.3. Microstructural changes identified by resistivity measurements and SEM in Ti-6Al-7Nb

The comparison of resistivity measurements and SEM observations is less convincing in Ti-6Al-7Nb alloy. The microstructure remains unchanged after heating up to 440°C, which is consistent with resistivity measurements. However, no obvious microstructure changes were observed in the condition after heating up to 550°C despite resistivity evolution suggests some microstructural transformation to occur. (Note that the sample heated up to 550°C was exposed to temperatures above 500°C only for 10 minutes.) The same alloy annealed at 500°C for 1 hour showed recovery process (identified by X-ray diffraction) and the beginning of recrystallization (observed by TEM) [14]. Fig. 8d shows partly recrystallized structure of the sample heated to 660°C, which is consistent with resistivity measurements and observations of material annealed at 600°C for 1 hour [14]. We believe that resistivity measurements captured the recovery and recrystallization processes also in Ti-6Al-7Nb, despite that the beginning of the process cannot be unambiguously proven by SEM observations.

4.4. Open issues and future work

Resistivity measurements show two distinct peaks. However, recovery and recrystallization processes seem to operate simultaneously. The distinction between both effects might be revealed by isothermal annealing similarly to [21]. Microstructural observations require samples prepared with precise temperature control and should include TEM and/or in-situ microstructural observations. The possible effect of the rearrangement of beta phase particles during annealing of Ti-6Al-7Nb alloy on electrical resistivity remains also unclear.

5. Conclusions

The following conclusions can be drawn from this experimental study

- In-situ measurements revealed differences in electrical resistivity between UFG and annealed condition obtained by linear heating of both CP Ti and Ti-6Al-7Nb alloy
- The effects in electrical resistivity evolution of UFG condition of CP Ti were identified by SEM observations as recovery and recrystallization.
- Similar effects observed in Ti-6Al-7Nb alloy occur in the range of temperatures where recovery and recrystallization were also identified

- UFG structure of CP Ti and Ti-6Al-7Nb alloy is stable up to 440°C.

Acknowledgements

This work was financially supported by Ministry of Education, Youth and Sports under the project Kontakt II LH12217. Partial support by GACR under the project 14-36566G is also acknowledged. The authors wish to express their thanks to Dr. Kaveh Hazijadeh for ECAP processing of CP Ti.

References

- [1] Geetha M, Singh A K, Askomanani R, Gugia A K 2009 *Prog. Mat. Sci.* **54** pp 397-425
- [2] Long M, Rack H J 1998 *Biomaterials* **19** pp 1621
- [3] Stolyarov V V, Zhu Y T, Lowe T C, Islamgaliev R K, Valiev R Z 1999 *NanoStruct Mat* **11** 947 - 954
- [4] Islamgaliev R K, Kazyhanov V I, Shestakova L I, Sharafutdinov A V, Valiev R Z 2008 *Mat. Sci. Eng. A* **493** pp 190-194
- [5] Wang Y C, Langdon T G 2013 *Mat. Sci. Eng. A* **559** pp 861 – 867
- [6] Saitova L R, Hoppel H W, Goken M, Semenova I P, Valiev R Z 2009, *Int. J. Fatigue* **31** 322 – 331
- [7] Valiev R Z, Semenova I P, Jakushina E, Latysh V V, Rack H, Lowe T C, Petruzelka J, Dluhos L, Hrusak D, Sochova J 2008 *Mat Sci Forum* **584-586**
- [8] Kim H S, Yoo S J, Ahn J W, Kim D H, Kim W J 2011 *Mat. Sci. Eng. A* **528** pp 8479-8485
- [9] Suresh K S, Gurao N P, Satyaveer Singh D, Suwas S, Chattopadhyay K, Zhrebtsov S V, Salishchev G A 2013 *Mat. Char.* **82** pp 73 – 85
- [10] Zhang Z B, Hao Y L, Li S J, Yang R 2013 *Mat. Sci. Eng. A* **577** pp 225 – 233
- [11] Yilmazer H, Niinomi M, Nakai M, Cho K, Hieda J, Todaka Y, Miyazaki T 2013 *Mat. Sci. Eng. C* **33** pp 2499-2507
- [12] Yilmazer H, Niinomi M, Nakai M, Hieda J, Todaka Y, Akahori T, Miyazaki T 2012 *J Mech. Behav. Biomed. Mat.* **10** pp 235-245
- [13] Hoseini M, Pourian M H, Bridier F, Vali H, Szpunar J A, Bocher P 2012 *Mat. Sci. Eng. A* **532** 58-63
- [14] Polyakova V, Semenova I P, Valiev R Z 2010 *Mat. Sci. Forum* **667 – 669** pp 943-948
- [15] Sajadifar S V, Yapici G G, 2014 *Mat. Design* **53** pp 749-757
- [16] Leyens C, Peters M 2003 *Titanium and Titanium Alloys*, WILEY-VCH Verlag
- [17] Collings E W, *Materials Properties Handbook: Titanium Alloys*, ASM International, 1994
- [18] Prima F, Vermaut P, Ansel d, Debuigne J 2000 *Mat. Trans.* **41** pp 1092 1097
- [19] Feudenberg J, Kaufmann A, Klauss H, Marr T, Nenkov K, Subramanya Sarma V Schultz L 2010 *Acta Mater.* **58** pp 2324-2329
- [20] Liang M, Lu Y F, Sun L F, Yu X Y, Wang P F, Liu G Q Li C S 2013 *Phys. Proced.* **45** pp 105-108
- [21] Kamel Kazemi-Choobi, Khalil-Allafi J, Abbasi-Chianeh V 2012 *Mat. Sci. Eng. A* **551** 122-127
- [22] Hajizadeh K, Eghbali B, Topolski K, Kurzydowski K J 2014 *Mat. Chem. and Phys.* **143** pp 1032-1038
- [23] Janecek M, Strasky J, Cizek J, Harcuba P, Vaclavova K, Polyakova V V, Semenova I P 2014 *Met. Mat. Trans.* **45A** pp 7 - 15
- [24] Cormier M, Claisse F 1976 *J Less Comm. Mat.* **48** pp 309-314
- [25] Powell R W, Tye R P 1961 *J Less Comm. Mat.* **48** pp 309-314
- [26] Malinov S, Markovsky P, Sha W, Guo Z 2001 *J Alloys Comp.* **314** pp 181-192
- [27] Ueda M, Matsuhira H, Takasaki Y, Ikeda M, Toda Y 2012 *Supplemental Proceedings Volume 1: Materials Processing and Interfaces TMS 2012*, pp 895-902



Lattice defects in severely deformed biomedical Ti-6Al-7Nb alloy and thermal stability of its ultra-fine grained microstructure



Kristína Bartha ^{a,*}, Pavel Zháňal ^a, Josef Stráský ^a, Jakub Čížek ^b, Milan Dopita ^c, František Lukáč ^{b,d}, Petr Harcuba ^a, Michal Hájek ^a, Veronika Polyakova ^e, Irina Semenova ^e, Miloš Janeček ^a

^a Department of Physics of Materials, Charles University, Prague, Czech Republic

^b Department of Low Temperature Physics, Charles University, Prague, Czech Republic

^c Department of Physics of Condensed Matter, Charles University, Prague, Czech Republic

^d Department of Materials Engineering, Institute of Plasma Physics, The Czech Academy of Sciences, Prague, Czech Republic

^e Institute of Physics of Advanced Materials, Ufa State Aviation Technical University, Ufa, Russia

ARTICLE INFO

Article history:

Received 19 October 2018

Received in revised form

16 January 2019

Accepted 13 February 2019

Available online 15 February 2019

Keywords:

Titanium alloys

Equal channel angular pressing

Microstructure

Electrical resistance

Positron annihilation spectroscopy

ABSTRACT

Biomedical Ti-6Al-7Nb alloy was prepared by a dedicated thermal treatment followed by equal-channel angular pressing (ECAP) and extrusion. Ultra-fine grained duplex microstructure consisting of deformed primary α -grains and fragmented $\alpha + \beta$ region was achieved. Microstructural changes during heating with the rate of 5 °C/min were studied by in-situ electrical resistance. Microstructure after deformation and also after subsequent heating was thoroughly characterized by scanning electron microscopy, X-ray diffraction, and positron annihilation spectroscopy (PAS). X-ray diffraction and positron annihilation spectroscopy proved a very high dislocation density and the presence of high concentration of vacancy clusters in deformed material.

The ultra-fine grained microstructure of Ti-6Al-7Nb alloy is stable up to 440 °C, while upon heating to 550 °C and to 660 °C, the dislocation density decreases and vacancy clusters disappear. Enhanced microhardness can be achieved by ECAP followed by aging at 500 °C. Upon heating to 660 °C, the microhardness decreases due to ongoing recovery and recrystallization. Coincidence Doppler broadening (CDB), a special method of PAS, proved that dislocation cores are preferentially occupied by Al atoms that are known to cause substitutional solid solution strengthening.

© 2019 Elsevier B.V. All rights reserved.

1. Introduction

Titanium alloys are the ultimate choice for load-bearing orthopedic implants for big joints replacement [1]. Among them, two-phase $\alpha + \beta$ alloys and also metastable β Ti alloys are perspective candidates for use in medicine [2,3]. The workhorse of the titanium alloys industry and the most widely used titanium alloy for biomedical applications is the Ti-6Al-4V alloy [4–6]. However, this alloy contains vanadium that is known to be a toxic element [7]. Despite its harmful effect was not unambiguously proven, new vanadium-free Ti-6Al-7Nb alloy was developed which contains biocompatible niobium instead of potentially harmful vanadium [3,8]. Niobium is, similarly to vanadium, a β -stabilizing element,

even though its effect on β -transus temperature is lower [9]. As a result, Ti-6Al-7Nb alloy has similar mechanical and physical properties and undergoes similar phase transformations as thoroughly investigated and commonly used Ti-6Al-4V alloy [10,11].

Severe plastic deformation (SPD) methods can be used for improving the mechanical properties of materials by microstructural refinement. Ultra-fine grained (UFG) Ti-6Al-7Nb alloy was previously prepared by two most popular SPD methods - equal-channel angular pressing (ECAP) [12,13] and high pressure torsion (HPT) [14]. The UFG Ti-6Al-7Nb alloy exhibited superior mechanical properties – namely the strength and the fatigue performance [15,16] which can be attributed to the reduced grain size and increased concentration of defects in this two-phase material [14].

This work focuses on the investigation of thermal stability of the UFG microstructure and of the structure of lattice defects in the ultra-fine grained Ti-6Al-7Nb alloy prepared by ECAP. UFG microstructure is characterized by the grain size <1 μm and the high

* Corresponding author.

E-mail address: kristina.bartha@met.mff.cuni.cz (K. Bartha).

density of dislocations. However, the UFG structure is not thermodynamically stable and undergoes recovery and possibly recrystallization when exposed to elevated temperatures.

The thermal stability, i.e. the resistance of a material to thermally activated processes such as changes of the density of lattice defects, changes in crystallite size, precipitation and dissolution of particles, element partitioning in UFG Ti-6Al-7Nb alloy was studied. For that purpose, several experimental techniques were used. In-situ measurement of electrical resistance during heating provided the first insight into the recovery of the UFG structure. This method was previously successfully used for the investigation of the phase transformations in metastable β -Ti alloys and recovery and recrystallization in commercially pure Ti [17–19]. The microstructure of the ECAP deformed Ti-6Al-7Nb alloy was studied by scanning electron microscopy (SEM) post-mortem. Finally, lattice defects were studied by X-ray diffraction (XRD) and positron annihilation spectroscopy (PAS). Two different techniques of PAS were employed: measurement of positron lifetimes [20] and coincidence Doppler broadening (CDB) [21,22]. Measurement of positron lifetimes enables us to identify the type and the density of defects in the material. The chemical environment of the defects trapping positrons in solids was inspected by CDB.

2. Experimental materials and methods

2.1. Experimental material

The material in the form of a rod with a diameter of 22 mm in as-rolled condition was supplied by ATI Alvac Ltd. The initial microstructure of Ti-6Al-7Nb alloy (not shown here) consists of more than 60 vol% of primary α -phase particles. Based on previous experience, a thermal treatment (TT) is necessary for subsequent successful ECAP processing [15]. The thermal treatment consists of 2 annealing steps: the first annealing at the temperature just above the β -transus (985 °C) for 1 h followed by water quenching and the second annealing at the temperature of 780 °C for 4 h. The microstructure after TT may be characterized as the standard “duplex” structure consisting of 18 vol% of primary α -phase particles with the average grain size of 5.3 μm . This condition will be referred to as the initial condition.

The ECAP die with a diameter of 20 mm and channel angles of $\Phi = 120^\circ$ and $\Psi = 0^\circ$ was employed. The pressing was repeated six times (6 passes) at the temperature of 600 °C. ECAPed billets were finally extruded to 10 mm at 300 °C (hereafter for simplicity referred to as ECAP). The total equivalent deformation imposed by ECAP was 4 and the extrusion ratio $ER = 4$. More details about the material and its processing can be found elsewhere [16].

2.2. Electrical resistance measurement

Electrical resistance was measured in-situ during heating of the sample by a self-made experimental setup. The four-point method of resistance measurement and rapid commutation of direct current were implemented in order to minimize parasitic effects. High precision Keithley 2182A nanovoltmeters employed for the measurement of voltage and current provide very precise resistance measurement with a relative error lower than 0.0001 within each measured point and relatively fast acquisition rate of 2 points per second. Samples for electrical resistance measurement were approx. 1 mm thick, 10 mm wide and 15 mm long plates and were prepared using Struers Accutom-50.

The electrical resistance was measured during linear heating with a rate of 5 °C/min up to 800 °C. The absolute resistance (R) of the sample was measured. Note that specific electrical resistivity of the material cannot be calculated due to the complicated shape of

the sample.

For comparison between different samples, relative resistance was computed by the formula

$$\text{Relative resistance} = \frac{R}{R_0}, \quad (1)$$

where R_0 is the absolute resistance of the sample at the temperature of 25 °C. ECAP sample was measured in three runs, i.e. it was heated to 800 °C, cooled to room temperature in the furnace (uncontrolled cooling) and heated again to 800 °C; altogether three times.

Based on the results of electrical resistance measurements (see below in the Results section), three temperatures of interest were selected. The samples were subsequently heated to three post-mortem conditions 440 °C, 550 °C and 660 °C using the same heating rate of 5 °C/min as during in-situ electrical resistance measurements. After heating to the desired temperature, the sample was water quenched.

2.3. Scanning electron microscopy

Microstructural changes were observed post-mortem by high resolution scanning electron microscope Zeiss Auriga Crossbeam operated at 10 kV using backscattered electrons. Chemical contrast (Z-contrast) allowed us to distinguish α - and β -phases in Ti-6Al-7Nb alloy and the channeling contrast revealed the grain structure. Specimens for SEM observations were prepared by automatic grinding in Struers Accutom-50 precision cut-off machine (0.3 mm removed), followed by standard metallographic grinding and vibratory polishing in three 8-h steps using successively 0.3 μm alumina, 0.05 μm alumina and colloidal silica.

2.4. X-ray diffraction

XRD measurements were performed at room temperature post-mortem on one ECAPed sample and one ECAPed and heated sample. XRD measurements were carried out on powder X-ray diffractometer Bruker D8 Discover in vertical para-focusing Bragg-Brentano geometry (2.5° Soller slits in both primary and secondary beam and 0.5° divergence slit) with filtered copper radiation (Ni β filter in the secondary path), $\text{CuK}\alpha$ radiation $\lambda = 0.15418 \text{ nm}$. Diffraction patterns were acquired in the angular range 2θ from 20° to 135° with the step of $\Delta 2\theta = 0.04^\circ$. The measured X-ray diffraction patterns were fitted using the whole powder pattern fitting method (Rietveld method) employing computer program MStruct [23]. The X-ray measurement yielded the information about the phase composition, the lattice parameters, the size of coherently diffracting domains (crystallite size), and the dislocation density in individual crystalline phases.

2.5. Positron annihilation spectroscopy

The lifetime of positron and coincidence Doppler broadening on Ti-6Al7Nb alloy was measured by positron annihilation spectroscopy (PAS). The PAS measurement was performed post-mortem using the same samples as in XRD measurements. The $^{22}\text{NaCl}$ radioactive source deposited on a 2 μm thick mylar foil was used and placed between two identical samples of the studied material. Positron lifetime was measured by a digital spectrometer with a time resolution of 145 ps (FWHM ^{22}Na) [24]. The CDB investigations were performed using a digital spectrometer equipped with two HPGe detectors having an energy resolution of 0.9 keV at 511 keV [25]. At least 10^8 events were collected in each two-dimensional CDB spectrum, which was subsequently reduced into the one-

dimensional Doppler profile and instrumental resolution cuts. In order to inspect the nature of positron annihilation sites, the relative change of Doppler profile was determined as the ratio of the measured normalized profile and normalized reference profile of the well-annealed defect free pure Ti.

2.6. Microhardness measurement

Vickers microhardness measurements were carried out using the automatic microhardness tester Qness Q10a. The computer program QPix Control automatically processed and evaluated microhardness values of individual indents. The force applied by the indenter to the samples was 0.5 kgf and the dwell time 10 s. The average values of microhardness, as well as standard deviation, were computed from 20 indentations.

3. Results

3.1. Electrical resistance measurement

The temperature dependence of the electrical resistance of the initial and ECAP material is shown in Fig. 1. The relative resistance increases concavely and, above 650 °C, it starts to decline. The relative increase of resistance is approximately 10%. More importantly, the difference between the initial and ECAP samples is well visible. The ECAP curve shows a small peak at around 550 °C. In order to accentuate the differences between both conditions, the second derivative of electrical resistance with respect to temperature was calculated numerically and is plotted in the Fig. 2. Four curves are shown in Fig. 2: the initial material and three runs of ECAP sample. The second and the third run curves of ECAP sample coincide and differ only slightly from the curve of the initial material. On the other hand, the first run of ECAP sample significantly differs from all other curves suggesting that non-reversible processes must have occurred during the first heating run of ECAP specimen. Based on these results the temperatures of 440 °C, 550 °C and 660 °C (marked also by vertical lines in Fig. 2) were chosen for subsequent (post-mortem) characterization of ongoing processes in the material. The above mentioned selected temperatures may not coincide exactly with the global extremes of the second derivation of the electrical resistance. However, they are consistent with the temperatures selected for microstructural characterization of commercially pure Ti and Ti-6Al-7Nb in our

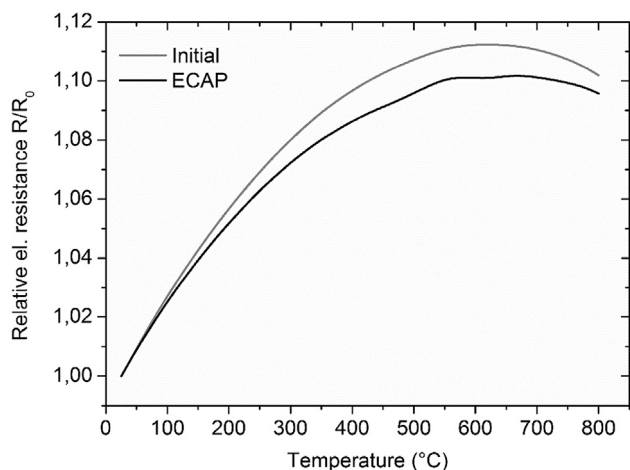


Fig. 1. Temperature dependence of the relative resistance of the Ti-6Al-7Nb alloy for initial and ECAP conditions.

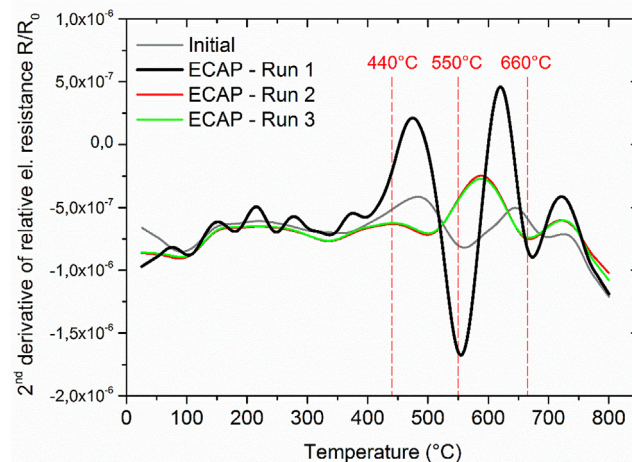


Fig. 2. Temperature dependence of the second derivative of the relative resistance of the Ti-6Al-7Nb alloy for the initial condition and three heating runs of the ECAP specimen. The highlighted temperatures were chosen for subsequent observations.

previous work [19].

3.2. Scanning electron microscopy

Note, that ECAP specimens for post-mortem SEM observations were heated to the respective temperatures (440 °C, 550 °C, 660 °C) using the same heating rate of 5 °C/min as during in-situ electrical resistance measurements in order to keep the same thermal processing regime. After reaching the desired temperature each sample was water quenched.

Fig. 3a shows the microstructure of the specimen in the initial condition after TT. It is a typical duplex microstructure consisting of primary α -phase grains (appearing dark) and lamellar $\alpha + \beta$ region in which α lamellae are divided by thin β -phase that appears white. Furthermore, distinct darker and lighter areas can be distinguished within individual primary α -grains. EDS measurement showed that the content of Al increases by 1.5 wt% in the interior of primary α -phase grains and is reduced by 2 wt% in the β -phase. The differences in Nb content are even more pronounced. The interior of primary α grains contains less than 5 wt% of Nb, while Nb content in the β -phase exceeds 16 wt%.

In Fig. 3b the typical microstructure of refined material after ECAP is illustrated. The microstructure can be characterized as a mixture of heavily deformed primary α -phase grains and elongated and fragmented $\alpha + \beta$ region. Fig. 3c corresponds to the ECAP sample heated up to 440 °C. No significant difference from ECAP specimen was observed (cf. Fig. 3b and c). Fig. 3d (the sample heated to 550 °C) shows the onset of globularization of β phase particles. Continuing β phase particles globularization and also new bigger α -phase grains are seen in Fig. 3e (the sample heated to 660 °C). SEM micrographs in Fig. 4 compare the microstructures of an ECAPed sample (Fig. 4a) and the sample subsequently heated to 660 °C (Fig. 4b) using higher magnification. Globularization of β phase particles is clearly visible and defect free grains (having uniform contrast) appear.

3.3. Crystallite size and dislocation density by X-ray diffraction results

X-ray diffraction measurements confirmed the presence of phases α (hcp, space group $P6_3/mmc$, #194) and β (fcc, space group $Fm-3m$, #225). All studied samples contained approximately 90% of

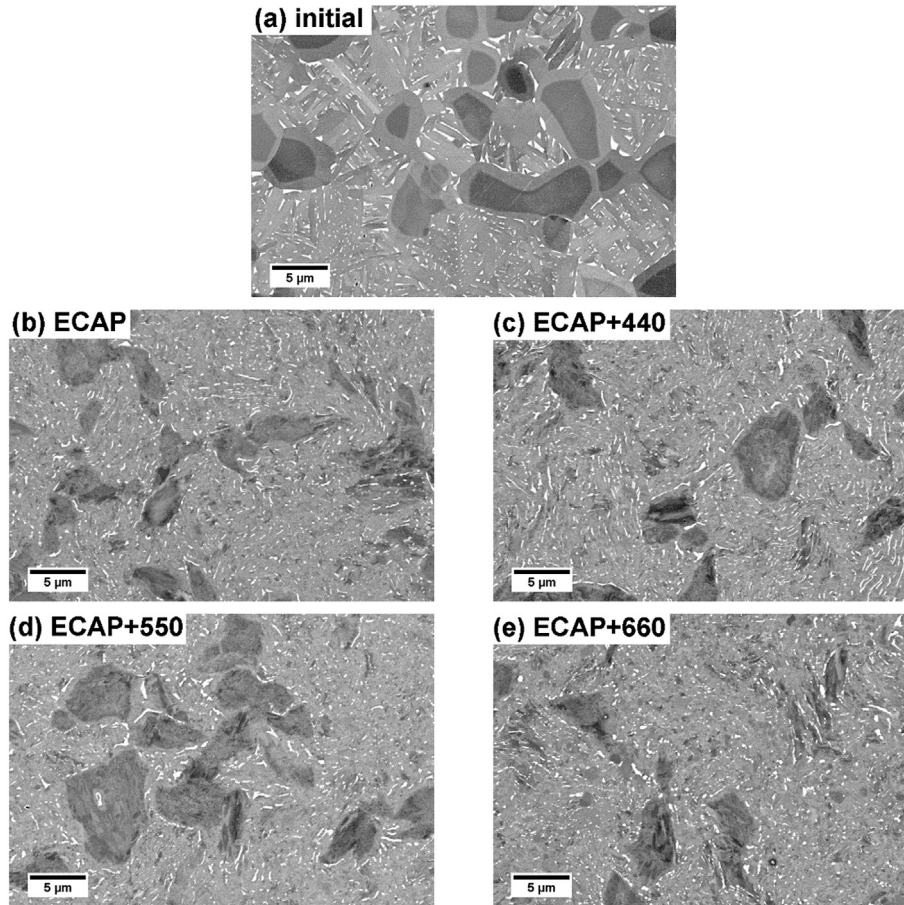


Fig. 3. SEM micrographs of Ti-6Al-7Nb alloy in different conditions: (a) initial - after TT, (b) ECAP, (c) ECAP + heating up to 440 °C, (d) ECAP + heating up to 550 °C, (e) ECAP + heating up to 660 °C.

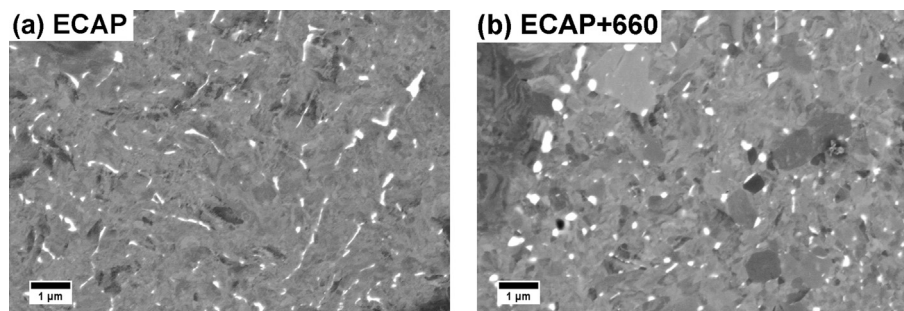


Fig. 4. Detailed SEM micrographs of Ti-6Al-7Nb alloy in conditions: (a) ECAP and (b) ECAP + heating up to 660 °C.

α -phase. The exact quantitative phase analysis was complicated due to the presence of the rather complex preferred orientation of crystallites (texture) caused by the ECAP and extrusion sample processing. The evolution of refined lattice parameters and the volume of the unit cell are shown in Fig. 5. In both phases, α and β , the lattice parameters, as well as the volume of unit cell, continuously decreased with increasing annealing temperature. The shrinkage of lattice parameters with increasing annealing temperature is a consequence of lattice defect annihilation (mainly dislocations) during the annealing.

Dislocation density and the size of coherently diffracting domains (crystallite size), were determined from peak broadening of both α - and β -phases. The crystallite sizes were modeled using the

log-normally distributed spherical crystallites [26,27]. The mean crystallite sizes in both phases increase with increasing terminal temperature of heating. The most pronounced increase in crystallite size is observed between 550 °C and 660 °C.

The dislocation density was determined using the Wilkens theory and models given in Refs. [26,28]. The dislocation contrast factors from Ref. [29] were adopted for the calculation. Dislocation density in ECAP sample and samples after subsequent heating is shown in Fig. 6a. In both α - and β -phases the dislocation densities decrease with the increasing terminal temperature, whereas the dislocation densities are in the order of $\rho_D \sim 10^{15} \text{ m}^{-2}$ and 10^{14} m^{-2} for α - and β -phase, respectively. Similarly to crystallite sizes, the most pronounced change in the dislocation density is observed

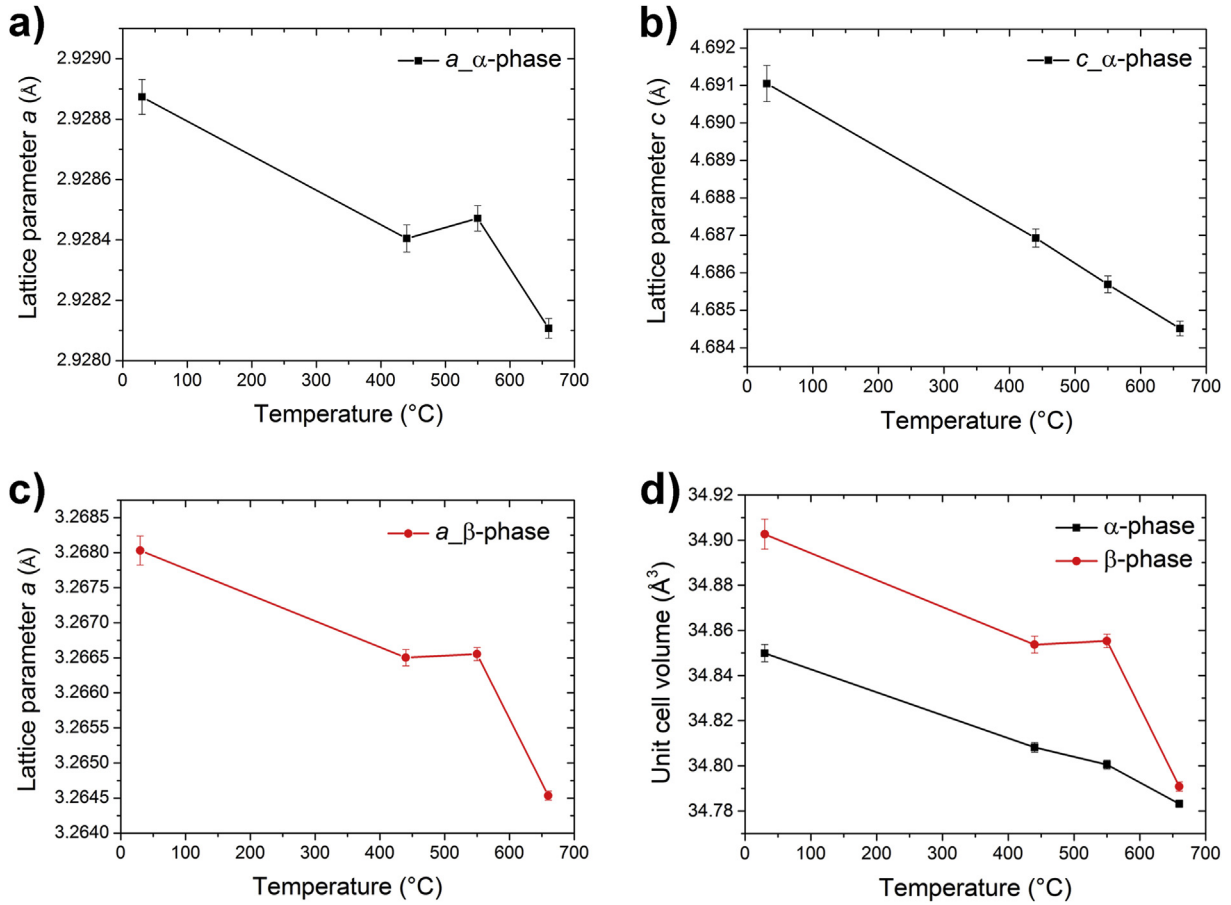


Fig. 5. Evolution of the lattice parameters (a) a and (b) c of the α -phase and (c) the parameter a of the β -phase, and (d) evolution of the unit cell volumes of α - and β -phases. Of the ECAP sample with subsequent heating to 3 temperatures.

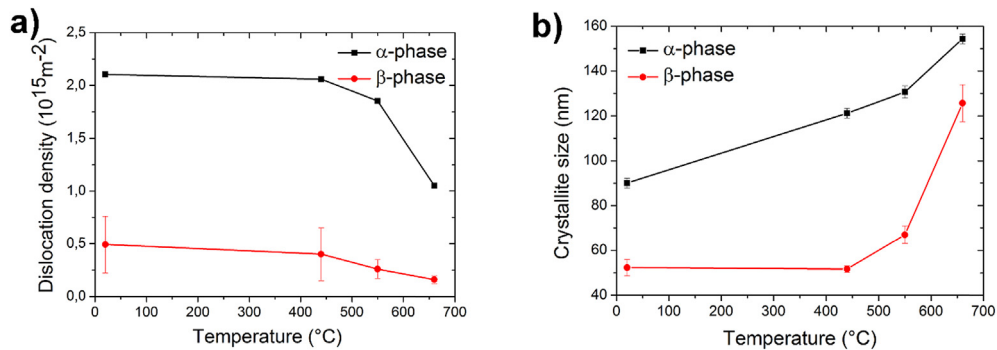


Fig. 6. Evolution of the (a) dislocation density and (b) crystallite size of the ECAP sample with subsequent heating.

between 550 °C and 660 °C.

3.4. Evolution of lattice defects with annealing of the material (PAS)

The defect structure of Ti-6Al-7Nb alloy after ECAP and subsequent heating to selected temperatures was investigated by measurements of positron lifetimes (LT) and coincidence Doppler broadening (CDB).

Information about defects in the material can be obtained from the decomposition of the LT spectrum. The lifetimes and intensities provide information about the type and density/concentration of lattice defects, respectively. Two types of defects: dislocations and

vacancy clusters were identified in the studied material. The temperature dependence of positron lifetimes and intensities of the two components is shown in Fig. 7a and b, respectively.

The ECAP sample exhibits so-called saturated trapping in two types of defects: dislocations and vacancy clusters. Saturated trapping refers to the situation when short-lived component corresponding to the annihilation of free positrons is negligible and virtually all positrons are trapped in defects before annihilation [30]. The component with lifetime ~ 170 ps represents a contribution of positrons trapped at dislocations. The long-lived component with the lifetime ~ 260 ps can be attributed to positrons trapped at vacancy clusters. If the saturated trapping in defects occurs one can

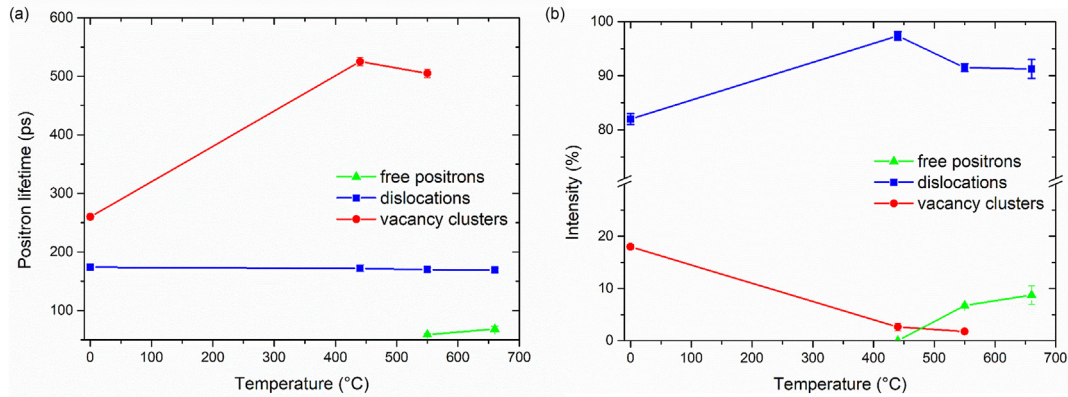


Fig. 7. Temperature dependence of (a) positron lifetimes and (b) the intensities of the individual exponential components resolved in positron lifetime spectra of the ECAP and annealed specimens.

claim that the average dislocation density in the ECAP sample is higher than $\rho_D \sim 5 \times 10^{15} \text{ m}^{-2}$ and the concentration of vacancy clusters is higher than $c_V \sim 20$ ppm (see Table 1). From comparison of the lifetime ~ 260 ps with theoretical calculations of positron lifetimes for vacancy clusters of various sizes in Ti [31] one can conclude that vacancy clusters in the ECAP sample are composed of two to three vacancies.

During heating to 440 °C vacancy clusters merge into larger objects (clusters) characterized by increased lifetime of 500 ps (see Fig. 7a). Simultaneously, their concentration decreases significantly (cf. Fig. 7b). The increase of dislocation component after heating to 440 °C observed in Fig. 7b is only relative and is caused by a significant decrease of concentration of vacancy clusters. Evolution of dislocation density during heating to the terminal temperature of 440 °C cannot be assessed from this measurement.

After heating to 550 °C, the further decline of the concentration of vacancy clusters takes place. The density of dislocations decreased as well and the free positron component appeared in the spectrum (relative intensity of the free positron component exceeds 5%). Heating to 660 °C leads to a further decrease in dislocation density and disappearance of the vacancy clusters completely (the relative intensity decreases below 5%). The abrupt decrease of the density of defects indicates a partial recrystallization of the material.

The concentration of defects (i.e. density of dislocations and concentration of vacancy clusters) can be estimated from the simple trapping model (STM) [20] when the free positron component is present

$$\rho_D = \frac{I_D}{\nu_D} \left(\frac{1}{\tau_f} - \frac{1}{\tau_D} \right), \quad (2)$$

where τ_f is the lifetime component of free positrons, τ_D is the lifetime component attributed to the positrons trapped at dislocations, I_D is the intensity of the positrons trapped at dislocations and $\nu_D \approx 0.5 \times 10^{-4} \text{ s}^{-1} \text{ m}^{-2}$ is the specific positron trapping rate for

dislocations [32]. Obtained results are summarized in Table 1. Dislocation density significantly decreases between 440 °C and 550 °C but even after heating to 660 °C the sample still contains relatively high dislocation density $\rho_D \sim 2 \times 10^{15} \text{ m}^{-2}$. The concentration of vacancy clusters can be calculated from STM as well

$$c_V = \frac{I_V}{n \cdot \nu_V} \left(\frac{1}{\tau_f} - \frac{1}{\tau_V} \right). \quad (3)$$

In the above equation $\nu_V \approx 10^{14} \text{ s}^{-1}$ is the specific positron trapping rate for vacancies [33], n is the number of vacancies constituting the cluster, I_V , and τ_V are the intensity and lifetime of component of vacancies, respectively. One can see in Table 1 that the concentration of vacancy clusters drops significantly even after heating to 440 °C, which can be estimated from the relative intensities of vacancies and dislocations. The concentration of vacancy clusters continuously decreases with increasing annealing temperature and after heating up to 660 °C they completely disappear.

The CDB technique was employed to characterize the chemical environment of defects in specimens deformed by ECAP. The momentum distribution of annihilating electron-positron pairs is obtained from precise coincidence measurement of the Doppler shift in energies of annihilation of γ -rays. Note that the momentum of the annihilating electron-positron pair is determined by the momentum of electron since the thermalized positron has a negligible momentum. In heavily deformed materials, the momentum distribution is affected by the overall concentration of defects (i.e. the population of positrons annihilated in the trapped state) and by the type of atoms surrounding the defects. Therefore, the shape of momentum distribution acquired from the CDB measurement carries information about local chemical environment of defects.

Fig. 8 shows the measured CDB ratio curves (related to a well annealed Ti reference) of ECAP specimen (open blue circles) and the specimen heated to 660 °C after ECAP (open red circles). Note that the majority of annihilation events occurs for electrons with very low momentum p .

At very low momenta $p < 5 \times 10^{-3} m_0 c$, the ratio curves are higher than 1, indicating that the fraction of positrons annihilated by low momentum electrons is higher than in well annealed pure Ti. Low momenta region corresponds to the contribution of valence electrons forming a band structure in the material. The higher intensity in this region refers to the fact that most positrons annihilate in a trapped state in defects and therefore predominantly with valence electrons. For elemental analysis, the ratio curves can be compared with those measured for reference samples of pure

Table 1
Dislocation density ρ_D and the concentration of vacancy clusters c_V of the ECAP and annealed samples of Ti-6Al-7Nb alloy calculated using the STM.

	$\rho_D (10^{15} \text{ m}^{-2})$	$c_V (\text{ppm})$
ECAP sample	>5	>20
ECAP sample heated up to 440 °C	>5	1.58
ECAP sample heated up to 550 °C	2.05	0.26
ECAP sample heated up to 660 °C	1.6	0

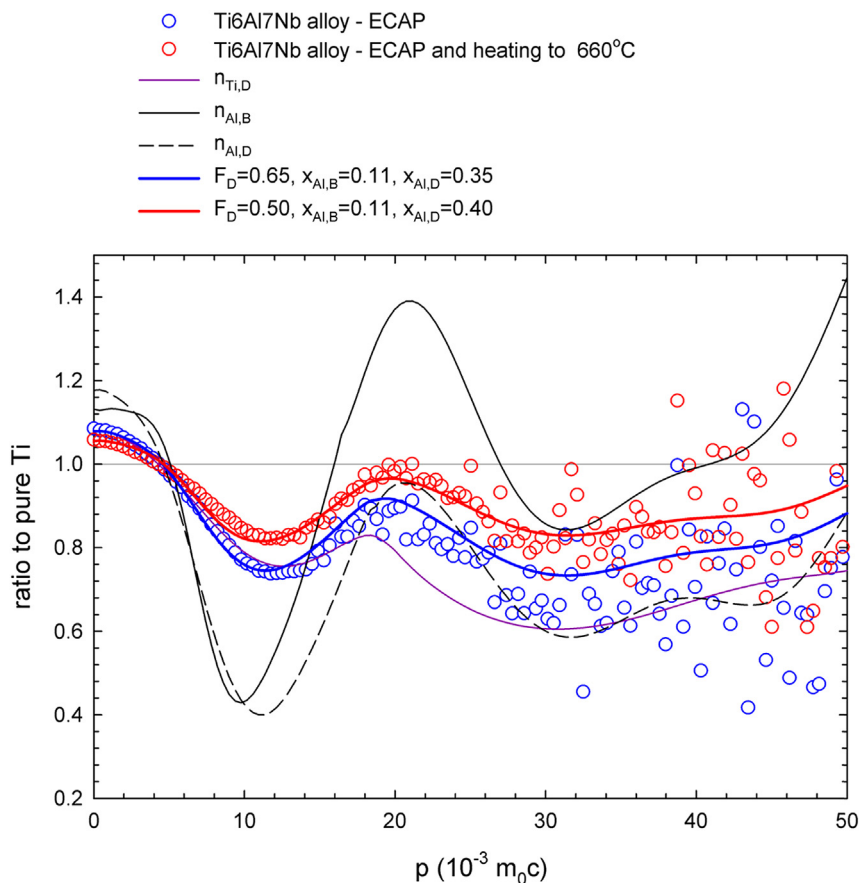


Fig. 8. CDB ratio curves (relative to pure Ti) for the specimen deformed by ECAP and the specimen heated up to 660 °C. Ratio curves for well annealed pure Al reference ($n_{Al,B}$), for positrons trapped at dislocations in Ti ($n_{Ti,D}$) and Al ($n_{Al,D}$) are also shown. The solid red and blue lines represent special superposition of aforementioned curves for quantitative estimation of measured curves of the material (for details see the section Results). (For interpretation of the references to colour in this figure legend, the reader is referred to the Web version of this article.)

elements. Fig. 8 presents CDB ratio curves also for the reference samples: (i) pure Ti with dislocation density high enough for saturated trapping (solid purple line), (ii) pure defect-free Al (solid black line), and (iii) pure Al with high dislocation density sufficient for saturated trapping (dashed black line). Similar curves for Nb were considered, but it did not improve the modeling of measured CDB curves and the contribution of the electrons of Nb to the annihilation of the positrons in the material is negligible.

The ratio curve of the measured ECAP sample (open blue circles) partially follows the CDB ratio curve of the positrons trapped at dislocations and annihilated in Ti. However, the peak at $p \sim 20 \times 10^{-3} m_0c$ is significantly higher. Near to the $p \sim 20 \times 10^{-3} m_0c$ the measured curve partly follows the CDB ratio curve of the positrons trapped at dislocations and annihilated in Al.

The CDB ratio curve of the ECAP sample subsequently heated to 660 °C exhibits a similar tendency with respect to the ratio curve of the ECAP sample. However, the curve is enhanced in the high momentum region ($p > 10 \times 10^{-3} m_0c$) and reduced in the low momentum region ($p < 5 \times 10^{-3} m_0c$). This is consistent with the recovery of the defects in the material.

Two other curves (solid blue and red line) going through the measured points are also shown in the Fig. 8. These curves aim on modeling the measured data and correspond to the superposition of four reference curves: Ti with dislocations ($n_{Ti,D}$), defect-free bulk Al ($n_{Al,B}$), Al with dislocations ($n_{Al,D}$) and also a constant function with intensity equal to 1, which technically represents defect-free Ti ($n_{Ti,B}$). The ratio curve for Ti-6Al-7Nb alloy is expressed as

$$n = (1 - F_D)(x_{Ti,B} + x_{Al,B}n_{Al,B}) + F_D(x_{Ti,D}n_{Ti,D} + x_{Al,D}n_{Al,D}), \quad (4)$$

where F_D is the fraction of positrons trapped at defects and was calculated from results of LT spectroscopy. The coefficients $x_{Ti,B}$, $x_{Al,B}$ represent fractions of free positrons annihilated in the vicinity of Ti and Al atoms, respectively. Similarly, the coefficients $x_{Ti,D}$, $x_{Al,D}$ are fractions of trapped positrons annihilated in the vicinity of Ti and Al atoms, respectively. Since these coefficients must fulfill normalization conditions $x_{Ti,B} + x_{Al,B} = 1$ and $x_{Ti,D} + x_{Al,D} = 1$, there are only two fitting parameters $x_{Al,B}$ and $x_{Al,D}$. It follows from results of ECAP sample presented in Fig. 8 that $x_{Al,B} = 0.11$ which perfectly corresponds to the atomic concentration of Al in the Ti-6Al-7Nb alloy. On the other hand, $x_{Al,D} = 0.35$ is more than three times bigger. It means that in the vicinity of dislocation core, the Al concentration is more than three times higher than the average concentration in the alloy. It can be concluded that either Al atoms tend to segregate along dislocations or, more plausibly, dislocations are preferentially stuck on Al atoms.

After heating to 660 °C, (model curve is plotted by red line in Fig. 8), the parameter F_d corresponding to annihilation at dislocations decreases, but the chemical environment around the defects is not significantly changed.

3.5. Microhardness

The microhardness of the initial condition and ECAP sample as

well as the specimens that were subsequently heated at 440 °C, 550 °C and 660 °C was determined. The evolution of Vickers hardness with the heating temperatures is shown in Fig. 9. The initial sample exhibits the lowest microhardness ($HV \sim 325$) and the microhardness of ECAP sample increases only slightly. Subsequent heating of the initial sample led to a slight increase of microhardness up to the temperature of 550 °C and to an insignificant decrease upon further heating. The ECAP specimen is the most sensitive to subsequent heating and after heating to 550 °C it exhibits the highest microhardness ($HV \sim 380$). All tested conditions show a microhardness decrease after heating to 660 °C. The detailed explanation of the microhardness evolution is described in the following section.

4. Discussion

4.1. Electrical resistance measurement

The increase of the electrical resistance of Ti-6Al-7Nb alloy in both initial and ECAP conditions upon heating is concave and at higher temperatures, it even declines (cf. Fig. 1). The decrease of the resistance above 700 °C is caused by the increased amount of the β -phase, which has lower resistance than the α -phase. Similar behavior was reported in Ti-6Al-4V which contains around 15% of β -phase at 750 °C and 20% of β -phase at 800 °C [34]. The second derivative of the evolution of electrical resistance (Fig. 2) indicates that only the first run of the ECAP sample significantly differs from the other two runs. This confirms the fact that non-reversible processes must have occurred during the first heating run of the material which do not take place during subsequent heating runs. Recovery processes can be therefore successfully identified by electrical resistance measurement as it was also shown in our previous work [19].

4.2. Microstructure and lattice defects after ECAP

SEM observations indicate that the microstructure of Ti-6Al-7Nb alloy after ECAP is partly refined, but significantly less deformed than after processing by high pressure torsion (HPT) [14]. Very high dislocation density ρ_D exceeding $5 \times 10^{15} m^{-2}$ and the high concentration of vacancy clusters $c_V > 20$ ppm were determined by PAS.

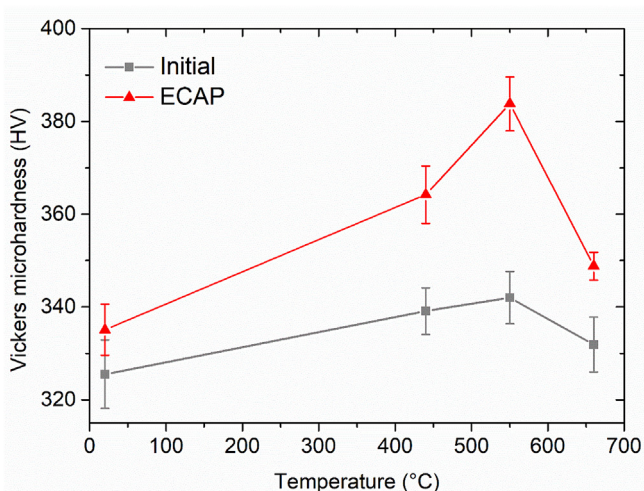


Fig. 9. Temperature dependence of the Vickers microhardness in the initial and ECAP conditions. The annealing temperatures were 440 °C, 550 °C, and 660 °C.

The formation of vacancy clusters depends on the crystalline structure of the material. While vacancy clusters are observed after severe plastic deformation in the studied Ti-6Al-7Nb alloy which consists mainly of hexagonal close packed (HCP) α -phase [14], they are not observed in similarly deformed Ti-15Mo alloy which contains only the body centered cubic (BCC) β -phase [32]. This can be associated with increased diffusivity of single vacancies in BCC material which prevents the formation of vacancy clusters.

In summary, defect structure and microstructure after severe plastic deformation is in thermodynamically unstable condition and contains excessive amounts of point defects (vacancy clusters), line defects (dislocations) and planar defects (refined grain structure).

4.3. Recovery and recrystallization processes

After heating of the ECAP sample up to 440 °C, the concentration of vacancy clusters decreases, while their average size increases. On the other hand, the density of dislocations does not change significantly and no microstructural changes can be observed by SEM. It is consistent with the fact that point defects recover before line and planar defects [35]. Note also that electrical resistance measurement is not sensitive to the recovery of vacancy clusters [35].

Upon heating to 550 °C and 660 °C, the dislocation density decreases significantly as observed both by XRD and PAS. However, the precise comparison of the results achieved by these two methods is not straightforward because XRD is influenced mainly by dislocations in the interior of the sub-grains (crystallites, coherently diffracting domains) that cause peak broadening. On the other hand, PAS detects all dislocation (positrons get trapped at them) disregarding their structure [36]. The crystallite size determined by XRD significantly increased after heating to 550 °C and 660 °C, which is consistent with dislocation density evolution and electrical resistance measurement. It can be concluded that microstructure undergoes recovery processes at temperatures above 440 °C. However, no apparent microstructure changes were observed by SEM in the condition after heating even up to 550 °C. Only SEM observations of the sample heated up to 660 °C showed defect free α -phase grains and significant globularization of the β -phase particles. This is consistent with the electrical resistance measurements and also with the observations of material annealed at 600 °C for 1 h in Ref. [16].

Distinction between recovery and recrystallization is not obvious from the achieved results. As reviewed in Ref. [37], severely deformed materials often undergo process of *continuous static recrystallization* (CSRX), which does not include the nucleation of new grains, but rather a rapid static recovery of dislocations, followed by grain boundary migration, spheroidization of grains/particles and grain growth. This theory is consistent with the achieved results.

4.4. Microhardness

The annealing of the Ti-6Al-7Nb alloy in the initial condition leads to the strengthening of the material which is caused by the precipitation of the Ti_3Al particles [9]. This thermo-mechanical treatment is typical for titanium alloys and results in the superior strength [38,39]. On the other hand, the decrease of the microhardness of the initial sample after heating up to 660 °C can be attributed to the dissolution of the Ti_3Al particles.

Formation of Ti_3Al particles can be experimentally proven neither by SEM nor by XRD as they are extremely small. The particles were observed by advanced methods of TEM and 3D atom probe tomography after 5 weeks of aging of Ti-6Al-4V alloy at

500 °C [40]. Note, however, that Ti₃Al particles affect the strength and microhardness of the material even though they have not been directly observed, yet [41]. The kinetics of formation of Ti₃Al particles are strongly dependent on element partitioning in the $\alpha + \beta$ alloy, namely on the content of Al. The formation of Ti₃Al is therefore easier in the primary α phase that contains a higher amount of Al. In this case, the formation of Ti₃Al is enhanced by thermomechanical processing before ECAP causing significant element partitioning as it is shown in Fig. 3a and quantified by EDS. Furthermore, diffusion of Al atoms required for the formation of Ti₃Al particles is enhanced in the severely deformed material due to increased concentration of vacancies and increased dislocation density. This results in the significant microhardness increase in the ECAP condition.

In the material prepared by ECAP at 600 °C and subsequent extrusion at 300 °C (ECAP sample), Ti₃Al particles could not precipitate. This heavily deformed condition exhibits only slightly enhanced microhardness when compared to the initial condition. Microstructural refinement itself, therefore, does not provide significant additional strengthening in a two-phase $\alpha + \beta$ alloy, contrary to single phase β -alloys [42]. On the other hand, upon heating, the strengthening of deformed material is significantly enhanced.

In conclusion, the microhardness level achieved for severely deformed (ECAP) and subsequently annealed material could not be achieved by a thermal treatment only.

4.5. Coincidence Doppler broadening

The main conclusion from the unique observation by coincidence Doppler broadening (CDB) is that Al atoms are present at the dislocation cores with three times higher concentration ($x_{Al,D} = 0.35$ for ECAP specimen and even $x_{Al,D} = 0.40$ for specimen after heating to 660 °C) than is the average atomic concentration of Al in the alloy (11 at.%).

The interaction between Al atoms and dislocation is clearly proven, however, dislocations can be pinned on substitutionally solved Al atoms or on the Ti₃Al particles or both.

Microhardness measurement suggests that Ti₃Al particles are formed during annealing, which is further partially supported by the fact that the concentration of Al atoms at dislocation cores $x_{Al,D}$ is even increased after annealing. Note that utilization of the CDB method for assessing chemical environment of defects is possible only for material with very high defect densities, such as severely deformed materials.

5. Conclusions

The following conclusions can be drawn from this experimental study:

- The ultra-fine grained condition of biomedical Ti-6Al-7Nb alloy was achieved by equal channel angular pressing. The duplex microstructure of this condition is characterized by deformed primary α -grains and fragmented $\alpha + \beta$ region.
- X-ray diffraction and positron annihilation spectroscopy proved a very high dislocation density and the presence of high concentration of vacancy clusters in the material after ECAP.
- Measurement of electrical resistance is capable to detect microstructural changes during heating and allowed to select the temperatures of 440 °C, 550 °C and, 660 °C for post-mortem characterization of the material.
- During heating to the terminal temperature of 440 °C, vacancy clusters significantly recovered, while dislocation density remained unchanged. The dislocation density decreased after heating to 550 °C. The recovery and recrystallization processes

after heating to temperature 660 °C were clearly proven also by SEM.

- Enhanced microhardness can be achieved by ECAP followed by annealing treatment.
- Preferential pinning of dislocations by Al atoms was proven by coincidence Doppler broadening method (CDB) method.

Author contributions

V. Polyakova and I. Semenova performed the ECAP deformation. P. Zháňal and M. Hájek performed the in-situ electrical resistance measurement. K. Bartha in collaboration with P. Harcuba performed the SEM observations. F. Lukáč and M. Dopita performed the XRD measurements and integrated refinements using the XRD data. J. Čížek performed the PAS and CDB measurement and also evaluated the measured data. The microhardness measurement was done by K. Bartha. Particular parts were written by authors responsible for measurements. K. Bartha, J. Stráský and M. Janeček wrote majority of the manuscript text. All authors reviewed and approved the final draft of the manuscript.

Conflicts of interest

The authors declare no conflict of interests.

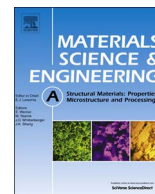
Acknowledgement

This work was financially supported by the Czech Science Foundation under the project 16-12598S. Partial financial support by the Ministry of Education, Youth and Sports under the project LTARF18010 are also gratefully acknowledged. One of the authors, J.C. acknowledges financial support by the Czech Science Foundation under the project 17-17016S. The student K-B acknowledges financial support by Grant Agency of Charles University project no. 1106216 and by SVV-260442.

References

- [1] M. Geetha, A.K. Singh, R. Asokamani, A.K. Gogia, Ti based biomaterials, the ultimate choice for orthopaedic implants – a review, *Prog. Mater. Sci.* 54 (2009) 397–425. <https://doi.org/10.1016/j.pmatsci.2008.06.004>.
- [2] S. Ehtemam-Haghighi, K.G. Prashanth, H. Attar, A.K. Chaubey, G.H. Cao, L.C. Zhang, Evaluation of mechanical and wear properties of Ti-xNb-7Fe alloys designed for biomedical applications, *Mater. Des.* 111 (2016) 592–599. <https://doi.org/10.1016/j.matdes.2016.09.029>.
- [3] K.S. Katti, Biomaterials in total joint replacement, *Colloids Surfaces B Bio-interfaces* 39 (2004) 133–142. <https://doi.org/10.1016/j.colsurfb.2003.12.002>.
- [4] C. Leyens, M. Peters, *Titanium and Titanium Alloys: Fundamentals and Applications*, Wiley-VCH, 2003.
- [5] M. Niinomi, Recent research and development in titanium alloys for biomedical applications and healthcare goods, *Sci. Technol. Adv. Mater.* 4 (2003) 445–454. <https://doi.org/10.1016/j.stam.2003.09.002>.
- [6] H.J. Rack, J.I. Qazi, Titanium alloys for biomedical applications, *Mater. Sci. Eng. C* 26 (2006) 1269–1277. <https://doi.org/10.1016/j.msec.2005.08.032>.
- [7] S.G. Steinemann, Titanium – the material of choice, *Periodontology* 2000 (17) (1998) 7–21. <https://doi.org/10.1111/j.1600-0757.1998.tb00119.x>.
- [8] M. Niinomi, Mechanical biocompatibilities of titanium alloys for biomedical applications, *J. Mech. Behav. Biomed.* 1 (2008) 30–42. <https://doi.org/10.1016/j.jmbbm.2007.07.001>.
- [9] G. Welsch, R. Boyer, E.W. Collings, *Materials Properties Handbook: Titanium Alloys*, ASM International, 1993.
- [10] X. Liu, P.K. Chu, C. Ding, Surface modification of titanium, titanium alloys, and related materials for biomedical applications, *Mater. Sci. Eng. R* 47 (2004) 49–121. <https://doi.org/10.1016/j.mser.2004.11.001>.
- [11] M. Niinomi, Mechanical properties of biomedical titanium alloys, *Mater. Sci. Eng. A* 243 (1998) 231–236. [https://doi.org/10.1016/S0921-5093\(97\)00806-X](https://doi.org/10.1016/S0921-5093(97)00806-X).
- [12] V.M. Segal, Materials processing by simple shear, *Mater. Sci. Eng. A* 197 (1995) 157–164. [https://doi.org/10.1016/0921-5093\(95\)09705-8](https://doi.org/10.1016/0921-5093(95)09705-8).
- [13] R.Z. Valiev, T.G. Langdon, Principles of equal-channel angular pressing as a processing tool for grain refinement, *Prog. Mater. Sci.* 51 (2006) 881–981. <https://doi.org/10.1016/j.pmatsci.2006.02.003>.

- [14] M. Janeček, et al., Mechanical properties and dislocation structure evolution in Ti6Al7Nb alloy processed by high pressure torsion, *Metall. Mater. Trans. A* 45 (2014) 7–15. <https://doi.org/10.1007/s11661-013-1763-2>.
- [15] V.V. Polyakova, V.N. Anumalasetty, I.P. Semenova, R.Z. Valiev, Influence of UFG structure formation on mechanical and fatigue properties in Ti-6Al-7Nb alloy, *IOP Conf. Ser. Mater. Sci. Eng.* 63 (2014), 012162. <https://doi.org/10.1088/1757-899X/63/1/012162>.
- [16] V. Polyakova, I.P. Semenova, R.Z. Valiev, Influence of annealing on the structure and mechanical properties of ultrafine-grained alloy Ti-6Al-7Nb, processed by severe plastic deformation, *Mater. Sci. Forum* 667–669 (2011) 943–948. <https://doi.org/10.4028/www.scientific.net/MSF.667-669.943>.
- [17] F. Prima, P. Vermaut, D. Ansel, J. Debuigne omega, Precipitation in a beta metastable titanium alloy, resistometric study, *Mater. Trans. JIM.* 41 (2000) 1092–1097. <https://doi.org/10.2320/matertrans1989.41.1092>.
- [18] P. Zháňal, et al., Evolution of ω phase during heating of metastable β titanium alloy Ti-15Mo, *J. Mater. Sci.* 53 (2018) 837–845. <https://doi.org/10.1007/s10853-017-1519-2>.
- [19] P. Zháňal, et al., Thermal stability of ultrafine-grained commercial purity Ti and Ti-6Al-7Nb alloy investigated by electrical resistance, microhardness and scanning electron microscopy, *Mater. Sci. Eng. A* 651 (2016) 886–892. <https://doi.org/10.1016/j.msea.2015.11.029>.
- [20] P. Hautojärvi, *Positrons in Solids*, Springer-Verlag, Berlin Heidelberg, 1979.
- [21] M. Alatalo, et al., Identification of vacancy defects in compound semiconductors by core-electron annihilation: application to InP, *Phys. Rev. B* 51 (1995) 4176–4185. <https://doi.org/10.1103/PhysRevB.51.4176>.
- [22] P. Asoka-Kumar, M. Alatalo, V.J. Ghosh, A.C. Kruseman, B. Nielsen, K.G. Lynn, Increased elemental specificity of positron annihilation spectra, *Phys. Rev. Lett.* 77 (1996) 2097–2100. <https://doi.org/10.1103/PhysRevLett.77.2097>.
- [23] Z. Matěj, A. Kadlecová, M. Janeček, L. Matějová, M. Dopita, R. Kužel, Refining bimodal microstructure of materials with MSTRUCT, *Powder Diffr.* 29 (2014) S35–S41. <https://doi.org/10.1017/S0885715614000852>.
- [24] F. Bečvář, J. Čížek, I. Procházka, J. Janotová, The asset of ultra-fast digitizers for positron-lifetime spectroscopy, *Nucl. Instrum. Methods A* 539 (2005) 372–385. <https://doi.org/10.1016/j.nima.2004.09.031>.
- [25] J. Čížek, M. Vlček, I. Procházka, Digital spectrometer for coincidence measurement of Doppler broadening of positron annihilation radiation, *Nucl. Instrum. Methods A* 623 (2010) 982–994. <https://doi.org/10.1016/j.nima.2010.07.046>.
- [26] P. Scardi, M. Leoni, Whole powder pattern modelling, *Acta Crystallogr.* 58 (2002) 190–200. <https://doi.org/10.1107/S0108767301021298>.
- [27] G. Ribárik, T. Ungár, J. Gubicza, MWP-fit: a program for multiple whole-profile fitting of diffraction peak profiles by ab initio theoretical functions, *J. Appl. Crystallogr.* 34 (2001) 669–676. <https://doi.org/10.1107/S0021889801011451>.
- [28] M. Wilkens, The determination of density and distribution of dislocations in deformed single crystals from broadened X-ray diffraction profiles, *Phys. Status Solidi* 2 (1970) 359–370. <https://doi.org/10.1002/pssa.19700020224>.
- [29] I.C. Dragomir, T. Ungár, Contrast factors of dislocations in the hexagonal crystal system, *J. Appl. Crystallogr.* 35 (2002) 556–564. <https://doi.org/10.1107/S0021889802009536>.
- [30] J. Čížek, et al., Evolution of defects in copper deformed by high-pressure torsion, *Acta Mater.* 59 (2011) 2322–2329. <https://doi.org/10.1016/j.actamat.2010.12.028>.
- [31] J. Čížek, O. Melikhova, Z. Barno vská, I. Procházka, R.K. Islamgaliev, Vacancy clusters in ultra fine grained metals prepared by severe plastic deformation, *J. Phys. Conf. Ser.* 443 (2013), 012008.
- [32] M. Janeček, et al., Microstructure evolution in solution treated Ti15Mo alloy processed by high pressure torsion, *Mater. Char.* 98 (2014) 233–240. <https://doi.org/10.1016/j.matchar.2014.10.024>.
- [33] IOS Press Ebooks - Positron Spectroscopy of Defects in Metals and Semiconductors, 2018. <http://ebooks.iospress.nl/volumearicle/32922>. (Accessed 25 June 2018).
- [34] S. Malinov, P. Markovsky, W. Sha, Z. Guo, Resistivity study and computer modelling of the isothermal transformation kinetics of Ti-6Al-4V and Ti-6Al-2Sn-4Zr-2Mo-0.08Si alloys, *J. Alloys. Compd.* 314 (2001) 181–192. [https://doi.org/10.1016/S0925-8388\(00\)01227-5](https://doi.org/10.1016/S0925-8388(00)01227-5).
- [35] E. Smith, M.S. Stagg, Production and mobility of point defects in titanium and zirconium, *Nature* 189 (1961) 300–301. <https://doi.org/10.1038/189300a0>.
- [36] J. Čížek, et al., Structural characterization of ultrafine-grained interstitial-free steel prepared by severe plastic deformation, *Acta Mater.* 105 (2016) 258–272. <https://doi.org/10.1016/j.actamat.2015.12.039>.
- [37] T. Sakai, A. Belyakov, R. Kaibyshev, H. Miura, J.J. Jonas, Dynamic and post-dynamic recrystallization under hot, cold and severe plastic deformation conditions, *Prog. Mater. Sci.* 60 (2014) 130–207. <https://doi.org/10.1016/j.pmatsci.2013.09.002>.
- [38] G. Welsch, G. Lütjering, K. Gazioglu, W. Bunk, Deformation characteristics of age hardened Ti-6Al-4V, *MTA* 8 (1977) 169–177. <https://doi.org/10.1007/BF02677278>.
- [39] S. Guo, Q. Meng, G. Liao, L. Hu, X. Zhao, Microstructural evolution and mechanical behavior of metastable β -type Ti-25Nb-2Mo-4Sn alloy with high strength and low modulus, *Prog. Nat. Sci.* 23 (2013) 174–182. <https://doi.org/10.1016/j.msea.2018.09.002>.
- [40] Z. Wu, et al., The influence of precipitation of α_2 on properties and microstructure in TIMETAL 6-4, *Metall. Mater. Trans. A* 44 (2012) 1706–1713. <https://doi.org/10.1007/s11661-012-1530-9>.
- [41] D.-G. Lee, S. Lee, Y. Lee, Effect of precipitates on damping capacity and mechanical properties of Ti-6Al-4V alloy, *Mater. Sci. Eng. A* 486 (2008) 19–26. <https://doi.org/10.1016/j.msea.2007.08.053>.
- [42] K. Václavová, et al., Microhardness and microstructure evolution of ultra-fine grained Ti-15Mo and TIMETAL LCB alloys prepared by high pressure torsion, *Mater. Sci. Eng. A* 682 (2017) 220–228. <https://doi.org/10.1016/j.msea.2016.11.038>.



Microhardness and microstructure evolution of ultra-fine grained Ti-15Mo and TIMETAL LCB alloys prepared by high pressure torsion

Kristína Václavová^{a,*}, Josef Stráský^a, Veronika Polyakova^b, Jitka Stráská^a, Jitka Nejezchlebová^c, Hanuš Seiner^d, Irina Semenova^b, Miloš Janeček^a

^a Charles University in Prague, Department of Physics of Materials, Ke Karlovu 5, Prague 121 16, Czech Republic

^b UFA State Aviation Technical University, Institute of Physics of Advanced Materials, K. Marx Street 12, Ufa 450 000, Russia

^c Czech Technical University in Prague, Faculty of Nuclear Sciences and Physical Engineering, Trojanova 13, Prague 120 00, Czech Republic

^d Academy of Sciences of the Czech Republic, Institute of Thermomechanics, Dolejškova 5, 18 200 Prague, Czech Republic

ARTICLE INFO

Keywords:

Metastable β -Ti alloys
High pressure torsion
Microhardness
Microstructure evolution
Twinning-induced grain refinement
Decreasing elastic constants

ABSTRACT

Two metastable β -Ti alloys, Ti-15Mo and Ti-6.8Mo-4.5Fe-1.5Al (TIMETAL LCB) were solution treated and subjected to severe plastic deformation by high pressure torsion. The evolution of microhardness, microstructure and elastic constants with increasing strain imposed by high pressure torsion was investigated.

Fragmentation of the microstructure with increasing strain was observed by scanning electron microscopy. Significant twinning in system $\{1\ 1\ 2\} \langle 111 \rangle$ after high pressure torsion was observed in both studied alloys by electron backscatter diffraction. Multiple twinning contributes significantly to the fragmentation of grains and consequently to the overall refinement of the microstructure.

Microhardness significantly increases with increasing strain and was fitted using the Hollomon and Voce laws. Hollomon's hardenability exponent is much higher for both studied β -Ti alloys than for the commonly used Ti-6Al-4V alloy. It reflects high capability of strengthening β -Ti alloys by intensive plastic deformation.

The measurement of elastic constants using resonant ultrasound spectroscopy showed that the deformation by high pressure torsion increases the Young's modulus as compared to solution treated material. On the other hand, further straining causes subsequent decrease of the Young's modulus.

1. Introduction

The importance of the β -titanium alloys in commercial practice has been increasing in the last few decades due to successful utilizing their unique properties such as high strength, low specific density, strengthening capability, high fracture toughness, and excellent corrosion resistance [1,2]. β -Ti alloys are extensively used in aircraft industry [3] and considered as prospective candidates for biomedical implants manufacturing due to their excellent biocompatibility and relatively low Young's modulus preventing the stress shielding [4–8]. However, a high strength condition is usually achieved by advanced thermo-mechanical treatment involving precipitation of α -phase particles, which significantly increases the Young's modulus [9,10].

Severe plastic deformation (SPD) methods strengthen metallic materials via reducing the grain size and increasing the dislocation density [11]. Furthermore, Young's modulus can be reduced by the microstructural refinement. It was also reported that the functional properties such as corrosion resistance and biocompatibility might be also improved by the microstructure refinement [12].

Ultra-fine grained (UFG) commercially pure titanium (CP Ti) was prepared by high pressure torsion (HPT) [13] and equal-channel angular pressing (ECAP) [14] almost two decades ago. Furthermore, UFG $\alpha+\beta$ Ti alloys such as Ti-6Al-4V alloy and specialized biocompatible Ti-6Al-7Nb alloy were also studied in detail [15,16] and exhibited significantly improved strength and fatigue resistance [17,18].

On the other hand, there is only limited literature on the UFG metastable β -Ti alloys. Reports focused primarily on the study of the enhanced strength, fatigue performance [19,20] and microstructural refinement [21,22]. The elastic properties of UFG β -Ti alloy were studied only in alloys containing niobium as the main alloying element [23,24].

The mechanism of the grain refinement in the β -titanium alloys can vary widely, depending on the specific alloy composition, grain size, deformation mode, temperature and pressure [25]. The classical mechanism of the grain refinement is based on the movement of dislocations, formation of dislocation walls and sub-grain boundaries followed by lattice rotation forming high-angle grain boundaries [26]. However, the grain refinement can be also induced by twinning

* Corresponding author.

E-mail address: kristina.vaclavova@gmail.com (K. Václavová).

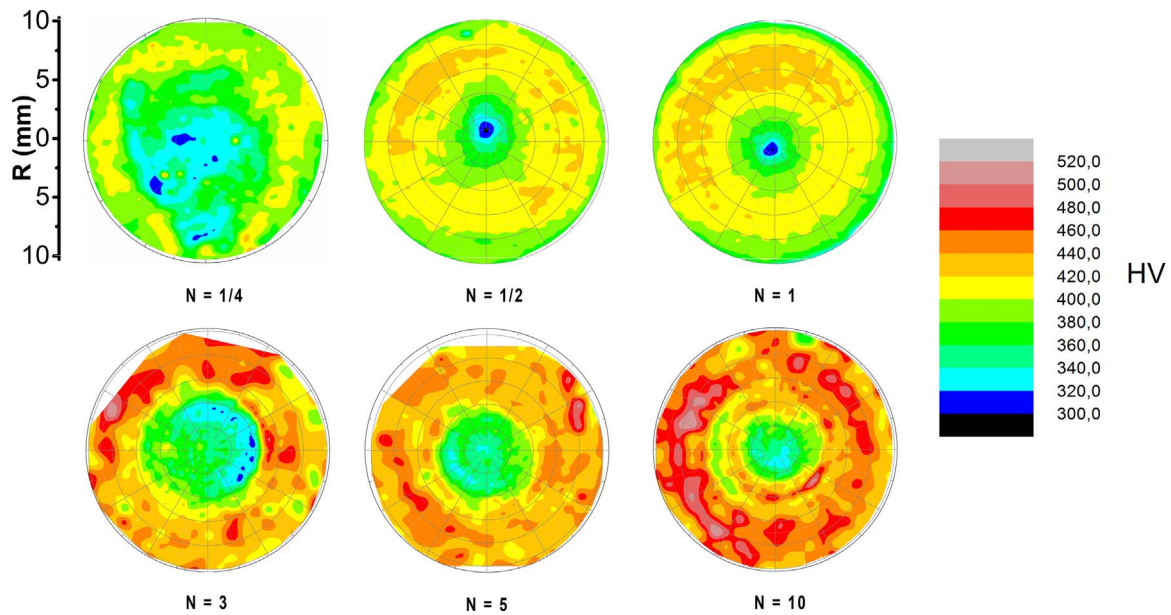


Fig. 1. Microhardness of Ti-15Mo alloy after various numbers of HPT turns represented by color-coded polar diagram. (For interpretation of the references to color in this figure, the reader is referred to the web version of this article.)

followed by lattice rotation. The two main mechanical twinning systems in bcc materials including β -Ti alloys are $\{1\ 1\ 2\} \langle 1\ 1\ 1 \rangle$ [27–30] and $\{3\ 3\ 2\} \langle 1\ 1\ 3 \rangle$ [31,32], the latter one being activated especially at low temperatures and at high strain rates.

Two metastable β -Ti alloys were used in this study: Ti-15Mo alloy and Ti-6.8Mo-4.5Fe-1.5Al alloy (TIMETAL LCB). Ti-15Mo alloy exhibits good mechanical properties, does not contain any toxic elements such as vanadium and therefore is suitable for a medical use. The TIMETAL LCB (low-cost beta) alloy is characterized by lower production costs due to the partial replacement of the relatively expensive β stabilizing alloying elements such as vanadium or molybdenum by iron. The TIMETAL LCB alloy was commercially used for suspension springs manufacturing, since the weight of a suspension spring can be reduced by 60% thanks to the high strength, low density and reduced Young's modulus of the alloy [9] when compared to previously used steels.

The objective of the present study is to examine the evolution of the microstructure, mechanical and elastic properties of two metastable β -Ti alloys with imposed equivalent strain.

2. Experimental

Ti-15Mo alloy was supplied by Carpenter Technology Corp. in a form of a rod with the diameter of 10.5 mm. Ti-6.8Mo-4.5Fe-1.5Al alloy was produced on demand by Huizhou Top Metals Ltd. using magnetic levitation melting and finally wire-cut to the diameter of 20 mm. The as-delivered material was solution treated (1083 K, 20 min) in a protective Ar atmosphere and water quenched. Ti-15Mo alloy was further cut to cylinders (diameter 10.5 mm, height approx. 5 mm) and pressed in HPT machine at room temperature to obtain the desired diameter of 20 mm. The principle of HPT method is described in detail in [33].

Samples with the diameter of 20 mm and the thickness of 1 mm were prepared by HPT at Ufa State Aviation Technical University (USATU) Ufa, Russia at room temperature and the pressure of 2 GPa. A series of samples after $N=1/4, 1/2, 1, 3, 5$ and 10 turns and $N=1/4, 1/2, 1$ and 5 turns of HPT was prepared from Ti-15Mo alloy and TIMETAL LCB alloy, respectively. The total equivalent strain imposed in the sample by HPT can be expressed by the von Mises approach, which utilizes a simple torsion, and the strain is then expressed by the linear relation [34]:

$$\epsilon_{\text{vonMises}} = \frac{2\pi Nr}{\sqrt{3}h}, \quad (1)$$

where N is the number of rotations, r represents the distance from the sample centre and h is the final thickness of the specimen. The equivalent strain imposed by pressing is about 1.5, while equivalent strains imposed by the torsion are by two decades higher. The thickness is therefore neglected.

Microhardness measurements were carried out using the automatic microhardness tester Qness Q10a by Vickers method; 1 kg load and dwell time of 10 s were applied. More than 1000 indents were automatically evaluated along concentric circles, which allows a detailed investigation of microhardness variations on both the surface and the cross-section of the disc.

The scanning electron microscope FEI Quanta 200 FX operated at 10 kV was used for microstructural observations and electron backscatter diffraction (EBSD) analysis.

Young's modulus and Poisson's ratio were evaluated by the resonant ultrasound spectroscopy (RUS) [35] using a fully contactless laser-based RUS set-up described in detail in [36]. This set-up utilizes focused laser pulses for generating the vibrations in the examined sample and the scanning laser beam for the interferometric detection of the modal response. Five different conditions after different stages of straining were used for RUS measurements for each alloy. All samples were rectangular parallelepipeds with the approximate dimensions of $2 \times 2 \times 1 \text{ mm}^3$. For the RUS measurements, the materials of all samples were considered as elastically isotropic, with only two independent elastic constants: Young's modulus E and Poisson's ratio ν .

3. Results

3.1. Microhardness

3.1.1. Ti-15Mo

The microhardness evolution with the increasing number of HPT turns on the specimen's surface is depicted as a series of color-coded images in the Fig. 1. The variations of the microhardness in the cross-section of the specimens are shown in the Fig. 2. The microhardness increases with the increasing distance r from the centre and with the increasing number N of HPT turns. In each image in the Fig. 1, two distinct regions are clearly visible – a central region with a low

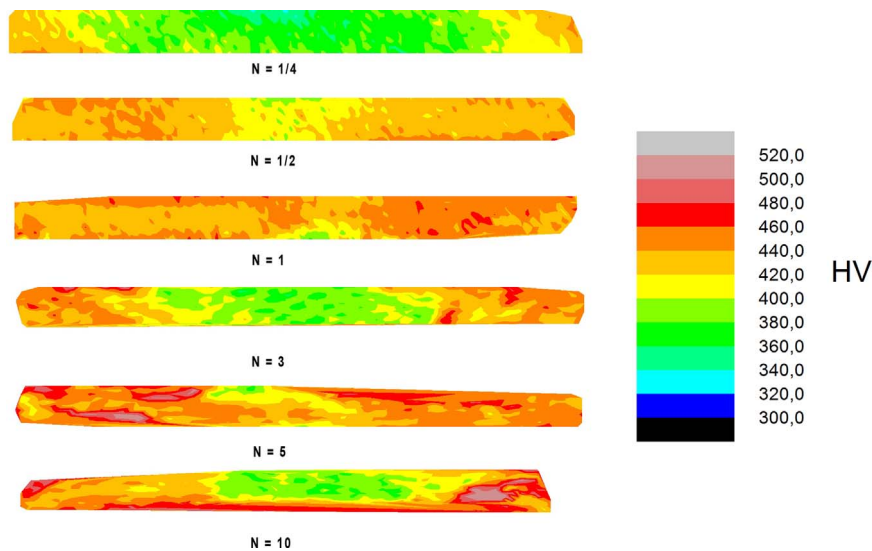


Fig. 2. Microhardness variations through thickness of Ti-15Mo alloy processed by HPT (vertical axis is extended for better visibility). (For interpretation of the references to color in this figure, the reader is referred to the web version of this article.)

microhardness (blue color) and the peripheral region with an increased microhardness (red color). The microhardness in the peripheral region increases with the increasing number of HPT turns. The decrease of the microhardness near the edge of the sample is caused by the material outflow during HPT processing. The microhardness is not homogeneous through the sample thickness (Fig. 2). However, no systematic differences were identified.

3.1.2. TIMETAL LCB

The microhardness evolution in the TIMETAL LCB alloy after different number of HPT turns is presented similarly as for the Ti-

15Mo alloy. Vickers microhardness of the TIMETAL LCB alloy after $N = 1/4, 1/2, 1$ and 5 HPT turns was measured on the sample surface (Fig. 3.) and in the cross-section (Fig. 4). Similarly as in the Ti-15Mo alloy, the microhardness increases with the number of HPT turns and also with the increasing distance from the centre of the specimen with exception of specimen edge, where the decreased microhardness is caused by the material outflow. The microhardness in TIMETAL LCB is more homogenous than in the case of Ti-15Mo, especially after 5 rotations.

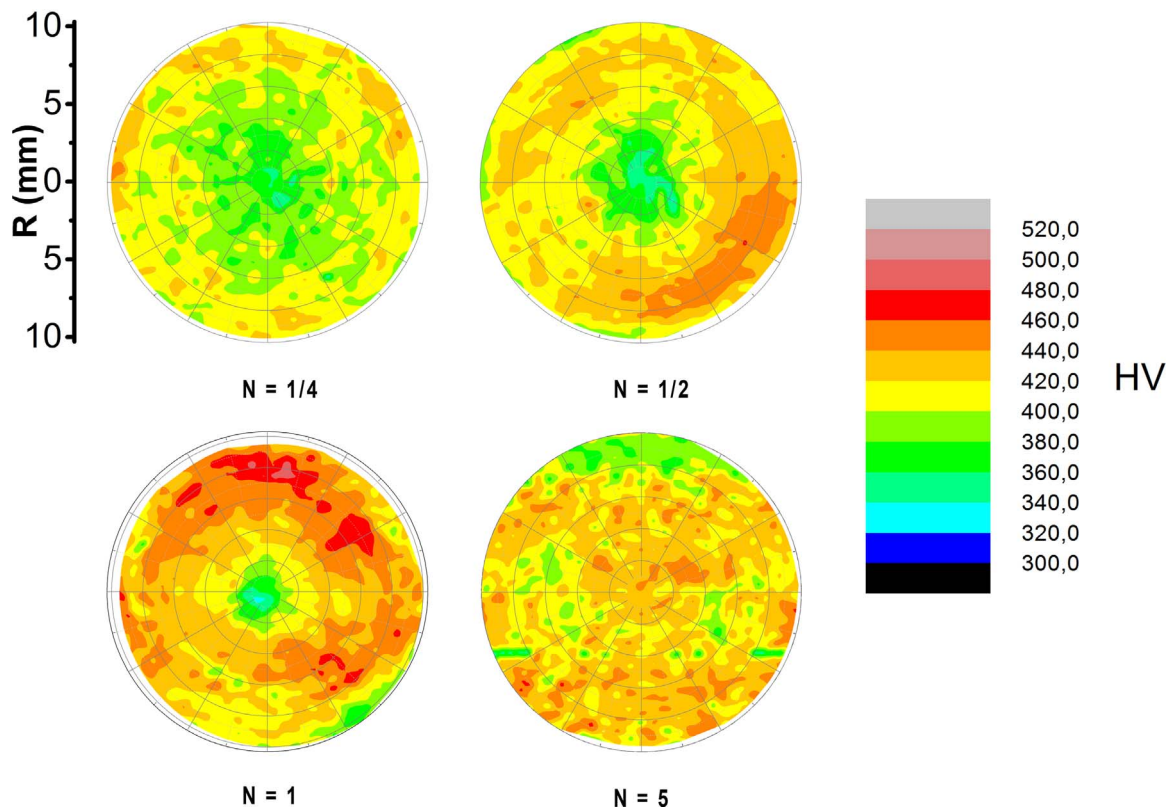


Fig. 3. Microhardness of TIMETAL LCB alloy after various number of HPT turns represented on color-coded polar diagram. (For interpretation of the references to color in this figure, the reader is referred to the web version of this article.)

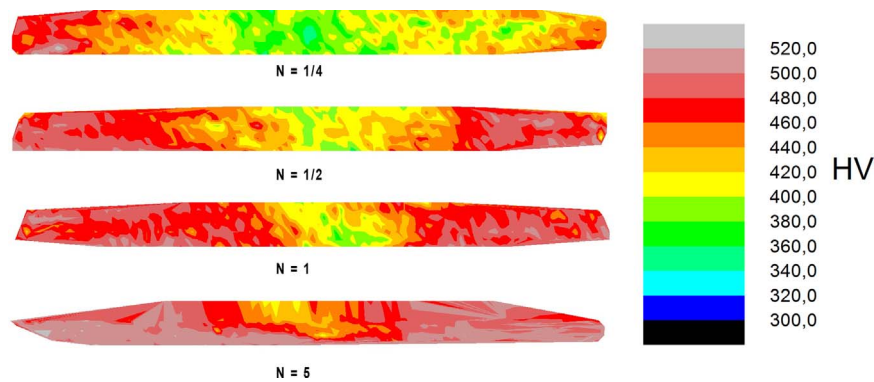


Fig. 4. Microhardness variations through thickness of TIMETAL LCB alloy processed by HPT (vertical axis is extended for better visibility). (For interpretation of the references to color in this figure, the reader is referred to the web version of this article.)

3.2. Microstructure evolution/refinement

Scanning electron microscopy was used to study initial stages of the microstructure refinement in both alloys during HPT. Due to the expected lateral inhomogeneity of the microstructure caused by an inhomogeneous character of the imposed strain by HPT, the microstructure was investigated in three regions, namely in the centre of the disc, near the half of the radius of the disc (referred to as “middle”) and near the disc periphery.

3.2.1. Ti-15Mo

Ti-15Mo alloy in the β solution treated condition before HPT processing (not shown) consists of equiaxed grains with the average size of 20 – 50 μm . In the Fig. 5. the microstructure of the Ti-15Mo alloy sample after $N = 1/4$ HPT turns is shown. Comparatively large ($\sim 20 \mu\text{m}$) heavily deformed grains were observed in the disc centre (Fig. 5a). In the “middle” region the microstructure is more deformed and inhomogeneous consisting of bigger grains surrounded by small grains (Fig. 5b). On the disc periphery, a refined grain structure is observed (Fig. 5c).

Contrast in the SEM images is given predominantly by the channelling of electrons along differently oriented crystallographic planes. However, it was proven by energy dispersive X-ray (EDX) analysis that the observed bands in Fig. 5c are caused by segregation of Mo atoms. The average chemical composition of lighter and darker parts in Fig. 5 is summarized in Table 1. It is obvious that darker parts contain less Mo. The same segregation of Mo atoms is claimed in [37]. However, the mechanism of element partitioning is unknown.

3.2.2. TIMETAL LCB

The cast and solution treated TIMETAL LCB alloy consists of very large grains with size up to 1 mm (not shown). The microstructure of the TIMETAL LCB alloy after $N = 1/4$ HPT turn is depicted in the Fig. 6. In the centre part, original large though deformed grains were observed (Fig. 6a). In the “middle” part, bigger grains are surrounded by small grains and the microstructure is clearly heavily twinned [32]. In the

Table 1

EDX analysis of bands occurring in the periphery of the sample.

wt%	Ti	Mo
Darker bands	85.65	14.35
Lighter bands	83.26	16.74

periphery, grains are not clearly distinguishable and lighter bands can be observed (Fig. 6c).

The microstructure of the specimens with higher imposed strain ($N > 1/4$) could not be resolved by SEM due to the strong grain refinement. Refined microstructure of Ti-15Mo alloy prepared by HPT was shown by transmission electron microscopy in our previous study [38].

The initial stages of the microstructure refinement by HPT were investigated by the EBSD. Fig. 7. shows a high-resolution inverse pole figure (IPF) map from the centre part of the Ti-15Mo alloy after $N = 1/4$ HPT turn. High ($\theta > 15^\circ$) and low-angle grain boundaries ($5^\circ < \theta < 15^\circ$) are highlighted in black and red color, respectively (θ denotes the misorientation angle).

The microstructure consists of heavily deformed and twinned grains. The fragmentation of grains and formation of a UFG microstructure is visible especially in the right part of the image. Black areas in IPF map correspond to the points which could not be successfully indexed due to high deformation.

In the Fig. 8, the IPF image from the middle part of the TIMETAL LCB alloy after $N = 1/4$ HPT rotation is shown. Regular black squares in the image are indents from the preceding microhardness measurement. Lattice rotation within grains and significant twinning can be observed. Twinning-induced grain refinement is clearly visible in the bottom right corner.

3.3. Measurement of elastic constants of β -Ti alloys

Elastic constants of Ti-15Mo and TIMETAL LCB alloys in the

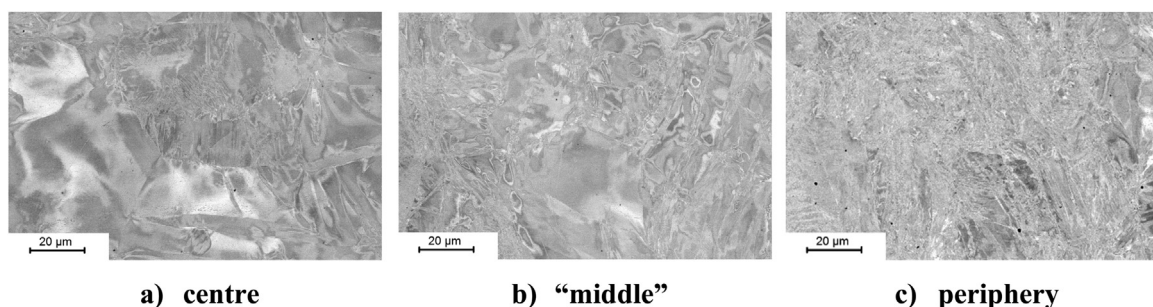


Fig. 5. SEM images of Ti-15Mo alloy after $N = 1/4$ HPT turns (channelling contrast). a) centre. b) “middle”. c) periphery.

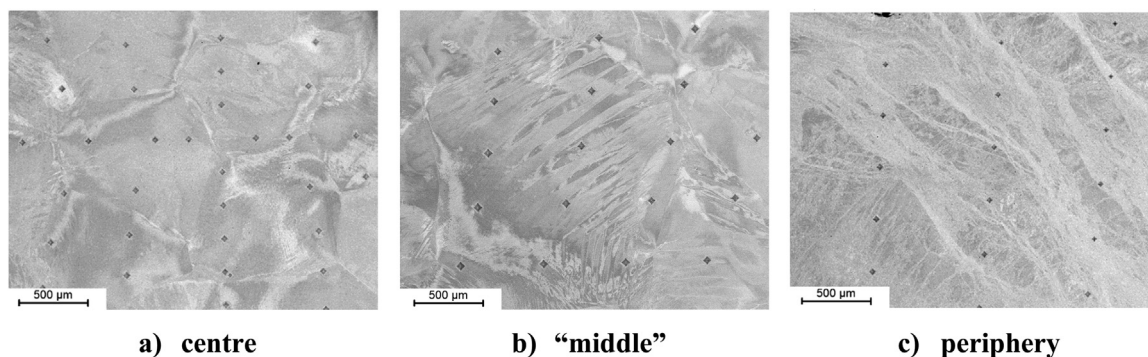


Fig. 6. SEM images of TIMETAL LCB alloy after $N = 1/4$ HPT turns (channelling contrast). a) centre. b) “middle”. c) periphery.

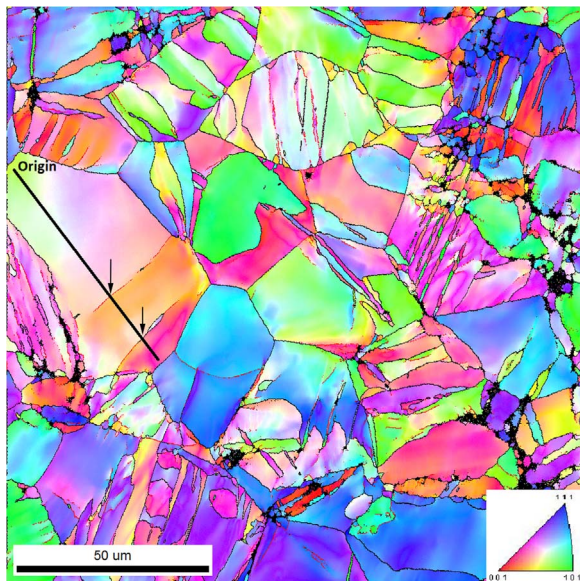


Fig. 7. Inverse pole figure map from the centre part of the Ti-15Mo alloy after $N = 1/4$ HPT turn; misorientation measured along the highlighted black line. (For interpretation of the references to color in this figure, the reader is referred to the web version of this article.)

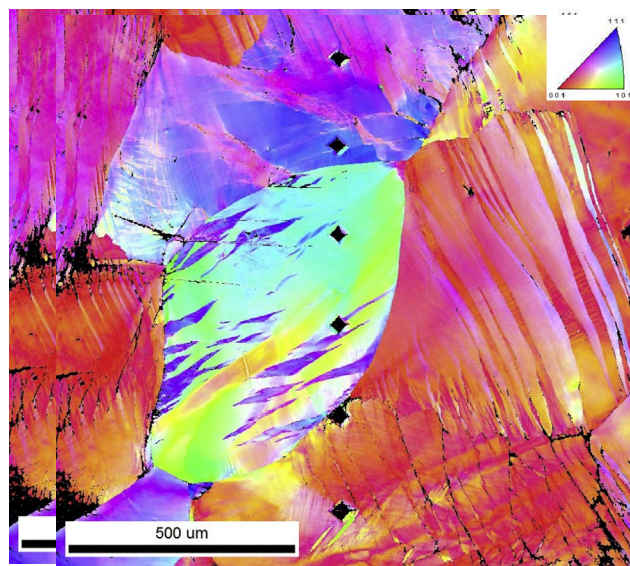


Fig. 8. Inverse pole figure map of TIMETAL LCB alloy after $1/4$ HPT turn (middle part). (For interpretation of the references to color in this figure, the reader is referred to the web version of this article.)

Table 2

Young's modulus and Poisson's ratio of Ti-15Mo and TIMETAL LCB alloys after different number of HPT turns.

	Young's modulus E (GPa)		Poisson's ratio ν	
	Centre	Periphery	Centre	Periphery
Ti-15Mo ST	91.0		0.361	
Ti-15Mo $N=1$	98.1	92.8	0.348	0.359
Ti-15Mo $N=5$	96.6	91.4	0.357	0.367
TIMETAL LCB ST	80.1		0.38	
TIMETAL LCB $N=1$	91.2	88.6	0.362	0.367
TIMETAL LCB $N=5$	89.7	86.7	0.367	0.377

solution treated (ST) condition and after $N = 1$ and 5 HPT turns were measured. Table 2 contains results of the Young's modulus and the Poisson's ratio ν of alloy after different number of HPT rotations and in different regions of the disc. The standard deviations of the Young's modulus and the Poisson's ratio is ± 1 GPa and ± 0.01 , respectively.

4. Discussion

4.1. Microhardness

The microhardness of the Ti-15Mo alloy increases from HV ≈ 310 (solution treated coarse-grained material) to HV ≈ 450 (heavily deformed material after HPT). Maximum strength achieved in a ductile $\alpha+\beta$ aged condition is 1150 MPa [39], which corresponds approximately to HV ≈ 390 . HPT deformation of the β ST condition therefore results in higher hardness than in the $\alpha+\beta$ aged condition. Contrary to the precipitation hardening, SPD increases the strength while retaining the β phase with lower Young's modulus. Achieving high strength and low modulus simultaneously is crucial for potential application of the material in biomedicine as an implant material.

Vickers microhardness of the β ST condition of the TIMETAL LCB alloy HV ≈ 340 is slightly higher than that of Ti-15Mo alloy due to solid solution strengthening by Fe and Al as reported in [40,41]. The microhardness achieved by HPT deformation exceeds the hardness of the aged two-phase $\alpha+\beta$ condition [42].

Three types of strength evolution with increasing strain during HPT were proposed for different metals and alloys: strain hardening without recovery, strain hardening with recovery and strain softening [43]. In the present study, strain hardening without recovery is dominant since recovery processes in Ti alloys are not activated at room temperature.

The microhardness increase due to imposed equivalent strain can be modelled by empirical work hardening models such as Hollomon model [44] or Voce model [45]. The Von Mises equivalent strain by HPT was calculated according to the Eq. (1) and the evolution of microhardness was depicted for the Ti-15Mo alloy (Fig. 9) and the TIMETAL LCB alloy (Fig. 10). All data points were used for the calculation, i.e. both from the measurement on the disc surface and

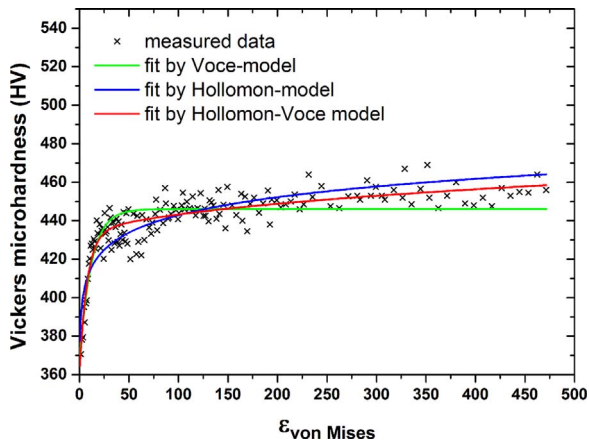


Fig. 9. Evolution of the microhardness with equivalent strain in Ti-15Mo alloy. The red line denotes the fitted microhardness according to the Eq. (4), blue and green line according to the Eq. (2) and Eq. (3), respectively. (For interpretation of the references to color in this figure, the reader is referred to the web version of this article.)

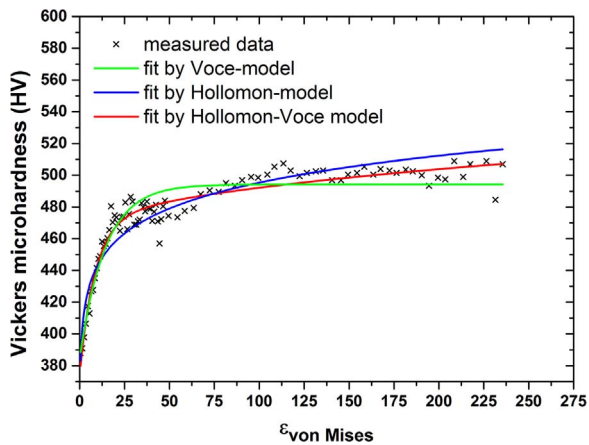


Fig. 10. Variation of the measured microhardness values with equivalent strain of TIMETAL LCB alloy. The red line denotes the fitted microhardness according to the Eq. (4), blue and green line according to the Eq. (2) and Eq. (3), respectively. (For interpretation of the references to color in this figure, the reader is referred to the web version of this article.)

cross-section. Data corresponding to the leaking off the material near the edge of the discs were neglected. Fitting with weighting was employed.

According to [44], the hardness evolution with strain was first fitted by the Hollomon-type equation:

$$HV(\varepsilon) = K \cdot \varepsilon^m + HV_0^H, \quad (2)$$

where ε is the Von Mises equivalent strain, $HV(\varepsilon)$ is the measured Vickers microhardness of the material, m is the hardenability exponent, K is a material constant and HV_0^H is a fitting parameter which corresponds to the microhardness of the initial material.

The Hollomon model (Eq. (2)) does not account for the microhardness saturation which occurs at high strains. Eq. (3) represents Voce-type equation, which assumes exponential saturation of microhardness at a value HV_{max}^V :

$$HV(\varepsilon) = HV_{max}^V - (HV_{max}^V - HV_0^V) \exp(-L \cdot \varepsilon), \quad (3)$$

where HV_0^V is a fitting parameter corresponding to the initial microhardness at $\varepsilon=0$, HV_{max}^V is a fitting parameter corresponding to the saturation value of the hardness and L can be regarded as the saturation rate.

The microhardness of the studied alloys increases very fast with increasing Von Mises strain up to the strain $\varepsilon \approx 50$. However, the microhardness does not completely saturate even for very high strains.

Table 3

Fitting parameters for Ti-15Mo, TIMETAL LCB and Ti-6Al-4V alloys.

	HV_0	HV_{max}	m	K	L
Ti-15Mo	358	458	0.44	2.13	0.13
TIMETAL LCB	372	461	0.46	3.68	0.12
Ti-6Al-4V[43]	311	364	1.4×10^{-8}	3.87	0.06

Consequently, none of the models resulted in a satisfactory fit. Therefore, the sum of the Hollomon-type and Voce-type model (hereinafter referred to as Hollomon-Voce model) was used for modelling of hardening of studied alloys (Eq.(4)):

$$HV(\varepsilon) = HV_{max}^V + HV_0^H + K \cdot \varepsilon^m - (HV_{max}^V - HV_0^V) \exp(-L \cdot \varepsilon) \quad (4)$$

Resulting fits are shown in Figs. 9 and 10 (red line). The fits by the Hollomon model (blue line) and the Voce model (green line) are also displayed. It is clear, that the combined Hollomon-Voce curve matches the experimental data much better than the individual models. Fitting parameters observed from Hollomon-Voce model are listed in Table 3. Initial microhardness HV_0 represents the sum of fitting parameters HV_0^H and HV_0^V . HV_{max} represents the sum of maximum microhardness of the fitting function, i.e. $HV_{max} = HV_{max}^V + K \cdot \varepsilon_{max}^m$. For comparison, analogous fitting procedure was employed for the microhardness data for the Ti-6Al-4V alloy deformed by HPT reported in [43].

Note, that the HV_0 values of 358 and 372 HV from the fit for the Ti-15Mo and the TIMETAL LCB alloys, respectively, are significantly higher than the values measured for the initial coarse-grained material (310 and 340 HV for the studied alloys, respectively). The reason is that the increase of microhardness at low strains is very sharp and HV_0 value is sensitive to fitting procedure. Additionally, neglecting the reduction of sample thickness in the calculation of the Von Mises strain may also affect the result of fitting at low strains.

Negligible Hollomon hardenability exponent m for the Ti-6Al-4V alloy [43] means that the microhardness increase in this case can be completely modelled by Voce model. The strengthening capability of the studied β -Ti alloys is much higher than that of Ti-6Al-4V alloy and therefore SPD processing of solution treated β -Ti alloys is even more beneficial than in the case of pure Ti or $\alpha+\beta$ alloys. Very high microhardness of the investigated β -Ti alloys can be attributed to the increased dislocation density [38] and the grain fragmentation. Strengthening can be also caused by deformation-induced ω -phase [46,47]. However, the confirmation of this hypothesis needs further investigation which is beyond the scope of this paper.

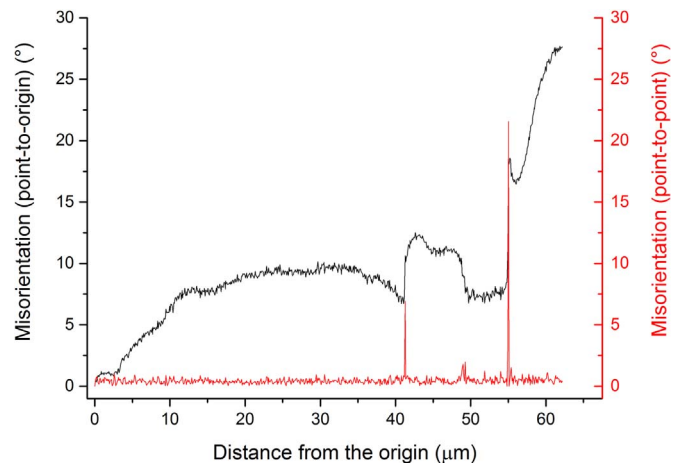


Fig. 11. Misorientation variations along the highlighted black line in Fig. 9. (For interpretation of the references to color in this figure, the reader is referred to the web version of this article.)

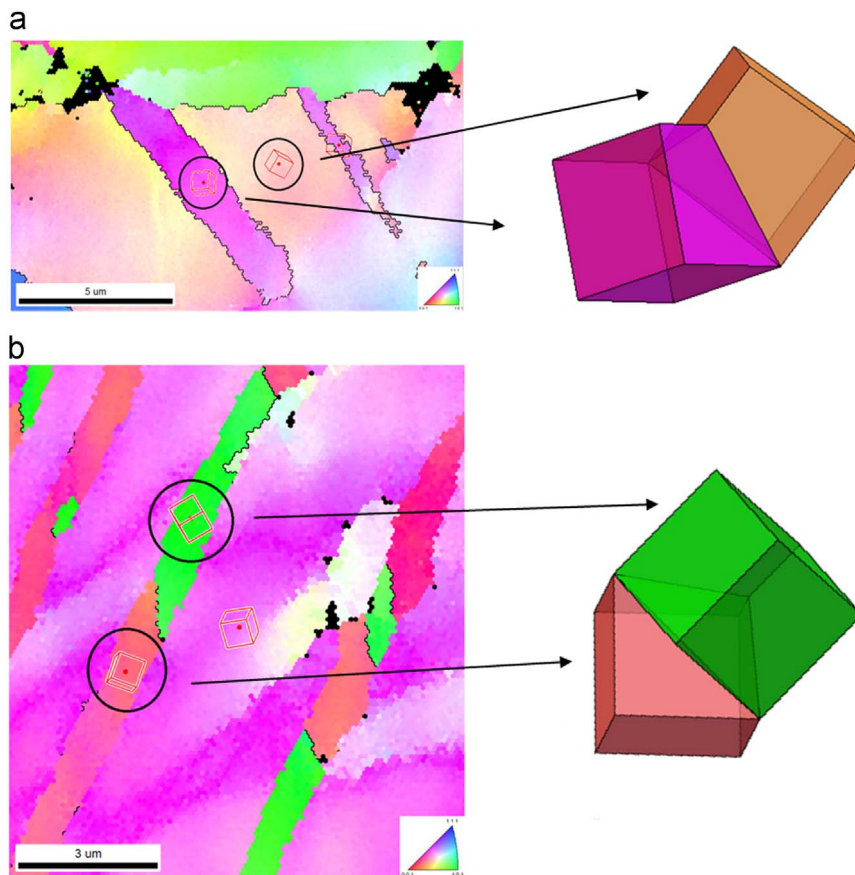


Fig. 12. The detail of the inverse pole figure from Fig. 7 (Ti-15Mo, $N=1/4$) showing the primary and secondary twins. a. Left figure: IPF image - the orientations of the matrix and twins are indicated. Right sketch: Graphical representation of the twinning system between the matrix and the twin. b. Left figure: The orientation of the primary and secondary twins are indicated. Right sketch: Graphical representation of the secondary twinning. (For interpretation of the references to color in this figure, the reader is referred to the web version of this article.)

4.2. Multiple twinning as the mechanism of grain refinement

The activity of twinning system $\{1\ 1\ 2\} \langle 1\ 1\ 1 \rangle$ in Ti-15Mo alloy is clearly documented by EBSD mapping. Moreover, it can be shown that the primary twins undergo additional secondary twinning. It is concluded that multiple mechanical twinning significantly contributes to the microstructure refinement.

EBSD observations prove the common mechanism of the grain refinement consisting of the combination of dislocation density accumulation, lattice rotation, formation of dislocation walls and subgrain boundaries. The lattice rotation within a grain was identified by misorientation variations along the black line shown in Fig. 7. The point-to-origin and point-to-point misorientations are shown in Fig. 11 by a black and red line, respectively. The misorientation within the grain increases up to 10° which suggests a high degree of imposed strain and a high density of dislocations stored in the material deformed by HPT. In the distances of approximately $42\ \mu\text{m}$ and $55\ \mu\text{m}$ from the selected origin, the point-to-point misorientation abruptly changes. It corresponds to the position of sub-grain boundaries, which are also clearly visible in Fig. 7 (marked by arrows).

Detail analysis of the EBSD observations revealed an alternative mechanism of grain refinement, namely twinning-induced grain refinement.

Fig. 12a shows the detail from the Fig. 7 along with a schematic illustration of the twin orientation. From the graphic representation it is clearly visible that twinning occurs in the system $\{1\ 1\ 2\} \langle 1\ 1\ 1 \rangle$. Consequently, the misorientation between the parent matrix and the twin is approx. 55° .

In the Fig. 12b the secondary twinning is shown and graphically

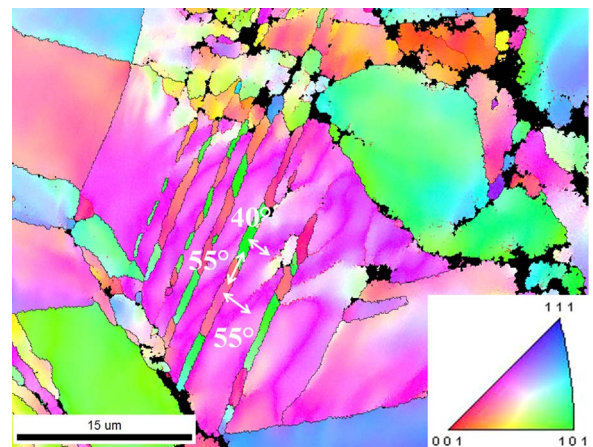


Fig. 13. Inverse pole figure map of twinned grain of Ti-15Mo alloy after $N=1/4$ HPT turn. (For interpretation of the references to color in this figure, the reader is referred to the web version of this article.)

illustrated. It is unambiguously proven that the system of secondary twinning is again $\{1\ 1\ 2\} \langle 1\ 1\ 1 \rangle$.

Fig. 13 is a bigger excerpt from Fig. 7 showing that the multiple twinning in Ti-15Mo alloy contribute to grain refinement of material. The misorientation values prove that the twin shown in red is a primary twin formed from the matrix, whereas the twin shown in green is a secondary twin which was formed from the primary one.

Twinning induced grain refinement was also reported in magnesium alloys (hcp structure) [48,49], stainless steel (fcc structure) [50],

copper (fcc structure) [51]. In commercially pure Ti (hcp structure) the twinning-induced grain refinement is well documented [52–54]. On the other hand, to our knowledge, grain refinement by multiple twinning has not yet been reported in metastable β -Ti alloys (bcc structure) deformed by SPD.

4.3. Elastic constants of HPT deformed β -Ti alloys

HPT deformation affects the elastic properties of the studied alloys. The Young's modulus of Ti-15Mo alloy after N=1 HPT turn in the centre of the specimen (lowest deformation) is 98.1 GPa while the Young's modulus of initial ST material was 91 GPa. The Young's modulus decreases with further straining, i.e. with increasing number of HPT turns and increasing distance from the centre of the sample and the final Young's modulus (98.4) is comparable to that of ST material. Similar trend can be observed for TIMETAL LCB alloy: the Young's modulus of HPT deformed material in the centre of the sample (91.2 GPa) is higher than the Young's modulus of the ST condition (80.1 GPa). Increasing deformation leads to a decrease of Young's modulus, but the final value for (N=5, periphery) remains higher than that of solution treated material. Alterations in Young's modulus might be caused by the deformation induced ω -phase observed in [37,55]. The Young's modulus of ω -phase reaches 200 GPa [56] and even a small fraction of ω -phase affects the elastic properties. According to [57], 10% ω -phase forms from the β -matrix after 1 HPT turn, while further deformation by 10 HPT turns leads to a reverse phase transformation. In the case of TIMETAL LCB, the recovery of the Young's modulus is not complete, which suggests that the deformation induced ω -phase is not fully reverted. A decrease of Young's modulus with increasing deformation might be further caused by increasing density of free-volume defects such as non-equilibrium grain boundaries and the density dislocations (see [57] and other references therein).

The first HPT turn induces also a measurable decrease of the Poisson's ratio, especially in the central part of samples. This can be again explained by formation of a small volume fraction of the ω -phase, as the isotropic Poisson's ratio for the ω -phase is apparently low, $\nu=0.27$ [56]. With increasing deformation, the value of ν fully recovers. The experimental results from the measurement of the Young's modulus of Ti-15Mo alloy are comparable with the results indicated in [58].

The increase of Young's modulus due to the formation of ω -phase is adverse for potential application in biomedicine, where low Young's modulus is required. It might be beneficial to use alloys less prone to ω -phase formation, for instance Ti-Nb based alloys if low Young's modulus is the major concern. However, the Young's modulus of ultra-fine grained Ti-15Mo and TIMETAL LCB alloys with increased hardness is still significantly lower than the Young's modulus of Ti-6Al-4V alloy [6].

5. Conclusions

In the present work, the microstructure and the microhardness evolution in ultra-fine grained metastable β -titanium alloys prepared by HPT were investigated. The most important results of this investigation can be summarized as follows:

- Microhardness of Ti-15Mo and TIMETAL LCB alloys increases with increasing von Mises equivalent strain. The highest microhardness of β solution treated material deformed by HPT exceeds significantly the microhardness of commonly used aged two phase $\alpha+\beta$ condition of the same alloys.
- The capability of deformation hardening by HPT in both studied β -Ti alloys is much higher than in common $\alpha+\beta$ Ti-6Al-4V alloy.
- Scanning electron microscopy demonstrated the increasing grain fragmentation with the increasing equivalent strain. Bands with

higher Mo content were identified in severely deformed Ti-15Mo alloy.

- Twinning system $\{112\} \langle 111 \rangle$ is active during HPT deformation. Multiple twinning contributes to the grain refinement in bcc β -Ti alloys.
- The Young's modulus' variations with the strain due in the investigated β -Ti alloys were nonmonotonous. Young's modulus first increases after the initial stage of the HPT deformation, while it decreases with further straining. This can be explained by the enhanced stress-induced ω -phase formation in the initial stages of HPT straining and is further supported by the simultaneous decrease of the Poisson's ratio during the first HPT turn.

Acknowledgement

This work was financially supported by Czech Science Foundation under the project GB 14-36566G. K.V. acknowledges the student project of Grant Agency of Charles University GAUK No. 1106216 and the project SVV-2016–260213.

References

- [1] G. Lütjering, J.C. Williams, *Titanium*, Springer-Verlag, Berlin, Heidelberg, 2003.
- [2] M. Niinomi, Mechanical properties of biomedical titanium alloys, *Mater. Sci. Eng. A* 243 (1998) 231–236. [http://dx.doi.org/10.1016/S0921-5093\(97\)00806-X](http://dx.doi.org/10.1016/S0921-5093(97)00806-X).
- [3] R.R. Boyer, An overview on the use of titanium in the aerospace industry, *Mater. Sci. Eng. A* 213 (1996) 103–114. [http://dx.doi.org/10.1016/0921-5093\(96\)10233-1](http://dx.doi.org/10.1016/0921-5093(96)10233-1).
- [4] D. Kuroda, M. Niinomi, M. Morinaga, Y. Kato, T. Yashiro, Design and mechanical properties of new β type titanium alloys for implant materials, *Mater. Sci. Eng. A* 243 (1998) 244–249. [http://dx.doi.org/10.1016/S0921-5093\(97\)00808-3](http://dx.doi.org/10.1016/S0921-5093(97)00808-3).
- [5] D.F. Williams, *Titanium for Medical Applications*, Springer-Verlag, Berlin, Heidelberg, 2001.
- [6] M. Geetha, A.K. Singh, R. Asokamani, A.K. Gogia, Ti based biomaterials, the ultimate choice for orthopaedic implants – a review, *Prog. Mater. Sci.* 54 (2009) 397–425. <http://dx.doi.org/10.1016/j.pmatsci.2008.06.004>.
- [7] E.S.N. Lopes, R.J. Contieri, S.T. Button, R. Caram, Femoral hip stem prosthesis made of graded elastic modulus metastable β Ti alloy, *Mater. Des.* 69 (2015) 30–36. <http://dx.doi.org/10.1016/j.matdes.2014.11.040>.
- [8] M. Niinomi, Recent research and development in titanium alloys for biomedical applications and healthcare goods, *Sci. Technol. Adv. Mat.* 4 (2003) 445–454. <http://dx.doi.org/10.1016/j.stam.2003.09.002>.
- [9] C. Leyens, M. Peters, *Titanium and Titanium Alloys*, WILEY-VCH Verlag, Weinheim, 2003.
- [10] J.C. Fanning, Properties of TIMETAL 555 (Ti-5Al-5Mo-5V-3Cr-0.6Fe), *J. Mater. Eng. Perform.* 14 (2005) 788–791. <http://dx.doi.org/10.1361/105994905x75628>.
- [11] A.P. Zhilyaev, T.G. Langdon, Using high-pressure torsion for metal processing: fundamentals and applications, *Prog. Mater. Sci.* 53 (2008) 893–979. <http://dx.doi.org/10.1016/j.pmatsci.2008.03.002>.
- [12] R.Z. Valiev, et al., Nanostructured SPD processed titanium for medical implants, *Mater. Sci. Forum* 584–586 (2008) 49–54.
- [13] A.A. Popov, et al., Structural and mechanical properties of nanocrystalline titanium processed by severe plastic deformation, *Scr. Mater.* 37 (1997) 1089–1094. [http://dx.doi.org/10.1016/S1359-6462\(97\)00210-8](http://dx.doi.org/10.1016/S1359-6462(97)00210-8).
- [14] R.Z. Valiev, Structure and mechanical properties of ultrafine-grained metals, *Mater. Sci. Eng. A* 234–236 (1997) 59–66. [http://dx.doi.org/10.1016/S0921-5093\(97\)00183-4](http://dx.doi.org/10.1016/S0921-5093(97)00183-4).
- [15] I.P. Semenova, G.I. Raab, L.R. Saitova, R.Z. Valiev, The effect of equal-channel angular pressing on the structure and mechanical behaviour of Ti-6Al-4V alloy, *Mater. Sci. Eng. A* 387–389 (2004) 805–808. <http://dx.doi.org/10.1016/j.msea.2004.02.093>.
- [16] M. Janeček, et al., Mechanical properties and dislocation structure evolution in Ti6Al7Nb alloy processed by high pressure torsion, *Metall. Mater. Trans. A* 45A (2014) 7–15. <http://dx.doi.org/10.1007/s11661-013-1763-2>.
- [17] L.R. Saitova, H.W. Hoppel, M. Göken, I.P. Semenova, R.Z. Valiev, Cyclic deformation behaviour and fatigue lives of ultrafine-grained Ti-6Al-4V EEL alloy for biomedical use, *Int. J. Fatigue* 31 (2009) 322–331. <http://dx.doi.org/10.1016/j.ijfatigue.2008.08.007>.
- [18] V. Polyakova, I.P. Semenova, R.Z. Valiev, Influence of annealing on the structure and mechanical properties of ultrafine-grained alloy Ti-6Al-7Nb, processed by severe plastic deformation, *Mater. Sci. Forum* 667–669 (2010) 943–948.
- [19] Z.B. Zhang, Y.L. Hao, S.J. Li, R. Yang, Fatigue behaviour of ultrafine-grained Ti-24Nb-4Zr-8Sn multifunctional biomedical titanium alloy, *Mater. Sci. Eng. A* 577 (2013) 225–233. <http://dx.doi.org/10.1016/j.msea.2013.04.051>.
- [20] D. Kent, G. Wang, Z. Yu, X. Ma, M. Dargusch, Strength enhancement of a biomedical titanium alloy through modified accumulative roll bonding technique, *J. Mech. Behav. Biomed. Mater.* 4 (2011) 405–416. <http://dx.doi.org/10.1016/j.jmbbm.2010.11.013>.
- [21] T. Li, D. Kent, G. Sha, M. Dargusch, J.M. Cairney, Precipitation of the α -phase in an

- ultrafine grained beta-titanium alloy processed by severe plastic deformation, *Mater. Sci. Eng. A* 605 (2014) 144–150. <http://dx.doi.org/10.1016/j.msea.2014.03.044>.
- [22] D. Kent, W.L. Xiao, G. Wang, Z. Yu, M.S. Dargusch, Thermal stability of an ultrafine grain β -Ti alloy, *Mater. Sci. Eng. A* 556 (2012) 582–587. <http://dx.doi.org/10.1016/j.msea.2012.07.030>.
- [23] M. Geetha, A.K. Singh, R. Asokamani, A.K. Gogia, Ti based biomaterials, the ultimate choice for orthopaedic implants – a review, *Prog. Mater. Sci.* 54 (2009) 397–425.
- [24] Kelvin Y. Xie, et al., Nanocrystalline β -Ti alloy with high hardness, low Young's modulus and excellent in vitro biocompatibility for biomedical applications, *Mater. Sci. Eng. C* 33 (2013) 3530–3536.
- [25] I. Weiss, S.L. Semiatin, Thermomechanical processing of beta titanium alloys – an overview, *Mater. Sci. Eng. A* 243 (1998) 46–65. [http://dx.doi.org/10.1016/S0921-5093\(97\)00783-1](http://dx.doi.org/10.1016/S0921-5093(97)00783-1).
- [26] G. Gottstein, *Physical Foundations of Materials Science*, Springer-Verlag, 2004.
- [27] H. Paxton, Experimental verification of the twin system in alpha-iron, *Acta Metall.* 1 (1953) 141–143. [http://dx.doi.org/10.1016/0001-6160\(53\)90052-2](http://dx.doi.org/10.1016/0001-6160(53)90052-2).
- [28] J.W. Christian, S. Mahajan, Deformation twinning and its effect on crack extension, *Prog. Mater. Sci.* 39 (1995) 1–157. [http://dx.doi.org/10.1016/0079-6425\(94\)00007-7](http://dx.doi.org/10.1016/0079-6425(94)00007-7).
- [29] Y. Wang, et al., Deformation twinning during nanoindentation of nanocrystalline Ta, *Appl. Phys. Lett.* 86 (2005) 101915. <http://dx.doi.org/10.1063/1.1883335>.
- [30] Y. Yang, S. Wu, G. Li, Y. Li, Y. Lu, K. Yang, P. Ge, Evolution of deformation mechanisms of Ti–22.4Nb–0.73Ta–2Zr–1.34O alloy during straining, *Acta Mater.* 58 (2010) 2778–2787. <http://dx.doi.org/10.1016/j.actamat.2010.01.015>.
- [31] X.H. Min, et al., {3 3 2} <1 1 3> Twinning system selection on a β -type Ti–15Mo–5Zr polycrystalline alloy, *Mater. Sci. Eng. A* 579 (2013) 164–169. <http://dx.doi.org/10.1016/j.msea.2013.04.119>.
- [32] X.H. Min, K. Tsuzaki, S. Emura, K. Tsuchiya, Heterogeneous twin formation and its effect on tensile properties in Ti–Mo based β titanium alloys, *Mater. Sci. Eng. A* 554 (2012) 53–60. <http://dx.doi.org/10.1016/j.msea.2012.06.009>.
- [33] R.Z. Valiev, A.V. Korznikov, R.R. Mulyukov, Structure and properties of ultrafine-grained materials produced by severe plastic deformation, *Mater. Sci. Eng. A* 168 (1993) 141–148.
- [34] R.Z. Valiev, et al., Structure and deformation behaviour of Armcro iron subjected to severe plastic deformation, *Acta Mater.* 44 (1996) 4705–4712. [http://dx.doi.org/10.1016/S1359-6454\(96\)00156-5](http://dx.doi.org/10.1016/S1359-6454(96)00156-5).
- [35] A. Migliori, J.L. Sarrao, W.M. Visscher, T.M. Bell, M. Lei, Z. Fisk, R.G. Leisure, Resonant ultrasound spectroscopic techniques for measurement of the elastic moduli of solids, *Physica B Phys. Condens. Matter* 183 (1993) 1–24.
- [36] P. Sedlák, H. Seiner, J. Zidek, M. Janovská, M. Landa, Determination of all 31 Independent Elastic Coefficients of Generally Anisotropic Solids by Resonant Ultrasound Spectroscopy: Benchmark Ex. Exp. Mech. 54 (2014) 1073–1085. <http://dx.doi.org/10.1007/s11340-014-9862-6>.
- [37] B. Jiang, K. Tsuchiya, S. Emura, X. Min, Effect of high-pressure torsion process on precipitation behaviour of α phase in β -type Ti–15Mo alloy, *Mater. Trans.* 55 (2014) 877–884.
- [38] M. Janeček, et al., Microstructure evolution in solution treated Ti15Mo alloy processed by high pressure torsion, *Mater. Charact.* 98 (2014) 233–240. <http://dx.doi.org/10.1016/j.matchar.2014.10.024>.
- [39] ATI 15Mo Titanium Alloy Technical Sheet, (https://www.atimetals.com/Documents/ati_15Mo_Titanium_Alloy_en_v4%20final.pdf).
- [40] J. Stráský, M. Janeček, P. Hrcuba, M. Landa, Plastic deformation and elastic properties of Ti–Nb–Zr–Ta(–Fe–Si) biomedical alloys, *Adv. Mater. Res.* 922 (2014) 734–739. <http://dx.doi.org/10.4028/www.scientific.net/AMR.922.734>.
- [41] E.W. Collings, *Materials Properties Handbook: Titanium Alloys*, ASM International, 1993.
- [42] J. Šmilauerová, *Phase Transformations and Microstructure Changes in TIMET LCB Alloy* (Master thesis), Charles University in Prague, 2012.
- [43] Y.C. Wang, T.G. Langdon, Effect of heat treatment on microstructure and microhardness evolution in a Ti–6Al–4V alloy processed by high pressure torsion, *J. Mater. Sci.* 48 (2013) 4646–4652. <http://dx.doi.org/10.1007/s10853-012-7071-1>.
- [44] J.H. Hollomon, *Trans. Metall. Soc. AIME* 162 (1945) 268.
- [45] E. Voce, The relationship between stress and strain for homogeneous deformations, *J. Inst. Met.* 74 (1948) 537–562.
- [46] F. Sun, et al., Investigation of early stage deformation mechanisms in a metastable β titanium alloy showing combined twinning-induced plasticity and transformation-induced plasticity effects, *Acta Mater.* 61 (2013) 6406–6417.
- [47] S. Gatina, I. Semenova, M. Janeček, J. Stráský, Effect of high pressure torsion on the aging kinetics of β -titanium Ti–15Mo alloy, *IOP Conf. Ser. Mater. Sci. Eng.* 63 (2014).
- [48] Y. Li, et al., Grain refinement due to complex twin formation in rapid hot forging of magnesium alloy, *Ser. Mater.* 68 (2013) 171–174. <http://dx.doi.org/10.1016/j.scriptamat.2012.10.007>.
- [49] H. Miura, M. Ito, X. Yang, J.J. Jonas, Mechanisms of grain refinement in Mg–6Al–1Zn alloy during hot deformation, *Mater. Sci. Eng. A* 538 (2012) 63–68. <http://dx.doi.org/10.1016/j.msea.2012.01.014>.
- [50] H.W. Zhang, Z.K. Hei, G. Liu, J. Lu, K. Lu, Formation of nanostructured surface layer on AISI 304 stainless steel by means of surface mechanical attrition treatment, *Acta Mater.* 51 (2003) 1871–1881. [http://dx.doi.org/10.1016/S1359-6454\(02\)00594-3](http://dx.doi.org/10.1016/S1359-6454(02)00594-3).
- [51] K. Wang, N.R. Tao, G. Liu, J. Lu, K. Lu, Plastic strain-induced grain refinement at the nanometer scale in copper, *Acta Mater.* 54 (2006) 5281–5291. <http://dx.doi.org/10.1016/j.actamat.2006.07.013>.
- [52] S.V. Zherebtsov, et al., Evolution of grain and subgrain structure during cold rolling of commercial-purity titanium, *Mater. Sci. Eng. A* 528 (2011) 3474–3479. <http://dx.doi.org/10.1016/j.msea.2011.01.039>.
- [53] D.H. Hong, S.K. Hwang, Microstructural refinement of CP-Ti by cryogenic channel-die compression involving mechanical twinning, *Mater. Sci. Eng. A* 555 (2012) 106–116. <http://dx.doi.org/10.1016/j.msea.2012.06.040>.
- [54] C.S. Meredith, A.S. Khan, The microstructural evolution and thermo-mechanical behaviour of UFG Ti processed via equal channel angular pressing, *J. Mater. Process. Technol.* 219 (2015) 257–270. <http://dx.doi.org/10.1016/j.jmatprotec.2014.12.024>.
- [55] B. Koch, B. Skrotzki, Strain controlled fatigue testing of the metastable β -titanium alloy Ti–6.8Mo–4.5Fe–1.5Al (Timetal LCB), *Mater. Sci. Eng. A* 528 (2011) 5999–6005. <http://dx.doi.org/10.1016/j.msea.2011.04.031>.
- [56] M. Tane, Y. Okuda, Y. Todaka, H. Ogi, A. Nagakubo, Elastic properties of single-crystalline ω phase in titanium, *Acta Mater.* 61 (2013) 7543–7554.
- [57] A.B. Lebedev, Y.A. Burenkov, A.E. Romanov, V.I. Kopylov, V.P. Filonenko, V.G. Gyaznov, Softening of the in submicrocrystalline copper, *Mater. Sci. Eng. A* 203 (1995) 165–170.
- [58] S. Gatina, I. Semenova, J. Leuthold, R. Valiev, Nanostructuring and phase transformations in the β -alloy Ti–15Mo during high-pressure torsion, *Adv. Eng. Mater.* 17 (2015) 1742–1747.



Effect of the severe plastic deformation by ECAP on microstructure and phase transformations in Ti-15Mo alloy

K. Bartha^{a,*}, A. Veverková^a, J. Stráský^a, J. Veselý^a, P. Minárik^a, C.A. Corrêa^{a,b}, V. Polyakova^c, I. Semenova^c, M. Janeček^a

^a Department of Physics of Materials, Charles University, Prague, Czech Republic

^b Institute of Physics of the Czech Academy of Sciences, Prague, Czech Republic

^c Institute of Physics of Advanced Materials, Ufa State Aviation Technical University, Ufa, Russia

ARTICLE INFO

Keywords:

Metastable β titanium alloy
Equal channel angular pressing
 α phase precipitation
Microstructure
Transmission Kikuchi diffraction
Phase composition

ABSTRACT

Ti-15Mo alloy in a metastable β solution treated condition was processed by equal channel angular pressing (ECAP) at an elevated temperature of 250 °C. The resulting microstructure is highly deformed, contains twins and shear bands, but is not ultra-fine grained. Both the initial solution treated material and the material after ECAP were subjected to ageing at 400 °C and 500 °C in order to study the effect of deformation on phase transformations, namely the α phase precipitation. The phase composition was studied by X-ray diffraction measurement; the microstructure was investigated using conventional EBSD and an advanced method of transmission Kikuchi diffraction (TKD). It was shown that the α phase precipitation is accelerated in areas with higher density of lattice defects, which provide a dense net of preferred sites for nucleation and also fast diffusion paths necessary for accelerated growth. Upon further annealing, discontinuous lamellar coarsening occurs, which had not been previously reported in metastable β -Ti alloys. The microhardness is governed mainly by the formation of ω phase particles. The fraction of ω phase increases during annealing at 400 °C and the specimen aged at 400 °C/16 h shows the highest value of microhardness of 520 HV for both ECAP and undeformed material. Upon annealing at 500 °C, the microhardness is significantly lower.

1. Introduction

Titanium and its alloys are widely used as biomedical materials due to their light weight, high strength, excellent biocompatibility and corrosion resistance [1]. Over the last decades, extensive research has been devoted to the development of metastable β -titanium alloys containing only non-toxic elements and having a low Young's modulus to avoid stress shielding [2–5]. The most promising alloys are Ti-29Nb-13Ta-4.6 Zr (TNTZ), Ti-15Mo or Ti-Zr-based alloys [6,7].

In this study, Ti-15Mo, a binary metastable β -Ti alloy containing only biocompatible elements was used. This alloy exhibits the tensile strength of 690 MPa and the modulus of elasticity of 78 GPa in a solution treated (ST) condition [8]. The strength of this alloy can be further enhanced by methods of severe plastic deformation (SPD) by introducing a high density of dislocations into the material and reducing its grain size [9,10]. The most widely used SPD methods are equal channel angular pressing (ECAP) [11] and high pressure torsion (HPT) [12]. ECAP is capable of producing specimens with a reasonable size for various biomedical applications [13].

Mechanical properties of metastable β -Ti alloys are significantly affected by phase transformations during processing and subsequent thermal treatment. In some metastable β -Ti alloys (including Ti-15Mo alloy) the thermodynamically metastable ω phase may form during rapid cooling from the high-temperature single β phase field, referred to as ω_{ath} (athermal ω). The mechanism of ω_{ath} phase formation was described as a shift of two neighboring $(111)_\beta$ planes along the body diagonal of the cubic cell to their intermediate position, while one $(111)_\beta$ plane between two pairs of collapsed planes is left unchanged [14]. Typically at temperatures in the range of 300–400 °C, the ω phase particles become stabilized by a diffusion process by rejecting β stabilizer elements [15] and is referred to as ω_{iso} phase. The presence of ω phase increases both the strength and the Young's modulus of the alloy and causes the embrittlement of the material [16]. The size of ω_{ath} does not exceed several nanometers, while the size of ω_{iso} phase particles is typically in tens of nanometers [17]. It has been reported previously that the shuffle $\beta \rightarrow \omega$ transformation is complete only in the central part of an ω particle [18,19], and advanced XRD measurements in [20] proved that in small ω_{ath} particles, the transformation is incomplete

* Corresponding author.

E-mail address: kristina.bartha@met.mff.cuni.cz (K. Bartha).

<https://doi.org/10.1016/j.mtcomm.2019.100811>

Received 13 May 2019; Received in revised form 28 August 2019; Accepted 26 November 2019

Available online 27 November 2019

2352-4928/ © 2019 Elsevier Ltd. All rights reserved.

throughout the whole volume of a particle.

During ageing at higher temperatures (400 °C–700 °C), α phase particles form by nucleation and growth. α particles act as barriers for dislocation motion and strengthen the material without detrimental embrittlement, which is caused by presence of ω_{iso} phase particles [21]. Nucleation of the α phase is heterogeneous and therefore preferentially located at grain boundaries, dislocations or other lattice defects [22–24]. ω phase can also act as nucleation site for α phase precipitation [18,25]. Due to the heterogeneous nature of α phase nucleation, a dense net of nucleation sites (grain boundaries, dislocations) introduced by SPD significantly affects its precipitation. Lattice defects in the β matrix do not only serve as preferred sites for nucleation but also provide fast diffusion paths necessary for accelerated growth.

The effect of SPD deformation on α phase precipitation has been rarely studied. Our previous studies [26,27] focused on improved mechanical properties and grain refinement in Ti-15Mo alloy deformed by HPT at room temperature. Enhanced α phase precipitation in more β -stabilized Ti-20Mo alloy after HPT was reported in [24,28]. The most relevant study is a detail report by Xu et al. [29] who studied Ti-20Mo alloy prepared by ECAP and documented α phase precipitation upon ageing within shear bands in the severely deformed material. Another study by Jiang et al. reported the influence of equiaxed α phase formation in Ti-5Al5Mo-5V-3Cr (Ti-5553) alloy after HPT on the improvement of the ductility of the material [30].

In this study, the effect of the ECAP-deformed microstructure on the ongoing phase transformations upon ageing is thoroughly investigated. Successful ECAP processing of Ti alloys is generally challenging due to their high strength, high toughness and limited ductility. An ECAP die with the outer angle of 120° (i.e. not the most common 90°) and processing at elevated temperatures are usually required [31,32]. Processing of metastable β -Ti alloys in the metastable β solution treated condition at elevated temperatures can be associated with ω phase formation and the loss of ductility. A detailed analysis of the microstructure of the ECAP-deformed Ti-15Mo alloy was carried out by scanning (SEM) and transmission electron microscopy (TEM) as well as by transmission Kikuchi diffraction (TKD). The change of the phase content upon ageing was determined by X-ray diffraction (XRD) measurement. The change of mechanical properties was characterized by microhardness measurements.

2. Experimental materials and methods

The metastable β -Ti alloy used in this study, Ti-15Mo, contains 15 wt % of molybdenum and a negligible amount of other elements [33]. The alloy supplied from Carpenter Co. was solution treated in an inert Ar atmosphere at the temperature of 810 °C for 4 h and quenched in water (hereafter referred to as undeformed samples). Subsequent deformation by ECAP was carried out at Ufa State Aviation Technical University (USATU) in the Russian Federation at the temperature of 250 °C in a die with channel angles $\Phi = 120^\circ$ and $\psi = 0^\circ$ (see Fig. 1). The alloy was subjected to $N = 2$ ECAP passes. The equivalent strain of N ECAP passes can be calculated according to the von Mises equation [34]:

$$\varepsilon_{VM} = N \cdot \frac{1}{\sqrt{3}} \left[2 \cotg \left(\frac{\Phi}{2} + \frac{\psi}{2} \right) + \psi \operatorname{cosec} \left(\frac{\Phi}{2} + \frac{\psi}{2} \right) \right] \quad (1)$$

For $N = 2$ ECAP passes the total equivalent strain is $\varepsilon_{VM} = 1.33$. ECAPed samples were produced in a shape of a rod with the diameter of 10 mm and the length of about 60 mm. Undeformed and ECAPed samples were aged at 400 °C and 500 °C for 1, 4 and 16 h. The samples were immersed in a preheated molten salt bath to avoid oxygen contamination and to ensure a high heating rate; the samples were subsequently quenched in water.

Zeiss Auriga Compact CrossBeam scanning electron microscope equipped with an electron backscatter diffraction (EBSD) camera and

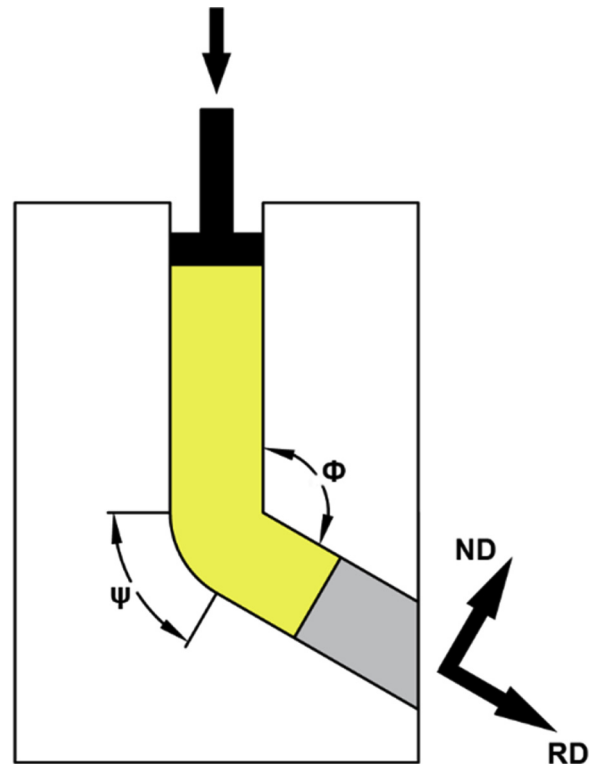


Fig. 1. Schematic representation of the ECAP process and the orientation of the sample (rolling (RD) and normal (ND) directions).

focused ion beam (FIB) was used for SEM analysis. The microscope was operated at 10 kV for standard back-scattered electrons (BSE) observations and EBSD analysis, while the acceleration voltage of 20 kV was used for BSE observations of a thin lamella prepared by FIB and for transmission Kikuchi diffraction (TKD) analysis also referred to as “transmission EBSD” (t-EBSD) [35]. EBSD analysis was carried out in two different planes – parallel to the direction of processing (rolling direction – RD) and perpendicular to the direction of processing (normal direction –ND); see Fig. 1. Thin lamella was prepared by FIB from a selected area for detailed investigation of the deformed microstructure using transmission electron microscope JEOL 2200 FS operated at 200 kV and using the above mentioned TKD method. In the TKD, primary electrons are forward-scattered in a thin lamella and may diffract at various plane systems in a crystalline material (similarly to back-scattered electrons in EBSD analysis). Kikuchi pattern is subsequently detected using a standard EBSD camera. The signal of standard EBSD origins from a narrow layer at the specimen surface while the TKD signal origins from a narrow layer (50–100 nm) at the bottom surface of the prepared thin lamella (150–200 nm).

X-ray powder diffraction (XRD) data were measured on a Bruker D8 Advance diffractometer, Bragg-Brentano geometry, Cu K_{α} radiation, variable divergence slit, and a Sol-X detector. Diffraction patterns were collected at room temperature in the 2θ range from 30° to 130° with a step size of 0.02° and an exposure time of 5 s/step. The patterns were fitted and refined by the program Jana2006 [36] employing the Le Bail algorithm with a pseudo-Voigt profile and ten terms of Legendre polynomials for the background.

Vickers microhardness measurements were performed by an automatic microhardness tester Qness Q10a; 0.5 kg load and a dwell time of 10 s were applied. Size of a microhardness indent is approximately 20 μm . 20 indents were evaluated for each sample.

Samples for SEM, XRD and microhardness measurements were prepared by mechanical grinding followed by a three-step vibratory polishing. Thin TEM foils were prepared by electrochemical thinning using Tenupol-5 jet polishing unit at –20 °C followed by ion polishing

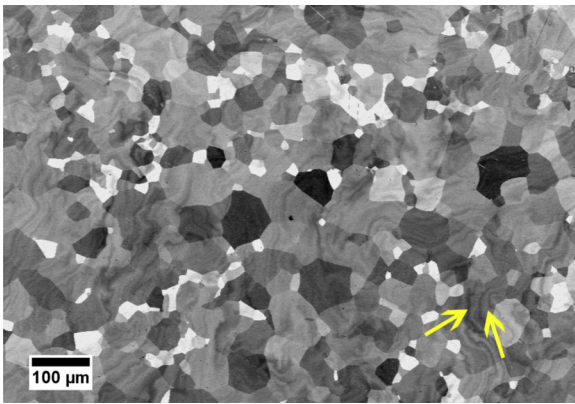


Fig. 2. BSE micrograph of the solution treated (undeformed) sample. The arrows indicate chemical inhomogeneities present throughout the material.

using a Leica EM RES102 ion polisher. A site-specific lamella was cut and thinned using a gallium FIB.

3. Results

3.1. Initial microstructure of Ti-15Mo alloy

Fig. 2 shows the initial microstructure of the Ti-15Mo alloy after solution treatment. Coarse-grained structure with the grain size of $\sim 50 \mu\text{m}$ is well visible due to channelling contrast. Z-contrast shows chemical inhomogeneities observed as wavy features and present everywhere in the initial material. A region containing well visible chemical inhomogeneity is marked by arrows in Fig. 2. Energy dispersive X-ray spectroscopy (EDS) point analyses were carried out at different positions in order to quantify the differences in Mo content. Brighter parts contain $16.7 \pm 0.5 \text{ wt.}\% \text{ Mo}$, while darker parts $14.5 \pm 0.4 \text{ wt.}\% \text{ Mo}$. This slight difference may affect the phase stability of the parent β phase matrix. The nanometer sized ω_{ath} phase, which is present in the ST Ti-15Mo alloy [15], cannot be observed by SEM.

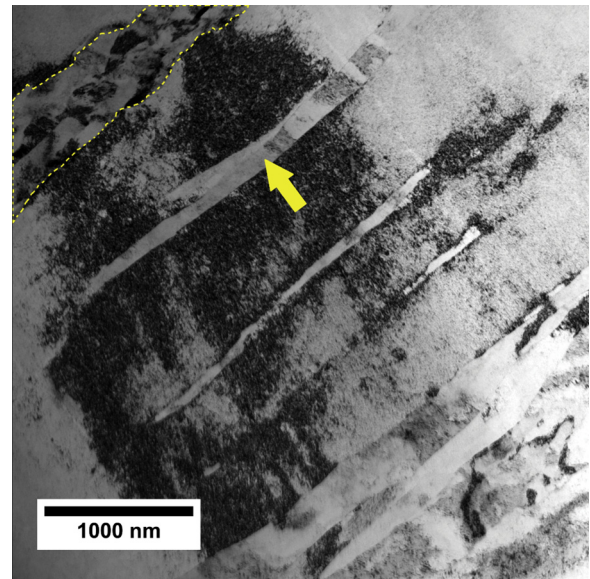


Fig. 4. Bright field TEM image of the microstructure of Ti-15Mo alloy after N = 2 ECAP passes.

3.2. Ti-15Mo alloy after deformation by ECAP

The microstructure of the ECAPed sample after N = 2 ECAP passes in both rolling and normal directions (Fig. 3(a) and (b), respectively) was studied by EBSD. IPF maps in Fig. 3 indicate a highly deformed, but not ultra-fine grained structure of the material. The orientation of the black areas could not be successfully indexed due to a poor quality of diffraction patterns. Grain interiors are significantly deformed as it can be inferred from continuous changes of orientation (color) within individual grains. The activity of the twinning process during ECAP deformation is also visible in Fig. 3, some twins are highlighted by arrows. Twinning in the system $\{112\} < 111 >$ was confirmed from the inverse pole figure (IPF) maps using the values of misorientation. This result is consistent with previous reports in Ti-15Mo alloy [27,37]. Interior of observed twins is also significantly deformed.

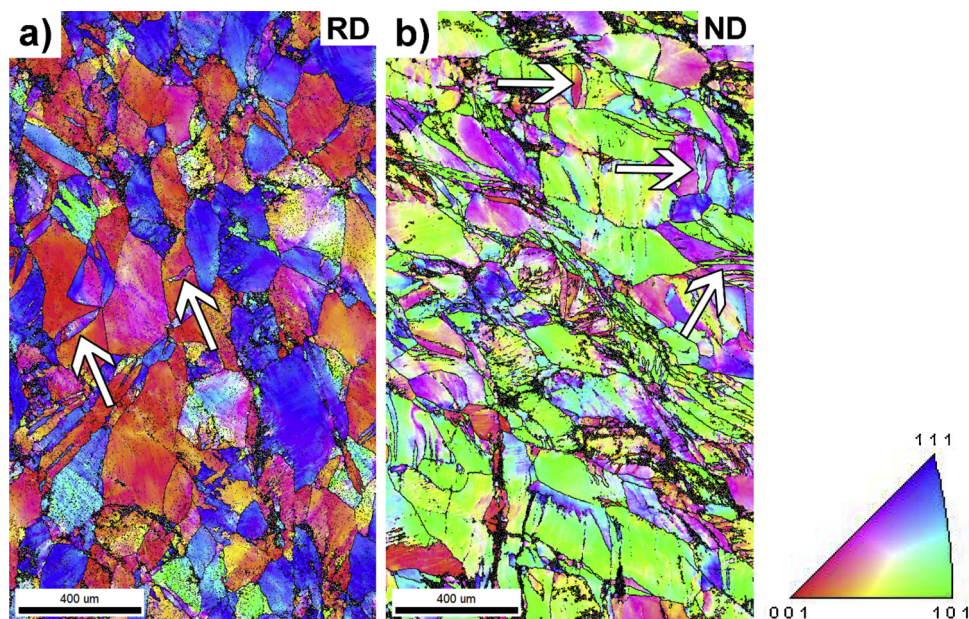


Fig. 3. IPF maps of ECAPed samples in (a) rolling and (b) normal direction of the deformation and the corresponding orientation triangle for BCC structure. The white arrows indicate twins.

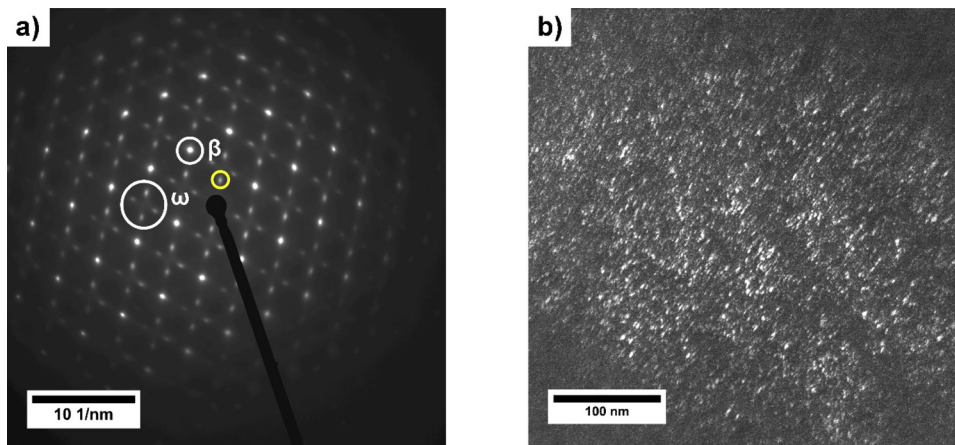


Fig. 5. (a) Diffraction pattern of the parent β matrix in the direction $[110]$ containing ω phase particles and; the yellow circle indicates the ω phase reflection selected for dark field TEM image (b) dark field TEM image of ω phase particles (For interpretation of the references to colour in this figure legend, the reader is referred to the web version of this article).

The deformed microstructure of the specimen after $N = 2$ ECAP passes in the rolling direction was studied in detail by TEM. In the bright field (BF) image in Fig. 4, a severely deformed and twinned grain with a high dislocation density can be observed (one twin is marked by a yellow arrow). Furthermore, in the upper left corner a highly deformed band-like structure consisting of subgrains with a high density of dislocations can be observed (delimited by a yellow dashed line).

Fig. 5(a) shows the $[110]$ zone axis selected area electron diffraction (SAED) pattern from the coarse β grain shown in Fig. 4, clearly exhibiting ω phase reflections at the $1/3$ and $2/3$ $\{112\}_{\beta}$ positions. Dark field (DF) TEM image from one of the ω phase reflections (shown by yellow circle in Fig. 5(a)) is shown in Fig. 5(b). The appearance of the ω phase after ECAP is similar to that previously reported for the ST condition [15]. However, volume fraction and exact size of the ω phase particles cannot be determined from TEM images.

3.3. Microstructure of the ST and ECAPed Ti-15Mo alloy after thermal treatment

Fig. 6 shows SEM micrographs of the microstructure of undeformed specimens after ageing at $400\text{ }^{\circ}\text{C}$ and $500\text{ }^{\circ}\text{C}$ for 4 and 16 h. α phase is not observed after ageing at $400\text{ }^{\circ}\text{C}$ for 4 and 16 h (Figs. 6(a) and (b)). On the other hand, ageing at $500\text{ }^{\circ}\text{C}$ (Fig. 6(c) and (d)) resulted in precipitation of thick and continuous α phase along grain boundaries (indicated by the white arrow in Fig. 6(c)). Apart of large grain boundary α particle, lamellar α phase particles precipitated in the material aged at $500\text{ }^{\circ}\text{C}/16\text{ h}$ (Fig. 6(d)). Recently it has been proven by TEM [38] that elliptical particles in the undeformed material after ageing (Fig. 6(d)) are ω_{iso} particles similar to those observed in [15]. This result is also consistent with XRD measurement presented below.

Fig. 7 shows BSE micrographs of the ECAPed specimen after the same ageing treatment. Deformation contours in large β grains are seen in Fig. 7(a) and (b). Small polygonal equiaxed α phase particles can be observed already after ageing at $400\text{ }^{\circ}\text{C}$ for 4 h (Fig. 7(a), marked with an arrow). The particles are arranged in chains in areas with a higher concentration of lattice defects. After a longer ageing time ($400\text{ }^{\circ}\text{C}/16\text{ h}$, Fig. 7(b)), α phase particles became larger and their overall volume fraction increased; however, they are still found only inside the bands. An increased amount of the α phase is observed after ageing at $500\text{ }^{\circ}\text{C}/4\text{ h}$ (Fig. 7(c)). Ageing of the ECAPed material at $500\text{ }^{\circ}\text{C}$ for 16 h (Fig. 7(d)) resulted in an abnormal growth of the β grains in shear bands (SBs). These β grains with size exceeding $1\text{ }\mu\text{m}$ contain significantly coarser α lamellae when compared to α particles in undeformed aged material.

3.4. Microstructure observation of the aged ECAPed samples by TKD

In Fig. 7(b), the area selected for the site-specific lamella

preparation by focused ion beam (FIB) is shown. A thin lamella was cut in the position of the green rectangle (perpendicular to the sample surface) intentionally across a fine-grained strip containing α phase particles. A detailed investigation of the lamella was carried out using TKD.

In Fig. 8(a) the BSE micrograph of the analyzed area within the thin lamella is shown. Darker areas can be associated with Mo depleted α phase particles. Fig. 8(b) shows the phase map of refined β matrix and small α particles. Black areas could not be indexed by TKD method (indexing procedure is equivalent to common EBSD) due to poor quality of diffraction pattern. This is caused by induced severe deformation and by overlapping of α phase particles and β matrix within thickness of the lamella. Figs. 8(c) and (d) show the TKD IPF maps of the β phase and α phase, respectively. The microstructure within the observed $\alpha + \beta$ layer (shear band) is ultra-fine grained composed of refined β phase matrix and equiaxed α phase particles. TEM analysis presented in our previous study [39] proved that observed UFG bands contain also ω phase. However, ω phase particles could not be identified by TKD due to their small size and similarity of Kikuchi patterns of ω and β phases.

Note that the theoretical interaction depth for generation of back-scattered electrons ($> 200\text{ nm}$) is larger than the thickness of the lamella, which is approximately $150\text{--}200\text{ nm}$. Thus, the observed chemical contrast (Fig. 8(a)) is averaged over the full thickness of the lamella, while small α -particles may not span through the whole thickness. On the other hand, the signal from TKD arises only from the (bottom) surface layer having the thickness of approximately $50\text{--}100\text{ nm}$ [40,41]. Hence, BSE micrograph and IPF maps do not coincide perfectly.

A TKD IPF map from a coarse β grain outside the refined layer is shown in Fig. 9. The coarse grain was determined as a pure β phase by TKD. However, the material contains also ω phase particles [39] which could not be resolved by TKD. The observed β grain is strongly deformed and contains low-angle grain boundaries. The degree of the deformation within one β grain was measured by the change of the point-to-origin orientation along the red line highlighted in Fig. 9(a) from the origin of the red line marked as O. Fig. 9(b) shows the dependence of the misorientation on the distance from the origin (point-to-origin misorientation). The misorientation increases to 25° within $2\text{ }\mu\text{m}$ distance which indicates a highly deformed microstructure, however, without presence of high angle grain boundaries. Achieved material therefore cannot be referred to as ultra-fine grained (UFG).

3.5. Evolution of phase composition with ageing

The evolution of phases in the aged undeformed and ECAPed samples was determined using XRD measurement. Measured (black curves) and fitted (colored curves) XRD patterns of ST and ECAPed samples are compared in Fig. 10 (note, that the vertical axis is displayed in the

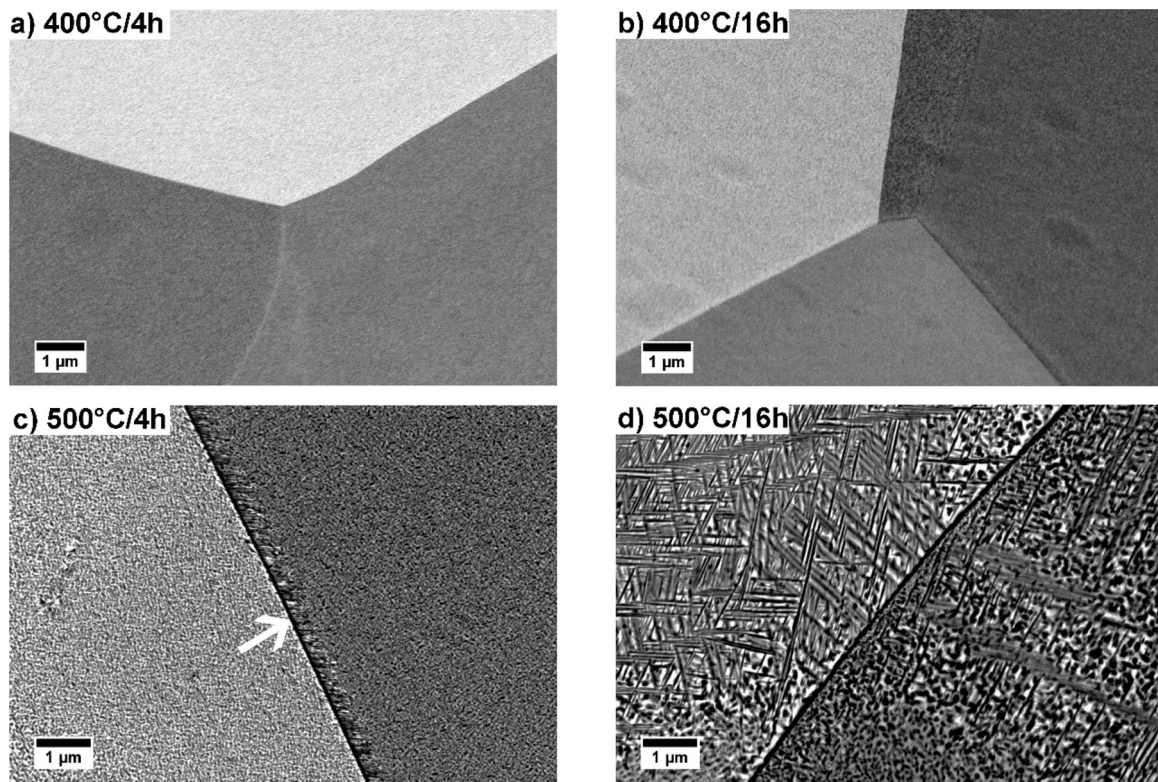


Fig. 6. BSE micrographs of the undeformed samples aged at (a) 400 °C for 4 h, (b) 400 °C for 16 h, (c) 500 °C for 4 h, (d) 500 °C for 16 h. The white arrow indicates the grain boundary α phase.

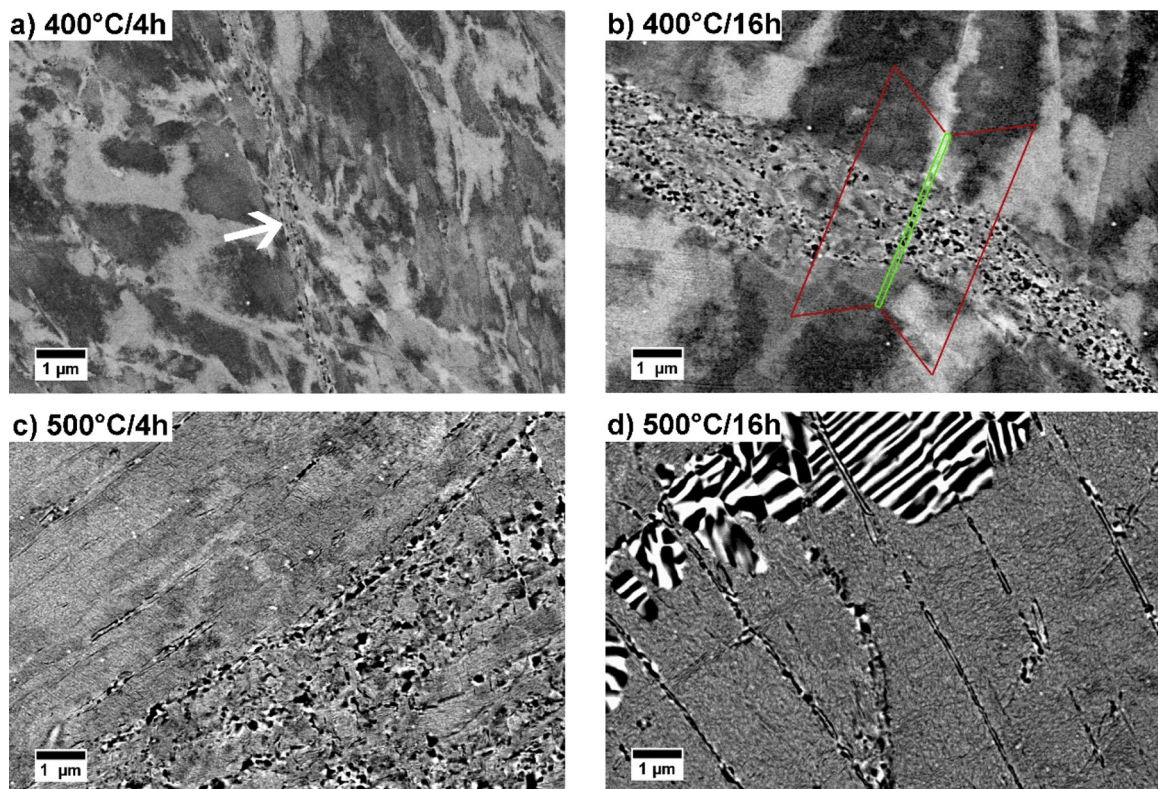


Fig. 7. BSE micrographs of the ECAPed samples aged at (a) 400 °C for 4 h, (b) 400 °C for 16 h (with the highlighted area of site-specific thin lamella preparation), (c) 500 °C for 4 h, (d) 500 °C for 16 h.

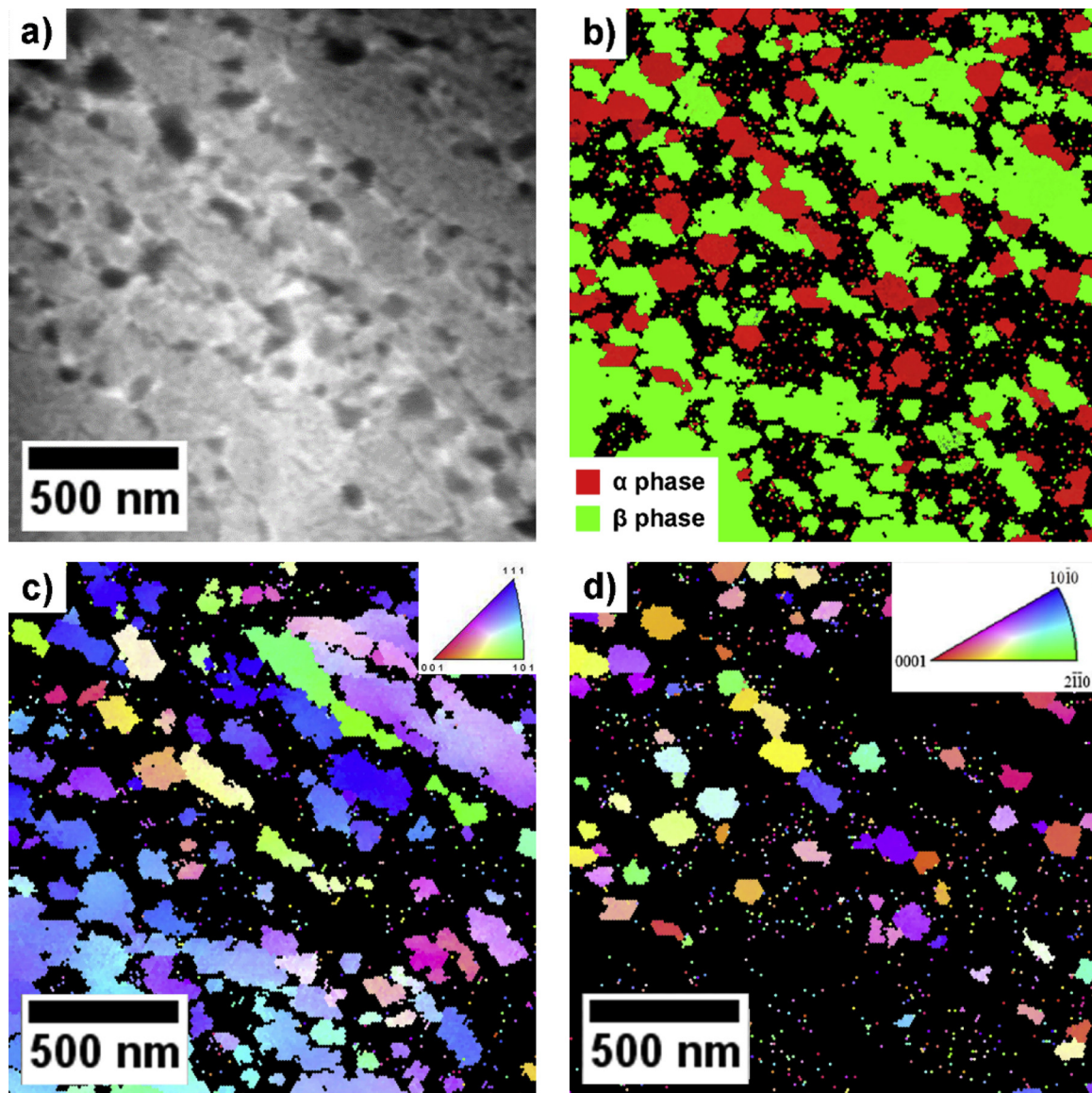


Fig. 8. (a) BSE micrograph, (b) phase map from α and β phase (c) IPF map from the β phase and (d) IPF map from the α phase of the shear band of the ECAPed and aged sample at 400 °C for 16 h.

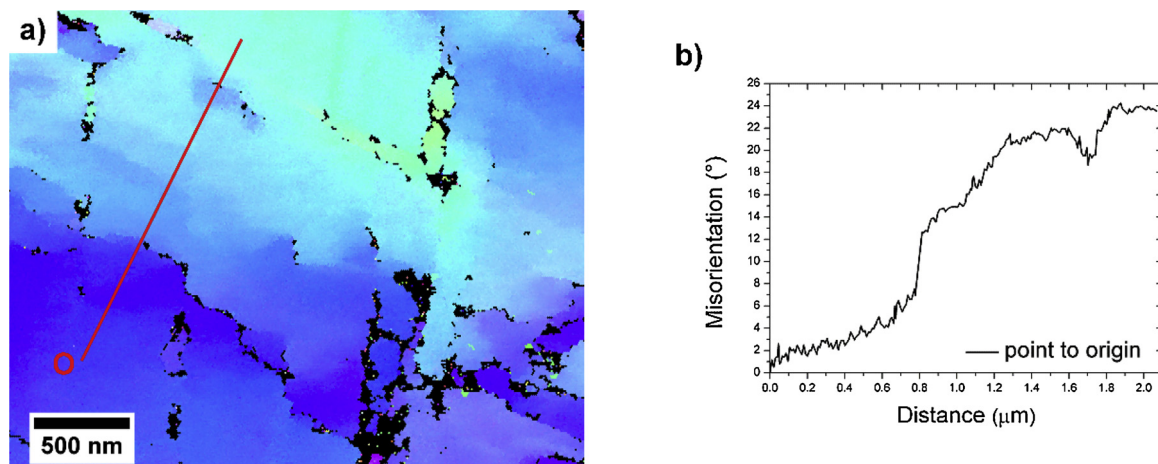


Fig. 9. (a) IPF map from the β matrix with a highlighted line, along which the dependence of the misorientation on the distance from the origin (O) was measured (b).

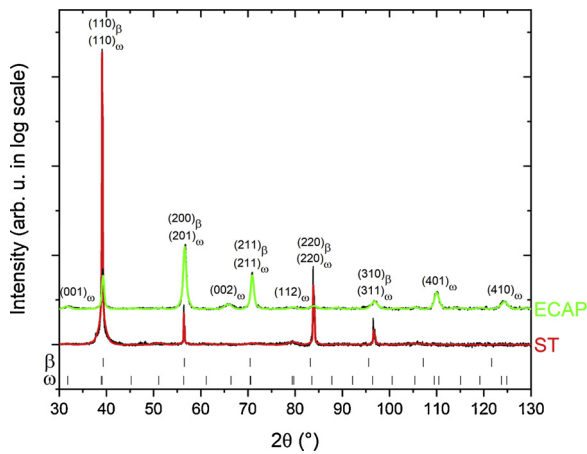


Fig. 10. XRD patterns of the Ti-15Mo alloy in ST and ECAPed conditions. The patterns are shifted vertically for clarity.

logarithmic scale in order to accentuate small peaks). Both specimens contain large grains with the size of hundreds of micrometres, and have preferred orientation of grains, as can be inferred from the relative intensity of the peaks. These facts complicate the quantitative analysis of the XRD patterns and only qualitative conclusions can be made.

The ST Ti-15Mo alloy contains β and ω phase, which can be identified in the XRD pattern only by a tiny peak at 79° . The XRD pattern of the material after ECAP deformation exhibits significantly broadened peaks due to an increased dislocation density and reduced crystallite size in the severely deformed material. Furthermore, due to residual stresses in the ECAPed material, the peaks are slightly shifted to higher 2θ angles, i.e. to shorter interplanar distances. The intensity of ω peaks indicates increased volume fraction of the ω phase in the ECAPed material due to deformation at the elevated temperature of 250°C which is sufficient for the irreversible formation of the diffusion stabilized ω_{iso} phase.

In Fig. 11(a) and (b), the evolution of the XRD patterns with ageing is shown for undeformed and ECAPed specimens, respectively. The vertical axis is again displayed in logarithmic scale. The most significant peaks, where the evolution of emerging phases is most apparent, are marked with arrows – filled and open arrows for α and ω phase, respectively. Note, that for better visibility only fitted data are shown in Fig. 11(a) and (b).

Ageing of undeformed material at $400^\circ\text{C}/1\text{h}$ (red curve in Fig. 11(a)) causes an increase of the intensity of the peaks of ω phase (open arrows). Small peaks from the α phase are also visible in the pattern (full arrows). XRD patterns of undeformed material aged at 400°C for 1, 4 and 16 h and at 500°C for 1 h are very similar. After ageing at $500^\circ\text{C}/4\text{h}$, the α phase is clearly present (filled arrows in Fig. 11(a)) and its volume fraction increases after ageing at 500°C for 16 h, which is consistent with SEM observations. Even after ageing at 500°C for 16 h, ω phase is still present according to XRD.

In the ECAPed material, volume fraction of the ω phase increases after ageing at $400^\circ\text{C}/1\text{h}$, similarly to the undeformed material (red curve in Fig. 11(b), open arrows). Contrary to the undeformed material, volume fraction of α phase is significantly higher in the ECAPed samples aged at 500°C for 1 h and increases with the time of ageing (green curve in Fig. 11(b), full arrows). Volume fraction of α phase is even significantly higher in samples aged at 500°C and increases with time of ageing. Increased amount of α phase is accompanied by a decrease of volume fraction of ω phase. After ageing at 500°C for 4 and 16 h the ECAPed material does not contain ω phase.

3.6. Evolution of the microhardness with ageing

The evolution of the microhardness of undeformed and ECAPed

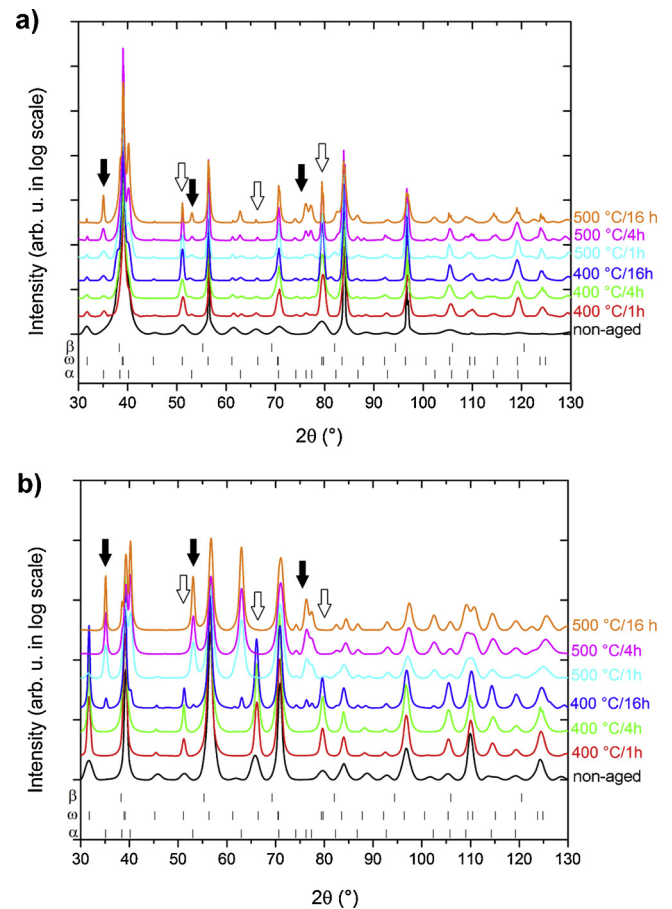


Fig. 11. XRD patterns of the (a) undeformed and (b) ECAPed specimens alloy and their evolution with ageing of the material. Black and white arrows indicate significant α and ω peaks, respectively (see the text). The patterns are shifted vertically for clarity.

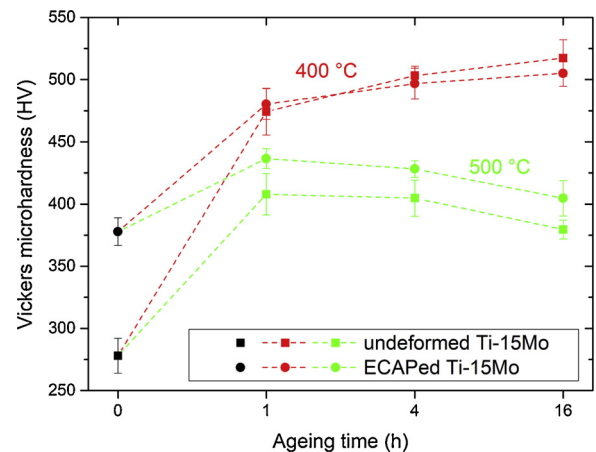


Fig. 12. Dependence of the microhardness of undeformed and ECAPed samples aged at 400°C and 500°C on the ageing time.

condition with ageing time is shown in Fig. 12 for both ageing temperatures. The microhardness of the ST Ti-15Mo alloy is approximately $\sim 280\text{HV}$, while the ECAPed condition exhibits an increased microhardness of $\sim 380\text{HV}$. At the lower ageing temperature the microhardness increases with increasing ageing time both in the undeformed and ECAPed conditions. However, the microhardness values are the same in both materials. Ageing of both types of the material at 500°C leads to a lower microhardness compared to ageing at 400°C . Contrary

to 400 °C, the microhardness decreases with increasing ageing time at 500 °C. ECAPed aged at 500 °C exhibit slightly higher microhardness than their undeformed counterparts.

4. Discussion

4.1. Deformation by ECAP

The deformation of initial β solution treated alloy by ECAP results in the formation of deformed and twinned structure, however, the grain fragmentation is insignificant. The equivalent deformation after $N = 2$ ECAP passes according to von Mises (Eq. 1) is approx. 1.33 which is not sufficient for pronounced grain fragmentation of the β matrix. Nevertheless, according to TEM observations (Fig. 4) areas with higher concentration of the lattice defects (particularly dislocations) appear in the ECAP deformed microstructure. Formation of shear bands (SB) in ECAP deformed materials has already been reported elsewhere [28,42].

XRD results suggest that the amount of the ω phase may have increased after ECAP either due to severe deformation [43] or due to processing at elevated temperature of 250 °C. In order to assess the effect of temperature, solution treated benchmark sample was annealed at 250 °C for 30 min, which corresponds approximately to the time of ECAP processing by $N = 2$ passes including pre-heating of material. The achieved microhardness of 340 HV (compared to 280 HV of ST material and 380 HV of ECAP material) suggests that processing at the elevated temperature of 250 °C is sufficient for the formation of ω_{iso} phase particles stabilized by diffusion [44].

4.2. Effect of ageing on phase composition and microstructure

Both undeformed and ECAPed materials were subjected to ageing treatment in order to reveal the differences between ongoing phase transformations and the morphology of α phase particles. According to the XRD measurement, the amount of the α phase is slightly increased in the undeformed material after ageing at 400 °C for 1 and 4 h. On the other hand, in the material after ECAP, the α phase precipitation is already significant after ageing at 400 °C for 1 and 4 h. Indeed, small equiaxed particles were observed in SEM images of ECAPed and aged specimens (see Fig. 7).

Accelerated and localized precipitation of the α phase in the deformed β -Ti alloy is strongly correlated with the pre-existing SBs created by ECAP deformation. Such SBs with a high density of lattice defects are favorable areas for preferential nucleation of the α phase because less energy is required for nucleation at defects [45]. Once nucleated, the growth of α nuclei is diffusion-controlled [46] and the coarsening of the α phase is therefore controlled by the diffusion of Mo (β stabilizing element) in the β matrix. It is known, that diffusion rate along grain boundaries and pipe diffusion along dislocation cores are several orders of magnitude higher than the volume diffusivities [45,47]. Therefore, in the ECAPed material the heterogeneous precipitation (both nucleation and growth) of the α phase is accelerated.

Enhanced diffusion should also promote diffusional stabilization and growth of ω_{iso} particles. However, ω particles do not form by the standard nucleation mechanism and therefore the overall effect of deformed microstructure on ω_{iso} phase evolution might be weaker. Furthermore, α phase precipitation is a competitive process to ω_{iso} phase growth. Mo atoms are expelled from α phase particles causing the thermodynamic stabilization of surrounding β phase and the reduction of the volume fraction of metastable ω phase [22].

In the deformed material, equiaxed morphology of α phase precipitates is observed after ageing at 400 °C. The growth of individual α phase particles is limited by the high amount of α nuclei via two processes. First, each α nucleus forms a barrier for the growth of another α precipitate due to impingement. Second, each α nucleus forms a barrier for diffusion of Mo which limits the growth of α particles due to additional β stabilization of surrounding β matrix. As a result, after ageing,

α phase particles remain equiaxed in shear bands of the ECAPed material, which is similar to α phase precipitation in a highly deformed material after HPT [24,29,48].

A significant difference in the evolution of the phases in undeformed and ECAPed specimens can be found after ageing at 500 °C. While the ω phase is retained in the undeformed material, volume fraction of the ω phase in the ECAPed material decreased after ageing at 500 °C. It can be attributed to α phase precipitation causing additional thermodynamic stabilization of the β matrix due to expelling of Mo atoms. The presence of incoherent α phase precipitates also relieve internal elastic stresses in the matrix which may otherwise also promote ω phase formation [49]. Similar preference of α phase precipitation over ω phase formation was observed in cold-rolled Ti-25Nb-2Mo-4Sn alloy [50].

Heterogeneous growth of α phase lamellae occurs in the material after ECAP (see Fig. 7(d)). The resulting microstructure resembles a discontinuous coarsening of the lamellar structure which was observed in various alloying systems [51–53]. Discontinuous coarsening typically originates at grain boundaries [51] and arises from lowering the total energy of the system by simultaneous decreasing of amount of grain boundaries and interfaces between phases. Parallel α lamellae are observed in Fig. 7(d) which suggests that only one variant of α lamellae evolved in each β grain. It is typical for discontinuous coarsening [54–56]. As the result the microstructure of aged ECAP is coarser, at least in some areas, than in the aged undeformed counterpart.

4.3. Microhardness

The microhardness of the Ti-15Mo alloy increases from HV \approx 280 of the solution treated coarse-grained material to HV \approx 380 of the deformed material after ECAP. The increase is attributed to strengthening by grain fragmentation, twinning, the high dislocation density [9,10] and importantly to the evolution of ω_{iso} phase particles as discussed above.

Despite limited knowledge of interaction between ω particles and dislocations, it can be assumed, that dislocations overcome ω_{ath} particles in the ST material by cutting through precipitates. These particles are small, coherent and moreover, the $\beta \rightarrow \omega_{ath}$ transformation may be incomplete - only small shifts of atomic planes may take place after quenching [20]. The shear stress required for a dislocation to pass through a precipitate increases with the size of the particle and, in particular, with the obstacle strength [57,58].

During ECAP processing at 250 °C, ω particles become stabilized by expelling Mo and the shift of atomic planes associated with $\beta \rightarrow \omega$ transformation is more pronounced [15,19]. The evolution of ω particles may increase the obstacle strength for dislocation motion and hardening by ω phase is more pronounced in the ECAPed material than in the ST material despite the overall volume fraction of the ω phase and the average size of ω particles might be comparable.

The values of microhardness after ageing at 400 °C for 1 h significantly increased to \sim 480 HV for both undeformed and ECAPed materials. As the α phase is not present in the material, the increase of the microhardness can be attributed to the evolution of ω phase particles as discussed above. With further ageing at 400 °C for 4 and 6 h, a slight increase of the microhardness was observed and the microhardness would possibly saturate similarly as in metastable Ti-6.8Mo-4.5Fe-1.5Al alloy [59]. The microhardness of the ECAPed material does not exceed the microhardness in the undeformed material after ageing at 400 °C. In comparison, the maximum microhardness of the Ti-15Mo alloy after one HPT turn attains very similar value of \sim 500 HV [60].

Microhardness of the specimens aged at 500 °C is significantly increased when compared to initial ST and ECAPed conditions. This is attributed to the presence of ω phase and also to the α phase precipitation, which is observed both by XRD and SEM. On the other hand, microhardness after ageing at 500 °C is significantly lower than after ageing at 400 °C, see Fig. 12. This decrease is related to the lower

amount of the ω phase, as observed in XRD patterns, especially for ECAPed material (see Fig. 11(b)). Lower amount of ω phase in the aged ECAPed material is attributed to a massive increase of the content of thermodynamically stable α phase. A slight decrease of the microhardness with the ageing time is associated with coarsening of both ω and α phase particles. Recovery of the defects and possible recrystallization can also play a role in the microhardness decrease in ECAPed material. A positive effect of ECAP processing on microhardness is suppressed by subsequent ageing and concurrent phase transformations.

5. Conclusions

Ti-15Mo alloy in a β solution treated condition was subjected to deformation by ECAP. Undeformed and ECAPed materials were subjected to ageing at temperatures 400 °C and 500 °C. The effect of the deformation on microhardness and phase transformations, namely the α phase precipitation was studied. The most important results of this study can be summarized as follows:

- ECAP processing performed at an elevated temperature of 250 °C results in the formation of deformed but not ultra-fine grained structure and in an increased amount of the ω phase in the material.
- Contrary to the undeformed material, small and equiaxed α phase particles precipitate already after ageing at 400 °C for 1 h in the ECAPed material in shear bands containing a high density of lattice defects.
- ω particles play a major role in hardening of the alloy. Upon ageing at higher temperatures and longer times, the ω phase content decreases and the microhardness evolution is governed by α phase precipitation.

Author contributions

V. Polyakova and I. Semenova performed the deformation by ECAP. K. Bartha and A. Veverková performed the SEM observations and microhardness measurements. K. Bartha in collaboration with J. Veselý performed the TEM analysis, in collaboration with P. Minárik prepared the thin lamella and performed the TKD measurement. C. A. Corrêa performed the XRD measurements and integrated refinements using the XRD data. Particular parts were written by authors responsible for each measurement. K. Bartha, J. Stráský and M. Janeček were finalizing the text. All authors reviewed and approved the final draft of the manuscript.

Declaration of Competing Interest

The authors declare no conflict of interests.

Acknowledgements

This work was financially supported by the Czech Science Foundation under the project 1720700Y. Partial financial support by the Ministry of Education Youth and Sports under the project LTARF18010 is also gratefully acknowledged. C. A. Corrêa and M. Janeček acknowledge the financial support from the Czech Ministry of Education, project NanoCent (OP VVV) No. CZ.02.1.01/0.0/0.0/15_003/0000485.






References

- [1] C. Leyens, M. Peters, *Titanium and Titanium Alloys*, Wiley-VCH, 2003.
- [2] Y.L. Hao, S.J. Li, S.Y. Sun, R. Yang, Effect of Zr and Sn on Young's modulus and superelasticity of Ti-Nb-based alloys, *Mater. Sci. Eng. A* 441 (2006) 112–118, <https://doi.org/10.1016/j.msea.2006.09.051>.
- [3] D. Kuroda, M. Niinomi, M. Morinaga, Y. Kato, T. Yashiro, Design and mechanical properties of new β type titanium alloys for implant materials, *Mater. Sci. Eng. A* 243 (1998) 244249, [https://doi.org/10.1016/S0921-5093\(97\)00808-3](https://doi.org/10.1016/S0921-5093(97)00808-3).
- [4] M. Geetha, A.K. Singh, R. Asokamani, A.K. Gogia, Ti based biomaterials, the ultimate choice for orthopaedic implants – a review, *Prog. Mater. Sci.* 54 (2009) 397–425, <https://doi.org/10.1016/j.pmatsci.2008.06.004>.
- [5] J. Brems, E. Eisenbarth, V. Biehl, Titanium and its alloys for medical applications, in: C. Leyens, M. Peters (Eds.), *Titanium and Titanium Alloys*, Wiley-VCH, 2003, pp. 423–451.
- [6] M. Niinomi, Y. Liu, M. Nakai, H. Liu, H. Li, Biomedical titanium alloys with Young's moduli close to that of cortical bone, *Regen. Biomater.* 3 (2016) 173–185, <https://doi.org/10.1093/rb/rbw016>.
- [7] D.R.N. Correa, et al., Development of Ti-15Zr-Mo alloys for applying as implantable biomedical devices, *J. Alloys. Compd.* 749 (2018) 163–171, <https://doi.org/10.1016/j.jallcom.2018.03.308>.
- [8] J. Disegi, *Implant materials, Wrought Titanium -15% Molybdenum, Synthes*, (2009).
- [9] E.O. Hall, The deformation and ageing of mild steel: III discussion of results, *Proc. Phys. Soc. Sect. B* 64 (1951) 747, <https://doi.org/10.1088/0370-1301/64/9/303>.
- [10] N.J. Petch, The cleavage strength of polycrystals, *J. Iron Steel Inst.* 174 (1953) 25–28.
- [11] V.M. Segal, Materials processing by simple shear, *Mater. Sci. Eng. A* 197 (1995) 157–164, [https://doi.org/10.1016/0921-5093\(95\)09705-8](https://doi.org/10.1016/0921-5093(95)09705-8).
- [12] A.P. Zhilyaev, T.G. Langdon, Using high-pressure torsion for metal processing: fundamentals and applications, *Prog. Mater. Sci.* 53 (2008) 893–979, <https://doi.org/10.1016/j.pmatsci.2008.03.002>.
- [13] F.H. Froes, M. Qian, *Titanium in Medical and Dental Applications*, Woodhead Publishing, 2018.
- [14] D. De Fontaine, Mechanical instabilities in the b.c.c. Lattice and the beta to omega phase transformation, *Acta Metall.* 18 (1970) 275–279, [https://doi.org/10.1016/0001-6160\(70\)90035-0](https://doi.org/10.1016/0001-6160(70)90035-0).
- [15] P. Zháňal, et al., Evolution of omega phase during heating of metastable beta titanium alloy Ti-15Mo, *J. Mater. Sci.* 53 (2018) 837–845, <https://doi.org/10.1007/s10853-017-1519-2>.
- [16] M. Tane, Y. Okuda, Y. Todaka, H. Ogi, A. Nagakubo, Elastic properties of single-crystalline ω phase in titanium, *Acta Mater.* 61 (2013) 7543–7554, <https://doi.org/10.1016/j.actamat.2013.08.036>.
- [17] A. Devaraj, R.E.A. Williams, S. Nag, R. Srinivasan, H.L. Fraser, R. Banerjee, Three-dimensional morphology and composition of omega precipitates in a binary titanium–molybdenum alloy, *Scripta. Mater.* 61 (2009) 701–704, <https://doi.org/10.1016/j.scriptamat.2009.06.006>.
- [18] Y. Zheng, et al., Role of ω phase in the formation of extremely refined intragranular α precipitates in metastable β -titanium alloys, *Acta Mater.* 103 (2016) 850–858, <https://doi.org/10.1016/j.actamat.2015.11.020>.
- [19] A. Devaraj, et al., Experimental evidence of concurrent compositional and structural instabilities leading to ω precipitation in titanium–molybdenum alloys, *Acta Mater.* 60 (2012) 596–609, <https://doi.org/10.1016/j.actamat.2011.10.008>.
- [20] J. Šmilauerová, P. Harcuba, D. Krieger, V. Holý, On the completeness of the $\beta \rightarrow \omega$ transformation in metastable β titanium alloys, *J. Appl. Crystallogr.* 50 (2017) 283–287, <https://doi.org/10.1107/S1600576716020458>.
- [21] E. Orowan, Zur Kristallplastizität. I, *Z Für Phys.* 89 (1934) 605–613.
- [22] K. Václavová, et al., Ultra-fine grained microstructure of metastable beta Ti-15Mo alloy and its effects on the phase transformations, *IOP Conf. Ser. Mater. Sci. Eng.* 194 (2017) 012021, <https://doi.org/10.1088/1757-899X/194/1/012021>.
- [23] A. Zafari, K. Xia, Formation of equiaxed α during ageing in a severely deformed metastable β Ti alloy, *Scripta. Mater.* 124 (2016) 151–154, <https://doi.org/10.1016/j.scriptamat.2016.07.012>.
- [24] B. Jiang, K. Tsuchiya, S. Emura, X. Min, Effect of high-pressure torsion process on precipitation behavior of α phase in β -Type Ti-15Mo alloy, *Mater. Trans.* 55 (2014) 877–884, <https://doi.org/10.2320/matertrans.M2013469>.
- [25] N.G. Jones, R.J. Dashwood, M. Jackson, D. Dye, B Phase decomposition in Ti-5Al-5Mo-5V-3Cr, *Acta. Mater.* 57 (2009) 3830–3839, <https://doi.org/10.1016/j.actamat.2009.04.031>.
- [26] M. Janeček, et al., Microstructure evolution in solution treated Ti15Mo alloy processed by high pressure torsion, *Mater. Charact.* 98 (2014) 233–240, <https://doi.org/10.1016/j.matchar.2014.10.024>.
- [27] K. Václavová, et al., Microhardness and microstructure evolution of ultra-fine grained Ti-15Mo and TIMETAL LCB alloys prepared by high pressure torsion, *Mater. Sci. Eng. A* 682 (2017) 220–228, <https://doi.org/10.1016/j.msea.2016.11.038>.
- [28] W. Xu, et al., Promoting nano/ultrafine-duplex structure via accelerated α precipitation in a β -type titanium alloy severely deformed by high-pressure torsion, *Scripta. Mater.* 68 (2013) 67–70, <https://doi.org/10.1016/j.scriptamat.2012.09.023>.
- [29] W. Xu, et al., On the formation of an ultrafine-duplex structure facilitated by severe shear deformation in a Ti-20Mo β -type titanium alloy, *Acta Mater.* 60 (2012) 5067–5078, <https://doi.org/10.1016/j.actamat.2012.05.042>.
- [30] B. Jiang, S. Emura, K. Tsuchiya, Improvement of ductility in Ti-5Al-5Mo-5V-3Cr alloy by network-like precipitation of blocky α phase, *Mater. Sci. Eng. A* 722 (2018) 129–135, <https://doi.org/10.1016/j.msea.2018.03.025>.
- [31] I.P. Semenova, G.I. Raab, L.R. Saitova, R.Z. Valiev, The effect of equal-channel angular pressing on the structure and mechanical behavior of Ti-6Al-4V alloy, *Mater. Sci. Eng. A* 387–389 (2004) 805–808, <https://doi.org/10.1016/j.msea.2004.02.093>.
- [32] L.R. Saitova, H.W. Höppel, M. Göken, I.P. Semenova, R.Z. Valiev, Cyclic deformation behavior and fatigue lives of ultrafine-grained Ti-6Al-4V ELL alloy for medical use, *Int. J. Fatigue* 31 (2009) 322–331, <https://doi.org/10.1016/j.ijfatigue.2008.08.007>.

- [33] Supplier Technical Sheet, Carpenter Co., Belgium, 2012.
- [34] Y. Iwahashi, J. Wang, Z. Horita, M. Nemoto, T.G. Langdon, Principle of equal channel angular pressing for processing of ultra-fine grained materials, *Scripta Mater.* 35 (1996) 143–146, [https://doi.org/10.1016/1359-6462\(96\)00107-8](https://doi.org/10.1016/1359-6462(96)00107-8).
- [35] R.R. Keller, R.H. Geiss, Transmission EBSD from 10 nm domains in a scanning electron microscope, *J. Microsc.* 245 (2011) 245–251, <https://doi.org/10.1111/j.1365-2818.2011.03566.x>.
- [36] V. Petříček, M. Dušek, L. Palatinus, Crystallographic computing system JANA2006: general features, *Z Für Krist – Cryst. Mater.* 229 (2014) 345–352, <https://doi.org/10.1515/zkri-2014-1737>.
- [37] X. Zhou, X. a Min, S. Emura, K. Tsuchiya, Accommodative {332} <113> primary and secondary twinning in a slightly deformed β -type Ti-Mo titanium alloy, *Mater. Sci. Eng. A* 684 (2017) 456–465, <https://doi.org/10.1016/j.msea.2016.12.025>.
- [38] K. Bartha, Phase Transformations in Ultra-fine Grained Titanium Alloys, Doctoral Thesis Charles University, Prague, 2019.
- [39] K. Bartha, et al., Inhomogeneous precipitation of the α -Phase in Ti15Mo alloy deformed by ECAP, *Mater. Sci. Forum* 941 (2018) 1183–1188, <https://doi.org/10.4028/www.scientific.net/MSF.941.1183>.
- [40] J. Kozlík, J. Stráský, P. Harcuba, I. Ibragimov, T. Chráška, M. Janeček, Cryogenic milling of titanium powder, *Metals* 8 (31) (2018), <https://doi.org/10.3390/met8010031>.
- [41] T. Tokarski, G. Cios, A. Kula, P. Bała, High quality transmission Kikuchi diffraction analysis of deformed alloys - Case study, *Mater. Charact.* 121 (2016) 231–236, <https://doi.org/10.1016/j.matchar.2016.10.013>.
- [42] G. Lütjering, J. Albrecht, C. Sauer, T. Krull, The influence of soft, precipitate-free zones at grain boundaries in Ti and Al alloys on their fatigue and fracture behavior, *Mater. Sci. Eng. A* 468–470 (2007) 201–209, <https://doi.org/10.1016/j.msea.2006.07.168>.
- [43] A.R. Kilmametov, et al., The $\alpha \rightarrow \omega$ and $\beta \rightarrow \omega$ phase transformations in Ti-Fe alloys under high-pressure torsion, *Acta Mater.* 144 (2018) 337–351, <https://doi.org/10.1016/j.actamat.2017.10.051>.
- [44] P. Zháňal, et al., Phase transformations in Ti-15Mo investigated by in situ electrical resistance, *Acta Phys. Pol. A* 128 (2015) 779–783, <https://doi.org/10.12693/APhysPolA.128.779>.
- [45] H.I. Aaronson, M. Enomoto, J.K. Lee, *Mechanisms of Diffusional Phase Transformations in Metals and Alloys*, CRC Press, Florida, 2010.
- [46] S.L. Semiatin, S.L. Knisley, P.N. Fagin, D.R. Barker, F. Zhang, Microstructure evolution during alpha-beta heat treatment of Ti-6Al-4V, *Metall. Mater. Trans. A* 34 (2003) 2377–2386, <https://doi.org/10.1007/s11661-003-0300-0>.
- [47] M. Legros, G. Dehm, Observation of Giant diffusivity along dislocation core, *Science* 319 (2008) 1646–1649, <https://doi.org/10.1126/science.1151771>.
- [48] B. Jiang, S. Emura, K. Tsuchiya, Formation of equiaxed α phase in Ti-5Al-5Mo-5V-3Cr alloy deformed by high-pressure torsion, *J. Alloys. Compd.* 738 (2018) 283–291, <https://doi.org/10.1016/j.jallcom.2017.12.201>.
- [49] J. Šmilauerová, et al., Ordered array of particles in -Ti matrix studied by small-angle X-ray scattering, *Acta Mater.* 81 (2014) 71–82, <https://doi.org/10.1016/j.actamat.2014.06.042>.
- [50] S. Guo, Q. Meng, L. Hu, G. Liao, X. Zhao, H. Xu, Suppression of isothermal ω phase by dislocation tangles and grain boundaries in metastable β -type titanium alloys, *J. Alloys. Compd.* 550 (2013) 35–38, <https://doi.org/10.1016/j.jallcom.2012.09.081>.
- [51] J.D. Livingston, J.W. Cahn, Discontinuous coarsening of aligned eutectoids, *Acta Metall.* 22 (1974) 495–503, [https://doi.org/10.1016/0001-6160\(74\)90103-5](https://doi.org/10.1016/0001-6160(74)90103-5).
- [52] G.W. Qin, et al., Discontinuous coarsening of the lamellar structure of γ -TiAl-based intermetallic alloys and its control, *Metall. Mater. Trans. A* 32 (2001) 1927–1938, <https://doi.org/10.1007/s11661-001-0005-1>.
- [53] M. Shaarbaf, R.A. Fournelle, Discontinuous coarsening of lamellar discontinuous precipitate in an Al-29.5at.%Zn alloy, *Mater. Sci. Eng. A* 102 (1988) 271–279, [https://doi.org/10.1016/0025-5416\(88\)90582-4](https://doi.org/10.1016/0025-5416(88)90582-4).
- [54] N. Stanford, P.S. Bate, Crystallographic variant selection in Ti-6Al-4V, *Acta Mater.* 52 (2004) 5215–5224, <https://doi.org/10.1016/j.actamat.2004.07.034>.
- [55] P. Harcuba, K. Václavová, J. Čapek, J. Stráský, M. Janeček, M. Janovská, Alpha variant selection determined from grain misorientations in Ti-6Al-7Nb alloy with a duplex microstructure, *Acta Phys. Pol. A* 128 (2015) 570–573, <https://doi.org/10.12693/APhysPolA.128.570>.
- [56] A. Bhattacharjee, P. Ghosal, A.K. Gogia, S. Bhargava, S.V. Kamat, Room temperature plastic flow behaviour of Ti-6.8Mo-4.5Fe-1.5Al and Ti-10V-4.5Fe-1.5Al: Effect of grain size and strain rate, *Mater. Sci. Eng. A* 452–453 (2007) 219–227, <https://doi.org/10.1016/j.msea.2006.10.166>.
- [57] J. Friedel, *Dislocations*, 1st ed., Pergamon Press, 1964.
- [58] R. Labusch, A statistical theory of solid solution hardening, *Phys. Status Solidi B* 41 (1970) 659–669, <https://doi.org/10.1002/pssb.19700410221>.
- [59] J. Šmilauerová, et al., Ageing response of sub-transus heat treated Ti-6.8Mo-4.5Fe-1.5Al alloy, *J. Alloys. Compd.* 724 (2017) 373–380, <https://doi.org/10.1016/j.jallcom.2017.07.036>.
- [60] K. Václavová, et al., Evolution of Microstructure and Microhardness in Ti-15Mo β Ti Alloy Prepared by High Pressure Torsion, *Mater. Sci. Forum* 879 (2017) 2555–2560, <https://doi.org/10.4028/www.scientific.net/MSF.879.2555>.

Article

Effect of the High-Pressure Torsion (HPT) and Subsequent Isothermal Annealing on the Phase Transformation in Biomedical Ti15Mo Alloy

Kristína Bartha ^{1,*}, Josef Stráský ¹, Anna Veverková ¹, Pere Barriobero-Vila ², František Lukáč ³, Petr Doležal ⁴, Petr Sedlák ⁵, Veronika Polyakova ⁶, Irina Semenova ⁶ and Miloš Janeček ¹

¹ Department of Physics of Materials, Charles University, 12000 Prague, Czech Republic;

josef.strasky@gmail.com (J.S.); annaterynkova@gmail.com (A.V.); janecek@met.mff.cuni.cz (M.J.)

² Institute of Materials Research, German Aerospace Center (DLR), 51147 Cologne, Germany; Pere.BarrioberoVila@dlr.de

³ Institute of Plasma Physics, Czech Academy of Sciences, 18000 Prague, Czech Republic; lukac@ipp.cas.cz

⁴ Department of Physics of Condensed Matter, Charles University, 12000 Prague, Czech Republic; petr.dolezal@mff.cuni.cz

⁵ Institute of Thermomechanics, Czech Academy of Sciences, 18000 Prague, Czech Republic; petr.sedlak@jfifi.cvut.cz

⁶ Institute of Physics of Advanced Materials, Ufa State Aviation Technical University, 450000 Ufa, Russia; vnurik@gmail.com (V.P.); semenova-ip@mail.ru (I.S.)

* Correspondence: kristina.bartha@met.mff.cuni.cz; Tel.: +420-95155-1361

Received: 17 October 2019; Accepted: 5 November 2019; Published: 7 November 2019



Abstract: Ti15Mo metastable beta Ti alloy was solution treated and subsequently deformed by high-pressure torsion (HPT). HPT-deformed and benchmark non-deformed solution-treated materials were annealed at 400 °C and 500 °C in order to investigate the effect of UFG microstructure on the α -phase precipitation. Phase evolution was examined using laboratory X-ray diffraction (XRD) and by high-energy synchrotron X-ray diffraction (HEXRD), which provided more accurate measurements. Microstructure was observed by scanning electron microscopy (SEM) and microhardness was measured for all conditions. HPT deformation was found to significantly enhance the α phase precipitation due the introduction of lattice defects such as dislocations or grain boundaries, which act as preferential nucleation sites. Moreover, in HPT-deformed material, α precipitates are small and equiaxed, contrary to the α lamellae in the non-deformed material. ω phase formation is suppressed due to massive α precipitation and consequent element partitioning. Despite that, HPT-deformed material after ageing exhibits the high microhardness exceeding 450 HV.

Keywords: β titanium alloys; severe plastic deformation; α phase precipitation; phase composition; high energy synchrotron X-ray diffraction

1. Introduction

The interest in metastable β -Ti alloys has gradually increased due to their high specific strength, which make them ideal for applications in the aerospace industry [1]. Manufacturing of medical implants and devices is another high-added-value field and constitutes a prospective application of metastable β titanium alloys [2]. These alloys offer higher strength levels than commonly used $\alpha + \beta$ alloys due to controlled precipitation of tiny particles of α phase [3]. The strength of titanium and Ti-based alloys can be further improved by achieving an ultra-fine grained (UFG) structure via severe plastic deformation methods (SPD) [4–7]. Manufacturing of UFG metastable β -Ti alloys is of significant

interest as demonstrated by recent reports [8–11]. This study focuses on the effect of microstructure refinement by SPD on the precipitation of α phase upon subsequent thermal treatment.

The α phase forms in metastable β Ti alloys by a standard mechanism of nucleation and growth. The kinetics of α phase formation in a solution-treated material is generally given by chemical composition of the alloy and the temperature of ageing. However, α phase precipitation also strongly depends on the microstructure since α phase particles nucleate at preferential sites such as grain and subgrain boundaries and dislocations [12,13].

In some β -Ti alloy, nanosized ω phase particles can also act as preferential nucleation sites for precipitation of α phase, although the exact mechanism of ω formation has not been fully resolved yet [14–18]. It is therefore of significant interest to investigate α phase precipitation in the presence of high concentration of lattice defects (UFG material) in an alloy prone to the ω phase formation. Binary metastable Ti15Mo alloy used in this study consists, similarly to other β -Ti alloys with similar degree of β stabilization, of a mixture of β and ω_{ath} (athermal ω) phases in the solution-treated (ST) condition [19,20]. This ω_{ath} phase forms during quenching of the alloy from the temperatures above β transus by a displacive diffusionless mechanism [21]. However, it was also reported that ω phase can form as a result of high deformation, and is referred to as deformation induced ω [8,22]. The $\beta \rightarrow \omega_{\text{ath}}$ transformation is reversible up to a temperature of 110 °C [23]. Upon ageing at higher temperatures, the ω_{ath} particles become stabilized by diffusion i.e., in Ti15Mo alloy by expelling Mo. This phase is referred to as ω_{iso} (isothermal ω) [24]. The size of particles of ω_{iso} phase is typically in the range of few nanometers up to 100 nm [19,24].

Solution-treated Ti15Mo alloy was processed by high-pressure torsion (HPT) [5] in order to achieve ultra-fine grained (UFG) microstructure with a high density of lattice defects. The equivalent von Mises strain achieved by HPT is heterogeneous and can be calculated according to Equation (1) [25]:

$$\varepsilon_{vM} = \frac{2\pi Nr}{\sqrt{3}h} \quad (1)$$

where r represents the distance from the center of the sample, h is the thickness of the specimen, and N is the number of revolutions. The equivalent inserted von Mises strain after a single HPT rotation ($N = 1$, $r = 10$ mm and thickness h of 1 mm) ranges from 0 (the exact center) up to 35 = 3500% (periphery). Such extreme strain results in a dislocation density exceeding $\rho = 5 \times 10^{14} \text{ m}^{-2}$ and grain size in the range of hundreds of nanometers [11,26].

The objective of this study was to investigate the effect of SPD on the mechanisms and kinetics of α phase precipitation and to compare it with the precipitation in the non-deformed solution-treated material. Both laboratory X-ray diffraction (XRD) and high-energy XRD using synchrotron radiation (HEXRD) were employed for this experimental study.

2. Materials and Methods

Ti15Mo (wt%) alloy was supplied by Carpenter Co. (Richmond, VA, USA) in the form of a rod with the diameter of 10 mm. The as-received material was solution treated (ST) in an inert Ar atmosphere at the temperature of 810 °C for 4 h and subsequently water quenched. The cylindrical samples of the length of 5 mm were first cut from the rod and pressed with 6 GPa to achieve disk-shaped samples with the diameter of 20 mm and the thickness of approximately 1 mm. Disk samples were subsequently subjected to HPT deformation at room temperature at Ufa State Aviation Technical University (USATU), Russian Federation. Note that this pre-HPT deformation induced deformation of about 75% is significantly lower than the actual HPT deformation. The detailed description of the HPT method can be found elsewhere [5]. For this study, samples after $N = 1$ HPT rotation were prepared.

ST and HPT deformed samples (hereafter referred to as non-deformed and HPT-deformed, respectively) were aged at temperatures of 400 °C and 500 °C for 1, 4, and 16 h. The ageing was performed by immersing the samples to preheated salt-bath (i.e., with very high heating rate) without air access and subsequently water quenched. HPT samples for scanning electron microscopy (SEM)

and microhardness study were prepared from the periphery part of the disks (>5 mm from the center) where the imposed strain is maximum. For XRD measurements, a quarter of a disk-shaped sample was used. All samples were mechanically grinded and polished by standard methods followed by a three-step vibratory polishing.

The microstructure of the specimens was observed using SEM Zeiss Auriga Compact Cross Beam (Jena, Germany) equipped with the energy dispersive spectroscopy (EDS) detector operated at 4 kV. K-line and L-line for Ti and Mo, respectively, were used for quantification of EDS data.

XRD measurement of the non-deformed Ti15Mo alloy was performed employing a Bruker D8 Advance powder X-ray diffractometer using Cu K_{α} radiation (Bruker AXS GmbH, Karlsruhe, Germany), with a variable divergent slit and a Sol X detector. The width of the beam was 6 mm and the sample was rotated, allowing it to probe the whole specimen surface. XRD measurements of the HPT-deformed Ti15Mo alloy were carried out on Bruker D8 Discover powder X-ray diffractometer. Vertical Bragg-Brentano geometry (2.5° Soller slits in both primary and secondary beam and 0.24° divergence slit) with filtered Cu K_{α} radiation was used. Beam size of $20 \text{ mm} \times 5\text{--}15 \text{ mm}$ (depending on the θ angle) was used. Note that the beam size is comparable to the size of the HPT disk. Diffraction patterns in both cases were collected at room temperature in the 2θ range from 30° to 130° and were analyzed using LeBail approach in the program Jana2006 (Václav Petříček, Michal Dušek and Lukáš Palatinus, Institute of Physics Academy of Sciences, Prague, Czech Republic).

The HEXRD measurement was carried out at the P07-HEMS beamline of PETRA III (Deutsches Elektronen-Synchrotron, Hamburg, Germany) [27] using the energy of 100 keV ($\lambda = 0.124 \text{ \AA}$) in a transmission mode perpendicular to the HPT surface. Patterns of entire Debye–Scherrer rings were acquired ex-situ from the bulk of Ti15Mo samples at room temperature. A PerkinElmer XRD 1621 image plate detector was used. The samples were kept fixed during the acquisition and measured 5 mm from the center of the sample with an incident beam of slit size of $1 \times 1 \text{ mm}^2$. The acquired diffraction patterns were processed by Rietveld structural refinement using FullProf software (Juan Rodriguez Carvajal, ILL Grenoble, France). Azimuthal averaging over 360° was performed first. HEXRD diffractograms after azimuthal averaging were treated by the March–Dollase approach in order to obtain at least rough estimates of volume fractions of individual phases. In fact, β phase peaks, which are the most intensive, could be fitted without the March–Dollase ‘adjustment’. Nevertheless, diffractions of evolving α and ω phases had to be treated by the March–Dollase approach to achieve reasonable agreement with the measured data [28]. Even with the use of the March–Dollase approach the resulting R-factors of the fit accuracy range between 15–20 for α and ω phases, while R-factor for β phase is around 10.

The microhardness of the samples was measured using the Vickers method with the use of microhardness tester Qness Q10a (Golling, Austria). Note that all samples from HPT disks were cut from the area at least 5 mm distant from the center where microhardness of HPT $N = 1$ condition is saturated [8]. For each specimen 0.5 kg load and the dwell time of 10 s were applied. At least 20 indents were evaluated for each sample in order to get satisfactory statistical results.

3. Results

3.1. Initial Conditions

Microstructure

The initial microstructure of the ST Ti15Mo alloy is shown in Figure 1. A coarse-grained (CG) structure consisting of grains of the average size of $\sim 50 \mu\text{m}$ is well visible due to the channeling contrast. In addition, brighter and darker areas are also visible in the material due to the chemical contrast (marked by yellow arrows in Figure 1). These chemical inhomogeneities were investigated by EDS. Table 1 summarizes the results of the EDS point analysis. Note that results were obtained by standardless EDS in which the measured spectra are compared to the data collected from standards by the EDS manufacturer under different conditions (namely different beam conditions). Such data

are therefore subjected to systematic error and as such they are not fully reliable in terms of exact quantitative Mo content determination. However, the relative difference in chemical composition between different areas is accurate and unambiguous.

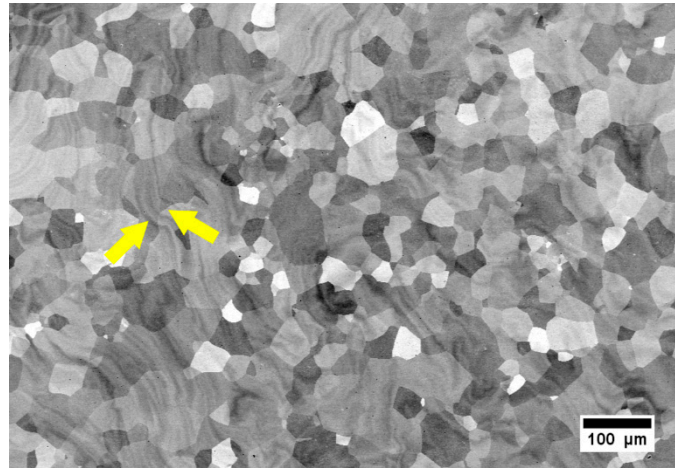


Figure 1. Scanning electron microscopy–back-scattered electrons (SEM–BSE) micrograph of the solution-treated (ST) Ti15Mo alloy (the yellow arrows indicate chemical inhomogeneities in the material).

Table 1. Chemical composition of the darker and brighter bands (marked by yellow arrows in Figure 1) as determined by energy dispersive spectroscopy (EDS) point analysis.

Element	Brighter Part (wt.%)	Darker Part (wt.%)
Ti	83.3 ± 0.5	85.7 ± 0.4
Mo	16.7 ± 0.5	14.3 ± 0.4

Local chemical inhomogeneities in the ST material were also investigated by EDS mapping. In Figure 2a, several β -grains and darker and lighter areas (visible especially in the top left corner of the image) are visible due to channeling contrast and chemical contrast (Z-contrast), respectively. EDS mapping confirms the chemical inhomogeneity—darker areas in Figure 2a contain less Mo as shown in Figure 2b. Variations in the local content of Mo (β stabilizing element) may affect the phase stability of the β phase matrix.

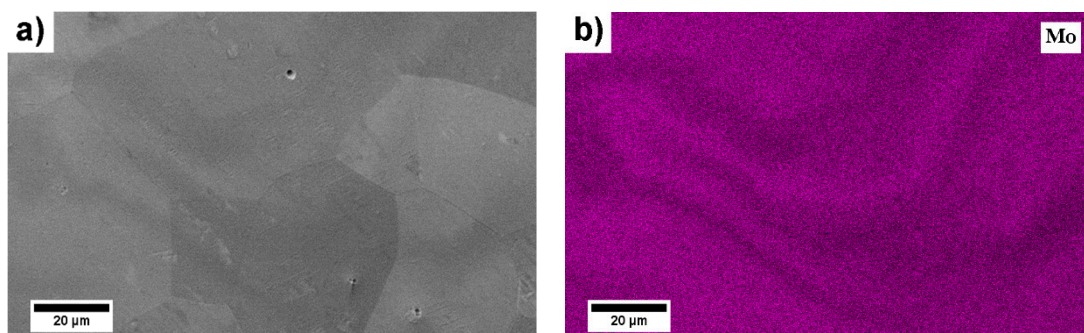


Figure 2. Local chemical inhomogeneities in ST Ti15Mo alloy: (a) scanning electron microscopy–secondary electrons (SEM–SE) micrograph of the area of interest, (b) corresponding element map of Mo using EDS.

The chemical inhomogeneities were also studied in the HPT-deformed sample. The SEM–BSE micrograph in Figure 3 clearly shows lighter and darker bands corresponding to the chemical

composition differences, which were also confirmed by EDS. Darker areas with lower Mo were formed from curly bands in the non-deformed material (Figure 1). In HPT deformed material, they are elongated in the direction of the deformation (Figure 3).

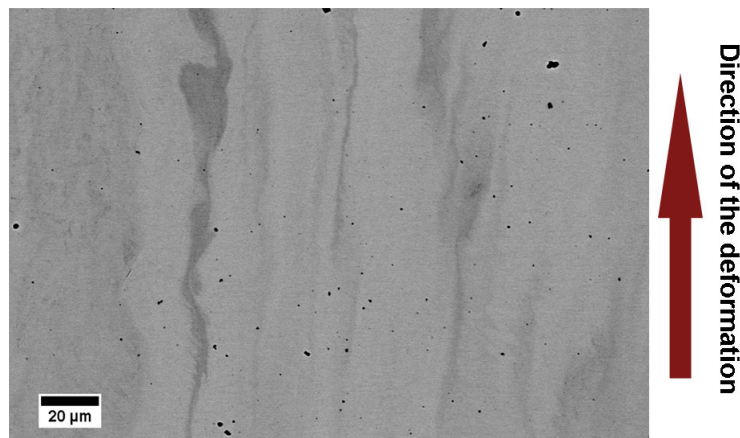


Figure 3. SEM–BSE micrograph of Ti15Mo alloy after high-pressure torsion (HPT) processing. Surface of HPT disk with highlighted direction of deformation (azimuthal direction). Darker and brighter areas are caused by the difference in chemical composition (black dots are polishing artefacts).

3.2. Non-Deformed and HPT-Deformed Material after Ageing

3.2.1. The Evolution of Microstructure during Ageing

SEM–BSE micrographs in Figure 4 show the evolution of the microstructures of the non-deformed material after ageing at 400 °C and 500 °C for 1–16 h. The microstructure consists of coarse-grained β matrix. At least one triple-junction is shown in each image. After ageing at 400 °C for 1 and 4 h, only β matrix is observed. In the specimen aged for a longer time (400 °C/16 h), nanometer-sized precipitates are seen in the SEM–BSE micrograph (note the higher magnification of this micrograph). These small ellipsoidal particles are particles of ω phase, which are visible due to chemical partitioning— ω phase particles are slightly Mo depleted [29]. Ageing at the higher temperature of 500 °C resulted in a precipitation of continuous and coarse α phase along grain boundaries (hereafter referred to as grain boundary α or GB α), which is also Mo depleted and appears as a long dark particle along the former β/β boundary (indicated by a yellow arrow). In the vicinity of the β grain boundaries, α phase particles with a typical lamellar morphology precipitated. Small ellipsoidal particles in the grain interior belong to ω phase. The contrast of these particles increases with the increasing ageing time due to ongoing chemical partitioning. After ageing at 500 °C for 16 h, tiny ellipsoidal ω particles are clearly seen in grain interiors, GB α is visible along the former β/β grain boundaries and α lamellae span from the GB α to the grain interiors. In conclusion, ω particles with ellipsoidal morphology can be observed by SEM in the grain interior after ageing at 500 °C and the fraction of α phase particles with lamellar morphology increases with increasing time of ageing at 500 °C. The coexistence of all three β , α , and ω phases is observed.

Figure 5 shows the microstructures of the HPT-deformed samples after ageing. Already after ageing at 400 °C/1 h, significant differences between the non-deformed and HPT-deformed specimens can be observed. In the non-deformed material, there is no evidence of α phase particles. On the other hand, small and equiaxed α particles already precipitated in HPT sample. In specimens aged at 400 °C for longer times of 4 h and 16 h, the volume fraction of the α phase increased and, simultaneously, α precipitates coarsened. Moreover, the precipitation is not homogeneous—some areas contain clearly more α phase particles. Ageing at 500 °C resulted in the formation of larger α particles, which are generally equiaxed, but not round—rather polygonal and sharp edged.

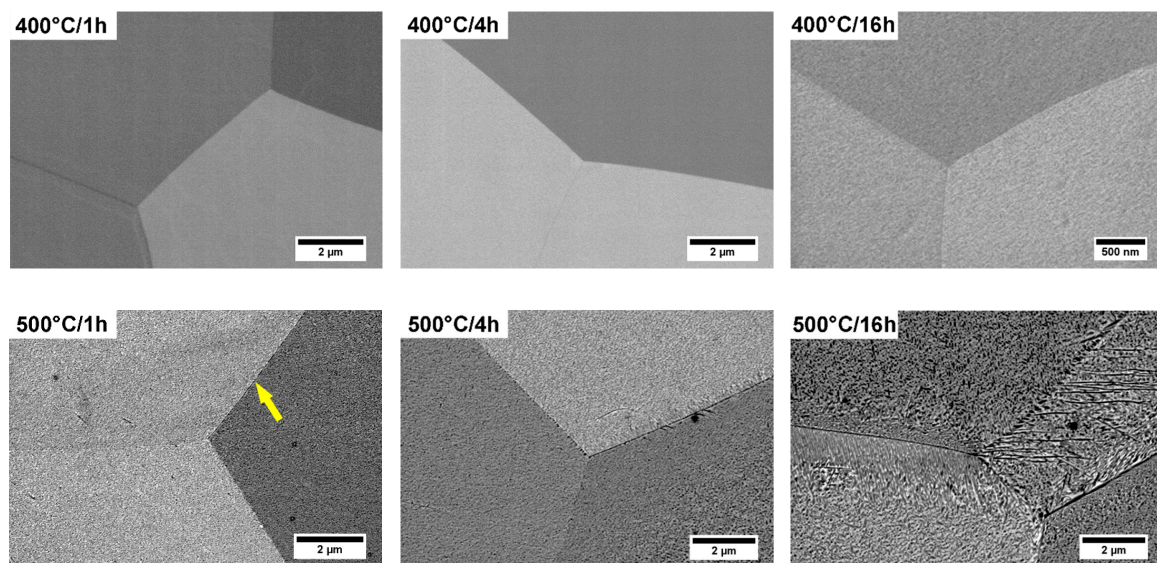


Figure 4. SEM–BSE micrographs of the non-deformed samples after ageing.

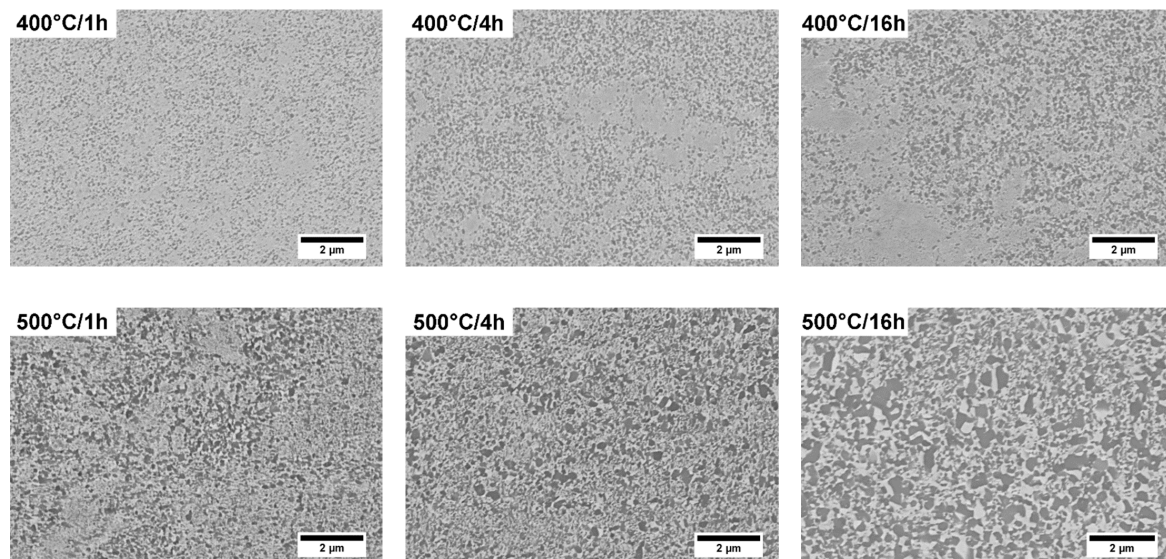


Figure 5. SEM–BSE micrographs of the samples deformed by high-pressure torsion (HPT-deformed samples) after ageing.

3.2.2. Evolution of Phase Composition during Ageing

The phase composition of the non-deformed and HPT-deformed samples before and after ageing is shown in laboratory XRD patterns in Figures 6 and 7, respectively. Both the measured (thin black curves) and fitted (colored curves) XRD patterns are shown. The interplanar distance is displayed on the horizontal axis for the comparison to the HEXRD data, while the y-axis shows the intensity in a logarithmic scale, allowing one to distinguish small peaks. The most important peaks, which best describe the evolution of emerging phases, are marked with arrows—full and open arrows for α and ω phase, respectively. A quantitative determination of phase content is not possible. The non-deformed specimen contains large grains with the size of hundreds of micrometers while HPT-deformed material is severely plastically deformed with high dislocation density and high internal stress resulted in the broadening of XRD peaks. Moreover, in both conditions, the grains have a preferred orientation as can be revealed from the relative intensity of the peaks. Therefore, laboratory XRD patterns could not be successfully fitted by any other method than the simple LeBail approach. However, several qualitative comparisons can be made.

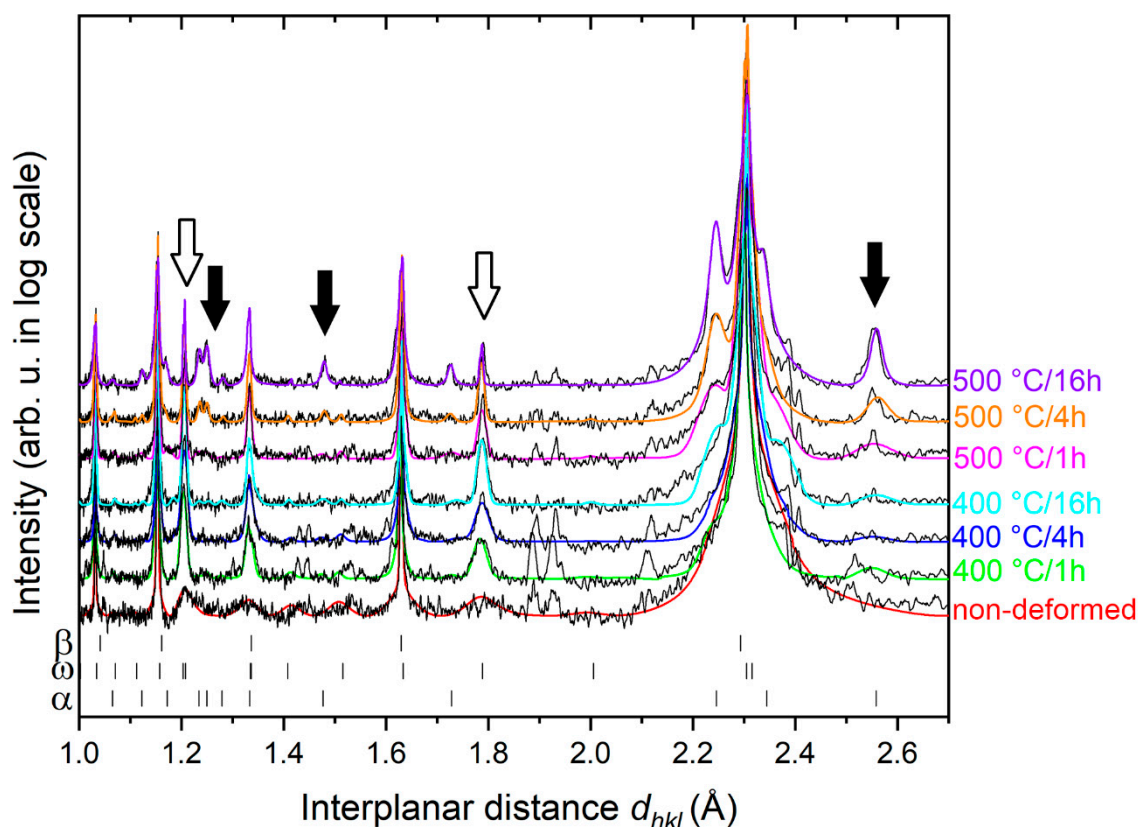


Figure 6. X-ray diffraction (XRD) patterns (in log-scale) of aged conditions of the non-deformed Ti15Mo alloy. Black thin curves correspond to data, colored curves are numerical fits. Non-deformed without ageing (red curve) and aged conditions (other colored curves) are displayed. The patterns are vertically shifted for clarity. The most important peaks are marked by full and open arrows for α and ω phase, respectively. Two unfitted peaks around $d_{hkl} = 1.9$ originated from the sample holder.

The non-deformed Ti15Mo alloy contains a mixture of β and ω phases. However, the identification of the ω phase content is difficult due to overlapping peaks of β and ω peaks. Nevertheless, ω peaks $(11-22)_{\omega}$ and $(11-21)_{\omega}$ can be observed at the interplanar distances $d_{hkl} \approx 1.2$ Å and $d_{hkl} \approx 1.8$ Å, respectively, as shown in Figure 6. Ageing of the non-deformed specimen at 400 °C/1 h (red curve in Figure 8) resulted in an increase of the intensity and narrowing of ω peaks (open arrows). In addition, small α phase peaks are also visible (full black arrows). XRD patterns of the non-deformed material aged at 400 °C for 1, 4, and 16 h are very similar. In the specimen aged at 500 °C for 1 h, the α phase is clearly present (full arrows in Figure 6). Moreover, its volume fraction increases with increasing ageing time (4–16 h), as also confirmed by SEM observations (cf. Figure 5); ω phase is still present in the specimen aged 500 °C even for the longest time of 16 h reported in [29].

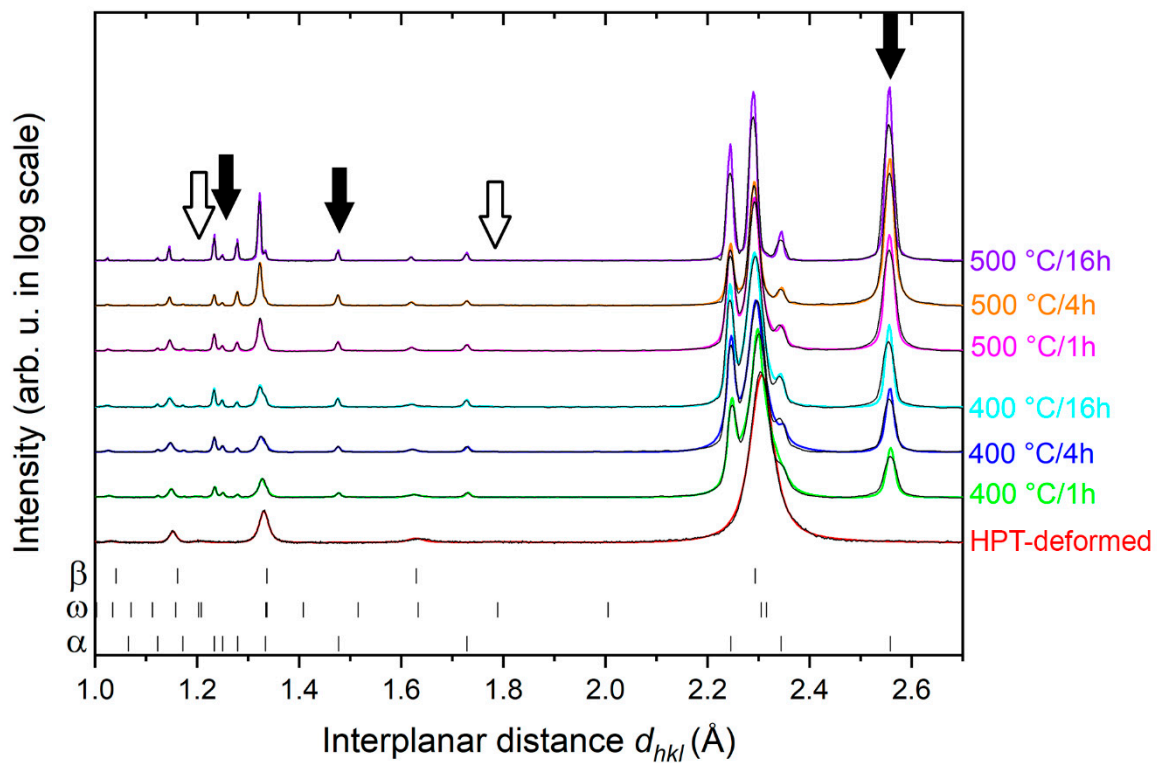


Figure 7. XRD patterns of aged conditions of the HPT-deformed Ti15Mo alloy: HPT-deformed without ageing (black curve) and aged under different conditions (colored curves) are displayed. The patterns are vertically shifted for clarity. The most important peaks are marked by full and open arrows for α and ω phase, respectively.

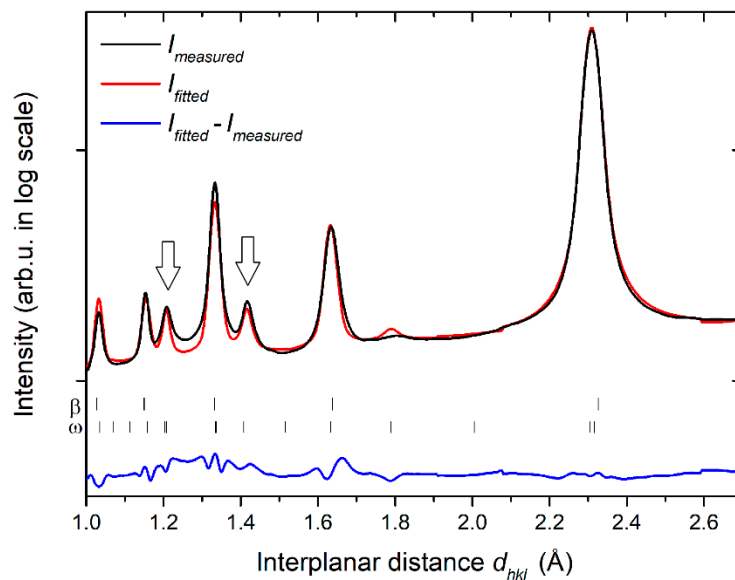


Figure 8. High-energy synchrotron X-ray diffraction (HEXRD) pattern of the HPT-deformed sample.

The XRD pattern of the HPT deformed specimen exhibits significantly broadened peaks due to enhanced dislocation density and reduced crystallite size in this specimen. Moreover, the peaks are slightly shifted to different values of interplanar distances due to residual stresses in the deformed material—the direction of the shift depends on the type of the residual stress [30].

The ω phase content in the HPT sample seems to be inferior to that in the non-deformed sample; only a tiny peak can be resolved at the interplanar distance $d_{hkl} \approx 1.2 \text{ \AA}$. However, the most intensive peaks of the ω phase coincide with the peaks of the β phase.

In order to obtain more precise information about volume fraction of individual phases, HEXRD measurement was carried out on the HPT-deformed sample. In contrast to the laboratory XRD, HEXRD provides a better signal-to-noise ratio and the simultaneous measurement of the scattering signal in various directions due to the use of a 2D detector and subsequent azimuthal averaging. Consequently, a better resolution of small peaks, namely those of the ω phase, is achieved. Figure 8 shows the HEXRD pattern of the HPT specimen. Both the measured and fitted intensities as well as the difference curve between the fitted and measured intensity are shown in Figure 8. The results indicate that the HPT-deformed alloy is a two-phase material with volume fractions of the β and ω phase of 72% and 28%, respectively (the error of the volume fractions estimation is approximately $\pm 5\%$).

In order to get more accurate results, the selected HPT-deformed specimen after ageing at 400 °C/1 h was examined using HEXRD. Both the measured and fitted intensity and the difference between the fitted and measured data are displayed in Figure 9.

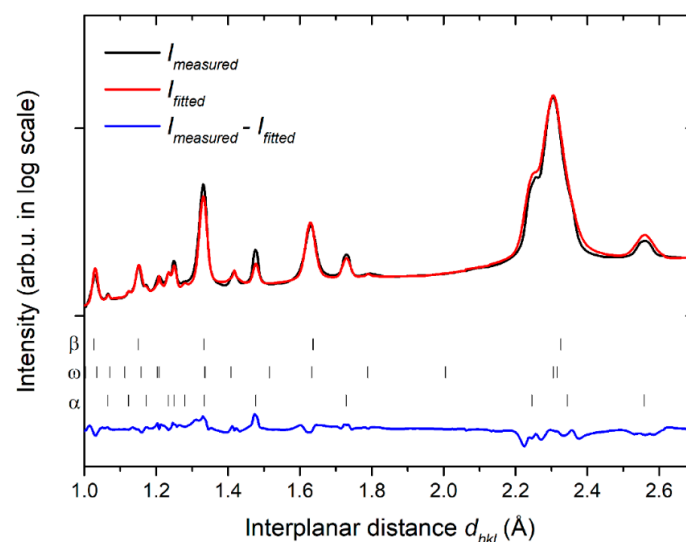


Figure 9. HEXRD pattern of the HPT-deformed sample after ageing 400 °C/1 h.

The volume fractions of individual phases in HPT-deformed sample before and after ageing at 400 °C/1 h are summarized in Table 2. The non-aged HPT-deformed material contains a high-volume fraction of the ω phase (28%). After ageing, the volume fraction decreases to approximately 9%. This is caused by enhanced volume fraction of the α phase, which reaches 23% in the aged condition.

Table 2. Volume fraction of individual phases in HPT-deformed Ti15Mo alloy as determined from high energy synchrotron X-ray diffraction (HEXRD). The experimental errors are also shown.

Material	Volume Fraction of the β Phase	Volume Fraction of the ω Phase	Volume Fraction of the α Phase
Ti15Mo HPT	72% \pm 5%	28% \pm 5%	-
Ti15Mo HPT + ageing 400 °C/1 h	67% \pm 5%	9% \pm 3%	23% \pm 4%

3.2.3. Microhardness Evolution during Ageing

Figure 10 shows the dependence of Vickers microhardness on ageing of the non-deformed and HPT-deformed samples. Ageing of both samples at 400 °C resulted in an abrupt increase of microhardness. In the non-deformed specimen, the microhardness increases with increasing ageing

time at 400 °C. On the other hand, in the HPT-deformed sample aged at 400 °C for 1 h the microhardness reaches the maximum (500 HV). With increasing ageing time at 400 °C the microhardness continuously decreases. Specimens aged at 500 °C exhibit lower microhardness than specimens aged at 400 °C. The microhardness of HPT sample aged at 500 °C for 16 h even drops below the microhardness of the non-aged HPT specimen.

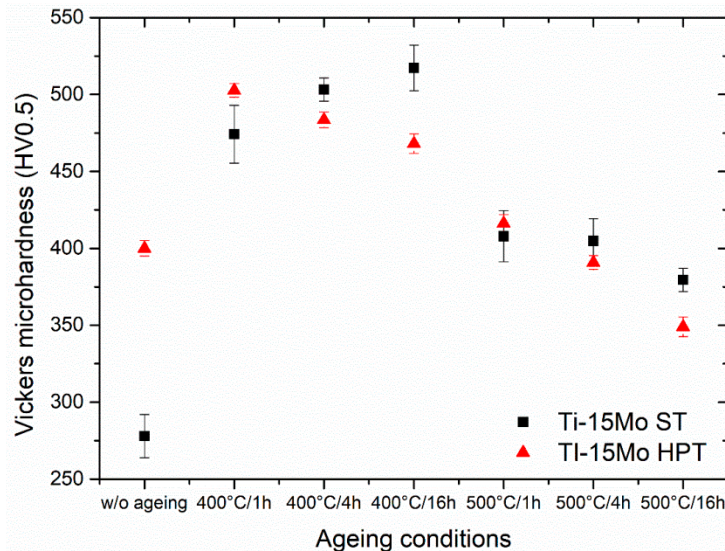


Figure 10. The evolution of the microhardness during ageing in the non-deformed and HPT-deformed samples.

4. Discussion

4.1. Enhanced α Phase Precipitation

A significant difference in the evolution of α phase in the non-deformed and the HPT-deformed conditions was observed. α phase is known to precipitate preferentially along the grain boundaries as so-called grain boundary α (GB α) [31]. Enhanced α phase precipitation was also found in pre-deformed materials due to the high dislocation density [32,33]. High concentration of defects in the HPT-deformed condition reduce the energy barrier for the nucleation of α phase. The growth of an α nuclei and its coarsening is controlled by the diffusion of Mo (β stabilizing element) in the β matrix [34]. It is well-known that the pipe diffusion along dislocation cores as well as the diffusion rate along grain boundaries are several orders of magnitude higher than the bulk diffusion [35]. As a consequence, the growth of the α precipitates along grain boundaries is also accelerated. The enhanced precipitation of the α phase in severely deformed metastable β Ti alloys was reported in several studies [36,37]. In the coarse-grained material, α phase particles precipitate in the form of lamellae, because certain mutual orientations of neighboring α and β lattices are associated with the significantly lower interfacial energy and therefore, lamellar shape is optimal for the reduction of the total interfacial energy of a precipitate [38]. On the other hand, α particles in the HPT-deformed materials are equiaxed, but not round—detailed inspection of Figure 5 reveals that particles are rather polygonal and sharp edged. It is assumed that α phase particles nucleate at triple junctions and all observed α particles are in fact GB α .

Ageing of HPT-deformed material (particularly at 400 °C/16 h) resulted in an inhomogeneous precipitation of α particles. Such inhomogeneity was reported to be caused by shear bands formed in the HPT deformed material [36,37,39,40]. However, we did not find any shear bands in the HPT material. On the other hand, we observed chemical inhomogeneities both in the non-deformed and in the HPT-deformed sample. In the latter case, the inhomogeneities are extended in the direction of HPT deformation (cf. Figure 3). As a consequence, the nucleation of the α phase particles may

be therefore promoted in the areas depleted in Mo, even if the shape and the scale of precipitation inhomogeneities in Figure 5 cannot be directly compared to Mo-depleted regions in Figure 3 due to very different magnification (zone of observation).

In the specimen aged at 500 °C, ω phase was retained in the non-deformed material while it was completely absent in the HPT-deformed specimen. Enhanced precipitation of the α phase results in the rejection of the β stabilizing Mo to the surrounding β matrix causing a thermodynamic stabilization of the β matrix and suppression of the formation of the ω phase HPT deformed material [26]. Similar behavior, i.e., the preferred α phase precipitation over the formation of the ω phase, was observed in Ti-25Nb-2Mo-4Sn alloy deformed by cold-rolling [41].

4.2. Microhardness Evolution

Microhardness is significantly increased by HPT deformation as discussed in detail in [8] due to the microstructural refinement, the introduction of high dislocation density, and increased content of ω phase. Ageing of both non-deformed and HPT-deformed materials at 400 °C resulted in microhardness increase. Moreover, similar microhardness values were observed in both conditions. However, the similar increase of the microhardness can be attributed to different effects in both conditions.

The hardening of the non-deformed material aged at 400 °C is caused by the ω particles—the nano-sized ω particles are stabilized by diffusion, their size increases, and they act as much stronger obstacles for motion of dislocations. One may assume that a moving dislocation can pass through (cut) ω_{ath} particles (known as Friedel effect [42]) as they are small and coherent. It is well known that the shear stress required for a dislocation to pass through a precipitate increases with its increasing size (within the Friedel's limit) and/or with increasing strength of the obstacle to dislocation motion [42,43]. Due to this and also because of the increasing volume fraction of ω phase, the hardness of the non-deformed material increases with increasing ageing time at 400 °C.

In HPT-deformed material, ageing at 400 °C already for 1 h results in the precipitation of tiny α phase particles, which are incoherent and cause significant Orowan strengthening. On the other hand, ω phase content is relatively low. The decreasing microhardness of the HPT material aged at 400 °C for longer times (4 and 16 h) may be related to the coarsening of the $\alpha + \beta$ microstructure. Both β matrix grains and α phase precipitates coarsen with increasing ageing time. The same process is even more pronounced during ageing at 500 °C. The microhardness was found to monotonically decrease with increasing ageing temperature and time. The maximum microhardness is therefore achieved in the HPT specimen aged at 400 °C. In a recent study [44], HPT deformation of Ti15Mo/TiB composite was performed at 400 °C and very high microhardness values (650 HV after $N = 1$ HPT revolution) were achieved.

The microhardness of the non-deformed material aged at 500 °C is inferior to that of the material aged at 400 °C for all ageing times. The relative decrease of microhardness of the non-deformed material with increasing temperature of ageing may be attributed to the decreasing volume fraction and increasing size of ω particles, whose size is well beyond the Friedel's limit.

Severe plastic deformation of the parent β phase and the introduction of high density of defects significantly accelerates the α phase precipitation. An important additional effect of this enhancement is the reduction of the content of ω phase and its disappearance at comparatively low ageing temperatures.

5. Conclusions

Metastable β titanium Ti15Mo alloy was prepared by HPT and subsequently aged at 400 °C and 500 °C. Phase transformations were observed by XRD and SEM. The following conclusions can be drawn from this study:

Precipitation of the α phase in the HPT-deformed material is significantly enhanced by the high density of lattice defects such as dislocations or grain boundaries, which act as preferential nucleation sites for α phase precipitation.

α phase particles in the non-deformed material precipitate in the form of lamellae, while in the HPT-deformed material, α precipitates are small, equiaxed, and polygonal in shape suggesting that they all formed as grain boundary α at the β grains triple junctions.

Two-phase $\alpha + \beta$ microstructure continuously coarsens with increasing temperature and time of ageing.

Deformation by HPT significantly increases the microhardness due to microstructural refinement, but also due to the formation of ω phase.

During annealing, the microhardness of the non-deformed material is governed mainly by the evolution of ω phase. In the HPT-deformed material, the main strengthening mechanism is the precipitation of fine α phase particles.

Author Contributions: K.B. conducted SEM experiments, interpreted the results, and wrote the majority of the manuscript. J.S. and M.J. discussed achieved results and wrote parts of the manuscript. A.V. cooperated on SEM observations and microhardness measurements. P.S. interpreted achieved mechanical properties. P.B.-V. conducted HEXRD experiment. F.L. and P.D. conducted laboratory XRD experiments. V.P. and I.S. prepared material by HPT.

Funding: This work was financially supported by the Czech Science Foundation under the project 17-04871S and by ERDF, project No. CZ.02.1.01/0.0/0.0/15_003/0000485. The Deutsches Elektronen-Synchrotron (DESY) is acknowledged for the provision of synchrotron radiation facilities in the framework of the proposal I-20150533 EC. Partial financial support by the Czech Ministry of Education, Youth and Sports under the project LTARF18010 is also gratefully acknowledged.

Conflicts of Interest: The authors declare no conflict of interest.

References

1. Boyer, R.R. An overview on the use of titanium in the aerospace industry. *Mater. Sci. Eng. A* **1996**, *213*, 103–114. [[CrossRef](#)]
2. Steinemann, S.G. Titanium—the material of choice? *Periodontol 2000* **1998**, *17*, 7–21. [[CrossRef](#)]
3. Weiss, I.; Semiatin, S.L. Thermomechanical processing of beta titanium alloys—An overview. *Mater. Sci. Eng. A* **1998**, *243*, 46–65. [[CrossRef](#)]
4. Valiev, R.Z.; Islamgaliev, R.K.; Alexandrov, I.V. Bulk nanostructured materials from severe plastic deformation. *Prog. Mater. Sci.* **2000**, *45*, 103–189. [[CrossRef](#)]
5. Zhilyaev, A.P.; Langdon, T.G. Using high-pressure torsion for metal processing: Fundamentals and applications. *Prog. Mater. Sci.* **2008**, *53*, 893–979. [[CrossRef](#)]
6. Kawabe, Y.; Muneki, S. Strengthening and Toughening of Titanium Alloys. *ISIJ Int.* **1991**, *31*, 785–791. [[CrossRef](#)]
7. Valiev, R.Z.; Langdon, T.G. Principles of equal-channel angular pressing as a processing tool for grain refinement. *Prog. Mater. Sci.* **2006**, *51*, 881–981. [[CrossRef](#)]
8. Václavová, K.; Stráský, J.; Polyakova, V.; Stráská, J.; Nejezchlebová, J.; Seiner, H.; Semenova, I.; Janeček, M. Microhardness and microstructure evolution of ultra-fine grained Ti-15Mo and TIMETAL LCB alloys prepared by high pressure torsion. *Mater. Sci. Eng. A* **2017**, *682*, 220–228. [[CrossRef](#)]
9. Kent, D.; Wang, G.; Yu, Z.; Ma, X.; Dargusch, M. Strength enhancement of a biomedical titanium alloy through a modified accumulative roll bonding technique. *J. Mech. Behav. Biomed.* **2011**, *4*, 405–416. [[CrossRef](#)]
10. Yilmazer, H.; Niinomi, M.; Nakai, M.; Cho, K.; Hieda, J.; Todaka, Y.; Miyazaki, T. Mechanical properties of a medical β -type titanium alloy with specific microstructural evolution through high-pressure torsion. *Mater. Sci. Eng. C* **2013**, *33*, 2499–2507. [[CrossRef](#)]
11. Janeček, M.; Čížek, J.; Stráský, J.; Václavová, K.; Hruška, P.; Polyakova, V.; Gatina, S.; Semenova, I. Microstructure evolution in solution treated Ti15Mo alloy processed by high pressure torsion. *Mater. Charact.* **2014**, *98*, 233–240. [[CrossRef](#)]
12. Ivasishin, O.M.; Markovskiy, P.E.; Semiatin, S.L.; Ward, C.H. Aging response of coarse- and fine-grained β titanium alloys. *Mater. Sci. Eng. A* **2005**, *405*, 296–305. [[CrossRef](#)]
13. Makino, T.; Chikaizumi, R.; Nagaoka, T.; Furuhashi, T.; Makino, T. Microstructure development in a thermomechanically processed Ti15V3Cr3Sn3Al alloy. *Mater. Sci. Eng. A* **1996**, *213*, 51–60. [[CrossRef](#)]

14. Barriobero-Vila, P.; Requena, G.; Schwarz, S.; Warchomicka, F.; Buslaps, T. Influence of phase transformation kinetics on the formation of α in a β -quenched Ti-5Al-5Mo-5V-3Cr-1Zr alloy. *Acta Mater.* **2015**, *95*, 90–101. [[CrossRef](#)]
15. Barriobero-Vila, P.; Requena, G.; Warchomicka, F.; Stark, A.; Schell, N.; Buslaps, T. Phase transformation kinetics during continuous heating of a β -quenched Ti-10V-2Fe-3Al alloy. *J. Mater. Sci.* **2015**, *50*, 1412–1426. [[CrossRef](#)]
16. Zheng, Y.; Williams, R.E.A.; Sosa, J.M.; Talukder, A.; Wang, Y.; Banerjee, R.; Fraser, H.L. The indirect influence of the ω phase on the degree of refinement of distributions of the α phase in metastable β -Titanium alloys. *Acta Mater.* **2016**, *103*, 165–173. [[CrossRef](#)]
17. Zheng, Y.; Williams, R.E.A.; Wang, D.; Shi, R.; Nag, S.; Kami, P.; Banerjee, R.; Wang, Y.; Fraser, H.L. Role of ω phase in the formation of extremely refined intragranular α precipitates in metastable β -titanium alloys. *Acta Mater.* **2016**, *103*, 850–858. [[CrossRef](#)]
18. Li, T.; Kent, D.; Sha, G.; Liu, H.; Fries, S.G.; Ceguerra, A.V.; Dargusch, M.S.; Cairney, J.M. Nucleation driving force for ω -assisted formation of α and associated ω morphology in β -Ti alloys. *Scripta Mater.* **2018**, *155*, 149–154. [[CrossRef](#)]
19. Zháňal, P.; Hrcuba, P.; Hájek, M.; Smola, B.; Stráský, J.; Šmilauerová, J.; Veselý, J.; Janeček, M. Evolution of ω phase during heating of metastable β titanium alloy Ti-15Mo. *J. Mater. Sci.* **2018**, *53*, 837–845. [[CrossRef](#)]
20. Nag, S.; Banerjee, R.; Srinivasan, R.; Hwang, J.Y.; Harper, M.; Fraser, H.L. ω -Assisted nucleation and growth of α precipitates in the Ti-5Al-5Mo-5V-3Cr-0.5Fe β titanium alloy. *Acta Mater.* **2009**, *57*, 2136–2147. [[CrossRef](#)]
21. Šmilauerová, J.; Hrcuba, P.; Kriegner, D.; Holý, V. On the completeness of the $\beta \rightarrow \omega$ transformation in metastable β titanium alloys. *J. Appl. Crystallogr.* **2017**, *50*, 283–287. [[CrossRef](#)]
22. Kuan, T.S.; Ahrens, R.R.; Sass, S.L. The stress-induced omega phase transformation in Ti-V alloys. *Metall. Trans. A* **1975**, *6*, 1767–1774. [[CrossRef](#)]
23. Zháňal, P.; Hrcuba, P.; Šmilauerová, J.; Stráský, J.; Janeček, M.; Smola, B.; Hájek, M. Phase Transformations in Ti-15Mo Investigated by in situ Electrical Resistance. *Acta Phys. Pol. A* **2015**, *128*, 779–783. [[CrossRef](#)]
24. Devaraj, A.; Nag, S.; Srinivasan, R.; Williams, R.E.A.; Banerjee, S.; Banerjee, R.; Fraser, H.L. Experimental evidence of concurrent compositional and structural instabilities leading to ω precipitation in titanium-molybdenum alloy. *Acta Mater.* **2012**, *60*, 596–609. [[CrossRef](#)]
25. Valiev, R.Z.; Ivanisenko, Y.V.; Rauch, E.F.; Baudalet, B. Structure and deformation behaviour of Armco iron subjected to severe plastic deformation. *Acta Mater.* **1996**, *44*, 4705–4712. [[CrossRef](#)]
26. Václavová, K.; Stráský, J.; Zháňal, P.; Veselý, J.; Polyakova, V.; Semenova, I.; Janeček, M. Ultra-fine grained microstructure of metastable beta Ti-15Mo alloy and its effects on the phase transformations. *IOP Conf. Ser. Mater. Sci. Eng.* **2017**, *194*, 012021. [[CrossRef](#)]
27. Schell, N.; King, A.; Beckmann, F.; Fischer, T.; Müller, M.; Schreyer, A. The High Energy Materials Science Beamline (HEMS) at PETRA III. *Mater. Sci. Forum* **2014**, *772*, 57–61. [[CrossRef](#)]
28. Dollase, W.A. Correction of intensities for preferred orientation in powder diffractometry: Application of the March model. *J. Appl. Crystallogr.* **1986**, *19*, 267–272. [[CrossRef](#)]
29. Bartha, K. Phase transformation in ultra-fine grained titanium alloys. Ph.D. Thesis, Charles University, Prague, Czech Republic, 19 June 2019.
30. Hauk, V. *Structural and Residual Stress Analysis by Nondestructive Methods*, 1st ed.; Elsevier: Amsterdam, Netherlands, 1997.
31. Šmilauerová, J.; Janeček, M.; Hrcuba, P.; Stráský, J.; Veselý, J.; Kužel, R.; Rack, H.J. Ageing response of sub-transus heat treated Ti-6.8Mo-4.5Fe-1.5Al alloy. *J. Alloy. Compd.* **2017**, *724*, 373–380. [[CrossRef](#)]
32. Furuhashi, T.; Nakamori, H.; Maki, T. Crystallography of α Phase Precipitated on Dislocations and Deformation Twin Boundaries in a β Titanium Alloy. *Mater. Trans. JIM* **1992**, *33*, 585–595. [[CrossRef](#)]
33. Zhang, B.; Yang, T.; Huang, M.; Wang, D.; Sun, Q.; Wang, Y.; Sun, J. Design of uniform nano α precipitates in a pre-deformed β -Ti alloy with high mechanical performance. *J. Mater. Res. Technol.* **2019**, *8*, 777–787. [[CrossRef](#)]
34. Semiatin, S.L.; Knisley, S.L.; Fagin, P.N.; Barker, D.R.; Zhang, F. Microstructure evolution during alpha-beta heat treatment of Ti-6Al-4V. *Metall. Mater. Trans. A* **2003**, *34*, 2377–2386. [[CrossRef](#)]
35. Legros, M.; Dehm, G. Observation of Giant diffusivity along dislocation core. *Science* **2008**, *319*, 1646–1649. [[CrossRef](#)] [[PubMed](#)]

36. Jiang, B.; Tsuchiya, K.; Emura, S.; Min, X. Effect of High-Pressure Torsion Process on Precipitation Behavior of α Phase in β -Type Ti–15Mo Alloy. *Mater. Trans.* **2014**, *55*, 877–884. [[CrossRef](#)]
37. Zafari, A.; Xia, K. Formation of equiaxed α during ageing in a severely deformed metastable β Ti alloy. *Scr. Mater.* **2016**, *124*, 151–154. [[CrossRef](#)]
38. Furuhashi, T.; Makino, T.; Idei, Y.; Ishigaki, H.; Takada, A.; Maki, T. Morphology and Crystallography of α Precipitates in β Ti–Mo Binary Alloys. *Mater. Trans. JIM* **1998**, *39*, 31–39. [[CrossRef](#)]
39. Xu, W.; Wu, X.; Stoica, M.; Calin, M.; Kühn, U.; Eckert, J.; Xia, K. On the formation of an ultrafine-duplex structure facilitated by severe shear deformation in a Ti–20Mo β -type titanium alloy. *Acta Mater.* **2012**, *60*, 5067–5078. [[CrossRef](#)]
40. Xu, W.; Edwards, D.P.; Wu, X.; Stoica, M.; Calin, M.; Kühn, U.; Eckert, J.; Xia, K. Promoting nano/ultrafine-duplex structure via accelerated α precipitation in a β -type titanium alloy severely deformed by high-pressure torsion. *Scr. Mater.* **2013**, *68*, 67–70. [[CrossRef](#)]
41. Guo, S.; Meng, Q.; Hu, L.; Liao, G.; Zhao, X.; Xu, H. Suppression of isothermal ω phase by dislocation tangles and grain boundaries in metastable β -type titanium alloys. *J. Alloy. Compd.* **2013**, *550*, 35–38. [[CrossRef](#)]
42. Friedel, J. *Dislocations*, 1st ed.; Smoluchowski, R., Kurti, N., Eds.; Pergamon Press: Oxford, UK, 1964.
43. Labusch, R. A Statistical Theory of Solid Solution Hardening. *Phys. Status Solidi (b)* **1970**, *41*, 659–669. [[CrossRef](#)]
44. Zherebtsov, S.; Ozerov, M.; Klimova, M.; Stepanov, N.; Vershinina, T.; Ivanisenko, Y.; Salishchev, G. Effect of High-Pressure Torsion on Structure and Properties of Ti-15Mo/TiB Metal-Matrix Composite. *Materials* **2018**, *11*, 2426. [[CrossRef](#)] [[PubMed](#)]



© 2019 by the authors. Licensee MDPI, Basel, Switzerland. This article is an open access article distributed under the terms and conditions of the Creative Commons Attribution (CC BY) license (<http://creativecommons.org/licenses/by/4.0/>).

Review

Developing Nanostructured Ti Alloys for Innovative Implantable Medical Devices

Ruslan Z. Valiev ^{1,2,*}, Egor A. Prokofiev ², Nikita A. Kazarinov ², Georgy I. Raab ¹, Timur B. Minasov ³ and Josef Stráský ⁴

¹ Institute of Physics of Advanced Materials, Ufa State Aviation Technical University, 12 K. Marx street, 450008 Ufa, Russia; giraab@mail.ru

² Laboratory of Mechanics of Advanced Bulk Nanomaterials, Saint Petersburg State University, Universitetskiy prospekt 28, Peterhof, 198504 St. Petersburg, Russia; egpro@mail.ru (E.A.P.); n.kazarinov@spbu.ru (N.A.K.)

³ Department of Traumatology and Orthopedics, Bashkir State Medical University, 3 Lenin street, 450008 Ufa, Russia; m004@yandex.ru

⁴ Department of Physics of Materials, Charles University, Ke Karlovu 3, 121 16 Prague, Czech Republic; josef.strasky@gmail.com

* Correspondence: ruslan.valiev@ugatu.su

Received: 31 October 2019; Accepted: 14 February 2020; Published: 21 February 2020



Abstract: Recent years have witnessed much progress in medical device manufacturing and the needs of the medical industry urges modern nanomaterials science to develop novel approaches for improving the properties of existing biomaterials. One of the ways to enhance the material properties is their nanostructuring by using severe plastic deformation (SPD) techniques. For medical devices, such properties include increased strength and fatigue life, and this determines nanostructured Ti and Ti alloys to be an excellent choice for the engineering of implants with improved design for orthopedics and dentistry. Various reported studies conducted in this field enable the fabrication of medical devices with enhanced functionality. This paper reviews recent development in the field of nanostructured Ti-based materials and provides examples of the use of ultra-fine grained Ti alloys in medicine.

Keywords: nanostructured Ti alloys; severe plastic deformation; enhanced strength and fatigue life; medical implants with improved design; shape-memory NiTi alloy; functionality

1. Introduction

Presently, Ti and its alloys represent the top choice when a combination of high strength, light weight, and affordable cost are required, such as in the area of medical device manufacturing. However, the clinical demands for implantable medical devices are growing rapidly, and nowadays new Ti alloys are being investigated in terms of their chemical composition optimization, manufacturing processes and modification of surface to meet the appropriate medical standards and comply with regulation [1,2]. One possibility to design and manufacture new materials with enhanced properties focuses on nanostructuring of metallic materials using the so-called severe plastic deformation (SPD) techniques, which have become a cutting edge and promising area in materials science and engineering [3,4].

Different SPD techniques are applied to refine grains in metallic materials to below micrometer range or even to the nanosized range. SPD techniques are also efficient for the formation of nanoclusters and nanoprecipitates of secondary phases, enhancing the mechanical and functional properties of the materials [4,5]. A whole variety of SPD techniques have been developed and put forward to provide very high strains ($\epsilon > 5$) under high applied pressure, such as accumulative roll bonding

(ARB), including multiple forging, twist extrusion, and others [6–8]. However, equal channel angular pressing (ECAP) and high pressure torsion (HPT), introduced already in the pioneering works [3], remain the most used methods for the production of ultrafine-grained (UFG) materials. Principles of these techniques, developed devices and microstructure evolution during processing steps have been thoroughly reviewed in numerous studies [3–7,9,10]. Recently, these deformation techniques have been further upgraded for practical application [11,12].

Nanostructuring of metallic materials increases material strength due to work hardening and grain refinement [13,14], consequently, fatigue life can be also significantly increased by microstructure refinement [15]. Understanding material processing by SPD techniques is essential for designing of medical devices with improved functionality as it not only improves mechanical properties but also affects corrosion and biomedical properties [16–18]. Improved strength and enhanced biomedical response of a nanostructured material can be efficiently used in dental implants; a stent of such permanent implant manufactured from nanostructured Ti can be significantly smaller due to the increased strength and therefore less harmful for a patient [19].

Recently, materials scientists have been exploring possibilities of improved interaction of nanostructured materials with body tissues, for instance bones. In this respect, surface modifications of bulk nanomaterials demonstrate encouraging results [17,18,20,21]. These improvements provide the possibility for development and design of implantable medical devices that perform better and provide improved functionality in comparison to their counterparts manufactured from common coarse-grained materials. This review article outlines the progress in engineering of advanced nanostructured Ti alloys and medical implants/devices manufactured from those advanced materials.

2. SPD Processing of Nanostructured Titanium Materials

2.1. Commercially Pure Ti

The first studies devoted to Ti-based materials potentially applicable in medicine were applied to commercial purity titanium (CP Ti) due to its high biocompatibility with living tissues [22]. Unparalleled biocompatibility of Ti was the main interest of many clinical studies of medical devices and tools applied in traumatology, orthopedics, and dentistry. Unfortunately, CP Ti is characterized by reduced strength when compared to other metallic materials used in biomedical devices such as steels or cobalt-based alloys. Achieving higher strength level is possible by alloying or thermo-mechanical processing, but then the Ti-based materials usually lose their biometric response or fatigue performance. Therefore, SPD processing was considered as an alternative strategy proving that nanostructuring of CP Ti may become a novel approach to improve the mechanical properties of this material to achieve its high-performance [13,17,19,20,23]. Apart from enhancing mechanical properties, this strategy is also advantageous in improving the biological response of the surface of the CP titanium based products [18,20].

The first results on nanostructured CP Ti Grade 4 (O–0.34%, Fe–0.3%, C–0.052%, N–0.015%, all in wt.%, balance–Ti) were achieved by Valiev et al. aiming on manufacturing rods with significantly enhanced mechanical properties and superior biomedical response for the fabrication of dental implants [19]. The processing route involved equal-channel angular pressing (ECAP) as an SPD technique [9] followed by thermo-mechanical treatment by forging and, finally, drawing. Continuous SPD processing by ECAP-Conform (ECAP-C) and subsequent drawing, was capable of producing rods with the diameter of 7 mm and the length of 3 m with homogeneous ultrafine-grained (UFG) structure along the entire length of the rods [23,24]. Furthermore, ECAP-Conform represents an economical SPD-based fabrication procedure for mass production of ‘nanoTi’.

After combined severe plastic deformation and thermo-mechanical processing, the grain size was significantly reduced from 25 μm in the initial Ti rods to 150 nm in the processed material. Figure 1 illustrates the effect of ECAP-C strain on the density of high-angle boundaries (HAB) and mechanical strength of CP Ti Grade 4 [21].

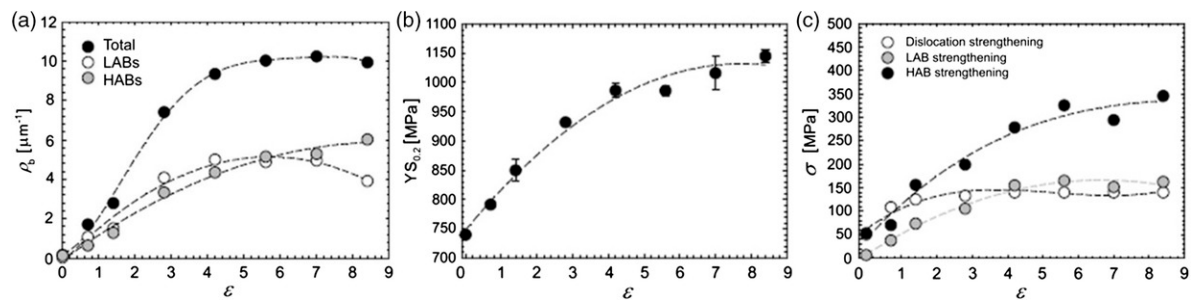


Figure 1. Influence of ECAP-C strain on (a) grain boundary (GB) density, (b) yield strength and (c) the contribution of various strengthening mechanisms [21].

Table 1 shows the improved mechanical properties of CP Ti after nanostructuring by ECAP and subsequent thermomechanical treatment. The strength of the nanostructured titanium is doubled when compared to the conventional CP titanium. The increase in strength was achieved without reduction of ductility (total elongation to failure is above the limit of 10%), which is otherwise commonly observed after intensive drawing or rolling.

Table 1. Mechanical properties of coarse-grained (CG) and nanostructured CP Grade 4 Ti. Annealed Ti-6Al-4V ELI (extra low interstitials) alloy for comparison.

State	Processing	UTS, MPa	YS, MPa	Elongation, %	Reduction Area, %	Fatigue Strength at 10^6 Cycles
1	Initial CG Ti	700	530	25	52	340
2	nanoTi	1240	1200	12	42	620
3	Annealed Ti-6Al-4V ELI	940	840	16	45	530

Fatigue tests of conventional and nanostructured CP Ti were conducted in air at room temperature in accordance with ASTM E 466-96 with the loading frequency of 20 Hz and $R = 0.1$. Table 1 shows that the fatigue strength of nanoTi [17,24] after one million cycles is almost doubled when compared to the conventional CP titanium and even exceeds the fatigue performance of the Ti-6Al-4V alloy [22,25]. Significant enhancement of fatigue properties and improved strength of nanostructured Ti allow us to produce smaller sizes of implants and therefore to reduce the extent of a surgical intervention (see also Section 3).

CP Ti is known for its considerable biocompatibility which results from the presence of the protective oxide film. Titanium dioxide TiO_2 forms naturally on the surface of CP Ti and represents a stable protective layer on that a mineralized bone matrix can be attached. This film is usually 5–10 nm thick and biologically inert, thus it prevents a potentially negative reaction between the surrounding body environment and the metal [22].

NanoTi with UFG structure containing high density of non-equilibrium grain boundaries achieved by SPD is also characterized by significantly increased internal energy of the material [3]. This fact may result in considerable change in the morphology of the oxide film on the material surface. NanoTi with polished surface exhibits improved biological reaction of the surface as confirmed by recent studies in a series of experiments through cytocompatibility tests using mouse fibroblast cells [20,26–29]. At the same time, additional improvement of biomedical properties of nanostructured titanium can be achieved by dedicated surface modifications such as chemical etching or bioactive coatings [17,18].

2.2. Titanium Alloys

Two-phase ($\alpha + \beta$) titanium alloys such as Ti-6Al-4V and Ti-6Al-7Nb continue to be the most important metallic materials in the dental and orthopedic fields due to their excellent mechanical properties and satisfactory biocompatibility [2,22,30,31].

Several recent studies reported improved mechanical and functional properties of nanostructured titanium alloys.

Microstructure and mechanical properties of Ti-6Al-4V ELI (extra low interstitial alloys for medical applications) prepared by SPD are reported in [15,32,33]. Round rods of the two-phase alloy with the diameter of 40 mm (Intrinsic Devices Company, San Francisco, CA, USA) and with chemical composition: Ti-base, Al-6.0%; V-4.2%; Fe-0.2%; O-0.11%; N-0.0025%; H-0.002%, C-0.001% (wt.%) had the grain size of about 8 μm in a cross-section and 20 μm in a longitudinal section. X-ray diffraction analysis proved that the volume fractions of α and β phases were approximately 85% and 15%, respectively. 250 mm length rods were processed in two steps. The rods were subjected to ECAP via route Bc at 600 $^{\circ}\text{C}$ and subsequently extruded, altogether with total strain of 4.2 [33]. The extrusion steps were carried out at 300 $^{\circ}\text{C}$ with the last pass at room temperature for additional strengthening. The rods with the diameter of 18 mm and length up to 300 mm were produced. The rods were finally annealed in the temperature range from 200 $^{\circ}\text{C}$ to 800 $^{\circ}\text{C}$ for 1 h and subsequently cooled in air.

Transmission electron microscopy (TEM) studies showed that SPD leads to a complex UFG structure containing refined grains and subgrains with a mean size of about 300 nm.

Stress–strain curves for the initial coarse-grained and UFG material shown in Figure 2 demonstrate that the alloy after grain refinement by SPD underwent significant strengthening. Tensile elongation of the UFG material (curve 2) is reduced from 17% to 9%. Strength/ductility trade off, however, improved after subsequent annealing at 500 $^{\circ}\text{C}$. The results of tensile tests correspond to the measurement of microhardness [32,33].

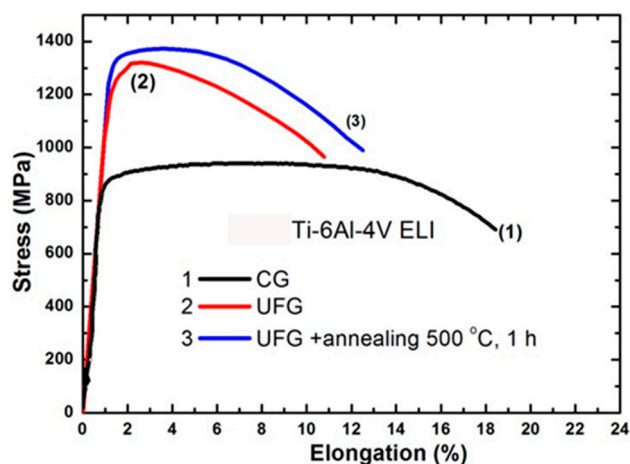


Figure 2. Engineering stress–strain tensile curves of the Ti-6Al-4V ELI alloy: coarse-grained material (initial) (1); UFG condition (2) and UFG condition after annealing at 500 $^{\circ}\text{C}$ (3).

In accordance with [10], enhancement of the ductility in the UFG material by annealing is clearly associated with a decrease of internal elastic stress and dislocation density. Simultaneous additional strengthening of the alloy can be explained by the observed decrease in content of metastable β -phase after cooling from the annealing temperature. Its volume fraction in the UFG alloy annealed at 500 $^{\circ}\text{C}$ can be higher than before annealing, as shown in [10], due to quenching from the annealing temperature. Despite no visible particles of any secondary phase, aging processes might have caused grain boundary segregations associated with additional improvement of the properties of the annealed UFG material [34].

Fine tuning of mechanical properties by annealing after the SPD processing is limited mainly by grain growth occurring at elevated temperatures. Thermal stability of UFG structure of commercially pure Ti follows classical grain growth depending on temperature via Arrhenius equation [35] and limited to approximately 450 °C [36]. Nanostructured $\alpha + \beta$ exhibit enhanced thermal stability up to 550 °C [37].

Fatigue properties of the Ti-6Al-4V ELI alloy with UFG structure were investigated. High strength and enhanced ductility (1370 MPa and 12%) after SPD processing and subsequent annealing at 500 °C; resulted in an enhancement of fatigue limit to 740 MPa after 10^7 cycles in comparison to 600 MPa in the initial coarse-grained condition (Figure 3) [32].

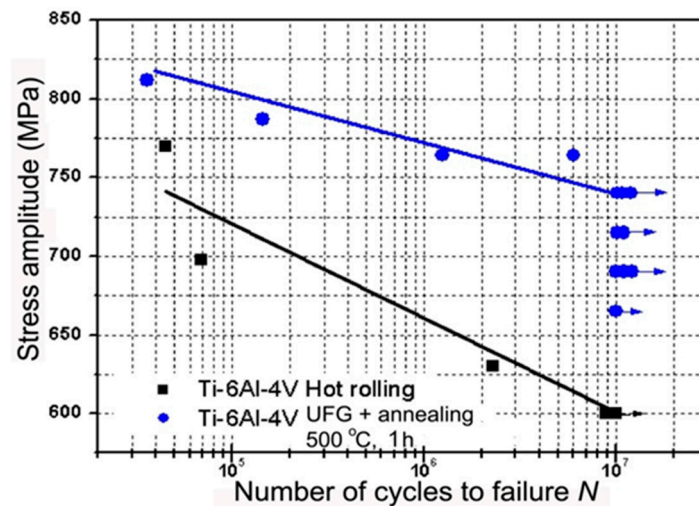


Figure 3. Fatigue test results of initial coarse-grained material and UFG material after annealing at 500 °C, 1 h.

The fatigue limit of the Ti-6Al-4V alloy in UFG condition reported in [32] tested by rotating bending was slightly higher than the values in [32,38] proving that measured fatigue properties depend on the choice of the measurement technique.

Achieved results show that high strength can be achieved in UFG Ti-6Al-4V ELI alloy by processing by ECAP and subsequent thermo-mechanical treatment. Selection of SPD regimes and adjustment of processing parameters of SPD processing such as temperature, strain rate and strain allow us to manipulate the grain boundary structure and phase morphology in the two-phase UFG alloy. As the result, the best combination of strength and ductility can be achieved along with the improved fatigue endurance limit. Enhancement of strength and ductility of the biomedical Ti-6Al-7Nb alloy was reported in another comprehensive study [39]. In comparison to Ti-6Al-4V, the Ti-6Al-7Nb alloy represents a better choice for biomedical use due to avoiding the toxic vanadium [40]. This study shows that processing by ECAP and consequent thermo-mechanical treatment causing formation of UFG structure results in high strength (1400 MPa) and ductility (elongation of 10%). These achieved properties are attractive for designing, developing and manufacturing of high-performance medical devices and implants.

Considering that vanadium and partly also aluminum are rather toxic elements and, simultaneously, that reducing of the Young's modulus is required for avoiding so-called stress-shielding [39], the development of brand new biomedical alloys represents a current relevant challenge for researchers. A new generation of titanium alloys must provide improved strength, better biocompatibility, and lower Young's modulus than Ti6Al4V alloy. Current research focuses on new alloying systems, in particular Ti-Nb and Ti-Mo.

Given the above mentioned requirements, the interest is drawn to titanium alloys containing high content of the β phase, because this phase is characterized by lower Young's modulus in the range of

55–90 GPa, and thus exhibit lower stress shielding [39,41–43]. Moreover, these Ti alloys are designed to contain only non-toxic constituents such as Nb, Mo, Zr, and Ta. On the other hand, these materials are characterized by comparatively low strength, because the lowest Young's modulus is obtained only in solution treated single phase β -Ti alloys. Achieving low Young's modulus and high strength simultaneously is a challenging task. Ageing treatments that induce a fine and uniform precipitation of ω and α phase components provides significant strengthening. On the other hand, this inevitably increases the Young's modulus of the alloy [41–43]. Only few studies present successful results in development of thermal treatments without detrimental effect on some of the relevant mechanical properties [44,45].

Advancements in the areas of orthopedics and dentistry called for new strategies for development of new generation of β -Ti alloys with reduced Young's modulus and high strength, which would be more suitable for such applications. Recently, SPD processing has been proposed to fabricate nanocrystalline β -Ti alloys with high strength, low modulus of elasticity and excellent biocompatibility [46–51]. Nanostructuring of these alloys leads to improved strength due to grain refinement and substructure evolution [52]. In particular, solution treated β -Ti Ti15Mo alloy, which is qualified for medical use, can be significantly refined by HPT as demonstrated in Figure 4a. Grain size can be decreased well below 100 nm [53]. Significant disadvantage, apart from limited size of HPT samples, is formation of deformation induced ω phase causing sharp increase of elastic modulus [54]. Subsequent aging of UFG Ti15Mo alloy leads to two-phase $\alpha + \beta$ structure which is also characterized by increased modulus of elasticity [55–57]. More promising is using Ti-Nb-Ta-Zr based alloys which are less prone to ω phase formation. Ti-29Nb-13Ta-5Zr alloy prepared by HPT exhibited increased yield stress from 550 to 800 MPa with unchanged elastic modulus [58,59]. Significant microstructure refinement was recently also achieved in Ti-35Nb-6Ta-7Zr biomedical alloy by ECAP (Figure 4b).

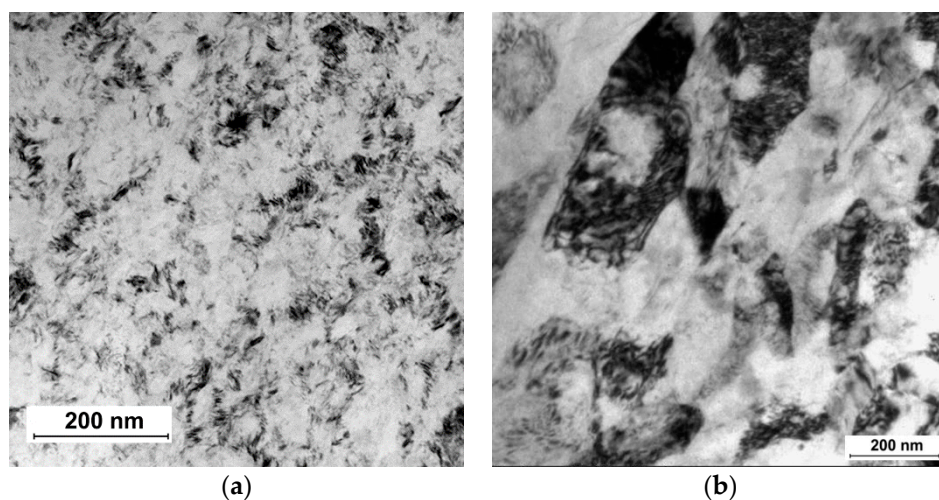


Figure 4. Microstructure of (a) Ti15Mo alloy prepared by HPT and (b) Ti-35Nb-6Ta-7Zr alloy prepared by ECAP (cross-section).

Microstructural refinement in β -Ti alloys can be also enhanced by multiple twinning and/or martensitic transformation $\beta \rightarrow \alpha''$ [60]. The nanocrystalline β -Ti alloys also display excellent *in vitro* biocompatibility as shown by enhanced cell attachment and proliferation [48]. These novel nanocrystalline β -Ti alloys have high chances to meet the challenge of next-generation implant material with significant prospects in load bearing biomedical applications.

2.3. Nanostructured NiTi Shape Memory Alloys

NiTi alloys exhibit unique mechanical behavior—shape memory effect (SME) and superelasticity, which arise from a transformation between martensite and austenite phases [61,62]. NiTi alloys are

important materials which are already used in advanced medical devices due to the above mentioned mechanical properties and, additionally, due to functional properties such as good biocompatibility and corrosion resistance in vivo [61,63]. At the same time, new, advanced applications will require enhanced properties (higher strength, higher recovery strain and stress, etc.) of NiTi shape memory alloys.

During the past two decades, there has been interest in the application of SPD methods to NiTi alloys because the formation of nanocrystalline and UFG structures allows enhancing mechanical and functional properties in comparison to coarse grained materials [63,64].

HPT processing of NiTi alloys leads to a transformation from crystalline to amorphous phase. Microstructural changes in deformed NiTi during thermal treatment are of key interest as they are responsible for the shape memory effect [65,66]. During following thermal treatments nanocrystalline (NC) structure can be obtained in NiTi alloys via crystallization process (Figure 5) [64,67]. Nanocrystalline NiTi alloys with grain size about 20 nm demonstrate very high strength up to 2000 MPa [64].

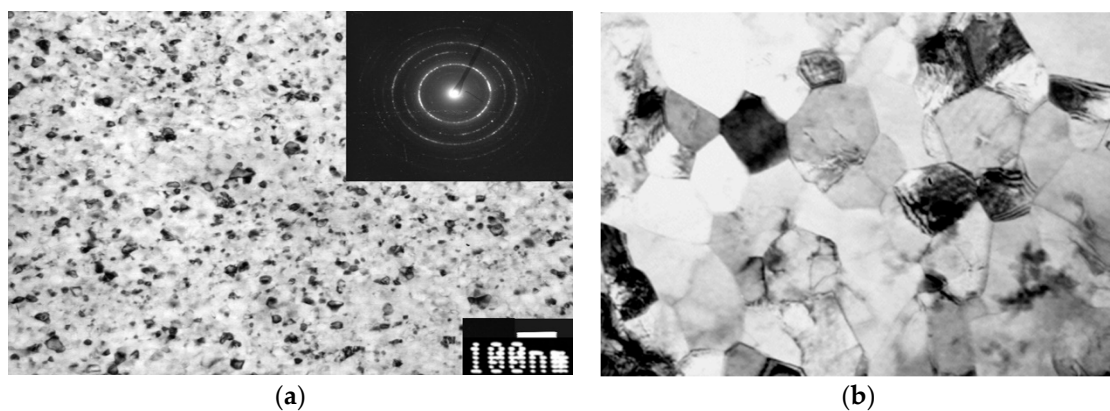


Figure 5. Microstructure of (a) NC and (b) UFG NiTi alloys processed by HPT and ECAP, respectively.

Equal channel angular pressing is another SPD processing technique applied for producing uniform UFG structure in bulk NiTi alloys. The ECAP processing of NiTi at 400–450 °C results in formation of UFG structure with grain size of about 200 nm (Figure 5).

UFG structure formation leads to significant improvement of mechanical and functional properties of NiTi-based alloys [64,68–70]. The ultimate tensile strength (UTS) of UFG NiTi alloy attains 1400 MPa, which is 50% higher than in CG alloys; and the yield stress (YS) increases after ECAP from 500 MPa to 1100 MPa (Figure 6a). The functional shape-memory effect of NiTi after ECAP is also improved (Figure 6b). The maximum completely recoverable strain ϵ_r^{\max} increases from 6% (in CG state) to 9% after ECAP and the maximum recovery stress σ_r^{\max} reaches 1120 MPa, which is twice more than the level of CG alloys (about 500 MPa) [69]. UFG structure formation in Ni-rich NiTi alloys by ECAP results in an emergence of superelasticity at temperature close to the human body temperature. Superelasticity in UFG NiTi is characterized by a narrow mechanical hysteresis and low residual strain [71].

The high-strength NC and UFG NiTi alloys with improved functional characteristics are very promising for medical applications in particular for manufacturing of stents, embolic protection filters, guide wires, and other peripheral vascular devices (see Section 4).

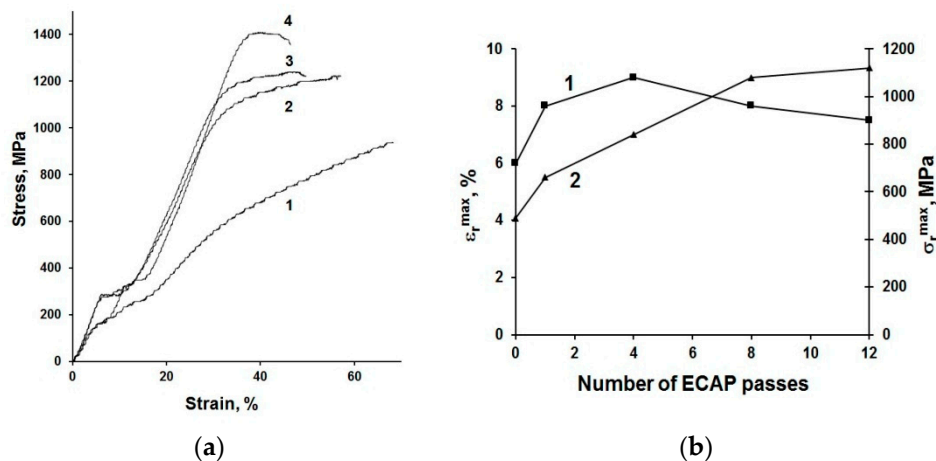


Figure 6. Mechanical properties of NiTi alloy in CG condition and after ECAP. (a) Engineering stress–strain curves for tensile tests in CG state (1) and after ECAP using 4 (2), 8 (3) and 12 (4) passes and (b) functional properties (ϵ_r^{\max} and σ_r^{\max}) as a function of number of ECAP passes [61].

3. Design of Miniaturized Implants

Enhanced mechanical properties of nanostructured metals allow development of medical implants with better design, for instance with a more subtle design which is less harmful for human body [17].

Application of stronger nanostructured CP Ti instead of common CG Ti, allows for altering the design of devices. Recently, detailed computations were conducted to analyze the possible geometries of miniplates for maxillofacial surgery manufactured from nanostructured Ti [72].

CP Ti miniplate specified by ASTM F 67, was considered by Conmet Company (Moscow, Russia) as the benchmark for redesigning the product dimensions of mini-plates manufactured from nanostructured CP Ti. The mechanical properties in a cross-section of a newly designed plate were calculated with the use of estimates of the fatigue performance limit for coarse-grained Grade 4 CP Ti and nanostructured Grade 4 CP Ti. In practical use, the mini-plates are subjected to bending loads, therefore bending strength of mini-plates from conventional and nanostructured CP Ti was compared. The result indicates that the plate from nanostructured Ti has significantly improved bending strength and therefore, it is clearly advantageous over the standard device currently manufactured from CG Ti.

Recently, three-dimensional finite element models (FEM) were developed using CAE software (KOMPAS-3D v15, ASCON Group, Saint Petersburg, Russia) and then imported into ANSYS Workbench 18.2 (ANSYS Inc., Canonsburg, PA, USA) [73] for geometry analysis of nanoTi dental implants. In addition to static strength, calculations of virtual fatigue testing were carried out using the built-in fatigue module. For all tested models, mesh sensitivity testing was performed in order to obtain mesh-independent results.

The following procedure was used to assess possible ways to miniaturize the implants. The device with a standard geometry was assumed to be made from the conventional coarse-grained CP Ti. The model was designed in a way to obtain nearly critical stress state both in terms of static and fatigue failure. Afterwards, the same loading was applied to a model with reduced dimensions but with the properties of nano CP Ti.

A one-stage dental implant with generic geometry was considered in the study. The shape of the implant is similar to the implant geometry produced from nano CP Ti by company Timplant s.r.o. (Ostrava, Czech Republic) [74]. Figure 7 shows a technical drawing of the geometry of this nanoimplant with a corresponding numerical model.

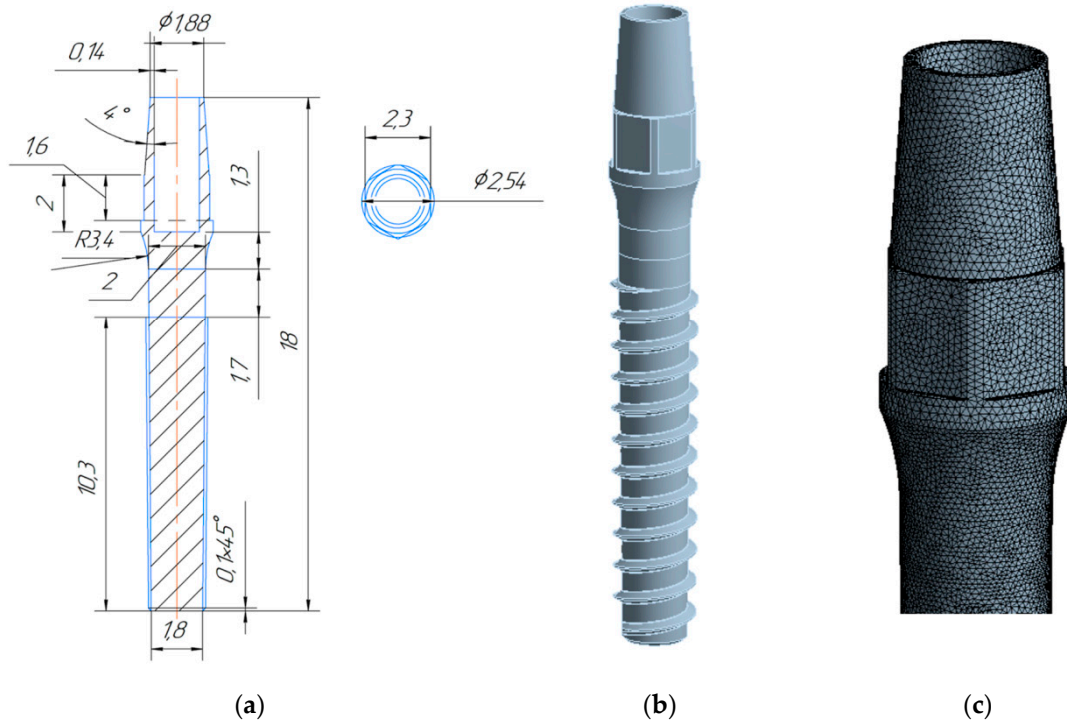


Figure 7. Geometry of the dental nanoimplant: (a) technical drawing with dimensions in mm; (b) 3D model; (c) enlarged FEM mesh.

The applied loading scheme was inspired by the testing procedures used in the ISO 14801 standard. The performed calculations revealed that application of the nanoTi allows reduction of the diameter of implant by at least 10%, while 20% diameter reduction leads to an unacceptable decrease of the device’s fatigue strength. Maximal principal stress zone for the implant with the diameter reduced by 10% loaded with a 67.75 N force is shown in Figure 8.

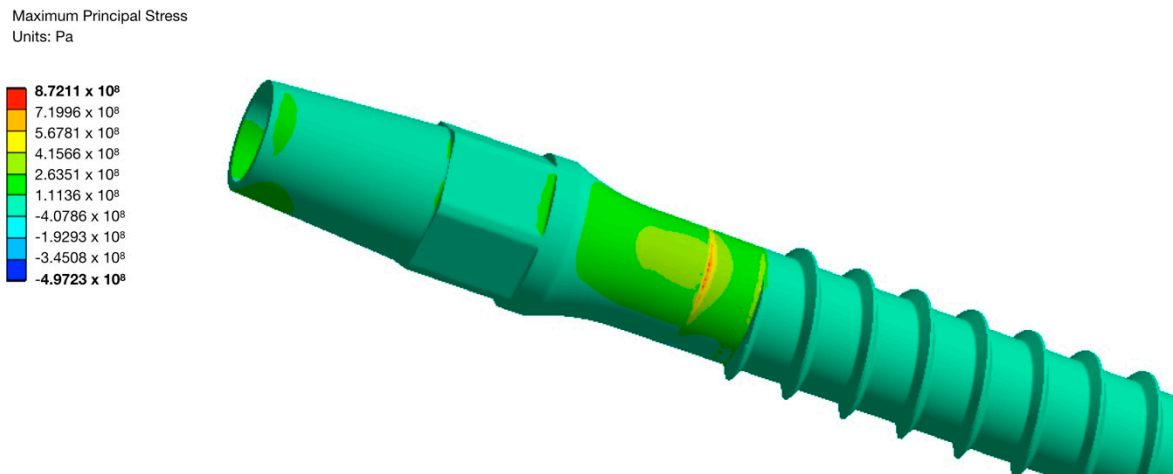


Figure 8. Maximal principal stress for the UFG Ti implant with a 10% reduced diameter and 67.75 N force.

4. Fabrication and Tests of Medical Nanoimplants

Recently, manufacturing and successful testing of several medical implants fabricated from nanostructured Ti have been considered in detail [17]. Another example of the innovative development is the manufacturing and testing of the implant pins designed for surgery in the bone tissue of the hip, which increases bone strength and prevents its fracture (Figure 9) [75]. The pins of two types

(Figure 10) were produced from nanostructured Ti rods of 3 mm diameter with very high strength ($\sigma = 1300$ MPa). These implants were used to study their effect on the bone strength of the hip, which was evaluated by means of bench testing [76]. For this purpose, a special device (Figure 11) was used to analyze the mechanical properties of implant systems under compression along the axis of the hip. Such systems were subjected to a defined load along the axis of the hip, as well as in the perpendicular direction with a force directed to the region of the greater trochanter to complete fracture at a rate of 5 mm/min using the INSTRON 5982 (Instron®, High Wycombe, Buckinghamshire, UK) multipurpose one pin dynamometer. A total of 3 systems were studied: three pins, a spiral, and a spiral + pin system. As a result [76], the use of different implants demonstrated high efficiency in improving the strength of bone tissue in the hip. In particular, the use of a spiral and a pin in the bone-implant system made it possible to increase the axial load resistance by 72.6% in comparison to the tests excluding implants. This demonstrated the prospect of integration of surgical reinforcement of the hip made of nano CP Ti into clinical practice to prevent broken bones.

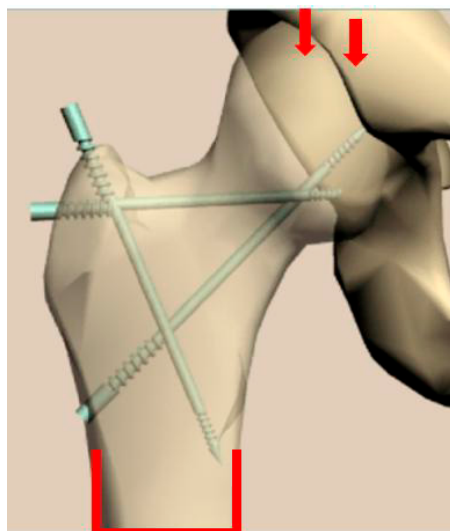


Figure 9. The image of the hip after the insertion of reinforcing implants.

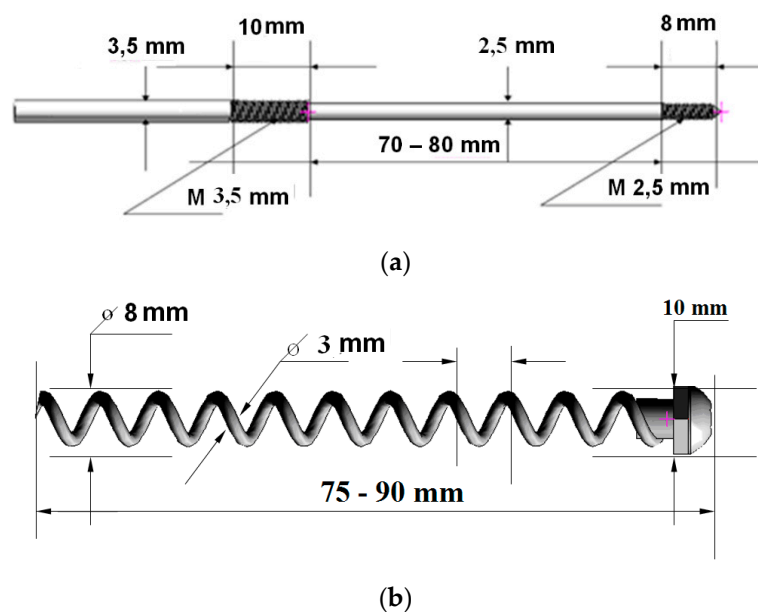


Figure 10. Two types of the implant systems used: ((a) a pin; (b) a spiral) and their application using the INSTRON 5982 dynamometer.

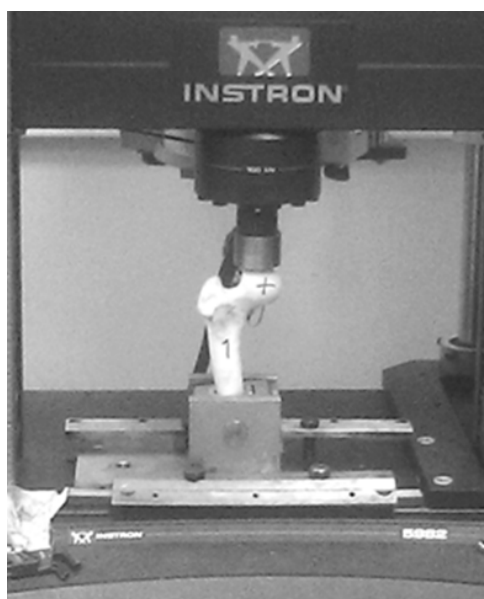


Figure 11. Testing procedure of the reinforced hip sample.

Another interesting example of the innovative application is the removable clipping device for blood vessels, tubular structures, and soft tissues fabricated from UFG NiTi with enhanced shape-memory effect and designed for bleeding control during laparoscopic operations. This device has been created and tested in collaboration between Ufa State Aviation Technical University (USATU) and National University of Science and Technology “MISIS” [24].

The conducted tests demonstrated that the removable clipping devices produced from UFG NiTi alloy obtain several advantages when compared to the standard counterpart. Table 2 provides the most important properties of the clipping device for the UFG and conventional CG alloy. The maximum opening angle of the jaws, at which no residual deformation was observed, increases up to 160°, which is significantly higher than that of benchmark CG alloy. The value of the reversible shape memory effect (up to 4 mm) and the maximum rated force that develops at triggering the clipping device (up to 0.9 N) also doubles in the product from UFG alloys.

Table 2. Service characteristics of the clipping device produced from the NiTi alloys.

Material	Opening Angle of the Jaws, °	Opening of the Jaws at Reversible Shape Memory Effect, mm	Max Rated Force of the Clipping Device, H
CG	<110	2	0.44
UFG	160	4	0.9

Higher completely recoverable strain allows for a more convenient shape of the clipping device to be used for laparoscopy and manipulation; it also helps to reduce the diameter of a laparoscope tube, i.e., to create more comfortable surgery conditions for a doctor and a patient. Due to higher deformation with a reversible shape memory effect, it is possible to improve non-invasiveness when removing the clipping device. Increased maximum recovery stress provides high force that develops at triggering the clipping device, high reliability of tissue crimping and fixation, and also makes it possible to reduce the weight of the clipping device.

5. Conclusions

Recent studies have proven that nanostructuring of titanium materials by means of severe plastic deformation (SPD) techniques achieving grain refinement, increase of dislocation density, dissolution,

and formation of secondary phase precipitations allows for considerable improvement of the strength and fatigue properties. In the present paper the advantages of nanostructuring were demonstrated for CP Ti, Ti alloys including new β -Ti alloys as well as the NiTi alloy with shape memory effect. The approaches to computer design of a number of miniaturized medical implants made from high-strength nanomaterials have been suggested. In addition, the paper includes the examples of manufacturing and tests of selected advanced medical devices for traumatology and surgery from Ti nanobiomaterials. Taking into account the results of recent studies on surface modification, including chemical etching of nanometals and deposition of bioactive coatings, it is assumed that the developments of Ti-based nanomaterials opens new possibilities for advanced medical implants and devices with improved design and functionality.

Author Contributions: R.Z.V. introduced the concept and contents of the present paper, together with co-authors conducted the analysis and description of the resulting data. E.A.P. prepared the results of studies on the structure and properties of UFG TiNi alloy with shape memory effect. N.A.K. provided the results of the design of miniaturized implants (Section 3). G.I.R. provided the description of SPD techniques for processing CP Ti and Ti alloys to produce UFG structure. T.B.M. introduced the original data on manufacturing and testing of the implant pins designed for surgery in the bone tissue of the hip. J.S. reviewed the results of studies on biomedical Ti alloys subjected to SPD processing. All authors have read and agreed to the published version of the manuscript.

Funding: This research was funded by Russian Science Foundation grant № 19-49-02003 and by Ministry of Education, Youth and Sports of the Czech Republic (project №LTARF18010). The authors gratefully acknowledge the financial support from Saint Petersburg State University in the framework of Call 3 project (id 26130576 for R.Z.V., E.A.P. and N.A.K.). This work was also financially by Ministry of Industry and Trade of the Czech Republic (project № FV20147).

Conflicts of Interest: The authors declare no conflict of interest.

References

1. Hanawa, T. Overview of metals and applications. In *Metals for Biomedical Devices*; Elsevier BV: Amsterdam, The Netherlands, 2010; pp. 3–24.
2. Froes, F.H.; Qian, M. *Titanium in Medical and Dental Applications*, 1st ed.; Woodhead Publishing: Duxford, UK, 2018.
3. Valiev, R.; Islamgaliev, R.; Alexandrov, I. Bulk nanostructured materials from severe plastic deformation. *Prog. Mater. Sci.* **2000**, *45*, 103–189. [[CrossRef](#)]
4. Valiev, R.Z.; Estrin, Y.; Horita, Z.; Langdon, T.G.; Zehetbauer, M.J.; Zhu, Y.T. Producing bulk ultrafine-grained materials by severe plastic deformation: Ten years later. *JOM* **2016**, *68*, 1216–1226. [[CrossRef](#)]
5. Valiev, R.Z.; Estrin, Y.; Horita, Z.; Langdon, T.G.; Zehetbauer, M.J.; Zhu, Y.T. Fundamentals of superior properties in bulk nanoSPD materials. *Mater. Res. Lett.* **2016**, *4*, 1–21. [[CrossRef](#)]
6. Whang, S.H. *Nanostructured Metals and Alloys: Processing, Microstructure, Mechanical Properties and Applications*, 1st ed.; Woodhead Publishing Limited: Cambridge, UK, 2011.
7. Rosochowski, A. *Severe Plastic Deformation Technology*; Whittles Publishing: Scotland, UK, 2017.
8. Estrin, Y.; Vinogradov, A. Extreme grain refinement by severe plastic deformation: A wealth of challenging science. *Acta Mater.* **2013**, *61*, 782–817. [[CrossRef](#)]
9. Valiev, R.Z.; Langdon, T.G. Principles of equal-channel angular pressing as a processing tool for grain refinement. *Prog. Mater. Sci.* **2006**, *51*, 881–981. [[CrossRef](#)]
10. Rack, H.J.; Qazi, J.; Allard, L.; Valiev, R.Z. Thermal Stability of Severe Plastically Deformed VT-6 (Ti-6Al-4V). *Mater. Sci. Forum* **2008**, *584*, 893–898. [[CrossRef](#)]
11. Takizawa, Y.; Masuda, T.; Fujimitsu, K.; Kajita, T.; Watanabe, K.; Yumoto, M.; Otagiri, Y.; Horita, Z. Scaling up of High-Pressure Sliding (HPS) for Grain Refinement and Superplasticity. *Met. Mater. Trans. A* **2016**, *47*, 4669–4681. [[CrossRef](#)]
12. Fakhretdinova, E.I.; Raab, G.I.; Valiev, R.Z. Modeling of Metal Flow during Processing by Multi-ECAP-Conform. *Adv. Eng. Mater.* **2015**, *17*, 1723–1727. [[CrossRef](#)]
13. Valiev, R.Z. Nanostructuring of metals by severe plastic deformation for advanced properties. *Nat. Mater.* **2004**, *3*, 511–516. [[CrossRef](#)]

14. Polyakova, V.; Semenova, I.; Valiev, R. Influence of annealing on the structure and mechanical properties of ultrafine-grained alloy Ti-6Al-7Nb, processed by severe plastic deformation. *Mater. Sci. Forum* **2011**, *667–669*, 943–948. [[CrossRef](#)]
15. Semenova, I.; Yakushina, E.; Nurgaleeva, V.; Valiev, R. Nanostructuring of Ti-alloys by SPD processing to achieve superior fatigue properties. *Int. J. Mat. Res.* **2009**, *100*, 1691–1696. [[CrossRef](#)]
16. Lowe, T.C.; Valiev, R.Z. Frontiers of bulk nanostructured metals in biomedical applications. In *Advanced Biomaterials and Biodevices*; Tiwari, A., Nordin, A.N., Eds.; Wiley-Scrivener Publ.: Beverly, MA, USA, 2014; pp. 3–52.
17. Valiev, R.Z.; Sabirov, I.; Zemtsova, E.G.; Parfenov, E.V.; Dluhoš, L.; Lowe, T.C. Nanostructured pure Ti for development of miniturized biomedical implants. In *Titanium in Medical and Dental Applications*; Froes, F., Qian, M., Eds.; Woodhead Publishing: Duxford, UK, 2018; pp. 393–418.
18. Zemtsova, E.; Arbenin, A.; Valiev, R.Z.; Smirnov, V.M. Modern techniques of surface geometry modification for the implants based on titanium and its alloys used for improvement of the biomedical characteristics. In *Titanium in Medical and Dental Applications*; Elsevier BV: Amsterdam, The Netherlands, 2018; pp. 115–145.
19. Valiev, R.Z.; Semenova, I.P.; Latysh, V.V.; Rack, H.; Lowe, T.C.; Petruzalka, J.; Dluhos, L.; Hrusak, D.; Sochova, J. Nanostructured Titanium for Biomedical Applications. *Adv. Eng. Mater.* **2008**, *10*, B15–B17. [[CrossRef](#)]
20. Estrin, Y.; Lapovok, R.; Medvedev, A.E.; Kasper, C.; Ivanová, E.; Lowe, T.C. Mechanical performance and cell response of pure titanium with ultrafine-grained structure produced by severe plastic deformation. In *Titanium in Medical and Dental Applications*; Elsevier BV: Amsterdam, The Netherlands, 2018; pp. 419–454.
21. Dyakonov, G.; Mironov, S.; Semenova, I.P.; Valiev, R.Z.; Semiatin, S.L. Microstructure evolution and strengthening mechanisms in commercial-purity titanium subjected to equal-channel angular pressing. *Mater. Sci. Eng. A* **2017**, *701*, 289–301. [[CrossRef](#)]
22. Brunette, D.M.; Tengvall, P.; Textor, M.; Thomsen, P. *Titanium in Medicine*; Springer-Verlag: Berlin/Heidelberg, Germany, 2003.
23. Gunderov, D.; Polyakov, A.; Semenova, I.; Raab, G.; Churakova, A.; Gimaltdinova, E.; Sabirov, I.; Segurado, J.; Sitdikov, V.; Alexandrov, I.; et al. Evolution of microstructure, macrotexture and mechanical properties of commercially pure Ti during ECAP-conform processing and drawing. *Mater. Sci. Eng. A* **2013**, *562*, 128–136. [[CrossRef](#)]
24. Mishnaevsky, L.; Levashov, E.; Valiev, R.Z.; Segurado, J.; Sabirov, I.; Enikeev, N.; Prokoshkin, S.; Solov'Yov, A.V.; Korotitskiy, A.; Gutmanas, E.; et al. Nanostructured titanium-based materials for medical implants: Modeling and development. *Mater. Sci. Eng. R Rep.* **2014**, *81*, 1–19. [[CrossRef](#)]
25. Boyer, R.; Welsch, G.; Collings, E. *Materials Properties Handbook: Titanium Alloys*; ASM International: Materials Park, OH, USA, 1998.
26. Petruželka, J.; Dluhoš, L.; Hrušák, D.; Sochová, J. Nanostructured titanium - application in dental implants. *Trans. VSB Tech. Univ. Ostrava* **2006**, *52*, 177–186.
27. Faghihi, S.; Azari, F.; Zhilyaev, A.; Szpunar, J.; Vali, H.; Tabrizian, M. Cellular and molecular interactions between MC3T3-E1 pre-osteoblasts and nanostructured titanium produced by high-pressure torsion. *Biomater.* **2007**, *28*, 3887–3895. [[CrossRef](#)]
28. Estrin, Y.; Ivanova, E.P.; Michalska, A.; Truong, V.K.; Lapovok, R.; Boyd, R. Accelerated stem cell attachment to ultrafine grained titanium. *Acta Biomater.* **2011**, *7*, 900–906. [[CrossRef](#)]
29. Nie, F.L.; Zheng, Y.F.; Wei, S.C.; Wang, D.S.; Yu, Z.T.; Salimgareeva, G.K.; Polyakov, A.V.; Valiev, R.Z. In vitro and in vivo studies on nanocrystalline Ti fabricated by equal channel angular pressing with microcrystalline CP Ti as control. *J. Biomed. Mater. Res. – Part A* **2013**, *101A*, 1694–1707. [[CrossRef](#)]
30. Geetha, M.; Singh, A.; Asokamani, R.; Gogia, A. Ti based biomaterials, the ultimate choice for orthopaedic implants – A review. *Prog. Mater. Sci.* **2009**, *54*, 397–425. [[CrossRef](#)]
31. Nakai, M.; Niinomi, M.; Akahori, T.; Ohtsu, N.; Nishimura, H.; Toda, H.; Fukui, H.; Ogawa, M. Surface hardening of biomedical Ti-29Nb-13Ta-4.6Zr and Ti-6Al-4V ELI by gas nitriding. *Mater. Sci. Eng. A* **2008**, *486*, 193–201. [[CrossRef](#)]
32. Saitova, L.; Höppel, H.W.; Göken, M.; Semenova, I.; Valiev, R. Cyclic deformation behavior and fatigue lives of ultrafine-grained Ti-6Al-4V ELI alloy for medical use. *Int. J. Fatigue* **2009**, *31*, 322–331. [[CrossRef](#)]

33. Semenova, I.P.; Saitova, L.R.; Raab, G.I.; Korshunov, A.I.; Zhu, Y.T.; Lowe, T.C.; Valiev, R.Z. Microstructural features and mechanical properties of the Ti-6Al-4V ELI alloy processed by severe plastic deformation. *Mater. Sci. Forum* **2006**, *503–504*, 757–762. [[CrossRef](#)]
34. Valiev, R.Z.; Zhilyaev, A.P.; Langdon, T.G. *Bulk Nanostructured Materials: Fundamentals and Applications*; John Wiley & Sons: Hoboken, NJ, USA, 2014.
35. Hoseini, M.; Pourian, M.H.; Bridier, F.; Vali, H.; Szpunar, J.A.; Bocher, P. Thermal stability and annealing behaviour of ultrafine grained commercially pure titanium. *Mater. Sci. Eng. A* **2012**, *532*, 58–63. [[CrossRef](#)]
36. Zháňal, P.; Václavová, K.; Hadzima, B.; Harcuba, P.; Stráský, J.; Janeček, M.; Polyakova, V.; Semenova, I.P.; Hájek, M.; Hajizadeh, K. Thermal stability of ultrafine-grained commercial purity Ti and Ti-6Al-7Nb alloy investigated by electrical resistance, microhardness and scanning electron microscopy. *Mater. Sci. Eng. A* **2016**, *651*, 886–892.
37. Bartha, K.; Zháňal, P.; Stráský, J.; Čížek, J.; Dopita, M.; Lukáč, F.; Harcuba, P.; Hájek, M.; Polyakova, V.; Semenova, I.P.; et al. Lattice defects in severely deformed biomedical Ti-6Al-7Nb alloy and thermal stability of its ultra-fine grained microstructure. *J. Alloys Compd.* **2019**, *788*, 881–890. [[CrossRef](#)]
38. Zherebtsov, S.; Salishchev, G.; Galejev, R.; Maekawa, K. Mechanical Properties of Ti-6Al-4V Titanium Alloy with Submicrocrystalline Structure Produced by Severe Plastic Deformation. *Mater. Trans.* **2005**, *46*, 2020–2025.
39. Niinomi, M. Mechanical biocompatibilities of titanium alloys for biomedical applications. *J. Mech. Behav. Biomed. Mater.* **2008**, *1*, 30–42.
40. Steinemann, S.G. Titanium—The material of choice? *Periodontology 2000* **1998**, *17*, 7–21.
41. Raabe, D.; Sander, B.; Friák, M.; Ma, D.; Neugebauer, J. Theory-guided bottom-up design of β -titanium alloys as biomaterials based on first principles calculations: Theory and experiments. *Acta Mater.* **2007**, *55*, 4475–4487. [[CrossRef](#)]
42. Hou, F.; Li, S.; Hao, Y.; Yang, R. Nonlinear elastic deformation behaviour of Ti-30Nb-12Zr alloys. *Scr. Mater.* **2010**, *63*, 54–57. [[CrossRef](#)]
43. Niinomi, M.; Nakai, M.; Hieda, J. Development of new metallic alloys for biomedical applications. *Acta Biomater.* **2012**, *8*, 3888–3903. [[CrossRef](#)] [[PubMed](#)]
44. Sun, F.; Zhang, J.Y.; Vermaut, P.; Choudhuri, D.; Alam, T.; Mantri, S.A.; Svec, P.; Gloriant, T.; Jacques, P.J.; Banerjee, R.; et al. Strengthening strategy for a ductile metastable β -titanium alloy using low-temperature aging. *Mater. Res. Lett.* **2017**, *5*, 547–553. [[CrossRef](#)]
45. Najdahmadi, A.; Zarei-Hanzaki, A.; Farghadani, E. Mechanical properties enhancement in Ti-29Nb-13Ta-4.6Zr alloy via heat treatment with no detrimental effect on its biocompatibility. *Mater. Des.* **2014**, *54*, 786–791. [[CrossRef](#)]
46. Xu, W.; Wu, X.; Figueiredo, R.B.; Stoica, M.; Calin, M.; Eckert, J.; Langdon, T.G.; Xia, K. Nanocrystalline body-centred cubic beta-titanium alloy processed by high-pressure torsion. *Int. J. Mater. Res.* **2009**, *100*, 1662–1667. [[CrossRef](#)]
47. Zafari, A.; Wei, X.; Xu, W.; Xia, K. Formation of nanocrystalline β structure in metastable beta Ti alloy during high pressure torsion: The role played by stress induced martensitic transformation. *Acta Mater.* **2015**, *97*, 146–155. [[CrossRef](#)]
48. Xu, W.; Wu, X.; Calin, M.; Stoica, M.; Eckert, J.; Xia, K. Formation of an ultrafine-grained structure during equal-channel angular pressing of a β -titanium alloy with low phase stability. *Scr. Mater.* **2009**, *60*, 1012–1015. [[CrossRef](#)]
49. Polyakov, A.V.; Semenova, I.P.; Ivanov, E.; Valiev, R.Z. Ultra-fine grained β -type TNZT ELI alloy with high strength and low elastic modulus. *IOP Conf. Ser.: Mater. Sci. Eng* **2019**, *461*, 012077. [[CrossRef](#)]
50. Xie, K.; Wang, Y.-B.; Zhao, Y.; Chang, L.; Wang, G.; Chen, Z.; Cao, Y.; Liao, X.; Lavernia, E.J.; Valiev, R.Z.; et al. Nanocrystalline β -Ti alloy with high hardness, low Young's modulus and excellent in vitro biocompatibility for biomedical applications. *Mater. Sci. Eng. C* **2013**, *33*, 3530–3536. [[CrossRef](#)]
51. Stráský, J.; Janeček, M.; Semenova, I.; Čížek, J.; Bartha, K.; Harcuba, P.; Polyakova, V.; Gatina, S. Microstructure and lattice defects in ultrafine grained biomedical $\alpha+\beta$ and metastable β Ti alloys. In *Titanium in Medical and Dental Applications*; Froes, F., Qian, M., Eds.; Woodhead Publishing: Duxford, UK, 2018; pp. 455–475.
52. Valiev, R.Z. Superior Strength in Ultrafine-Grained Materials Produced by SPD Processing. *Mater. Trans.* **2014**, *55*, 13–18. [[CrossRef](#)]

53. Janeček, M.; Čížek, J.; Stráský, J.; Bartha, K.; Hruška, P.; Polyakova, V.; Gatina, S.; Semenova, I. Microstructure evolution in solution treated Ti15Mo alloy processed by high pressure torsion. *Mater. Charact.* **2014**, *98*, 233–240. [[CrossRef](#)]
54. Bartha, K.; Stráský, J.; Polyakova, V.; Stráská, J.; Nejezchlebová, J.; Seiner, H.; Semenova, I.; Janeček, M. Microhardness and microstructure evolution of ultra-fine grained Ti-15Mo and TIMETAL LCB alloys prepared by high pressure torsion. *Mater. Sci. Eng. A* **2017**, *682*, 220–228.
55. Gatina, S.; Semenova, I.; Janeček, M.; Stráský, J. Effect of high pressure torsion on the aging kinetics of β -titanium Ti-15Mo alloy. *IOP Conf. Series: Mater. Sci. Eng.* **2014**, *63*, 012068. [[CrossRef](#)]
56. Bartha, K.; Stráský, J.; Veverková, A.; Barriobero-Vila, P.; Lukáč, F.; Doležal, P.; Sedlák, P.; Polyakova, V.; Semenova, I.P.; Janeček, M. Effect of the High-Pressure Torsion (HPT) and Subsequent Isothermal Annealing on the Phase Transformation in Biomedical Ti15Mo Alloy. *Metals* **2019**, *9*, 1194. [[CrossRef](#)]
57. Bartha, K.; Veverková, A.; Stráský, J.; Veselý, J.; Minárik, P.; Correa, C.; Polyakova, V.; Semenova, I.; Janeček, M. Effect of the severe plastic deformation by ECAP on microstructure and phase transformations in Ti-15Mo alloy. *Mater. Today Commun.* **2020**, *22*, 100811. [[CrossRef](#)]
58. Yilmazer, H.; Niinomi, M.; Nakai, M.; Hieda, J.; Todaka, Y.; Akahori, T.; Miyazaki, T. Heterogeneous structure and mechanical hardness of biomedical α -type Ti-29Nb-13Ta-4.6Zr subjected to high-pressure torsion. *J. Mech. Behav. Biomed. Mater.* **2012**, *10*, 235–245. [[CrossRef](#)]
59. Yilmazer, H.; Niinomi, M.; Nakai, M.; Cho, K.; Hieda, J.; Todaka, Y.; Miyazaki, T. Mechanical properties of a medical β -type titanium alloy with specific microstructural evolution through high-pressure torsion. *Mater. Sci. Eng. C* **2013**, *33*, 2499–2507. [[CrossRef](#)]
60. Lin, Z.; Wang, L.; Xue, X.; Lu, W.; Qin, J.; Zhang, D. Microstructure evolution and mechanical properties of a Ti-35Nb-3Zr-2Ta biomedical alloy processed by equal channel angular pressing (ECAP). *Mater. Sci. Eng. C* **2013**, *33*, 4551–4561. [[CrossRef](#)]
61. Otsuka, K.; Ren, X. Physical metallurgy of Ti-Ni-based shape memory alloys. *Prog. Mater. Sci.* **2005**, *50*, 511–678. [[CrossRef](#)]
62. Brailovski, V.; Prokoshkin, S.; Terriault, P.; Trochu, F. *Shape Memory Alloys: Fundamentals, Modeling and Applications*; École de technologie supérieure (ETS): Montreal, QC, Canada, 2003; p. 851.
63. Pushin, V.G.; Stolyarov, V.V.; Valiev, R.Z.; Kourov, N.I.; Kuranova, N.N.; Prokofiev, E.A.; Yurchenko, L.I. Features of structure and phase transformation in shape memory TiNi-based alloys after severe plastic deformation. *Ann. Chim. Sci. Mater.* **2002**, *27*, 77–88. [[CrossRef](#)]
64. Valiev, R.; Gunderov, D.; Prokofiev, E.; Pushin, V.; Zhu, Y. Nanostructuring of TiNi alloy by SPD processing for advanced properties. *Mater. Trans.* **2008**, *49*, 97–101. [[CrossRef](#)]
65. Malard, B.; Pilch, J.; Sittner, P.; Delville, R.; Curfs, C. In situ investigation of the fast microstructure evolution during electropulse treatment of cold drawn NiTi wires. *Acta Mater.* **2011**, *59*, 1542–1556. [[CrossRef](#)]
66. Burow, J.; Frenzel, J.; Somsen, C.; Prokofiev, E.; Valiev, R.; Eggeler, G. Grain Nucleation and Growth in Deformed NiTi Shape Memory Alloys: An In Situ TEM Study. *Shape Mem. Superelasticity* **2017**, *3*, 347–360. [[CrossRef](#)]
67. Waitz, T.; Kazykhanov, V.; Karnthaler, H. Martensitic phase transformations in nanocrystalline NiTi studied by TEM. *Acta Mater.* **2004**, *52*, 137–147. [[CrossRef](#)]
68. Prokoshkin, S.D.; Khmelevskaya, I.; Dobatkin, S.; Trubitsyna, I.; Tatyannin, E.; Stolyarov, V.; Prokofiev, E. Alloy composition, deformation temperature, pressure and post-deformation annealing effects in severely deformed Ti-Ni based shape memory alloys. *Acta Mater.* **2005**, *53*, 2703–2714. [[CrossRef](#)]
69. Stolyarov, V.V.; Prokofiev, E.A.; Prokoshkin, S.D.; Dobatkin, S.V.; Trubitsyna, I.B.; Khmelevskaya, I.Y.; Pushin, V.G.; Valiev, R.Z. Structural features, mechanical properties, and the shape-memory effect in TiNi alloys subjected to equal-channel angular pressing. *Phys. Met. Metall.* **2005**, *100*, 608–618.
70. Tong, Y.; Guo, B.; Chen, F.; Tian, B.; Li, L.; Zheng, Y.; Prokofiev, E.; Gunderov, D.V.; Valiev, R.Z. Thermal cycling stability of ultrafine-grained TiNi shape memory alloys processed by equal channel angular pressing. *Scr. Mater.* **2012**, *67*, 1–4. [[CrossRef](#)]
71. Prokofiev, E.; Burow, J.; Frenzel, J.; Gunderov, D.; Eggeler, G.; Valiev, R. Phase transformations and functional properties of NiTi alloy with ultrafine-grained structure. *Mater. Sci. Forum* **2011**, *667–669*, 1059–1064. [[CrossRef](#)]
72. Semenova, I.P.; Klevtsov, G.V.; Klevtsova, N.A.; Dyakonov, G.; Matchin, A.A.; Valiev, R.Z. Nanostructured Titanium for Maxillofacial Mini-Implants. *Adv. Eng. Mater.* **2016**, *18*, 1216–1224. [[CrossRef](#)]

73. ANSYS Workbench. Available online: <https://cae-expert.ru/product/ansys-workbench> (accessed on 24 October 2019).
74. Timplant ®-Dental Implants. Available online: <http://www.timplant.cz/en/> (accessed on 24 October 2019).
75. Minasov, T.B.; Bakusov, L.M.; Nasyrov, R.V. *Intratissular Tension in the Segments of the Musculoskeletal System*; LAP LAMBERT Acad. Publ.: Saarbrucken, Germany, 2012.
76. Minasov, T.B.; Minasov, B.S. The effectiveness of combined therapy of postmenopausal osteoporosis using dual-action medicine. *Traumatol. Orthop.* **2011**, *4*, 92–94.



© 2020 by the authors. Licensee MDPI, Basel, Switzerland. This article is an open access article distributed under the terms and conditions of the Creative Commons Attribution (CC BY) license (<http://creativecommons.org/licenses/by/4.0/>).